

Advances in Science, Technology & Innovation  
IEREK Interdisciplinary Series for Sustainable Development

Haytham El Atfy · Bandar I. Ghassal  
*Editors*

# Advances in Petroleum Source Rock Characterizations: Integrated Methods and Case Studies

A Multidisciplinary Source Rock Approach



---

# Advances in Science, Technology & Innovation

## IEREK Interdisciplinary Series for Sustainable Development

### Editorial Board

Anna Laura Pisello, Department of Engineering, University of Perugia, Italy

Dean Hawkes, University of Cambridge, Cambridge, UK

Hocine Bougdah, University for the Creative Arts, Farnham, UK

Federica Rosso, Sapienza University of Rome, Rome, Italy

Hassan Abdalla, University of East London, London, UK

Sofia-Natalia Boemi, Aristotle University of Thessaloniki, Greece

Nabil Mohareb, Faculty of Architecture—Design and Built Environment,  
Beirut Arab University, Beirut, Lebanon

Saleh Mesbah Elkaffas, Arab Academy for Science, Technology & Maritime Transport, Egypt

Emmanuel Bozonnet, University of la Rochelle, La Rochelle, France

Gloria Pignatta, University of Perugia, Italy

Yasser Mahgoub, Qatar University, Qatar

Luciano De Bonis, University of Molise, Italy

Stella Kostopoulou, Regional and Tourism Development, University of Thessaloniki,  
Thessaloniki, Greece

Biswajeet Pradhan, Faculty of Engineering and IT, University of Technology Sydney,  
Sydney, Australia

Md. Abdul Mannan, Universiti Malaysia Sarawak, Malaysia

Chaham Alalouch, Sultan Qaboos University, Muscat, Oman

Iman O. Gawad, Helwan University, Egypt

Anand Nayyar , Graduate School, Duy Tan University, Da Nang, Vietnam

### Series Editor

Mourad Amer, International Experts for Research Enrichment and Knowledge Exchange  
(IEREK), Cairo, Egypt

**Advances in Science, Technology & Innovation (ASTI)** is a series of peer-reviewed books based on important emerging research that redefines the current disciplinary boundaries in science, technology and innovation (STI) in order to develop integrated concepts for sustainable development. It not only discusses the progress made towards securing more resources, allocating smarter solutions, and rebalancing the relationship between nature and people, but also provides in-depth insights from comprehensive research that addresses the **17 sustainable development goals (SDGs)** as set out by the UN for 2030.

The series draws on the best research papers from various IEREK and other international conferences to promote the creation and development of viable solutions for a **sustainable future and a positive societal** transformation with the help of integrated and innovative science-based approaches. Including interdisciplinary contributions, it presents innovative approaches and highlights how they can best support both economic and sustainable development, through better use of data, more effective institutions, and global, local and individual action, for the welfare of all societies.

The series particularly features conceptual and empirical contributions from various interrelated fields of science, technology and innovation, with an emphasis on digital transformation, that focus on providing practical solutions to **ensure food, water and energy security to achieve the SDGs**. It also presents new case studies offering concrete examples of how to resolve sustainable urbanization and environmental issues in different regions of the world.

The series is intended for professionals in research and teaching, consultancies and industry, and government and international organizations. Published in collaboration with IEREK, the Springer ASTI series will acquaint readers with essential new studies in STI for sustainable development.

**ASTI series has now been accepted for Scopus (September 2020). All content published in this series will start appearing on the Scopus site in early 2021.**

---

Haytham El Atfy • Bandar I. Ghassal  
Editors

Advances in Petroleum  
Source Rock  
Characterizations: Integrated  
Methods and Case Studies

A Multidisciplinary Source Rock Approach

*Editors*

Haytham El Atfy  
Department of Geology  
Faculty of Science  
Mansoura University  
Mansoura, Egypt

Bandar I. Ghassal  
EXPEC Advanced Research Center  
Saudi Aramco  
Dhahran, Saudi Arabia

Research Fellow of the Alexander  
von Humboldt Foundation  
University of Tübingen  
Germany

ISSN 2522-8714                      ISSN 2522-8722 (electronic)  
Advances in Science, Technology & Innovation  
IEREK Interdisciplinary Series for Sustainable Development  
ISBN 978-3-031-16395-1              ISBN 978-3-031-16396-8 (eBook)  
<https://doi.org/10.1007/978-3-031-16396-8>

© The Editor(s) (if applicable) and The Author(s), under exclusive license to Springer Nature  
Switzerland AG 2023

This work is subject to copyright. All rights are solely and exclusively licensed by the Publisher, whether the whole or part of the material is concerned, specifically the rights of translation, reprinting, reuse of illustrations, recitation, broadcasting, reproduction on microfilms or in any other physical way, and transmission or information storage and retrieval, electronic adaptation, computer software, or by similar or dissimilar methodology now known or hereafter developed.

The use of general descriptive names, registered names, trademarks, service marks, etc. in this publication does not imply, even in the absence of a specific statement, that such names are exempt from the relevant protective laws and regulations and therefore free for general use.

The publisher, the authors, and the editors are safe to assume that the advice and information in this book are believed to be true and accurate at the date of publication. Neither the publisher nor the authors or the editors give a warranty, expressed or implied, with respect to the material contained herein or for any errors or omissions that may have been made. The publisher remains neutral with regard to jurisdictional claims in published maps and institutional affiliations.

This Springer imprint is published by the registered company Springer Nature Switzerland AG  
The registered company address is: Gewerbestrasse 11, 6330 Cham, Switzerland

*Dedicated to my mother's soul to whom I owe everything*

*Haytham El Atfy*

*Dedicated to my mother's and father's souls who I wished they are here to see  
this book*

*Bandar I. Ghassal*

---

## Preface

The rapid increase in unconventional resources around the world has promoted several technologies and research trends to assess potential source rocks by efficiently utilizing integrated methods. Most of this work in the last 20 years has been disseminated in numerous journals and conference papers. Thus, we thought of this book with several invited geoscientists from around the world to have a consolidated publication that discusses the recent technological advancements, as well as recent and multidisciplinary case studies.

The book comes in three parts. Chapter “[Sedimentary Organic Matter: Origin, Productivity, Preservation and Role in Source-Rock Development](#)” discusses and provides an extensive overview of source rock formation mechanisms and how this affects the generated hydrocarbons later on upon maturation. The second part discusses select advancements in source rock characterization methods, which comprises chapter “[Practical Guide for Petroleum Source Rock Interpretation](#)” to “[Effective Source-Rock Evaluation Strategies for the Identification of Profitable Plays in the Permian Basin, USA](#)”. Chapter “[Practical Guide for Petroleum Source Rock Interpretation](#)” provides a detailed overview of source rock sampling and assessment techniques covering wide spectra including classical and recent advanced technologies and interpretation methods. Chapter “[Maturity Determination of Contaminated Source Rocks by Pyrolysis and Thermal Oxidation Methods: A Review](#)” introduces a novel thermal maturity parameter that replaces the conventional  $T_{\max}$  pyrolysis parameter. Chapter “[Source Rocks Forward Modelling: Significance and Approach](#)” discusses a new method of source rock stratigraphic modeling in marine environments. Chapter “[Optical Kerogen Analysis](#)” presents several optical methods of source rock and kerogen analysis. Chapter “[Effective Source-Rock Evaluation Strategies for the Identification of Profitable Plays in the Permian Basin, USA](#)” discusses new strategies for source rock evaluation on a regional scale. The last part of the book includes multidisciplinary case studies covering several basins from the USA, Libya, Egypt, Southwest Africa, Iraq, Pakistan, and China.

We very much appreciate the effort and contributions of the 39 authors in this book, as well as all of the technical reviewers who gave their time to improve the quality of the book.

Mansoura, Egypt  
Dhahran, Saudi Arabia

Haytham El Atfy  
Bandar I. Ghassal

---

## Acknowledgments

The editors gratefully appreciate fruitful discussions and comments from all reviewers (arranged in alphabetical order) whose careful, constructive, and perceptive critical comments greatly improved the chapters of this book: Esam Abd El-Gawad, Rania Abu-Ali, Mohammed Abu Al Reesh, Mohamed A. Ahmed, Khaled Arouri, Ibrahim Atwah, Samer Bou Daher, Salah Y. El Beialy, Waleed Sh. El Diasty, Mohamed M. El Nady, Moataz El-Shafeiy, Maher I. El-Soughier, Annette Götz, Henry Halpern, Mohamed I. Ibrahim, Ahmed Mansour, Feng Lu, Sebastian Lüning, Maria-Fernanda Romero-Sarmiento, Sedat Inan, and Rainer Zuhlke. Technical support from Springer as well as IEREK, especially Dr. Nabil Khelifi, Toka Amer, and Nareshkumar Mani, is highly appreciated.

Haytham El Atfy is greatly indebted to the Alexander von Humboldt Foundation for their funding and continuous support as Research Fellow at the University of Tübingen. I should also record my sincere appreciation to Mansoura University for its help during the preparation of this book.

The editors are sincerely thankful to Saudi Artist Esrraa Abunar for the beautiful book cover design and drawings.

From Haytham to Noha, thank you so much my lovely wife for your continuous help, support, and patience—it is challenging to express the gratitude that I owe you. Still, enough to say, ‘without you, I would never have accomplished this work’.

From Bandar to his wife Esrraa Abunar, you have always been a partner in every success I encounter in my life. Thank you from the bottom of my heart for the tremendous support.

Last but not least, we record our sincere thanks to our families who always encouraged us and gave us moral support. A bouquet should go to our children: Kanzy, Mohamed (Haytham’s), Jory, and Rakan (Bandar’s), for their understanding and coping with our minimal attention during the preparation of this work.



---

# Contents

## Introduction

- Sedimentary Organic Matter: Origin, Productivity, Preservation, and Role in Source Rock Development** ..... 3  
Bandar I. Ghassal and Haytham El Atfy

## Methods

- Practical Guide for Petroleum Source Rock Interpretation** ..... 25  
Bandar I. Ghassal, Sattam S. Mutairi, and Haytham El Atfy
- Maturity Determination of Contaminated Source Rocks by Pyrolysis and Thermal Oxidation Methods: A Review** ..... 47  
Sedat İnan
- Source Rocks Forward Modelling: Significance and Approach** ..... 59  
Samer Bou Daher, Benoit Chauveau, Erwan Leguerroue, Paul Jermannaud, Alcide Thebault, Maria-Fernanda Romero-Sarmiento, and Emerson Marfisi
- Optical Kerogen Analysis** ..... 81  
Hartmut Jäger
- Effective Source-Rock Evaluation Strategies for the Identification of Profitable Plays in the Permian Basin, USA** ..... 97  
Mohamed K. Zobaa and David Entzminger

## Case Studies

- High-Resolution Palynostratigraphy and Palynofacies of the Upper Cretaceous and K/Pg Boundary, SE Sirt Basin, Libya: A Case Study** ..... 109  
Ali Daw El-Mehdawi
- Viability of the Upper Member of the Mississippian Lodgepole Formation as an Economic Source Rock in the Williston Basin** ..... 181  
Murray Dighans and Mohamed K. Zobaa
- Integration of Palynological and Foraminiferal Analyses Toward Evaluation of the Paleoenvironment and Hydrocarbon Potential in the Orange Basin, SW Africa** ..... 193  
Marissa K. Spencer, Damián Cárdenas, Francisca E. Oboh-Ikuenobe, and Tapas Chatterjee
- Palynofacies, Organic Petrography, and Source Rock Potential of the Toarcian Quse Formation Oil Shale in the Tibetan Tethys, China** ..... 213  
Ahmed Mansour, Thomas Gentzis, Guoqing Xia, Humberto Carvajal-Ortiz, Seare Ocubalidet, Haisheng Yi, and Haytham El Atfy

---

<b>Palynology and Petroleum Source Rock Geochemistry of the Cretaceous Mancos and Gallup Formations, San Juan Basin, New Mexico</b> .....	227
Ashton B. Faulkner and Mohamed K. Zobaa	
<b>Petroleum System Analysis of the Main Paleozoic Source Rocks in Western Iraq: A 1D Basin Modelling Approach</b> .....	243
Qusay Abeed	
<b>Source Rock Quality and Continuous Petroleum System in the Ranikot Formation (Kirthar Foldbelt, Pakistan) Based on Principal Organic Geochemistry</b> .....	257
Michał Makos, Richard J. Drozd, Ishtiaq Noor, Zdzisław Kołodziejczyk, Mateusz Górniak, Ihtesham Ul Wahab, Muhammad Javid Akhtar, and Shifaat Alam Muhammad	
<b>Characterization of the Upper Cretaceous-Paleogene Black Shale of the Southern Tethys Margin, Egypt</b> .....	279
Rania Abu-Ali, Ahmed El-Kammar, and Jochen Kuss	

---

## Contributors

**Qusay Abeed** Halliburton, Landmark Solutions, Abingdon, UK

**Rania Abu-Ali** Department of Geology, Cairo University, Giza, Egypt;  
Department of Geosciences, Bremen University, Bremen, Germany

**Muhammad Javid Akhtar** Polish Oil and Gas Company (PGNiG SA) Pakistan Branch,  
Islamabad, Pakistan

**Samer Bou Daher** Division of Global Solutions, Beicip-Franlab, Rueil-Malmaison, France

**Humberto Carvajal-Ortiz** Core Laboratories, Houston, TX, USA

**Tapas Chatterjee** Department of Earth Sciences, University of the Western Cape, Cape  
Town, South Africa

**Benoit Chauveau** IFP Energies Nouvelles, Directions Géoscience, Rueil-Malmaison, France

**Damián Cárdenas** Geosciences and Geological and Petroleum Engineering, Missouri  
University of Science and Technology, Rolla, MO, USA;  
Smithsonian Tropical Research Institute, Panamá, Panama

**Murray Dighans** Endeavor Energy Resources, LP, Midland, Texas, USA

**Richard J. Drozd** Stratum Reservoir, Houston, USA

**Haytham El Atfy** Department of Geosciences, University of Tübingen, Tübingen, Germany;  
Geology Department, Faculty of Science, Mansoura University, Mansoura, Egypt

**Ahmed El-Kammar** Department of Geology, Cairo University, Giza, Egypt

**Ali Daw El-Mehdawi** Exploration Department, National Oil Corporation, Tripoli, Libya

**David Entzminger** Entzminger Geoscience Services, LLC, Midland, TX, USA

**Ashton B. Faulkner** Beryl Oil and Gas, Midland, TX, USA

**Thomas Gentzis** Core Laboratories, Houston, TX, USA

**Bandar I. Ghassal** Saudi Aramco, Dhahran, Saudi Arabia

**Mateusz Górniak** Polish Oil and Gas Company (PGNiG SA) Pakistan Branch, Islamabad,  
Pakistan

**Sedat İnan** Faculty of Mines, Department of Geological Engineering, Istanbul Technical  
University, Maslak-Istanbul, Turkey

**Paul Jermannaud** Division of Global Solutions, Beicip-Franlab, Rueil-Malmaison, France

**Hartmut Jäger** GeoResources STC, Bensheim, Germany

**Zdzisław Kołodziejczyk** Polish Oil and Gas Company (PGNiG SA), Exploration and  
Production Branch in Warsaw, Warsaw, Poland

- 
- Jochen Kuss** Department of Geosciences, Bremen University, Bremen, Germany
- Erwan Leguerroue** Division of Global Solutions, Beicip-Franlab, Rueil-Malmaison, France
- Michał Makos** Polish Oil and Gas Company (PGNiG SA) Pakistan Branch, Islamabad, Pakistan
- Ahmed Mansour** Geology Department, Faculty of Science, Minia University, Minia, Egypt
- Emerson Marfisi** Division of Global Solutions, Beicip-Franlab, Rueil-Malmaison, France
- Shifaat Alam Muhammad** Pakistan Petroleum LTD., Gerry's Center, Islamabad, Pakistan
- Sattam S. Mutairi** Saudi Aramco, Dhahran, Saudi Arabia
- Ishtiaq Noor** HyRes Geoscience, Islamabad, Pakistan
- Francisca E. Oboh-Ikuenobe** Geosciences and Geological and Petroleum Engineering, Missouri University of Science and Technology, Rolla, MO, USA
- Seare Ocubalidet** Core Laboratories, Houston, TX, USA
- Maria-Fernanda Romero-Sarmiento** IFP Energies Nouvelles, Directions Géoscience, Rueil-Malmaison, France
- Marissa K. Spencer** Geosciences and Geological and Petroleum Engineering, Missouri University of Science and Technology, Rolla, MO, USA
- Alcide Thebault** Division of Global Solutions, Beicip-Franlab, Rueil-Malmaison, France
- Ihtesham Ul Wahab** Polish Oil and Gas Company (PGNiG SA) Pakistan Branch, Islamabad, Pakistan
- Guoqing Xia** State Key Laboratory of Oil and Gas Reservoir Geology and Exploitation, Chengdu University of Technology, Chengdu, China
- Haisheng Yi** State Key Laboratory of Oil and Gas Reservoir Geology and Exploitation, Chengdu University of Technology, Chengdu, China
- Mohamed K. Zobaa** Department of Geosciences, The University of Texas Permian Basin, Odessa, TX, USA

## Introduction



# Sedimentary Organic Matter: Origin, Productivity, Preservation, and Role in Source Rock Development

Bandar I. Ghassal and Haytham El Atfy 

## Abstract

Accurate source rock characterizations via geochemical and optical methods require advanced knowledge of the processes of their formation and the factors that control their development. The current chapter starts by addressing the fundamentals of sedimentary organic matter's origin and chemical compositions and how they interact with the atmosphere, lithosphere, and hydrosphere through comprehensive elucidations of the biogeochemical cycles of carbon, nitrogen, sulfur, and phosphorus. Then, it discusses the deposition and transportation of organic matter in different habitats and the physical and chemical factors that affect its preservations. The third part of the chapter provides insights into the kerogen formation pathways, classifications, and alteration processes. Finally, the chapter introduces the common terrestrial and marine source rock depositional environments and the processes that control the organic productivity and source rock development richness and quality. The knowledge in this chapter represents a reliable base for accurate source rocks and petroleum data interpretations. Furthermore, it can assist in explaining the changes in organofacies and thermal maturity, identifying sweet spots in unconventional resources, types of generated hydrocarbons (sweet versus sour oils), and maturing basin modeling calibrations.

B. I. Ghassal (✉)  
Saudi Aramco, Dhahran, Saudi Arabia  
e-mail: [Bandar.ghassal@aramco.com](mailto:Bandar.ghassal@aramco.com)

H. El Atfy  
Department of Geosciences, University of Tübingen, 72076  
Tübingen, Germany  
e-mail: [El-Atfy@daad-alumni.de](mailto:El-Atfy@daad-alumni.de)

Geology Department, Faculty of Science, Mansoura University,  
Mansoura, 35516, Egypt

## 1 Introduction

Source rocks are fine-grained sedimentary carbonate or siliciclastic rocks that are rich in organic matter and are expected to generate fluid hydrocarbons upon attaining sufficient thermal maturity (Littke et al., 1997). They are an essential petroleum system element whose organic matter, mineralogical compositions, and thermal maturity determine generated fluids' chemical and physical properties. The focus in the last two decades on unconventional resources, such as gas and oil shale plays, has advanced source rock characterization methods. These methods investigate controls over quantity, quality, thermal maturity, and hydrocarbon generative potential of organic matter, which, among other factors, control sweet spots and their properties. Furthermore, several new assessment parameters and techniques have advanced and matured basin modeling and petroleum systems analysis, resulting in minimizing petroleum charge risk. Examples of recent advancements in source rock characterizations methods are found in (Romero-Sarmiento et al., 2013; Inan et al., 2017; Ghassal et al., 2017; Maende et al., 2017; Al-Hajeri et al., 2020). In order to use state-of-the-art technologies effectively, a comprehensive understanding of source rock formation mechanisms is essential. The current chapter reviews the source rock development in various depositional environments by providing detailed insights into organic matter composition, types, and factors controlling their preservation and hydrocarbon productivities.

Understanding all aspects of sedimentary organic matter formation is the primary step toward advanced source rock assessment. Hence, the chapter synopsis the classification, biogeochemical cycles, and the processes that produce, preserve, and transport organic matter in different geological environments. Knowing the exact chemical compositions of kerogens in potential source rocks allows for an accurate prediction of potentially generated hydrocarbons. Moreover, the kerogen chemistry characterization enables better determination of generation kinetics and thermal maturity

windows for the different hydrocarbon products (Dieckmann et al., 2000; Pepper & Corvi, 1995).

Organic matter and its related hydrocarbons are composed mainly of hydrogen, carbon, oxygen, sulfur, nitrogen, phosphorous, and other elements. The cycles of these elements in nature play crucial roles in the evolution of sedimentary organic matter throughout geological history (Summons, 1993). Thus, the dynamics and the reactions of each of these elements in the different Earth pools impact the productivity and preservation of organic matter and, consequently, the generation, type (e.g., oil versus gas), and quality of hydrocarbons (e.g., sweet versus sour).

Sedimentary organic matter undergoes a series of processes that include productivity, deposition or transportation, and then preservation or decomposition. These processes are followed by kerogen formation via diagenesis, catagenesis, and, finally, metagenesis, depending upon the subsurface processes and conditions. The kerogen formation and thermal maturity pathways differ based on the depositional environments. The current review covers both the organic geochemistry and palynology aspects related to sedimentary organic matter formation and evaluation.

## 2 Origin of Sedimentary Organic Matter

Organic matter varies in chemical composition depending on the original biological precursor. These compositional differences, together with the syn- and post-depositional conditions, determine the levels of its preservation. Thus, the biological and biogeochemical processes in different environments throughout the Earth's history are primary controls on the type of organic matter in any specific locality in time and space.

According to several properties, such as their morphology and physiological and biochemical capacities, the organisms are classified into main taxonomic groups (Summons, 1993). The three domains of organisms are archaea, bacteria, and eukarya (Woese et al., 1990), as in Fig. 1a.

Prokaryotes are unicellular, tiny spheroidal bodies ranging in size from 0.1 to 5  $\mu\text{m}$  (Summons, 1993). They lack a membrane-bound nucleus, mitochondria, and chloroplast. Their extremely flexible metabolic and respiratory systems enable them to live and adapt to aerobic and anaerobic conditions. Some obtain their energy from chemical sources (Fig. 1b). They include the archaea and bacteria domains. These characteristics allow the prokaryotes to survive over 4 billion years (Gregory & DeSalle, 2005; Magalon et al., 2012).

Archaeobacteria are prokaryotes that mostly occupy extreme environments, such as hypersaline and volcanic settings (Parker, 2001). The three main examples of archaeobacteria are methanogens, halophilic, and thermophilic. First,

methanogens are anaerobic archaeobacteria that produce methane from the conversion of  $\text{CO}_2$ , hydrogen, formate, acetate, and other simple carbon compounds (Summons, 1993). Their growth depends on the temperature and absence of oxygen. Second, the halophilic archaeobacteria are aerobic and inhabit hypersaline environments (Irwin, 2020). Third, the thermophilic sulfate-dependent archaeobacteria are either aerobic or anaerobic. They occupy very high-temperature or sulfide-rich environments (Summons, 1993).

Eukaryotes, on the other hand, contain a membrane-bound nucleus, mitochondria, and chloroplast. Unlike prokaryotes, they are multicellular and have larger cell sizes that range from 10 to 100  $\mu\text{m}$  (Summons, 1993). They include animals, plants, fungi, and protists (Parker, 2001; Summons, 1993). The latter are unicellular or form simply organized colonies. The microorganisms, which are prokaryotes and protists, constitute the vast majority of living biomass. They are the most prevalent organisms throughout the Earth's history and extend over broad geographic areas and environments (Summons, 1993).

The availability of carbon type (e.g., organic and inorganic), energy resources, and chemical substances classifies the microorganisms based on their biochemical capacities, which in turn determine their habitats (Fig. 1c). For example, autotrophs utilize inorganic sources, such as  $\text{CO}_2$ ,  $\text{NO}_3^-$ , or  $\text{HCO}_3^-$ , to generate new biomass. They either reduce  $\text{CO}_2$  through energy obtained from sunlight, hence called phototrophs, or through inorganic reactions, hence called chemoautotrophs (Sage, 2008). The phototrophs use photosynthesis to convert  $\text{CO}_2$  to carbohydrates. They are the primary producer of organic matter. The prokaryotes cyanobacteria and purple and green photosynthetic bacteria are typical examples of phototrophs, while algae and higher plants represent eukaryotic phototrophs (Summons, 1993).

Conversely, heterotrophic organisms cannot produce their food and rely on other organic sources (Gaedke, 2021). Therefore, they return the organic carbon into the geosphere mainly through organic carbon oxidation to obtain energy through various processes. They play significant roles in biogeochemical cycles. The aerobes are heterotrophic organisms that utilize oxygen as an oxidant. Furthermore, anaerobes are organisms that use nitrates or sulfates to oxidize organic matter. Typical examples of heterotrophic organisms include heterotrophic bacteria and fungi (Ritz, 2005; Summons, 1993).

### 2.1 Organic Matter Compositions

Biomass is composed mainly of proteins, carbohydrates, lignin, and lipids (Fig. 2) (Selly, 1998). The proportions of these components determine the organic matter types and their stability under various geological conditions. Proteins

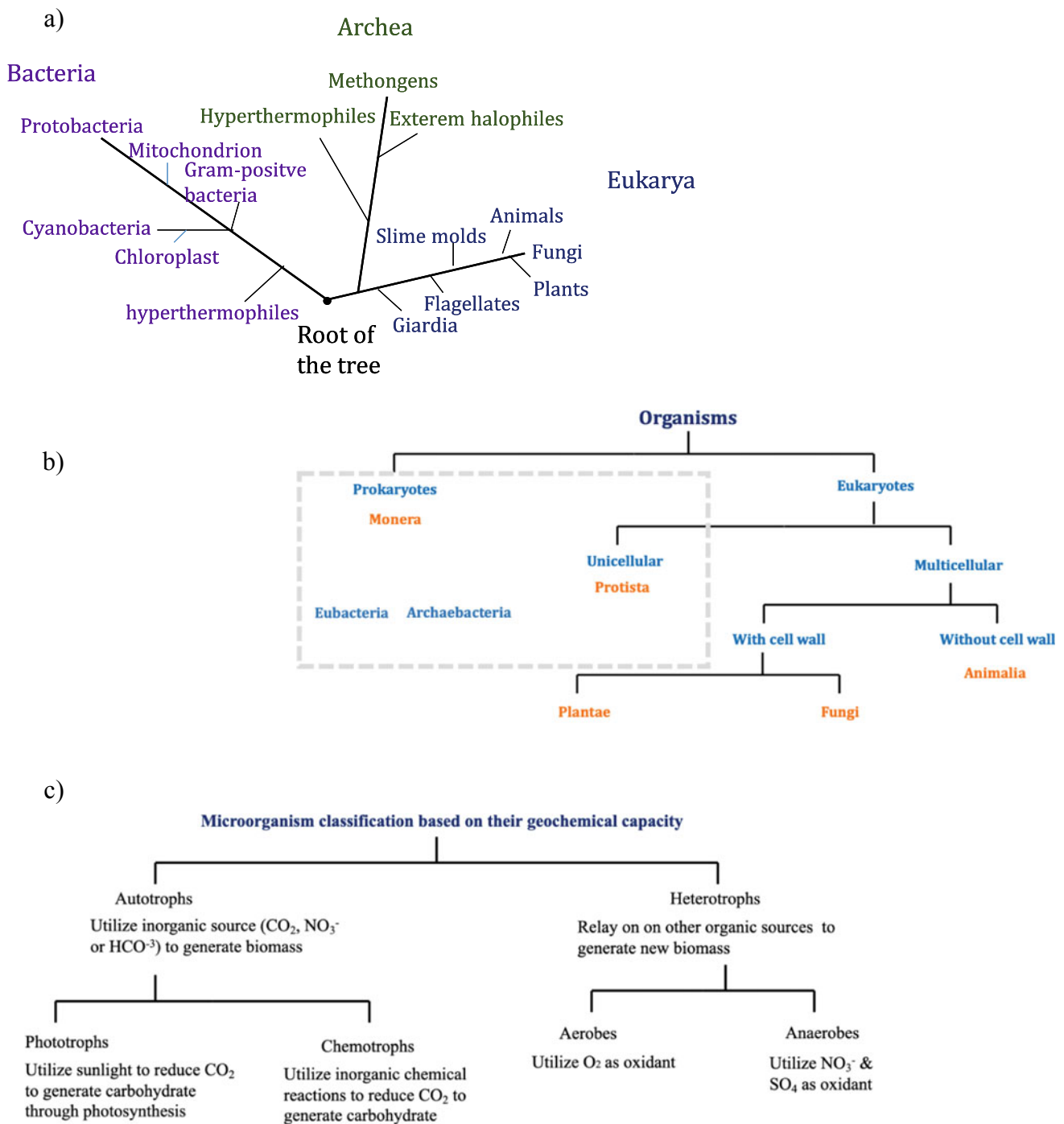


**Fig. 1** Classification of organisms based on a) three domains of life, b) cell types, and c) biochemical capacities

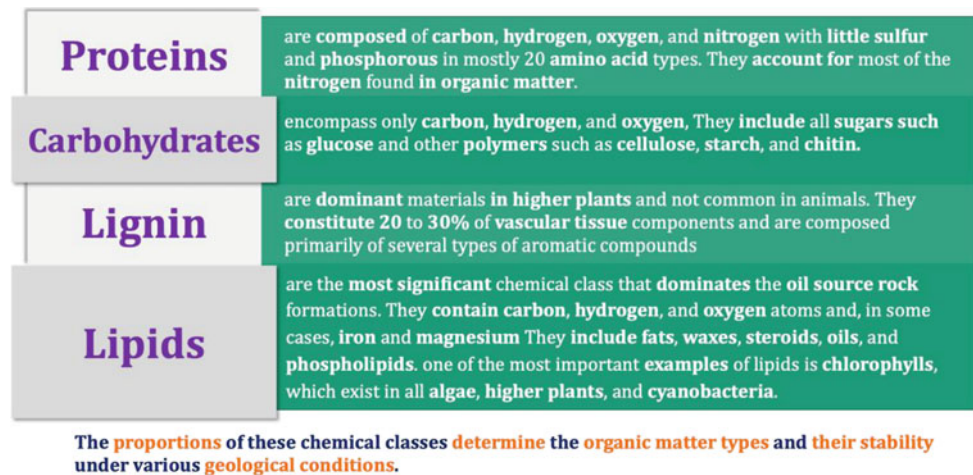
are composed of carbon, hydrogen, oxygen, and nitrogen with little sulfur and phosphorous in mostly 20 amino acid types. They predominantly exist in animals (Selly, 1998) and account for most of the nitrogen found in organic matter (Killops & Killops, 2013). Proteins constitute a significant fraction of organic nitrogen in organisms (Killops & Killops, 2013).

Carbohydrates occur in most organisms as an essential energy source. They encompass only carbon, hydrogen, and oxygen, with the basic formula  $C_n(H_2O)_n$ . They include all sugars, such as glucose, and other polymers, such as cellulose, starch, and chitin (De Leeuw and Largeuw, 1993).

Lignins are dominant constituents in higher plants and are not common in animals. They constitute 20 to 30% of



**Fig. 2** Summary of chemical classes found in organic matters, see text for references



vascular tissue components, are composed primarily of several types of aromatic compounds (Selly, 1998), and represent the second dominant biopolymer after cellulose (Killops & Killops, 2013).

Lipids are the most significant chemical class that dominates the oil source rock formations and are present widely in most organisms (Selly, 1998). They contain carbon, hydrogen, and oxygen atoms and, in some cases, iron and magnesium (De Leeuw and Largeuw, 1993). They are insoluble in water and soluble in nonpolar organic solvents, such as hexane and chloroform. Lipids include fats, waxes, steroids, oils, and phospholipids (Selly, 1998; Killops & Killops, 2013). One of their most important examples is chlorophylls, which exist in all algae, higher plants, and cyanobacteria.

## 2.2 Biogeochemical Cycles

Biogeochemical cycles are defined as the interactions, movements, and cyclization of elements between the biotic (biosphere) and abiotic factors. The latter includes the atmosphere, geosphere, and hydrosphere. Six primary elements comprise the organic molecules and inhabit several biotic and abiotic reservoirs in various chemical forms: carbon, hydrogen, nitrogen, oxygen, phosphorus, and sulfur (Summons, 1993). Their movements between these pools occur through spontaneous oxidizing or reducing chemical reactions or biological interactions. These cycles are primarily interlinked and fueled by sunlight through photosynthesis. In some cases, hydrothermal activities source the energy needed for carbon fixation. Understanding these processes improves the realization of the factors controlling organic matter richness, quality, and isotopic variation (Brusseau, 2019).

Oxygen is not discussed separately due to its complexity as a by-product of numerous reactions linked to other

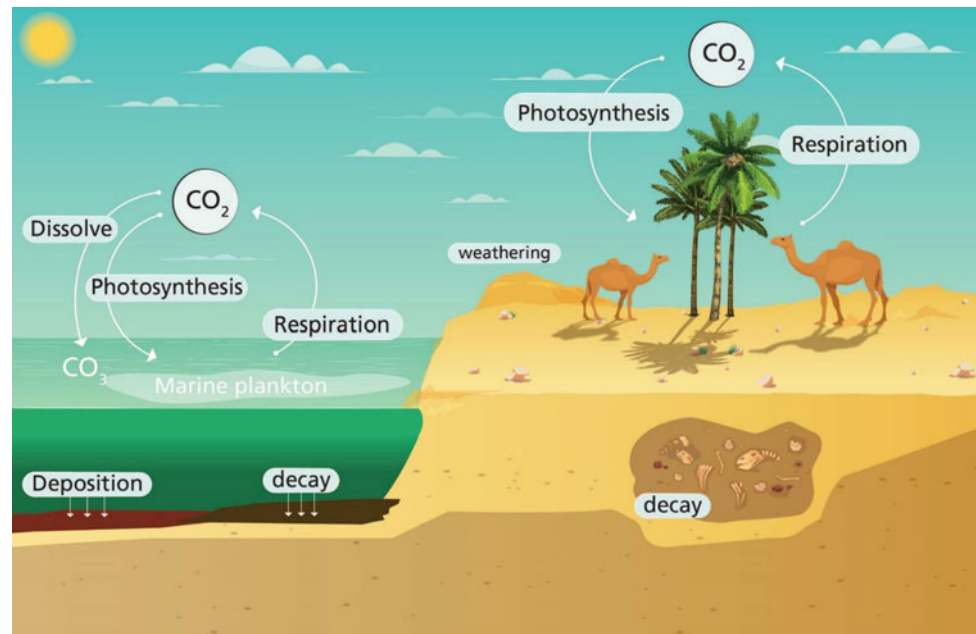
element cycles. The main processes that transfer the oxygen between the various reservoirs are respiration, photosynthesis, and the decay and combustion of organic matter. The primary oxygen producers are phytoplankton and plants. The oxygen released during the sunlight reaction with water vapor is also an essential source (Summons, 1993).

### 2.2.1 Carbon Cycle

Carbon is an essential element in all living organisms and acts as an energy source for most species. However, most of the carbon is preserved in the lithosphere, with fossil fuel constituting one-fifth of it (Brusseau, 2019; Vallero, 2014). The atmosphere is another primary reservoir of carbon. In these reservoirs, carbon exists in either oxidized or reduced chemical forms. The carbon cycle consists of two interlinked sub-cycles that occur at various temporal and spatial scales (Fig. 3). The first sub-cycle takes place on a short timescale (days–months) and within the biosphere. During photosynthesis, autotrophs convert CO<sub>2</sub> into simple organic intermediates and then to carbohydrates, such as glucose. Heterotrophs that feed on these autotrophs metabolize the carbohydrate to obtain energy through respiration. The carbon returns to the atmosphere through decomposition, excretion, and respiration (Summons, 1993).

The second sub-cycle occurs over a long timescale (hundred–thousand years) through geological processes. CO<sub>2</sub>, which is the dominant form of carbon in the atmosphere, plays a critical role in regulating and maintaining Earth's temperature and oxygen concentrations. The exchange of CO<sub>2</sub> between the atmosphere, biosphere, and geosphere predominantly controls its concentrations in the atmosphere and influences its oxygen abundance (Summons, 1993). Phytoplankton converts CO<sub>2</sub> through photosynthesis into nutrients for other higher-level organisms, which return the carbon to the atmosphere through respiration. The CO<sub>2</sub> in the atmosphere dissolves in the oceans and transforms into other inorganic compounds such as HCO<sub>3</sub><sup>−</sup> and CO<sub>3</sub>.

**Fig. 3** Simplified diagram illustrating the carbon cycle



Some organisms assimilate Ca with CO<sub>3</sub> to form CaCO<sub>3</sub>, which composes the hard bodies of most marine shells. These taxa deposit on the seafloor after they die, contributing to the sedimentary pile. Over thousands of years, these sediments solidify to form various carbonate rocks through several geological processes (Wigley and Schimel, 2005). The carbon in the organic reservoir, on the other hand, is found in the reduced form either in living biomass, dissolved or suspended in seawater, or recently deposited on the seafloor. When deposited and preserved, this organic matter is encompassed in sediments to eventually form petroleum source rocks (Summons, 1993; Brusseau, 2019).

### 2.2.2 Nitrogen Cycle

Nitrogen is one of the primary nutrient sources for most living biomass in oceans and lands. Its concentration controls primary organic productivity and organic matter decay. It also plays a significant role in regulating atmospheric temperature. Moreover, nitrogen is an essential constituent in chlorophyll composition responsible for photosynthesis processes and is one of the main elements of living biomass tissues. The consecutive transfer of nitrogen by several processes between the various reservoirs (atmosphere, geosphere, and biosphere) defines its cycle, converting it into different end products (Fig. 4). These processes are fixation, nitrification, assimilation, ammonification, and denitrification, all involving reduction or oxidation of nitrogen compounds by biological, physical, or chemical processes (Brusseau, 2019; Hayes, 2018; Summons, 1993).

Nitrogen in the atmosphere is present in the inert form (N<sub>2</sub>), which is not usable by living biomass. It precipitates in

soil from air or surface water. Bacteria such as cyanobacteria, phototrophic bacteria, and Rhizobiaceae convert N<sub>2</sub> to ammonia through the nitrogen fixation process. Furthermore, nitrogen fixation can occur by the light energy in the atmosphere that breaks N<sub>2</sub> into nitrogen oxide (Bernhard, 2010).

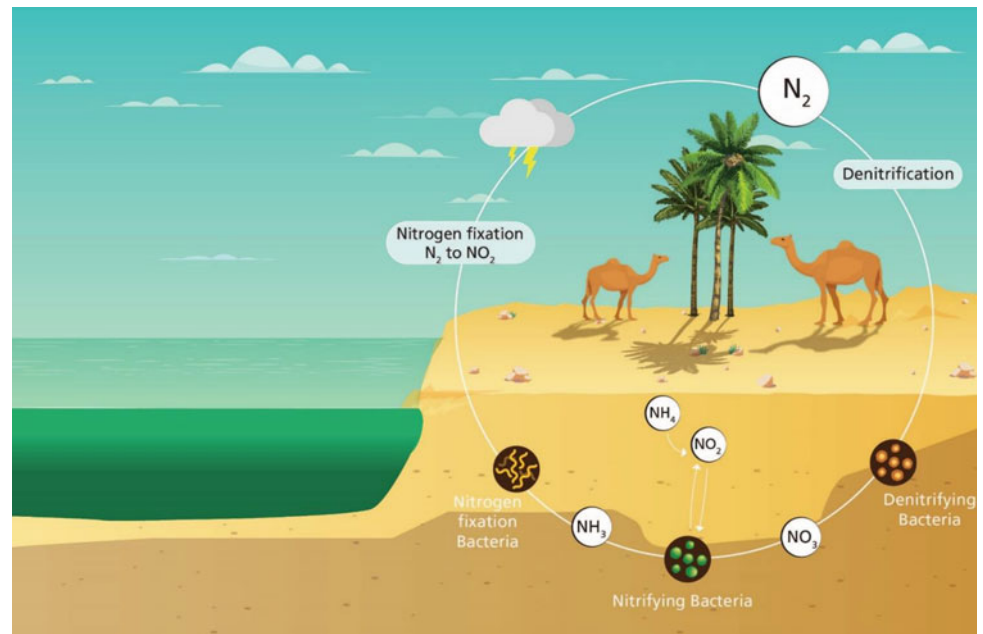
Nitrification is a successive biological process of converting ammonia to nitrites by bacterial oxidation. The Nitrobacter subsequently converts nitrites to nitrates. The other essential nitrogen cycle process is assimilation, which is transferring the ammonia and the nitrite, nitrate, and ammonium ions from soil to plants to form tissues and proteins. Ammonification is the decay of organic matter after burial. Bacteria and fungi decompose nitrogen compounds into ammonia. The last process of the nitrogen cycle is denitrification, where nitrogen is released back into the atmosphere. The process involves the bacterial conversion of nitrate to N<sub>2</sub> in reduced conditions. In marine environments, nitrogen compounds are deposited with the sediments, forming sedimentary rocks over geological time (Bernhard, 2010; Brusseau, 2019).

### 2.2.3 Sulfur Cycle

Sulfur is one of the Earth's most abundant elements, which exists in different forms in all reservoirs in the ecosystem. Organic sulfur is usually amino acid found in protein, hormones, and vitamins. Sulfur abundance and cyclization within marine environments control, to a large degree, organic matter preservation and quality (Brimblecombe, 2003).

The sulfur cyclization is driven mostly by biological activities, weathering, and hydrological activities (Fig. 5).

**Fig. 4** Simplified diagram illustrating the nitrogen cycle



Sulfur is leached from the lithosphere to the atmosphere via weathering processes before its oxidation to sulfate ( $\text{SO}_4$ ). Some bacteria groups utilize sulfate in their respiration as an oxidant. Also, other plants and microorganisms reduce sulfate to produce biomass through the assimilatory sulfate reduction process. On the other hand, animals uptake sulfur from consuming amino acids from other living organisms (Brusseau, 2019; Summons, 1993). The two significant bacterial groups that play a primary role in sulfur cyclization are the sulfate-reducing bacteria (SRB) and sulfide oxidizer bacteria (Zavarzin, 2008). Benthic communities feed on the organic matter deposited on the seafloor, where oxygen is available for respiration. Moreover, this zone witnessed metal reductions, such as  $\text{Fe(III)}$  to  $\text{Fe}^{+2}$  and  $\text{Mn(IV)}$  to  $\text{Mn}^{+2}$ . Beneath this zone, the oxygen becomes depleted. In these anaerobic conditions, the SRB and archaea utilize the dissimilatory sulfate reduction (DSR) process to oxidize sulfate as an oxidant to gain energy from buried organic carbon and methane to generate hydrogen sulfide ( $\text{H}_2\text{S}$ ),  $\text{HS}^-$ , and  $\text{S}^{2-}$  (e.g., Jørgensen et al., 2019; Simon and Krock, 2013). It is in this anoxic zone where pyrite is formed via bacteria by reducing the dissolved sulfates to sulfide.

The sulfide oxidizer bacteria obtain their energy from oxidizing sulfides in magmatic regions in chemolithotrophic or phototrophic processes. The sulfur returns from the biosphere to the soil via organic matter decay. Some sulfur is leached from terrestrial environments and is transferred through rivers to oceans and lakes. The sulfur cycles back to the atmosphere or moves to the marine biosphere (Summons, 1993).

### 2.2.4 Phosphorus Cycle

Phosphorus is another crucial element for living biomass occurring in DNA, RNA, and animal bones. Notwithstanding its vast abundance in the lithosphere, it is less abundant than other organic elements, especially in fossil organic matter. Phosphorus primarily regulates the fertility of the ecosystem and cycles between the lithosphere, hydrosphere, and biosphere. The cycle involves three main processes: geological weathering, absorption by living organisms, and organic matter decay (Fig. 6). The phosphate salts are removed from rocks during weathering processes and then deposit in soils. Note that the phosphate salts do not dissolve in water completely; therefore, aquatic living organisms absorb phosphorus from the lower water layers. In terrestrial environments, plants absorb phosphorus from the soil. Animals gain their phosphorus from consuming these plants. The phosphorus returns to the lithosphere again through the decay of organic matter. (Summons, 1993; Rittenberg, 2003; Macdonald et al., 2018).

### 2.3 Primary Organic Productivity

Primary organic productivity is defined as the carbon fixation rate by converting inorganic carbon into hydrocarbons through photosynthetic organisms (Killops & Killops, 2013; Littke et al., 1997; Selley, 1998). The primary reaction that occurs in plants and algae yields water and glucose. The produced glucose acts as the onset for the formation of complex carbon compounds such as polysaccharides

**Fig. 5** Simplified diagram illustrating the sulfur cycle

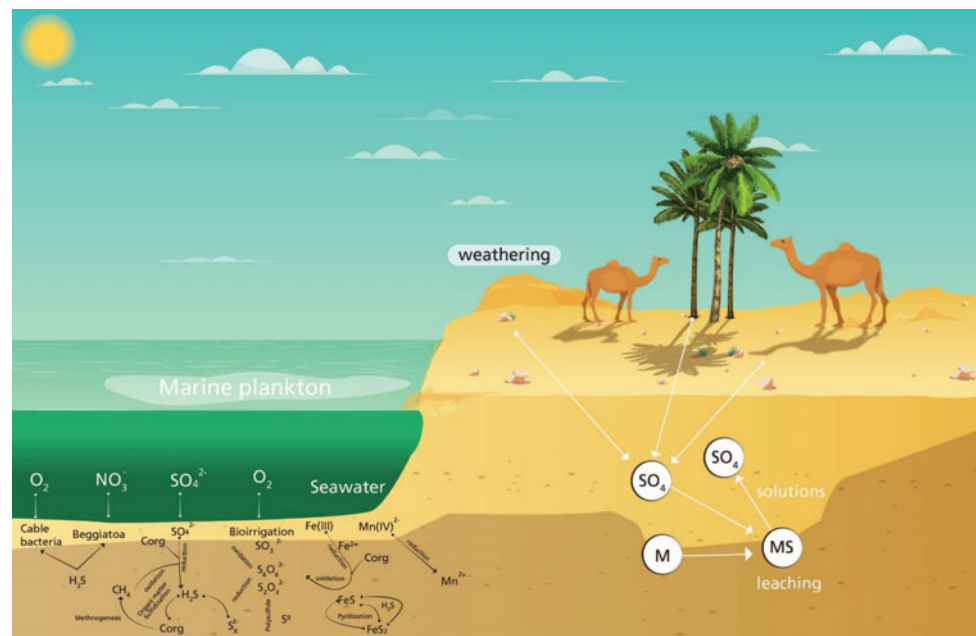
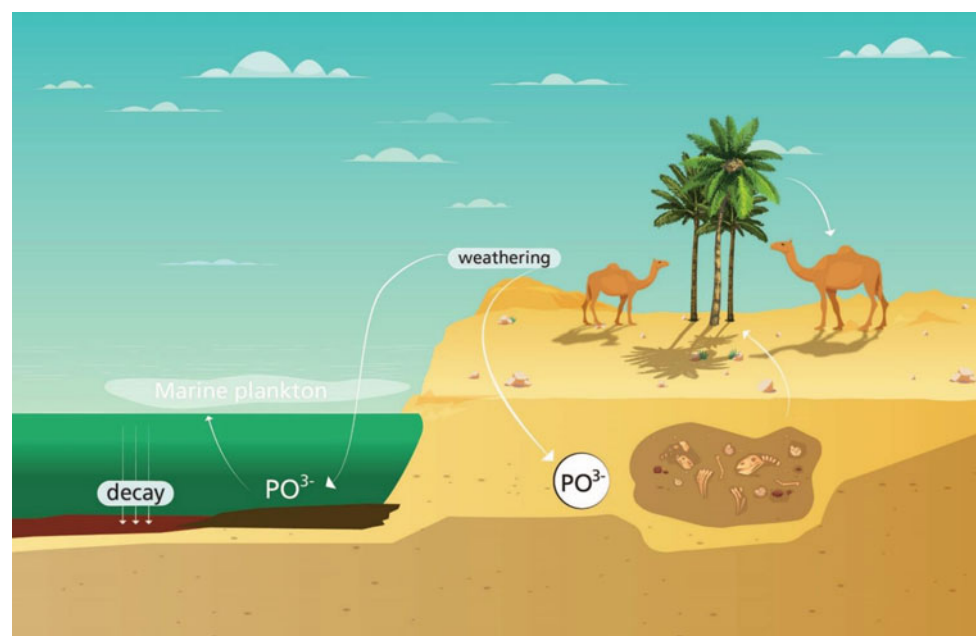


**Fig. 6** Simplified diagram illustrating the phosphorus cycle



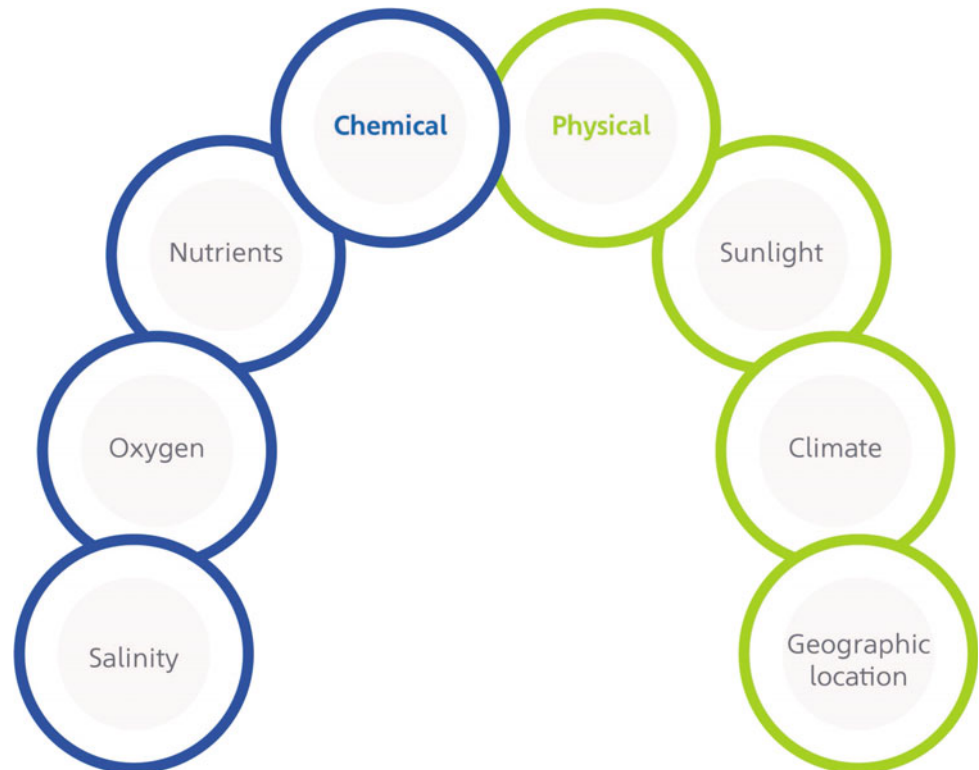
occurring in plants and their consuming animals (Selly, 1998). The second process that converts inorganic carbon to organic carbon is chemosynthesis—another form of bio-productivity but only significant locally (Sorokin, 1966).

Physical and chemical factors that control the occurrence and the intensity of the primary organic productivity are shown in Fig. 7. The physical parameters include the temperature and amount of light, in the case of aquatic environments, the photic zone thickness, and the water turbidity (Selly, 1998). Crucial factors that control the intensity of primary organic productivity are the Earth's climate and

atmospheric green gas levels. The primary productivity intensifies with increasing  $\text{CO}_2$  and temperature and light availability (Littke et al., 1997). The chemical and physical factors are in essence, interlinked and are expected to vary temporally and spatially in different geographic locations and geological settings.

Chemical factors play integral roles in primary organic productivity. Phosphates and nitrates are essential for plant and animal growth and are considered a preferred ingredients for organic matter productivity (Selly, 1998). In addition, oxygen is a by-product of photosynthesis, allowing

**Fig. 7** Summary of the factors controlling the primary productivity



phytoplankton to flourish, thereby improving zooplankton productivity. These factors are maximized in two high primary productivity belts between the polar and equatorial oceans attributed to high-latitude upwelling manifested in modern days (Littke et al., 1997). In the upwelling zones, deep cold nutrient-rich oceanic currents upwell to shallower waters to enrich the shelf and coastal areas with phosphates and nitrates, consequently increasing bioproductivity (Selly, 1998). Wind direction, Earth rotation, and Earth climate control these settings.

Sunlight intensity, as a primary control over photosynthesis and bioproductivity, varies based on climate, weather, and geographic location, as well as on geological settings that can prevent access to surface water. Bioproduction is the highest in the upper part of the photic oxygen-rich zone and steadily diminishes deeper with decreasing light and temperature (Selly, 1998).

Water provides hydrogen for the photosynthesis process, which intensifies the bioproductivity. Its availability plays a primary role in terrestrial environments. For example, high rainfall environments characterize the great coal-forming forest (Killops & Killops, 2013). The bioproductivity is also controlled by geographic and climatic factors. In high-latitude or cold regions with ice cover, plant growth is limited. On the other hand, the very high temperature reduces photosynthesis as it destroys or alters enzymes and cellular components (bioproductivity). In marine environments, temperature and rainfall cause the algae breed to

overgrow. Therefore, humid, subtropical, and tropical climates favor high bioproductivity (Li et al., 2015).

Water salinity has a vital role in the composition of primary producers in fresh, saline, or hypersaline waters. Greater diversity of primary producers occurs in fresh and sea waters than in hypersaline waters (Killops & Killops, 2013). The diversity may not affect bioproductivity but the composition of the preserved organic matter later on. In restricted basins, positive water balance traps nutrients, resulting in increasing bioproductivity (Li et al., 2015).

The four main contributors to the formation of sedimentary organic matter are phytoplankton, zooplankton, higher plants, and bacteria with an insignificant contribution from higher organized animals such as sharks (Mendonça Filho et al., 2012; Tissot & Welte, 1984).

## 2.4 Deposition and Transportation of Organic Matter

Organic matters are the black or dark-colored remains of plants and/or animals deposited during rock sedimentation. Apart from coal seams, which are nearly composed of only organic constituents, most sedimentary rocks encompass minor organic matter amounts. In marine environments, organic matter availability and generation and their preservation versus destruction in the sediment–water interface are the primary constraints that control the organic matter richness

in the sedimentary rock. Marine organisms occupying ocean surfaces biosynthesize most organic matter before their deposition on the seafloor (Wakeham & Lee, 1993).

The alteration of organic matter composition continues at the sediment–water interface, which changes their original composition. The majority of the produced marine organic matter is recycled in the epipelagic zones, but only small fractions precipitate in the mesopelagic and bathypelagic zones (Fig. 8). In the epipelagic zones, the bacteria and zooplankton recycle more than 90% of the produced organic matter through photosynthesis to generate other biomass, degraded or dissolved organic matter. The organic matter that survives the water column recycling processes and accumulates on the seafloor (10–30%) constitutes the sedimentary organic matter records.

In terrestrial environments, mainly swamps, bog, fen moor, musky, and peatlands, only a small fraction of the original organic matter is preserved in peat deposits. Mires is the term that describes these peat-forming ecosystems. There are two types of mires, which are topogenous and ombrogenous (Taylor et al., 1998). The former refers to marshes, fen, and swamps formed in reduced rainfall climates and high groundwater levels. The ombrogenous mires are more affluent than the topogenous in organic nutrients and inorganic inputs and form in heavy rainfall systems with a water table lower than the peat surface. Three factors are responsible for the mire formation, which are flora development, geographic location, and climate (Taylor et al., 1998).

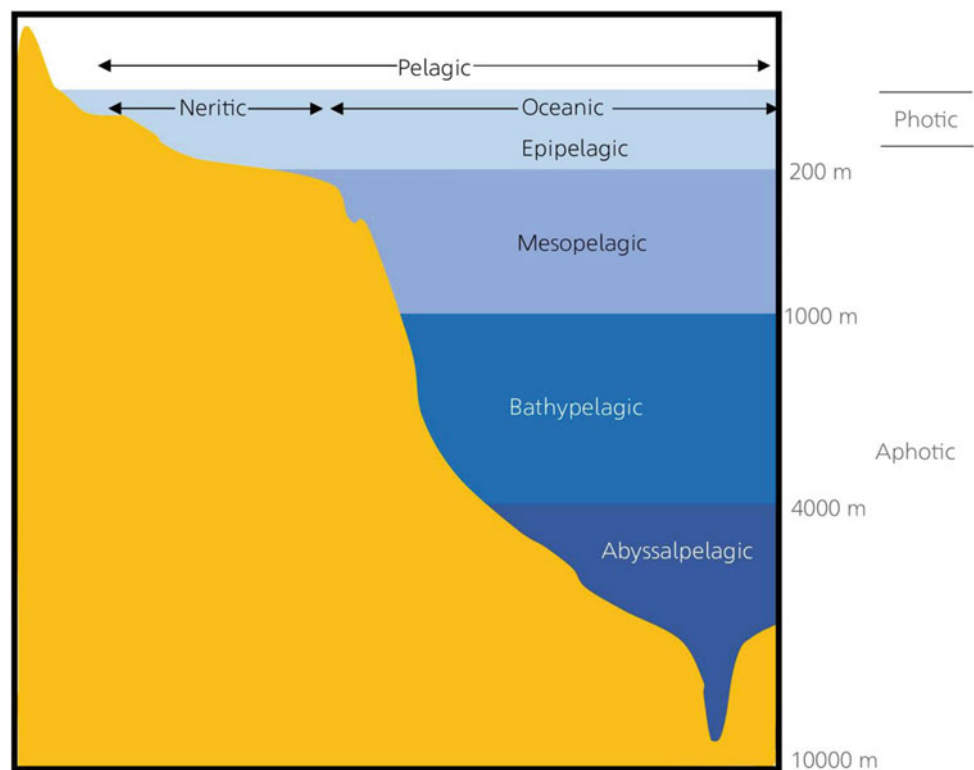
## 2.5 Preservation of Organic Matter

The preserved organic matter is the one that survives the biosynthesis processes by predators during transportation through the water column, escaping degradation at the sediment–water interface, and is buried in the sediments (Canfield, 1994; Piper & Calvert, 2009). Five factors principally affect organic matter preservation: primary productivity, anoxicity, mineral surface area, sedimentation rate, and wave and current energy (Fig. 9).

The deposited organic matter on the seabed is generally comparable to the primary productivity and decreases with water depth (Suess, 1980). In that case, it is evident that primary productivity is a critical factor in the amount of preserved organic matter. However, it is a vital variable but not a sole factor.

Anoxicity is the second factor that controls the organic matter preservations. Intense primary productivity and the decay of organic materials and their oxidation to  $\text{CO}_2$  tend to reduce the oxygen level and create a low-oxygen water layer called the oxygen-minimum zone, OMZ (Killops & Killops, 2013; Tissot & Welte, 1984). This zone is characterized by elevated  $\text{H}_2\text{S}$  concentrations produced by sulfate-reducing bacteria (Fig. 10). The low-oxygen level and the presence of  $\text{H}_2\text{S}$  reduce the rate of organic matter degradation and enhance preservation. The organic matter oxidation to  $\text{CO}_2$  is seized in this zone, but anaerobic oxidation such as sulfate reduction, denitrification, or methanogenesis occurs

**Fig. 8** Simplified diagram illustrating various marine settings



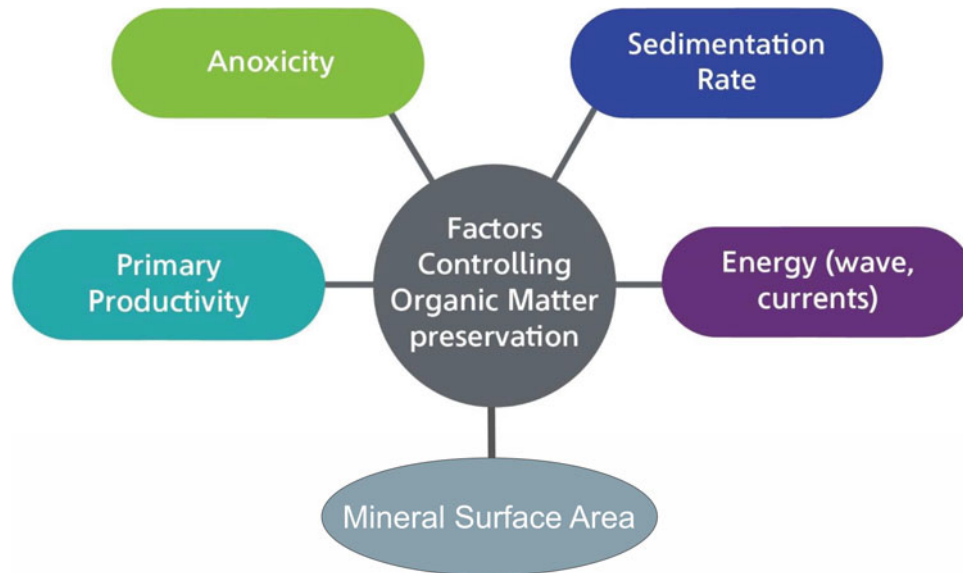


**Fig. 9** Summary of the factors controlling organic matter preservation

(Canfield et al., 2021). In this case, the destruction of organic matter occurs at a slow rate. The OMZ persists in the middle of the water column interlayered between two highly oxygenated water layers (Diaz et al., 2013; Fenchel et al., 2012).

Grain size and mineralogical composition play a vital role in organic matter preservation. The fine-grained sediments inhibit or prevent the oxygen exchange between the pore-water and the free-water column. Moreover, the clays inactivate bacteria digestive enzymes, increasing organic matter preservation (Dean & Gorham, 1998). Mayer (1994) suggested that mineral surface is responsible for organic matter

preservation in marine environments apart from deltas. The organic matter forms a monolayer adsorbed by the mineral surface (Killops and Killpos, 2013). This process is considered a conversion of dissolved to particulate organic matter (Tissot & Welte, 1984). This adsorption is irreversible and can protect even labile constituents such as sugar, thereby enhancing preservation (Henriches, 1992; Killops and Killpos, 2013). The length of exposure to oxygenated water during deposition is a critical factor.

The sedimentation rate has a direct impact on organic matter preservation and its types. For example, most of the

### Fate of organic matter

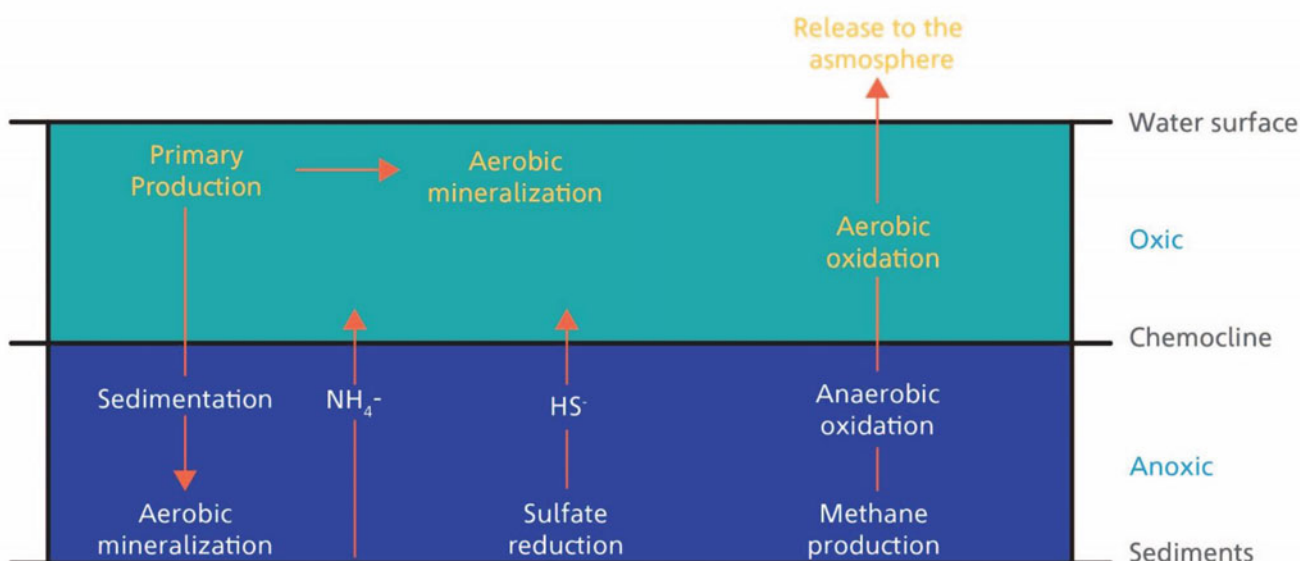


**Fig. 10** Summary of the factors contributing to the preservation and fate of organic matters

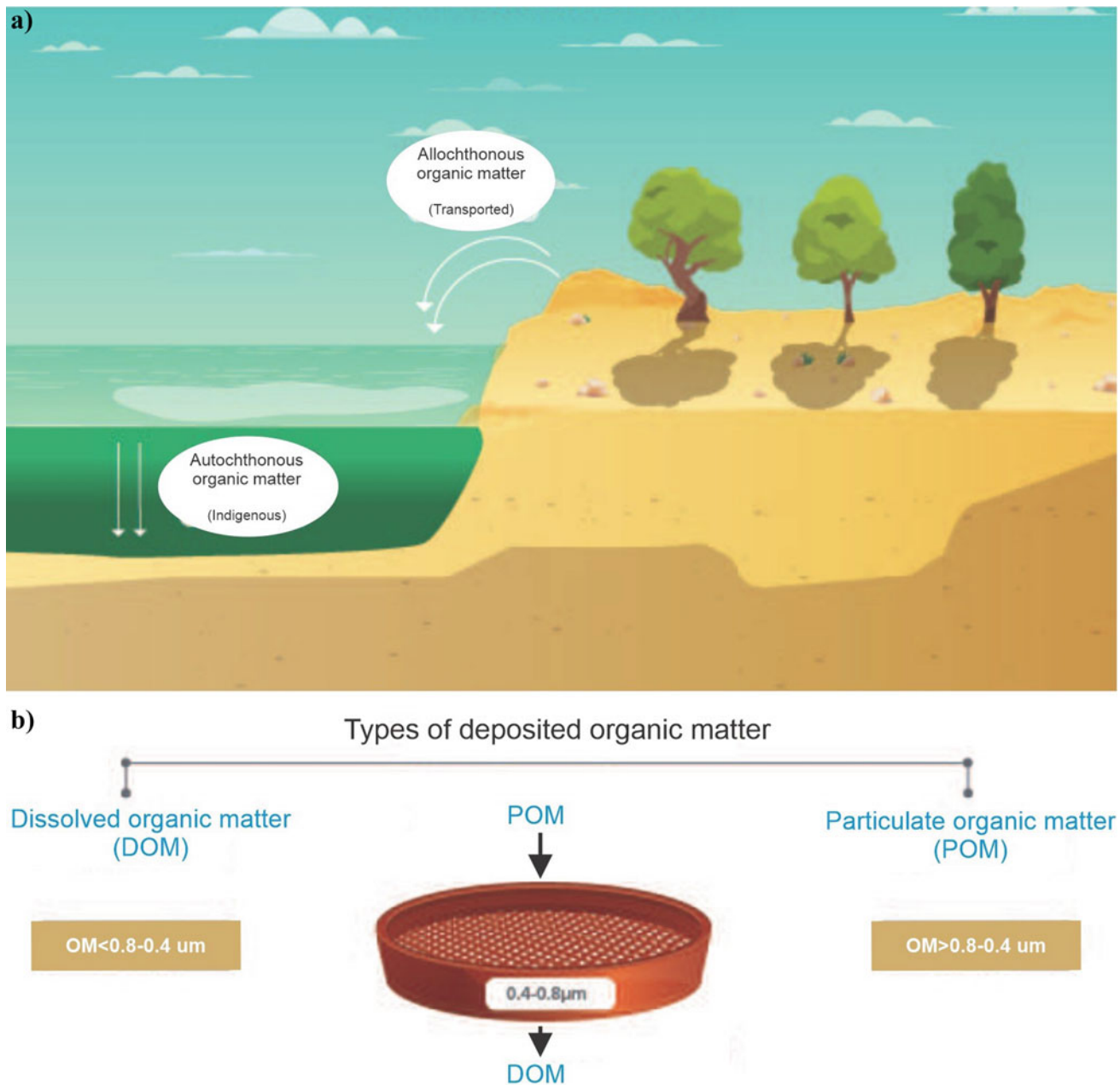


**Fig. 11** Calcification of organic matter based on their proximity to the depositional environments

preserved organic matter in deltaic systems is allochthonous (Fig. 11) (e.g., Ghassal et al., 2016a). The high sediment inputs outweigh the amount of organic matter required to form monolayers, reducing marine organic matter preservation (Henriches, 1992). Besides, terrestrial organic matter is generally more resistant to degradation compared to marine ones. Moreover, assuming the rate of organic matter input is constant, and then the sedimentation is inversely proportional to the preserved organic matter concentration (Fig. 12). The foregoing dissection explains the increase in richness and quality of organic matter in more distal and deeper settings. High-energy waves and currents cause the

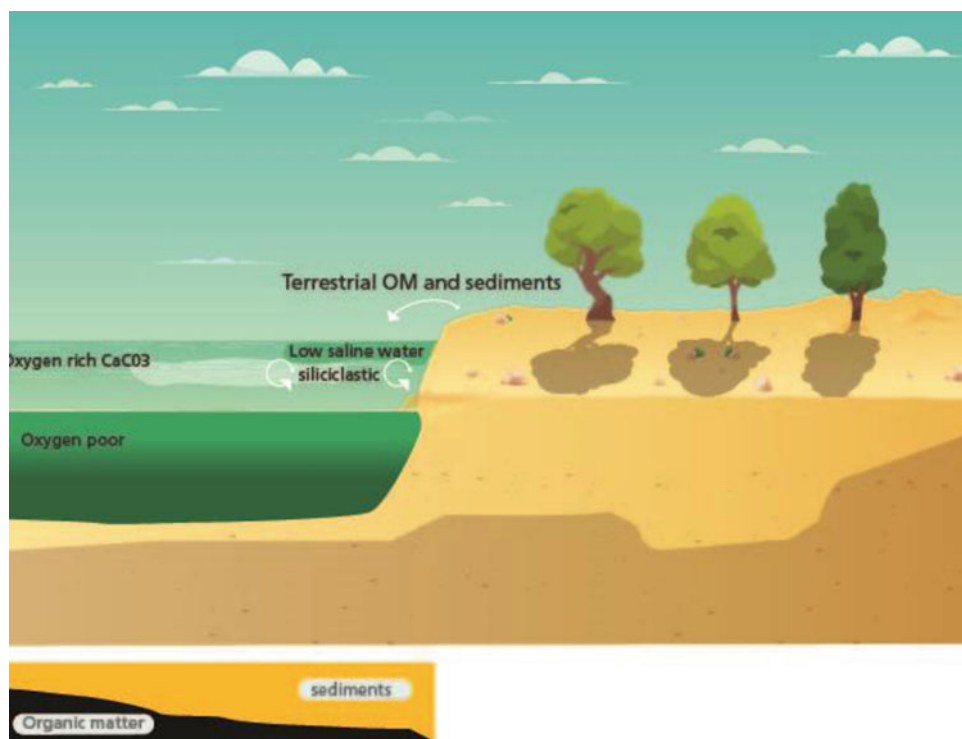
oxygen to circulate and destabilize the chemical and physical conditions of the water column, affecting all of the above-mentioned factors.

### 3 Kerogen Formation, Classifications, and Alteration

Kerogen is the most common term used to describe the fossil organic matter in sedimentary rocks. It is the fraction of the organic matter in sedimentary rocks, which is insoluble in organic solvents. Chemically, it is a macromolecule made of



**Fig. 12** Simplified diagram illustrating organic matter richness and preservation from proximal to distal settings



condensed cyclic nuclei linked by heteroatomic bonds or aliphatic chains (Tissot & Welte, 1984). In the absence of migrated hydrocarbons, kerogen usually accounts for more than 95% of total organic matter in sedimentary rocks (Tyson, 1995). Humins are the early precursor of kerogen in young sediments, insoluble in the soil or marine sediments (e.g., Hayes et al., 2017). The primary distinction between humins and kerogen is the presence of hydrolyzable fractions in humins that diminish with burial (Tissot & Welte, 1984).

An array of physical and chemical analytical techniques provides reliable information on the structure and composition of kerogen. These include elemental analysis (C, H, N, and S), infrared spectroscopy, microscopic examination including palynology, degradative oxidation, and various pyrolysis techniques such as Rock-Eval, hydrous pyrolysis, laser micro-pyrolysis, and Raman spectroscopy (Mendonça Filho et al., 2012). Collectively, four types of kerogen can be identified (Figs. 13 and 14). Type-I kerogen contains many aliphatic chains and a few aromatic nuclei. The elemental H/C ratio is originally high, and the potential for oil and gas generation is also high. This kerogen type is mainly derived from algal lipid or organic matter enriched in lipids by microbial activity. It typifies kerogens of lacustrine source rocks. Type-II kerogen comprises more aromatic and naphthenic rings. The H/C ratio and the oil and gas potential are lower than observed for Type-I kerogen. It is usually related to marine organic matter deposited in reducing environments, with a low to high sulfur content. Pollen grains, spores, cuticles, and marine organic matter are important

components in this type of kerogen, but their assemblages may vary depending on the proximity to the shorelines and source rock age. Type-III kerogen encompasses mostly condensed polyaromatics and oxygenated functional groups, with minor aliphatic chains. The H/C ratio is low, and oil potential is moderate, although this kerogen may still generate abundant gas at greater depths. The O/C ratio is comparatively higher than for the other types of kerogen. It is mostly derived from terrestrial higher plants. Type-IV kerogen is a secondary type of kerogen and contains practically only aromatic components. The organic matter is carbonized by oxidation before or during deposition and possesses no potential to form hydrocarbon source rocks.

Organic matter is subjected to various compositional alterations in the sediment–water interface and during burial. The changes are caused by microbial activities, oxidations, and thermal effects at a later stage (Fig. 15). The maturation of organic matter starts with diagenesis, followed under successively higher burial temperatures by catagenesis, metagenesis, and finally metamorphism in extreme thermal regimes (Horsfield and Rullkotter, 1994).

Diagenesis includes physical, chemical, and microbiological processes occurring within a few hundred meters of overburden. It is a process through which the system approaches equilibrium under shallow burial, low temperature, and pressure, where the sediments consolidate. Catagenesis is the stage where kerogen is converted to petroleum hydrocarbons due to increasing burial and thermal stress. Tectonism and volcanism affect the geothermal regimes by

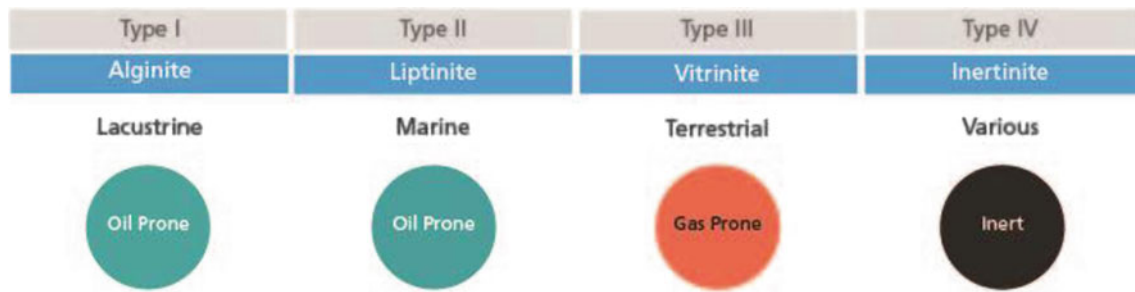


**Fig. 13** Summary of main kerogen types

intensifying catagenesis and altering geothermal gradients. Metagenesis is the last stage of thermal maturation of organic matter at very high temperatures, commonly associated with very deep burial (Tissot & Welte, 1984). At this stage, only methane is generated, and inert carbon and graphite are formed in the rock. Finally, metamorphism is the last thermal evolution stage when the sediments are deeply buried and exposed to very high pressure (>300 MPa) and temperature above 200 °C (Mendonça Filho et al., 2012; Tissot & Welte, 1984). At this stage, the remaining organic carbon converts to inorganic carbon.

## 4 Common Source Rock Depositional Environments

### 4.1 Terrestrial Environments

#### 4.1.1 Mires

Mires are wetlands with heavy vegetation where the water table is near or above topsoil (Rydin et al., 1999). They include swamps, fen, bogs, moors, musky, and peatland (McCabe, 1991). They form peats, which are the primary precursor for coal formation. Mire characteristics are dependent on the development of flora, geographical location, climate, and structural framework (Taylor et al., 1998). The early Carboniferous period witnessed a significant flourishing of vascular plants, which resulted in extensive peat mires for the first time (Glasspool & Scott, 2005). No significant peat development was recorded before Carboniferous.

The water balance between the groundwater and rainfall must exceed evaporation to enhance organic production. The water balance maintains water depth that controls the aerobic versus anaerobic zones (Taylor et al., 1998), a condition that varies seasonally and due to climate changes. Accumulation of peat in mires requires a continued gradual increase in the water table, isolation from seawater flooding, and low fluvial sediment supply (Stach et al., 1982). Mires are classified based on the vegetation types, which depend on the geological age and the abovementioned factors related to water balance. As a result, only a small fraction of the original

organic matter is developed into coal (Taylor et al., 1998). Based on their hydrological system, Taylor et al. (1998) classified mires (Fig. 16) as follows:

1. Topogeneous mires: where peat formation is caused primarily by high water levels. They include marshes, fen, and swamps.
2. Ombrogenous mires: form in high rainfall regions and where the groundwater level is below peat-forming layers. They include bogs.

The topogeneous mires are generally more affluent than the ombrogenous in the inorganic substance and plant nutrients.

#### 4.1.2 Lacustrine

Lakes are landlocked water bodies isolated from marine access (Fig. 17). They constitute less than 0.1% of the hydrosphere, yet they are considered primary source rock depositional environments (Killops & Killops, 2013). They can originate from several geological and hydrological processes such as glacial, tectonic, volcanic, fluvial, coastal, and chemical. These processes generate enclosed depressions and water bodies to form lakes (Branstrator, 2009). The lake size, morphology, climate, and river inputs control the water chemistry, salinity, and thermal regime, as well as organic matter productivity and preservation (Demaison and Moor, 1980; Selly, 1998; Katz, 2012; Killops & Killops, 2013). Best organic primary productivity and preservation occur in density stratified water columns. Water density stratifications occur seasonally when warm water caps cooler water or low salinity water sets on hypersaline water in low-wind areas.

The first condition that favors organic matter productivity and optimum preservation in lakes is water column stratification caused by temperature differences. This process is seasonal and dependent on lake depth and size as well as the sunlight and wind intensity. During the summer season, abundant light and nutrients promote phytoplanktonic bio-productivity and higher oxygen levels in the upper layer, compared to an oxygen-depleted anoxic and more dense water layer underneath. The density contrast inhibits water

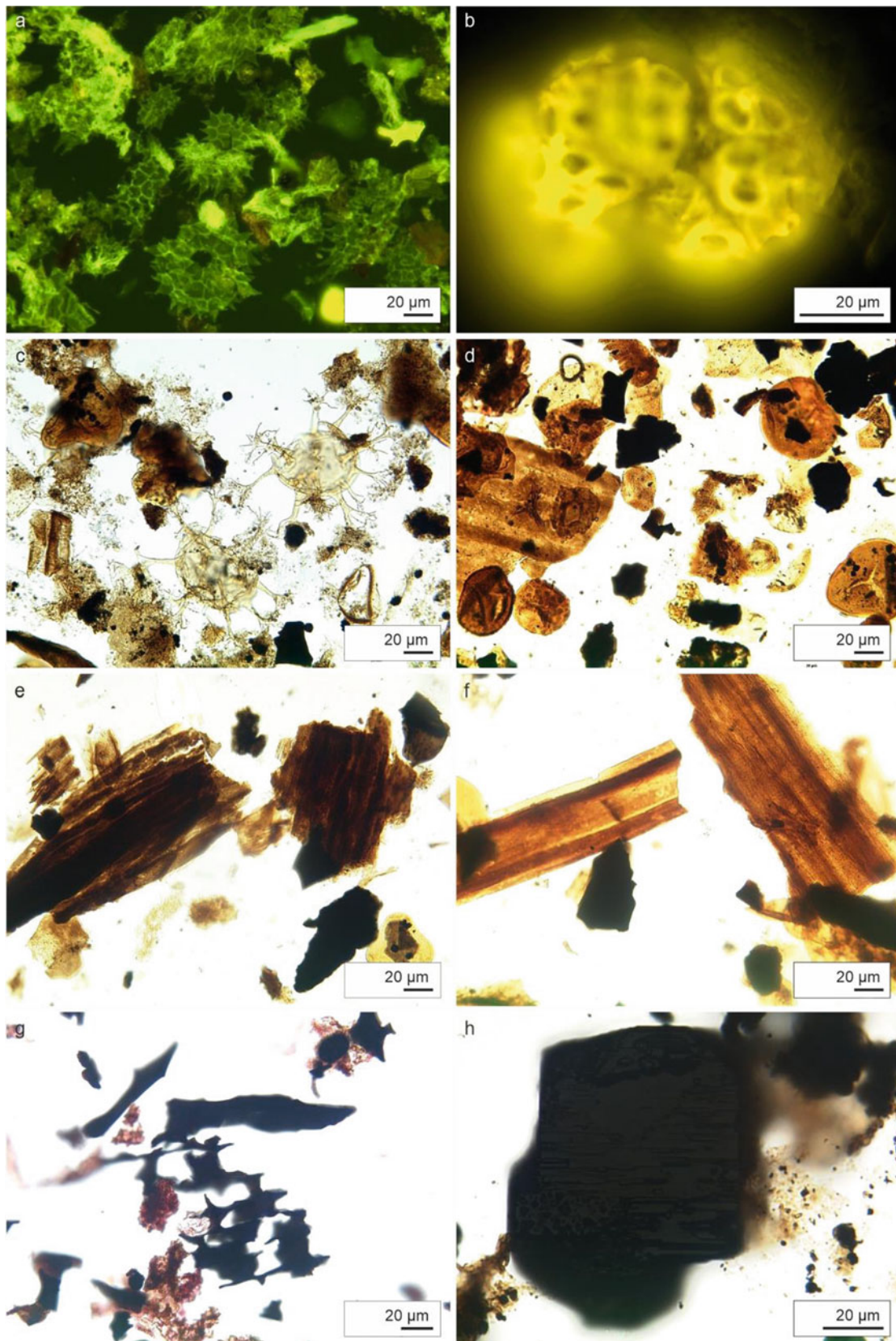
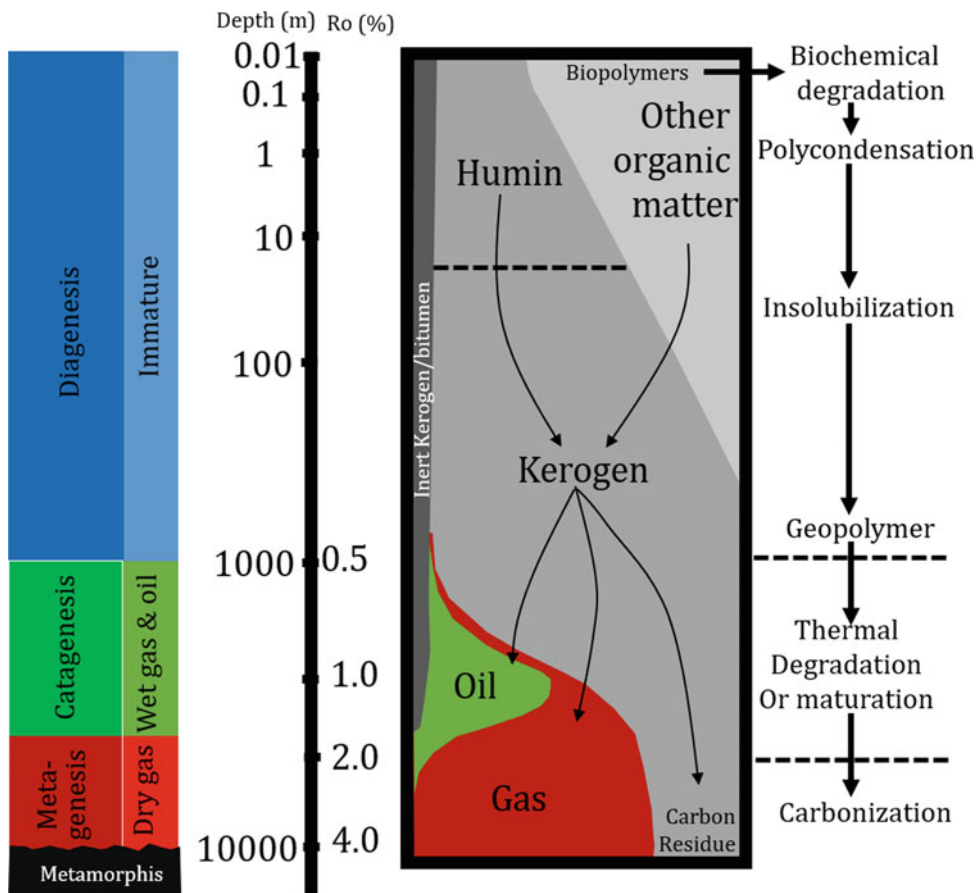


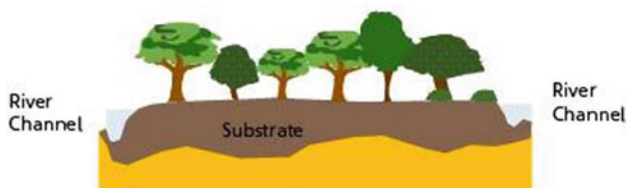
**Fig. 14** Selected images of several kerogen types seen under microscope. **a-b:** Organic matter (*Pediastrum* and *Botryococcus* algae) related to the kerogen Type-I. **c-d:** Organic matter (dinocysts, spores, pollen, and phytoclasts) related to kerogen Type-II. **e-f:** Organic matter

(wood tissues: non-opaque phytoclasts) related to the kerogen Type-III. **g-h:** Organic matter (carbonized and charred wood tissues: opaque phytoclasts) related to the kerogen Type-IV

**Fig. 15** Summary of the kerogen thermal evolutions



**Topogeneous Mires**



**Ombrogenous Mires**

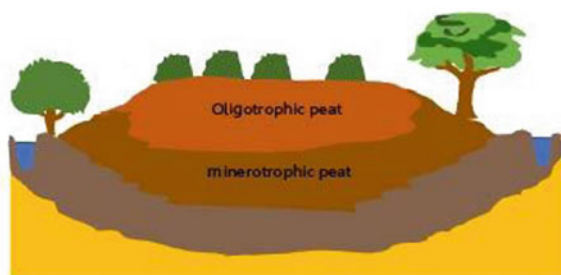


**Fig. 16** Simplified diagram illustrating types of mires

circulation, resulting in water stratification and improved organic preservation (Selly, 1998; Killops & Killops, 2013). Salinity variations also play a significant role in water stratification, as changes in water temperature are sensitive to its salinity.

Differences in salinity cause the second water density stratification condition. It initiates in regions where subsurface saline springs intrude the lakes or where salt diffuses from evaporites at the sediment–water interface (Killops & Killops, 2013).

Based on their access to water flows, lakes are classified as hydrologically open and closed, with some lakes alternating between the two types during their geological histories (Killops & Killops, 2013). They are also classified based on their mixing into amictic lakes, meromictic lakes, and holomictic lakes (Hutchinson & Löffler, 1956). Amictic lakes are usually located in polar regions or high mountains. Their permanent ice cover prevents water mixing. Meromictic lakes, on the other hand, partially mix, especially in the upper layer, while holomictic lakes mix annually at various degrees based on geographic locations. The

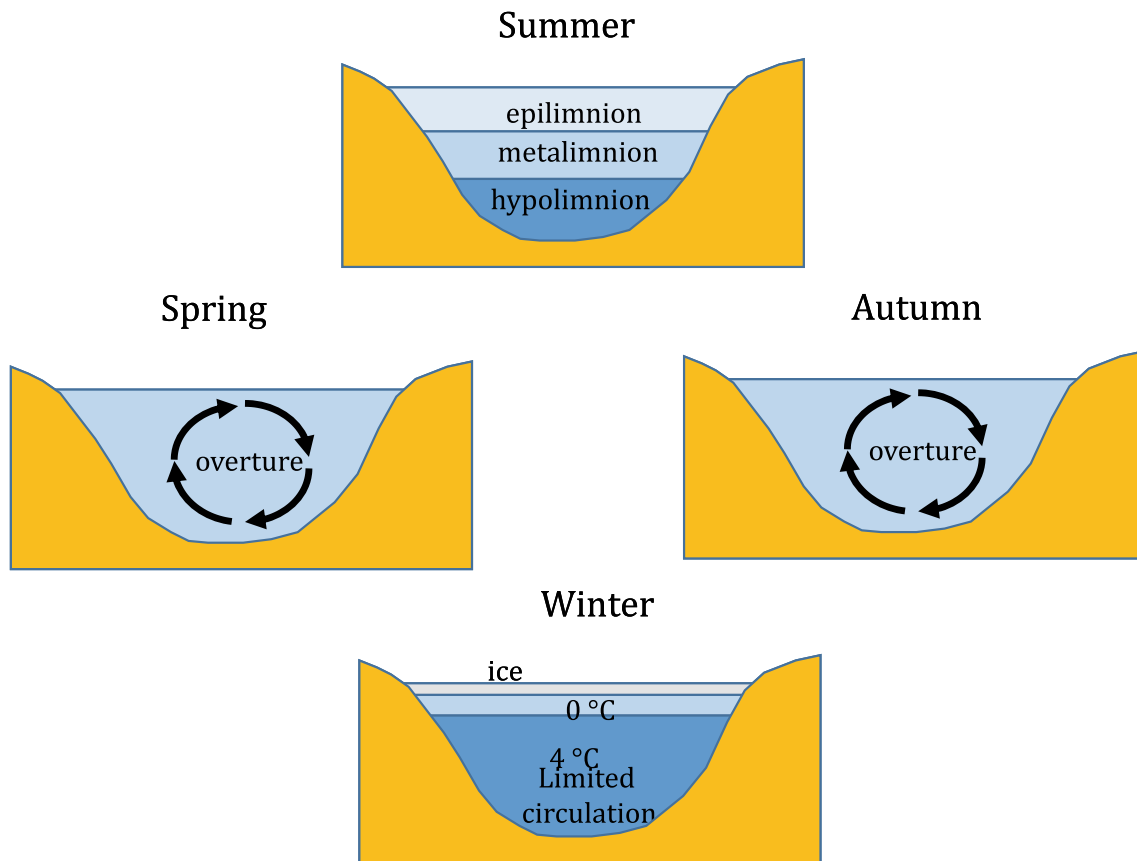


**Fig. 17** Summary of lacustrine hydrological settings in the four seasons, depositional environment follows Killops and Killops (2013)

differences between these types are best described in Hutchinson and Löffler (1956).

The hydrologically closed lakes are usually formed by tectonic activities, volcanism, or glaciation, primarily in open regions where evaporation exceeds precipitation (Langbein, 1961; Waiser & Robarts, 2009). The evaporation and precipitation change substantially, affecting the lake water level and shorelines, which cause sediment reworking. During high lake water levels, water stratification and anoxic conditions prevail in the central part allowing for the deposition of organic-rich layers with carbonate and evaporitic minerals (Killops & Killops, 2013; Waiser & Robarts, 2009).

The hydrologically open lakes receive a balanced water inflow from rivers and precipitation and outflow from evaporation, allowing the shorelines and water level to stabilize (Reading, 1986). Lake sedimentation is controlled by its size, depth, and river inputs that change seasonally. The river inputs are higher during the summer and decrease during the wintertime. Moreover, lakes are usually surrounded by vegetation (Killops & Killops, 2013). Therefore, the nearshore deposits are dominated by siliciclastic deposition and allochthonous organic matter sourced from plants

surrounding the lakes. The siliciclastic inputs diminish toward the more distal or central part, replaced mostly by carbonates enriched with organic matter (Allen & Collinson, 1986). Similar to marine environments, the organic matter richness is greatly affected by sediment dilution. Thus, the richness of organic matter in the nearshore area is less than in the distal area due to the difference in sedimentation rates. Due to the rapid changes in fluvial inputs, the lake sedimentation and organic matter types and richness are remarkably heterogeneous. A common example of source rock deposited in a lacustrine environment is the Green River Formation in the USA.

## 4.2 Marine Environments

Marine source rocks are deposited in four main settings: broad flooded continental shelves (deltaic settings), oxygen-minimum zones along continental shelves, upwelling zones, and rift/barred basins (e.g., Katz, 2012; Kisters et al., 2000; Littke, 1993). The oxygen-minimum zones in aquatic environments are defined as mid-layers deficient in oxygen concentrations compared to the layers below and above in

oceans and lakes. They persist over millions of km<sup>2</sup> and over long periods of geological time (Diaz et al., 2013). They are created by the deposition of organic matter, where oxygen can, in some instances, be reduced to complete anoxia.

#### 4.2.1 Deltaic Settings

Deltas represent transitional depositional environments between completely terrestrial and completely marine and are considered some of the favorable settings to accommodate organic-rich sediments. Several factors control the delta formation and characteristics, including climate, sediment and water discharge, wave intensities, tides, and tectonic regime (Boggs et al., 2006; Allen and Allen, 2013). There are several criteria to classify deltas, yet in this chapter, the classification of Galloway (1975) is adopted. He classified deltas based on their front regimes into (1) wave dominated, (2) tide dominated, and (3) fluvial dominated.

The wave-dominated deltas are characterized by their destructive nature, as wave force inhibits fine-grained sedimentation and casts the shorelines to form a cusped shape (Nienhuis et al., 2015). This high-energy type of delta does not commonly host petroleum source rocks.

On the other hand, the tide- and fluvial-dominated delta types are characterized by their constructive nature and their tendency to host prolific source rock beds (Allen and Allen, 2013). Tide-dominated deltas occur on a large scale (hundreds of km) with cyclic variant energy sediments (Goodbred & Saito, 2012).

The depositional characteristics of the deltaic environments classify deltaic source rocks into offshore and onshore types. The onshore source rocks are mostly peat and mire deposits during transgressive system tract events behind the landward stepping shorelines (Kosters et al., 2000). The offshore deltaic source rocks are primarily siliciclastics and characterized by low to good total organic carbon values that range from 0.5 to 3.0% with dominated kerogen Types-III/IV and minor marine organic matter input. The kerogen in deltaic systems is mostly transported with high proportions of higher plant tissues (allochthonous) and aquatic algae (autochthonous) (Bustin, 1988; Ghassal et al., 2016a; Tissot & Welte, 1984). Due to the high-sedimentation rates and oxygen-level fluctuations, the organic matter richness and preservation are variably reduced. Examples of deltaic source rocks include the Mississippi, Niger, and Ganges River deltas, representing fluvial-dominated, wave-dominated, and tide-dominated systems, respectively.

Rivers transport terrestrial organic matter such as vitrinite, inertinite, coal particles, and freshwater algae as well as pollen and spores and other cuticles and plant tissues to coastal areas where marine algae deposit. River discharges and sea-level changes control the relative proportions of terrestrial and marine organic inputs. In addition, the intensity of water circulation modifies the oxygen level, resulting

in partial oxidation of organic matter. These conditions vanish in more distal settings, as discussed below.

#### 4.2.2 Marine Continental Shelves

Marine continental shelves are some of the most favorable depositional environments for source rock development (Fig. 18a). The source rocks are deposited over a wide area depending on the size of the shelf and the OMZ. The source rock organofacies vary from proximal to distal setting. The source rocks in the proximal settings are rich in terrestrial organic matter and siliciclastic minerals. Further to more distal settings, the carbonate to siliciclastic proportions increase with more marine organic matter. The most distal settings are rich in carbonate contents with high sulfur-rich kerogen (Ghassal et al., 2018). A common source rock deposited in a continental shelf environment is the *Posidonia* Shale in Germany.

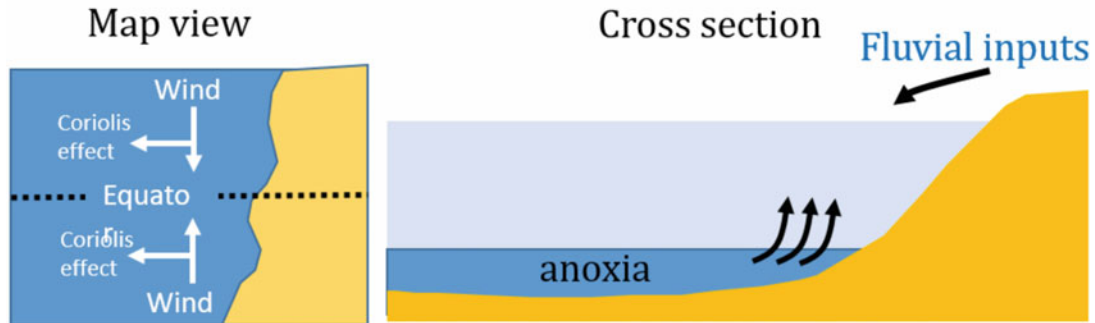
#### 4.2.3 Upwelling Zones

About half of the world's organic-rich source rocks were formed in upwelling zone conditions (Parrish, 1987). This is due to the higher biological activities that surpass the productivity encountered in regular shelves (Katz, 2012; Koblenz-Mishke et al., 1970). During an elevated greenhouse warm climate, the warm winds move the marine coastal waters toward the ocean, and deep nutrient-rich waters rise and replace them, which intensify bioproductivity. Upwelling activities decrease during cold climates (Bakun, 1990; Parrish, 1987). Moreover, the upwelling zones mainly prevail in the western continental margins due to wind directions and the Coriolis effect caused by the Earth's rotation affecting mid-latitude zones (Fig. 18b) (e.g., Katz, 2012; Ghassal et al., 2016b). The prominent bioproductivity increases the amount of deposited organic matter and reduces the bottom-water oxygen levels, which leads to enhanced organic matter preservation (Katz, 2012; Littke et al., 1997). The spatial distribution of preserved organic matter depends on seabed bathymetry. The source rocks formed in upwelling zones are dominated by liptinitic kerogen. The dilution of terrestrial and reworked organic matter and sediment sourced by fluvial discharges are usually reduced relative to purely marine organic matter. The cold upwelling water reduces the air humidity in the shoreline vicinity, inhibiting fluvial runoff (Robinson & Davies, 2016). A common example of source rock deposited in an upwelling setting is Tarfaya Cenomanian/Turonian marlstone section in Morocco.

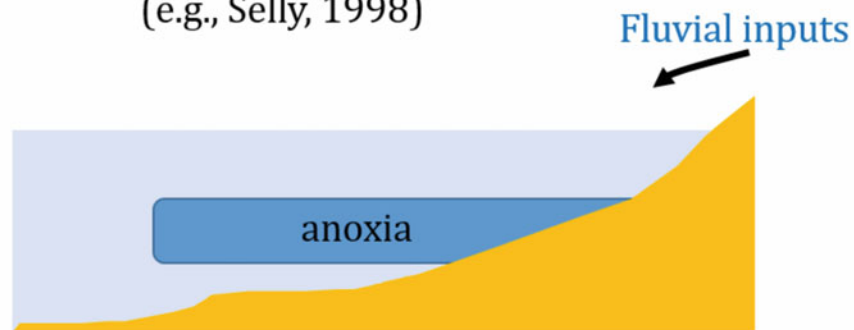
#### 4.2.4 Restricted Marine Basins

Silled or barred basins are depressions on the seafloor where water circulation is restricted (Fig. 18c). This restriction makes them good areas to trap nutrients, intensifying the bioproductivity and oxygen depletion and consequently

**a. Upwelling Depositional Environment**  
(e.g., Selly, 1998)

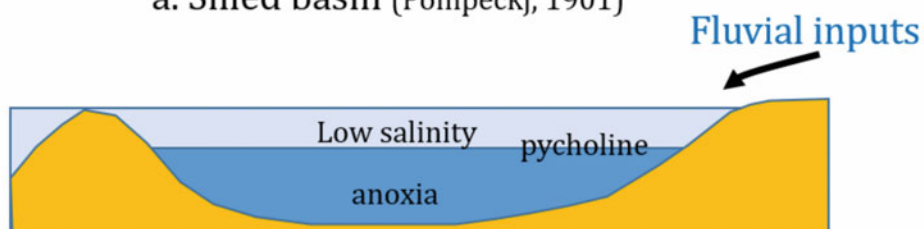


**b. Continental Shelf Depositional Environment**  
(e.g., Selly, 1998)



**c. Restricted Marine Depositional Environment**

**a. Silled basin (Pompeckj, 1901)**



**b. Irregular bathymetry (Hallam & Bradshaw, 1979)**

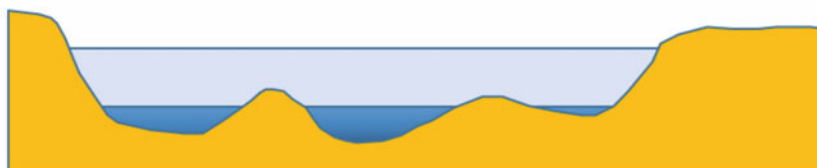


**Fig. 18** Summary of the various marine settings, depositional environment in **a**) and **b**) follow Selly (1998), **c**) follow Hallam and Bradshaw (1979) and Pompeckj (1901)

increasing the organic matter deposition and preservation (e.g., Allen and Allen, 2013; Selley, 1998). The aquatic organic matter here is expected to be less diversified compared to open marine settings. Due to the shallow nature and proximity to shorelines, these settings receive fair terrigenous inputs. The richness of the preserved organic matter is highly variable due to the rapid fluctuation in sea level and turbidity of the water column. Source rock development in these settings is caused by thermal density or salinity stratifications.

## References

- Al-Hajeri, M., Sauerer, B., Furmann, A., Amer, A., Akbar, H., & Abdallah, W. (2020). Maturity estimation for Type II-S kerogen using Raman spectroscopy—A case study from the Najmah and Makhul Formations in Kuwait. *International Journal of Coal Geology*, 217, 103317.
- Allen, P. A., & Allen, J. R. (2013). Basin analysis: Principles and application to petroleum play assessment. Wiley. 632 p.
- Allen, P. A., & Collinson, J. D. (1986). Lakes. In H. G. Reading (Ed.), *Sedimentary environments and facies* (pp. 63–94). Blackwell Scientific Publications, Oxford.
- Bakun, A. (1990). Global climate change and intensification of coastal ocean upwelling. *Science*, 247(4939), 198–201.
- Bernhard, A. (2010). The nitrogen cycle: Processes, players, and human impact. *Nature Education Knowledge*, 3(10), 25.
- Boggs, D. A., Boggs, G. S., Eliot, L., & Knott, B. (2006). Regional patterns of salt lake morphology in the lower Yarra Yarra drainage system of Western Australia. *Journal of Arid Environments*, 64(1), 97–115.
- Branstrator, D. K. (2009). Origins of types of lake basins. In *Encyclopedia of inland waters* (pp. 624–613). Elsevier Inc.
- Brimblecombe, P. (2003). 8.14—The global sulfur cycle. *Treatise on Geochemistry*, 8, 645–682.
- Brusseau M. L. (2019). Ecosystems and ecosystem services (Chap. 6). In *Environmental and Pollution Science* (3rd ed., pp. 89–102).
- Bustin, R. M. (1988). Sedimentology and characteristics of dispersed organic matter in Tertiary Niger Delta: Origin of source rocks in a deltaic environment. *AAPG Bulletin*, 72(3), 277–298.
- Canfield, D. E. (1994). Factors influencing organic carbon preservation in marine sediments. *Chemical Geology*, 114(3–4), 315–329.
- Canfield, D. E., van Zuilen, M. A., Nabhan, S., Bjerrum, C. J., Zhang, S., Wang, H., & Wang, X. (2021). Petrographic carbon in ancient sediments constrains Proterozoic Era atmospheric oxygen levels. *Proceedings of the National Academy of Sciences*, 118(23).
- De Leeuw, J. W., & Largeau, C. (1993). A review of macromolecular organic compounds that comprise living organisms and their role in kerogen, coal, and petroleum formation. In *Organic Geochemistry* (pp. 23–72).
- Dean, W. E., & Gorham, E. (1998). Magnitude and significance of carbon burial in lakes, reservoirs, and peatlands. *Geology*, 26(6), 535–538.
- Demaison, G. J., & Moore, G. T. (1980). Anoxic environments and oil source bed genesis. *AAPG Bulletin*, 64(8), 1179–1209.
- Diaz, R. J., Eriksson-Hägg, H., & Rosenberg, R. (2013). Hypoxia (Chap. 4). In *Managing Ocean Environments in a Changing Climate. Sustainability and Economic Perspectives*, (pp. 67–96). Elsevier.
- Dieckmann, V., Horsfield, B., & Schenk, H. J. (2000). Heating rate dependency of petroleum-forming reactions: Implications for compositional kinetic predictions. *Organic Geochemistry*, 31(12), 1333–1348.
- Fenchel, T., King, G. M., & Blackburn, T. H. (2012). The water column. In *Bacterial Biogeochemistry* (pp. 67–88).
- Gaedke, U. (2021). Trophic dynamics and food webs in aquatic ecosystems. *Reference Module in Earth Systems and Environmental Sciences*. <https://doi.org/10.1016/B978-0-12-819166-8.00009-8>
- Galloway, W. E. (1975). Process framework for describing the morphologic and stratigraphic evolution of deltaic depositional systems. In M. L. Broussard (Ed.), *Deltas: Models for Exploration*. Houston Geological Society; 87–98.
- Ghassal, B. I., El Atfy, H., Sachse, V., & Littke, R. (2016a). Source Rock Potential of the Middle Jurassic to Middle Pliocene, Onshore Nile Delta Basin. *Egypt. Arabian Journal of Geosciences*, 9, 744.
- Ghassal, B. I., Littke, R., Sachse, V., Sindern, S., & Schwarzbauer, J. (2016b). Depositional environment and source rock potential of upper Albian to Turonian sedimentary rocks of the Tarfaya Basin, Southwest Morocco. *Geologica Acta*, 14, 419–441.
- Ghassal, B. I. H., Littke, R., & Sindern, S. (2017). *Source rock depositional processes in different marine settings: examples from North African basins* (No. RWTH-2017-06977). Fachgruppe für Geowissenschaften und Geographie.
- Ghassal, B. I., Littke, R., El Atfy, H., Sindern, S., Scholtysik, G., El Beialy, S., & El Khoriby, E. (2018). Source rock potential and depositional environment of Upper Cretaceous sedimentary rocks, Abu Gharadig Basin, Western Desert, Egypt: An integrated palynological, organic and inorganic geochemical study. *International Journal of Coal Geology*, 186, 14–40.
- Glasspool, I. J., & Scott, A. C. (2005). An early Carboniferous (Mississippian), Tournaisian, megaspore assemblage from Three Mile Plains, Nova Scotia, Canada. *Review of Palaeobotany and Palynology*, 134, 219–236.
- Goodbred, S. L., & Saito, Y. (2012). Tide-dominated deltas. *Principles of tidal sedimentology* (pp. 129–149). Springer.
- Gregory, T. R., & DeSalle, R. (2005). Comparative genomics in prokaryotes. In T. R. Gregory (Ed.), *The Evolution of the Genome* (pp. 585–675). Elsevier.
- Hallam, A., & Bradshaw, M. J. (1979). Bituminous shales and oolithic ironstones as indicators of transgressions and regressions. *Geological Society of London Journal*, 136, 157–164.
- Hayes, M. H., Mylotte, R., & Swift, R. S. (2017). Humins: Its composition and importance in soil organic matter. *Advances in Agronomy*, 143, 47–138.
- Hayes, W. (2018). Genetics as a tool to understand structure and function. In *Molecular Biology of Symbiotic Nitrogen Fixation* (pp. 1–11). CRC Press.
- Henrichs, S. M. (1992). Early diagenesis of organic matter in marine sediments: Progress and perplexity. *Marine Chemistry*, 39(1–3), 119–149.
- Horsfield, B., & Rullkötter J. (1994). Diagenesis, catagenesis and metagenesis. In L. Magoon, W. G. Dow (Eds.), *The Petroleum System from Source to Trap* (pp. 189–199). AAPG Memoir 60.
- Hutchinson, G. E., & Löffler, H. (1956). The thermal classification of lakes. *Proceedings of the National Academy of Sciences of the United States of America*, 42(2), 84.
- Inan, S., Henderson, S., & Qathami, S. (2017). Oxidation Tmax: A new thermal maturity indicator for hydrocarbon source rocks. *Organic Geochemistry*, 113, 254–261.
- Irwin, J. A. (2020). Overview of extremophiles and their food and medical applications (Chap. 6). In *Physiological and Biotechnological Aspects of Extremophiles* (pp. 65–87).
- Jørgensen, B. B., Findlay, A. J., & Pellerin, A. (2019). The biogeochemical sulfur cycle of marine sediments. *Frontiers in Microbiology*, 10, 849.



- Katz, B. (2012). *Petroleum source rocks* (p. 325). Springer Science & Business Media.
- Killops, S. D., Killops, V. J. (2013). *Introduction to Organic Geochemistry* (p. 408). Wiley.
- Koblentz-Mishke, O. J., Volkovinsky, V. V., & Kabanova, J. G. (1970). Plankton primary production of the World Ocean. In W. S. Wooster (Ed.), *Scientific Exploration of the South Pacific* (pp. 183–193).
- Kosters, E. C., VanderZwaan, G. J., & Jorissen, F. J. (2000). Production, preservation and prediction of source-rock facies in deltaic settings. *International Journal of Coal Geology*, 43, 13–26.
- Langbein, W. B. (1961). Salinity and hydrology of closed lakes: A study of the long-term balance between input and loss of salts in closed lakes (Vol. 412). US Government Printing Office.
- Li, Y. F., Lu, H., Zhang, Y., Zhang, X. L., Shao, D. Y., Yan, J. P., & Zhang, T. W. (2015). U-Mo covariation in marine shales of Wufeng-Longmaxi Formations in Sichuan Basin, China and its implication for identification of watermass restriction. *Geochimica (beijing)*, 44(2), 109–116.
- Littke, R. (1993). Migration of oil and gas coals. In *Deposition, Diagenesis and Weathering of Organic Matter-Rich Sediments* (pp. 135–169).
- Littke, R., Baker, D. R., & Rullkötter, J. (1997). Deposition of petroleum source rocks. In D. H. Welte, B. Horsfield, & D. R. Baker (Eds.), *Petroleum and Basin Evolution* (pp. 271–333). Springer.
- Macdonald, C. A., Delgado-Baquerizo, M., Reay, D. S., Hicks, L. C., & Singh, B. K. (2018). Soil nutrients and soil carbon storage: Modulators and mechanisms (Chap. 6). In *Soil Carbon Storage. Modulators, Mechanisms and Modeling* (pp. 167–205).
- Maende, A., Pepper, A., Jarvie, D., & Weldon, D. (2017). Advanced pyrolysis data and interpretation methods to identify unconventional reservoir sweet spots in fluid phase saturation and fluid properties (API gravity) from drill cuttings and cores. *Petroleum Geology*, 12(4), 417–452.
- Magalon, A., Arias-cartin, R., & Walburger, A. (2012). Supramolecular organization in prokaryotic respiratory systems. In R. K. Poole (Ed.), *Advances in Microbial Physiology* (Vol. 61, pp. 217–266). Elsevier.
- Mayer, L. M. (1994). Surface area control of organic carbon accumulation in continental shelf sediments. *Geochimica Et Cosmochimica Acta*, 58(4), 1271–1284.
- McCabe, P. J. (1991). Tectonic controls on coal accumulation. *Bulletin De La Societe Geologique De France*, 162(2), 277–282.
- Mendonça Filho, J. G., Menezes, T. R., Mendonça, J. O., de Oliveira, A. D., da Silva, T. F., Rondon, N. F., & da Silva, F. S. (2012). Organic facies: Palynofacies and organic geochemistry approaches. In *Geochemistry* (pp. 211–248). [www.intechopen.com](http://www.intechopen.com). <https://doi.org/10.5772/47928>
- Nienhuis, J. H., Ashton, A. D., & Giosan, L. (2015). What makes a delta wave-dominated? *Geology*, 43(6), 511–514.
- Parker, J. (2001). Bacteria. In *Encyclopedia of Genetics* (pp. 146–151).
- Parrish, J. T. (1987). Palaeo-upwelling and the distribution of organic-rich rocks. *Geological Society, London, Special Publications*, 26(1), 199–205.
- Pepper, A. S., & Corvi, P. J. (1995). Simple kinetic models of petroleum formation. Part I: Oil and gas generation from kerogen. *Marine and Petroleum Geology*, 12, 291–319.
- Piper, D. Z., & Calvert, S. E. (2009). A marine biogeochemical perspective on black shale deposition. *Earth-Science Reviews*, 95(1–2), 63–96.
- Pompeckj, J. F. (1901). *Der Jura Zwischen Regensburg Und Regensburg: Geognostische Jahreshefte*, 14, 139–220.
- Reading, H. G. (1986). Sedimentary Environments and Facies (p. 615).
- Ritz, K. (2005). Fungi. In *Encyclopedia of Soils in the Environment* (pp. 110–119).
- Robinson, L., & Davies, A. (2016). Upwelling zones as controls on source rock deposition—is the present the key to the past? *Neflex Exploration Insights magazine (March Edition)*, 15.
- Romero-Sarmiento, M. F., Ducros, M., Carpentier, B., Lorant, F., Cacas, M. C., Pegaz-Fiornet, S., Wolfa, S., Rohaisa, S., & Moretti, I. (2013). Quantitative evaluation of TOC, organic porosity and gas retention distribution in a gas shale play using petroleum system modeling: Application to the Mississippian Barnett Shale. *Marine and Petroleum Geology*, 45, 315–330.
- Ruttenberg, K. C. (2003). 8.13 - The Global Phosphorus Cycle. *Treatise on Geochemistry*, 8, 585–643.
- Rydin, H., Sjörs, H., & Löfroth, M. (1999). 7. Mires. In *Swedish Plant Geography, Acta Phytogeographica Suecica* (pp. 91–112). Svenska Västgeografiska Sällskapet, Uppsala.
- Sage, R. F. (2008). Autotrophs. In *Encyclopedia of Ecology* (pp. 291–300).
- Selley, R. C. (1998). *Elements of petroleum geology* (2nd ed., p. 470). Academic Press.
- Simon, J., & Kroneck, P. M. (2013). Microbial sulfite respiration. *Advances in Microbial Physiology*, 62, 45–117.
- Sorokin, Yu. I. (1966). On the trophic role of chemosynthesis and bacterial biosynthesis in water bodies., In C. R. Goldman (Ed.), *Primary productivity in aquatic environments* (pp. 187–250). Univ. California Press.
- Stach, E., Mackowsky, M. T., Teichmüller, M., Taylor, G. H., Chandra, D., & Teichmüller, R. (1982). *Coal petrology*. Gebrüder Borntraeger.
- Suess, E. (1980). Particulate organic carbon flux in the oceans—surface productivity and oxygen utilization. *Nature*, 288(5788), 260–263.
- Summons, R. E. (1993). Biogeochemical cycles. In *Organic Geochemistry* (pp. 3–21). Springer.
- Taylor, G. H., Teichmüller, M., Davis, A. C. F. K., Diessel, C. F. K., Littke, R., & Robert, P. (1998). *Organic petrology*.
- Tissot, B., & Welte, D. H. (1984). *Petroleum Formation and Occurrence* (p. 699). Springer.
- Tyson, R. V. (1995). *Sedimentary organic Matter—Organic Facies and Palynofacies* (p. 615). Chapman and Hall.
- Vallero, D. (2014). *Fundamentals of Air Pollution* (p. 996). Academic Press, Technology & Engineering.
- Waiser, M. J., & Robarts, R. D. (2009). Saline inland waters. In: Gene E. Likens, (Editor) *Encyclopedia of Inland Waters*. volume 2, pp. 634–644 Oxford: Elsevier.
- Wakeham, S. G., & Lee, C. (1993). Production, transport, and alteration of particulate organic matter in the marine water column. In *Organic Geochemistry* (pp. 145–169). Springer.
- Wigley, T. M., & Schimel, D. S. (Eds.). (2005). *The carbon cycle* (Vol. 6). Cambridge University Press. 312 p.
- Woese, C. R., Kandler, O., & Wheelis, M. L. (1990). Towards a natural system of organisms: Proposal for the domains Archaea, Bacteria, and Eucarya. *Proceedings of the National Academy of Sciences of the United States of America*, 87, 4576–4579.
- Zavarzin, G. A. (2008). A planet of bacteria. *Herald of the Russian Academy of Sciences*, 78, 144–151.

## Methods



# Practical Guide for Petroleum Source Rock Interpretation

Bandar I. Ghassal, Sattam S. Mutairi, and Haytham El Atfy 

## Abstract

The progressive increase in the demand for unconventional resource assessments such as gas and oil shale, as well as shale gas and oil plays in the last two decades, boosted the development of source rock characterization methods and techniques. Additionally, it advanced more research in geochemistry, palynology, and organic microscopy. The interpretation of source rocks appears straightforward; therefore, many industry professionals and researchers make common mistakes when interpreting source rocks. These are repeatedly observed, especially in kerogen typing, thermal maturity assessments, and disregarding the drilling-fluid contamination effects. This chapter addresses the leading causes of these interpretation errors and provides a detailed review of sampling techniques and analytical methods with their advantages and limitations. The methods mainly characterize source rocks for their richness, quality, and thermal maturity. The approaches include thermal oxidation, pyrolysis, organic microscopy, molecular geochemistry (e.g., biomarkers), isotope geochemistry (including mud gas isotopes), inorganic geochemistry, palynology, and other advanced techniques.

B. I. Ghassal (✉) · S. S. Mutairi  
Saudi Aramco, Dhahran, Saudi Arabia  
e-mail: [Bandar.ghassal@aramco.com](mailto:Bandar.ghassal@aramco.com)

S. S. Mutairi  
e-mail: [sattam.mutairi.4@aramco.com](mailto:sattam.mutairi.4@aramco.com)

H. El Atfy  
Department of Geosciences, University of Tübingen,  
72076 Tübingen, Germany  
e-mail: [El-Atfy@daad-alumni.de](mailto:El-Atfy@daad-alumni.de)

H. El Atfy  
Geology Department, Faculty of Science,  
Mansoura University, Mansoura, 35516, Egypt

## 1 Introduction

Petroleum source rock characterization methods have witnessed significant developments in the last 50 years, especially in the last two decades. This is due to the international unconventional resource exploration boom, the easy access to public data, and progressive technological developments.

The interpretation of source rock seems straightforward; thus, many researchers and industry professionals fall into interpretation common mistakes. These are observed in numerous peer-reviewed articles and conference proceedings, especially in kerogen typing, thermal maturity evaluations, and disregarding effects of drilling fluid contamination, and sulfur effect. Some of these erroneous interpretations occur due to (1) the utilization of unsuitable interpretation schemes for sample sets, (2) using insufficient methods to reach conclusions, (3) unawareness of the limitations of each technique, and (4) the unfamiliarity of sampling pitfalls. This and the incremental demand for source rock assessments necessitate a comprehensive interpretation guide. This is because the interpretations of the fundamental source rock analyzes are the bases for all subsequent unconventional (and conventional) play developments. The previous chapter discussed the factors controlling the source rock development, richness, organic matter types, thermal maturity, and distribution. This chapter presents a practical source rock characterization workflow that can guide researchers and industry professionals toward optimum evaluations. The discussion elaborates on the most prevalent geochemical and optical methods, their limitations, and how to interpret their parameters.

## 2 Source Rock Sampling

A correct sampling strategy is a critical step toward accurate source rock assessment. The selection strategy depends on the study objectives, sample type, and the size of the sampling program. For example, source rocks are obtained either

for resource assessment or research purposes. Dense and systematic sampling is essential to ascertain the thickness and distribution of source rock richness, quality, and thermal maturity. In contrast, sampling for research purposes requires specifying types and intervals based on the study objectives. For example, if the research aims to investigate the source rock evolution with time, a detailed sampling is required. But, if the aim is to investigate the kinetics of different organofacies then a selective sampling program is required. Prior knowledge of the depositional environments and petrophysical and well data is very beneficial for narrowing down the scope of investigations.

There are three main types of samples: outcrop, core, and drilling cuttings. The advantages and disadvantages of each type are discussed below and summarized in Table 1.

Outcrop sampling has many benefits, as the source rock layers can be easily traced and sampled in large areas. Moreover, the geological relationships with adjacent layers are easily observed. The most significant advantage of the outcrop sample is that they can be collected in large amounts and on frequent trips, as well as being autochthonous and free of contamination commonly associated with drilling, such as reworking, caving, and drilling mud. On the other hand, outcrop samples have several shortcomings, such as exposure to geological weathering and oxidation, human activity pollution, and, in some cases, access difficulties.

Drillcore sampling is the best type to investigate source rock potential, as it affords a good understanding of the source rock spatial distributions and thicknesses. Cores cannot be sampled in large amounts, and once consumed, they cannot be resampled again. Drilling fluids heavily influence the core sample quality. In general, water-based mud fluids have a negligible effect on the samples if some polymers are avoided.

On the other hand, oil-based drilling fluids significantly overprint source rock geochemical characteristics. They

invade the samples and, in some cases, cannot be removed, even with strong organic solvents.

Cuttings samples are the most commonly and widely available sample types, mainly due to the lower cost of drilling and recovery. However, they are less favorable than the other sample types. Depending on the mud logging speed, each sample weighs approximately 15 g collected from an interval of 10 to 30 feet. This practice significantly reduces the sampling resolution, making accurate depth assignment and geological interpretation elusive, especially for thin and interbedded layers. There are two techniques of cuttings sampling in the lab: (1) handpicking, where only the dark grains are selected (2) bulk sampling, taking a sample from the whole bag. Drilling fluids and additives pose more severe challenges to the sample quality compared to drillcore samples.

### 3 Source Rock Characterization Methods

Source rocks are assessed for their organic richness, organic matter types, thermal maturity, and depositional environments. Characterization methods vary depending on the needed amount of details. Some methods provide direct measurements or results, while others are utilized to make broad interpretations. As with any geochemical study, conclusive understanding is only possible when combining at least three of the following techniques.

#### 3.1 Thermal Oxidation

Several methods use oxidation to measure the total organic carbon (TOC) content, one example is discussed here. The total inorganic carbon (TIC) content is usually measured with the same method and the same run.

**Table 1** Summary of advantages and disadvantages of different source rock sample types

Sample type	Advantages	Disadvantages
Outcrop	<ul style="list-style-type: none"> <li>Stratigraphic relationships can be visualized on large scales</li> <li>Can be collected in a large amount</li> <li>Can be resampled frequently</li> </ul>	<ul style="list-style-type: none"> <li>Exposure to geological weathering</li> <li>Exposure to human pollution</li> <li>Access difficulties in some cases</li> </ul>
Drillcore	<ul style="list-style-type: none"> <li>Provide a good understanding of vertical and aerial source rock quality and distribution in the subsurface with excellent quality even at very deep sections</li> <li>It can be preserved for tens of years</li> </ul>	<ul style="list-style-type: none"> <li>Vulnerable to drilling fluid contamination</li> <li>Cannot be resamples</li> <li>Sampled as very small amounts</li> </ul>
Drill cuttings	<ul style="list-style-type: none"> <li>Low cost compared to core samples</li> <li>Available for the entire od thick sections of wells</li> </ul>	<ul style="list-style-type: none"> <li>Highly vulnerable to drilling additives contamination</li> <li>Each sample represents a thick interval (&gt;10 m)</li> </ul>

First, tens of milligrams from a powdered sample passing through the 60-mesh size (based on instrument calibration) are transferred into a crucible. The samples are then combusted in an oxidation oven at 550 °C for 3 min to measure the TOC. Then the sample is combusted at 1100 °C to calculate the TIC. The method is highly accurate; however, it has some limitations. The presence of some carbonate minerals that oxidize at a similar temperature as organic matter, such as siderite, causes analytical errors as they deceptively increase the apparent TOC values. Thus, inspecting the oxidation curve is essential to the quality control and quality assurance processes. In addition, reviewing the mineralogical data is required. These steps are critical when evaluating source rocks deposited in environments that produce siderite.

### 3.2 Pyrolysis Methods

There are several pyrolysis methods of source rock characterization that can be classified into two categories. The first category includes programmed pyrolysis methods with flame ionization (FID) and infrared (IR) detectors. They are used to provide a robust and rapid assessment of hydrocarbon richness and thermal maturity. Rock–Eval is the most common source rock evaluation method (Espitalié et al., 1985; Peters, 1986). More recent methods gained attention: the IFPEN Shale Play Method (Romero-Sarmiento et al., 2016) and the Petroleum System Method PSM (Maende et al., 2017). The sample preparation methods are very similar to the thermal oxidation method (e.g., Ghassal et al., 2018).

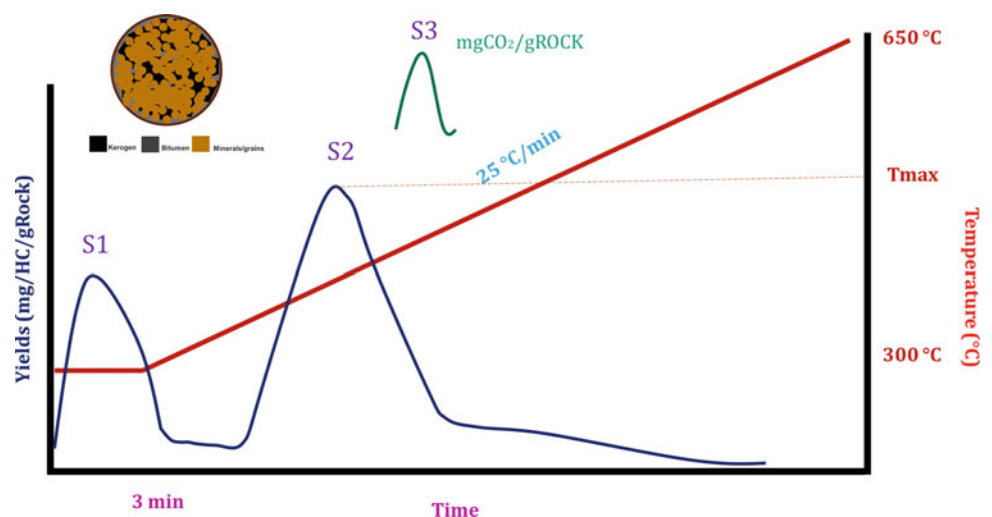
The Rock–Eval method pyrolyzes the rock samples starting at 300 °C for 3 min to yield the first peak (S1) detected by the FID. Then, the temperature increases at a rate of 25 °C/min to reach 650 °C. During this temperature ramp, two peaks are detected. The S2 peak measures the

amount of thermally cracked hydrocarbons by FID. During the same temperature ramp between 300 and 390 °C, the released CO<sub>2</sub> is detected by the IR detector as an S3 peak (Fig. 1). The temperature of the maximum S2 peak is termed T<sub>max</sub>. These parameters are used to calculate additional values in combination with TOC. A summary of these parameters is provided in Table 2.

The IFPEN Shale Play method by Romero-Sarmiento et al. (2016) provides a new parameter to quantify absorbed gas in shale gas resource assessment. The method provides higher resolution results of the free hydrocarbons compared to the conventional Rock–Eval method. The rock is pyrolyzed starting from 100 °C, with temperature increasing at 25 °C/min to reach 200 °C and plateau for 3 min to generate the first free-hydrocarbon peak (Sh0). Then the temperature increases at the same previous rate to reach 350 °C and stabilizes for three 3 min to yield (Sh1) peak. The temperature increases to 650 °C at the previous rate to generate the Sh2 peak. The first two peaks represent the thermovaporization products of the free hydrocarbons. However, the Sh2 peak represents the pyrolyzable portions of the remaining hydrocarbons (e.g., kerogen or pyrobitumen). The Shale Play Method parameters and a sample of the pyrogram are summarized in Fig. 2.

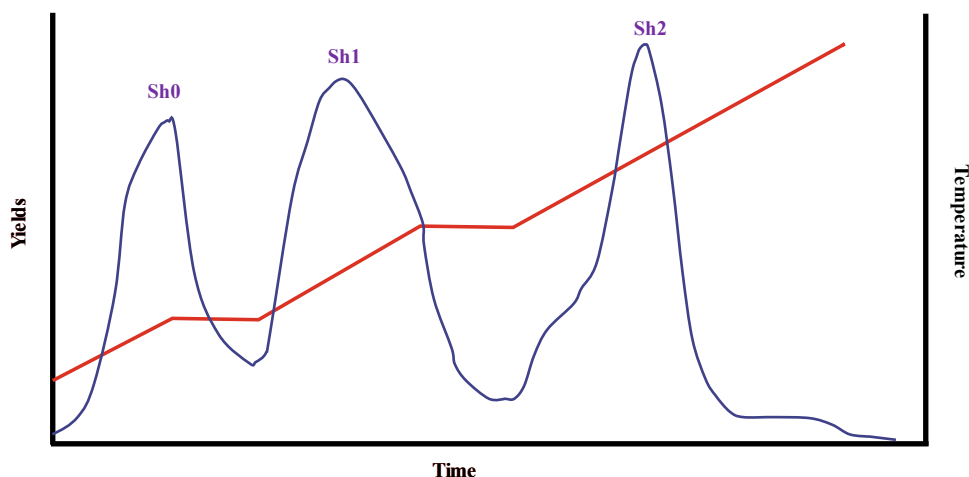
The petroleum system method (PAM-HAWK) provides a higher resolution assessment of hydrocarbons and classifies them based on chemical grouping. Five different peaks released at five stepwise pyrolysis stages with a temperature ramp of 25 °C/min distinguish this method, which is instrumental in assessing oil shale plays and oil-mature source rocks. The first four peaks (Oil-1 to Oil-4) separate the free hydrocarbons into four petroleum fractions, which are C<sub>4</sub>–C<sub>5</sub>, C<sub>6</sub>–C<sub>10</sub>, C<sub>11</sub>–C<sub>19</sub>, C<sub>20</sub>–C<sub>36</sub>. The Oil-1 peak evolves at the temperature ramp from 50 to 100 °C and the Oil-2 peak is recorded at 100 °C isotherm. The Oil-3 and Oil-4 peaks are detected at two temperature ramps from 100

**Fig. 1** Example of Rock-Eval 6 pyrogram



**Table 2** Summary of Rock Eval parameters (Peters, 1986)

Parameter	Definition	Unit	Uses
S1	Free hydrocarbons (solvent extractable)	mgHC/gRock	Richness
S2	Thermally crackable hydrocarbons (Kerogen/pyrobitumen)	mgHC/gRock	Richness
S3	CO <sub>2</sub> released from kerogen breakdown during pyrolysis	mgCO <sub>2</sub> /gRock	Richness
T <sub>max</sub>	The temperature of the maximum S2 yield	°C	Thermal maturity
Hydrogen index (HI)	(S2/TOC) * 100	mgHC/TOC	Kerogen typing
Oxygen index (OI)	(S3/TOC) * 100	mgCO <sub>2</sub> /TOC	Kerogen typing
Production index (PI)	S1/(S1 + S2)		Thermal maturity

**Fig. 2** Example of shale play method pyrogram, red curve represents temperature

to 180 °C, and from 180 to 350 °C, respectively. Then, the temperature increases to 650 °C to generate the K-1 peak representing the kerogen or non-free hydrocarbons, such as pyrobitumen or asphaltene. The method provides estimates of fluid API gravity, original reservoir phase saturation, and compositions. The high resolution of the method enables it to quantify the absorbed free hydrocarbons usually present as shoulder in the conventional Rock–Eval method. The forgoing information on PAM-HAWK is summarized by Maende et al. (2017), however, Fig. 3 summarizes the parameters of the PAM method.

The second analytical pyrolysis method category possesses integrated pyrolysis and gas chromatography (Py-GC) with either FID or mass spectrometer (MS). The technique is used to determine the kerogen chemical composition. Although not widely used routinely, this type of analysis is useful for determining the kerogen types and estimating the expected generated hydrocarbons composition upon expulsion. Details of the optimum utilization of Py-GC can be found in Dembicki (2009); di Primio and Horsfield (2006); Ghassal et al. (2018).

Various pyrolysis techniques assess source rock for either their bulk or compositional kinetics. The most common

techniques are open and closed system pyrolysis, and their inputs are essential for calibrating basin and hydrocarbon generation models using Arrhenius equations.

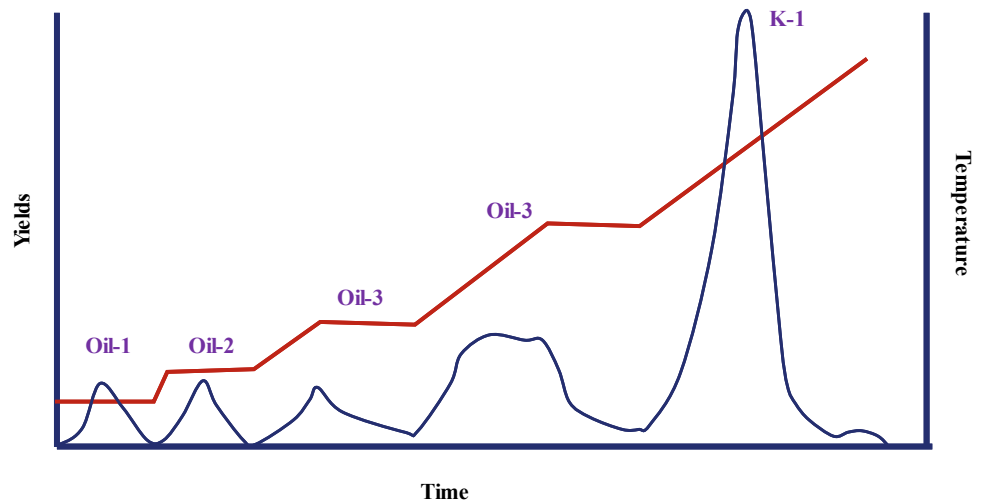
The kinetic models of Pepper and Corvi (1995) are the most widely used techniques as they classify petroleum generation based on lithology, organofacies, and depositional environments.

### 3.3 Organic Microscopy

Kerogen typing, maceral identification, and thermal maturity measurements are the common applications of organic microscopy. The development of most of the techniques utilized in petroleum source rock studies stemmed from the coal industry. The organic microscopy methods are the most accurate techniques for assessing maceral and kerogen assemblages, as well as thermal maturity. Organic matter is assessed either under incident or fluorescent lights.

The incident lights are better used to identify and measure the reflectance of vitrinite and inertinite kerogens, and the fluorescent light is used in liptinite maceral group classification. The organic petrology methods described by Taylor

**Fig. 3** Example of petroleum assessment method pyrogram, red curve represents temperature



et al. (1998) are highly recommended for vitrinite reflectance measurements and maceral counting.

The bulk core sample is cut perpendicular to the bedding and embedded in a mixture of epoxy resin and hardener. After overnight drying in a low-temperature oven, the surface is ground and polished.

The vitrinite reflectance measurements are ideally conducted in a dark room using a microscope for incident white light with a tungsten-halogen lamp calibrated with a standard. A minimum of 50 vitrinite particles are normally measured to reach the best results.

Maceral counting is conducted utilizing white incident light (to count for vitrinite and inertinite) and fluorescent light (to count for bituminite, telalginite, lamalginite, and liptodetrinite). For each sample, about 500 maceral counts are performed along bisects perpendicular to bedding.

The volume % of whole-rock of each maceral is calculated. Then the following equation by Littke (1993) can be used to estimate the percentage of each maceral:

$$\text{TOC (wt\%)} = (\rho_{\text{OM}}/\rho_{\text{Rock}}) \times (\text{C\%/100}) \times \text{OM (vol.\%)}$$

where C% is the carbon content of the organic matter.

Note that the submicroscopic macerals (e.g., amorphous organic matter) are non-countable. Thus, the submicroscopic OM is calculated from the difference between the calculated OM from the equation and the counting.

### 3.4 Molecular Geochemical Methods

The free hydrocarbons (bitumen) are extracted from source rocks by high polarity organic solvents. The most common organic solvents are mixtures of hexane, dichloromethane (DCM), and methanol. Depending on the study aims, several geochemical characterization methods can assess the

extracted sample. Here, we discuss the commonly used techniques in both the industry and academia.

The first molecular geochemical method is fractionating the extracted free hydrocarbons into saturates, aromatics, resins, and asphaltenes (SARA analysis). The method comprises asphaltene separation (deasphaltening) that separates the asphaltene from the maltene, followed by maltene liquid chromatography. There are several fractionation methods, but one example is discussed here.

De-asphaltening is the process where source rock extracts are separated into maltene and asphaltene by mixing the extract with a paraffinic solvent (e.g., n-pentane) and vibrating the mixture overnight. The resultant maltene is usually fractionated into three fractions: saturates, aromatic, and resins using several liquid chromatography options, such as standard wet chemistry, medium pressure liquid chromatography (MPLC), and high-performance liquid chromatography (HPLC). The concept is the same, as all depend on fractionating the samples based on polarity and polarizability to the different chemical classes (Fan & Buckley, 2002). Different methods might generate different results and quality; thus, every run needs to be verified by other methods, such as gas chromatography.

An extended fractionation method, developed by Schwarzbauer et al. (2000), that fractionates the source rock extracts into six fractions (saturates, monoaromatic, diaromatic, polyaromatic, semipolar, and polar) is also beneficial for detailed studies. The technique requires a microcolumn filled with 2 g of 40 mm silica gel. The column is saturated with n-pentane. The raw sample is injected onto the top of the column. Then a sequence of organic solvents with variable polarities are injected in the following sequence:

- n-pentane (5 mL)
- n-pentane/DCM 95/5 v/v (8.5 mL),
- n-pentane/DCM 90/10 v/v (5 mL),

- n-pentane/DCM 40/60 v/v (5 mL),
- DCM (5 mL),
- methanol (5 mL)

Gas chromatography is one of the most common techniques used to screen the composition of liquid hydrocarbons such as bitumen and crude oil. It separates the thermally vaporized hydrocarbons based on their boiling points and polarity, without decomposition, in order to identify or quantify the chemical compounds. Samples are injected into a column with a carrier gas (usually helium) in a temperature-controlled oven. Various detectors, such as flame ionization (FID) or mass spectrometry (MS) detect the separated compounds, and the length and type of the columns and temperature program determine the separation resolution. Examples of GC-FID and GC-MS methods can be found in Ghassal et al. (2018). Bulk source rock extracts are usually first assessed using GC-FID, and the saturates and aromatic are evaluated by GC-MS. Comprehensive discussions of the analytical techniques and common biomarkers are published in Peters et al. (2005).

### 3.5 Isotope Geochemistry

Stable isotope analyses are carried out on the whole rock, kerogen concentrates, and rock extracts for various purposes. The most common stable isotopes used in source rock studies are carbon, oxygen, sulfur, and hydrogen. The isotopes are mainly measured utilizing gas chromatography— isotope ratio mass spectrometry (GC-IRMS). The applications of stable isotope analysis are comprehensively discussed in Galimov (2006).

One of the most advanced isotopic techniques to infer source rock properties is mud gas isotope logging (MGIL). It uses carbon isotopic ratios of mud stream gases to provide a diagnostic fingerprint of reservoir hydrocarbons while the well is being drilled. Carbon isotope ratios provide a powerful means for understanding gas origins and, unlike gas compositions, are not fractionated as gas is liberated from the mud system. Although there are many potential applications, the MGIL is particularly useful for identifying completion zones, assessing the lateral and vertical extent of reservoir and source rocks, and determining whether two fluid zones might be in communication. The methodologies are best described in Ellis (2004) and Haworth et al. (1985). Figure 13 summarizes the MGIL workflow.

The samples are collected in Isotubes, small single-use containers of about 110 mL ( $\leq 80$  psig in pressure), which are used for sampling mud gases for chemical and isotopic analyzes. Isotubes are sealed at each end with a Schrader valve (as used for car tires) which needs to be opened by

applying pressure on the central pin, both to fill the tube with gas and to sample it subsequently.

All samples must first be analyzed by a GC to determine their gas composition and concentration. This includes both hydrocarbon and non-hydrocarbon components. Samples are analyzed in a GC customized for natural gas analysis. This GC system is equipped with thermal conductivity (TCD) and flame ionization (FID) detectors and measures  $C_1$ – $C_{6+}$  hydrocarbons and fixed gases  $N_2$ ,  $O_2 + Ar$ ,  $CO_2$ , and  $CO$ . Samples are introduced into the GC system using sample loops for precise and repeatable results. The GC utilizes several packed columns and valve switching to separate the various components. Helium is used as the carrier gas. Chromatograms are checked for accuracy, including monitoring raw totals and tracking results of internal standards to verify systems are operating within specified parameters. The raw percentage values for each sample are imported into the main sample database and are normalized for data reporting. The MGIL cylinders provide compositional and isotopic mud gas data. Drilling factors such as the use of oil-based mud (OBM) are known to cause data contamination, which is characterized by elevated ethane ( $C_2H_4$ ) content. This component is generally an artificial product of a chemical reaction that takes place due to the increased solubility of carbon components in OBM. The ethane content in each isotube is measured to account for contamination and eliminate affected data before interpretation.

Secondly, each hydrocarbon gas component ( $C_1$ – $C_5$ ) is analyzed by GC-IRMS, which provides a carbon isotopic ( $^{13}C/^{12}C$ ) value for each of the hydrocarbon gas components present in sufficient concentrations.

Thirdly, the deuterium ( $^2H/^1H$ ) isotopic composition is measured for methane, ethane, and propane by GC-IRMS. For samples with very low hydrocarbon gas concentrations below the instrument detection limits, enrichment preparation techniques using liquid nitrogen may be applied.

### 3.6 Inorganic Geochemistry

Various mineralogical and elemental data are used to characterize source rocks for depositional environments. These data provide excellent measures for assessing bottom water oxicity, organic paleoproductivity, weather, mineral alterations, and lithologies. This section provides an overview of selected basic methods used to assess source rock depositional environments.

X-ray fluorescence (XRF) and Inductively Coupled Plasma-mass spectrometry (ICP-MS) are the two main techniques for measuring major and minor elements of rock samples. These analytical methods are non-destructive and can analyze microscopic samples. However, in source rock



studies, bulk samples are usually characterized. In the XRF method, the primary X-ray source excites the sample and then ascertains the chemical composition by measuring the emitted fluorescent X-ray. The ICP-MS measures elements based on ionizing the elements and then quantifying them. X-ray diffraction (XRD) is a non-destructive analytical technique used to determine the mineral composition in rock samples, including clay minerals.

### 3.7 Palynological Methods

The value of palynology to the petroleum industry is well established and has been widely publicized in numerous publications. It is valuable in distinguishing continental and marine sedimentary facies. Many brackish-water and marine sediments contain abundant fossils from the continent. Fossil spores, pollen, and phytoclasts from the land can reveal the age and environment of the continent and complement similar determinations made from microfossils of marine environments. Another merit is that a functional palynology laboratory will complement geochemical results in addition to its low cost.

Palynology investigates all kinds of microscopic organic particles ranging from well-defined morphologies, such as spores, pollen, dinoflagellate cysts, wood and cuticle, to the origin and biological association of less structured remains (Fig. 4). Although palynology has varied applications in paleoenvironmental and paleoclimatic reconstructions, the biostratigraphic application of palynomorphs continues to be the most important area of activity. During the past few decades, however, increased attention has been paid to the wide variation in the composition of organic facies associated with different types of rocks, which has led to a rapid expansion of palynology to other applications, such as the source rock evaluation (Batten, 1982).

The term palynofacies was first introduced by Combaz (1964). Palynofacies has since found applications in the interpretation of environments of deposition and petroleum source rock identification (Tyson, 1995; Batten 1996a, 1996b; Gonçalves et al., 2020), thus aiding the general evaluation of the hydrocarbon potential of sedimentary basins, as well as in geosteering where high resolution in reservoir studies is needed (Batten, 1999; Bombardiere & Gorin, 2000; Dodsworth, 2016).

## 4 Source Rock Interpretation Methods

Source rocks are interpreted for their richness, quality, and thermal maturity. This is achieved by interpreting their depositional environments, organic matter types and factors

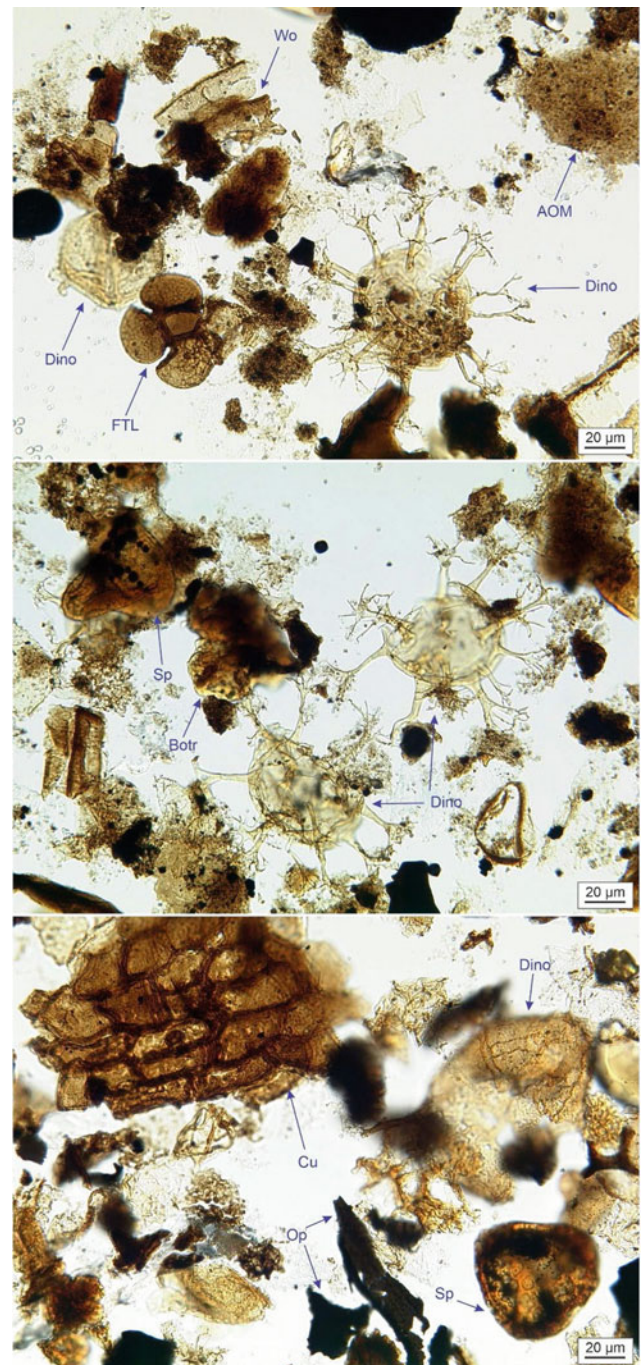


**Fig. 4** Palynofacies snapshots seen under transmitted white light from the Early Cretaceous Zubair Formation, Iraq, show a diverse group of palynofacies particles: palynomorphs (Dino = Dinocysts; Sp = Spores, Bot = *Botryococcus coenobia*, FTL = Foraminifer test linings), phytoclasts (Wo = wood; Cu = cuticle, Op = opaque) and amorphous organic matter (AOM)

controlling their richness and thermal maturity. This section covers several aspects and techniques to decode these factors.

#### 4.1 Richness, Quality, and Depositional Environments

The organic richness is assessed mainly by determining the total organic carbon content by thermal oxidation or the hydrocarbon yields by pyrolysis. It can also be assessed by organic petrology, which is more time-consuming and may not work on all sample types. It can also be difficult to quantify the free hydrocarbons that may exist. The common techniques of assessing the organic matter types and depositional environments are organic petrology or palynofacies analysis. It can be characterized indirectly using pyrolysis, molecular and stable isotope geochemical methods.

Kerogens in source rocks are usually reactive (Type-I, -II, and/or -III) and non-reactive (Type-IV). The TOC measurements account for both proportions, unlike the Rock-Eval S2 and S3 parameters that only determine the richness of the reactive kerogen. Therefore, the TOC alone is insufficient to ascertain the organic richness. The correlation between S2 (reactive kerogen) and TOC is an excellent measure for the richness and quality of remaining source rock potential. If source rock samples are related (e.g., same source rock), they should have robust linear correlations with a very high correlation coefficient ( $r^2$ ). The HI calculated from the slope represents the HI value of reactive kerogen, and the TOC intercept indicates the proportions of the inert kerogen. For example, in the siliciclastic source rock deposited in high-energy environments, the inert

kerogen content is higher than in the carbonate source rocks. Thus, higher TOC intercept values are expected in siliciclastic source rocks compared to carbonate-rich ones.

The S2/S3 ratio is utilized to define where the source rock has oil, gas, or mixed generative potential (Peters & Cassa, 1994). However, some carbonate minerals, such as siderite, influence the S2 and S3 yields. Apparently, the siderite decomposes at  $\sim 390$  °C, similar to the  $\text{CO}_2$  generation from organic matter, and absorbs generated hydrocarbons released during the pyrolysis run (Hazra et al., 2022). The concern extends to the HI and OI quality that are calculated based on S2 and S3, respectively.

The HI and OI are the relationships between the hydrocarbons and organic oxygen, in the reactive kerogen, to the TOC. This makes them ideal source rock quality parameters. The HI gives a proxy of hydrogen richness, and high values indicate better preservation and aquatic organic matter. In this case, the increased values should be accompanied by low OI, indicating low-oxygen depositional environments. On the other hand, lower HI and higher OI values usually characterize terrigenous depositional environments. Note that as the source rock thermal maturity increases, the reactive kerogen is consumed, thereby decreasing both the HI and OI values. The van Krevelen diagram (van Krevelen, 1950) classifies kerogen type, which can be used to imply organic matter type, thermal maturity and depositional environments, in a broad sense. This type of kerogen classification uses the kerogen elemental ratio of H/C versus

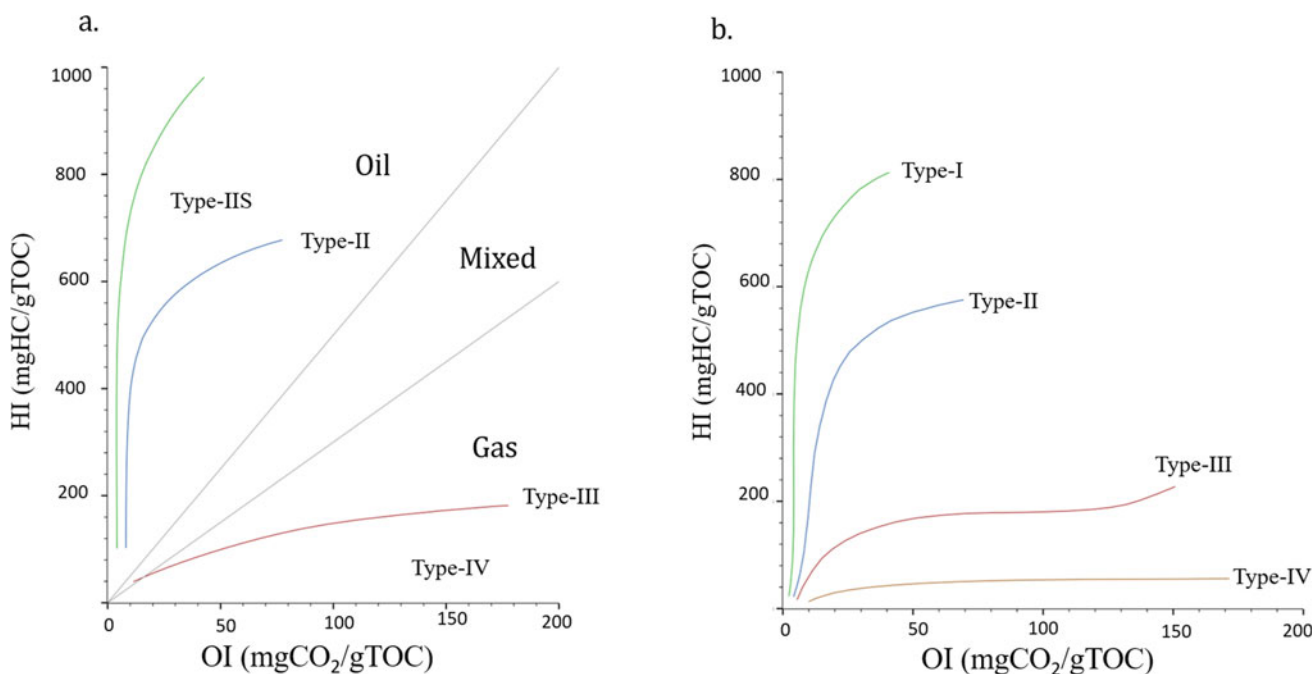


**Fig. 5** Two versions of pseudo van Krevelen diagram. **a)** classifies the kerogen based on their oxygen index (OI) and hydrogen index (HI) relationships to kerogen Type-I, -II, -III and -IV, **b)** classifies marine and non-marine kerogen into type-I, -II and III (Dembicki, 2009). Figures were captured from Pigi Software

O/C. Due to the relatively difficult analytical procedure of measuring elemental data on kerogens, the correlation between OI and HI is used alternatively. Figure 5 shows published source rock data plotted on a pseudo van Krevelen diagram (Peters and Cassa, 1994).

Many biomarkers are used to determine the organic matter types due to their direct relationship to the original organism that constituted the source rock kerogen. Some source-related biomarkers can be attributed to specific taxa of organisms or the whole kingdom, while others can be tied to certain geological settings. Here, we discuss the most common source biomarkers. Pristane (Pr) and Phytane (Ph) are two of the most abundant source biomarkers found in source rock extracts. They are crucial isoprenoids that elute in GC after  $n$ -C<sub>17</sub> and  $n$ -C<sub>18</sub> peaks, respectively (Fig. 6). They gain their abundance from their widespread and predominant sources, which are the phytol chain side bacteriochlorophyll-a and -b, and chlorophyll-a in purple sulfur bacteria and phototrophic organisms, respectively (e.g., Brooks et al., 1969; Powell et al., 1975; Peters et al., 2005; Fang et al., 2019).

Dihydrophytol, which is a constituent of the archaeal cell membranes, is also suggested as a source for pristane and phytane (Chappe et al., 1982). The Pr/Ph ratio indicates source-rock lithologies, thermal maturity and bottom water oxicity/anoxicity condition, although primarily a reflection of the primary organic input (Fang et al., 2019).

The Pr/Ph is a useful ratio to indicate bottom water oxicity/anoxicity. Ratios exceeding unity indicate suboxic to oxic conditions, while lower values suggest anoxic bottom water conditions (Didyk et al., 1978). Published Pr/Ph of Cenomanian to Turonian oil shales from the Trafaya Basin by Ghassal et al. (2016a) was plotted against a well-depth to track the change in values with time (Fig. 7). It shows substantial

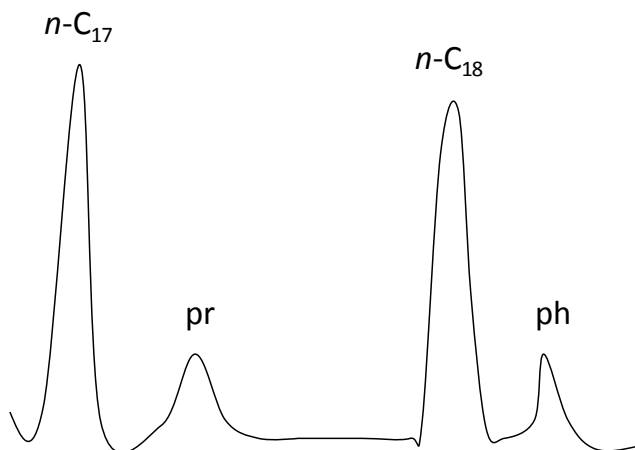


**Fig. 6** Example of  $n$ -C<sub>17</sub>, pristane,  $n$ -C<sub>18</sub> and phytane gas chromatography results

Pr/Ph reduction within the oceanic anoxic event 2 (OAE2). Figure 8 demonstrates an example of the ratio increasing in deltaic systems (Ghassal et al., 2016b). The pristane and phytane are controlled by other factors such as hypersalinity that lowers the ratio below 1, as ten Haven et al. (1987) suggested. Moreover, the Pr/Ph ratio increases with thermal maturity (Peters et al., 2005). Therefore, other biomarkers need to support the interpretation of the Pr/Ph values.

The crossplot of Pr/ $n$ -C<sub>17</sub> and Ph/ $n$ -C<sub>18</sub> reveals the organic matter type, thermal maturity, and alteration processes, such as biodegradation (Lijmbach, 1975), as shown in Fig. 9. This diagram cannot be used alone to indicate the organic matter type, similar to many other geochemical methods.

The normal alkane distribution is influenced primarily by the source organic types and thermal maturity. The abundance of short-chained compounds (e.g., <C<sub>20</sub>) characterizes oils or extracts generated from marine organic matter. On the other hand, samples rich in C<sub>30+</sub> typify hydrocarbon sourced from terrestrial organic matter, and bimodal alkane distributions indicate mixed sources. The lacustrine organic matter is indicated by chromatograms rich in a wide range that exceeds C<sub>30</sub>. Figure 10 illustrates two examples of gas chromatograms representing marine and deltaic depositional environments.

Various aliphatic and aromatic biomarkers can also assess the organic matter types, bottom water conditions, and source rock depositional environments. The steranes and hopanes are the most commonly used biomarkers in petroleum characterization. The steranes are derived from the eukaryotic cell membranes (e.g., algae and higher plants), whereas the hopanes originate from prokaryotic cell membranes, e.g., heterotrophic bacteria and phototrophic cyanobacteria (Mackenzie et al., 1982; Ourisson et al., 1979). Therefore, the steranes/hopanes ratio is used to elucidate the relative abundance of the eukaryotic/prokaryotic inputs.

The relationships between C<sub>27</sub>, C<sub>28</sub>, and C<sub>29</sub> steranes are plotted in a ternary diagram (Fig. 11) to indicate the depositional environments, which was constructed using an extensive study that included oils sourced from various depositional environments (Moldowan et al., 1985). The plot is insensitive to maturity variations, making it an excellent tool for source inference and correlation (Peters et al., 2000).

The Oleanane index (Oleanane/C<sub>30</sub>Hopane) is one of the most common source- and age-related aliphatic biomarker ratios. Oleanane constitutes the most widespread and essential group of triterpenoids in land plants, primarily angiosperms (Akihisa et al., 2016) that evolved in the Late Cretaceous (e.g., Peters et al., 2005). Therefore, it is a robust biomarker to indicate age and terrigenous inputs. It resists post-accumulation alteration processes such as water washing and biodegradation (Alberdi and Lopez, 2000).

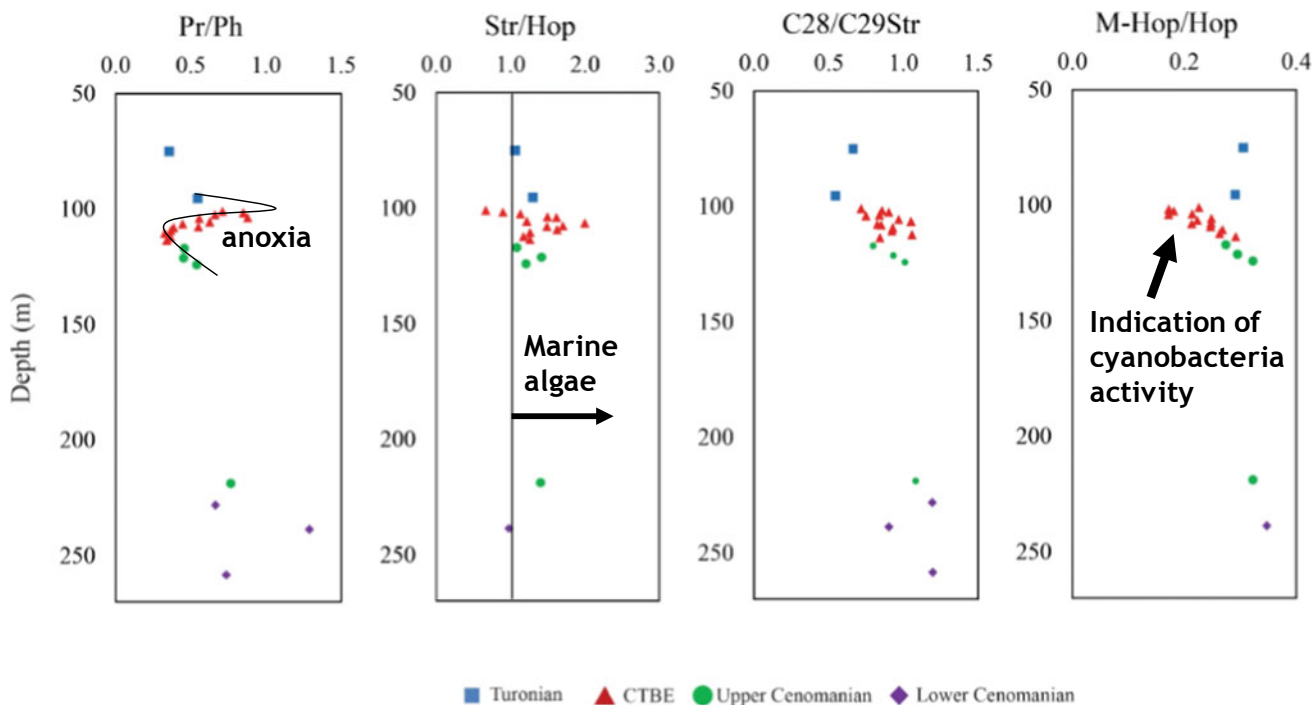


**Fig. 7** Examples of the anoxia effect on the Pr/Ph values compared to other biomarker ratios. CTBE = Cenomanian Turonian boundary event. Data from Ghassal et al. (2016a)

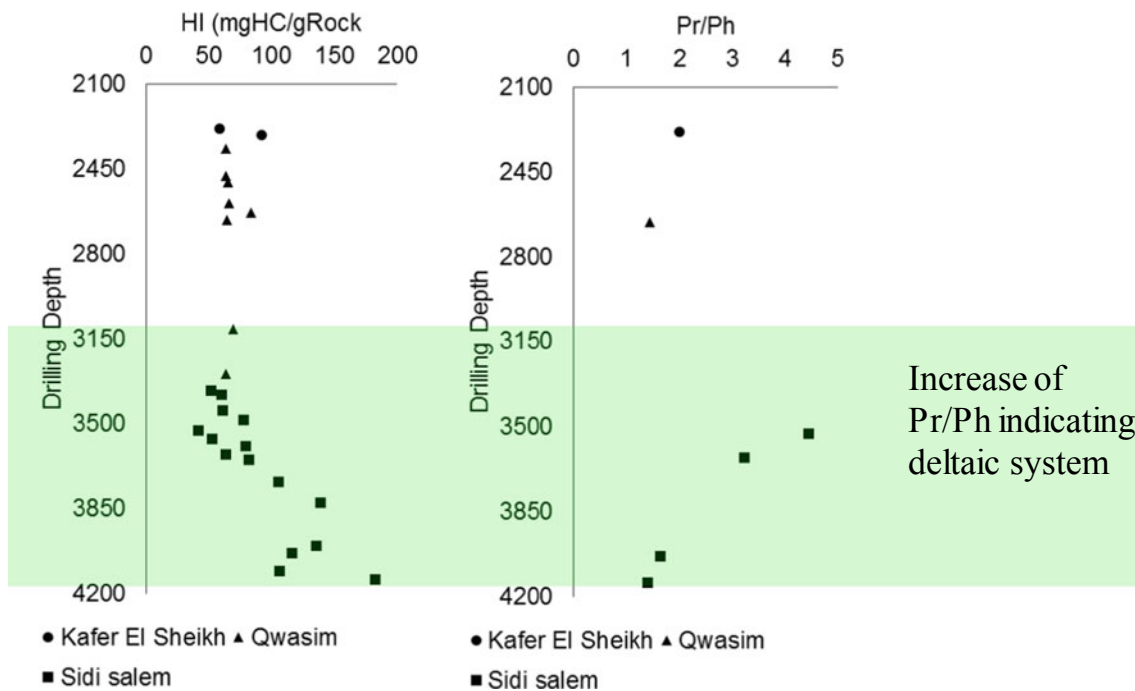


**Fig. 8** Examples of the oxic conditions in deltaic system effect on the Pr/Ph values compared to other biomarker ratios. Data from Ghassal et al. (2016b)

The gammacerane index (gammacerane/(gammacerane + C<sub>30</sub>hopane)) is used to indicate stratified water columns in marine or lacustrine depositional environments

primarily due to hypersalinity or temperature gradients, as discussed in Chap. 1 (Peters et al., 2005; Sinninghe Damsté et al., 1995). The ratio is maturity sensitive; therefore, this

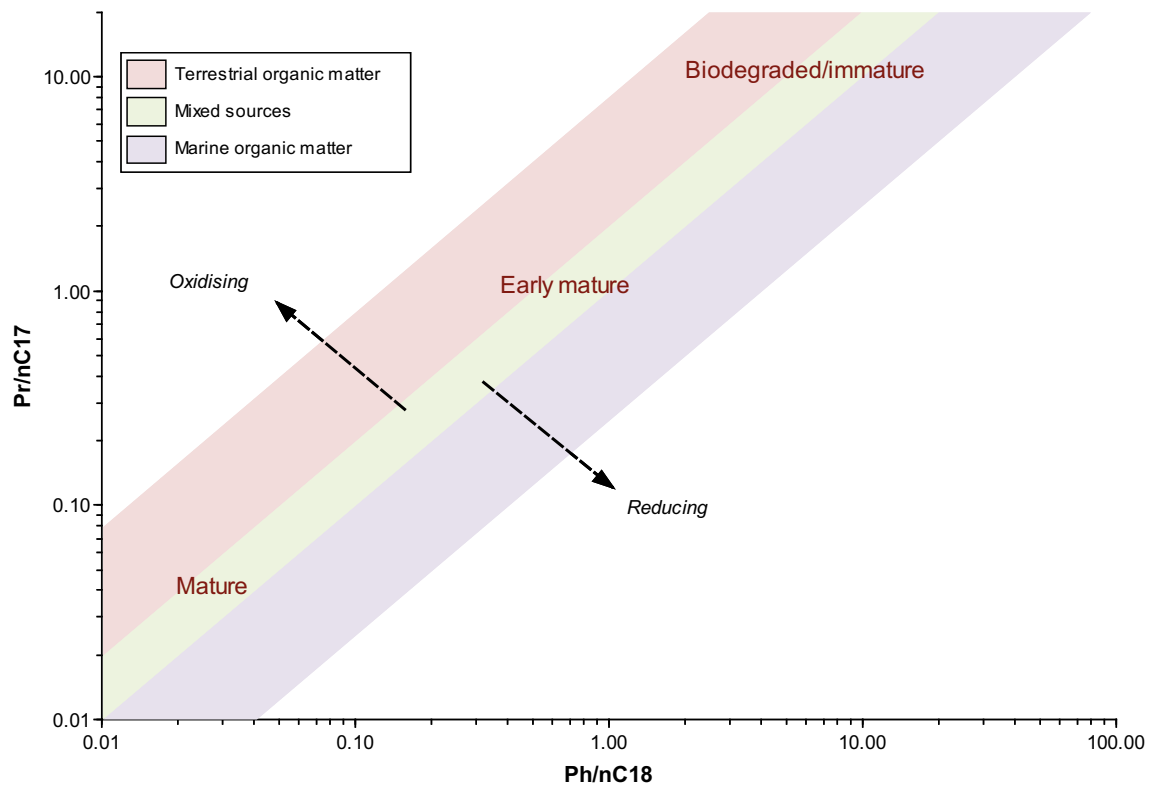


**Fig. 9** Phytane/ $n$ - $C_{18}$  versus Pristane/ $n$ - $C_{17}$  correlation to determine the organic matter type from gas chromatography data of source rock extracts or oils (Lijmbach, 1975)

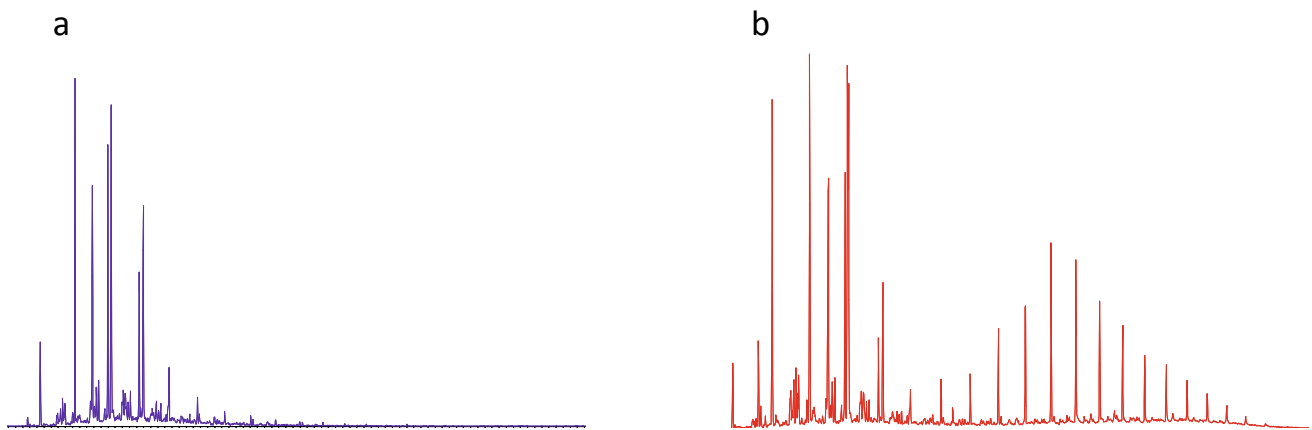


**Fig. 10** Examples from a) marine source rocks (a) and b) deltaic source rocks (b). Data from Ghassal et al. (2016b)

needs to be considered when studying samples with varying thermal maturity levels.

The  $C_{31}$  22R homohopane/ $C_{30}$  Hopane ratio is used to discriminate marine from lacustrine source rocks, as values higher than 0.25 characterize marine sources. It is best to be utilized in combination with  $C_{26}/C_{25}$  tricyclic terpanes (Peters et al., 2005).

Carbonate or marl source rocks deposited in anoxic bottom water conditions demonstrate a 30-norhopane/ $C_{30}$

hopane ratio higher than 1, unlike other depositional environments. The ratio is sensitive to thermal maturity, so this must be considered during interpretation (Peters et al., 2005).

Stable carbon isotopes of the source-rock extracts provide essential indications of the source rock depositional environment. For example, the correlation between stable carbon isotopes of saturates and aromatic fractions from bitumens are an excellent tool to distinguish marine from terrigenous

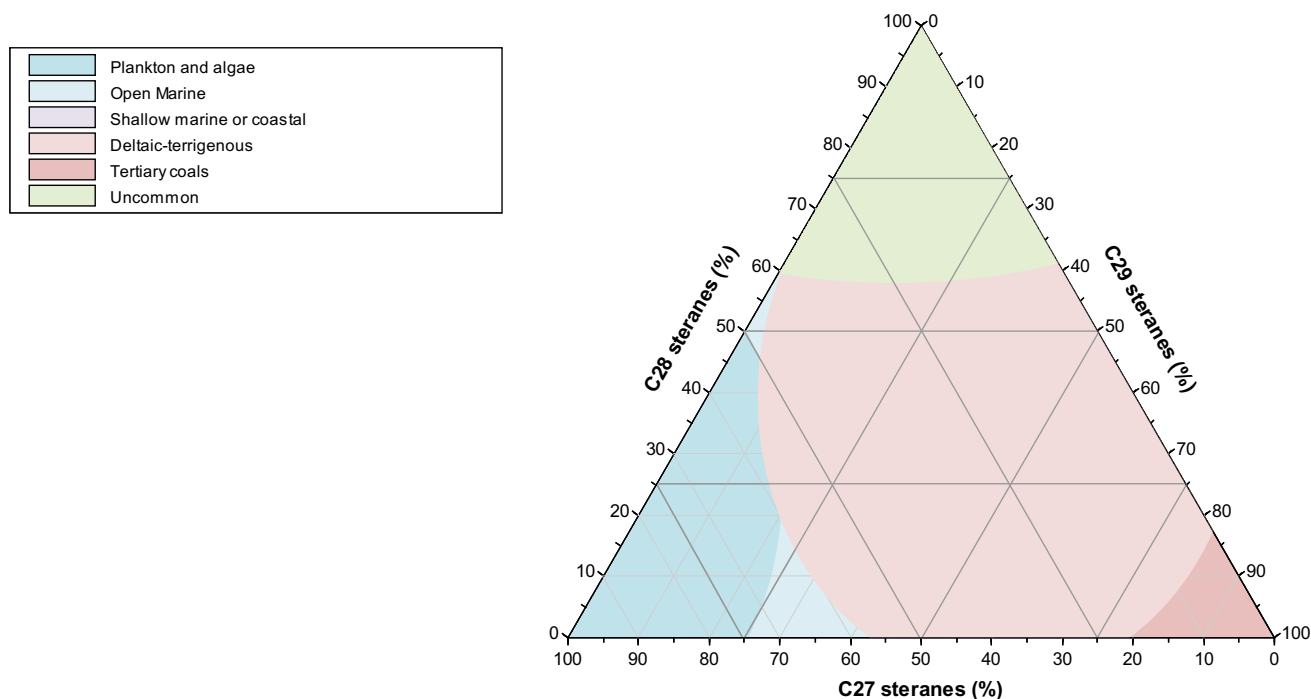


**Fig. 11** C<sub>27</sub>–C<sub>28</sub>–C<sub>29</sub> steranes ternary diagram by Huang and Meinschein (1979). Figure was captured from Pigi Software

organic matter (Sofer, 1984; Fig. 12). Moreover, samples with similar ages usually cluster together. Samples of the same source rock or oil family increase their isotope values with thermal maturity or biodegradation. The carbon and oxygen isotopes of carbonate rocks and kerogen concentrates are commonly used to indicate stratigraphic boundaries, diagenetic processes and anoxia (e.g., Clayton, 1991; Hesselbo et al., 2007; Tsikos et al., 2004). Therefore, it is used for stratigraphic correlations and depositional environment interpretations.

Gas collected from source rock interval during formation testing or retrieved in mud gas is an excellent method to assess organic matter type and maturity (e.g., Philp and Monaco, 2012). The data are usually used for gas-to-source correlation or production allocation studies. In addition to characterizing and verifying shows, the interpretation of MGIL data has other important applications for exploration and production, including:

- assessment of production tests and their failure cause roots
- providing detailed records of stratigraphic elements, such as seal, migration pathways and reservoir/source rocks quality
- identification of potential hydrocarbon accumulations
- typing of source rock and hydrocarbons
- assessment of thermal maturity of source rocks and reservoir fluids

- continuous gas sampling for accurate gas isotope calibration curves
- providing detailed petroleum system evaluation

Figure 13 is a standard MGIL analytical workflow. With respect to classical geochemical interpretations, carbon and hydrogen isotopic ratios of hydrocarbon gas are widely used for the identification of different gas origins. Variations in the isotopic ratios can be utilized to infer the gas source, biogenic, or thermogenic. The interpretation of gas isotopic signatures is the most useful tool in understanding the origin of subsurface hydrocarbon gases, their thermal maturities, migration trends and compartmentalization within the reservoir.

Gas isotope ratios are commonly analyzed from conventional gas sampling (pressurized gas samples) during production or formation testing procedures. The recent advanced development of GC-IRMS has allowed the analysis of hydrocarbon gases at relatively low concentrations and volumes. One of the most useful applications of this new technology is the unleashed potential of analyzing hydrocarbon gases dissolved in circulating drilling muds.

The standard mud gas analysis depends largely upon the ratios and the total of hydrocarbon species that occur within the mud stream. This technology is used in the oil and gas industry to assess the hydrocarbon productivity of a certain reservoir interval. The method can mask the true signature of the gas and can result in false high gas shows, where

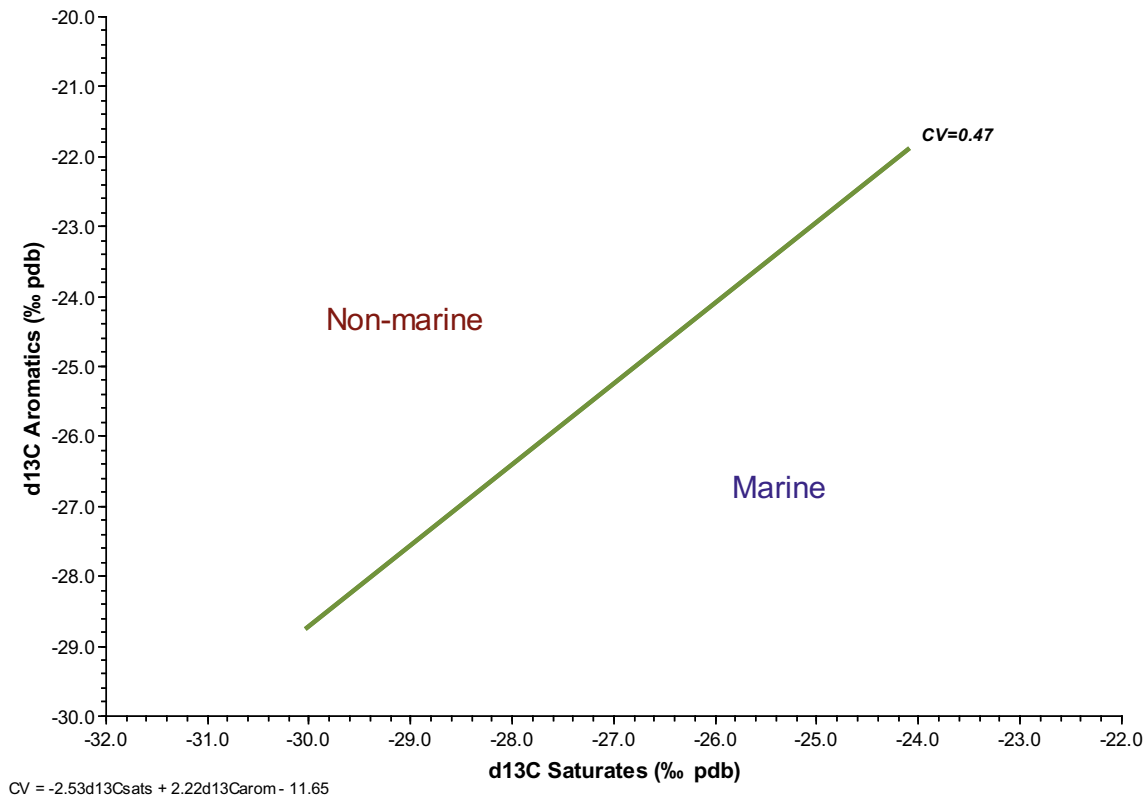


**Fig. 12** The  $\delta^{13}\text{C}$  of saturates versus  $\delta^{13}\text{C}$  of aromatic of source rock extracts or oil used to determine the source rock depositional environments (Sofer, 1984)

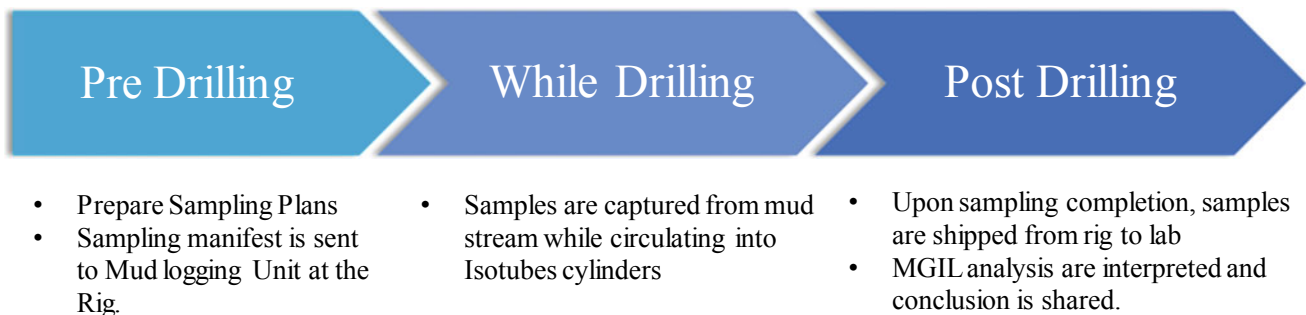


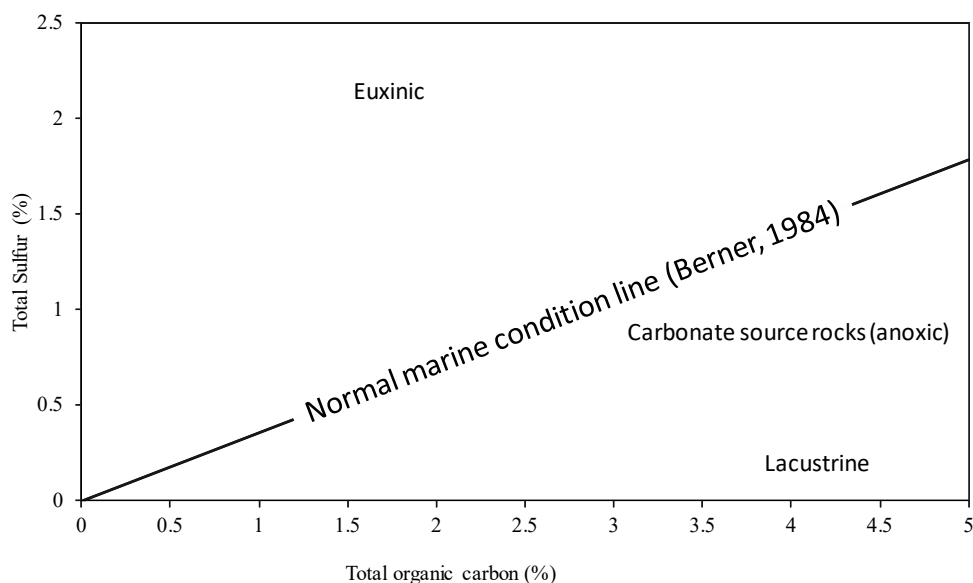
**Fig. 13** Simplified mud gas isotope logging (MGIL) analysis flowchart

artificial gas is generated due to the drilling condition for example. Conversely, the method could also miss a potential pay zone as a consequence of suppressed gas readings. Isotopic measurement of mud gas uses carbon isotopic ratios of mud stream gases to provide a diagnostic fingerprint of reservoir hydrocarbons while the well is being drilled. Carbon isotope ratios provide a powerful means for understanding hydrocarbon gas origins and they are particularly independent of gas concentrations. Due to the expensive well data acquisition tools, the MGIL sampling technology is considered relatively inexpensive.

The inorganic geochemistry of source rock plays an integral role in explaining the bottom water conditions, organic matter preservation and productivity, as well as the proximity to the shorelines. It becomes a powerful tool when it is combined with organic parameters. The following discussion provides examples of techniques for interpreting source rocks utilizing inorganic geochemistry.

As discussed in Chap. 1, the sulfate-reducing bacteria (SRB) oxidize the portions of organic matter in the bottom water to yield the  $\text{HS}^{-1}$  moiety that reacts with the Fe residing in pore water or clay minerals to form pyrite

**Fig. 14** Total Organic Carbon (TOC %) versus Total Sulfur (TS %) used to distinguish the source rock depositional environment



(Ghassal et al., 2016a, and references therein). Therefore, the ratio between TOC/S can be used as a proxy for preserved versus non-preserved organic matter to interpret the depositional environment. Sediments in oxic water and normal salinity have a TOC/S ratio of 2.8. Lower values typify euxinic and lacustrine depositional environments (Fig. 14; Berner, 1984). Moreover, carbonate-dominated sediments deposited in a distal environment away from iron-rich sediment inputs have low S/TOC ratios (Ghassal, 2017). Several additional factors control the pyrite formation and need to be considered before using the ratio as a proxy (Ghassal et al., 2016a, 2018). These are: (1) the organic matter type, (2) the metabolizable portion of organic matter (through

SRB), (3) the amount of the reactive iron, (4) the intensity of the SRB activity, and (5) rate of sedimentation.

The S/Fe ratio, termed the degree of pyritization, indicates the bottom water anoxicity. The stoichiometric ratio of the S to the Fe in pyrite is 1.15 and is plotted as a “pyrite line” on the Fe versus S crossplot (Fig. 15). Rock samples falling on the pyrite line means that all the Fe and the S have formed pyrite. Samples plotting below the line indicate iron-rich mineralization, while those plotting above the line represent other forms of sulfur, such as sulfate or organic sulfur (Dean & Arthur, 1989; Wortmann et al., 1999; Ghassal, 2017). Similar conclusions can be obtained using the TOC-Fe-Sulfur ternary plot (Fig. 17).

**Fig. 15** Total Iron (TI %) versus Total Sulfur (TS %), used to distinguish the source rock depositional environment

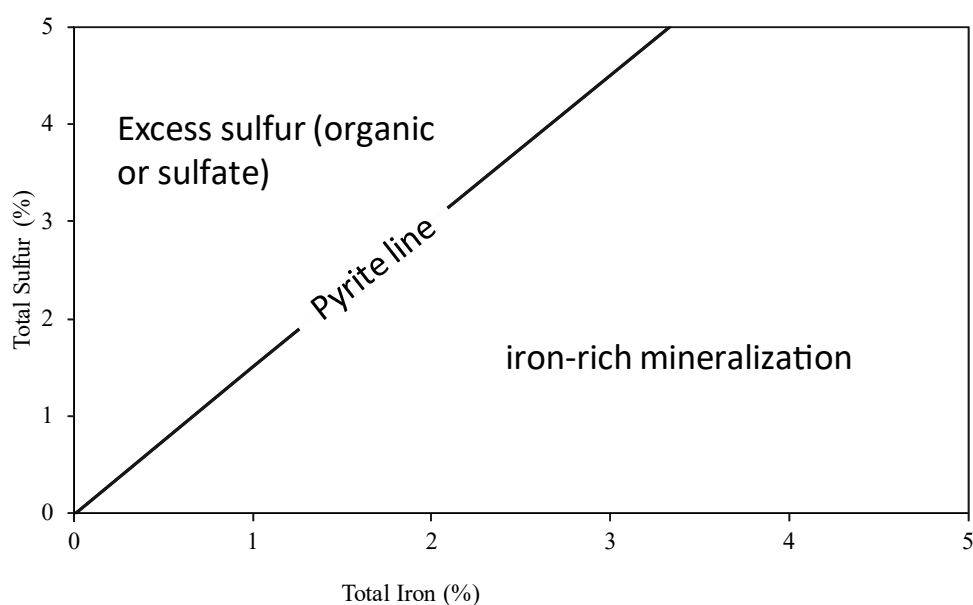
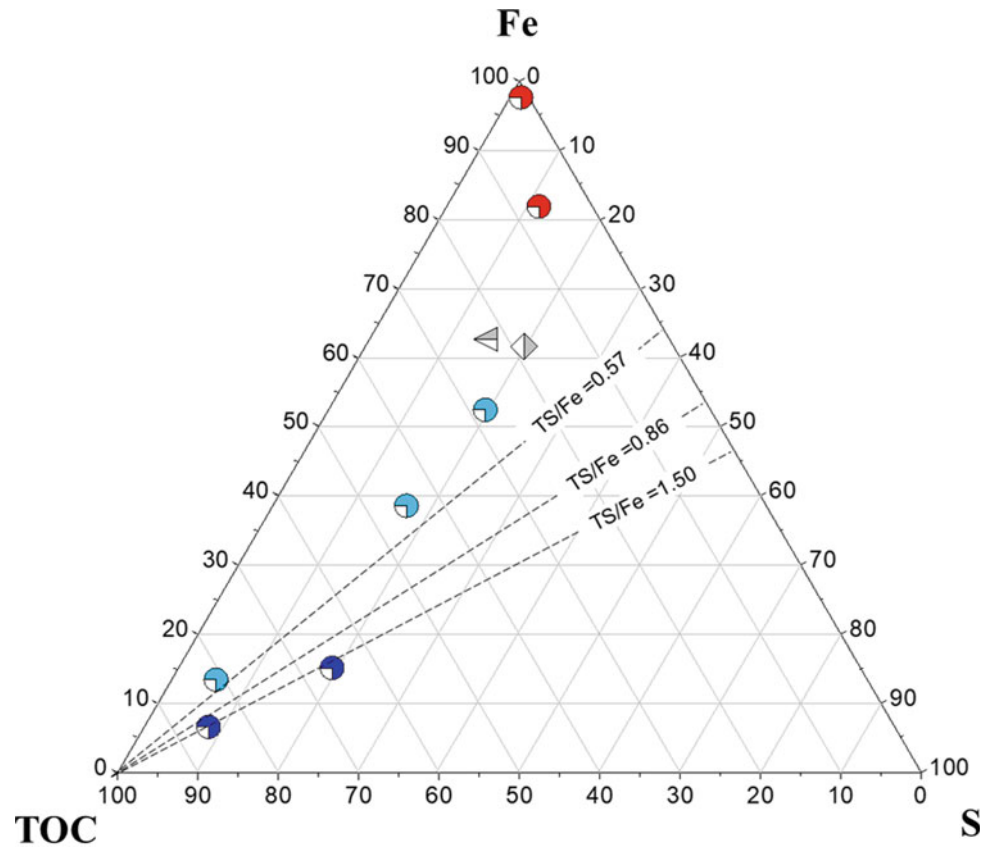




**Fig. 16** TOC-Fe-S ternary diagram used to determine the bottom water condition. Data modified from Ghassal et al. (2018)



Littke et al. (1997) have introduced a new method to calculate the original TOC from measured TOC and sulfur data as follows:

$$\text{TOC}_{\text{original}} = \text{TOC} + 2S * M_c/M_s$$

where  $M_c$  is the molecular weight of carbon, and  $M_s$  the molecular weight (Fig. 16).

The percentage of the original organic matter within the rock is calculated using the following equation:

$$\text{Original organic matter (OM)} = \text{TOC}_{\text{original}} * 100/C_{\text{OM}}$$

$C_{\text{OM}}$  is the carbon content of organic matter (Fig. 17).

Then, the carbonate and silicate percentages are calculated and plotted in a ternary diagram together with the OM % (Fig. 18). Method limitations are discussed in Littke et al. (1997).

Other inorganic elements can be measured to infer the type of organic matter inputs (terrigenous or biogenic) and associated diagenetic processes (Ghassal, 2017). The Si, Al, Ti, Fe, K, and Mn, for example, are used to indicate terrigenous inputs as they are found in the continental crust minerals. Si specifically can be sourced from a biogenic source its sources need to be verified before being used as a proxy for terrigenous inputs.  $\text{CaCO}_3$  in marine source rocks indicates biogenic inputs.

The  $\text{Al}_2\text{O}_3/\text{TOC}$  ratio indicates the sediment proximity to the shorelines (Isaksen & Bohacs, 1995). The same applies to other terrigenous elements such as the  $\text{TiO}/\text{TOC}$  and the  $\text{Fe}_2\text{O}_3/\text{TOC}$  ratios. Plotting the S/Fe ratio (degree of pyritization) versus the  $\text{Al}_2\text{O}_3/\text{TOC}$  ratio (proximity to the shorelines) provides a new tool for TOC predictions using the correlation equation. Similarly, the Rock-Eval HI versus the S/Fe ratio provides a new tool for predicting HI or degree of pyritization or bottom water anoxia (Ghassal, 2017; Ghassal et al., 2018).

## 5 Thermal Maturity

Thermal maturity measurement by vitrinite reflectance is the most common and robust technique. However, measuring the thermal maturity of pre-Devonian and vitrinite-barren samples represents a challenge. As discussed in Chap. 1, vitrinite originates from terrestrial plants that did not evolve until the Carboniferous. For samples lacking vitrinite, alternative microscopic and non-microscopic techniques have been developed for measuring thermal maturity. These methods include the reflectance of solid bitumen and or graptolite. The latter is age-specific and challenging to measure as it is controlled by polishing orientation and

**Fig. 17** Carbonates-organic matter-silicates ternary diagram used to infer organic paleoproductivity. Data from Ghassal et al. (2016a)

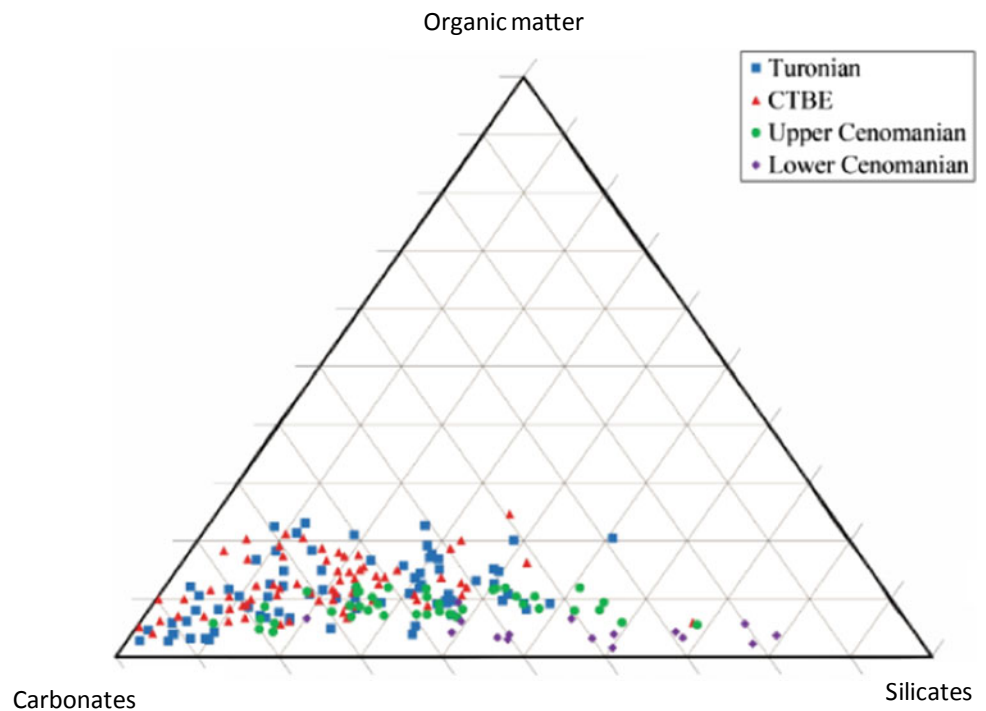
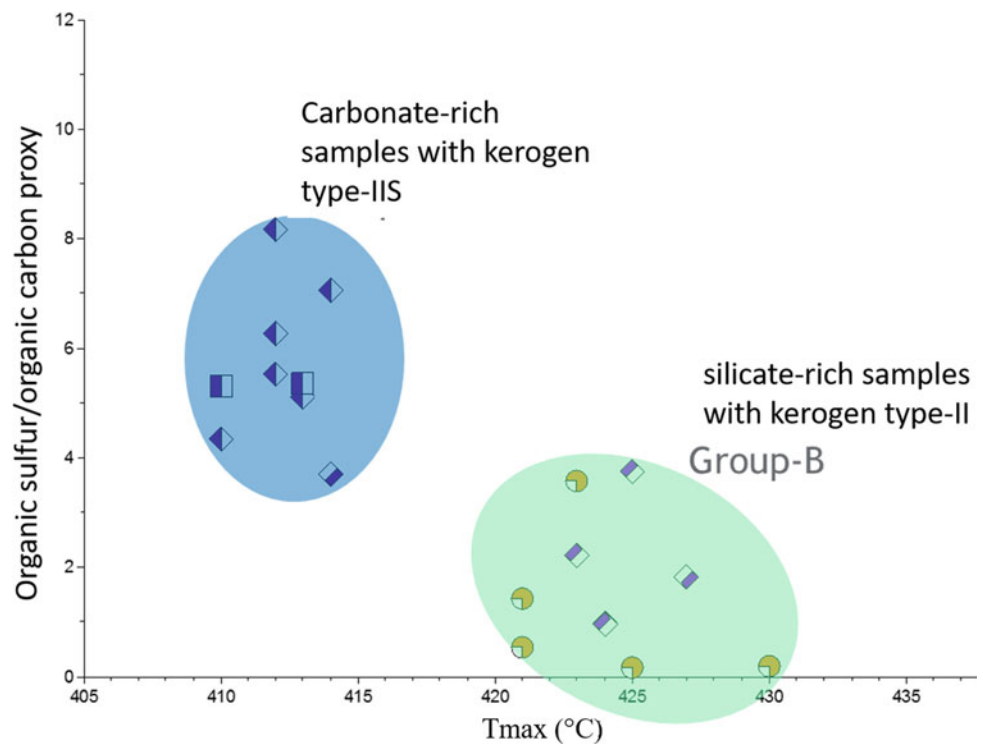


**Fig. 18**  $T_{max}$  of two sample groups with similar thermal maturity, measured by microscopy, but with different organic sulfur richness. Data from Ghassal et al. (2018)



quality. Therefore, alternative non-microscopic techniques are used routinely to measure thermal maturity.

Amongst optical maturity parameters, vitrinite and huminite reflectance, as well as miospore color (TAI, SCS, SCI) are most widely used. Nevertheless, optical and chemical

properties of other macerals, palynomorphs, and microfossils with organic compounds in their skeletons, and the molecular composition of bitumen also serve as parameters for thermal maturity (Hartkopf-Fröder et al., 2015). Additional parameters have been established, such as the conodont color

alteration (CAI, e.g. Kovács & Árkai, 1987), color changes in foraminifera tests (Foraminifera Colouration Index, FCI, e.g. McNeil et al., 1996), as well as the color evolution of other organic particles, such as the ostracod carapaces (e.g. Kontrovitz et al., 1992), conchostracan valves (Tasch, 1982), other arthropod cuticles (Bartram et al., 1987), and the ichthyoliths (e.g., Johns et al., 2012). Furthermore, color changes induced by heat have been conveyed from other fossil groups, such as the thecamoebians (McNeil et al., 2000), microbivalves, microgastropods (Ainsworth et al., 1990), and amniote eggshells (Janssen et al., 2011), in addition to other parameters discussed in detail in Hartkopf-Fröder et al. (2015). The rarity of these fossils hinders their wide applications as potential paleotemperature detectors.

The Palynomorph Darkness Index (PDI) was proposed by Goodhue and Clayton (2010) as a thermal maturity indicator. The PDI has been calculated from the measurements of the red, green, and blue (RGB) intensities of the white light transmitted through palynomorphs mounted on glass thin sections, using a standard palynological microscope and a digital camera.

The most commonly used non-microscopic alternative for thermal maturity assessment is the Rock-Eval  $T_{\max}$ , a standard technique for all source rock types. There are two main limitations to this technique. First, it depends on the kerogen compositions and kinetics. For example, high-sulfur kerogen usually has lower activation energies, and, consequently, the reported  $T_{\max}$  values are lower than those for low-sulfur kerogens (Ghassal et al., 2018; Pepper & Corvi, 1995). Reviewing published thermal maturity scales based on the  $T_{\max}$  indicates a drastic discrepancy in maturity level assignments, especially when converted to vitrinite reflectance equivalent (%VRe). Yang and Horsfield (2020) provide a detailed summary of the various published scales and discussed the uncertainty of the  $T_{\max}$  as a thermal maturity parameter, when not supported by other maturity indicators. Examples of published scales are also shown in Fig. 18 which illustrates the shift in the  $T_{\max}$  measured for source rocks of identical thermal maturity (based on organic microscopy) but with variable organic sulfur richness. Therefore, a specific thermal maturity classification scheme or calibration must be followed to evaluate the source rock of a particular formation within a basin. The second limitation of the use of the  $T_{\max}$  as a thermal maturity index is that the quality of those measurements relies on the amount of reactive kerogen in the samples. The  $T_{\max}$ , therefore, cannot be used for overmature samples or samples that lack reactive kerogen (e.g., non-source rocks). Finally, the sample richness (e.g., high TOC and HI) and high amount of bitumen can reduce/suppress the  $T_{\max}$  values by about 8 °C (Snowdon, 1995). Therefore, the  $T_{\max}$  (and other maturity indicators) of the adjacent intervals need to be observed prior to the final maturity interpretation.

Biomarkers also offer excellent thermal maturity indicators, however, they are limited to specific maturity ranges. Terpane biomarker ratios used for maturity assessment include the Ts (18 $\alpha$ -22, 29,30-trisnorhopane) to Tm (17 $\alpha$ -22, 29,30-trisnorhopane) measured on the m/z 191. The Ts/Tm ratio (also expressed as Ts/(Ts + Tm)) increases with increasing thermal maturity due to differences in the thermal stability of the two compounds. However, the source rock lithology also controls the ratio (Peters et al., 2005); therefore, the ratio is not recommended to compare the maturity of source rocks that have different lithologies. The crossplot of the C<sub>29</sub>  $\alpha\alpha\alpha$  20S/(20S + 20R) and the C<sub>29</sub>  $\alpha\beta\beta$ /( $\alpha\beta\beta$  +  $\alpha\alpha$ ) sterane ratios (Seifert & Moldowan, 1986) can be used to assess the thermal maturity for early-mature (<0.8% VR) source rocks and oils (Fang et al., 2019). The 22S/(22S + 22R) homohopane isomerization ratio is similarly suitable only for the low maturity ranges (Peters & Moldowan, 1991).

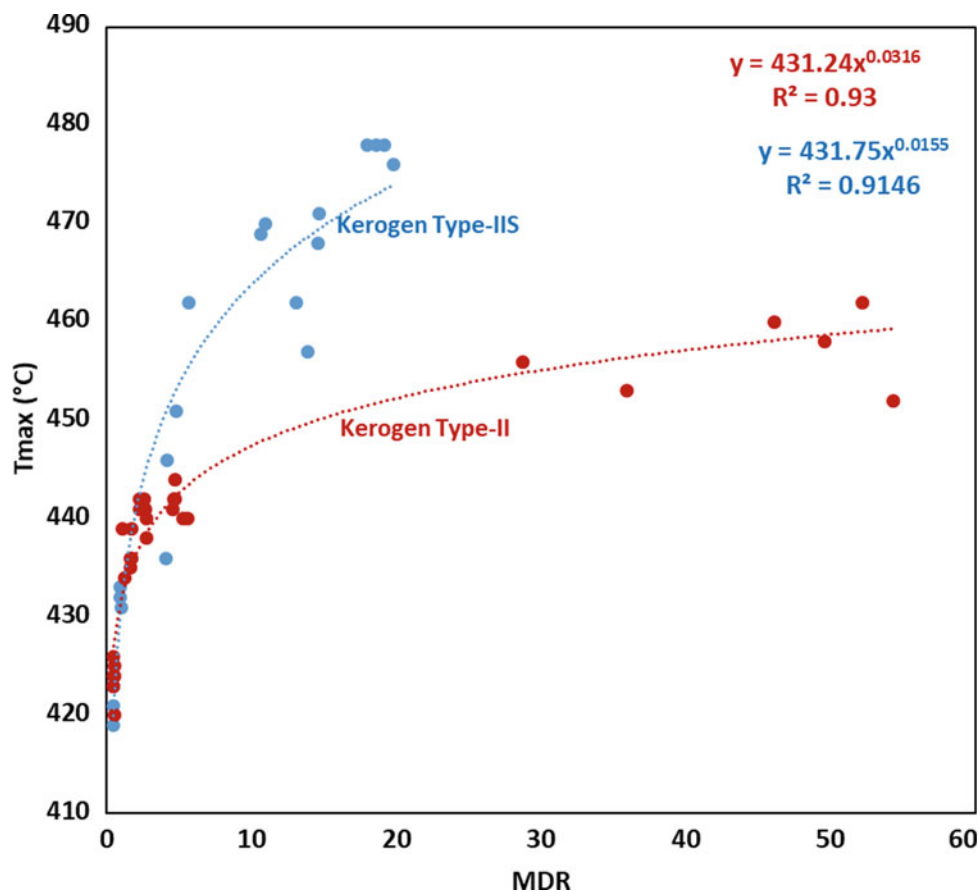
The C<sub>35</sub>-homohopane index C<sub>35</sub>/(C<sub>31</sub>-C<sub>35</sub>) decreases with thermal maturity; however, they are susceptible to bottom water anoxicity and the inputs of its primary precursor, bacteriohopanetetrol (Peters & Moldowan, 1991). The tricyclics/17 $\alpha$ -hopanes increases with thermal maturity as kerogens yield more tricyclic compounds than 17 $\alpha$ -hopanes with increasing maturity (Aquino Neto et al., 1982; Peters et al., 1990). This ratio must be used with caution as it is sensitive to the abundance of the diverse organic precursors (Peters et al., 2005). Another biomarker ratio suitable for immature to early mature source rocks is the moretane/hopane ratio. The value of the ratio decreases with increasing thermal maturity because C<sub>29</sub> and C<sub>30</sub> moretanes are less stable than the corresponding hopanes.

Unlike the aliphatic biomarkers, the aromatic compounds are more effective in assessing higher thermal maturity levels. Three aromatic maturity parameters are discussed here. The methylphenanthrene index (MPI) has been calibrated to actual vitrinite reflectance measurement on source rocks and can therefore be converted to %VRe values, the equation below (Kvalheim et al., 1987) for a wide range of maturity (0.5–1.2%VRe). The MPI is, however, sensitive to source rock lithologies (Cassani et al., 1988) and organofacies.

$$1.89 \times (3 - \text{MP} + 2 - \text{MP}) / (\text{P} + 1.26 \times (1 - \text{MP} + 9 - \text{MP}))$$

During source rock maturation, the monoaromatic steroids (MA) aromatize to triaromatic steroids (TA), allowing the TA/(TA + MA) ratio to be used as a thermal maturity marker (Mackenzie et al., 1981) for a wide range of thermal maturity. Because there are several published formulas to represent the conversion of MA to TA, the same formula needs to be used for each data set or when comparing with

**Fig. 19** MDR versus  $T_{\max}$  of source rock with kerogen Type-IIS (blue; Srinivasan et al., 2022) and kerogen Type-II (red; Fang et al., 2019)



data sets from other sources. A detailed discussion of the different versions of the ratio can be referred to in Peters et al. (2005).

The relationships between the various alkylated C1–C4 homologs of dibenzothiophene (DBT) indicate source rock thermal maturity. This is due to the variability of their thermal stability that depends on the position of the methyl group. The most thermally stable isomers are the 4-methyldibenzothiophene (4-MDBT) and the 4,6-dimethyldibenzothiophene (4,6-DMDBT). Therefore, the 4-/1-MDBT, 2,4-/(1,4 + 1,6)-DMDBT and 4,6/(1,4 + 1,6)-DMDBT ratios are utilized to determine source rock thermal maturity. For a specific source rock formation with a wide range of thermal maturity, the ratios can be calibrated to the Rock–Eval  $T_{\max}$  to predict the thermal maturity of produced petroleum from the unconventional play (Srinivasan et al., 2022). Figure 19 is a plot of  $T_{\max}$  versus published 4-/1-MDBT (methyldibenzothiophene ratio, MDR) data of the Posidonia Shale (Fang et al., 2019) and the Jurassic organic-rich marlstone from the Arabian basin (Srinivasan et al., 2022).

The methylnaphthalene ratio (MNR = 2-/1-methylnaphthalene) and the ethylnaphthalene ratio (ENR = 2-/1-ethylnaphthalene) both increase with thermal maturity, hence making them suitable as maturity parameters (Fang

et al., 2019; Peters et al., 2005; Radke et al., 1982; Srinivasan et al., 2022).

Thermal oxidation is another maturity parameter (described in Chap. 3 and in Henderson and Ghassal, 2019). Raman spectroscopy has also been proven excellent in providing accurate thermal maturity from various types of organic matter, such as graptolite, solid bitumen and vitrinite (Henry et al., 2019; Kelemen & Fang, 2001; Sauerer et al., 2017; Schmidt Mumm & Inan, 2016).

## References

- Ainsworth, N. R., Burnett, R. D., & Kontrovitz, M. (1990). Ostracod colour change by thermal alteration, offshore Ireland and Western UK. *Marine and Petroleum Geology*, 7, 288–297.
- Akihisa, T., Zhang, J., & Tokuda, H. (2016). Potentially chemopreventive Triterpenoids and other secondary metabolites from plants and fungi (Chap. 1). In *Studies in Natural Products Chemistry* (Vol. 51, pp. 1–50).
- Alberdi, M., & López, L. (2000). Biomarker 18 $\alpha$ (H)-oleanane: A geochemical tool to assess Venezuelan petroleum systems. *Journal of South American Earth Sciences*, 13, 751–759.
- Aquino Neto, F. R., Restle, A., Connan, J., Albrecht, P., & Ourisson, G. (1982). Novel tricyclic terpanes (C19, C20) in sediments and petroleums. *Tetrahedron Letters*, 23, 2027–2030.

- Bartram, K. M., Jeram, A. J., & Selden, P. A. (1987). Arthropod cuticles in coal. *Journal of the Geological Society*, *144*, 513–517.
- Batten, D. J. (1982). Palynofacies, palaeoenvironments and petroleum. *Journal of Micropalaeontology*, *1*, 107–114.
- Batten, D. J. (1996a). Palynofacies and palaeoenvironmental interpretation. In J. Jansonius, & D.C. McGregor (Eds.), *Palynology: Principles and Applications 3* (pp. 1011–1064). AASP Foundation.
- Batten, D. J. (1996b). Palynofacies and petroleum potential. In J. Jansonius, & D.C. McGregor (Eds.), *Palynology: Principles and Applications 3* (pp. 1065–1084). AASP Foundation.
- Batten, D. J. (1999). Palynofacies analysis. In T.P. Jones, & N. P. Rowe (Eds.), *Fossil Plants and Spores: modern techniques* (pp. 194–198). Geological Society.
- Berner, R. A. (1984). Sedimentary pyrite formation: An update. *Geochim Cosmochim Acta*, *48*, 605–615.
- Bombardiere, L., & Gorin, G. E. (2000). Stratigraphical and lateral distribution of sedimentary organic matter in Upper Jurassic carbonates of SE France. *Sedimentary Geology*, *132*, 177–203.
- Brooks, J. D., Gould, K., & Smith, J. W. (1969). Isoprenoid hydrocarbons in coal and petroleum. *Nature*, *222*, 257–259.
- Cassani, F., Gallango, O., Talukdar, S., Vallejos, C., & Ehrmann, U. (1988). Methylphenanthrene maturity index of marine source rock extracts and crude oils from the Maracaibo Basin. In *Organic Geochemistry In Petroleum Exploration Proceedings of the 13th International Meeting On Organic Geochemistry* (pp. 73–80). Venice, Italy.
- Chappe, B., Albrecht, P., & Michaelis, W. (1982). Polar lipids of archaeobacteria in sediments and petroleum. *Science*, *217*, 65–66.
- Clayton, C. (1991). Carbon isotope fractionation during natural gas generation from kerogen. *Marine and Petroleum Geology*, *8*, 232–240.
- Combaz, A. (1964). Les palynofaciès. *Revue De Micropaléontologie*, *7*, 205–218.
- Dean, W. E., & Arthur, M. A. (1989). Iron-sulfur-carbon relationships in organic-carbon-rich sequences; I, Cretaceous Western Interior Seaway. *American Journal of Science*, *289*, 708–743.
- Dembicki, H., Jr. (2009). Three common source rock evaluation errors made by geologists during prospect or play appraisals. *AAPG Bulletin*, *93*, 341–356.
- di Primio, R. & Horsfield, B. (2006). From petroleum-type organofacies to hydrocarbon phase prediction. *AAPG Bulletin*, *90*, 1031–1058.
- Didyk, B. M., Simoneit, B. R. T., Brassell, S. C., & Eglinton, G. (1978). Organic geochemical indicators of palaeoenvironmental conditions of sedimentation. *Nature*, *272*, 216–222.
- Dodsworth, P. (2016). Palynostratigraphy and palaeoenvironments of the Eagle Ford Group (Upper Cretaceous) at the Lozier Canyon outcrop reference section, west Texas. USA. *Palynology*, *40*, 357–378.
- Ellis, L. (2004). MGIL Maximizes Value of Mud Logging. The American Oil and Gas Reporter.
- Espitalié, J., Deroo, G., & Marquis, F. (1985). La pyrolyse Rock-Eval et ses applications (deuxième partie). *Revue Institut Français Du Pétrole*, *40*, 755–784.
- Fan, T., & Buckley, J. S. (2002). Rapid and accurate SARA analysis of medium gravity crude oils. *Energy & Fuels*, *16*, 1571–1575.
- Fang, Z., Huang, R., Chelme-Ayala, P., Shi, Q., Xu, C., & El-Din, M. G. (2019). Comparison of UV/Persulfate and UV/H<sub>2</sub>O<sub>2</sub> for the removal of naphthenic acids and acute toxicity towards *Vibrio fischeri* from petroleum production process water. *Science of the Total Environment*, *694*, 133686.
- Haworth, J. H., Sellens, M., & Whittaker, A. (1985). Interpretation of hydrocarbon shows using light (C<sub>1</sub>–C<sub>5</sub>) hydrocarbon gases from mud-log data. *AAPG Bulletin*, *69*, 1305–1310.
- Henry, D. G., Jarvis, I., Gillmore, G., & Stephenson, M. (2019). Raman spectroscopy as a tool to determine the thermal maturity of organic matter: Application to sedimentary, metamorphic and structural geology. *Earth-Science Reviews*, *198*, 102936.
- Galimov, E. M. (2006). Isotope organic geochemistry. *Organic Geochemistry*, *37*, 1200–1262.
- Ghassal, B. I. H. (2017). Source rock depositional processes in different marine settings: examples from North African basins (Doctoral dissertation, Universitätsbibliothek der RWTH Aachen).
- Ghassal, B. I., Littke, R., El Atfy, H., Sindern, S., Scholtysik, G., El Beialy, S., & El Khoriby, E. (2018). Source rock potential and depositional environment of Upper Cretaceous sedimentary rocks, Abu Gharadig Basin, Western Desert, Egypt: An integrated palynological, organic and inorganic geochemical study. *International Journal of Coal Geology*, *186*, 14–40.
- Ghassal, B. I., Littke, R., Sachse, V., Sindern, S., & Schwarzbauer, J. (2016a). Depositional environment and source rock potential of upper Albian to Turonian sedimentary rocks of the Tarfaya Basin, Southwest Morocco. *Geologica Acta*, *14*, 419–441.
- Ghassal, B. I., El Atfy, H., Sachse, V., & Littke, R. (2016b). Source rock potential of the Middle Jurassic to middle Pliocene, onshore Nile Delta basin. *Egypt. Arabian Journal of Geosciences*, *9*(20), 1–21.
- Gonçalves, P. A., Pinheiro, S., Mendonça Filho, J. C., Mendonça, J. O., & Flores, D. (2020). Study of a Silurian sequence of Domes region (Central Iberian Zone, Portugal): The contribution of organic petrology and palynofacies. *International Journal of Coal Geology*, *225*, 103501.
- Goodhue, R., & Clayton, G. (2010). Palynomorph darkness index (PDI)—A new technique for assessing thermal maturity. *Palynology*, *34*, 147–156.
- Hartkopf-Fröder, C., Königshof, P., Littke, R., & Schwarzbauer, J. (2015). Optical thermal maturity parameters and organic geochemical alteration at low grade diagenesis to anchimetamorphism: A review. *International Journal of Coal Geology*, *150–151*, 74–119.
- Hazra, B., Singh, D. P., Chakraborty, P., Das, H., Singh, V., Sahu, S. G., & Singh, P. K. (2022). Structural and thermal properties of vitrain lithotype in coal-inferences from TG-DTG-DSC, Rock-Eval and X-ray diffraction. *Journal of Earth System Science*, *131*, 98. <https://doi.org/10.1007/s12040-022-01849-6>
- Henderson, S. & Ghassal, I. (2019). Overmature and Vitrinite-Barren Source Rocks: A Novel Thermal Maturity Parameter. Paper presented at the SPE Middle East Oil and Gas Show and Conference, Manama, Bahrain, March 2019. SPE-194946-MS. <https://doi.org/10.2118/194946-MS>.
- Hesselbo, S. P., Jenkyns, H. C., Duarte, L. V., & Oliveira, L. C. V. (2007). Carbon-isotope record of the Early Jurassic (Toarcian) Oceanic Anoxic Event from fossil wood and marine carbonate (Lusitanian Basin, Portugal). *Earth and Planetary Science Letters*, *253*, 455–470.
- Huang, W. Y., & Meinschein, W. G. (1979). Sterols as ecological indicators. *Geochimica Et Cosmochimica Acta*, *43*, 739–745.
- Isaksen, G. H., & Bohacs, K. M. (1995). Geological controls of source rock geochemistry through relative sea level; Triassic, Barents Sea. *Petroleum source rocks* (pp. 25–50). Springer.
- Janssen, J. D., Mutch, G. W., & Hayward, J. L. (2011). Taphonomic effects of high temperature on avian eggshell. *Palaios*, *26*, 658–664.
- Johns, M. J., Trotter, J. A., Barnes, C. R., & Narayan, Y. R. (2012). Biostratigraphic, strontium isotopic, and geologic constraints on the landward movement and fragmentation of terranes within the Tofino Basin British Columbia. *Canadian Journal Earth Sciences*, *49*, 819–856.
- Kelemen, S. R., & Fang, H. L. (2001). Maturity trends in Raman Spectra from kerogen and coal. *Energy & Fuels*, *15*, 653–658.

- Kontrovitz, M., Ainsworth, N. R., Burnett, R. D., & Slack, J. M. (1992). Induced color in ostracode shells: An experimental study. *The University of Kansas Paleontological Contributions, New Series*, 2, 1–10.
- Kovács, S., & Árkai, P. (1987). Conodont alteration in metamorphosed limestones from northern Hungary, and its relationship to carbonate texture, illite crystallinity and vitrinite reflectance. In R. L. Austin (Ed.), *Conodonts: Investigative Techniques and Applications* (pp. 209–229). Ellis Horwood.
- Kvalheim, O. M., Christy, A. A., Telnæs, N., & Bjørseth, A. (1987). Maturity determination of organic matter in coals using the methylphenanthrene distribution. *Geochimica Et Cosmochimica Acta*, 51, 1883–1888.
- Lijmbach, G.W. (1975). On the origin of petroleum. In *Proceeding of the 9th World Petroleum Congress* (Vol. 2, pp. 357–369). Applied Science Publisher.
- Littke, R. (1993). Migration of oil and gas coals. In *Deposition, Diagenesis and Weathering of Organic Matter-Rich Sediments* (pp. 135–169).
- Littke, R., Baker, D. R., & Rullkötter, J. (1997). Deposition of petroleum source rocks. In D. H. Welte, B. Horsfield, & D. R. Baker (Eds.), *Petroleum and Basin Evolution* (pp. 271–333). Springer.
- Mackenzie, A. S., Brassell, S. C., Eglinton, G., & Maxwell, J. R. (1982). *Chemical Fossils: The geological fate of steroids*. *Science*, 217, 491–504.
- Mackenzie, A. S., Patience, R. L., & Maxwell, J. R. (1981). Molecular changes and the maturation of sedimentary organic matter. In G. Atkinson, & J. J. Zuckerman (Eds.), *Origin and Chemistry of Petroleum* (pp. 1–32). Pergamon Press.
- McNeil, D. H., Issler, D. R., & Snowdon, L. R. (1996). Colour alteration, thermal maturity, and burial diagenesis in fossil foraminifers. *Geological Survey of Canada Bulletin*, 499, 1–34.
- Maende, A., Pepper, A., Jarvie, D. M., & Weldon, W. D. (2017). Advanced pyrolysis data and interpretation methods to identify unconventional reservoir sweet spots in fluid phase saturation and fluid properties (API gravity) from drill cuttings and cores. *Petroleum Geology*, 12, 417–452.
- McNeil, D. H., Leckie, D. A., Kjarsgaard, B. A., Stasiuk, L. D. (2000). Agglutinated foraminiferal assemblages in Albian shales overlying kimberlite deposits in the Smeaton core from central Saskatchewan, Canada. In M.B. Hart, M.A. Kaminski, C.W. Smart (Eds.), *Proceedings of the Fifth International Workshop on Agglutinated Foraminifera* (pp. 299–309). Grzybowski Foundation, Kraków.
- Moldowan, J. M., Seifert, W. K., & Gallegos, E. J. (1985). Relationship between petroleum composition and depositional environment of petroleum source rocks. *AAPG Bulletin*, 69, 1255–1268.
- Ouirsson, G., Albrecht, P., & Rohmer, M. (1979). The hopanoids: Palaeochemistry and biochemistry of a group of natural products. *Pure and Applied Chemistry*, 51, 709–729.
- Pepper, A. S., & Corvi, P. J. (1995). Simple kinetic models of petroleum formation. Part I: Oil and gas generation from kerogen. *Marine and Petroleum Geology*, 12, 291–319.
- Peters, K. E. (1986). Guidelines for evaluating petroleum source rock using programmed pyrolysis. *AAPG Bulletin*, 70, 318–329.
- Peters, K. E., Snedden, J. W., Sulaeman, A., Sarg, J. F., & Enrico, R. J. (2000). A new geochemical-stratigraphic model for the Mahakam Delta and Makassar Slope, Kalimantan, Indonesia. *AAPG Bulletin*, 69, 12–44.
- Peters, K. E., Cassa, & M. R. (1994). Applied source rock geochemistry. In L. B. Magoon, & W. G. Dow (Eds.), *The Petroleum System—from Source to Trap* (pp. 93–120). AAPG Memoir 60.
- Peters, K. E., & Moldowan, J. M. (1991). Effects of source, thermal maturity, and biodegradation on the distribution and isomerization of homohopanes in petroleum. *Organic Geochemistry*, 17, 47–61.
- Peters, K. E., Moldowan, J. M., & Sundaraman, P. (1990). Effects of hydrous pyrolysis on biomarker thermal maturity parameters: Monterey Phosphatic and Siliceous members. *Organic Geochemistry*, 15, 249–265.
- Peters, K. E., Walters, C. C., & Moldowan, J. M. (2005). *The Biomarker Guide*. Cambridge University Press.
- Philp, R. P., & Monaco G. L. (2012). Applications of stable isotopes in hydrocarbon exploration and environmental forensics. In *Handbook of Environmental Isotope Geochemistry* (pp. 639–677).
- Powell, T. G., Cook, P. J., & McKirdy, D. M. (1975). Geologic factors controlling crude oil composition in Australia and Papua, New Guinea. *AAPG Bulletin*, 59, 1176–1197.
- Radke, M., Welte, D. H., & Willsch, H. (1982). Geochemical study on a well in the Western Canada Basin: Relation of the aromatic distribution pattern to maturity of organic matter. *Geochimica Et Cosmochimica Acta*, 46, 1–10.
- Romero-Sarmiento, M. -F., Pillot, D., Letort, G., Lamoureux-Var, V., Beaumont, V., Huc, A. -Y., & Garcia, B. (2016). New Rock-Eval method for characterization of unconventional shale resource systems. *Oil & Gas Science and Technology—Rev. IFP Energies nouvelles*, 71, 37.
- Sauerer, B., Craddock, P. R., AlJohani, M. D., Alsamadony, K. L., & Abdallah, W. (2017). Fast and accurate shale maturity determination by Raman spectroscopy measurement with minimal sample preparation. *International Journal of Coal Geology*, 173, 150–157.
- Schmidt Mumm, A., & Inan, S. (2016). Microscale organic maturity determination of graptolites using Raman spectroscopy. *International Journal of Coal Geology*, 162, 96–107.
- Schwarzbauer, J., Littke, R., & Weigelt, V. (2000). Identification of specific organic contaminants for estimating the contribution of the Elbe river to the pollution of the German Bight. *Organic Geochemistry*, 31, 1713–1731.
- Seifert, W. K., & Moldowan, J. M. (1986). Use of biological markers in petroleum exploration. *Methods in Geochemistry and Geophysics*, 24, 261–290.
- Sinninghe Damsté, J. S., Frewin, N. L., Kenig, F., & De Leeuw, J. W. (1995). Molecular indicators for palaeoenvironmental change in a Messinian evaporitic sequence (Vena del Gesso, Italy). I: Variations in extractable organic matter of ten cyclically deposited marl beds. *Organic Geochemistry*, 23, 471–483.
- Snowdon, L. R. (1995). Rock-Eval  $T_{max}$  suppression: Documentation and amelioration. *AAPG Bulletin*, 79, 1337–1348.
- Sofer, Z. (1984). Stable carbon isotope compositions of crude oils: Application to source depositional environments and petroleum alteration. *AAPG Bulletin*, 68, 31–49.
- Srinivasan, P., Jacobi, D., Atwah, I., Karg, H., & Azzouni, A. (2022). Integration of methylidibenzothiophene and pyrolysis techniques to determine thermal maturity in sulfur-rich Type II-S source rocks and oils. *Organic Geochemistry*, 163, 104333.
- Tasch, P. (1982). Experimental valve geothermometry applied to fossil conchostracan valves, Blizzard Heights, Antarctica. In C. Craddock (Ed.), *Antarctic Geoscience, Symposium on Antarctic Geology and Geophysics* (pp. 661–668). University of Wisconsin Press, Madison.
- Taylor, G. H., Teichmüller, M., Davis, A. C. F. K., Diessel, C. F. K., Littke, R., & Robert, P. (1998). *Organic petrology*. Borntraeger, Berlin-Stuttgart, 704 p.
- ten Haven, H. L., de Leeuw, J. W., Rullkötter, J., & Sinninghe Damsté, J. S. (1987). Restricted utility of the pristane/phytane ratio as a palaeoenvironmental indicator. *Nature*, 330, 641–643.
- Tsikos, H., Jenkyns, H. C., & Walsworth-Bell, B., et al. (2004). Carbon-isotope stratigraphy recorded by the Cenomanian-Turonian Oceanic Anoxic Event: Correlation and implications based on three key localities. *Journal of the Geological Society*, 161, 711–719.

- Tyson, R. V. (1995). *Sedimentary organic Matter—Organic Facies and Palynofacies* (p. 615). Chapman and Hall.
- van Krevelen, D. W. (1950). Graphical-statistical method for the study of structure and reaction processes of coal. *Fuel*, 29, 269–284.
- Wortmann, U. G., Hesse, R., & Zacher, W. (1999). Major-element analysis of cyclic black shales: Paleooceanographic implications for the Early Cretaceous deep western Tethys. *Paleoceanography*, 14, 525–541.
- Yang, S., & Horsfield, B. (2020). Critical review of the uncertainty of  $T_{\max}$  in revealing the thermal maturity of organic matter in sedimentary rocks. *International Journal of Coal Geology*, 225, 103500.



# Maturity Determination of Contaminated Source Rocks by Pyrolysis and Thermal Oxidation Methods: A Review

Sedat Inan

## Abstract

Open system pyrolysis (e.g., Rock-Eval) is widely used screening technique for hydrocarbon source rock characterization. It is preferred because it is rapid, practical and cost-effective. However, some pitfalls exist due mainly to sample conditions and care must be exercised. One of the major problems occurs when source rock samples are contaminated by organic additives from the drilling fluids. Analyses of contaminated samples inevitably result in misrepresentative conclusions, possibly leading to incorrect directions. This paper revisits some previously reported problems due to contamination and discusses available remedies. Decontaminating source rock samples is conventionally accomplished by solvent extraction. However, a recent method called thermo-vaporization is equally successful in decontaminating samples prior to pyrolysis. In the case of concern about determining the true thermal maturity of samples contaminated with persistent contaminants, we remind the reader and discuss a recently proposed method, namely Oxidation T<sub>max</sub>. Finally, although pyrolysis is a rapid screening technique, sole dependence upon pyrolysis for petroleum source rock characterization must be avoided. At the least, for some selected samples, assessments should be based on integrated organic geochemical and organic petrographic analysis methods.

## 1 Introduction

Source rock evaluation is very important for the initial assessment of hydrocarbon potential of a given basin. It has become a tradition to use open system pyrolysis for

geochemical screening of petroleum source rocks (Behar et al., 2001; Espitalié, 1986; Espitalié et al., 1977; Horsfield, 1984; Peters, 1986; Peters & Cassa, 1994). Recently, unconventional petroleum potential of source rocks have been evaluated by in-place hydrocarbon determination using modified pyrolysis cycles (Romero-Sarmiento, 2019). Geochemical screening aims for rapid determination of the total organic carbon (TOC) content, type of kerogen, and its thermal maturity. LECO TOC analyses may also be performed for determination of the TOC content (Carvajal-Ortiz & Gentzis, 2015). Determination of maturity has become even more important for unconventional reservoirs as proper determination of maturity enables more accurate estimates of gas oil ratio (GOR) and gas content of the formation by using basin modeling (Hakami & Inan, 2016).

Thermal maturity of source rock kerogen is determined mainly based on optical microscopy (e.g., Teichmüller & Durand, 1983; Tissot & Welte, 1984), pyrolysis (Espitalié et al., 1977; Peters, 1986; Tissot & Welte, 1984), Raman Spectroscopy (e.g., Schmidt Mumm and Inan, 2016), biomarker analyses of source rock bitumen (e.g., Peters et al., 2005; Philp & Lewis, 1987) among many other available techniques. Pyrolysis, by far, is the most frequently used technique because it is rapid, practical, and cost-effective.

Pyrolysis is simply heating organic matter in the absence of oxygen, while thermal oxidation is heating organic matter in presence of oxygen. Thermal maturity assessment from open system pyrolysis is based on Pyrolysis T<sub>max</sub>. Although slight differences exist for kerogen types, the oil window maturity is generally defined as  $435\text{ °C} \leq T_{\text{max}} \leq 470\text{ °C}$  (Behar et al., 2001; Espitalié, 1986; Espitalié et al., 1977). Although pyrolysis is an inexpensive and rapid screening method, this relatively practical approach unfortunately carries with it a large potential pitfalls in characterization of source rock in terms of quality and maturity (Inan et al., 2018; Snowdon, 1995).

S. Inan (✉)

Faculty of Mines, Department of Geological Engineering, Istanbul Technical University, 34467 Maslak-Istanbul, Turkey  
e-mail: [sedatinan@itu.edu.tr](mailto:sedatinan@itu.edu.tr)



In this chapter, we will discuss the state of the art of open system pyrolysis and some pitfalls related to samples used. First, we will discuss recent advancement in methodologies to overcome these problems in pyrolysis. Next, we will discuss thermal oxidation as a complimentary method to pyrolysis-based maturity determinations.

## 2 Open System Pyrolysis

Before discussing some pitfalls related to the nature of the source rock sample used in pyrolysis, it is appropriate to briefly provide information on the open system pyrolysis technique (Behar et al., 2001).

Figure 1 shows a typical analysis cycle and a pyrogram obtained from pyrolysis. Applications of the parameters obtained from the pyrolysis analysis are also shown. Main parameters obtained are hydrogen index in mg HC/g TOC, oxygen index in mg CO<sub>2</sub>/g TOC and the Tmax which is the temperature at which hydrocarbon generation is maximum. A cross-plot of HI versus OI, known as a modified van Krevelen diagram, is widely used to type organic matter (kerogen) contained in the sample as shown in Fig. 2a. A cross-plot of HI versus Tmax as shown in Fig. 2b also enables identification of kerogen type and its maturity with respect oil and gas generation. Broad two-way arrows drawn in Figs. 2a and 2b depict the case for contamination of source rock samples. Depending on the organic constituents of the drilling mud, HI of the sample may artificially increase or decrease; likewise, Tmax of the sample may increase or decrease. Deviation from true values will depend on the severity of contamination of the sample introduced to pyrolysis analysis without pre-treatment.

Open system pyrolysis of source rocks demonstrates a shift in Tmax with increasing thermal maturity of the sample. As shown in Fig. 3, thermal degradation products defined as S2 peak (and its apex named as Tmax) shifts to higher temperatures. In a suit of samples, lower Tmax depicts low maturity, whereas higher Tmax depicts higher maturity. The accuracy of Tmax of the pyrolysis instrument (discussed by Espitalié et al., 1977) was reported to be 1°3 °C (Peters, 1986). Recent pyrolysis instruments provide less than 2 °C accuracy (King, 2015).

Open system pyrolysis is performed on a ground source rock sample (usually <250 micron). Hydrocarbons and CO<sub>2</sub>/CO are detected by flame ionization detector (FID) and thermal conductivity detector (TCD), respectively. In routine pyrolysis cycle, pyrolysis temperature program is run from 300 to 650 °C. S1 peak (in mg HC/g rock) stands for free hydrocarbons released during isothermal heating at 300 °C for 5 min. Pyrolysis is then performed normally at 25 °C/min up to 650 °C to detect hydrocarbons generated from kerogen cracking. Pyrolysis products are represented by S2

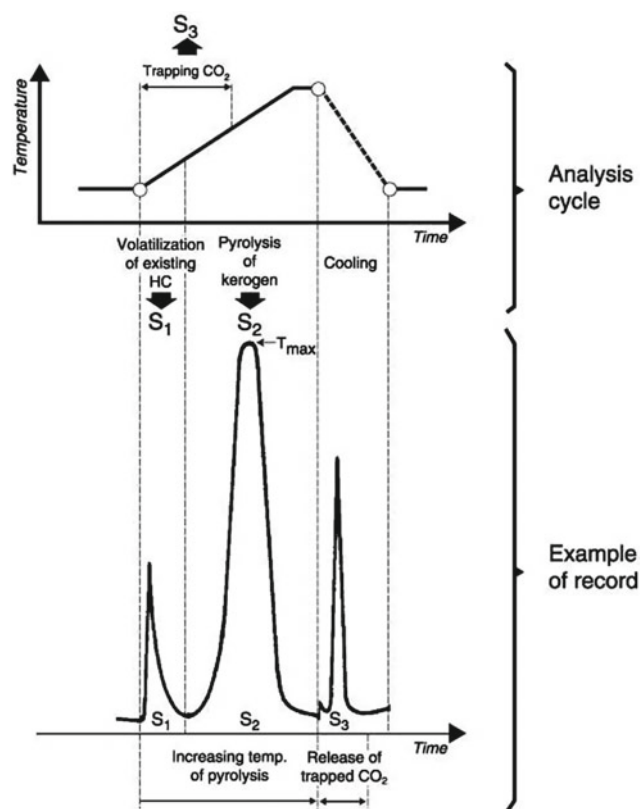


**Fig. 1** Open system pyrolysis oven temperature cycle and peak recording pyrograms

peak (in mg HC/g rock). With respect to the S2 peak, the Tmax (°C) is recorded, and it represents the apex of the S2 peak; the temperature at which hydrocarbon generation is at maximum during pyrolysis. During pyrolysis, oxygen-containing compounds are also liberated (from cracking of kerogen) and detected. This peak is called S3 peak and stands for mg CO<sub>2</sub>/g rock collected between 300 and 390 °C during the pyrolysis cycle.

## 3 Pitfalls in Pyrolysis Analysis Related to Sample Conditions

Pyrolysis analysis instruments have advanced and become more sophisticated since their development in the late 70s (Espitalié et al., 1977). In the new generation of pyrolysis instruments, hydrocarbon detection range, oven temperature stability, gas flow controllers, and many other aspects have been improved significantly and the accuracy and precision of the measurements are impressively high (King, 2015). However, many pitfalls still exist due to sample conditions. Despite continuous efforts toward achieving reliable guidelines for performing pyrolysis and interpreting results (e.g., Katz, 1983; Peters, 1986; Espitalié, 1986; Jarvie, 1991;

**Fig. 2** Kerogen typing and maturity determination based on pyrolysis (modified from Peters & Cassa, 1994). **a** HI versus OI plot, **b** HI versus Tmax plot where y-axis is as in A. Note that the HI versus OI plot cannot be used for high maturity samples to type kerogen. Green symbols, blue symbols, and red symbols depict Type I, Type II, and Type III kerogen, respectively. Arrows show possible dual effects of contamination on pyrolysis determined HI and Tmax; direction of the effect will naturally depend on the chemical composition of the contaminants (the drilling mud additives)

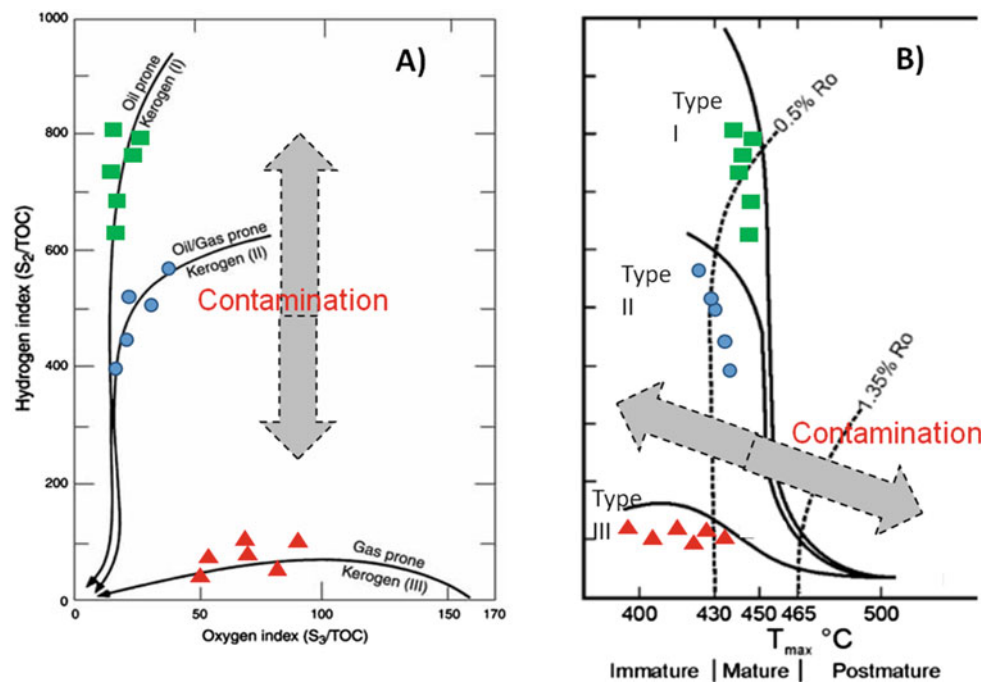
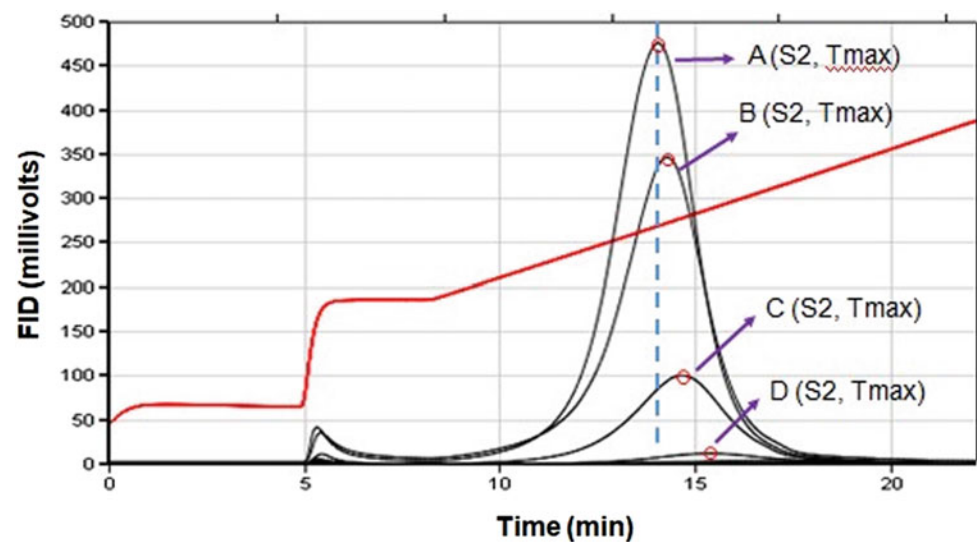


**Fig. 3** Pyrolysis analyses of samples of increasing maturity Inan et al., 2018 (modified from). Pyrolysis Tmax, the temperature recorded at apex of the S2 peak) shows a shift to higher temperatures for higher maturity samples (from least mature sample A to most mature sample D)



Peters & Cassa, 1994; Inan et al., 1998; Ohm et al., 2007; Dembicki, 2009; Carvajal-Ortiz & Gentzis, 2015; Akinlua et al., 2016; Inan et al., 2017; Inan et al., 2018), in practice, relying solely on pyrolysis for source rock characterization may lead to seriously misleading conclusions. Unfortunately, this easy-way approach may lead to erroneous evaluations of source rock richness and maturity. Moreover, when source rocks are considered unconventional reservoir rocks, the possible threat scale becomes higher (Hakami & Inan, 2016). A detailed account of problems related to source rock samples to be analyzed by pyrolysis has been dealt with by many workers (e.g., Katz, 1983; Peters, 1986; Skyes & Snowdon, 2002; Carvajal-Ortiz & Gentzis, 2015).

Below is a shortlist of these shortcomings related to source rock samples' conditions delivered to laboratories for analysis.

**High Maturity Samples:** Such samples yield insufficient pyrolysis products, and thus, the Tmax reading is obviously much higher than normal (Peters, 1986). Moreover, even slight contamination can dominate the programs, and this situation can easily perturb detection of true Tmax. For example, pyrograms of four mature and solvent-extracted samples are shown in Fig. 4. Since the S2 peaks are small, slight contamination left in the samples appears as broad shoulders on the right of programs (1, 2, and 3 in Fig. 4).

This indicates that resistant contaminants could not be removed by solvent extraction.

**Contaminated Samples:** Contamination of samples (cores or cuttings) obtained from boreholes drilled with OBM unfavorably affect Pyrolysis T<sub>max</sub>. Drilling engineers add a variety of organics for smoother operation, and some of these organic materials are quite persistent (Walker et al., 1986; Baker Hughes, 2006; Nciri et al., 2014). When sample contaminant is made up of low molecular weight organic material (e.g., diesel), removal by solvent extraction is relatively easy and the sample is mostly cleaned and ready for pyrolysis analysis for maturity determination. An example of this case is shown in Fig. 5. The pyrogram of the extracted sample shows that both S1 and S2 peaks are reduced and the shoulder of the S2 peak present for the as-received sample has disappeared. The decrease in S2 indicates some thermally stable extractable organic matter is carried over to the S2 peak (Delvaux et al., 1990) in the pyrolysis of the as-received sample. The apex of the S2 peak, the T<sub>max</sub>, has shifted to the right (increased) as expected in the extracted sample.

**Extremely Organic-Rich Samples and Coals:** Flame ionization detector (FID) saturation during pyrolysis of organically very rich samples or organically contaminated samples is another problematic case, whereby S2 and T<sub>max</sub> are not properly identified. In this case, reducing the sample size used for pyrolysis is the remedy for organically rich samples (Peters, 1986; Sykes & Snowdon, 2002). Contaminated samples require treatment as it will be discussed below.

**Organic Poor (Lean) Samples:** Pyrolysis of organically lean siliciclastic (e.g., shale) samples is known to produce higher than normal T<sub>max</sub> values due to retention of generated hydrocarbons on minerals. This phenomenon is known as mineral matrix effect (e.g., İnan et al., 1998; Peters, 1986).

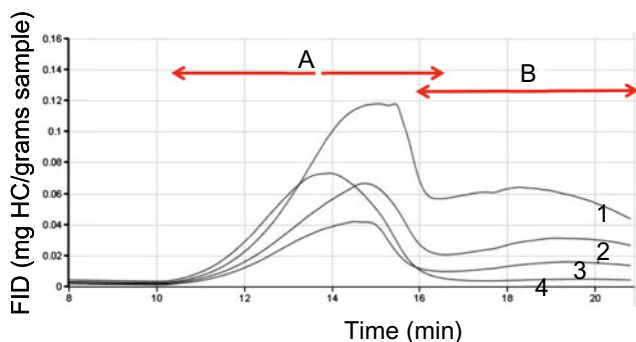


**Fig. 4** Pyrograms for four extracted samples of equivalent maturity (obtained within a 100 ft distance from a core). The measured T<sub>max</sub> is 465–475, so the samples are mature with respect oil generation

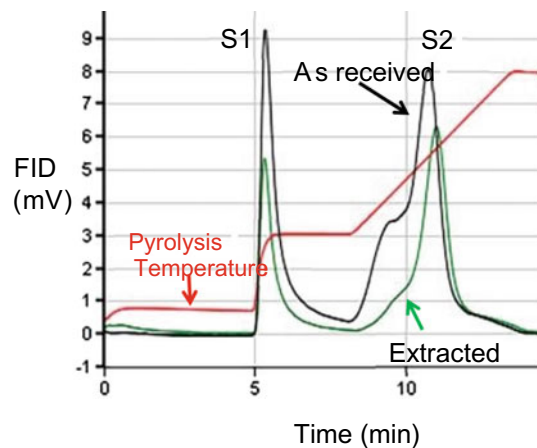


**Fig. 5** Pyrograms of parallel sample splits “as-received” and “solvent-extracted” King, 2015 (modified from). Pyrograms shown in black and green are for the as-received and extracted samples, respectively

#### 4 Remedies for Maturity Determination of Contaminated Samples

The conventional remedy for decontaminating a source rock sample prior to determining its maturity based on pyrolysis T<sub>max</sub> is extracting the sample with a strong organic solvent. Recently, proposals have been made on decontaminating samples by thermo-vaporization (İnan et al., 2018; İnan, 2020a) and oxidation T<sub>max</sub> as an alternative or complementary method (İnan et al., 2017) for maturity determination of contaminated samples. It is appropriate to revisit the salient points of the proposed methods, namely the thermo-vaporization for decontaminating samples and oxidation T<sub>max</sub> as a complementary method for determining source rock maturity. However, before doing this, it is worth summarizing the significant volume of publications on this subject to show how important the phenomenon of sample contamination has been in petroleum exploration and research.

Although use of oil-based mud (OBM) benefits drilling engineers, it leads to undesirable consequences for geochemists in charge of analyses and characterizations of source rocks. It is widely known that organic additives in the drilling mud may have adverse effect on the pyrolysis-based maturity of the samples. Pyrolysis of such samples leads to masking effect on the true pyrolysis T<sub>max</sub>. When this is undetected, erroneous T<sub>max</sub>-based maturity will be reported, and this will underestimate real thermal maturity (Akinlua et al., 2016; Hakami & İnan, 2016; İnan et al., 2018; İnan, 2020a; Peters, 1986; Petersen et al., 2017). The end result can be even more dramatic when such maturity data are used to calibrate basin modeling (Hakami & İnan, 2016). Akinlua et al. (2016) showed that pyrolysis of as-received

(unextracted) samples suggested Type III kerogen. However, pyrolysis analysis of the same sample after solvent extraction suggested the presence of both Types II/III and III kerogen. Most experts in petroleum exploration presume and argue that cores of tight source rock intervals do not get contaminated by oil-based mud or at least the mud will not penetrate the core.

On the contrary to this presumption, Petersen et al. (2017) have demonstrated that core samples are also contaminated and this adversely affects organic geochemical analyses on core samples. They showed that the drilling mud has invaded into the center of the 5–1/4 in. (13.34 cm) core and the contamination has not only affected pyrolysis results but also kinetic measurements, resulting in pseudo petroleum generation at low temperatures. They concluded that most of these low  $E_a$  peaks can be related to contamination. Rock–Eval pyrolysis S2 peaks from these samples have a “shoulder” indicating carry over from the S1 peak. So, the HI values (and possibly kerogen quality) were also overestimated (Petersen et al., 2017). Moreover, laboratory artificial maturation of source rock samples for oil expulsion studies (e.g., İnan, 2020b) require cleaned source rock samples; otherwise, miscalculation on oil expulsion efficiency is inevitable. These examples clearly demonstrate that cleaning source rock samples of contaminants is a must-follow step prior to geochemical analyses. Analysis of decontaminated source rock samples will no doubt yield more reliable results on TOC content, pyrolysis-based kerogen typing and maturity, as well as artificial maturation and oil expulsion efficiency studies.

In search for a more reliable analysis of contaminated source rock samples, İnan et al. (2017) reported a new maturity indicator, namely oxidation Tmax. Oxidation Tmax is derived from recording of the temperature of the maximum yield of kerogen’s thermal oxidation during Rock–Eval analysis. This peak is less influenced by OBM contamination (because most, if not all, contaminants will vanish during pyrolysis cycle), and therefore, it provides more robust maturity for contaminated source rocks. The authors pointed out that the oxidation method can be conducted by using both a LECO instrument and/ a standard Rock–Eval pyrolysis instrument with pyrolysis and oxidation cycles. Application of the oxidation Tmax method will gain more popularity in coming years, due mainly to decades of experience of laboratory scientists on application of pyrolysis. The pyrolysis method will continue to be important in geochemical labs for some time. As we presume that pyrolysis Tmax will continue to be used widely, decontaminating the samples before pyrolysis is a justified and well worthy practice. In decontamination of source rock samples, we mentioned the classical method of solvent extraction and more recent method called “thermo-vaporization.”

#### 4.1 Decontaminating Source Rock Samples Prior to Pyrolysis

There is no doubt that solvent extraction is an effective method for decontaminating source rocks from organic contaminants, but this method is costly and time-consuming. Moreover, if the solvents are not effectively removed from the sample, this may complicate geochemical analyses to be performed. An effective solvent extraction is normally performed by using a Soxhlet apparatus (e.g., Harwood & Moody, 1989). However, the method takes considerable time. When the sample turnover is high, relatively faster extraction is conducted by using the accelerated solvent extraction (ASE) system. On the other hand, it is known that removal of persistent contaminants like resin and asphaltic material may not be possible by solvent extraction. İnan et al. (2018) following the prior work of İnan (2017 published in 2020) reported an alternative method that is faster and low-cost. The method is called “thermo-vaporization” and has been shown to be a powerful alternative to solvent extraction process. Reportedly, thermo-vaporization method eliminates the need for time-consuming solvent extraction. İnan et al. (2018) stated that careful thermo-vaporization program warrants that the kerogen is not affected during thermo-vaporization process; only the contaminants are removed. However, they cautioned that removal of heavy organics like asphaltic material cannot be possible without breaking some part of the source rock kerogen at increased temperatures (>375 °C) required to remove contaminants with thermo-vaporization.

In developing the thermo-vaporization method, İnan et al. (2018) obtained a sample of oil-based mud (OBM). They pyrolyzed several splits of the OBM sample and found a Tmax of the OBM sample to be  $432 \pm 2$  °C. They later mixed the OBM with powder splits of immature- and mature-source rock samples with varying proportions. Figure 6 shows pyrolysis results of the as-received and the OBM-contaminated sample. While the recorded Tmax of the as-received (clean) source rock sample was 419 °C, the Tmax of the mixture turned out to be 429 °C. Since the Tmax of the OBM ( $432 \pm 2$  °C) was greater than the sample in as-received condition, the resultant Tmax of the mixture, as expected, turned out to be higher (429 °C).

Next, İnan et al. (2018) performed pyrolysis analysis of a sample produced by a mixture of OBM and as-received mature source rock sample (predetermined Tmax of 462 °C). The program given in Fig. 7 shows that the resultant Tmax of the mixture was 437 °C. The effect of the OBM in this case has been decreasing the Tmax of the as-received sample. Since the Tmax of the OBM ( $432 \pm 2$  °C) was lower than that of the sample (462 °C), the contamination led to determination of lower than real maturity. With these

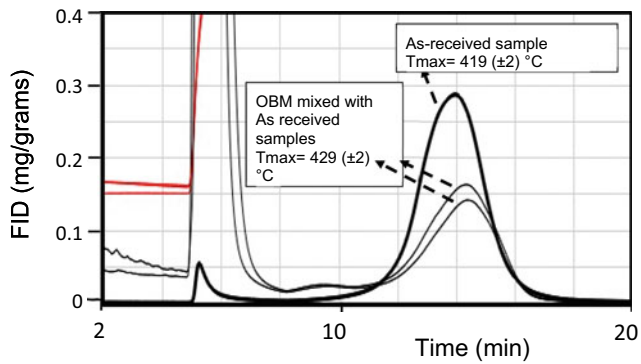


**Fig. 6** Comparison of pyrogram of as-received sample and pyrogram of OBM mixed with the as-received sample. The first 8 min show detection of volatile OBM components (modified from İnan et al., 2018)

experiments, İnan et al. (2018) were able to show that due to OBM contamination an “immature sample” was misidentified as “oil mature” and a “gas mature” sample was misidentified as “oil mature” based on the  $T_{max}$  of the pyrolysis.

After determining the adverse influence of the OBM on  $T_{max}$  maturity, İnan et al. (2018) prepared mixtures of mature rock sample with the addition of different amounts of OBM material. The mixed sample set was obtained by mixing 100 mg of sample with 40, 20, 10, and 5 mg OBM; the prepared sample set contained one original (as-received) and four contaminated samples. They conducted pyrolysis to determine  $T_{max}$  of the mixtures. Later, they performed decontamination by the classical solvent extraction method. The last step was to dry and pyrolyze the solvent-extracted samples. As shown in Fig. 8, it is clear that solvent extraction has removed much of the OBM and that  $T_{max}$  values of 455–460 °C of the extracted samples were found to be quite close to the  $T_{max}$  value of 462 °C of the original sample (shown by green filled circle).

By first contaminating source rock samples and later decontaminating them by conventional solvent extraction as

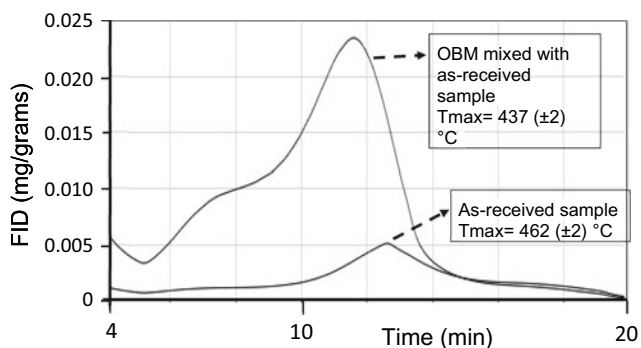


**Fig. 7** Comparison of pyrogram of the “As-received” sample ( $T_{max}$  462 °C) and the program of the mixture of OBM and the sample

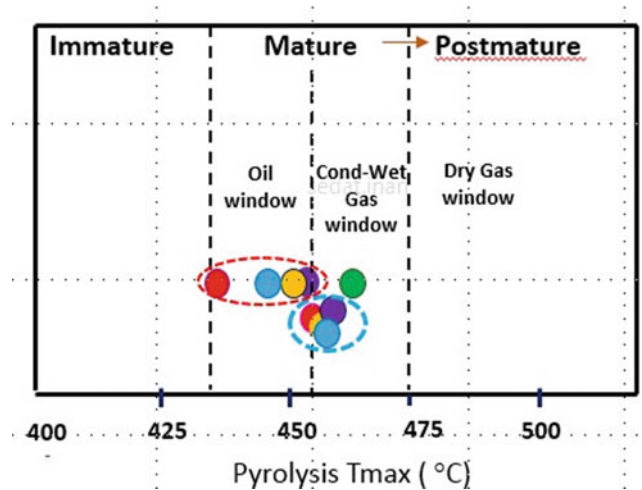


**Fig. 8** Plot depicting pyrolysis  $T_{max}$  variations between pre- and post-solvent extraction of the high maturity samples. The samples contain varying amount of OBM.  $T_{max}$  values enclosed in the red ellipse are of the contaminated samples.  $T_{max}$  values enclosed within the blue ellipse are of the solvent-extracted samples. Green circle is the  $T_{max}$  value of the original sample. Red, blue, orange, and purple circles depict source rock samples mixed with 40 mg, 20 mg, 10 mg, and 5 mg OBM, respectively

explained above, İnan et al. (2018) obtained a benchmark for developing the thermo-vaporization (TV) method. The TV method to be developed should be at least as successful as the solvent extraction method on the samples prepared. With this aim, they experimented TV to decontaminate source rock samples and achieve results comparable to solvent extraction (as shown in Fig. 8). Here, the critical challenge was to find out the best temperature threshold to clean the samples of the OBM without affecting the source rock kerogen (e.g., thermal cracking). Several changes made in the pyrolysis device’s temperature cycle resulted in an optimized temperature cycle as shown in Fig. 9.

Figure 10 shows pyrograms of pyrolysis analysis of thermo-vaporized splits of an immature source rock sample

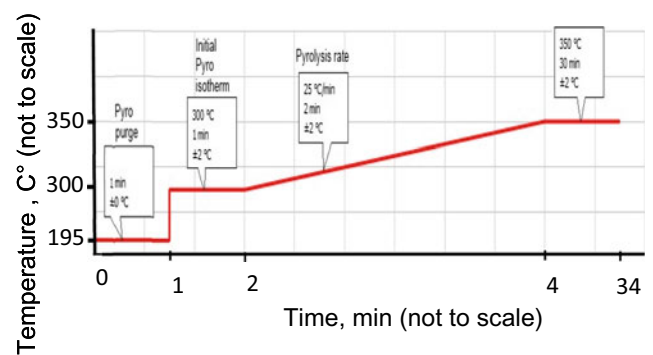


**Fig. 9** Pyrolysis chamber’s temperature cycle for thermo-vaporization (TV). This is for TV at 350 °C for 30 min (modified after İnan et al., 2018)

at 350 °C for varying durations from 5 to 30 min; a pyrogram of the original sample (not thermo-vaporized) is also shown for comparison. The results show that TV of an immature sample had a negligible effect on the source rock kerogen; increasing the maturity to Tmax of 425 °C compared to the original 419 °C Tmax. While 5 min TV resulted in 1 °C increase in Tmax, 30 min TV at 350 °C led to a 6 °C increase in the Tmax. Considering that this is a quite low maturity sample with a Tmax value of 419 °C, the effect of the TV on the kerogen is expected to be the maximum; an effect of TV causing only 6 °C increase was considered acceptable. Moreover, extrapolating to higher maturity samples, the impact of TV on more mature samples was considered to be quite insignificant to none. The conclusion was that TV did not alter the source rock kerogen at 350 for up to a 30 min duration so TV could be safely used for decontaminating source rock samples.

The next step was to experiment TV on OBM-contaminated samples and compare the results with solvent extraction. Figure 11 shows the pyrolysis Tmax determined after thermo-vaporization of OBM-contaminated splits of the high maturity (Tmax = 462 °C) source rock sample. TV was varied in temperature and duration such as 350 °C for 30 min, 60 min, and 90 min. At 375 °C TV, the duration was 30 min. Results showed that only TV at 350 °C continued for 90 min significantly increased the Tmax of the sample by about 8 °C. Other TV experiments cleaned the samples, and the resultant Tmax of the samples was very close to the original sample (Fig. 11). As a result, TV was considered adequate as the solvent extraction method and that TV was suitable for decontaminating source rock samples at 350 °C for 30 and 60 min or at 375 °C for 30 min.

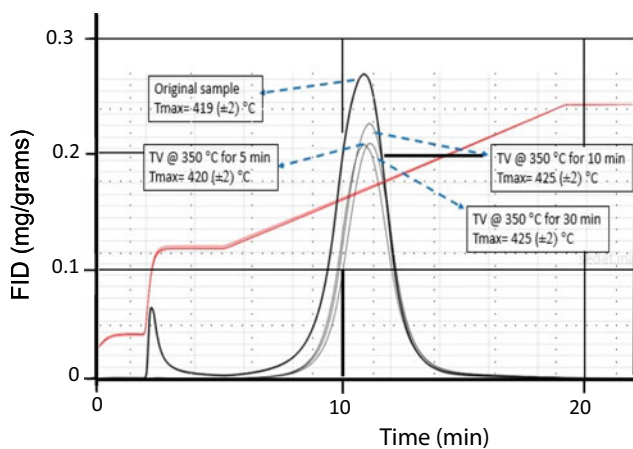


**Fig. 10** Pyrolysis of thermo-vaporized splits of an immature source rock sample at 350 °C for different durations (modified after Inan et al., 2018). The original sample's Tmax value (419 °C) increased to 425 °C when the sample was thermo-vaporized for 30 min

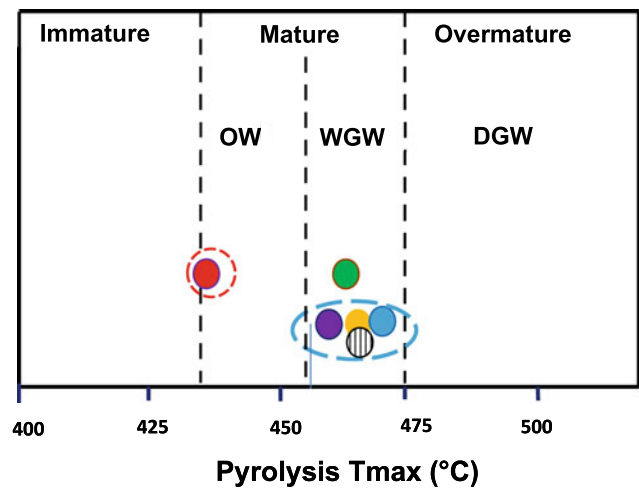


**Fig. 11** Plot showing pyrolysis Tmax after TV (for different durations) of OBM-contaminated splits of a sample. The original Tmax value for the sample is 462 °C. Tmax of the original sample (green filled circle) and Tmax of the OBM-contaminated sample (red filled circle) are shown. Purple-, orange-, and blue-filled circles depict the pyrolysis Tmax of samples thermo-vaporized at 350 °C for 30, 60, and 90 min durations, respectively. Lined-filled circle shows the Tmax of the sample thermo-vaporized at 375 °C for 30 min. Red ellipse encloses the Tmax values of the OBM-contaminated sample. Blue ellipse encloses the Tmax values of the samples after TV. Oil Window, Wet Gas Window, and Dry Gas Window maturity zones are shown as OW, WGW, and DGW, respectively

## 4.2 Thermal Oxidation of Contaminated Samples: Oxidation Tmax

From the above discussion, it is very clear that, prior to geochemical analyses, cleaning source rock (cuttings and/or core) samples obtained from a well drilled using OBM is necessary. Classical solvent extraction and thermo-vaporization are both suitable methods for cleaning. However, care must be exercised that during decontamination the kerogen is not altered. For relatively less resistant OBM components, removal is efficient and the kerogen will not be affected. However, resistant components of OBM (e.g., Walker et al., 1986; Baker Hughes, 2006) will be difficult to remove either by thermo-vaporization or solvent extraction and will certainly result in misleading pyrolysis results (both S2 and Tmax). For this reason, Inan et al. (2017) tried to estimate thermal maturity through oxidation rather than pyrolysis. The aim was to obtain a maturity from oxidation where decontamination fails and use oxidation-based maturity as further verification of pyrolysis Tmax.

The oxidation Tmax, the temperature at which oxidation product is maximum, has been shown to be affected less by contamination (Inan et al., 2017) and can easily be obtained using a LECO analyzer. Pyrolysis instrument equipped also with an oxidation furnace is also suitable for obtaining oxidation Tmax on a source rock sample. Pyrolysis is widely

known and used source rock screening method among petroleum geochemists (Carvajal-Ortiz & Gentzis, 2015). On the other hand, thermal oxidation is a commonly used method in the coal and oil shale industry for determination of reactivity of fuel chars and coal as well as for the development of combustion and coal gasification systems (e.g., Levy & Stuart, 1984; Lee et al., 1985; Kok & Pamir, 2000; Kastanaki & Vamvuka, 2006; Murphy & Shaddix, 2006; Wall et al., 2009; Syed et al., 2011). İnan et al. (2017) have shown that thermal oxidation is a technique petroleum geochemist can significantly benefit from when maturity assessment of source rock is concerned, provided that the method is properly calibrated against known maturity parameters.

As part of the experimental work aiming for development of the oxidation Tmax method, İnan et al. (2017) used a suite of shale samples of varying maturity determined and correlated by different geochemical and optical methods (İnan et al., 2016). The maturity of the samples, based on pyrolysis Tmax, ranged from 413 to 518 °C; covering a wide maturity range. The details of the methods are given in İnan et al. (2017) but it is useful to mention them here shortly. The oxidation of the ground splits of the sample was conducted using a LECORC-612 instrument. The temperature program for thermal oxidation was set operate from 400 to 600 °C at 25 °C/min or 50 °C/min. Powder samples used varied from

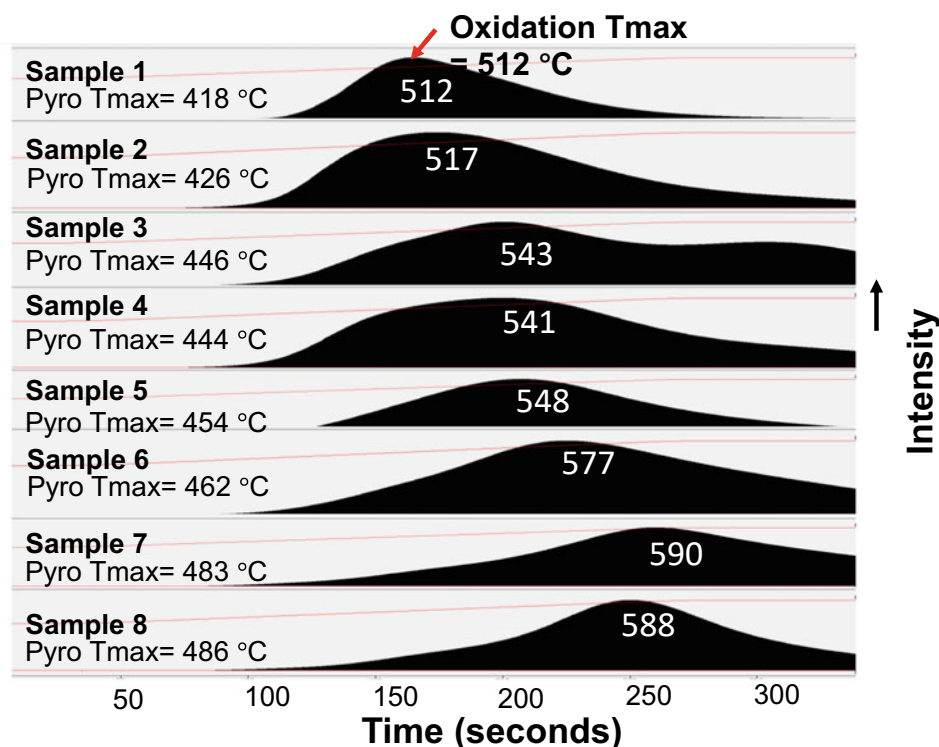
40 to 100 mg; Repeatability for oxidation Tmax was determined to be about  $\pm 2$  °C. The oxigrams (plots of detected oxidation products versus oxidation time) are shown in Fig. 12.

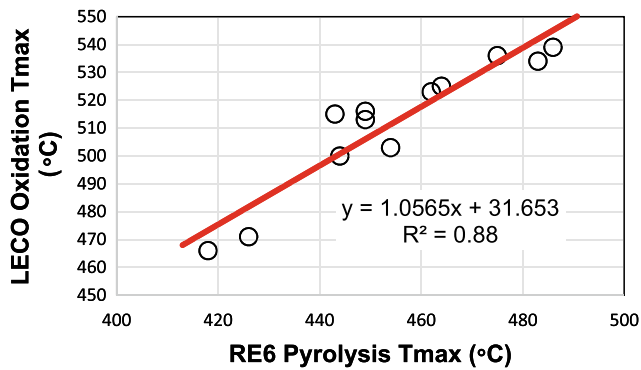
Plot in Fig. 13 shows the oxidation Tmax against pyrolysis Tmax. The correlation was strong and encouraging. Therefore, in the next step, the oxidation of the splits of the samples was run using Rock-Eval 6 (RE6) instrument methods. The oxidation products from residual organic carbon (S4) were trapped and detected between 400 and 650 °C.

Figure 14 shows a plot of oxidation Tmax versus pyrolysis Tmax, both obtained from RockEval 6 (RE 6) instrument cycles. The correlation is still impressively good. İnan et al. (2017) noted that using a pyrolysis instrument with an oxidation cycle for obtaining oxidation Tmax is very advantageous because charring is already achieved during the pyrolysis stage, meaning that free and pyrolyzable hydrocarbons are already removed at pyrolysis stage prior oxidation. So, following routine pyrolysis cycle, the Tmax from the oxidation of the residual carbon can be easily measured. As shown in Fig. 14, correlation between RE6 pyrolysis Tmax and RE6 oxidation Tmax yielded a very good coefficient (0.89); this suggests a strong relationship. As a result, the relationship was found to be.

RE6 (S2) pyrolysis Tmax (°C) = 1.7104 \* RE6 (S4) oxidation Tmax—272.82 ( $r^2 = 0.89$ ).

**Fig. 12** Oxiograms of samples from oxidation analyses using a LECO analyzer. Heating rate of 50 °C/min was employed. Pre-determined pyrolysis Tmax values showing progressive increase are given on the left of the plot. Oxidation Tmax values similarly show a progressive increase in good correlation with sample maturity based on Pyrolysis Tmax. Red lines are temperature profiles from 400 to 600 °C (modified from İnan et al., 2017)





**Fig. 13** Plot comparing RE6 Pyrolysis Tmax values and LECO oxidation Tmax values. Oxidation Tmax values are from LECO analyzer and are obtained from a cycle at a heating rate of 50 °C/min

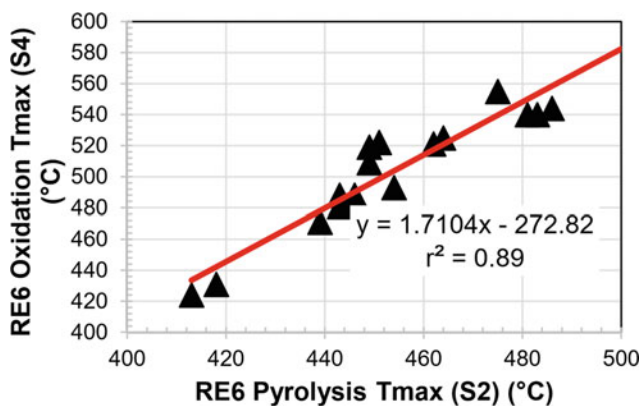


**Fig. 14** Correlation of oxidation Tmax (S4) and pyrolysis Tmax (S2), both obtained on samples using RE6 instrument

## 5 Conclusions

Carvajal-Ortiz and Gentzis (2015) have rightfully noted that pyrolysis is widely used by geochemists all over the World because the technique is easy and rapid to use. Moreover, the analyses results are relatively easy to interpret. However, they also noted that the users of pyrolysis method must be aware of the shortcomings and analytical pitfalls that may lead to less than desirable validity and quality of the results and their interpretation. We agree with the authors in that data quality of pyrolysis analyses is an important issue and the experience required to properly conduct quality assurance and quality check need to be satisfied. In this review, we have verified and concurred with Carvajal-Ortiz & Gentzis (2015)'s alerts and recommendations.

We have re-stated that pyrolysis is a rapid and cost-effective source rock screening technique that is widely applied across the world. We noted with satisfaction that technological improvements in pyrolysis instrumentation, from its first introduction by Espitalié et al. (1977) up to

present day, have been quite impressive. The range of detectors, sensors and gas flow controllers and stability of oven temperature have all been improved in many commercial pyrolysis instruments available in the market. The apparatus is not only used for fast characterization of source rock samples, but also is used for kinetic analysis and artificial maturation and oil expulsion efficiency studies. If there is a need to mention one limitation, this would be the sample size of the instrument that cannot exceed few hundred milligrams. Inan (2020b) has provided a solution to this shortcoming by introducing "restricted system pyrolysis system."

In summary, all commercially available pyrolysis instruments are efficient for source rock characterization. The main limitation in application of pyrolysis method is mainly related to the condition of source rock samples (in the form of core and/or cutting samples) received by laboratories. The major pitfalls are the contamination of samples by drilling mud containing organic additives or, sometimes, pure oil-based mud. Pyrolysis of such samples leads to erroneous results on source rock quality (TOC content, kerogen typing, and maturity). We conclude that decontaminating such contaminated source rock samples should be a routine practice prior to pyrolysis analysis. Classical solvent extraction is a proven method that can efficiently remove most soluble light- and medium-weight organic material. We have reminded the fact that solvent extraction is a process that can alter the sample in some instances. Therefore, we have discussed the thermo-vaporization method, which does not require special treatment of the sample. All needed is the thermo-vaporization of the sample in the crucible prior to full cycle pyrolysis analysis. It is important to note that samples decontaminated by solvent extraction and/or thermo-vaporization methods will lose their free hydrocarbons together with the contaminant material during the decontaminating process. So, pyrolysis S1 or S1/TOC ratio will no longer be a parameter to be used in interpretations. After decontamination, both the pyrolysis peak, S2, and the Tmax will most likely come out much better, representing the samples' true state. We need to caution that persistent organics (such as sulfonated thermoplastic polymers) added to, especially high temperature, drilling fluids could severely contaminate some source rock samples (sulfonated thermoplastic polymers (Walker et al., 1986)). We note that neither thermo-vaporization nor solvent extraction will be efficient in the decontamination of such samples. Oxidation Tmax introduced by Inan et al. (2017) can be obtained by thermal oxidation of the sample in a controlled instrument like LECO and Rock-Eval pyrolysis.

We recommend decontaminating source rock samples prior to pyrolysis analysis for characterization. However, we also recommend that dependence on pyrolysis for source rock characterizations in high-sample turnover laboratories should be avoided as much as possible.



At the least, some selected control samples should be analyzed by thermal oxidation and optical microscopy for further verification.

**Acknowledgements** I thank my former colleagues from Saudi Aramco EXPEC ARC; namely Salman Qathami, Mahmoud Zahrani, Mohammed Alsobaie, and Sebastian Henderson for collaboration and laboratory analyses. The manuscript was improved due to constructive comments of two anonymous reviewers. I thank the editors, Dr. Haytham El Atfy and Dr. Bandar I. Ghassal, for inviting me to write this chapter for their impressively efficient editorial handling.

## References

- Akinlua, A., Ajayi, T.R., & Jarvie, D. M. (2016). A re-appraisal of the application of Rock-Eval pyrolysis to source rock studies in the Niger Delta. *Journal of Petroleum Geology*, 28, 3948.
- Behar, F., Beaumont, V., & De B. Penteadó, H. L. (2001). Rock-Eval 6 technology: performances and developments. *Oil Gas Sci. Technol. Rev. Inst. Fr. Pet. Energ. Nouv.*, 56, 111–134.
- Carvajal-Ortiz, H., & Gentzis, T. (2015). Critical considerations when assessing hydrocarbon plays using Rock-Eval pyrolysis and organic petrology data: Data quality revisited. *International Journal of Coal Geology*, 152, 113–122.
- Delvaux, D., Martin, H., Leplat, P., & Paulet, J. (1990). Comparative Rock-Eval pyrolysis as an improved tool for sedimentary organic matter analysis. *Organic Geochemistry*, 16, 1221–1229.
- Dembicki, H., Jr. (2009). Three common source rock evaluation errors made by geologists during prospect or play appraisals. *Bulletin of the American Association of Petroleum Geologists*, 93, 341–356.
- Espitalié, J., Laporte, J. L., Madec, M., Marquis, F., Leplat, P., Pauletand, J., & Boutefeu, A. (1977). Method rapide de caractérisation des roches meres, de leur potential petrolieret de leudegré'evolution. *Inst. Fr. Pét.*, 32, 23–42.
- Espitalié, J. (1986). Use of Tmax as a maturation index for different types of organicmatter: Comparison with vitrinite reflectance. In J. Burrus (Ed.), *Thermal modelling in sedimentary basins* (pp. 475–496). Editions Technip.
- Hakami, A., & İnan, S. (2016). A basin modeling study of the Jafurah Sub-Basin, Saudi Arabia: Implications for unconventional hydrocarbon potential of the Jurassic Tuwaiq Mountain Formation. *International Journal of Coal Geology*, 165, 201–222.
- Harwood, L. M., & Moody, C. J. (1989). Experimental organic chemistry: Principles and practice (Illustrated ed., pp. 122–125). Wiley-Blackwell. ISBN 0-632-02017-2
- Hughes, B. (2006). Drilling fluid reference manual (Chap. 5). In *Oil/Synthetic Drilling Fluids* (pp. 205–279).
- Horsfield, B. (1984). Pyrolysis studies and petroleum exploration. In J. Brooks, & D. H. Welte (Eds.), *Advances in petroleum geochemistry* (pp. 247–298). Academic Press.
- İnan, S. (2020a). Decontaminating rock samples by thermovaporization. United States Patent # US 10,578,600 B2. Granted: 3March 2020a. (Application # 16/056,646, Filed: August 9, 2018).
- İnan, S. (2020b). Pyrolysis to determine hydrocarbon expulsion efficiency of hydrocarbon source rock. United States Patent # US 10,611,967 B2. Granted: 7 April 2020b. (Application # 15/637,932, Filed: June 29, 2017).
- İnan, S., Qathami, S., Zahrani M., Alsobaie, M. (2018). Thermovaporization for decontaminating hydrocarbon source rocks. *International Journal of Coal Geology*, 189, 111–121.
- İnan, S., Henderson, S., & Qathami, S. (2017). Oxidation Tmax: A new thermal maturity indicator for hydrocarbon source rocks. *Organic Geochemistry*, 113, 254–261.
- İnan, S., Goodarzi, F., Schmidt Mumm, A., Arouri, K., Qathami, S., Ardakani, O. H., İnan, T., & Tuwailib, A. A. (2016). The silurian qusaiba hot shales of Saudi Arabia: An integrated assessment of thermal maturity. *International Journal of Coal Geology*, 159, 107–119.
- İnan, S., Yalçın, M. N., & Mann, U. (1998). Expulsion of oil from petroleum source rocks: Inferences from pyrolysis of samples of unconventional grain size. *Organic Geochemistry*, 29, 45–61.
- Jarvie, D. M. (1991). Factors affecting Rock-Eval derived kinetic parameters. *Chemical Geology*, 93, 79–99.
- Kastanaki, E., & Vamvuka, D. (2006). A comparative reactivity and kinetic study on the combustion of coal–biomass char blends. *Fuel*, 85, 1186–1193.
- Katz, B. J. (1983). Limitations of “Rock-Eval” pyrolysis for typing organic matter. *Organic Geochemistry*, 4, 195–199.
- King, R.R. (2015). Modified method of interpretation of source rock pyrolysis for an unconventional world. AAPG Annual Convention and Exhibition, Denver-CO, USA, May 31–June 3, 2015. (Search and Discovery Article # 41704, 2015)
- Kök, M. V., & Pamir, M. R. (2000). Comparative pyrolysis and combustion kinetics of oil shales. *Journal of Analytical and Applied Pyrolysis*, 55, 185–194.
- Lee, I. C., Lee, M. D., & Dohn, H. Y. (1985). A DTA study of some oxidation characteristics of Colorado oil shale. *Thermochemica Acta*, 84, 371–375.
- Levy, J. H., & Stuart, W. I. (1984). Oxidative profiles of some Australian oil shales by thermal analysis and infrared spectroscopy. *Thermochemica Acta*, 74, 227–234.
- Murphy, J. J., & Shaddix, C. R. (2006). Combustion kinetics of coal chars in oxygen-enriched environments. *Combustion and Flame*, 144, 710–729.
- Nciri, N., Song, S., Kim, N., & Cho, N. (2014). Chemical characterization of Gilsonite Bitumen. *Journal of Petroleum & Environmental Biotechnology*, 5, 1–10. <https://doi.org/10.4172/2157-7463.1000193>
- Ohm, S. E., Karlsen, D. A., Backer-Owe, K., Pedersen, J. H., & Beeley, H. S. (2007). A drilling mud additive influencing the geochemical interpretations of hydrocarbon shows. *Petroleum Geoscience*, 13, 369–376.
- Peters, K. E. (1986). Guidelines for evaluating petroleum source rock using programmed pyrolysis. *Bulletin of the American Association of Petroleum Geologists*, 70, 318–329.
- Peters, K. E., & Cassa, M. R. (1994). Applied source rock geochemistry. In L. B. Magoon, & W. G. Dow (Eds.), *The petroleum system—from source to trap. American association of petroleum geologists memoir* 60 (pp. 93–120).
- Peters, K. E., Walters, C. C., & Moldowan, J. M. (2005). The biomarker guide: Biomarkers and isotopes in petroleum exploration and earth history. (Vol. 2, 1st ed., p. 471). Cambridge University Press.
- Petersen, H. I., Hertle, M., & Sulbrück, H. (2017). Upper Jurassic–lowermost Cretaceous marine shale source rocks (Farsund Formation), North Sea: Kerogen composition and quality and the adverse effect of oil-based mud contamination on organic geochemical analyses. *International Journal of Coal Geology*, 173, 26–39.
- Philp, R. P., & Lewis, C. A. (1987). Organic geochemistry of biomarkers. *Annual Review of Earth and Planetary Sciences*, 15, 363–395.
- Romero-Sarmiento, M. F. (2019). A quick analytical approach to estimate both free versus sorbed hydrocarbon contents in liquid-rich source rocks. *Bulletin of the American Association of Petroleum Geologists*, 103, 2031–2043.
- Schmidt Mumm, A., & İnan, S. (2016). Microscale organic maturity determination of graptolites using Raman spectroscopy. *International Journal of Coal Geology*, 162, 96–107.

- Snowdon, L. R. (1995). Rock-Eval Tmax suppression: Documentation and amelioration. *Bulletin of the American Association of Petroleum Geologists*, 79, 1337–1348.
- Syed, S., Qudaih, R., Talab, I., & Janajreh, I. (2011). Kinetics of pyrolysis and combustion of oil shale sample from thermogravimetric data. *Fuel*, 90, 1631–1637.
- Sykes, R., & Snowdon, L. R. (2002). Guidelines for assessing the petroleum potential of coaly source rocks using Rock-Eval pyrolysis. *Organic Geochemistry*, 33, 1441–1455.
- Teichmüller, M., Durand, B. (1983). Fluorescence microscopical rank studies on liptinites and vitrinites in peat and coals, and comparison with results of the Rock-Eval pyrolysis. *International Journal of Coal Geology*, 2, 197–230.
- Tissot, B. P., & Welte, D. H. (1984). *Petroleum Formation and Occurrence* (p. 699). Springer.
- Walker, T. O., Peiffer, D. G., Lundeberg, R. D. (1986). High temperature drilling fluids based on sulfonated thermoplastic polymers. US Patent # 4,579,669
- Wall, T., Yinghui, L., Spero, C., Elliott, L., Khare, S., Rathnam, R., Zeenathal, F., Moghtaderi, B., Buhre, B., Chanqdong, S., Gupta, R., Yamada, T., Makino, K., & Jianglong, Yu. (2009). An overview on oxyfuel coal combustion—State of the art research and technology development. *Chemical Engineering Research & Design*, 87, 1003–1016.



# Source Rocks Forward Modelling: Significance and Approach

Samer Bou Daher, Benoit Chauveau, Erwan Leguerroue, Paul Jermannaud, Alcide Thebault, Maria-Fernanda Romero-Sarmiento, and Emerson Marfisi

## Abstract

Organic matter rich rocks are the basis of any petroleum system. The nature and variability of organofacies in sedimentary rocks have been well documented for a large number of source rocks. Significant effects of these organofacies heterogeneities on the source rocks hydrocarbon generation potential and kinetics have also been reported, therefore highlighting the importance of numerical source rocks prediction tools in petroleum systems analysis. Efforts to numerically model organic matter deposition through earth's history have been made with various degrees of success. However, none of these efforts have yet been integrated in hydrocarbon exploration workflows due to the time and resource needed to properly do so. In this chapter, we present a new methodology to model marine organic matter. The

advantage of this methodology is that it is coupled with an established forward stratigraphic modelling workflow, therefore requiring minor additional input and time to provide a quantification of source rocks distribution and properties. The integration of this approach with traditional petroleum systems modelling solutions makes it a value adding tool in petroleum exploration efforts.

## 1 Introduction

Organic matter rich rocks are a prerequisite to any conventional and unconventional petroleum system, rendering an adequate quantification of their properties essential for a realistic estimation of petroleum resources. Lateral and vertical organofacies variations are well documented for many source rocks around the world (e.g. Bou Daher et al., 2014, 2015; Littke, 1993; Littke et al., 1991). Large differences in the timing of onset and peak hydrocarbon generation of various organofacies within the same source rock have also been documented (e.g. Bou Daher, 2016; Bou Daher et al., 2016; Keym et al., 2006). Most hydrocarbon kitchens in conventional petroleum systems are usually never sampled, and therefore, their properties are often qualitatively extrapolated from the nearest sampling location. This emphasizes the need for a reliable numerical methodology to predict source rock distribution on a basin scale away from available data points.

The production, transport, and preservation of organic matter are controlled by a complex combination of biological, physical, and chemical processes. Quantifying lateral and vertical source rock heterogeneities require therefore an integration of paleoclimatic, paleogeographic, and paleoceanographic reconstructions. Such an integration is both time consuming and demanding a high level of expertise that are rarely in line with timelines of the industry's operational needs.

S. Bou Daher (✉) · E. Leguerroue · P. Jermannaud · A. Thebault · E. Marfisi

Division of Global Solutions, Beicip-Franlab, Rueil-Malmaison, France

e-mail: [samer.boudaher@beicip.com](mailto:samer.boudaher@beicip.com)

E. Leguerroue

e-mail: [erwan.leguerroue@beicip.com](mailto:erwan.leguerroue@beicip.com)

P. Jermannaud

e-mail: [paul.jermannaud@beicip.com](mailto:paul.jermannaud@beicip.com)

A. Thebault

e-mail: [alcide.thebault@beicip.com](mailto:alcide.thebault@beicip.com)

E. Marfisi

e-mail: [emerson.marfisi@beicip.com](mailto:emerson.marfisi@beicip.com)

B. Chauveau · M.-F. Romero-Sarmiento

IFP Energies Nouvelles, Directions Géoscience, Rueil-Malmaison, France

e-mail: [benoit.chauveau@ifpen.fr](mailto:benoit.chauveau@ifpen.fr)

M.-F. Romero-Sarmiento

e-mail: [maria-fernanda.romero-sarmiento@ifpen.fr](mailto:maria-fernanda.romero-sarmiento@ifpen.fr)

In this chapter, we present a new methodology to quantitatively assess marine source rock properties on a basin scale. This methodology is integrated within a well-established forward stratigraphic modelling workflow using *DionisosFlow*<sup>®</sup> software that allows for an efficient and effective quantification of petroleum systems elements.

## 2 Source Rocks Heterogeneities

Organofacies is a term used to describe the nature and variability of the organic content of sedimentary rocks (Burwood et al., 1990 and references therein). The fraction of this sedimentary organic matter (OM) which is insoluble in organic solvents is well-defined as “kerogen” (Durand & Nicaise, 1980). Source rock deposition and kerogen composition through geological time are mainly controlled by the evolution of climatic conditions, biochemical precursors, and the balance between OM production and degradation.

The thermal decomposition of the initial kerogen (primary OM) during burial first generates heavy compounds (asphaltenes) at the oil-window thermal maturity stage, then generates low-molecular weight resins and liquid hydrocarbons from the secondary cracking of asphaltenes (e.g. Behar et al., 2008). The onset and outcome of these stages are controlled by the kerogen’s hydrocarbon generation kinetics which themselves reflect the depositional organofacies (e.g. Behar et al., 2008; Tissot & Espitalié, 1975 and references therein).

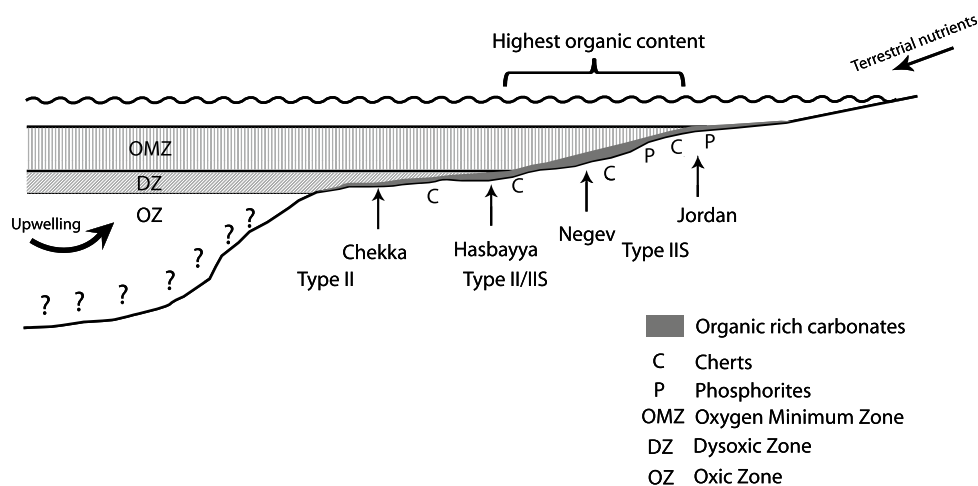
The sedimentary OM from source rock intervals has been widely investigated at the laboratory scale using open-system pyrolysis. The Rock-Eval<sup>®</sup> device quantifies the OM richness in terms of total organic carbon (TOC) content and the

OM type in terms of calculated hydrogen index (HI) (e.g. Espitalié et al., 1986; Lafargue et al., 1998; among others).

As with lithofacies variations, lateral and vertical organofacies variations (TOC and HI) play an important role in every petroleum system. In this section, some examples of such organofacies variations are discussed showing the magnitude of their effect on prospective hydrocarbon plays.

The Campanian–Maastrichtian source rock of the East-Mediterranean is a marine source rock deposited under an extensive upwelling system that extended approximately 300 km along the shelf. Several studies have sampled this source rock in outcrops and shallow wells in Jordan, Israel, Lebanon, and SE Turkey (Abed et al., 2005; Almogi-Labin et al., 1993, 2012; Ashckenazi-Polivoda et al., 2010, 2011; Bou Daher et al., 2014, 2015; Dercourt et al., 2000; Inan et al., 2010; Schneider-Mor et al., 2012). The documented organofacies variations along the Campanian–Maastrichtian East-Mediterranean shelf have been summarized in a conceptual model by Bou Daher et al. (2015), suggesting not only a change in TOC content, but also in hydrocarbon generation kinetics (Fig. 1). Bou Daher et al., (2015, 2016) showed that the observed variation in hydrocarbon generation kinetics within the East-Mediterranean Campanian–Maastrichtian source rock is controlled by the organic sulphur content, as aliphatic and aromatic sulphur compounds, which in turn correlates positively with the TOC (Vandembroucke & Largeau, 2007). The Campanian–Maastrichtian source rock is thermally immature in all sampled locations in Jordan, Israel, and Lebanon (Bein & Amit, 1982; Bou Daher et al., 2014; Gardosh et al., 2008). Thermal maturity of the Campanian–Maastrichtian succession is reached in the Levant Basin, however, its source rock properties are unknown, and its modelled timing of hydrocarbon

**Fig. 1** Conceptual model of the east Mediterranean Upper Cretaceous organic-rich carbonates illustrating the observed lateral variation in source rock properties in terms of quality and quantity (from Bou Daher et al., 2015)



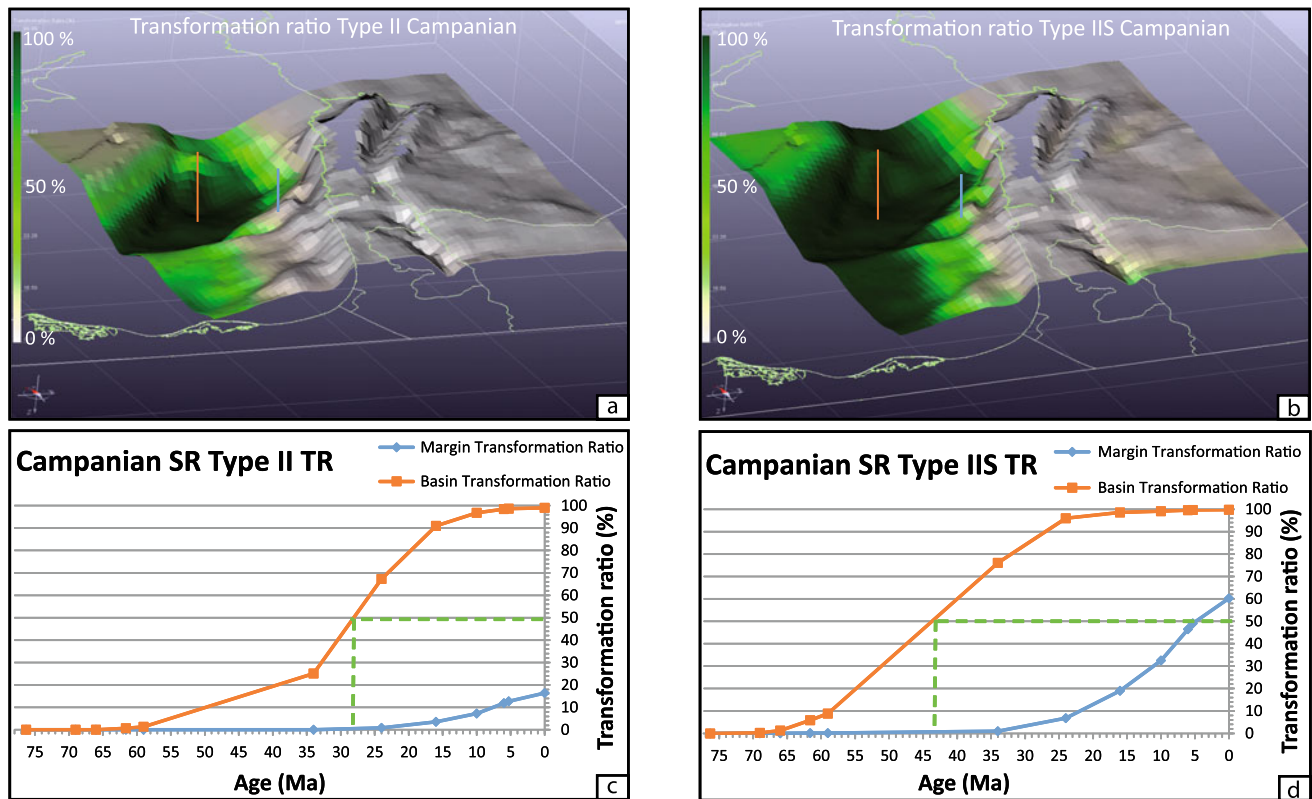


**Fig. 2** Modelled transformation ratios for the east Mediterranean Campanian source rock using measured hydrocarbon generation kinetics from the same source rock in two different sections 80 km apart. **a, b** transformation ratio map using measured Type II kinetics and Type IIS kinetics, respectively. **c, d** transformation ratio through time for two synthetic wells in the deep offshore and along the margin

generation varies considerably depending on the used kinetics (Fig. 2). Variation in hydrocarbon generation kinetics within the same marine source rock laterally and vertically is very common, especially in carbonate rich source rocks. These kinetics variations often correlate with TOC and HI, as shown in Fig. 3 for the Campanian–Maastrichtian of the East-Mediterranean (Bou Daher, 2016). This observed dynamic in marine source rocks suggests that predicting their TOC and HI not only provides a better assessment of the hydrocarbon generation potential, but also guides the basin modeller in selecting the most representative hydrocarbon generation kinetics for the usually unsampled kitchen areas, and better determines the limits of the oil generation window. The Upper Cretaceous succession of the eastern margin of the Levant Basin is an excellent example of a play that can be very promising or not at all based on the assumed source rock properties (Fig. 2). Such

using Type II and Type IIS kinetics, respectively, showing a 15 Ma difference for the timing of the critical moment (50%TR) in the basin and an even more important difference along the margin going from inactive to actively hydrocarbon generating source rock (from Bou Daher, 2016)

examples are common in frontier basins and require a reliable numerical source rock modelling approach to properly tackle.

### 3 Forward Stratigraphic Modelling

Forward stratigraphic modelling (FSM) is an approach to simulate the filling of sedimentary basins over geological time (Granjeon, 1996). *DionisosFlow*<sup>®</sup> is a 4D multi-lithology FSM software that reproduces the results of sedimentary and basinal processes, such as subsidence, sea level, erosion, sediment supply, and transport, in order to predict lateral and vertical facies and geometries at basin to reservoir scale (Fig. 4) (e.g. Granjeon, 1996, 2014; Granjeon & Joseph, 1999; Hawie et al., 2015a, 2015b, 2018). The advantages of such a process-based approach are in its

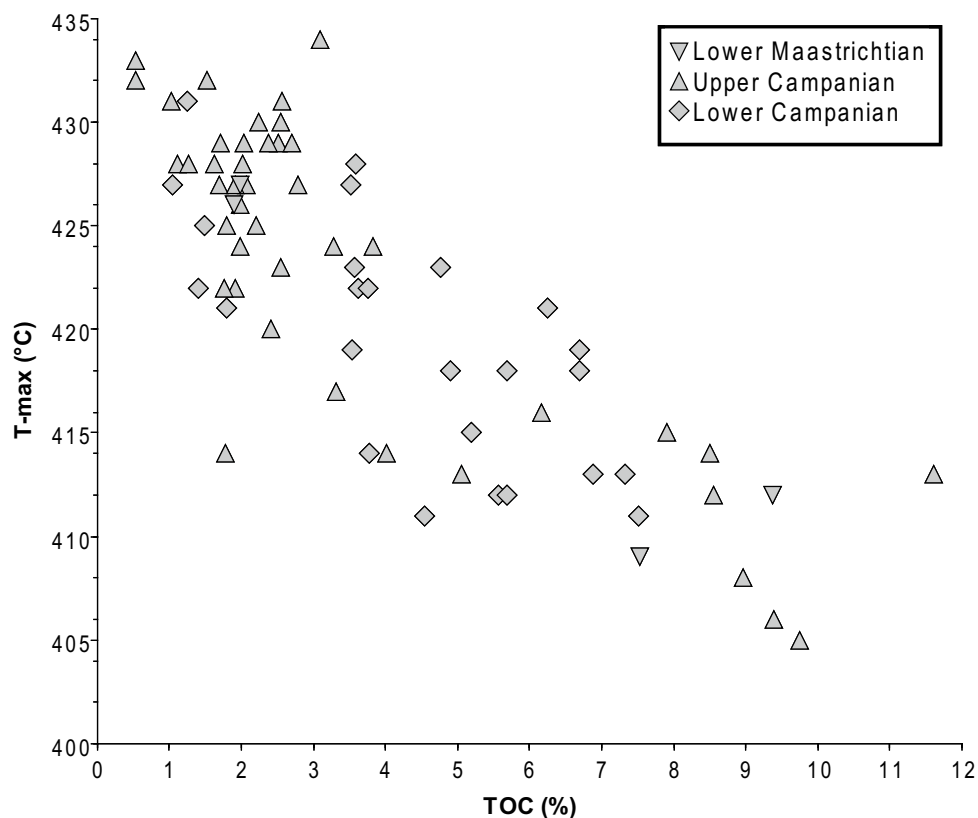


**Fig. 3** Rock-Eval<sup>®</sup> Tmax versus TOC data from the Upper Cretaceous east Mediterranean immature source rocks showing a negative correlation owed to the increase in organic sulphur with TOC which leads to hydrocarbon generation at lower temperatures and thus a lower Tmax (modified from Bou Daher, 2016)

ability to integrate and test the coherence of multiscale and multidisciplinary data and interpretation and provide a realistic interpolation between calibration points within a sequence stratigraphic framework (e.g. Liechoscki de Paula Faria et al., 2017; Hawie et al., 2018). The result of a *DionisosFlow*<sup>®</sup> forward stratigraphic simulation is a 4D block with sedimentological, environmental, and geometrical properties to characterize the filling of a sedimentary basin including its petroleum system elements.

## 4 Source Rocks Forward Modelling

FSM provides many of the essential physical parameters needed for source rock modelling, such as sedimentation rate, water depth, or sediment transport. Modelling source rocks properties and distribution require not only this

information, but also additional considerations related to the fate of organic carbon (Fig. 5). In this section, we present the concepts added in the stratigraphic forward model to estimate total organic carbon (TOC) and hydrogen index (HI) maps at the simulated sedimentary basin's scale. Complementary description of the model principles can be found in Granjeon and Chauveau (2014).

### 4.1 Concepts and Approach

Organic matter production, also referred to as primary productivity (PP), is introduced in the model through input maps that derive directly from external models or are created from our model by using simple empirical laws. Basically, these laws are designed to mimic the dependence of PP on the nutrients availability. Thereby, PP values can be

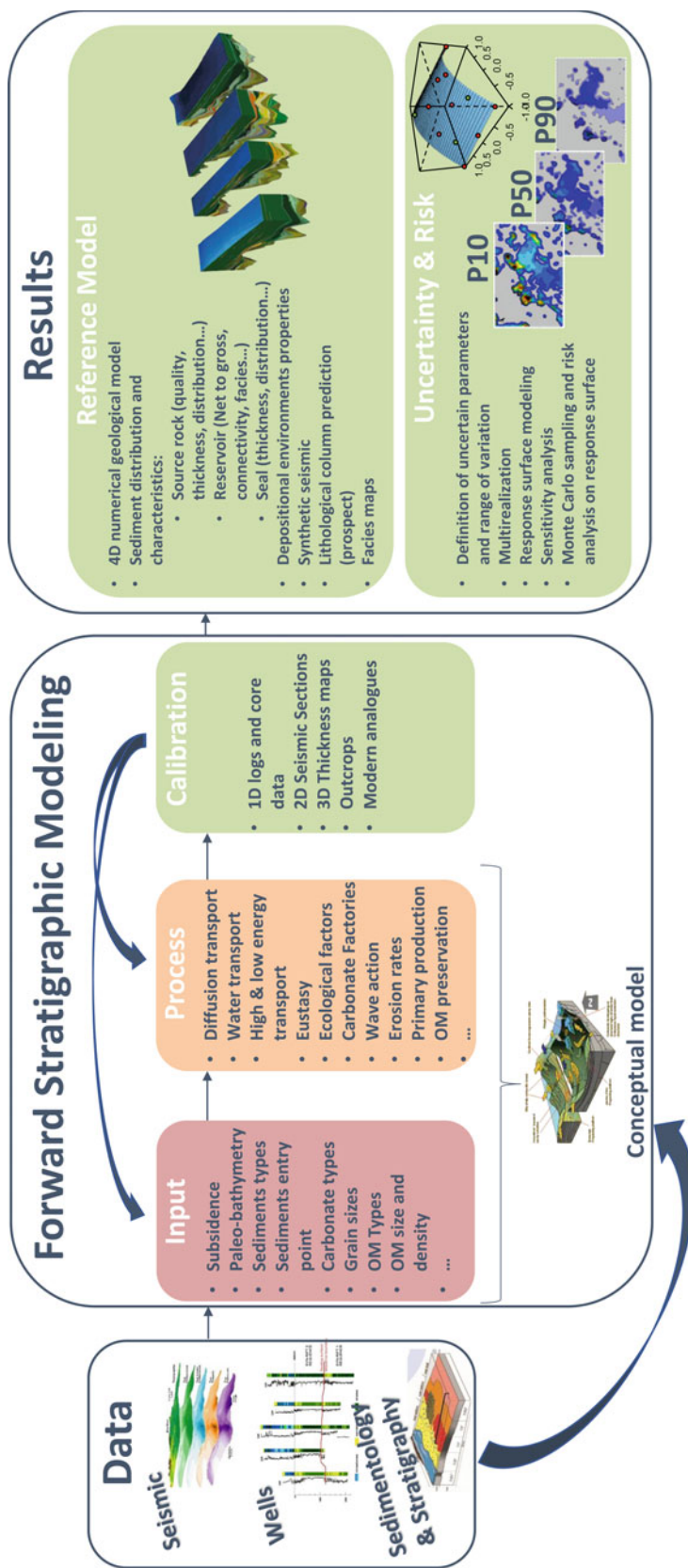
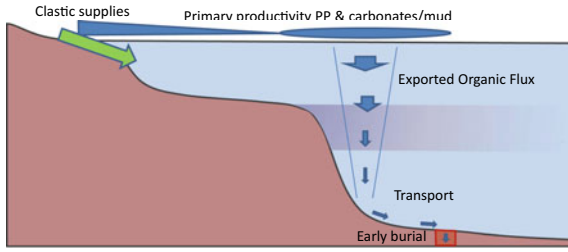


Fig. 4 Schematic illustrating the forward stratigraphic modelling approach, its associated results, and the uncertainty, sensitivity, and risk analysis workflow used in this chapter



**Fig. 5** Schematic view of the geological context simulated by the organic matter module

modulated by the distance from the coastline to reflect nutrients supply from continental area. High primary productivity zones can also be associated with a specific bathymetry range to simulate an upwelling area (“high productivity zone”) located at the continental slope or at the shelf break. Ecological constraints can finally be used to refine the conditions promoting the ignition of high productivity zones. These constraints can be specific values of water flux, turbidity, sediment proportion in the seafloor, wave action, or any other parameter simulated in the stratigraphic forward model.

Once organic matter is produced, it is exported from the photic zone to the seafloor interface and subjected to a degradation process occurring along the whole water column. Several power laws have been proposed (Suess & Müller, 1980; Betzer et al., 1980, 1984; Martin et al., 1987; Stein, 1991; Berelson, 2001) to reproduce the evolution of the organic matter flux with water depth. They all take the same general form:

$$\varphi_{\text{ORG}} = \text{ef} \frac{Z^{-n_0}}{Z_p} \quad \text{for } Z \geq Z_p \quad (1)$$

where ef is the export factor,  $n_0$  is the attenuation coefficient, and  $Z_p$  is the depth of the photic zone. Calibration is specific to each law and each of them presents its own  $f(\text{ef}, n_0)$  set. To make it usable for our purpose, the law must also describe the organic matter flux inside the photic zone to consider shallow water environments. As the organic matter flux measured inside the photic zone seems to be more or less constant (Suess, 1980), we suppose that re-suspension process by wave currents strongly impacts the net organic matter sedimentation rate. Thus, we assume that the net organic flux increases linearly between  $Z = 0$  and  $Z = Z_p$ . The main reasons invoked to explain the strong variations in  $(\text{ef}, n_0)$  deduced from measurements in different modern environments are variations in water temperature and the redox regime in the water column. As primary productivity depends largely on water temperature, estimated paleotemperature curves can be used to parametrize the

time-dependent productivity weighting curve. However, redox conditions can be estimated directly from the conditions simulated in the model. In this case, the impact on the organic flux will be provided with a coupling between the attenuation coefficient and the redox conditions.

An oxygen index ratio  $O_x$  is defined, ranging from 0 to 1 that reflects the concentration of dissolved oxygen in water  $[O_2]$ . Tyson and Pearson (1991) defined the redox regimes as oxic (8.0–2.0 ml/l  $O_2$ ), dysoxic (2.0–0.2 ml/l), suboxic (0.2–0.0 ml/l), and anoxic (0.0 ml/l). We follow this definition to define three redox regimes in our model: oxic ( $1-0 \cdot O_x$ ), dysoxic ( $0.25-0-0.06 \cdot O_x$ ), and strongly dysoxic to anoxic ( $0.06-0 \cdot O_x$ ). An oxygen index vertical curve is calculated for each numerical cell of the simulated marine domain based on a balance equation in which oxygen consumption rate and oxygen renewal rate are considered. Under the stationary assumption, the formulation is as follows:

$$\frac{\partial O_x(z)}{\partial t} = M(z) \cdot (1 - O_x(z)) - C \cdot O_x(z) = 0 \quad (2)$$

where  $M(z)$  ( $1 - O_x(z)$ ) is the net oxic water renewal rate ( $M(z)$  is the water mixing curve) and  $-C \cdot O_x(z)$  the oxygen consumption rate ( $C$  is the consumption coefficient). Calibration is provided in two phases. First, for an arbitrary fixed  $C$  value,  $M(z)$  is calibrated to reproduce typical oxygen profiles extracted from Garcia et al. (2013) database and illustrated in Hoogakker et al. (2018). In a second phase, the expression of  $C$  is defined. As the oxygen consumption is associated with the amount of organic matter degraded, we suppose a direct relation between  $C$  and PP. The  $C$  value used to define  $M(z)$  corresponds to  $C(\text{PP} = \text{PP}_{\text{anox}})$  where  $\text{PP}_{\text{max}}$  corresponds to the minimum PP required to initiate anoxic regime inside the OMZ as per the oxygen profiles published by Hoogakker et al. (2018). Following the same approach, we define  $\text{PP}_{\text{dysox}}$  as the minimum PP needed to initiate dysoxic regime inside the OMZ (Fig. 6). Finally,  $C$  (PP) relation is defined to respect these two conditions and to allow a nearly-linear relation between  $O_x$  and PP. Figure 6 shows two oxygen curves obtained with  $\text{PP}_{\text{dys}}$  and  $\text{PP}_{\text{anox}}$ . Minimum oxygen index value for  $\text{PP}_{\text{anox}}$  is  $O_x = 0.06$  and is  $O_x = 0.25$  for  $\text{PP}_{\text{dysox}}$  which are located at water depth around 300–350 m.

The default calibration of  $M(z)$  corresponds to an open ocean context. However, optional modulation of  $M(z)$  must be added to adjust it for more restricted environments. For that, we have decomposed the  $M(z)$  curve into two curves representing the surface and bottom water mixing parts (Fig. 7). The first curve ( $M_{\text{SURFACE}}(z)$ ) presents a maximum mixing regime in the photic zone (we assume that the surface mixing zone and the photic zone are the same even if it



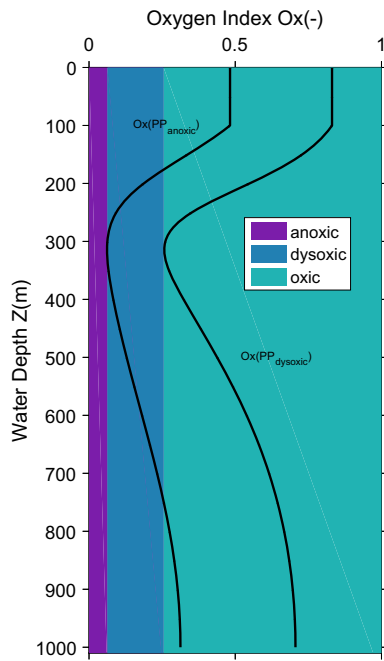


**Fig. 6** Vertical oxygen profiles simulated with the organic matter model for an open system and with two different primary productivities (PP = PP<sub>dysoxic</sub> and PP = PP<sub>anox</sub>). Colours represent oxic (cyan), dysoxic (blue), and anoxic (purple) regimes

is much more complex than this representation). Below the photic zone, mixing decreases exponentially over around two times of the mixing zone. The thickness of the mixing zone is defined by default at  $Z_p = 100$  m, to change the mixing efficiency. It allows us to reproduce for example high stratified surface waters. The second curve ( $M_{\text{BOTTOM}}(z)$ ) presents a maximum value for water depth above 1000 m. Below 1000 m, the mixing effect decreases until it reaches values close to 0 at surface. For this curve, a simple weighting coefficient  $A_{bc}$  is used to modulate the whole mixing efficiency. By acting on  $M(z)$  with variable  $Z_p$  or  $A_{bc}$ , the oxygen values decrease and dysoxic conditions, and even anoxic, can occur along the water column for lower PP. Thanks to this decomposition of the mixing curve, several geological configuration can be simulated. As an illustration, Fig. 8 allows to compare three distinct oxygen curves associated with three different bottom water mixing conditions ( $A_{bc} = 1$  for an open environment,  $A_{bc} = 0.1$  for a restricted environment, and  $A_{bc} = 0$  for a fully restricted basin).

The attenuation coefficient is finally no more a constant but a variable in depth based on the oxygen index following the empirical relation (Fig. 9):

$$\begin{cases} n = n_0 & \text{if } \text{Ox} > 0.25 \\ n = n_{\min} + (n_0 - n_{\min}) \frac{\text{Ox} - 0.06}{0.25 - 0.06} & \text{if } \text{Ox} \leq 0.25 \end{cases} \quad (3)$$

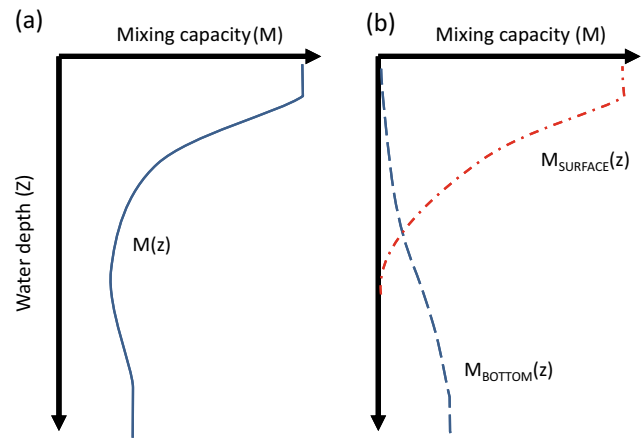


**Fig. 7** **a** Vertical mixing curve used by the model as a reference curve for an open environment, **b** decomposition of the reference mixing curve into  $M(z) = M_{\text{SURFACE}}(z) + M_{\text{BOTTOM}}(z)$ .  $M_{\text{SURFACE}}(z)$  and  $M_{\text{BOTTOM}}(z)$  can be modified to create adapted  $M(z)$  for more restricted basin or stratified water

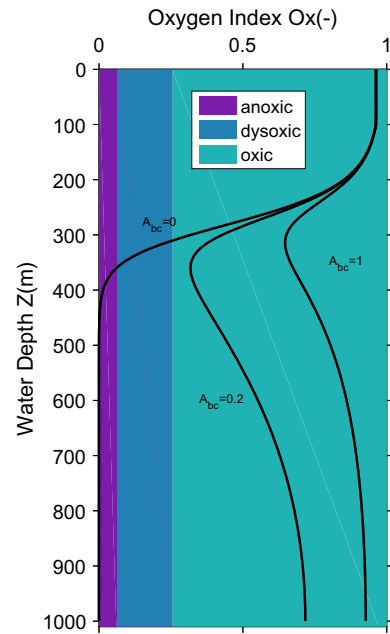


**Fig. 8** Vertical oxygen profiles simulated with the organic matter model for a constant primary productivity but with three different levels of restriction: open ( $A_{bc} = 1$ ), semi-restricted ( $A_{bc} = 0.2$ ), and fully restricted systems (without any bottom current circulation,  $A_{bc} = 0$ )

Using  $n_{\min} = 0.3$  and  $n_0 = 1.1$  and with adapted water mixing coefficients, different end-member configurations can be reproduced, from organic flux as those measured in modern East Pacific open ocean to organic fluxes recorded in the restricted Black Sea (Karl & Knauer, 1991; Lutz et al., 2002, 2007; Gogou et al., 2013; Dale et al., 2015).

Finally, as our target is the estimation of original TOC and HI maps before any “maturation” for it to be used as

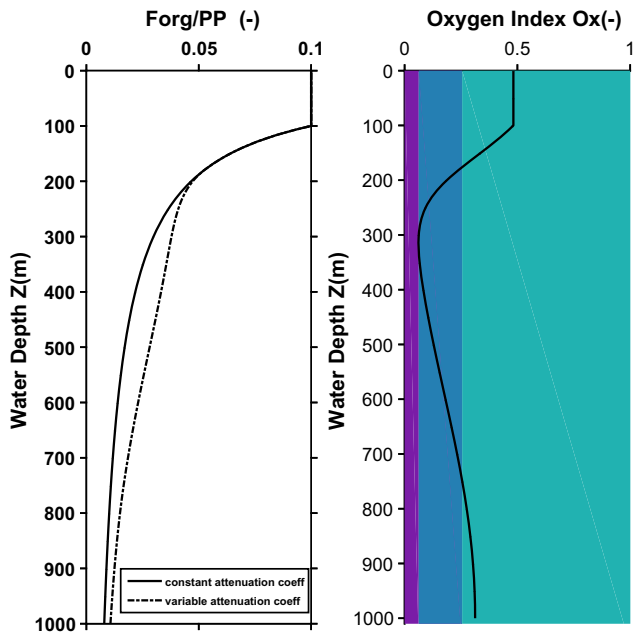


**Fig. 9** Exported organic flux, normalized to PP, and with  $ef = 0.1$ . Two organic flux curves are drawn: (1) with a constant attenuation coefficient  $n = 0.86$  and (2) with a variable  $n$  coefficient based on equation III. The attenuation coefficient is lower than the reference between  $Z = 200$  and  $Z = 720$  m. The maximum impact is for water depth comprises between 400 and 600 m

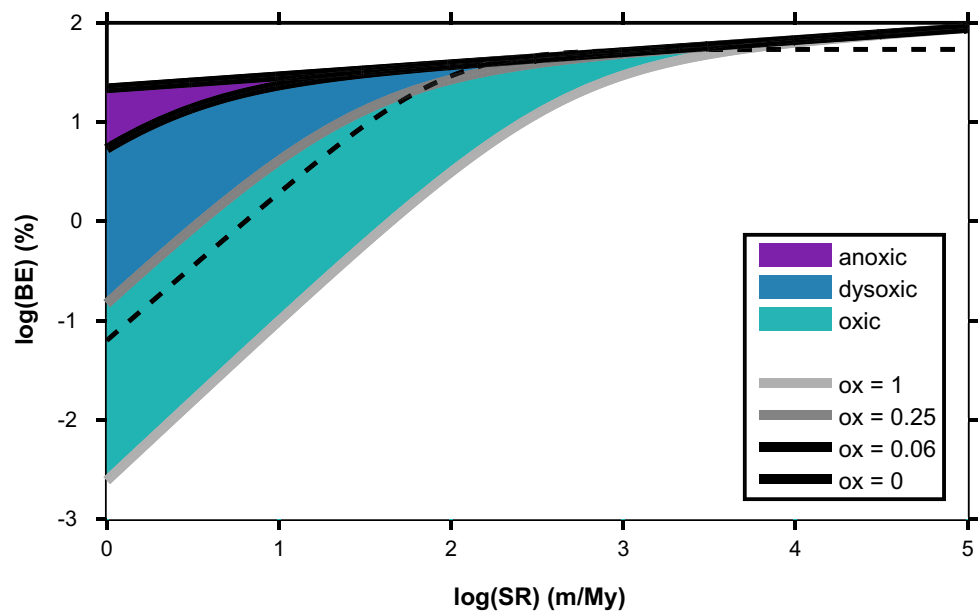
source rock input parameters in basin models, it is also needed to consider the organic matter degradation phase associated to the biological activity at the seafloor and in the first centimetres below. Having a quantitative and precise estimation of the amount of organic matter

preserved depending on the preservation conditions is highly uncertain. However, one of the most current approaches consists in using the notion of burial efficiency (BE), as used in Betts and Holland (1991), and discussed more recently in Burdige (2007). The burial efficiency is defined as the ratio between the organic matter outflows from the degradation zone to the organic matter inflow entering the sediment layer. Even if some authors initially used one BE curve for all the depositional environments (Betts & Holland, 1991), it is now recognized that two trends can be identified, such as one for oxic water and one for anoxic water (Stein, 1990).

For the purpose of the model, an empirical burial efficiency law was developed varying continuously with different sets of sedimentation rate and oxygen index values. Areas of BE associated with anoxic, dysoxic, and oxic conditions are in accordance with the data available from the literature (Betts & Holland, 1991; Burdige, 2007). Figure 10 shows four burial efficiency curves deduced from our model and associated with four constant oxygen values ( $Ox = 1$ ,  $Ox = 0.25$ ,  $Ox = 0.06$ ,  $Ox = 0$ ). Dashed line represents the BE curve defined by Betts and Holland (1991). The colours still indicate the redox regimes.

The innovative approach of this model lies in its ability to describe the organic matter production and degradation processes in the framework of a 3D numerical stratigraphic forward model. First strength of this coupling is that a part of the depositional context is explicitly simulated by the stratigraphic model itself, such as the bathymetry, the sedimentation rate, or the coastline location. Second, organic matter is viewed as a “classic” sediment in terms of transport and has its own transport capacity. Direct consequence is

**Fig. 10** Burial efficiency curves for different oxygen index values compared with the reference BE defined in Betts and Holland (1991). SR is the linear sedimentation rate (in m/My), and BE ranges from 0 to 100% of preservation. Colours represent the three redox regimes defined for this model (oxic, dysoxic, and anoxic)



that deposition in the continental shelf, where transport can play a major role, and re-erosion processes are fully considered and the organic-rich deposited layer stays in accordance with the deposition of the other inorganic sediment that are also subjected to transport. By default, *DionisosFlow*<sup>®</sup> simulates the bedload transport only. This transport regime is, however, well-adapted for the residual organic matter arriving at the seafloor, as demonstrated by Shieber et al. (2007), MacQuaker and Bohacs (2007), MacQuaker et al. (2010), or also in Trabucho-Alexandre et al. (2012).

The degree of organic matter preservation is expressed through a quality index that is considered to be representative to the Rock-Eval<sup>®</sup> hydrogen index. This principle has already been applied in Mann and Zweigel (2008) and simply consists in estimating HI as a function of the initial organic matter quality and of the total amount of degradation (water column and burial). An HI curve is defined as a function of the total degradation that has impacted the residual organic matter. To be calibrated, the HI (degradation) must pass through three key values representing typical HI for poorly ( $HI_{PP}$ ), moderately ( $HI_{MP}$ ), and well-preserved ( $HI_{WP}$ ) organic matter. Figure 11 presents the total organic carbon and the hydrogen indexes, and also the  $S2 = HI \times TOC$ , as a function of the sedimentation rate and of the primary productivity, for two constant water depths  $Z = 400$  m and  $Z = 1000$  m. For each case, two levels of basin restriction are simulated:  $A_{bc} = 1$  (fully open) and  $A_{bc} = 0.2$  (restricted environment). Calibration values used for this case are  $ef = 0.1$ ,  $PP_{ANOXIC} = 300$  gC/m<sup>2</sup>/yr,  $PP_{ANOXIC} = 150$  gC/m<sup>2</sup>/yr,  $HI_{WP} = 650$  mgHC/g,  $HI_{MP} = 300$  mgHC/g,  $HI_{PP} = 100$  mgHC/g. When primary productivity is high enough to initiate dys-oxic conditions at 400 m ( $PP \sim 180$  gC/m<sup>2</sup>/yr), the burial efficiency notably increases. As result, it vanishes the strong effect of the sedimentation rate at low SR regime. For weaker primary productivity, low SR regime is more impacted by the strong variation of BE with the sedimentation rate. It results in a TOC peak that corresponds to the optimal conditions between preservation and dilution. Hydrogen index, which is not impacted by dilution effect, is highest for high primary productivity and sedimentation rate. Effect of SR is to increase BE, whereas PP modifies the redox conditions, not only at the seafloor but in the whole water column. At 400 m, as the bathymetry is located in the centre part of the OMZ, preservation in the water column and during burial are both possibly strongly impacted by PP. At 1000 m, the burial efficiency is less impacted as bottom current tends to maintain a certain quantity of oxygen.

## 4.2 Upwelling Systems

Upwelling systems are responsible for the production and burial of large quantities of marine organic matter rich sediments in modern day and ancient oceans. Several forcing factors can contribute to the establishment of an upwelling system. These include paleolatitude, coastline geometry, shallow marine high, and trade wind direction (Jenkins & Bye, 2006). In this section, a methodology to model the outcome of an established upwelling system in terms of source rock quality and distribution is discussed.

Regardless of their nature or forcing factors, upwelling systems are organic rich due to the nutrient and oxygen rich deep ocean water that reaches the photic zone and induces primary productivity above a shelf or a submarine basinal high. These currents usually reach the photic zone above a bathymetry of around 400–100 m. In the methodology, we discuss here, and we define primary productivity above a user defined bathymetry in order to mimic upwelling induced primary productivity (Fig. 12).

In the simple synthetic model shown in Fig. 13, we illustrate an upwelling system where the nutrient rich water reaches the photic zone above a bathymetry range between 350 and 150 m (Fig. 13a). The induced primary productivity in the user defined photic zone/mixed layer results in a flux of marine organic matter to the seafloor (Fig. 13b) which is calculated according to the concepts discussed above. The organic sediments that reach the seafloor are then transported and distributed within the basin in the same way as the inorganic sediments using a diffusion equation that accounts for gravity, water, and wave driven transport. In the example illustrated in Fig. 13, however, we deactivated sediment transport and used a constant sea level in order to illustrate a simplified upwelling system behaviour. Due to the high flux of OM to the seafloor and its subsequent oxic degradation, an oxygen minimum zone is established resulting in an enhanced burial efficiency and an elevated TOC and HI (Fig. 13c, d). In real-case studies, the interplay between primary productivity, organic matter transport, and preservation combined with sea level and sedimentation rates variation results in important lateral and vertical source rock variations as illustrated in Fig. 14.

## 4.3 Riverine Systems and Restricted Versus Open Marine

Rivers transport minerals from the hinterland and into the ocean and thus are a major source of nutrients in modern and

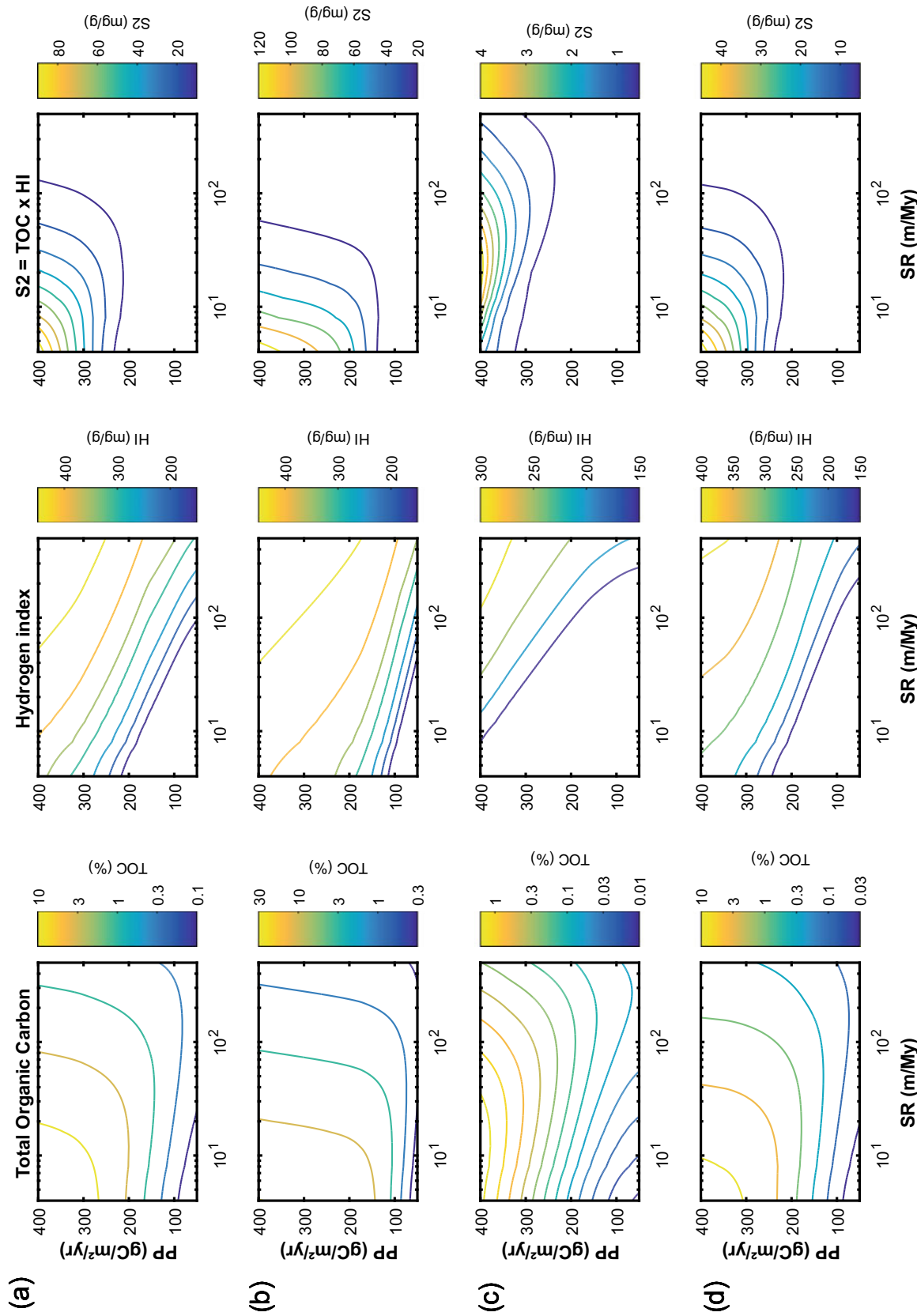


**Fig. 11** TOC-HI and thus S2 response of our model in the PP-SR regime diagram. 2 different water bathymetries are considered: 400 m (a, b) and 1000 m (c, d). 2 different restriction regimes are considered:  $A_{bc} = 1$  (a, c) and  $A_{bc} = 0.2$  (b, d)

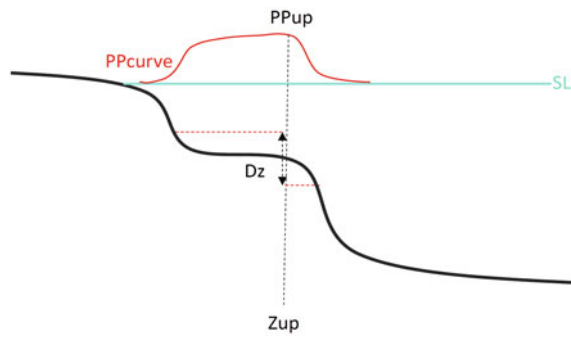


**Fig. 12** Schematic illustrating the approach used for upwelling systems, where SL is sea level, Dz is the bathymetry above which the primary productivity (PP) will occur in the photic zone/mixed layer, Zup is the bathymetry above which the PP will be highest (PPup)

ancient oceans. The riverine induced primary productivity combined with the basinal configuration (open vs. restricted) can lead to important source rock deposition. In the methodology presented here, we can induce primary productivity that decreases with distance to shore and thus mimic a riverine nutrient source (Fig. 15).

The effects of adapting an open marine setting versus a restricted basin are illustrated in Fig. 15. Identical primary productivity values can result in very different source rock quality depending on the basinal configuration and the renewal of oxygenated bottom waters (Fig. 16).

This synthetic example shown in Fig. 16 also illustrates the interplay between primary productivity and preservation

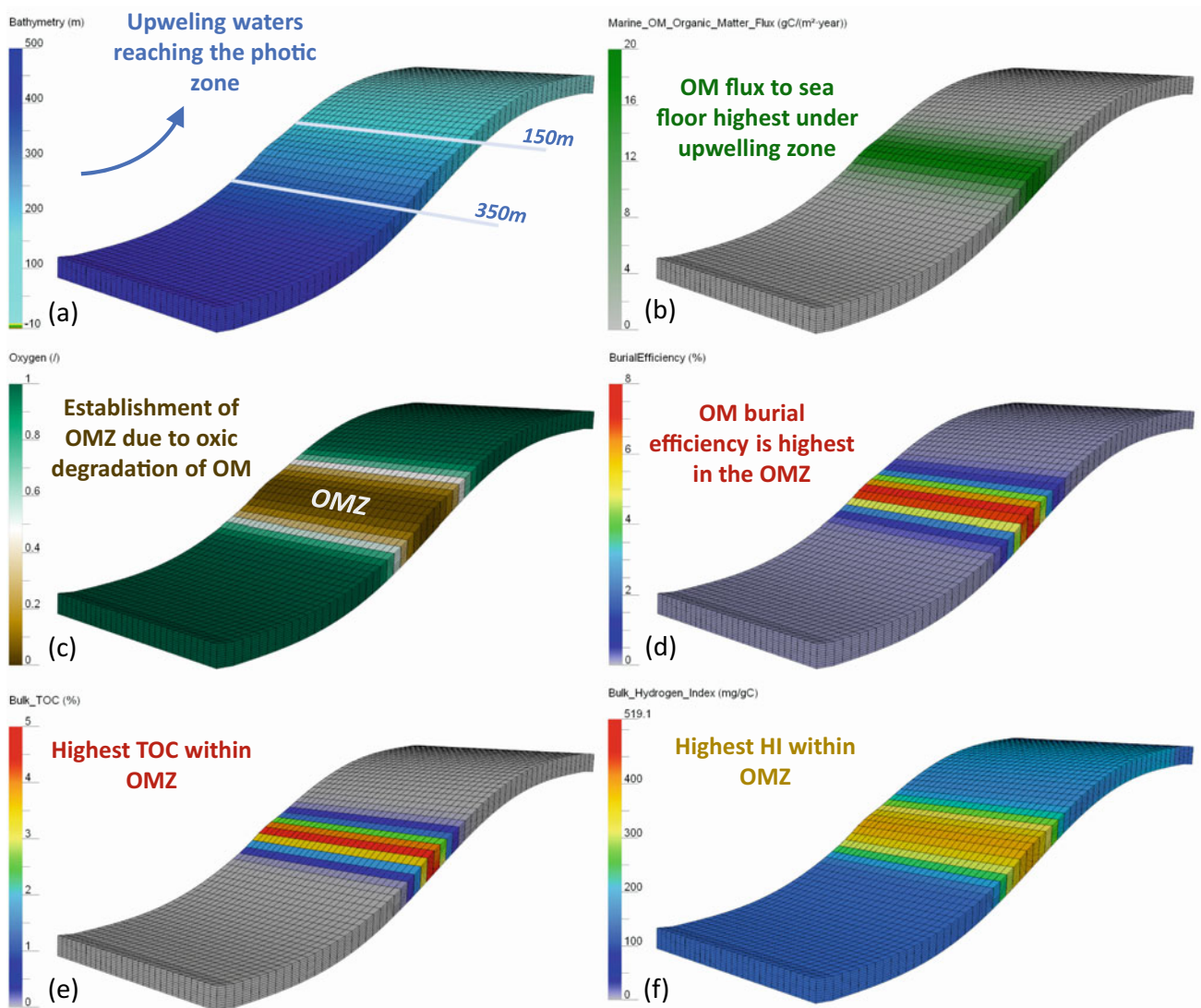


**Fig. 13** Synthetic model of an upwelling system showing **a** bathymetry with primary productivity in the photic zone above a bathymetry of 350–150 m, **b** OM flux to the seafloor, **c** oxygen minimum zone established due to oxic degradation of OM, **d** burial efficiency showing

highest values in OMZ as expected with constant sedimentation rate and minimal sediment transport used in this example, **e** highest TOC, and **f** highest HI established at OMZ

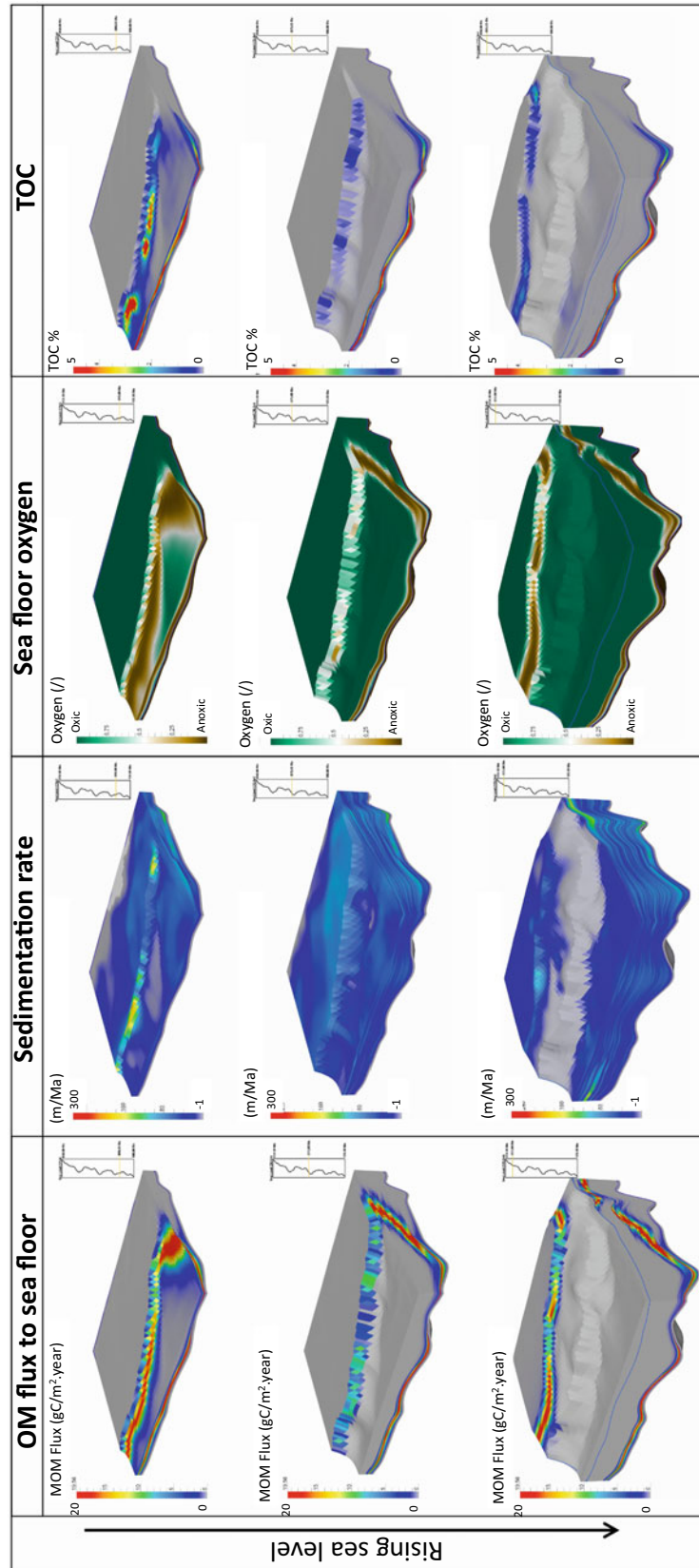


**Fig. 14** Forward stratigraphic model with an active upwelling system showing the effect of the interplay of flux of OM to seafloor, sedimentation rate, redox conditions, and sea level on source rock distribution

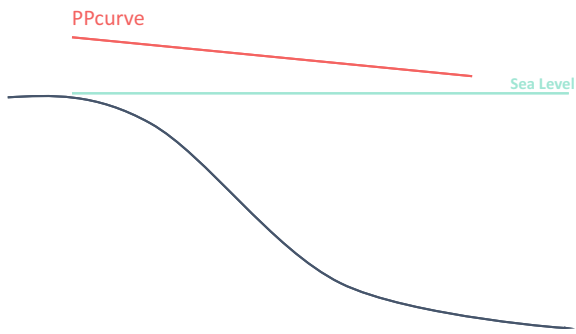


**Fig. 15** Schematic illustrating primary production (PP) input decreasing with distance to shore

and the effect that has on the lateral variation in source rock quality (TOC, HI).

## 5 Case Studies

Exploration offshore Newfoundland and Labrador hydrocarbon began in the 1960s. To date, over 160 exploration wells have been drilled in Newfoundland and Labrador's offshore jurisdiction. Many of these wells have been drilled in the Jeanne d'Arc basin, where currently, five fields are in production. Production to date has exceeded 1.8 billion barrels of oil. Exploration in the deeper waters of the Eastern

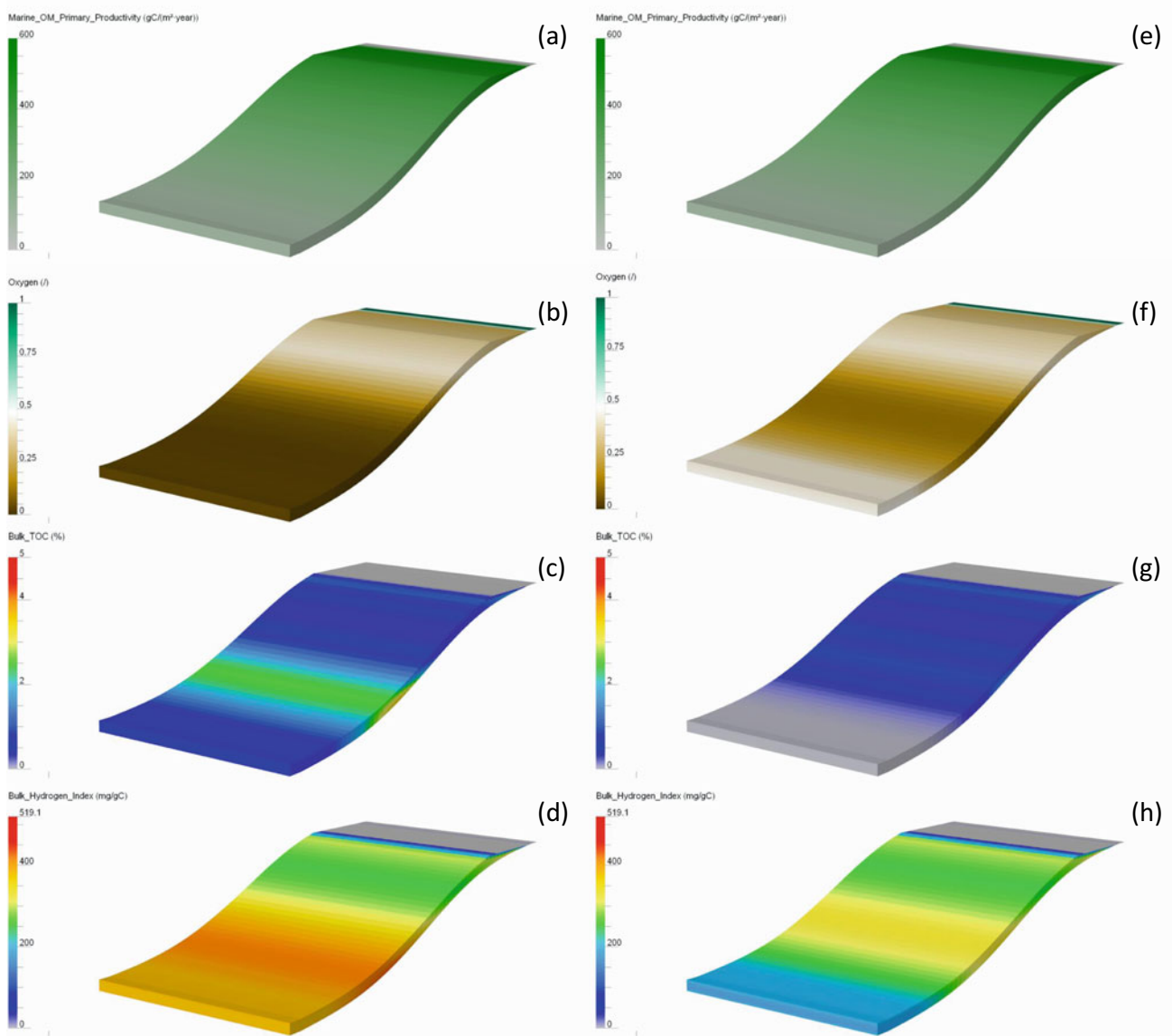


**Fig. 16** a–d Synthetic model with a restricted basinal configuration showing (a) primary productivity, (b) oxygen, (c) TOC, (d) hydrogen index. e–h Identical synthetic model with open marine basinal configuration showing (e) primary productivity, (f) oxygen, (g) TOC, (h) hydrogen index

Newfoundland Region (Orphan/Flemish Pass Basins) followed the initial exploration on the Grand Banks.

After a decade of no activity, exploration was renewed in the less successful basin of the Flemish Pass and Orphan. The comprehension of the petroleum system, well established in the Jeanne d'Arc basin, was challenged in places where only shows were demonstrated. New multi-client, exclusive seismic grids and the first 3D survey were collected allowing additional significant discoveries in the Flemish Pass basin notably. Recently, Nalcor Energy—Oil and Gas Inc. and Beicip-Franlab began resources assessments of the Orphan and Flemish Pass areas in order to account for recent seismic datasets and new modelling technologies. The focus of these assessments is to test the potential petroleum system through the maturity modelling of a sound source rock distribution (Jermannaud et al., 2016; Le Guerroué et al., 2019, 2020).

Classically, the proven Egret source rock (late Kimmeridgian to Tithonian in age) is the main source for hydrocarbon in the offshore Newfoundland basins while well record tends to demonstrate additional organic-rich levels with lateral extension and SPI potential that is poorly understood. We here present two case studies using regional calibrated *DionisosFlow*<sup>®</sup> models to characterize specific source rock potential.

## 5.1 Case Study 1: Orphan Basin Late Kimmeridgian Early Tithonian Source Rock Assessment

The eastern margin of Canada experienced successive rift episodes since Late Triassic times, propagating northward eventually leading to the rifting between Newfoundland and Iberia margins and then Newfoundland and Irish margins (Pichot et al., 2018), in the Orphan basin, the Kimmeridgian paleogeography is the one of a rifted continental crust with poorly connected, segmented rift basin. Passing to the Tithonian, as the rifting event continues, subbasin is connecting and sedimentary routes spread throughout the area (Jermannaud et al., 2020; Le Guerroué et al., 2017). This geodynamical change is synchronous with a significant eustatic flooding event (Fig. 17). In depth, reporting of this work is available within (Beicip-Franlab and Nalcor Energy—Oil and Gas Inc., 2020).

The depositional model is constrained with gross depositional environment maps combining seismic stratigraphic and structural mapping of sedimentary object using 3D dataset (Beicip-Franlab and Nalcor Energy—Oil and Gas Inc., 2020) in order to constrain a *DionisosFlow*<sup>®</sup> model. The model is calibrated in terms of stratigraphy and lithologies to wells within the model. The source rock depositional module

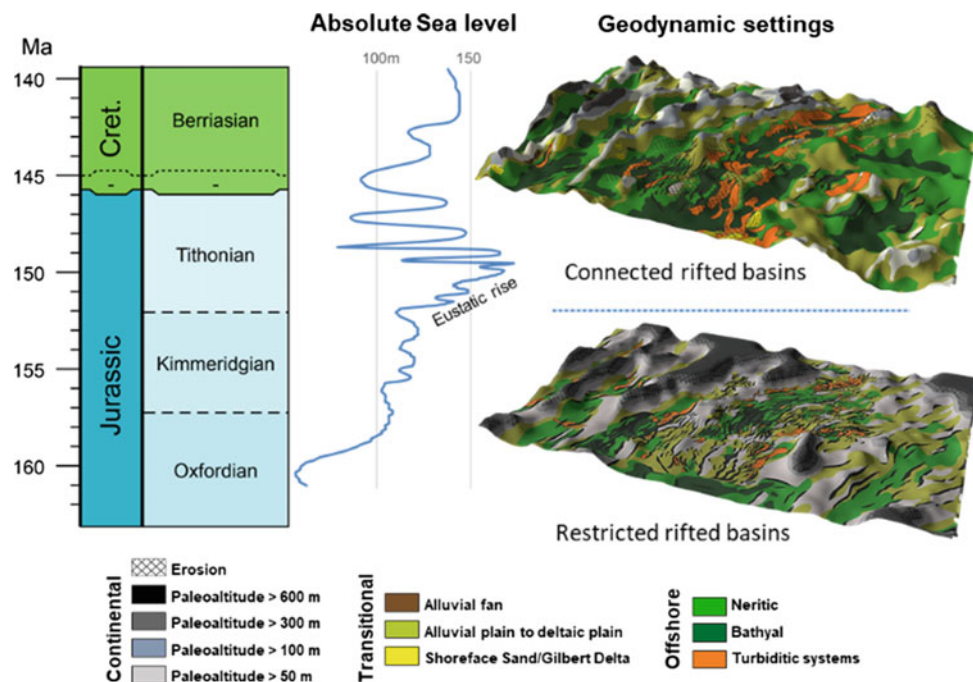


**Fig. 17** Eustatic and geodynamic settings of the area around the Kimmeridgian and Tithonian times recording the transition from continental to marine rifting (Beicip-Franlab, and Nalcor Energy—Oil and Gas Inc., 2020)



of *DionisosFlow*<sup>®</sup> is used and calibrated to Rock–Eval<sup>®</sup> data of the Great Barasway well (Fig. 18). Two different paleoenvironmental conditions are used to guide the organic matter deposition depending on the geodynamical setting of the basin. More restricted settings were adapted for the base of the model (Kimmeridgian), and more open marine settings were adapted for the Tithonian (Fig. 18). The complete basinal infilling is modelled and presented in Fig. 19 including the deposition of several levels of source rocks.

Since uncertainty exist on the exact timing of event happening in the upper Jurassic of the area (Fig. 17), two equiprobable models (scenarios) were designed. Scenario 1

(Fig. 20) considers the main geodynamical change (wide rift opening) to be synchronous with the main eustatic rise, implying enhanced marine flooding in oxic, ventilated, open basin. Scenario 2 (Fig. 20) tests this geodynamical change synchronously of a eustatic high stand implying limited basin drowning and prevalent anoxic subbasin (less ventilated).

The outcomes of the two equiprobable scenario are tested to assess sensitivity on source rock deposition and especially its lateral and vertical variations in terms of thickness, organic content (TOC), and potential (hydrogen index). Results of both hypotheses are shown in Fig. 20 and represented in a Wheeler diagram (plotted against geological age).

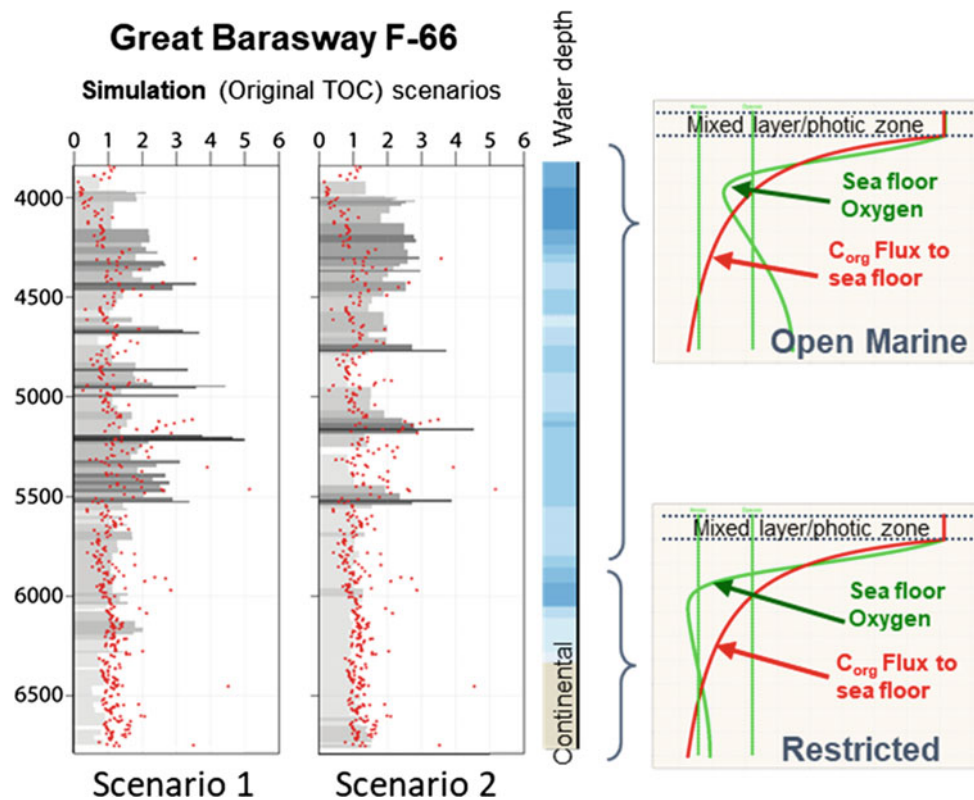


**Fig. 18** Models calibration at Great Barasway F-66 and paleoenvironment hypothesis (restricted marine versus open marine). Model is calibrated against rock eval lab measurements (red dots). Two calibrated scenarios are here considered (Beicip-Franlab and Nalcor Energy—Oil and Gas Inc., 2020)

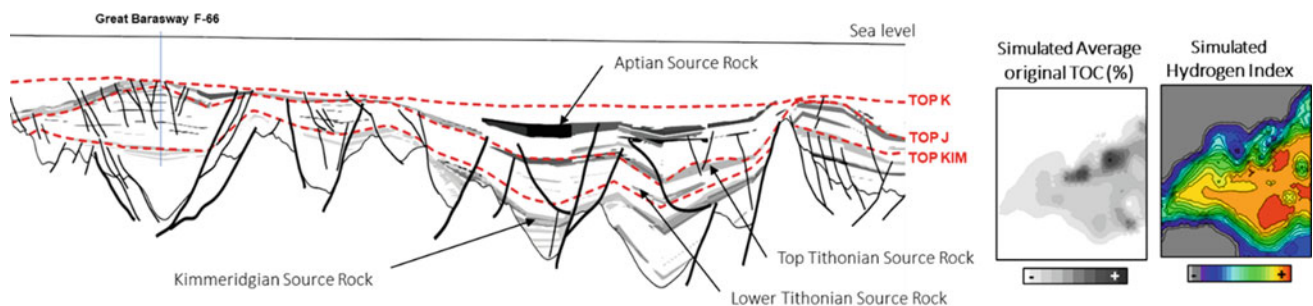


**Fig. 19** Simulated original TOC% result in section passing by the calibrated well and one source rock sample map of averaged original TOC% and simulated hydrogen index (Beicip-Franlab and Nalcor Energy—Oil and Gas Inc., 2020)

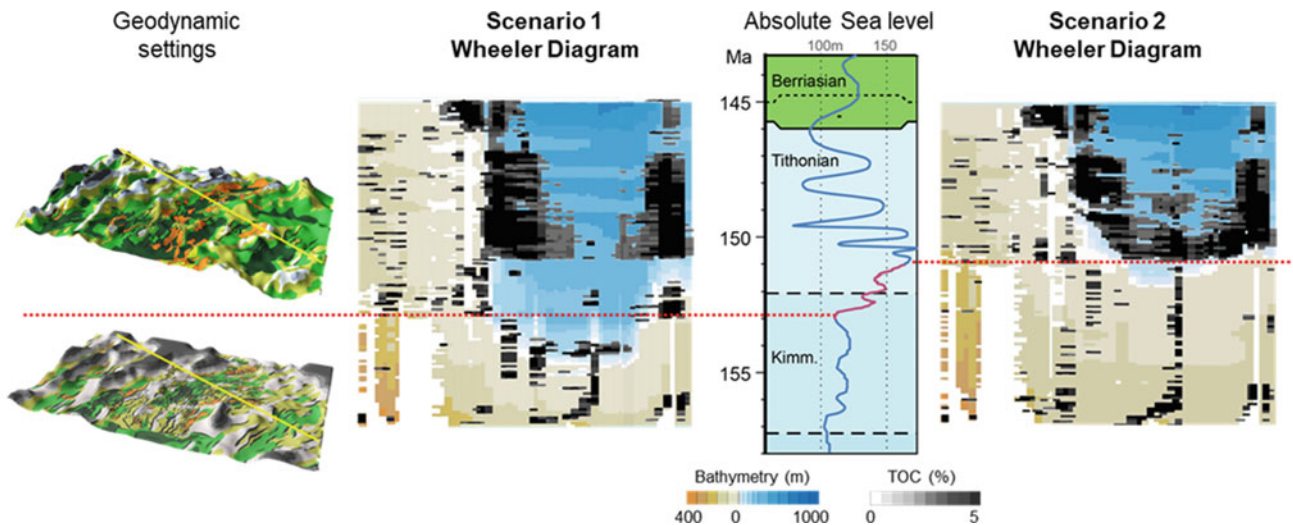


**Fig. 20** Tested hypothesis and results considering the synchronicity of a main geodynamical change (the transition from continental to marine rifting) against the late Kimmeridgian eustatic high. Was the sea level

rising, or already high during ongoing geodynamic change? Does it impact the organic matter deposition and preservation? (Beicip-Franlab and Nalcor Energy—Oil and Gas Inc., 2020)

Scenario 1 tests the deposition of organic matter in a widening rifted basin, while a large flooding event occurs enhancing basin drowning. Organic matter deposition is largely marine in oxic condition as the basins are largely ventilated, degrading the organic matter along the water column. Eventually higher up in the section (Cretaceous), as the drowning continues, organic deposition and preservation occur on the edges of the main Orphan trough (Fig. 20).

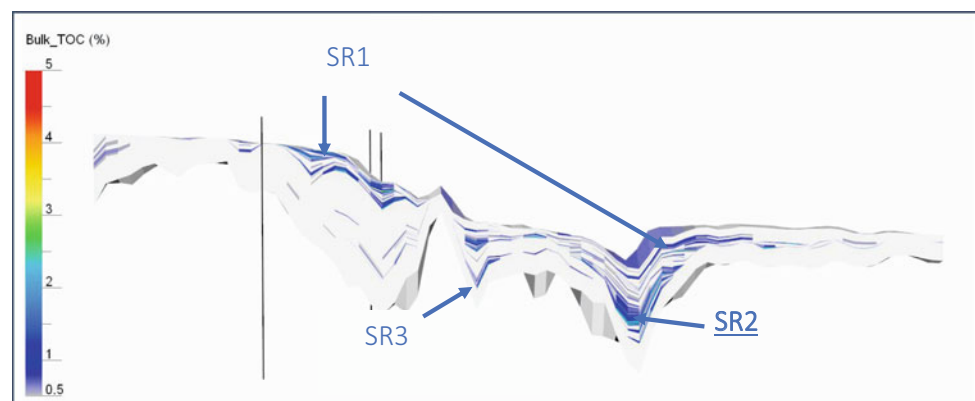
In Scenario 2, basins widening happens after the main sea level rise. Newly, structurally connected basins are not fully flooded, and marine circulation is restricted, limiting oxidation and hence favouring organic-rich level in early Tithonian times. Organic matter is significantly more widespread and better preserved in that scenario ultimately providing a better source rock potential. Reaching the Cretaceous time, as the drowning continues, the basin behaviour and organic matter preservation eventually matches Scenario 1 (Fig. 20).

Both scenarios provide sound alternative source rock models as they are both calibrated at the well, they are here assumed equiprobable given the current understanding of the basin setting and were both used to assess potential in places resources (Beicip-Franlab and Nalcor Energy—Oil and Gas Inc., 2020). To thoroughly assess the sensitivity of the system to uncertain parameters, a multirealization approach can be applied to better derisk the source rock presence and quality, as discussed in Case Study 2.

## 5.2 Case Study 2: Multiscenario Simulation of an Offshore Newfoundland SR

This case study concerns an offshore Newfoundland basin where the source rock deposition was simulated within a forward stratigraphic model. The resulting model identified three potential source rock intervals (Fig. 21). Based on the

**Fig. 21** Model cross section from offshore Newfoundland showing the identified source rocks



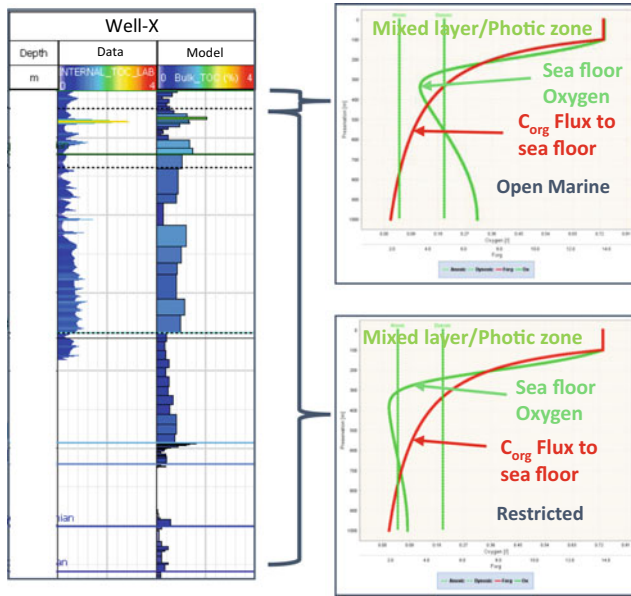


**Fig. 22** To the left an example of calibration of the model TOC to well data TOC. To the right, the preservation configurations used for the modelled succession based on paleogeographic information

study area’s paleogeographic setting, a restricted configuration was adapted for bottom water oxygen renewal for most of the modelled time followed by an open marine configuration with more aerated bottom waters (Fig. 22). The modelled TOC was then calibrated to TOC data available in one of the wells (Fig. 22). A variety of results can be extracted for each source rock, including TOC and HI which can be directly calibrated to available well data, in addition to bottom water oxygen which can be indirectly calibrated to redox sensitive geochemical proxies, and several other output properties that help better understand the deposition of the source rock. Results for source rock 2 (SR2) are shown in Fig. 23.

In this study, a sensitivity and uncertainty analysis using a response surface approach with *CougarFlow*<sup>TM</sup> was performed to assess the effect of uncertain parameter on the thickness of source rock 2 (SR2) (Fig. 24). A variation of  $\pm 20\%$  in primary productivity, organic matter quality (original HI), preservation factor (Martin’s exponent), and redox thresholds (burial efficiency) was tested through multirealization. A response surface to analyze the effect of

**Fig. 23** Panel showing maps of results for one of the source rocks identified (SR2) that can be obtained from the presented methodology. **a** TOC, **b** hydrogen index, **c** bottom water oxygen, **d** burial efficiency, **e** bathymetry, and **f** primary productivity

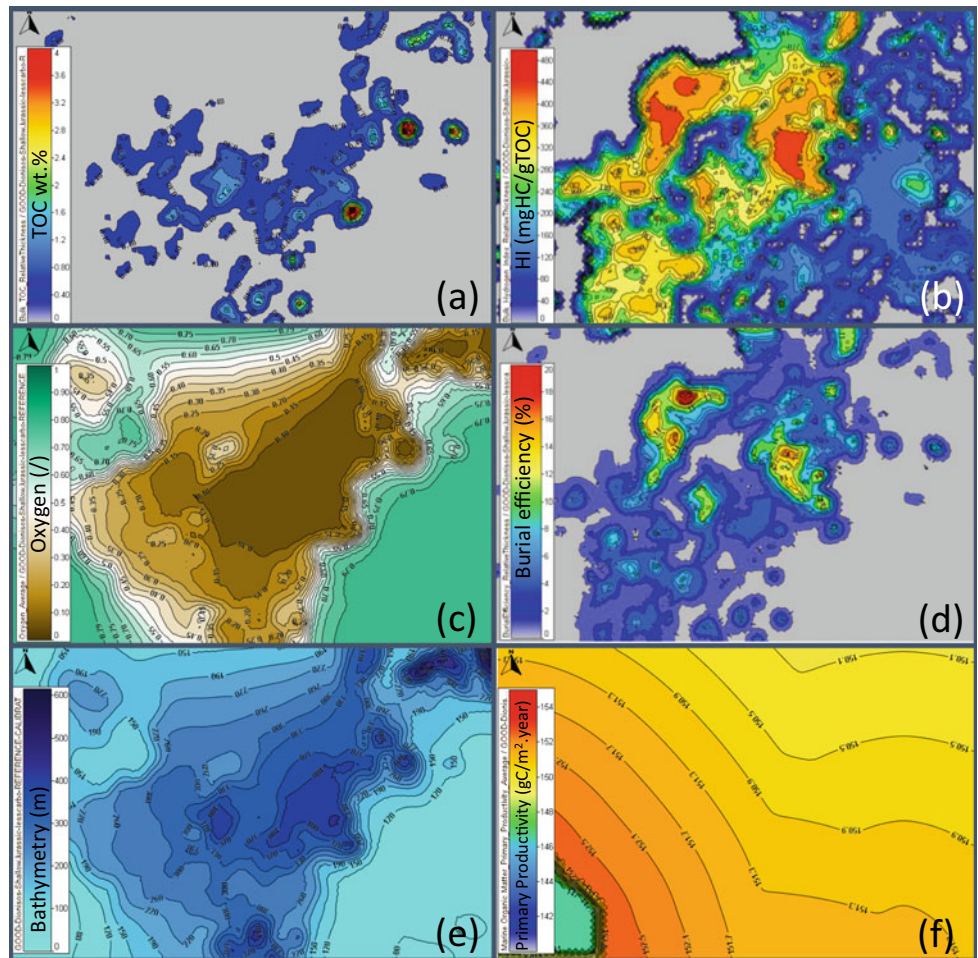


**Fig. 24** Schematic illustrating the response surface modelling approach used for sensitivity and risk analysis with CougarFlow™

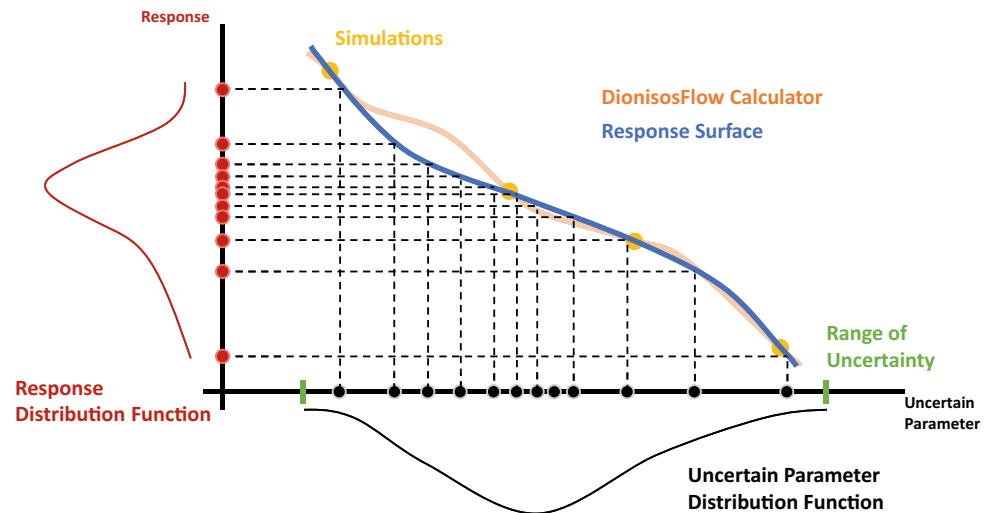
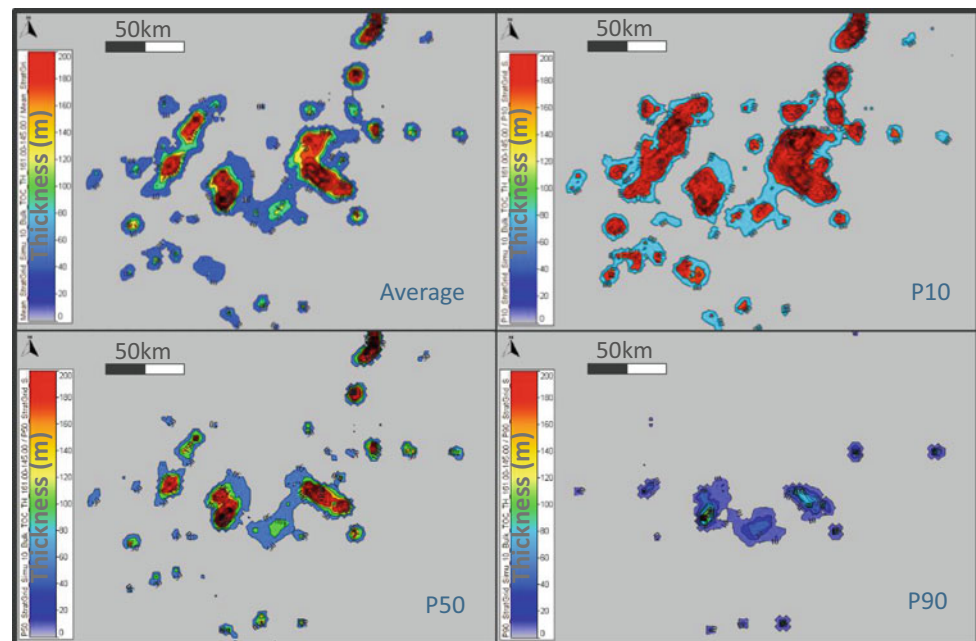


**Fig. 25** Results of risk analysis on the thickness of one of the identified source rocks (SR2). Thousands of response surface results can be used to produce average, P10, P50, and P90 maps showing the thickness of rock successions with TOC more than 1 wt.% and HI more than 300 mgHC/gTOC within the SR2 interval



these parameters on SR2 thickness was constructed and used to assess the risk of source rock presence (Fig. 25). This analysis shows that even in the worst-case scenario (P90), a kitchen area with around 50 m of source rock with TOC more than 1 wt.% and HI more than 300 mgHC/gTOC would still be present (Fig. 25).

## 6 Conclusions and Outlook

Forward stratigraphic models are able to provide precious information to simulate the evolution in time of depositional contexts experienced by a sedimentary basin. Associated to an organic matter model, FSM becomes a powerful tool to predict large-scale organic matter distribution and quality.

This coupling draws its strength from its capacity to transport not only inorganic sediments, but also organic matter while accounting for its degradation. Conditions of organic matter preservation are linked to stratigraphic variables such as bathymetry, sedimentation rate, and coastline location. The organic matter degradation rate is expressed with the oxygen index, a variable developed for the organic matter model to reflect the intensity of biological activity. Main results are TOC and HI maps that can be used as input for basin models and can be compared with TOC and HI maps resulting from more conceptual approaches to challenge and enhance geological models.

In this chapter, only results of marine organic matter modelling are presented. Terrestrial organic matter supply

can also currently be considered in this approach as an organic sediment defined with a constant HI. Additional developments are still necessary to go further and to simulate production and degradation processes of terrestrial and marine organic matter.

**Acknowledgements** The authors would like to thank Nalcor Energy Oil and Gas for their support and access to the data.

## References

- Abed, A. M., Arouri, K., & Boreham, C. (2005). Source rock potential of the phosphoritebituminous chalk-marl sequence in Jordan. *Marine and Petroleum Geology*, *22*, 413–425.
- Almogi-Labin, A., Bein, A., & Sass, E. (1993). Late Cretaceous upwelling system along the southern Tethys margin (Israel): Interrelationship between productivity, bottomwater environments, and organic matter preservation. *Paleoceanography*, *8*, 671–690.
- Almogi-Labin, A., Ashckenazi-Polivoda, S., Edelman-Furstenberg, Y., & Benjamini, C. (2012). Anoxia-dysoxia at the sediment-water interface of the southern Tethys in the late Cretaceous: Mishash Formation, southern Israel. In A. V. Altenbach, J. M. Bernhard, J. Seckbach (Eds.), *Anoxia: Evidence for eukaryote survival and paleontological strategies, cellular origin, life in extreme habitats and astrobiology* (21, pp. 553–572).
- Ashckenazi-Polivoda, S., Edelman-Furstenberg, Y., Almogi-Labin, A., & Benjamini, C. (2010). Characterization of lowest oxygen environments within ancient upwelling environments: Benthic foraminifera assemblages. *Paleoceanography, Palaeoclimatology, Palaeoecology*, *289*, 134–144.
- Ashckenazi-Polivoda, S., Abramovich, S., Almogi-Labin, A., Schneider-Mor, A., Feinstein, S., Püttmann, W., & Berner, Z. (2011). Paleoenvironments of the latest Cretaceous oil shale sequence, Southern Tethys, Israel, as an integral part of the prevailing upwelling system. *Paleoceanography, Palaeoclimatology, Palaeoecology*, *305*, 93–108.
- Behar, F., Lorant, F., & Lewan, M. (2008). Role of NSO compounds during primary cracking of a Type II kerogen and a Type III lignite. *Organic Geochemistry*, *44*, 387–397.
- Beicip-Franlab, and Nalcor Energy—Oil and Gas Inc. (2020). Offshore Newfoundland & Labrador Resource Assessment. Orphan basin Area NL20-CFB01. Public report. <https://oilandgas.nalcorenergy.com/wp-content/uploads/2020/09/2020-Orphan-Resource-Assessment-Public-Atlas-Final.pdf>
- Bein, A., & Amit, O. (1982). Depositional environments of the Senonian chert, phosphorite and oil shale sequence in Israel as deduced from their organic matter composition. *Sedimentology*, *29*, 81–90.
- Berelson, W. M. (2001). The flux of particulate organic carbon into the ocean interior. *Oceanography*, *14*(4), 59–67.
- Betts, J. N., & Holland, H. D. (1991). The oxygen content of ocean bottom waters, the burial efficiency of organic carbon, and the regulation of atmospheric oxygen. *Paleoceanography, Palaeoclimatology, Palaeoecology (Global and Planetary Change Section)*, *97*, 5–18.
- Betzler, P. R., Showers, W. J. Law, E. A. Winn, C. D. DiTullio, G. R., & Kroopnick, P. M. (1984). Primary productivity and particle fluxes on a transect of the equator at 153°W in the Pacific Ocean. *Deep-Sea Research*, *31*, 1–11.
- Bou Daher, S., Nader, F. H., Strauss, H., & Littke, R. (2014). Depositional environment and source-rock characterisation of organic-matter rich Upper Turonian—Upper Campanian carbonates, Northern Lebanon. *Journal of Petroleum Geology*, *37*, 1–20.
- Bou Daher, S., Nader, F. H., Müller, C., & Littke, R. (2015). Geochemical and petrographic characterization of Campanian-Lower Maastriichtian calcareous petroleum source rocks of Hasbayya, South Lebanon. *Marine and Petroleum Geology*, *64*, 304–323.
- Bou Daher, S., Ducros, M., Michel, P., Hawie, N., Nader, F. H., & Littke, R. (2016). 3D thermal history and maturity modelling of the Levant Basin and its eastern margin, offshore-onshore Lebanon. *Arabian Journal of Geosciences*, *9*, 440. <https://doi.org/10.1007/s12517-016-2455-1>
- Bou Daher, S. (2016). *Source rock characterization and petroleum generation modelling of the Levant Basin, onshore-offshore Lebanon: An integrated approach*, Ph.D. thesis, RWTH Aachen University, p. 158.
- Bruneau, B., Chauveau, B., Duarte, L. V., Desaubiaux, G., Moretti, I., & Baudin, F. (2018a). 3D numerical modelling of marine organic matter distribution: Example of the early Jurassic sequences of the Lusitanian Basin (Portugal). *Basin Research*, *30*, 101–123.
- Bruneau, B., Baudin, F., Villié, M., Moretti, I., Ducros, M., & Chauveau, B. (2018b). 3D numerical modelling and sensitivity analysis of the processes controlling organic matter distribution and heterogeneity—A case study from the Toarcian of the Paris Basin. *Geosciences*, *8*(11), 2076–3263.
- Bruneau, B., Chauveau, B., Baudin, F., & Moretti, I. (2017). 3D stratigraphic forward numerical modelling approach for prediction of organic-rich deposits and their heterogeneities. *Marine and Petroleum Geology*, *82*, 1–20.
- Burdige, D. J. (2007). Preservation of organic matter in marine sediments: Controls, mechanisms, and an imbalance in sediment organic carbon budgets? *Chemical Reviews*, *107*, 467–485.
- Burwood, R., Cornet, P. J., Jacobs, L., & Paulet, J. (1990). Organofacies variation control on hydrocarbon generation: A Lower Congo Coastal Basin (Angola) case history. *Organic Geochemistry*, *16*, 325–338.
- Chauveau, B., Granjeon, D., & Huc, A. (2013). Depositional model of marine organic matter coupled with a stratigraphic forward numerical model (DIONISOS): Application to the Devonian Marcellus Formation (Abstr.) In *AAPG Hedberg Conference Petroleum Systems: Modeling the Past*.
- Chauveau, B., Granjeon, D., & Ducros, M. (2016). 3D numerical stratigraphic model for basin scale modeling of the organic matter deposition in a marine environment: Application to the Natih formation (Late Cretaceous, Oman) (Abstr.) In *AAPG Geosciences Technology*.
- Dale, A. W., Sommer, S. Lomnitz, U., Montes, I., Treude, T., Liebetrau, V., Gierl, J., Hensen, C., Dengler, M., Stolpovsky, K., Bryant, L. D., & Wallmann, K. (2015). Organic carbon production, mineralisation and preservation on the Peruvian margin. *Biogeosciences*, *12*, 1537–1559
- Crasquin, S., & Sandulescu, M. (Eds.). (2000). Atlas Peri-tethys, Palaeogeographical Maps. 24 maps and explanatory notes: I-XX. CCGM/CGMW, Paris, p. 269.
- Durand, B., & Nicaise, G. (1980). Procedure for kerogen isolation. In B. Durand (Ed.), *Kerogen, insoluble organic matter from sedimentary rocks* (pp. 35–53). Editions Technip.
- Espitalié, J., Deroo, G., & Marquis, F. (1986). La pyrolyse Rock-Eval et ses applications. *Revue de l'Institut Français du Pétrole*, *41*, 73–89.
- Garcia, H. E., Locarnini, R. A., Boyer, T. P., Antonov, J. I., Mishonov, A. V., Baranova, O. K., Zweng, M. M. Reagan, J. R., & Johnson D. R. (2013). World Ocean Atlas 2013. Vol. 3: Dissolved oxygen, apparent oxygen utilization, and oxygen saturation. S. Levitus, Ed.; A. Mishonov, Technical Ed. NOAA Atlas NESDIS 75, 27 pp.
- Gardosh, M., Druckman, Y., Buchbinder, B., & Rybakov, M. (2008). The Levant Basin Offshore Israel: Stratigraphy, structure, tectonic

- evolution and implications for hydrocarbon exploration. *Geophysical Institute of Israel*, 429(328/08), 1–119.
- Gogou, A., Sanchez-Vidal, A., Durrieu de Madron, X., Stavarakakis, S., Calafat, A. M., Stabholz, M., Psarra, S., Canals, M., Heussner, S., Stavarakaki, I., & Papathanassiou, E. (2013). Carbon flux to the deep in three open sites of the Southern European Seas (SES). *Journal of Marine Systems*, 129(2014), 224–233.
- Granjeon, D. (2014). 3D forward modelling of the impact of sediment transport and base level cycles on continental margins and incised valleys. In A. W. Martinius, R. Ravnas, J. A. Howell, R. J. Steel, & J. P. Wonham (Eds.), *From depositional systems to sedimentary successions on the Norwegian Continental Margin: Somerset* (pp. 453–472). Wiley.
- Granjeon, D., & Chauveau, B. (2014). Sedimentary basin development method using stratigraphic simulation coupled with an organic matter production and degradation model. US 2014/0163883 A1.
- Granjeon, D., & Joseph, P. (1999). Concepts and applications of a 3-D multiple lithology, diffusive model in stratigraphic modelling. In J. W. Harbaugh, W. L. Watney, E. C. Rankey, R. Slingerland, R. H. Goldstein, & E. K. Franseen (Eds.), *Numerical experiments in stratigraphy: Recent advances in stratigraphic and sedimentological computer simulations*. SEPM Special Publication 62 (pp. 197–210). <https://doi.org/10.2110/pec.99.62.0197>
- Granjeon, D. (1996). *Modelisation stratigraphique deterministe—Conception et applications d'un modele diffusif 3D multilithologique*, Ph. D. thesis, Universite de Rennes 1, Rennes, France, 215 p.
- Hawie, N., Barrois, A., Marfisi, E., Murat, B., Hall, J., El-Wazir, Z., Al-Madani, N., & Aillud, G. (2015a). Forward stratigraphic modelling, Deterministic approach to improve carbonate heterogeneity prediction; Lower Cretaceous, Abu Dhabi. In *Abu Dhabi International Petroleum Exhibition and Conference*, November 9–12, 2015, SPE-177519-MS, 15 p. <https://doi.org/10.2118/177519-MS>
- Hawie, N., Deschamps, R., Granjeon, D., Nader, F. H., Gorini, C., Muller, C., Montadert, L., & Baudin, F. (2015b). Multi-scale constraints of sediment source to sink systems in frontier basins: A forward stratigraphic modeling case study of the Levant region. *Basin Research*, 29, 418–445. <https://doi.org/10.1111/bre.12156>
- Hawie, N., Covault, J. A., Dunlap, D., & Sylvester, Z. (2018). Slope-fan depositional architecture from high-resolution forward stratigraphic models. *Marine and Petroleum Geology*, 91, 576–585.
- Hoogakker, B. A. A., Lu, Z., Umling, N., Jones, L., Zhou, X., Rickaby, R. E. M., Thunell, R., Cartapanis, O., & Galbraith, E. (2018). Glacial expansion of oxygen-depleted seawater in the eastern tropical Pacific. *Nature*, 562(7727), 410–413. <https://doi.org/10.1038/s41586-018-0589-x>
- Inan, S., Alp Ugur, F., Inan, T., Yalcin, M. N., & Mann, U. (2010). Relationship between organic matter, sulphur and phosphate contents in upper cretaceous marine carbonates (Karabogaz Formation, SE Turkey): Implications for early oil generation. *Journal of Petroleum Geology*, 33(4), 319–338.
- Jenkins, A. D., & Bye, J. A. T. (2006). Some aspects of the work of V. W. Ekman. *Polar Record*, 42, 15–22.
- Jermannaud, P., Le Guerroué, E., Chenet, P. Y., Pitz, J., Gillis, E., Carter, J., Atkinson, I., McCallum, D., & Wright, R. (2016). Potential of the Eastern NL, Canada. In *78th EAGE Conference and Exhibition*. Vienna. <https://doi.org/10.3997/2214-4609.201600936>
- Jermannaud, P., Le Guerroué, E., Thomas, D., & Pérez-Drago, G. (2020). Six years exploring Offshore Newfoundland and Labrador: Insight from forward stratigraphic modeling to petroleum system assessment. In *82nd EAGE Annual Conference & Exhibition*. Amsterdam: European Association of Geoscientists & Engineers.
- Karl, D. & Knauer, G. (1991). Microbial production and particle flux in the upper 350 m of the Black Sea. *Deep-Sea Research*, 38(Suppl 2.), S921–S942.
- Keym, M., Dieckmann, V., Horsfield, B., Erdmann, M., Galimberti, R., Kua, L.-C., Leith, L., & Podlaha, O. (2006). Source rock heterogeneity of the Upper Jurassic Draupne Formation, North Viking Graben, and its relevance to petroleum generation studies. *Organic Geochemistry*, 37(2), 220–243.
- Lafargue, E., Marquis, F., & Pillot, D. (1998). Rock-Eval 6 applications in hydrocarbon exploration, production, and soil contamination studies. *Oil & Gas Science and Technology—Revue de l'IFP*, 53, 421–437.
- Le Guerroué, E., Chenet, P. Y., Lebreuilly, B., Jermannaud, P., McCallum, D., Mitchell, V., Montevecchi, N., Atkinson, I., & Wright, R. (2017). Potential of the Orphan basin, NL, Canada. In *79th EAGE Conference and Exhibition*. Paris. <https://doi.org/10.3997/2214-4609.201700888>
- Le Guerroué, E., Filleaudeau, P. Y., Thomas, D., Prélat, A., Pichot, T., Chenet, P. Y., Norris, D., Mitchell, V., Gillis, E., & Wright, R. (2019). Potential of the Eastern Jeanne d'Arc Basin, NL, Canada. In *81st EAGE Conference and Exhibition*. London. <https://doi.org/10.3997/2214-4609.201900724>
- Le Guerroué, E., Jermannaud, P., Pérez-Drago, G., Lebreuilly, B., Pichot, T., Chenet, P.Y., Norris, D., Gillis, E., & Wright, R. (2020). Geological equiprobable multi-models for resources assessment. Carson, Bonniton and Salar Basin, NL, Canada. In *82nd EAGE Annual Conference & Exhibition*, 2020: 1–5. Amsterdam: European Association of Geoscientists & Engineers. <https://doi.org/10.3997/2214-4609.202010664>
- Leiter, C., & Altenbach, A. V. (2010). Benthic foraminifera from the diatomaceous mud belt off Namibia: Characteristic species for severe anoxia. *Palaeontologia Electronica*, 13, 19.
- Liechoski de Paula Faria, D., Tadeu dos Reis, A., & Gomes de Souza, O. (2017). Three-dimensional stratigraphic-sedimentological forward modeling of an Aptian carbonate reservoir deposited during the sag stage in the Santos basin, Brazil. *Marine and Petroleum Geology*, 88, 676–695.
- Littke, R., Klussmann, U., Krooss, B., & Leythaeuser, D. (1991). Quantification of calcite-, pyrite-, and organic matter-loss due to weathering of Toarcian black shales and effects on kerogen and bitumen characteristics. *Geochimica et Cosmochimica Acta*, 55, 3369–3378.
- Littke, R. (1993). *Deposition, diagenesis and weathering of organic matter-rich sediments*. In *Lecture Notes in Earth Sciences* (p. 216). Springer.
- Lutz, M., Dunbar, R., & Caldeira, K. (2002). Regional variability in the vertical flux of particulate organic carbon in the ocean interior. *Global Biogeochemical Cycles*, 16(3), 1037.
- Lutz, M., Caldeira, K., Dunbar, R. B., & Behrenfeld, M. J. (2007). Seasonal rhythms of netprimary production and particulate organic carbon flux to depth describe the efficiency of biological pump in the global ocean. *Journal of Geophysical Research*, 112, C10011.
- Macquaker, J. H. S., & Bohacs, K. M. (2007). On the accumulation of mud. *Science*, 318, 1734–1735.
- Macquaker, J. H. S., Bentley, S., & Bohacs, K. M. (2010). Wave enhanced sediment-gravity flows and mud dispersal across continental shelves: Reappraising sediment transport processes operating in ancient mudstone successions. *Geology*, 38, 947–950.
- Mann, U., & Zweigel, J. (2008). Modelling source rock distribution and quality variations: The OF-Mod approach. In P. L. de Boer, G. Postma, C. J. van der Zwan, P. M. Burgess, & P. Kukla (Eds.), *Analogue and numerical forward modelling of sedimentary systems; from understanding to prediction* (pp. 239–274). Special Publication 40 of the International Association of Sedimentologists.
- Martin, J. H., Knauer, G. A., Karl, D. M., & Broenkow, W. W. (1987). VERTEX: Carbon cycling in the northeast Pacific. *Deep-Sea Research*, 34, 267–285.

- Pichot, T., Le Guerroué, E., Filleaudeau, P. Y., & Micarelli, L. (2018). Newfoundland Labrador Orphan basin: Structural key elements for the Northeast Atlantic Opening. In *Conjugate Margins Conference*.
- Schneider-Mor, A., Alsenz, H., Ashckenazi-Polivoda, S., Illner, P., Abramovich, S., Feinstein, S., Almogi-Labin, A., Berner, Z., & Püttmann, W. (2012). Paleocyanographic reconstruction of the late Cretaceous oil shale of the Negev, Israel: Integration of geochemical, and stable isotope records of the organic matter. *Palaeogeography, Palaeoclimatology, Palaeoecology*, 319–320, 46–47.
- Shieber, J., Southard, J., & Thaisen, K. (2007). Accretion of mudstone beds from migrating floccule ripples. *Science*, 318, 1760–1763.
- Stein, R. (1990). Organic carbon content/sedimentation rate relationship and its paleo environmental significance for marine sediments. *Geo-Marine Letters*, 10, 37–44.
- Stein, R. (1991). Accumulation of organic carbon in marine sediments: Results from the deep sea drilling project/ocean drilling program (DSDP/ODP). *Lecture Notes in Earth Sciences*, 34, 217.
- Suess, E., & Müller, P. J. (1980). Productivity, sedimentation rate and sedimentary organic matter in the oceans II.—Elemental fractionation. In *Biogéochimie de la Matière Organique à l'Interface Eau – Sédiment Marin. Colloque Internationaux du Centre des Recherches National des Sciences*, Paris, 293, 17–26.
- Suess, E. (1980). Particulate organic carbon flux in the oceans—Surface productivity and oxygen utilization. *Nature*, 288, 260–263.
- Tissot, B., & Espitalié, J. (1975). L'évolution de la matière organique des sédiments: application d'une simulation mathématique. *Oil and Gas Science and Technology*, 24, 470–501.
- Trabucho-Alexandre, J., Dirks, R., Veld, H., Klaver, G., & de Boer, P. L. (2012). Toarcian black shales In the Dutch Central Graben: Record of energetic, variable depositional conditions during an oceanic anoxic event. *Journal of Sedimentary Research*, 82(2), 104–120.
- Tyson, R. V. (2001). Sedimentation rate, dilution, preservation and total organic carbon: Some results of a modelling study. *Organic Geochemistry*, 32(2), 333–339.
- Tyson, R. V., & Pearson, T. H. (1991). Modern and ancient continental shelf anoxia, Geological Society Special Publication No. 58, pp. 1–24.
- Tyson, R. V. (1995). *Sedimentary organic matter. Organic facies and palynofacies* (615 pp.) Chapman and Hall.
- Vandenbroucke, M., & Largeau, C. (2007). Kerogen origin, evolution and structure. *Organic Geochemistry*, 38, 719–833.



# Optical Kerogen Analysis

Hartmut Jäger

## Abstract

A new approach of microscopic kerogen analysis—*Optical Kerogen Analysis*—identifies and quantifies the internal mixture of kerogen, regarding to composition, preservation and maturation. Kerogen composition is directly linked to the type of primary generated hydrocarbons. Kerogen preservation indicates the level of kerogen degradation and hydrocarbon generation, and organic maturation records the thermal history of the hydrocarbon system. This threefold approach leads to the quantification of productive versus unproductive proportions of the total kerogen (=net-TOC) in the hydrocarbon system, the estimation of HC generation from oil-prone and gas-prone parts of kerogen and the in situ basin maturation. It gives detailed insights on the internal variation of source rocks and highly reliable identification of effective source rock thickness (=net-source-rock unit) in source rock formations. It significantly improves the resolution and reliability of kerogen analysis compared to bulk rock geochemical analysis, usually used in source rock analysis.

## Keywords

Source rock analysis • Net-TOC • Net-source rock unit • Hydrocarbon system analysis

## 1 Introduction and Background

From the beginning, the definition and analysis of kerogen was based on geochemical analysis of sedimentary organic matter in organic-rich sediments. Until today, kerogen analysis is largely associated with geochemical analysis that

even microscopic kerogen analysis within hydrocarbon resource analysis mostly gets labeled as ‘geochemistry service’. Originally, kerogen was defined as the part of organic matter in sedimentary rocks that is not soluble in common organic solvents or aqueous alkaline solvents (Forsman & Hunt, 1958). This definition was extended to comprise all insoluble sedimentary organic matter not only in sedimentary rocks, but all types of rocks and sediments (Durand, 1980). Primarily, kerogen was supposed to have a homogeneous structure with little structural variations. But it turned out, that kerogen is a very heterogeneous and complex agglomerate of different types of organic matter. Thus, it is to be expected to have variations in the kerogen structures even over relatively small distances.

First chemical studies of organic matter were done in coals, because the organic matter was easier accessible than in sedimentary rocks. A first comprehensive compilation on coal analysis was published by van Krevelen (1961), which included the classification of organic matter in coals based on atomic ratios of H/C and O/C. These coal studies influenced and supported the analysis and classification of kerogen in sedimentary rocks and the influence of thermal alteration on changes in kerogen chemistry and hydrocarbon generation (Durand et al., 1972; Tissot & Welte, 1984; Tissot et al., 1974, 1975). This led to an extended kerogen classification scheme, defining four kerogen types based on chemical composition (H:C and O:C ratio, typical organic molecules), the biological origin of the organic matter, the depositional environments and the primary generated hydrocarbons (Tissot & Welte, 1984). These four kerogen types are commonly used as standard kerogen types until today.

Also, optical analysis of sedimentary organic matter developed as early as the 1960’s, introducing the concept of *palynofacies* (Combaz, 1964). It studies the total assemblage of particulate organic matter in a sediment, using mainly transmitted light microscopy, but also incident blue light fluorescence microscopy. It identifies the individual

H. Jäger (✉)  
GeoResources STC, Bensheim, Germany  
e-mail: [jaeger@georesources.de](mailto:jaeger@georesources.de)



particulate components, quantification of their proportions, size and preservation states to analyze the depositional settings and paleoenvironmental conditions. A compilation of the development of palynofacies analysis is given by Tyson (1995). The integration of palynofacies analysis and bulk rock geochemical methods led to the concept of *organic facies*, focused on the prediction of source rock quality. It is based on kerogen typing using organic matter composition derived from palynofacies analysis (e.g. Bujak et al., 1977; Burgess, 1974; Correia, 1971), using simple classification schemes: gas-prone (terrestrial, humic, ligneous), transitional (mixed) and oil-prone (marine, sapropelic) facies (Combaz, 1980; Raynaud & Robert, 1976). Based on coal petrology, the concept of organic petrology was developed for organic matter in sedimentary rocks (Stach et al., 1982; Taylor et al., 1998; Teichmüller, 1986). It characterizes and identifies the different organic constituents and determines the degree of maturity.

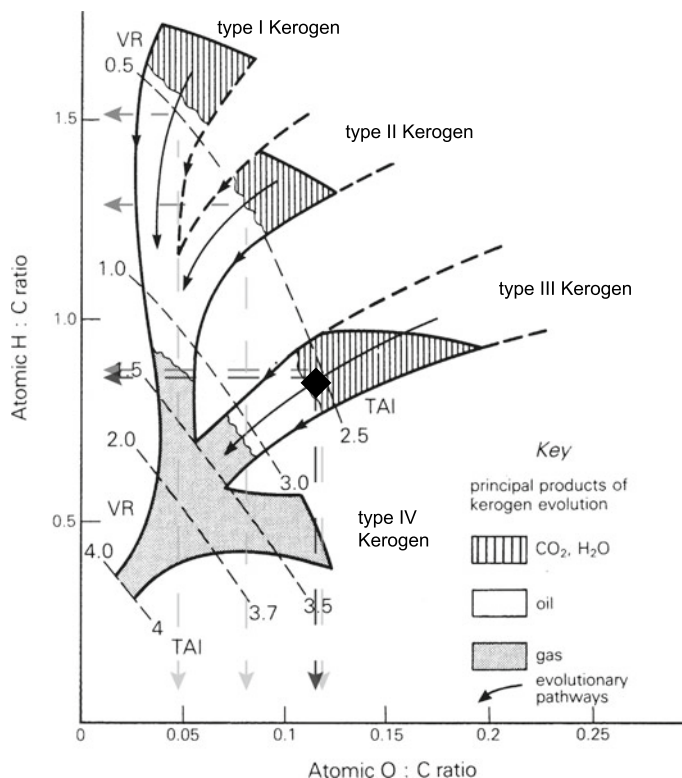
In *Optical Kerogen Analysis* (Jäger, 2013), the full range of microscopic analysis is used for the analysis of the total sedimentary organic matter, to obtain all information of the organic matter available from optical analysis. It is based on palynofacies and organic petrology, but has further developed the use and understanding of optical analysis of organic matter and its application to hydrocarbon generation in all three aspects: kerogen composition, kerogen preservation and kerogen maturation. Kerogen composition includes identification and characterization, but also full quantification of all organic matter components and its transformation into kerogen types. Kerogen preservation includes both, primary degradation during transport and deposition, but also secondary degradation from thermal alteration during burial and consequent hydrocarbon generation. Kerogen maturation provides detailed data on maturation of each organic matter group included in the total kerogen. This threefold approach of component specific optical analysis improves the understanding and interpretation of the generation, preservation and thermal history of the kerogen and its hydrocarbon generating potential.

## 2 Geochemical Versus Optical Kerogen Analysis

Although optical and geochemical kerogen analysis seem to be similar workflows leading to the same results in slightly different ways, there is a significant difference between both. Geochemical methods use whole rock samples for analysis. Thus, it is not a component specific analysis of the different organic matter components mixed in the kerogen, but a bulk analysis of all organic matter components together, leading to results mixed of the chemistry of all different types of organic matter in the rock. Kerogen classification based on

the bulk rock analysis assigns one kerogen type to each sample. The internal mixture of different organic matter groups in the kerogen is not recognized, just as internal differences in maturation and preservation between these groups. But this might be quite important for the evaluation of the hydrocarbon generating potential of the source rocks. The most common geochemical method in source rock analysis is Rock Eval Pyrolysis, which is no direct analysis of the chemistry of the organic matter, but an indirect interpretation of CO<sub>2</sub> levels generated during pyrolysis. This indirect analysis even more limits the identification of the internal mixture of the kerogen. Although Rock Eval Pyrolysis was developed as initial screening method for source rock analysis, it is the only method used in many geochemical source rock studies. But even if other geochemical methods are used, all are based on whole rock analysis, having the same problem to identify the internal mix of the kerogen. Geochemical methods that directly analyze the chemistry of organic matter can give some assumptions on mixed kerogen, but no direct identification and quantification and also no internal differences on preservation and maturation of different organic components. Therefore, kerogen characterization and the hydrocarbon generating potential based on these bulk rock chemistry data might differ significantly from the real kerogen composition and consequent hydrocarbon potential of the sample (Fig. 1). In *Optical Kerogen Analysis*, the organic matter is isolated from the rock and directly studied at the microscope. This enables the identification and quantification of all different organic matter groups mixed in the kerogen. The transformation from palynological organic matter groups into kerogen types enables the quantification of all four standard kerogen types in the total kerogen of each sample. Therefore, *Optical Kerogen Analysis* provides the exact proportion of all four kerogen types within the total kerogen of each sample and not by one bulk kerogen type as in geochemical analysis. Maturation and preservation of the different organic matter groups are analyzed too, providing additional insights in the hydrocarbon generating potential of each kerogen type in the total kerogen. This significantly improves the resolution and reliability of kerogen analysis compared to bulk rock geochemical analysis.

North (1985) gives an example of geochemical bulk rock analysis compared to component specific optical kerogen analysis (Fig. 1). The kerogen is classified as purely gas-prone type III kerogen by geochemical bulk analysis (black rhomb), but optical kerogen analysis shows that the real kerogen composition is quite different: only 50% gas-prone type III kerogen, but 20% oil-prone kerogen types I and II and 30% hydrocarbon unproductive type IV kerogen. This reduces the total hydrocarbon productivity in this source rock by 1/3. The real hydrocarbon generating potential of this source rock differs significantly from the interpretation of the



Microscopic analysis:

5% type I Kerogen  
15% type II Kerogen  
50% type III Kerogen  
30% type IV Kerogen

Maturation (VR) : 0,5%  $R_m$

Calculated H:C / O:C of total Kerogen:

H : C	O : C
$0,05 \times 1,5 = 0,075$	$0,05 \times 0,05 = 0,0025$
$0,15 \times 1,3 = 0,195$	$0,15 \times 0,08 = 0,012$
$0,50 \times 0,9 = 0,450$	$0,50 \times 0,12 = 0,060$
$0,30 \times 0,4 = 0,120$	$0,30 \times 0,14 = 0,042$
<b>H:C total = 0,840</b>	<b>O:C total = 0,1165</b>

Position of total kerogen

**Fig. 1** Kerogen composition from microscopic analysis transferred into van Krevelen diagram, typically used for geochemical kerogen classification. Modified from North (1985)

geochemical analysis. It differs regarding the kerogen composition, just as the type and timing of primary generated hydrocarbons and the total hydrocarbon productivity of the rock. In case the different groups of organic matter mixed in the total kerogen have different maturity, it becomes much more complicated. The same if the preservation levels of the different groups of organic matter differ too. Particularly if it is mainly primary degradation with a loss of initial hydrocarbon productivity, it becomes even more complicated. All this is not recognizable in geochemical bulk rock analysis, leading to the risk of misinterpretation of the source side in hydrocarbon system analysis.

Similar geochemical maturation analysis (e.g.  $T_{max}$  from Rock Eval pyrolysis), also based on whole rock analysis of chemical parameters interpreted for maturation, is unable to differentiate between different maturation levels of different organic matter groups mixed in the total kerogen. Due to recycling of highly mature organic matter and alteration of different groups of organic matter in the kerogen,  $T_{max}$  or other geochemical maturation indices, might produce results differing from the in situ maturity of the rocks, having a significant input on all further hydrocarbon system modeling and evaluation. This is an important issue in several basins worldwide, particularly the overestimation of organic maturation in several Paleozoic basins.

### 3 Sample Preparation and Analysis

All types of source rocks can be analyzed by optical kerogen analysis: claystones, siliceous and calcareous shales, marlstones, micritic carbonates and biogenic sediments. Sandy shales and siltstones do not work very well. The organic matter is extracted from the rock and mounted on slides for microscopical analysis to get analyzed separately and without any influence of the rock matrix. The quality of results of Optical Kerogen Analysis is not only depending on the quality of analysis and interpretation, but also on sampling and sample processing. Different from other palynological sample processing, minimal processing is obligatory for samples for Optical Kerogen Analysis: only maceration (HCl and HF acid treatment) and sieving; no oxidation or other chemical treatment and no ultrasound and microwave treatment. Sieving is necessary to remove the very fine-grained kerogen, which would produce an almost non-transparent layer in the kerogen slide. This would hamper the microscopic identification and analysis of the kerogen in the slide, which is the base for optical kerogen analysis. Therefore, optical kerogen analysis is based on kerogen particles  $>10 \mu\text{m}$  (depending on the mesh size of the sieve). But geochemical analysis shows the same results

for the isolated sieved kerogen sample and the bulk rock kerogen sample (Fig. 2). Minor differences are related to the impact of bitumen in the samples, which is present in the bulk rock sample only, but not in the sieved isolated kerogen sample. Also, the examination of the washed out very fine-grained kerogen by SEM shows that it has the same composition as the sieved kerogen in the slide. This means sieving does not change the kerogen composition.

Normally optical kerogen analysis is done by transmitted normal light microscopy. Additionally, incident blue light fluorescence microscopy is useful, particularly in samples rich in amorphous organic matter (AOM). Kerogen is

classified in up to 15 biologically defined groups, each with three subgroups regarding the level of preservation: well preserved, moderately degraded and strongly degraded. This detailed classification is important for reliable interpretation of the preservation mode of the total kerogen and its significance for hydrocarbon generating processes. A minimum of 300 particles are counted in each slide, using 2–3 traverses across the slide. Optical kerogen analysis is based on relative percentage of particle volumes, in contrast to palynofacies analysis based on relative percentage of particle abundances. Not only the number of particles is included, but also the size (volume) of the particle. The results of the volumetric quantification of each group are transformed into standard kerogen types I–IV, providing exact quantities of all four kerogen types within each sample for enhanced analysis of the hydrocarbon generation potential.

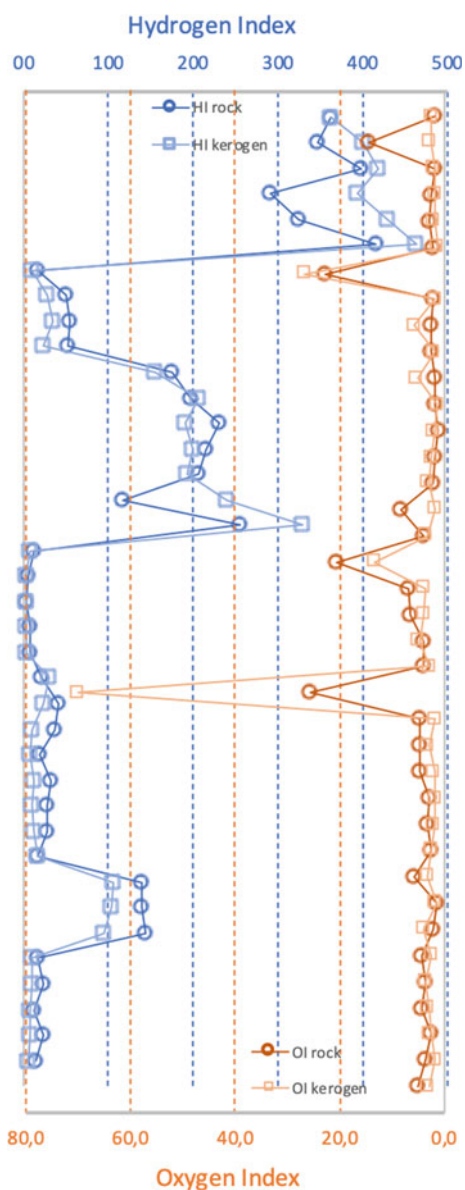


**Fig. 2** Correlation of Hydrogen Index (HI) and Oxygen Index (OI) derived from Rock Eval Pyrolysis of bulk rock samples and isolated kerogen of the same samples

## 4 Kerogen Composition

Microscopic analysis of kerogen composition is the part of the optical kerogen analysis workflow, which is developed and well known from palynofacies analysis and palynofacies-based kerogen typing, but also organic petrography. Kerogen composition refers directly to the primary type of hydrocarbons generated from the source rock. Therefore, it is an essential parameter of kerogen analysis. Kerogen is always a mixture of organic components when examined under the microscope (Tyson, 1995). Looking into the microscope, this mixture is directly visible (Fig. 3) and the different groups of organic matter can be identified and quantified. Most hydrocarbon systems are located in continental margin settings, representing shallow to deep marine shelf systems (Mann et al., 2003). The organic matter recorded in these settings is commonly mixed of terrestrial and marine organic matter, which represent different kerogen types according to the standard kerogen types of Tissot and Welte (1984).

In most marine environments, a certain input of terrestrial organic matter is preserved, but also in fully terrestrial environments, different types of organic matter are preserved, representing different kerogen types: aquatic and terrigenous (mainly debris of land plants). Even the terrigenous part is made of different kerogen types: oil-prone and gas-prone organic matter. Thus, in most kerogens, 3–4 of the standard kerogen types (Tissot & Welte, 1984) are mixed together. Monogenic kerogens, made of organic matter representing one type of kerogen only, are very rare. For the reliable interpretation and evaluation of the hydrocarbon generating potential, it is essential to know the quantities and hydrocarbon productivity of the different kerogen types within the total kerogen, which is available from optical kerogen analysis. Geochemical kerogen

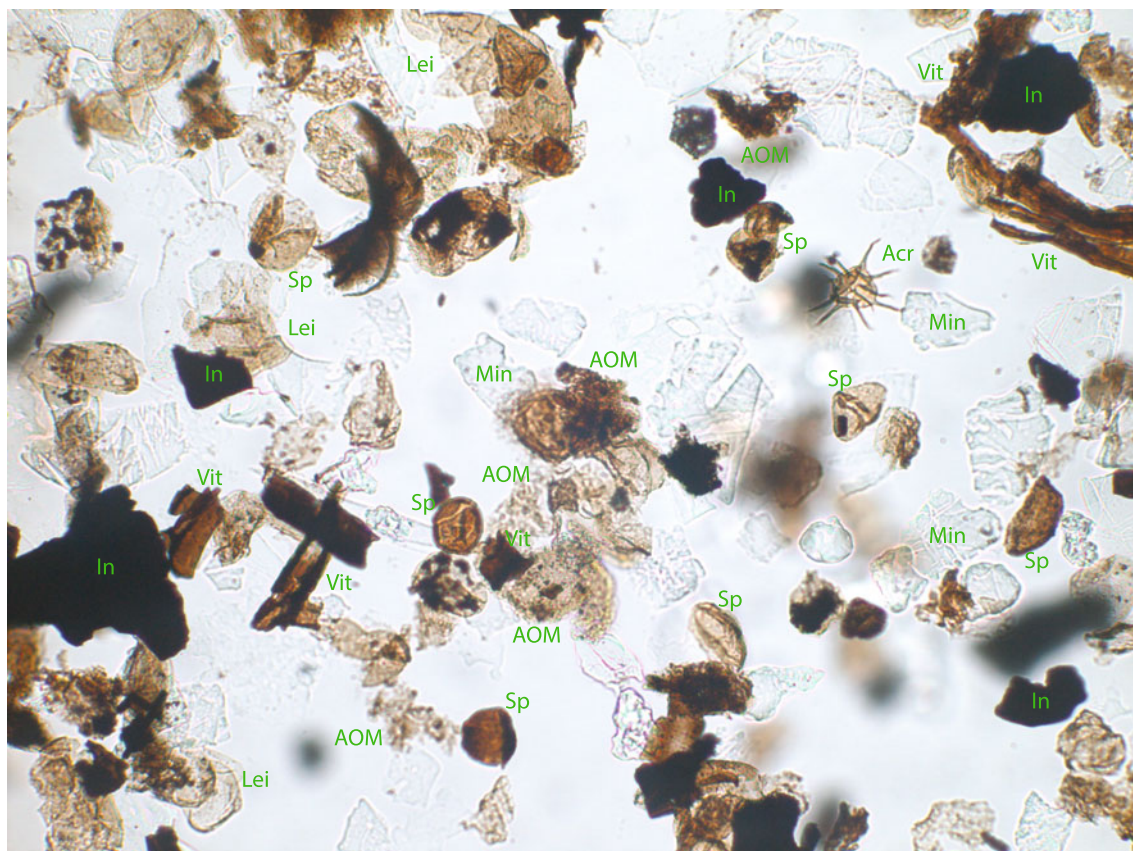


**Fig. 3** Microscope image of a slide of isolated kerogen showing the different organic matter components and some residual minerals (Sp: spores, Acr: acritarchs, Lei: leiospheres, AOM: amorphous organic matter, Vit: vitrinite, In: inertinite, Min: minerals)

analysis is unable to identify this mixture of different kerogen types within the total kerogen. Based on optical kerogen analysis the mixture of different organic matter within the total kerogen can be deciphered and the proportions of the different kerogen types and consequently the percentage of all four standard kerogen types are quantified for each sample.

Kerogen is isolated from the rock, concentrated on a slide and directly studied under the microscope, using well-established techniques employed in palynology and palynofacies analysis. Kerogen composition is analyzed by quantification of the different groups of organic matter mixed in the total kerogen similar to palynofacies analysis. In palynofacies analysis, different groups of organic matter are defined, according to the biological affinities of the organic components. In contrast to palynofacies analysis, optical kerogen analysis is based on volumetric quantification. Afterwards the proportions of the different palynological groups are combined into four supergroups, corresponding to the four standard kerogen types (Fig. 4). This transformation is the centerpiece of optical kerogen analysis. The link between palynological groups and kerogen types is based on

many publications, starting in the early 1970's (Bujak et al., 1977; Burgess, 1974; Correia, 1971). A comprehensive compilation is given by Tyson (1995).

Type I kerogen refers to hydrogen-rich organic matter, mainly lipids. It includes most of the phytoplankton group like prasinophytes and a wide range of planktonic algae, but also acritarchs in contrast to previous papers (compilation in Tyson, 1995). Acritarchs and prasinophytes are typical marine components, while other planktonic algae are typical from restricted marine to terrestrial (lacustrine) settings. Also, AOM *sensu strictu* is included, which is strongly degraded structureless organic matter of algal origin. All other strongly degraded organic matter, often generally referred to as AOM, is not included.

Type II kerogen has less hydrogen and is a mixture of lipids, aliphates and few aromates. It is particularly frequent in many petroleum systems and is usually related to marine sediments. Therefore, it is commonly interpreted as made of marine organic matter. But most of the organic matter referred to type II kerogen is of terrestrial origin: pollen, spores, cuticles, leaves and other lipid and wax-rich plant debris and herbaceous plants. The only marine component is

Environment	Palynological Groups		Maceral Groups		Kerogen types Tissot & Welte 1984	Hydrocarbon potential
AQUATIC MARINE	Phytoplankton	AOM (degraded algae)	Liptinite	Alginite	I	Highly Oil-prone
		Planctonic Algae				
		Prasinophytes				
		Leiospheres				
		Acritarchs				
		Dinocysts				
TERRESTRIAL	Sporomorphs	Spores	Vitrinite	Sporinite	II	Oil-prone
		Pollen				
	Phytoclasts	Cutinite*		Vitrinite	Vitrinite	III
		Vitrinite**				
		Inertinite***	Inertinite	Inertinite		
		Fungal debris				
MARINE	Zoomorphs	Chitinozoa	Faunal relics	Faunal relics	IV	Barren
		Graptolites				
		Forram Linings				
		Scolecodonts				
	Zooclasts					

\* Cuticles, epidermal tissues, herbaceous plants

\*\* Cortex & woody plant debris

\*\*\* Opaque phytoclasts

**Fig. 4** Organic matter classification scheme used in optical analysis, showing the transformation from palynological groups to kerogen types and primary generated hydrocarbons

dinoflagellate cysts (dinocysts). It also includes strongly degraded almost structureless AOM-like material originated from the degradation of aforementioned organisms.

Type III kerogen has low hydrogen content and is made of mostly humic organic matter. It includes carbohydrates (cellulose), lignin (tannin) and carboxylic acids. It is of terrestrial origin, derived from fibrous and woody plant debris (vitrinite) of mainly higher land plants, but also structureless colloidal humic organic matter. It also includes strongly degraded almost structureless AOM-like plant debris, often referred to as AOM.

Type IV kerogen has very low hydrogen content and includes highly carbonized humic organic matter. It is seen as residual kerogen by Tissot and Welte (1984) made of black opaque organic matter (inertinite), mainly oxidized woody plant debris, and has no potential for oil and gas. It is derived from microbial degradation during the rotting of the plants, but also from coalification by wildfires (charcoal) or long-term burial heating (coal). Inertinite also can be derived from all other groups of organic matter by carbonization during high thermal overprint. Beside inertinite, most chitinous organic components (chitinozoa, graptolites, scolecodonts) are included in type IV kerogen as well as most fungal remains (Tyson, 1995).

After the quantification of the palynologically defined organic matter groups, the groups are assigned to the four kerogen types (Fig. 4). The percentages of the groups are summed up, giving the total percentage for each of the four kerogen types in the total kerogen of each sample. In palynofacies and organic petrology usually particles are counted, but differences in size—and therefore volume—between the different types of organic matter are not considered. This works well for paleoenvironment analysis, but is a problem for the analysis of the hydrocarbon generating potential. For the analysis of the hydrocarbon generating potential of source rocks, the total volume of all four kerogen types is important, requiring volumetric quantification of the different kerogen types. This strongly limits the use of palynofacies and organic petrology derived kerogen composition data for optical kerogen analysis. If only data of percentages of particles are available, a new count has to be done for volumetric quantification used in optical kerogen analysis.

A simple scheme for presentation of kerogen composition data was introduced by Dow and O'Connor (1982). It plots oil-prone organic matter (AOM + Exinite) versus gas-prone organic matter (vitrinite) versus barren organic matter (inertinite) (Fig. 5a). In this plot, kerogen composition is directly linked to the primary generated hydrocarbons. It is

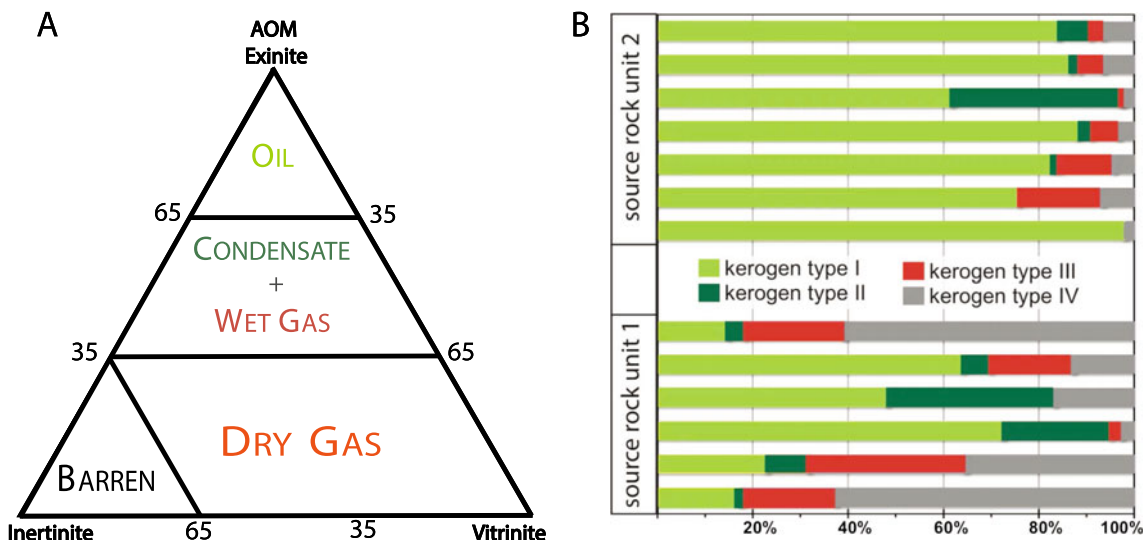


**Fig. 5** Presentation of results of optical analysis of kerogen composition. **a** Ternary plot of oil-prone versus gas-prone versus barren organic matter and generated products (Dow & O'Connor, 1982).

commonly used in palynofacies and organic petrology-based kerogen typing until today and works well for a first overview, but it has some limitations. A sample plotted in the dry gas field can yield up to 35% oil-prone material and can produce significant amounts of oil beside the gas. At low maturation, it only produces oil from the oil-prone part of the kerogen and no gas at all, although it plots in the dry gas field. Although plotting clearly in the field of dry gas, the observed generated hydrocarbons are different (oil). The same can happen in all other fields too.

Another way is the presentation of kerogen composition as added percentages of all four kerogen types in bar graph format (Fig. 5b) used in Optical Kerogen Analysis (Jäger, 2013). From this type of presentation, the proportion of each kerogen type can be read out easily, and it is clearly visible that different types of hydrocarbons will be generated from the kerogen according to the actual maturity. It also directly shows the amount of hydrocarbon unproductive organic matter in the kerogen (dead carbon) that has to be eliminated for further evaluation of the hydrocarbon source potential. The total organic carbon (TOC) content, including the proportion of unproductive type IV kerogen, has to be recalculated to the total amount of hydrocarbon productive organic carbon, the *net-TOC*. Deducting the percentage of type IV kerogen from the TOC gives the *net-TOC*. In source rock unit 2 (Fig. 5b), the *net-TOC* is very close to TOC (90–95% of TOC). The basal and uppermost sample in source rock unit 1 shows a clear difference between both. *Net-TOC* of both samples is about 40% of TOC only. The calculation of *net-TOC* significantly improves the evaluation of hydrocarbon potential and the calculation of volumes to be generated from the source rock.

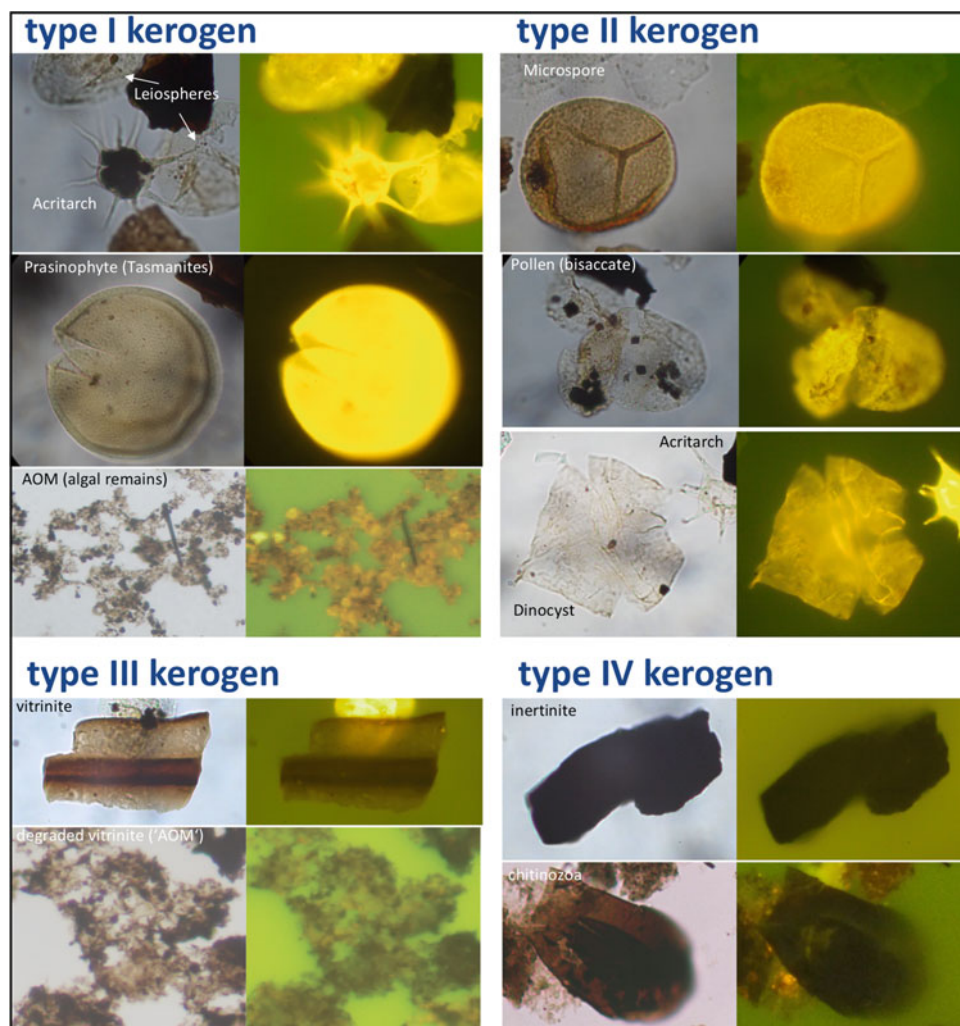
**b** Added percentages of all four kerogen types in bar graph format for better overview of kerogen composition (Jäger, 2013)

Furthermore, optical kerogen analysis provides accurate quantification of the proportion of oil-prone versus gas-prone kerogen in the hydrocarbon productive proportion of the total kerogen. It also quantifies the highly oil-prone type I kerogen versus the oil-prone type II kerogen. Based on the different quantities, the amount of productive kerogen can be further modified, according to the actual maturation of the hydrocarbon play. *Net-TOC<sub>gas</sub>* is the amount of kerogen that can produce hydrocarbons under dry gas conditions. This includes all kerogen that is transformed into gas directly (type III kerogen), but also type I and II kerogen, that produce gas by secondary cracking under gas maturity conditions. At low maturation (oil window), the amount of productive kerogen, the *net-TOC<sub>oil</sub>*, is even more reduced. It only covers the amount of oil-prone type I and II kerogen. Type III kerogen is unproductive in such low maturation. Within the oil window, kerogen productivity can be further differentiated. In the lower to middle oil window, only type I kerogen gets significantly transformed into hydrocarbons, reducing the *net-TOC* to the proportion of type I kerogen. At peak oil and higher maturation, all oil-prone kerogen (type I and II) contributes to hydrocarbon (oil) generation. For the exact calculation of *net-TOC*, not only kerogen composition has to be known, but also kerogen maturation.

#### 4.1 Fluorescence Microscopy

Additional to transmitted light microscopy, fluorescence microscopy (incident blue light) can also provide very useful additional information in optical kerogen analysis. Particularly in AOM-rich samples it supports the identification

**Fig. 6** Different groups of organic matter in transmitted normal light microscopy (left) and incident blue light fluorescence microscopy (right), grouped according to the four kerogen types



of the primary origin of the strongly degraded structureless organic matter. Based on fluorescence colors, four major groups can be distinguished, corresponding to the four standard kerogen types: In low maturation organic matter assigned to hydrogen-rich type I kerogen shows bright yellow colors. Dull yellow to yellow-orange colors are observed in organic matter assigned to type II kerogen. Brownish colors, almost equivalent to the color in normal light, are typical for organic matter assigned to type III kerogen and black colors are observed at organic matter assigned to type IV kerogen (Fig. 6). Fluorescence colors have to be analyzed very carefully with regard to kerogen maturation. With increasing maturation, fluorescence colors of type I and type II kerogen get darker and weaker (orange to reddish brown). At the end of the oil window, fluorescence disappears. Although the intensity of fluorescence colors decreases with increasing organic matter degradation, the fluorescence color doesn't change. Therefore, in AOM-rich samples, dominated by strongly degraded almost structureless organic matter, fluorescence microscopy can

support the identification of the initial origin of the organic matter (Fig. 6).

Often fluorescence of organic matter is taken as indicator for marine organic matter, interpreted as oil-prone kerogen, proposing that terrestrial organic matter, interpreted as gas-prone, shows no fluorescence. In some studies (unpublished internal reports), fluorescent organic matter is counted as highly oil-prone type I kerogen. But in fact, fluorescence of organic matter is more complex regarding the origin of the organic matter, but also the thermal overprint and is not a reliable indicator to distinguish between marine and terrestrial organic matter.

## 5 Kerogen Preservation

Kerogen preservation is the second important parameter of optical kerogen analysis. However, full analysis of kerogen preservation is not included in other methods, although it provides significant information on conditions during

transport, deposition and burial, which are relevant for the evolution and the evaluation of the hydrocarbon generating potential. On the one side, preservation is related to paleoenvironmental conditions during transport and deposition of the organic matter, defined as primary degradation. On the other side, it depends on the thermal degradation of organic matter during burial and consequent hydrocarbon generation, defined as secondary degradation. This secondary degradation indicates the level of hydrocarbon generation in the system. For the analysis of unconventional shale plays, kerogen preservation is of special interest. It indicates the level of micro-porosity within the organic matter, which is directly linked to the storage capacity of the shales, particularly in shale gas plays. Most kerogens show a mix of primary and secondary degradation, and there is no simple scheme to distinguish between both. It needs a detailed classification of organic matter groups and the preservation level within each group to decipher the effect of primary and secondary degradation within the total kerogen. Both have a significant but different impact on the hydrocarbon generating potential and for best practice kerogen analysis, it is significant to quantify the effect of each type separately.

## 5.1 Primary and Secondary Degradation

Primary degradation means the alteration of the primary organic matter during transport and deposition, mainly biologically by microbial activity, but also chemically. Microbial alteration and degradation start from weathering and is mainly active during depositional phases of the transport history. It leads to a loss of hydrogen, nitrogen, sulfur, phosphor, oxygen and others, while carbon is relatively enriched. These changes are similar to the process of carbonization and also lead to the darkening of the organic matter (Fig. 7), beside the degradation of the primary habitus. Primary degradation can also lead to hydrocarbon generation, e.g. biogenic methane. But due to the missing reservoir and open system during transport and deposition, these hydrocarbons disappear. The residual kerogen has

much lower hydrocarbon productivity or might be even completely unproductive. Chemical degradation happens during transport and deposition too. On the one side, chemical degradation is related to strongly oxic environments, where organic matter is oxidized. Oxidation leads to the thinning of the organic matter, and therefore to the 'bleaching' of organic matter (Fig. 7). But strongly anoxic environments with euxinic and reducing conditions can also lead to intense chemical weathering of organic matter. Commonly, this is combined with high microbial activity in these environments, leading to massive degradation of the primary habitus and strong darkening of the organic matter. Hence, strongly euxinic environments also produce massively degraded AOM-like kerogen.

Depending on the different sources, terrestrial to deep marine, of the different groups of organic matter mixed within the total kerogen, primary degradation of the different groups will be different. Most hydrocarbon systems are located in marine shelf systems (Mann et al., 2003) and therefore have mixed kerogens of terrestrial and marine origin. This means different transport histories for the allochthonous terrestrial organic matter and autochthonous marine ones, which lead to different degradation processes for each group. The terrestrial organic matter can be derived from coastal vegetation close to the marine depositional system or further away from the hinterland. Due to the different transport history of the terrestrial organic matter, kerogen preservation can differ even within this group. The longer the transport to the marine depositional system, the more degradational processes are expected. This can also include several cycles of deposition and remobilization (erosion) of the organic matter in certain fluvial environments or lakes. Each cycle will include certain degradational processes. Even within the autochthonous marine organic matter primary degradation will occur. From the sinking of the organic particles through the water column down to the seafloor to the deposition in seafloor sediments, the organic matter is exposed to degradational processes. It includes both: chemical degradation, mainly oxidation, but also reductive conditions mostly at the sea floor and within the upper sediment layers, and biological degradation mainly by microbial activity at the seafloor and within the upper sediment layers. This part of the degradation history is the same for marine and terrestrial organic matter, but terrestrial organic matter has an additional degradation history during the terrestrial transport.

Similar differences of kerogen degradation are also observed in lacustrine systems, although all organic matter is of terrestrial origin. In this case, the terrestrial plant-derived organic matter is the allochthonous part, and the aquatic organic matter of the lacustrine system is the autochthonous part of the kerogen. The degradational processes for both groups are similar to the ones described above.

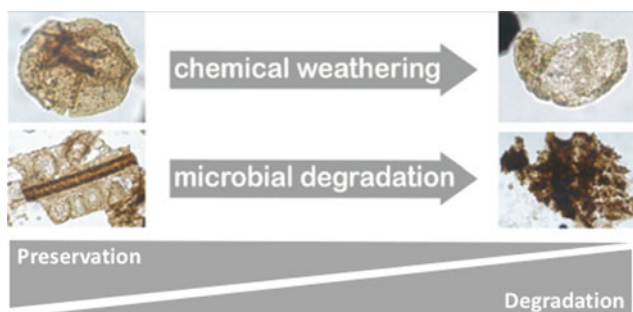


**Fig. 7** Effects of chemical and microbial degradation of organic matter



Intense primary degradation has a negative impact on the hydrocarbon generating potential. Chemical degradation can lead to a massive loss of organic matter decreasing the amount of kerogen available for hydrocarbon generation, while microbial degradation leads to less productive or even unproductive kerogen. Thus, source rocks with high amounts of poorly preserved kerogen related to primary degradation might have a high total content of organic carbon, but a very low amount of hydrocarbon productive organic matter and therefore a very low hydrocarbon generating potential.

Secondary degradation is chemical degradation during diagenesis and burial by the thermal alteration of organic matter and consequent generation of hydrocarbons. Increasing thermal overprint leads to the chemical transformation of primary organic matter into hydrocarbons and chemically and morphologically degraded residual organic matter. The increase of the thermal overprint leads to increasing rates of hydrocarbon generation and consequently increasing degradation of the primary organic matter. Therefore, the level of secondary degradation is directly linked to the level of hydrocarbon generation. Secondary degradation starts successive corresponding to the increasing thermal overprint. It starts with initial degradation of type I kerogen particles in the early oil window. Throughout the oil window, increasing degradation of type I and type II kerogen particles is observed. Type I kerogen particles are fully degraded in the late oil window. In the lower gas window, type II kerogen particles are fully degraded. Degradation of type III kerogen particles starts and continuously increases throughout the gas window.

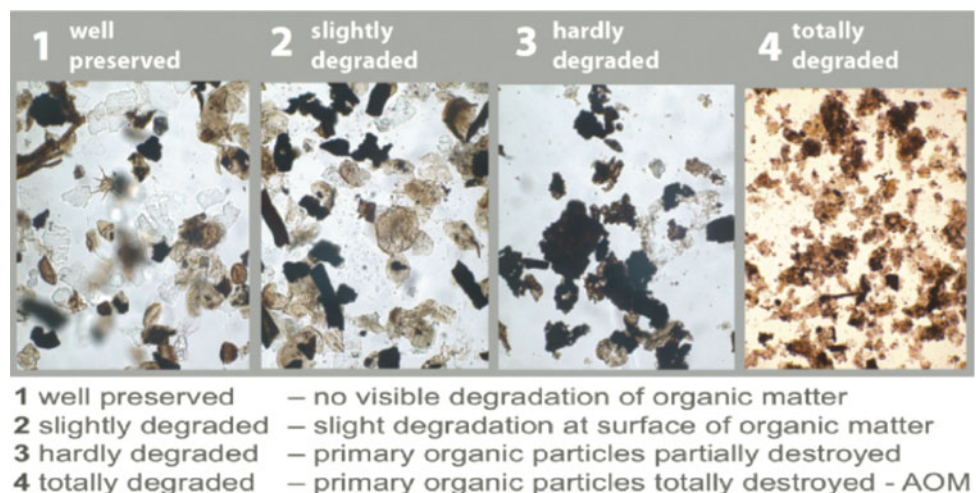
Kerogen preservation is analyzed separately for each group of organic matter, using a 4-stage scheme (Fig. 8). Kerogen preservation level 1, where all groups of organic matter are well preserved, clearly proves, that no hydrocarbons are generated. Kerogen preservation level 2 shows

significant degradation in type I kerogen particles and minor degradation in type II kerogen particles, indicating early oil generation. Increasing degradation of type II kerogen particles indicates increasing oil generation. Strong degradation of type I and II kerogen particles and initial degradation of type III kerogen particles indicate late oil generation and initial gas generation. Increasing gas generation leads to increasing degradation of type III kerogen particles. In highly oil generating systems, the massive generation of oil leads to additional alteration of all organic matter, because of the organic acids produced during the oil generation (Tissot & Welte, 1984), that are degrading organic matter. As secondary degradation is linked to hydrocarbon generation, the intensity of secondary degradation is a good indicator for the level of hydrocarbon generation. If primary and secondary degradation are separated and analysis is based on secondary degradation only, kerogen preservation can be used for the analysis of hydrocarbon generation similar to the Production Index (PI) or Transformation Index in geochemical kerogen analysis.

## 5.2 Organic Matter Porosity Development

Different types of organic matter have primary pores depending on the original biogenic structure. But this biogenic primary porosity gets almost completely lost during sediment compaction after the deposition, which leads to massive compaction of the initial organic matter within the sediment. Therefore, organic matter porosity observed in-situ in mudrocks and shales is post-compaction secondary porosity, related to the decomposition of organic matter during burial thermal alteration. Decomposition of the primary organic matter produces a porous texture. Increasing degradation and consequently increased decomposition leads to highly porous, ‘fluffy’ organic matter particles, commonly

**Fig. 8** Classification of kerogen preservation using four stages from well preserved (1) to totally degraded (4)



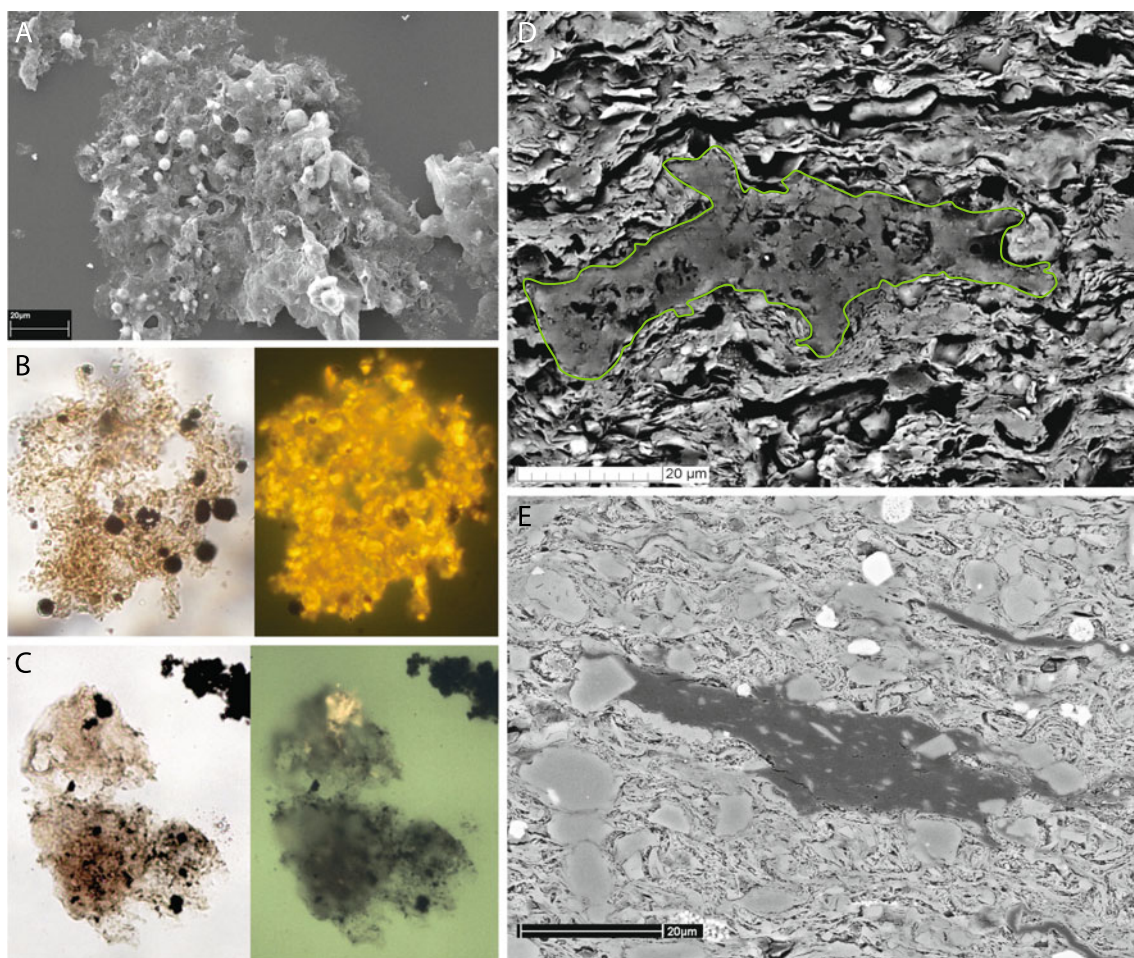


**Fig. 9** AOM isolated from the rock in SEM (a) and normal light and incident blue light fluorescence microscopy (b, c). AOM of algal origin with yellow fluorescence (b) and non-fluorescent AOM (c). SEM analysis of AOM in situ in shales: compacted with high porosity due to

post-compaction secondary degradation (d, surrounded by green line) and compacted with no porosity due to primary degradation and post-depositional compaction (e)

classified as AOM (Fig. 9). The higher the amount of AOM, the higher is the organic matter porosity, mainly micro-porosity. The amount of micro-porosity in organic matter is of great importance in the evaluation of unconventional shale plays, particularly shale gas plays. Shale storage capacity of shale gas plays is strongly linked to organic matter porosity, because adsorption of gas is much higher at organic matter surfaces than on mineral surfaces (Cheng & Huang, 2004). This is confirmed by the good correlation between gas adsorption and TOC observed in several studies (Li et al., 2015; Modica & Lapierre, 2012). But this correlation works only in organic-rich mature shales, but not in organic-rich immature shales (Ross & Bustin, 2009), proving the importance of maturation in this system. Although high percentages of highly porous AOM are recorded from kerogen slides of low mature organic-rich shales, the gas adsorption of these shales is very low, indicating very low in situ micro-porosity. All highly porous

AOM observed in the kerogen of these low mature shales is produced by primary degradation, representing the decomposition of organic matter during transport and deposition. During early diagenesis, the dewatering and massive compaction of the initial sediments leads to massive compaction of the highly porous AOM in the sediment too. It changes the fluffy AOM particles into compact almost non-porous organic matter particles with much smaller surface and therefore low gas adsorption (Fig. 9). In mature shales, the highly porous AOM is at least partially produced by secondary degradation related to maturation and hydrocarbon generation, starting long after sediment compaction. Hence, this porosity is retained open and available for gas adsorption in the shales (Fig. 9). Reliable quantification of productive organic matter micro-porosity available for gas adsorption cannot be done by the analysis of isolated kerogen in slides under the microscope, but has to be analyzed in situ in shale samples by SEM.

Due to the fact that retained organic matter porosity is a result of hydrocarbon generation, the onset of the porosity development corresponds with the beginning of oil generation. As shown in organic-rich mud rocks from the Cretaceous in Wyoming, it starts in the basal oil window increasing strongly until the late oil window. In the gas window, no more significant rise is observed (Modica & Lapierre, 2012). Upper Cretaceous organic lean calcareous mud rocks record the start of organic matter porosity development only in the middle oil window, increasing constantly throughout the oil window, but also in the gas window (Ko et al., 2016). The study of organic-rich mud rocks from the Upper Cretaceous Kimmeridge Clay shows the start of the organic matter porosity as late as the peak oil window (Cavelan et al., 2020). In contrast to these results in other studies, no organic matter porosity development is observed throughout the oil window, but starts as late as the early gas window (Chen & Xiao, 2014; Curtis et al., 2012; Ma et al., 2017). On the other hand, Chen and Xiao (2014) have observed decreasing pore volumes in the gas window. Another study of organic-rich mudstones in the Kimmeridge Clay (North Sea, UK) observes opposite porosity development, leading to the conclusion, that the variation of organic matter pores shows no general correlation to thermal maturity (Fishman et al., 2012).

In fact, organic matter porosity has no fixed starting point at a certain maturation level and no fixed development trend, but it depends on the type of organic matter mixed together in the kerogen. Cavelan et al. (2020) showed that phytoplanktonic rich and phytoplanktonic poor OM show different porosity development. Secondary OM degradation is linked to the chemical transformation of primary organic matter during hydrocarbon generation. It works gradational, corresponding to the increasing thermal overprint, from kerogen type I to IV (see above). Thus, depending on the specific mix of organic matter in the kerogen, porosity development will start at different maturation levels and follow different pathways. In kerogen type I dominated kerogens porosity development will start at the early oil window increasing into the late oil window, with almost no increase in porosity in the gas window. In kerogen type II dominated kerogens porosity development starts in the middle to peak oil window, continuing into late oil to condensate window. In kerogens dominated by type III, porosity development starts in the early gas window increasing throughout the gas window, mainly in the dry gas window. In mixed kerogens of types II and III, porosity development starts in the middle oil window and continues into the gas window, while a mix of kerogen type I and III would lead to porosity development from early to middle/peak oil window with no increase during late oil to early gas, but a second porosity development during dry gas window. So, the strongly heterogenous

porosity developments in the studies above are simply related to the different types of organic matter mixed in the studied kerogens. Knowing the specific organic matter composition from optical kerogen analysis enables the prediction of the specific porosity development of each kerogen.

## 6 Kerogen Maturation

Organic maturation analysis is done on the same organic matter slides as used before. It is based on palynomorph color analysis using normal light microscopy. With increasing maturation, palynomorph colors change from colorless/very light yellow through yellow, orange and brown to black (Fig. 10). Palynomorph colors are referred to well-established color indices: *Spore Color Index* (SCI) and *Thermal Alteration Index* (TAI). Although initially, these color indices were developed for spores, it works also very well for pollen, acritarchs and dinocysts, covering the full range from terrestrial to marine environments. Although all palynomorph groups show similar color trends, there are minor differences. Mostly, pollen grains are slightly lighter than spores due to thinner walls. The same is true for spores and acritarchs/dinocysts. For saccate pollen, it is better to use the central body not the saccus, because it is even thinner and less robust against alteration and damage. Within one study, the color analysis should be based on the same group of palynomorphs in all samples. Otherwise the results have to be adjusted carefully.

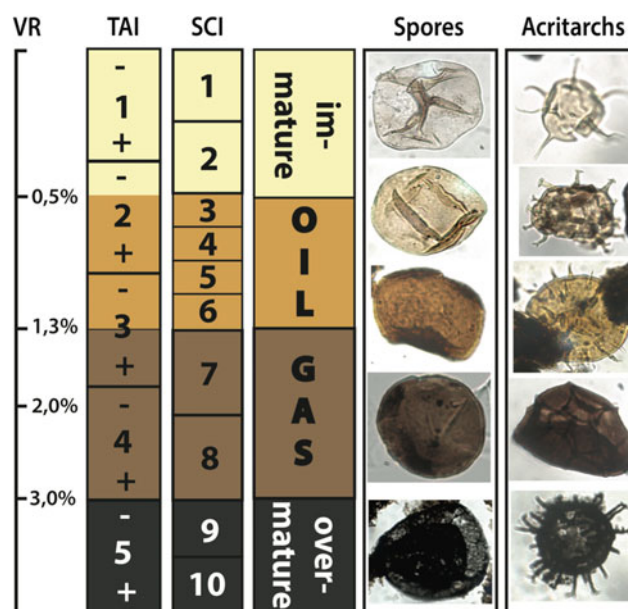


**Fig. 10** Color changes of palynomorphs in transmitted normal light according to increasing maturation in a correlation of SCI and TAI with VR

Palynomorphs used for color analysis have to meet certain requirements: a minimum of degradation, thin plain walls and no or very faint surface ornaments or folds. Complying to these requirements warrants high reliability of the results. Nevertheless, often palynomorph color analysis is strongly doubted, because it is a personal subjective method. To avoid this and make color analysis more objective, digital analysis of palynomorph colors is used.

First approaches are done by Smith (1983) and Marshall (1991), based on complex spectral analysis of light and colors, needing special equipment like a microspectrophotometer. Goodhue and Clayton (2010) developed a simplified approach—the Palynomorph Darkness Index (PDI). It only needs standard equipment commonly available in each lab: standard palynological microscopes, digital cameras and common image analysis software. PDI is based on grayscale, calculated from the red, green and blue (RGB) intensities of light transmitted through palynomorphs using the NTSC and JPEG grayscale conversion. For the calibration, the ‘white’ background of the kerogen slide is used, enabling simple calibration at each microscope in each lab worldwide. Tests with different microscope and camera combinations show excellent correlation, suggesting that the method is largely platform-independent. Analysis of artificially matured palynomorphs indicate good consistency of PDI from low to high maturity (Goodhue & Clayton, 2010). Analysis of PDI and vitrinite reflectance led to a first equation for conversion of both (Clayton et al. 2017). PDI analysis of different palynomorphs show good correlation of PDI with SCI (Spina et al. 2018). Correlation with other geochemical maturation parameters is good in one well and poor in another well (Spina et al. 2018), which might be controlled by differences of the geochemical data quality between both wells. Several studies of PDI analysis combined with vitrinite reflectance by the author (unpublished confidential reports) show good correlation of PDI and VR across a wide range of maturity. Therefore, PDI is a highly reliable method to assess organic maturation in optical kerogen analysis.

Palynomorph color analysis provides a fast first evaluation of the general maturation level. This is important for the analysis of the paleo-thermal history and the identification of the type of hydrocarbons that could be generated under these conditions. It improves the identification of recycled and altered just as caved or reworked palynomorphs, which have to be excluded from the material used for maturation analysis. For accurate and reliable organic maturation analysis, palynomorph color analysis has to be restricted to well preserved in situ palynomorphs only.

The determination of the maturity of the kerogen is also an important parameter for the distinction of primary and secondary degradation. Depending on the specific geochemistry, different types of organic matter are transformed

at different temperatures. Organic matter equivalent to kerogen type I and II get thermally altered and transformed within the oil window, while organic matter equivalent to kerogen type III is thermally degraded in the gas window. This means highly degraded plant debris (vitrinite, kerogen type III) in an oil-mature kerogen is completely related to primary degradation, because it would need higher temperatures (gas window) for thermally controlled secondary degradation. A kerogen composed of highly degraded marine and terrestrial oil-prone organic matter and well-preserved plant debris at peak oil maturity indicates that all degradation of the oil-prone organic matter is related to thermal secondary degradation. Because one part of the terrestrial organic matter (plant debris) is well preserved, it is assumed that the other part of the terrestrial organic matter (oil-prone terrestrial OM) was also deposited well preserved and got degraded by thermally controlled secondary degradation. This means that all oil-prone organic matter, marine and terrestrial fully contributes to the generation of hydrocarbons. Contrary a kerogen composed of highly degraded marine and terrestrial oil-prone organic matter and highly degraded plant debris at peak oil maturity indicates that a certain amount of degradation of the terrestrial oil-prone organic matter is related to primary degradation and not secondary degradation. The high degradation of the terrestrial gas-prone organic matter (plant debris) is not related to secondary degradation in the oil window, but to primary degradation during transport and deposition. Therefore, also a certain part of degradation of the terrestrial oil-prone organic matter is related to primary degradation. In this case, the terrestrial oil-prone organic matter has a lower hydrocarbon generating potential due to the decomposition and transformation of OM during primary degradation.

---

## 7 Data Integration and Interpretation

The approach of *Optical Kerogen Analysis* provides important information on the type and quality of the kerogen and its hydrocarbon generating potential. The integrated analysis of kerogen composition, preservation and maturation in *Optical Kerogen Analysis* goes much further than previous palynofacies and organic petrology-based kerogen studies, that provided parts of these informations only. The accurate calculation of the *net-TOC*, essential for the precise evaluation of the hydrocarbon resource potential, needs the data from kerogen composition and the maturation of the system. But it also needs the information of kerogen preservation, to check if parts of the kerogen are already degraded by primary degradation. This would lead to significant pre-depositional loss of hydrocarbon productivity that has to be included in the evaluation of the actual hydrocarbon generating potential. The integration of the

results from all three analyses directly reveals the detailed kerogen development, from transport to burial. This can significantly change the interpretation of the source rock and its hydrocarbon generating potential. It also can lead to very different interpretations of source rocks that look very similar in lithology and general geochemistry.

Optical Kerogen Analysis was applied to two oil shale units overlying each other up section within a carbonate shelf system, separated by are almost 110 m of limestones, marlstones and few claystones (Fig. 11). The lower oil shale is developed at the beginning of the transgression and is locally restricted to deep shelf settings. The upper oil shale is developed during maximum transgression and is widespread distributed across the shelf and can even be followed into other basins. Both are 30–35 m in thickness, dominated by dark-gray to black calcareous marlstones and less dark-gray to black claystones. They are rich in pyrite and pyritized fossils which are common in both. Several bioturbation levels are recorded from the lower unit, but are extremely rare in the upper unit. TOC is very similar. It is 5–12%

without bioturbation, but <1.5% within bioturbation levels. Despite all these similarities Rock Eval Pyrolysis showed some differences. S1 is generally higher in the upper oil shale, having a PI of 0.08–0.48, while the lower oil shale has a PI of 0.07–0.19. Also HI shows some differences, ranging from 200–600 in the upper oil shale and from 160–380 in the lower.

Microscopic analysis of isolated kerogen in normal transmitted light showed that most samples from both oil shale units are clearly dominated by strongly altered almost structureless organic matter, commonly assigned to AOM. It is mostly medium to dark brown, rarely gray to black colored, showing some variation within both units, but no clear difference. The rest of the organic matter components seems to be very similar in both units too. The proportion of barren type IV kerogen is low in both units (10–15%), showing a very high *net-TOC* of about 85–90% of the TOC in both oil shales (Fig. 11). But fluorescence colors using incident blue light microscopy revealed major differences. In the upper oil shale unit, most AOM shows light to dark

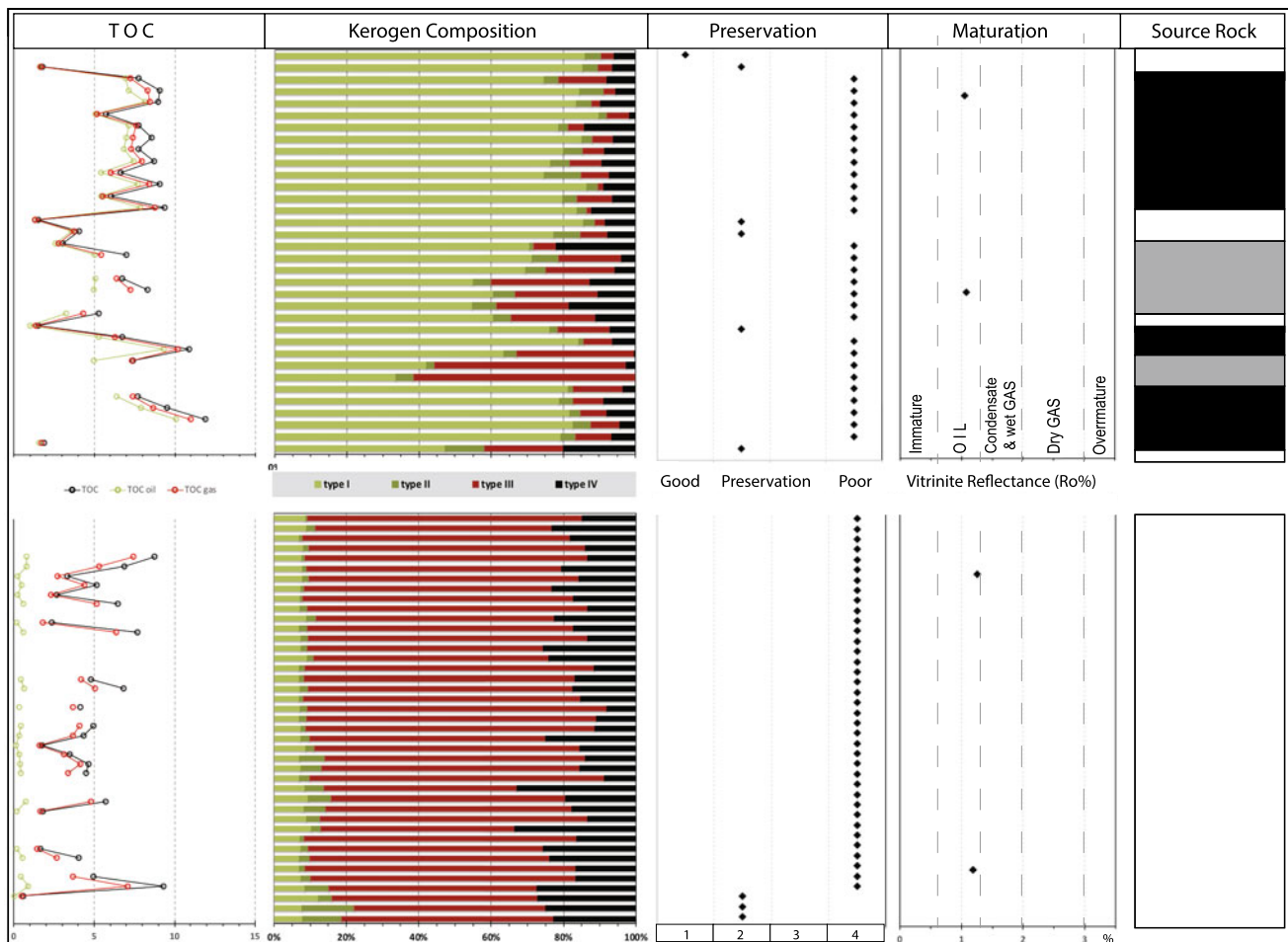


**Fig. 11** Full dataset of optical kerogen analysis of two overlying oil shale units for integrated interpretation of the hydrocarbon generating potential (black: highly oil-prone source rock, gray: oil-prone source rock, white: very low oil to no source rock)

yellow fluorescence, while in the lower unit, most AOM shows no fluorescence. If fluorescence is observed in the kerogen of the lower oil shale, it is from altered algal remains underneath the AOM-like material, which are difficult to recognize in normal light. The color of the AOM-like material doesn't change from normal transmitted light to incident blue light microscopy. This shows the major difference between kerogen of the upper and the lower oil shale. In the upper oil shale unit, most of the AOM is strongly altered algal origin, corresponding to highly oil-prone type I kerogen, making 70–85% of the total kerogen. In contrast, most of the AOM-like material in the samples from the lower oil shale is made of strongly altered terrestrial woody plant debris (vitrinite), corresponding to gas-prone type III kerogen. Preservation is poor (stage 4) in both units, which is an indicator for high kerogen transformation and hydrocarbon generation. Analysis of paly-nomorph colors indicates peak oil maturity, supported by vitrinite reflectance ( $R_o = 0.8–1.0\%$ ). According to the maturation, the degradation of the AOM in the upper oil shale is interpreted as secondary degradation of algal derived highly oil-prone type I kerogen. The strong decomposition—most of the type I kerogen is strongly transformed—indicates a high transformation ratio and high oil generation from the upper oil shale unit. The strong decomposition of most of the type III kerogen (primary vitrinite) in the lower oil shale is not related to secondary degradation during burial and hydrocarbon generation. It is no indicator for hydrocarbon generation, but shows strong primary degradation with a massive loss of hydrocarbon productivity. Even in higher maturation (dry gas window) the lower oil shale unit would not generate high amounts of gas, because most of the gas generating potential of the dominating type III kerogen got lost by the primary degradation. Gas generation would be almost completely related to the secondary cracking of the little amounts of primary generated oil in this interval. Therefore, in the lower oil shale unit, the  $net-TOC_{gas}$  is almost the same as the  $net-TOC_{oil}$ , while in the upper unit, the  $net-TOC_{gas}$  is commonly 5–10% higher than  $net-TOC_{oil}$ , except for some samples, where  $net-TOC_{oil}$  is low (<60%) and  $net-TOC_{gas}$  is 30–60% higher.

Based on the integration of all optical kerogen data, intervals of good hydrocarbon generating potential—*net source units*—can be defined for improved resource evaluation by enhanced volumetric calculations. About 60% of the upper oil shale unit is highly oil producing source rock (type I kerogen >70%,  $net-TOC_{oil}$  >75–80%). About 30% are good oil producing source rock (type I kerogen 50–60%,  $net-TOC_{oil}$  50–65%) and about 10% are poorly to no oil producing source rock. This is mainly related to low TOC. Only 6% of the unit are highly gas producing source rocks

(>65% type III kerogen). In the lower oil shale, the entire unit shows poor to no oil producing source rock. The  $net-TOC_{oil}$  is <1% in all samples, despite partially very high values of TOC. Due to the massive primary degradation of type III kerogen, no gas generating source rock is developed in the lower unit too.

Optical kerogen analysis has completely changed the hydrocarbon generating potential of the lower oil shale, showing a huge difference to the upper oil shale, although both seem to be similar source rock units based on lithology and geochemistry. Geochemical analysis shows partially higher oil potential and slightly higher TOC values in the upper oil shale, but both intervals seem to have a moderate to good hydrocarbon, particularly oil, generating potential. This seems to be supported by optical kerogen analysis, showing that kerogen is dominated by strongly degraded (AOM-like) organic matter in most samples. But in fluorescence microscopy, a huge difference is observed. The degraded organic matter in the upper oil shale shows fluorescence, indicating real AOM of algal origin, which is highly oil-prone type I kerogen. The strongly degraded organic matter in the lower oil shale shows mostly no fluorescence, indicating strongly degraded terrestrial derived plant material, which is gas-prone type III kerogen. Due to peak oil maturity in both units, the poor kerogen preservation in the upper oil shale is produced by secondary degradation, indicating significant kerogen transformation and oil generation from this oil shale. In opposite, the poorly preserved kerogen in the lower oil shale is a result of intense primary degradation, indicating a substantial loss of hydrocarbon generating potential of the kerogen during transport and deposition. Net-source units are identified by the integration of all data. 60% of the upper oil shale are highly oil-prone and 30% are oil-prone source rocks. The lower oil shale has changed from a previously assumed moderate oil to gas generating potential to a completely unproductive play, because of the substantial loss of hydrocarbon generating potential by intense primary kerogen degradation.

The integrated component specific analysis of the full kerogen mixture by *Optical Kerogen Analysis* improves the understanding and interpretation of the composition, preservation and thermal history of kerogen and its hydrocarbon generating potential. It is a highly sensitive tool for the identification of changes of the hydrocarbon source rock potential within source rock units, reducing the risk of failure in source rock evaluation. *Optical Kerogen Analysis* is an alternative workflow to classical geochemical kerogen analysis, providing additional information on kerogen quality and development and its results can get directly implemented into organofacies-based hydrocarbon system modeling.

## References

- Bujak, J. P., Barss, M. S., & Williams, G. L. (1977). Offshore east Canada's organic type and color and hydrocarbon potential. *The Oil and Gas Journal*, 75, 198–201.
- Burgess, J. D. (1974). *Microscopic examination of kerogen (dispersed organic matter) in petroleum exploration* (pp. 19–30). Geological Society of America, Special Paper 153.
- Cavelan, A., Boussafir, M., Mathieu, N., & Laggoun-Défarge, F. (2020). Impact of thermal maturity on the concomitant evolution of the ultrafine structure and porosity of marine mudstones organic matter; contributions of electronic imaging and new spectroscopic investigations. *The International Journal of Coal Geology*, 231, 103622.
- Chen, J., & Xiao, X. (2014). Evolution of nanoporosity in organic-rich shales during thermal maturation. *Fuel*, 129, 173–181.
- Cheng, A. L., & Huang, W. L. (2004). Selective adsorption of hydrocarbon gases on clays and organic matter. *Organic Geochemistry*, 35, 413–423.
- Combaz, A. (1964). Les palynofaciès. *Revue de Micropaléontologie*, 7, 205–218.
- Combaz, A. (1980). Les kéroènes vus au microscope. In B. Durand (Ed.), *Kerogen* (pp. 55–111). Editions Technip.
- Correia, M. (1971). Diagenesis of sporopollenin and other comparable organic substances: Application to hydrocarbon research. In J. Brooks, P. Grant, M. D. Muir, G. Shaw, & P. Van Gijzel (Eds.), *Sporopollenin* (pp. 569–620). Academic Press.
- Curtis, M. E., Cardott, B. J., Sondergeld, C. H., & Rai, C. S. (2012). Development of organic porosity in the Woodford Shale with increasing thermal maturity. *The International Journal of Coal Geology*, 103, 26–31.
- Clayton, G., Goodhue, R., Abdelbagi, S.T. & Vecoli, M. (2017). Correlation of Palynomorph Darkness Index and vitrinite reflectance in a submature Carboniferous well section in northern Saudi Arabia. *Revue de Micropaléontologie*, 60, 411–416.
- Dow, W. G., & O'Connor, D. I. (1982). Kerogen maturity and type by reflected light microscopy applied to petroleum exploration. In F. L. Staplin, W. G. Dow, C. W. O. Milner, C. W. D. Milner, D. I. O'Connor, S. A. J. Pocock, P. van Gijzel, D. H. Welte, M. A. Yukler (Eds.), *How to assess maturation and Paleotemperatures*. SEPM Short Course 7, 133–157.
- Durand, B., Espitalié, J., Nicaise, G., & Combaz, A. (1972). Étude de la matière organique insoluble (kéroène) des argiles du Toarcien du Bassin de Paris. I - Étude par les procédés optiques, analyse élémentaire, étude en microscopie et diffraction électroniques. *Oil & Gas Science and Technology—Revue d'IFP*, 27, 865–884.
- Durand, B. (Ed.). (1980). *Kerogen, insoluble organic matter from sedimentary rocks*. Éditions Technip.
- Fishman, N. S., Hackley, P. C., Lowers, H. A., Hill, R. J., Egenhoff, S. O., Eberl, D. D., & Blum, A. E. (2012). The nature of porosity in organic-rich mudstones of the Upper Jurassic Kimmeridge Clay Formation, North Sea, offshore United Kingdom. *The International Journal of Coal Geology*, 103, 32–50.
- Forsman, J. P., & Hunt, J. M. (1958). Insoluble organic matter (kerogen) in sedimentary rocks. *Geochimica et Cosmochimica Acta*, 15, 170–182.
- Goodhue, R. & Clayton, G. (2010). Palynomorph Darkness Index (PDI) - a new technique for assessing thermal maturity. *Palynology*, 34, 147–156.
- Jäger, H. (2013). Optical Kerogen analysis—A new workflow in unconventional shale play analysis. In *Unconventional Resources Technology Conference*, Denver. <https://doi.org/10.1190/urtec2013-091>
- Ko, L. T., Loucks, R. G., Zhang, T., Ruppel, S. C., & Shao, D. (2016). Pore and pore network evolution of Upper Cretaceous Boquillas (Eagle Ford-equivalent) mudrocks: Results from gold-tube experiments. *AAPG Bulletin*, 101, 1693–1772.
- Li, J., Yan, X., Wang, W., Zhang, Y., Yin, J., Lu, S., Chen, F., Meng, Y., Zhang, X., Chen, X., Yan, Y., & Zhu, J. (2015). Key factors controlling the gas adsorption capacity of shale: A study based on parallel experiments. *Applied Geochemistry*, 58, 88–96.
- Ma, L., Taylor, K. G., Dowey, P. J., Courtois, L., Gholinia, A., & Lee, P. D. (2017). Multi-scale 3D characterisation of porosity and organic matter in shales with variable TOC content and thermal maturity: Examples from the Lublin and Baltic Basins, Poland and Lithuania. *The International Journal of Coal Geology*, 180, 100–112.
- Mann, P., Gahagan, L., & Gordon, M. B. (2003). Tectonic setting of the world's giant oil and gas fields. In M. T. Halbouty (Ed.), *Giant oil and gas fields of the decade 1990–1999* (pp. 21–36). AAPG Memoir 47.
- Marshall J.E.A. (1991). Quantitative spore colour. *Journal of the Geological Society*, 148, 223–233.
- Modica, C. J., & Lapierre, S. G. (2012). Estimation of kerogen porosity in source rocks as a function of thermal transformation: Example from the Mowry shale in the powder River Basin of Wyoming. *AAPG Bulletin*, 96, 87–108.
- North, F. K. (1985). *Petroleum geology*. Allen & Unwin Inc.
- Raynaud J. F., & Robert P. (1976). Les methodes d'étude optique de la matiere organique. *Bulletin du Centre de recherche de Pau-SNPA*, 10, 109–127.
- Ross, D. J. K., & Bustin, R. M. (2009). The importance of shale composition and pore structure upon gas storage potential of shale gas reservoirs. *Marine and Petroleum Geology*, 26, 916–927.
- Smith P.M.R. (1983). Spectral Correlation of Spore Coloration Standards. *Geological Society, London, Special Publications*, 12, 289–294.
- Spina, A., Vecoli, M., Riboulleau, A., Clayton, G., Cirilli, S., Di Michele, A., Marcogiuseppe, A., Rettori, R., Sassi, P., Servais, T. & Riquier, L. (2018). Application of Palynomorph Darkness Index (PDI) to assess the thermal maturity of palynomorphs: A case study from North Africa. *International Journal of Coal Geology*, 188, 64–78.
- Stach, E., Mackowsky, M. Th., Teichmüller, M., Taylor, G. H., Chandra, D., & Teichmüller, R. (Eds.). (1982). *Coal petrology*. Gebrueder Borntraeger.
- Taylor, G. H., Teichmuller, M., Davis, A., Diessel, C. F. K., Littke, R., & Robert, P. (1998). *Organic petrology* (p. 704). Gebrüder Borntraeger.
- Teichmüller, M. (1986). Organic petrology of source rocks, history and state of the art. *Organic Geochemistry*, 10, 581–599.
- Tissot, B. P., & Welte, D. H. (1984). *Petroleum formation and occurrence* (2nd ed.). Springer.
- Tissot, B., Durand, B., Espitalie, J., & Combaz, A. (1974). Influence of nature and diagenesis of organic matter in formation of petroleum. *AAPG Bulletin*, 58, 499–506.
- Tissot, B., Deroo, G., & Espitalié, J. (1975). Étude comparée de l' époque de formation et d' expulsion du pétrole dans diverses provinces géologiques. In *Proceedings of the 9th World Petroleum Congress*, Applied Science Publishers, 2, 159–169.
- Tyson, R. (1995). *Sedimentary organic matter: Organic facies and palynofacies*. Chapman & Hall.
- van Krevelen, D. W. (1961). *Coal: Typology—Chemistry—Physics—Constitution*. Elsevier.



# Effective Source-Rock Evaluation Strategies for the Identification of Profitable Plays in the Permian Basin, USA

Mohamed K. Zobia and David Entzminger

## Abstract

Accurate determination of organic matter characteristics in hydrocarbon source rocks is of key importance in evaluating petroleum systems. Organic geochemical analysis is a powerful tool that can provide a wide range of crucial information to exploration geologists. Such information includes kerogen type, thermal maturity, transformation ratio, and generative petroleum potential. The scientific literature is full of case studies that provide evidence for the accuracy of organic geochemistry data and how they were successfully utilized to find economic discoveries. Nonetheless, like other exploration tools, organic geochemical data need to be strategically employed to avoid erroneous interpretations and obtain maximum benefit. Three examples of useful techniques for the identification of high-graded drilling targets within organic-rich unconventional and conventional reservoirs in the Permian Basin are presented from the Woodford Formation and the lower Permian Wolfcamp shales. For the unconventional examples, these techniques include mapping total organic carbon (TOC), vitrinite reflectance equivalents (VRe), transformation ratio (TR), and  $T_{\max}$  data to locate areas of high organic content, optimal thermal maturity, and favorable gas/oil ratios (GOR). Additionally, the use of pressure-depth plots to establish fluid contacts and migration pathways away from the “petroleum kitchen” is demonstrated for a conventional play.

## Keywords

Permian Basin • Woodford • Wolfcamp • Thermal maturity • TOC • Vitrinite reflectance • Pyrolysis

M. K. Zobia (✉)

Department of Geosciences, The University of Texas Permian Basin, Odessa, TX 79762, USA  
e-mail: [zobaa\\_m@utpb.edu](mailto:zobaa_m@utpb.edu)

D. Entzminger

Entzminger Geoscience Services, LLC, Midland, TX 79707, USA

## 1 Introduction

The four basic physical components of conventional hydrocarbon systems are the source rock, reservoir-rock, hydrocarbon trap, and a cap-rock (seal). In the case of unconventional systems, these traditional components are often combined in a single rock unit. Although all petroleum system components are nominally of equal importance, one can argue that the presence of organic-rich source-rock horizons is the essential foundation of any petroleum system. Therefore, it is of prime importance for petroleum geologists to carefully study and evaluate all plausible source-rock units in order to accurately locate sweet spots and make sound, lowest-risk drilling decisions. This evaluation has two components that often complement each other, analytical data and results of maturity modeling. Among the powerful analytical methods to characterize source-rock richness and generation potential are programmed pyrolysis, which generates a suite of key organic geochemical parameters such as total organic carbon (TOC), S1 (hydrocarbon shows), S2 (hydrocarbon yield from kerogen cracking), genetic potential, production index (PI), hydrogen index (HI), oxygen index (OI), and  $T_{\max}$  (thermal maturity). For explanation of the different pyrolysis parameters, the reader may refer to Dembicki (2017), Peters and Cassa (1994), and Tissot and Welte (1984).

Interpreting pyrolysis data requires experience to avoid making costly mistakes. It also requires sufficient knowledge about the geological, burial, and thermal history of the formation under investigation. Unfortunately, all too often geology, engineering, production, and geochemistry are not adequately integrated in the development of drilling locations for hydrocarbon plays. Therefore, the purpose of this paper is to show three examples of strategies using commonly obtainable datasets to find the best drilling targets within the Upper Devonian Woodford Formation and the lower Permian Wolfcamp shales in the Permian Basin.



## 2 The Permian Basin

The Permian Basin (Fig. 1) is one of the most-prolific hydrocarbon-producing basins in the USA, and perhaps the largest unconventional petroleum plays worldwide. According to the U.S. Energy Information Administration (EIA), as of September 2018, the Permian Basin has produced more than 33.4 billion barrels of oil and about 118 trillion cubic feet of natural gas over a period of about 100 years (EIA, 2018a). During 2017, the Permian Basin accounted for 20% of the total crude oil and about 9% of the total dry natural gas production in the USA, with estimated remaining proven reserves, as of 2016, to exceed 5 billion barrels of oil and 19.1 trillion cubic feet of natural gas (EIA, 2018a, 2018b).

The Upper Devonian Woodford is an organic-rich formation composed predominantly of black shales with large amounts of preserved marine organic matter (Comer, 1991). It extends over much of the Permian Basin and acts as both source- and unconventional reservoir-rock, the latter especially when it is highly fractured (Comer, 1991). The Woodford Formation has the highest TOC content (5–8 wt %) in portions of Crane, Ector, Pecos, Reeves, Ward, and Winkler counties (Fig. 2). It has also been the subject of several studies due to its favorable lithology, TOC, reservoir properties, thermal maturity, and saturation (Bammidi et al., 2011; Drake et al., 2018; Hemmesch et al., 2014). Organic geochemical data from additional examples of potential economic discoveries within the Woodford Formation in the Delaware Basin are discussed herein.

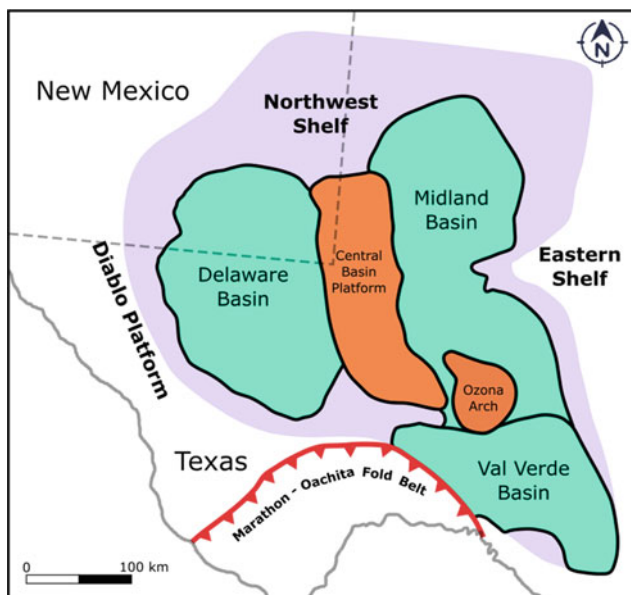


**Fig. 1** Location map of the Permian Basin showing its subbasins along with the main tectonic features. From MacRitchie and Zobaa (2019)

The Pennsylvanian–lower Permian Wolfcamp shales contain organic-rich horizons that exist throughout the greater Permian Basin area, including the Delaware Basin, Central Basin Platform, and the Midland Basin. Petroleum companies in the Permian Basin commonly subdivide the Wolfcamp shales into four operational units known from top to bottom as the Wolfcamp A, B, C, and D (Baumgardner et al., 2016). The Wolfcamp A and B units are the most drilled targets in the Permian Basin (EIA, 2018a). In 2016, the U.S. Geological Survey calculated technically recoverable mean resources of 20 billion barrels of oil and 16 trillion cubic feet of gas in the Wolfcamp shales in the Midland Basin (Gaswirth et al., 2016). The Wolfcamp shales have recently been under extensive scrutiny owing to their optimal geological, geochemical, and maturity characteristics for petroleum production (e.g., Baumgardner et al., 2016; Gaswirth et al., 2016; Hackley et al., 2020; Kvale and Rahman, 2016; MacRitchie & Zobaa, 2019). Additional discussion of potential commercial target areas within the lower Permian Wolfcamp shales in the Delaware Basin is introduced herein based on production and organic geochemical data.

## 3 Methodology

Programed pyrolysis data are obtained through the thermal decomposition of organic matter in an inert atmosphere. As described by Dembicki (2017), the process involves placing about 50–100 mg of ground rock samples in the pyrolysis oven and heating them to 550 °C in the presence of helium. Evolved volatile organic materials as well as CO<sub>2</sub> are measured and recorded as S1, S2, and S3 peaks on a pyrogram. The S1 peak represents the amount of free hydrocarbons that can be volatilized out of the rock without cracking the kerogen, while the S2 peak represents the existing potential of a rock to generate hydrocarbons (Peters & Cassa, 1994).

The S3 peak indicates the amount of oxygen associated with the kerogen in the sediment (Dembicki, 2017). Other reported parameters include TOC as well as  $T_{\max}$  which is the recorded temperature at maximum S2 generation. Using the aforementioned values, additional critical parameters such VRe can be calculated using Jarvie's (2018) equation:

$$\text{VRe} = 0.0165 \times T_{\max} - 6.51$$

$T_{\max}$  cutoff values used in this paper are after Peters and Cassa (1994). Mapping of TOC,  $T_{\max}$ , VRe, and TR was done manually using an open-source graphic designing software. Regional TOC and VRe data for the Woodford Formation are from Comer (1991) and Entzminger and Miller (2004). VRe and TR data for the Woodford's seven control wells in Loving, Ward, and Winkler counties were obtained with permission from Doug Waples, Sirius Exploration Geochemistry Inc.

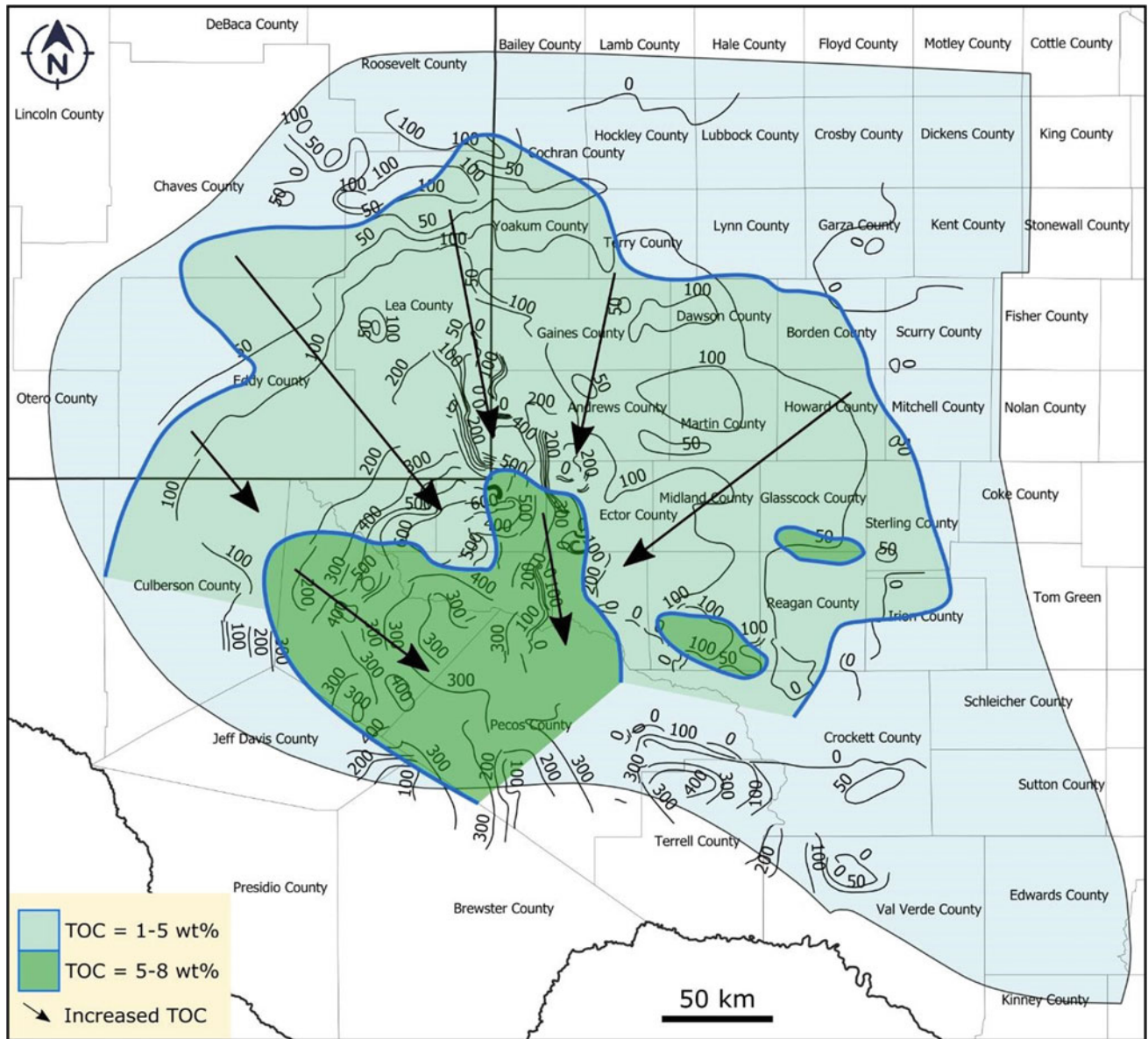


**Fig. 2** Thickness variation map for the Woodford formation within the greater Permian Basin area shows the distribution of TOC content along with the observed trends of increased TOC and formation thickness. Modified from Comer (1991) and Entzminger and Miller (2004)

For many small petroleum companies, datasets and resources are limited, thus finding ways to make the most use of the data available is critical. The three examples presented in this paper show that meaningful interpretations of organic geochemical data can lead to high-grade exploitation targets where minimal datasets are obtainable. But like any dataset, organic geochemical data are best used in integration with all the other available data for a given prospect or play.

## 4 Application of Best Tactics to Source-Rock Evaluation

### 4.1 Mapping VR, VRe, and TR

Vitrinite reflectance (VR) can be measured with reasonable accuracy on many rock samples, but measured VR values are not always reliable, for a variety of reasons. Such reasons

include misidentification of vitrinite-like solid bitumen, sample selection (core, cuttings, outcrop), contamination with particulate drilling additives, organic matter weathering and oxidation, among others (Cardott, 2012; Hackley et al., 2013). To replace or supplement measured VR values, we can calculate VR using standard modeling software, and we can estimate reflectance-equivalent values (VRe) for samples that were analyzed using a number of alternative techniques. Measured VR values in the Permian Basin are of questionable accuracy because of the nature of the Paleozoic organic matter. Thus, it is better in the Permian Basin to augment VR datasets with calculated VRe values from modeling. However, even the best VR and VRe datasets cannot resolve another issue; the increase in VR values with increasing thermal stress (the effects of temperature over geologic time) which is not directly related to hydrocarbon generation. The validity of VR and VRe as proxies for hydrocarbon generation across the broad range of maturities that constitute the hydrocarbon generation window requires local calibration, as shown by Waples and Marzi (1998). Mapping vitrinite reflectance equivalents helps high-grade an exploration area of interest (AOI) by suggesting the most likely areas for the necessary level of hydrocarbon generation to have been achieved. The main problem is that VR is not as accurate a technique as many people believe for mapping maturity and/or product types for similar unconventional plays across basins. Both mean activation energy and transformation ratio (TR) can be used to increase maturity accuracy. Mean activation energy is a measure of hydrocarbon generation which can be calculated from programmed pyrolysis (Waples, 2016; Waples et al., 2010). This parameter will not be discussed further in this paper, although it has been used successfully in the Permian Basin. Instead, we will discuss the use of TR as a direct measurement of hydrocarbon generation in the next section.

VR and VRe values do not directly quantify levels of hydrocarbon generation; they are indicators of thermal stress, and any application to estimating hydrocarbon generation from reflectance values involves calibration with some yardstick of generation, such as TR. Transformation ratio can be obtained from “as-received” samples, but Waples and Tobey (2015) have demonstrated the advantages of working only with extracted samples, especially within the main hydrocarbon generation window. With the original S2 and HI, one can determine the TR. With TOC, VRe, and TR, one can more accurately predict sweet spot areas where the source rock is most likely to be exploitable as an unconventional reservoir.

Mapping only VRe for a source-rock play can provide misleading results. In the mid-2000s, there was great interest in the Woodford unconventional oil play on the Central Basin Platform (CBP). In the same formation, an unconventional gas play in the Delaware Basin was developing

until gas prices collapsed. As oil became more commercially favorable, attention was turned to determining what areas would be most favorable in the same formation for oil. Figure 2 represents the thickness and TOC for the Woodford Formation, one of the richest source rocks in the Permian Basin. The Woodford was deposited in the Tobosa Basin, a precursor to the Permian Basin. Over most of the Tobosa Basin, preserved TOC is greater than 1% (Comer, 1991). The Woodford is thickest and has the highest TOC in Pecos, Reeves, Ward, and Winkler counties of Texas, within the Delaware Basin and CBP. Figure 3 shows the structural complexity and thermal maturity of the Woodford Formation. Throughout much of the southern Delaware Basin, the Woodford is in the gas window. Additionally, the Woodford is either absent or appears to be immature over a significant portion of the CBP, but there does seem to be an area along the western edge of the CBP that is in the oil window. This area is structurally complex, so knowing where to explore is a challenge (Fig. 3).

There have been numerous horizontal Woodford wells drilled in Andrews, Winkler, and Ward counties attempting to establish a commercial play, but without much success to date. This presents a puzzling question: why has a world-class source rock like the Woodford Formation not been more productive on the CBP where it is very thick? It is already established that the Woodford generated much of the oil in many fields on the CBP (Zumberger, 2013). This question can be answered by adding the TR into the equation. Rocks with  $> 0.7$  VRe are considered to be in the main oil window (Peters & Cassa, 1994). This general rule is applicable thus far for conventional plays and was used successfully in the Bakken play where Parshall and Sanish fields were discovered in the Williston Basin. To the contrary, the Woodford Formation in the Delaware Basin has proved to be different. Figure 4 (left) shows seven wells with VRe data that illustrate the areas of high maturity (gas:  $> 1.4$  VRe) as well as within the oil generation window ( $< 1.4$  VRe). The three wells with 0.68, 0.69, and 0.93 VRe did produce some oil but were noncommercial tests. Many more Woodford horizontal wells have since been drilled on the western edge of the CBP with similar noncommercial results. As mentioned previously, the VR and VRe proxies must be calibrated to correspond to hydrocarbon generation. Understanding how much source rock transforms from kerogen to petroleum is of critical importance when trying to establish a play from source rocks (Tobey & Campbell, 2016; Waples & Tobey, 2015). We find that the calculated TR of the kerogen is a critical element in appraising the level of hydrocarbon generation.

Figure 4 (right) shows the TR of the Woodford Formation in the area. Note the two wells of 0.68 and 0.69 VRe have a TR of only 0.01. This means about 1% of the potential generation has occurred, which means oil has

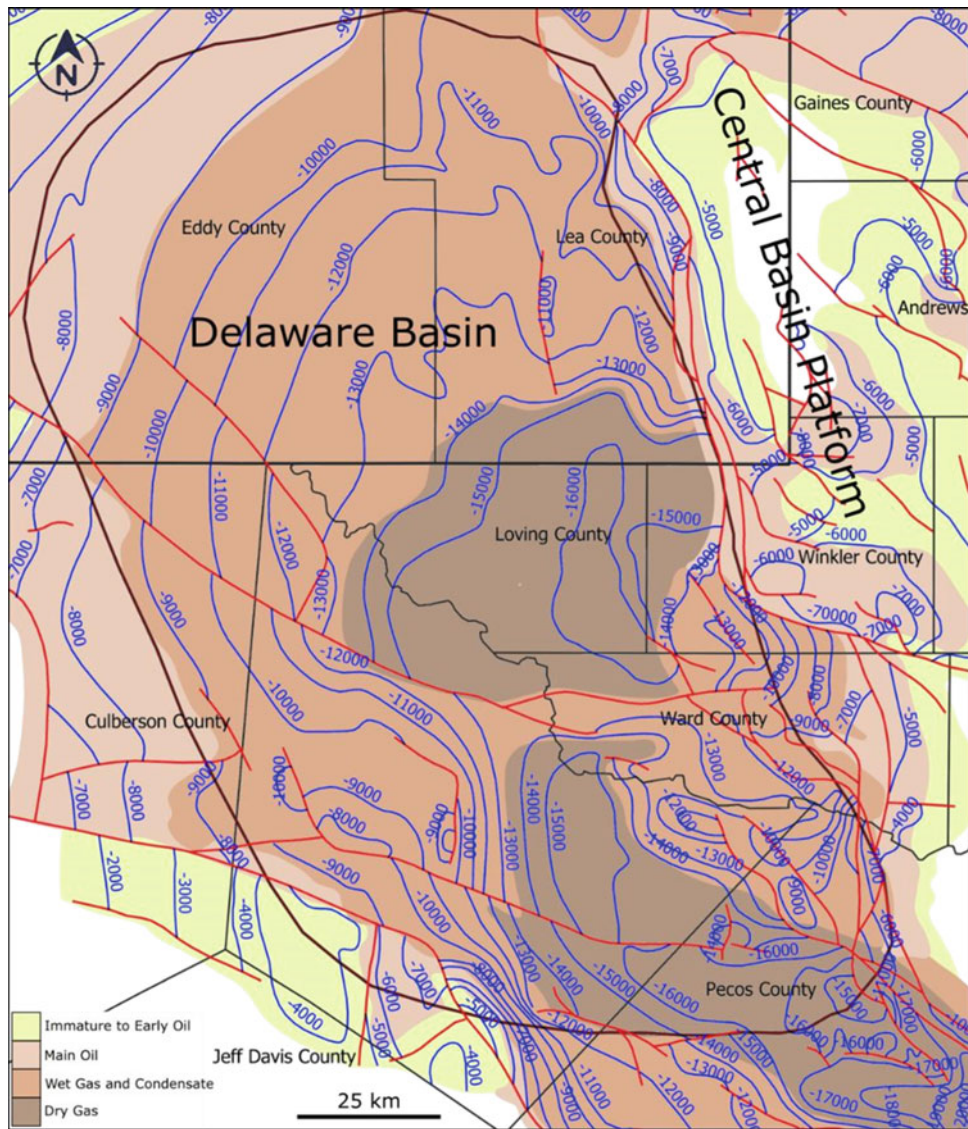


**Fig. 3** Structure contour map of the Woodford Formation in the Delaware Basin and the Central Basin Platform shows major faults (red lines) as well as the different zones of organic thermal maturity based on VRe data. Modified from Comer (1991) and Entzminger and Miller (2004)

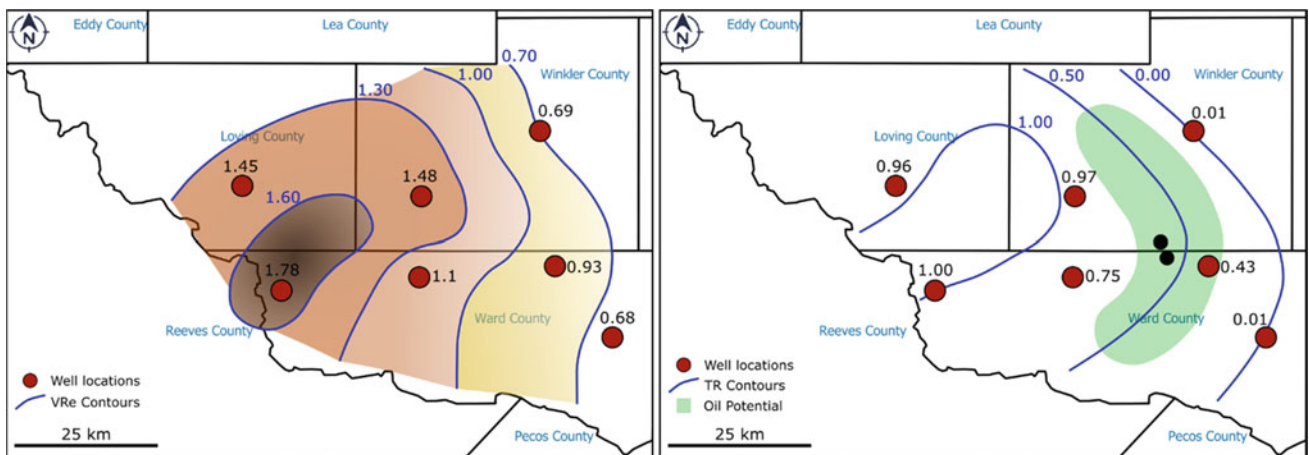


**Fig. 4** Woodford VRe and TR data for seven control wells within Loving, Ward, and Winkler counties, Texas show the prospective region (green zone) of optimal maturity and petroleum generation. Map data were obtained with permission from Doug Waples, Sirius exploration. Geochemistry Inc., however, interpretations are the authors'. Approximate locations of Marathon's recent Woodford horizontal wells are represented by the black dots

indeed been generated in the area but apparently not enough to be commercial. Combining both VRe and TR data (Fig. 4), the green zone outlines the area that is the most prospective for unconventional oil in this play. This green zone lies between the Woodford gas productive basin area and the Woodford Central Basin unproductive oil area round the 0.5 line mapped using TR data which appears to approximate peak oil for the Woodford in the Permian Basin. Recent discoveries now show this area is within the sweet spot for Woodford unconventional oil. Marathon oil announced in November 2019, two very productive Woodford horizontal wells in this green zone (Marathon Oil, 2019). The initial 30-day production of the two wells was 365 boepd/1000 ft of lateral (70% oil) and 240 boepd/1000 ft of lateral (48% oil).

## 4.2 Understanding Migration Pathways for Conventional Reservoirs

The use of pressure-depth plots helps establish fluid contacts and migration pathways for conventional plays. Pressure-depth plots can be produced with drill-stem test data, which are vital in forecasting well productivity. It is important to select tests where the final shut-in or flowing pressure has built to near reservoir pressure as can be seen in Fig. 5. Without test charts, scout ticket data can be utilized to select useable data where significant amounts of fluid were recovered. Tests should be from the same horizon or within pressure communication, as on a truncation boundary, with said horizon.

**Fig. 5** Example drill-stem test chart of a well drilled in Andrews County, Texas

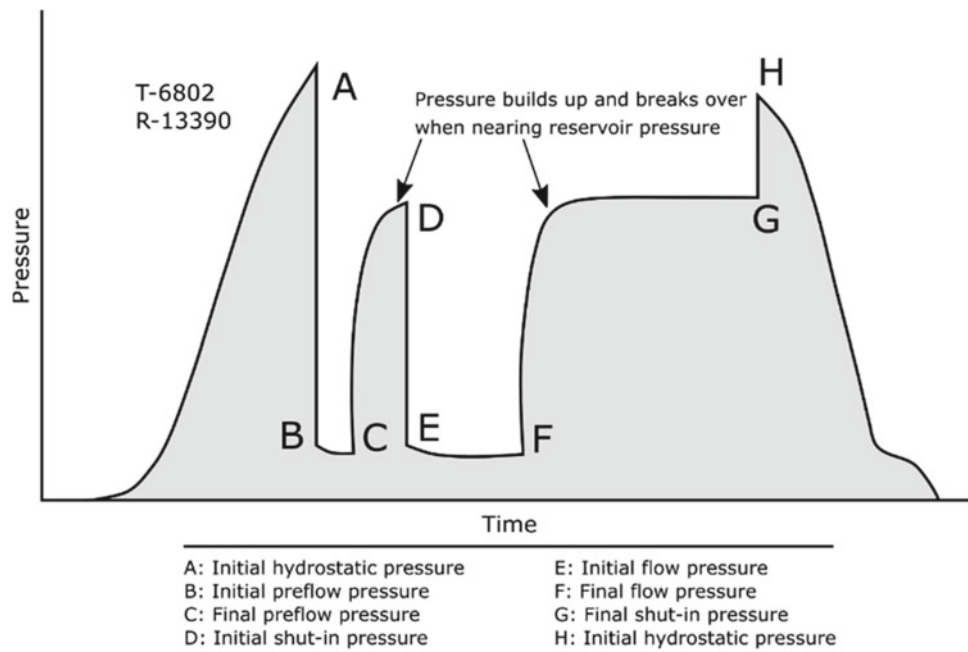
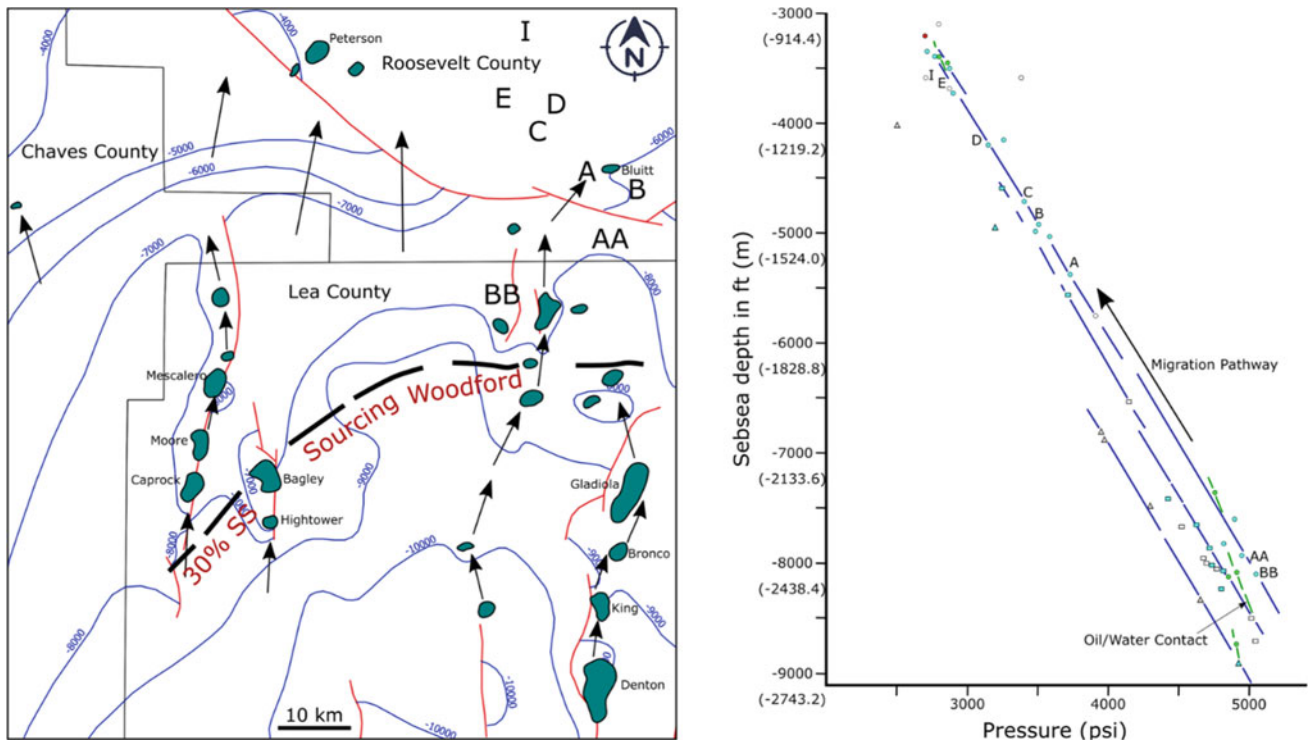


Figure 6 is a pressure versus depth plot of tests within the Woodford Formation in the northwest portion of the Permian Basin—Lea and Roosevelt counties, New Mexico (Entzminger & Miller, 2004). Three fluid compartments (circles, squares, and triangles) are plotted from the data in the region. Pressure versus depth plots show fluid contacts as the water is plotted on a 0.453 psi/ft gradient and oil or gas gradients are plotted based on the gravity of the fluid, where these gradients intersect is the fluid contact, see inset on Fig. 6.

Oil analysis by the ARCO research laboratory from the northern portion of the Delaware Basin revealed that many of the Silurian–Devonian fields like Denton, Gladiola, Bluit, and South Peterson are sourced from the Woodford Formation (Entzminger & Miller, 2004). The Woodford Shale truncates or has less than one percent TOC in northern Lea and Roosevelt counties of New Mexico (Fig. 2). For Woodford oil to be found in these northernmost reservoirs, it has likely migrated. Understanding the migration pathway(s) provides insights for other potential fields along migration routes. Following up the pressure versus depth plot for fields AA, BB, A, B, C, and D, one sees they are on the same pressure gradient and along a similar potential migration trend. Coupled with the structure map of the Woodford Formation, it is easy to follow the migration pathway the Woodford sourced oil likely took to the fields in the northwestern portion of the Permian Basin (Fig. 6). For an explorationist prospecting in areas away from a quality source rock, or a source rock that has not matured sufficiently to charge nearby reservoirs, it is critical to understand the petroleum system and how hydrocarbons could have migrated into a region.



**Fig. 6** Left: structure contour map of the Woodford Formation in the northwest portion of the Permian Basin—Lea and Roosevelt counties, New Mexico shows the location of major oil fields (green), and inferred hydrocarbon migration pathways (arrows). Structural data are after Comer (1991). Right: Pressure versus depth plot of tests within the

Woodford Formation for fields and wells AA, BB, A, B, C, and D show they are on the same pressure gradient and along a potential similar migration trend. Circles, squares, and triangles differentiate the datapoints representing the three fluid systems. After Entzminger and Miller (2004)

### 4.3 Mapping $T_{\max}$ and Production Data

Mapping  $T_{\max}$  from programmed pyrolysis data can be a very powerful tool guiding an unconventional play, if placed in context with other regional data. Figure 7 (left) provides five  $T_{\max}$  datapoints from cuttings and sidewall cores within the Wolfcamp A and B units in Reeves County, Texas. Using some general  $T_{\max}$  categories for product types, one can divide the area into high GOR (>5000 cfg/bo) and low GOR (<5000 cfg/bo) zones, but how that could be divided has several possibilities, depending on many factors such as kerogen organofacies and structural trends. Published regional faults (Ewing, 2013; Shumaker, 1992) suggest a northwest-southeast trend which would provide a reasonable divide between the high and low GOR zones. However, like most geological interpretations, it is best to integrate multiple proxies and data sources. In the present case, mapping  $T_{\max}$  alone would have led to drilling high GOR uneconomic wells. Integrating production data, provided another guide to optimal areas for the economic, low GOR wells. Figure 7 (right) of the production data suggests a northeast-southwest trend between the high and low GOR zones, which what was ultimately used for the MDC Texas Energy's drilling program. Other data like 3D seismic, which may not be

available or affordable, could have shown that the published fault trends did not include a deep fault trending northeast-southwest. This fault is located along the division line between the high and low GOR zones shown in Fig. 7 (right).

In early 2017, only a handful of wells were economic along this transition area between high GOR and low GOR zones. Today, over 100 economic unconventional wells exist, proving that combining pyrolysis and production data can be very powerful, when product type is essential in establishing an area for a commercial drilling program.

## 5 Conclusions

Whether evaluating conventional or unconventional reservoirs in any petroleum system, organic geochemical data are essential. Their value can be greatly maximized through the integration with other crucial information such as drill-stem test and production GOR data. Three useful examples were shown using data from the organic-rich Woodford Formation and Wolfcamp shales in the Permian Basin. The first example involves supporting VR and VRe data with TR to guide drilling economic unconventional horizontal wells.

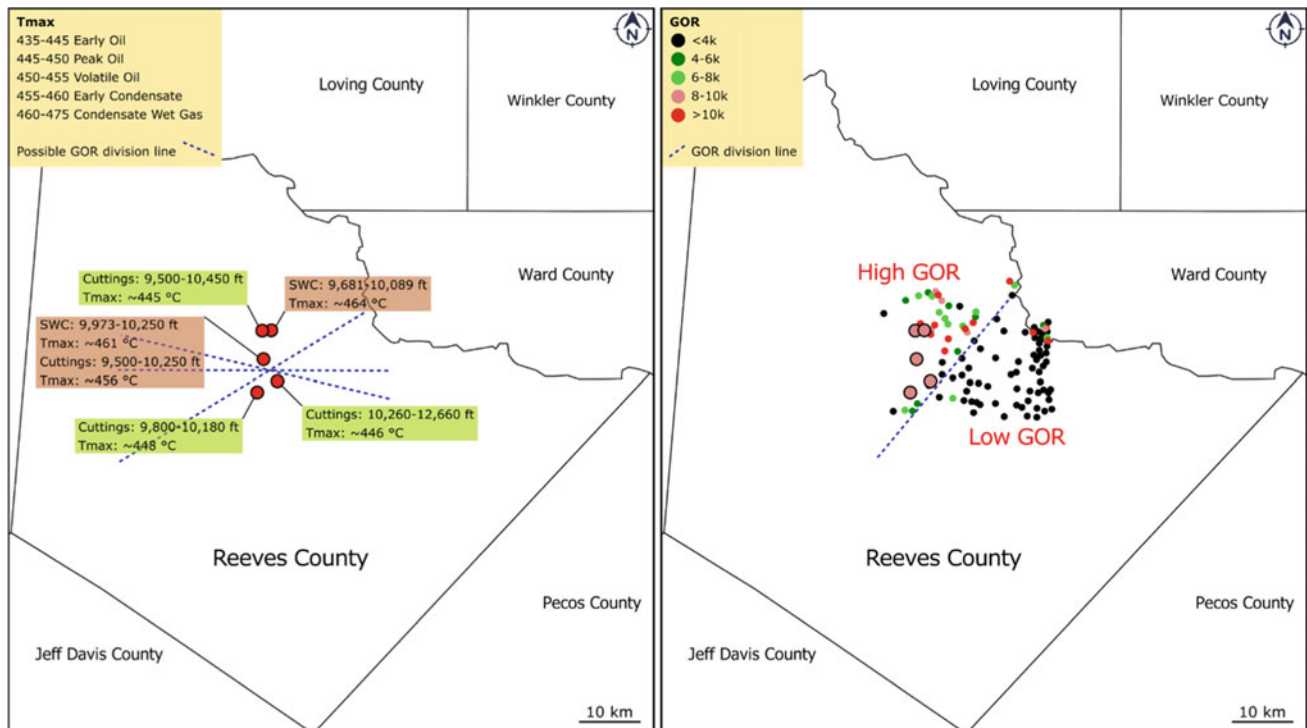


**Fig. 7** Left  $T_{\max}$  datapoints from cuttings and sidewall cores within the Wolfcamp A and B units in Reeves County, Texas. Several possible GOR division lines can be inferred based on  $T_{\max}$  alone, providing less target constraints and more drilling risk. Right GOR values based on

production data for the Wolfcamp A and B units in Reeves County, Texas. These data when combined with  $T_{\max}$  values provide much better constraints on zones of high (>5000 cfg/bo) and low (<5000 cfg/bo) GOR

The second example uses pressure-depth plots coupled with subsurface elevation data to determine hydrocarbon migration pathways along a given pressure gradient to predict further economic drilling targets near areas of economic discoveries. The third example involves mapping  $T_{\max}$  values assisted by previously available production-based GOR data to precisely delineate areas of high and low GOR for profitable, low GOR unconventional horizontal wells. As with most projects, utilizing several methods and datasets leads to better interpretations.

**Acknowledgements** We thank Dr. Doug Waples of Sirius Exploration Geochemistry Inc. for his insights on source rock kinetics and the power of the transformation ratio in unconventional plays. Dr. Waples' company also provided data for our Woodford play example, illustrating that even a few datapoints can make a significant difference in locating an economic play. We also acknowledge MDC Texas Energy LLC. for access to their well data.

## References

- Bammidi, V. S., Balch, R. S., & Engler, T. W. (2011). *Ranking the resource potential of the Woodford Shale in New Mexico*. Society of Petroleum Engineers, SPE-144576-MS, 10 p.
- Baumgardner, R. W., Jr., Hamlin, H. S., & Rowe, H. D. (2016). *Lithofacies of the Wolfcamp and lower Leonard intervals, southern Midland Basin Texas*: The University of Texas at Austin, Bureau of Economic Geology, Report of Investigations (Vol. 281, 97 p.).
- Cardott, B. J. (2012). Introduction to vitrinite reflectance as a thermal maturity indicator: AAPG search and discovery, Article #40928, 73 p.
- Comer, J. B. (1991). *Stratigraphic analysis of the Upper Devonian Woodford Formation, Permian Basin, West Texas and southeastern New Mexico*: The University of Texas at Austin, Bureau of Economic Geology, Report of Investigations (Vol. 201, 63 p.).
- Dembicki, Jr., H. (2017). *Practical petroleum geochemistry for exploration and production*. Elsevier.
- Drake, W. R., Longman, M. W., & Moses, A. (2018). Assessment of the Woodford Shale petroleum system within a deep subbasin on the Central Basin Platform, Permian Basin: AAPG Search and Discovery, Article #11105, 25 p.
- EIA. (2018b). U.S. crude oil and natural gas proved reserves. Year-End 2017: US Energy Information Administration Independent Statistics and Analysis, November 2018b, 48 p.
- EIA. (2018a). Permian Basin Wolfcamp Shale Play. Geology review: US Energy Information Administration Independent Statistics and Analysis, October 2018a, 15 p.
- Entzminger, D. J., & Miller, M. (2004). *Finding petroleum on the Roosevelt Arch, Roosevelt County*. New Mexico: AAPG Search and Discovery, Article #90025, Abstract.
- Ewing, T. E. (2013). Three scales of late Paleozoic structures in the West Texas basin—Description and genesis. *AAPG Search and Discovery, Article #30273*, 25 p.
- Gaswirth, S. B., Marra, K. R., Lillis, P. G., Mercier, T. J., Leathers-Miller, H. M., Schenk, C. J., Klett, T. R., Le, P. A., Tennyson, M. E., Hawkins, S. J., Brownfield, M. E., Pitman, J. K., & Finn, T. M. (2016). *Assessment of undiscovered continuous oil*

- resources in the Wolfcamp shale of the Midland Basin (4 p.), Permian Basin Province, Texas: U.S. Geological Survey, Fact Sheet 2016-3092.
- Hackley, P. C., Ryder, R. T., Trippi, M. H., & Alimi, H. (2013). Thermal maturity of northern Appalachian basin Devonian shales: Insights from sterane and terpane biomarkers. *Fuel*, 106, 455–462.
- Hackley, P. C., Zhang, T., Jubba, A. M., Valentine, B. J., Dulong, F. T., & Hatcherian, J. J. (2020). *Organic petrography and diagenesis of Leonardian (Wolfcamp A) mudrocks and carbonates, Midland Basin* (15 p). Texas: Marine and Petroleum Geology, v. 112, Article No. 104086.
- Hemmesch, N. T., Harris, N. B., Mnich, C. A., & Selby, D. (2014). A sequence stratigraphic framework for the upper Devonian Woodford Shale, Permian Basin, West Texas. *American Association of Petroleum Geologists Bulletin*, 98(1), 23–47.
- Jarvie, D. M. (2018). Petroleum systems in the Permian Basin: Targeting optimum oil production. In *Proceedings of the Houston Geological Society January Luncheon, Houston, TX* (pp. 1–33).
- Kvale, E. P., & Rahman, M. (2016). Depositional facies and organic content of upper Wolfcamp Formation (Permian) Delaware Basin and implications for sequence stratigraphy and hydrocarbon source. In *Unconventional Resources Technology Conference, URTEC-2457495-MS*, (11 p).
- MacRitchie, C., & Zobaa, M. K. (2019). *Multi-proxy sedimentary organic matter analysis of the upper Wolfcamp formation in the Collier-1201 well, southeastern Delaware Basin, Texas*: Interpretation (Vol. 7(4), pp. 1–8).
- Marathon Oil. (2019, November 6). *Third quarter financial and operational review*. Marathon Oil, 29 p. <https://ir.marathonoil.com/download/3Q+2019+Earnings+Presentation+%28PDF%29.pdf>
- Peters, K. E., & Cassa, M. R. (1994). Applied source-rock geochemistry. In L. B. Magoon, & W. G. Dow (Eds.), *The petroleum system. From source to trap*: American Association of Petroleum Geologists (pp. 93–120).
- Shumaker, R. C. (1992). Paleozoic structure of the Central Basin uplift and adjacent Delaware Basin. *West Texas: American Association of Petroleum Geologists Bulletin*, 76, 1804–1823.
- Tissot, B. P., & Welte, D. H. (1984). *Petroleum formation and occurrence*, 2nd edn. Springer.
- Tobey, M. H., & Campbell, C. E. (2016). Hydrogen index as a maturity proxy—Some pitfalls and how to overcome them: AAPG Search and Discovery, Article #41964, 31 p.
- Waples, D., & Tobey, M. H. (2015). Like space and time, transformation ratio is curved, AAPG Search and Discovery, Article #41713, 27 p.
- Waples, D. W. (2016). Petroleum generation kinetics: Single versus multiple heating-ramp opensystem pyrolysis. *American Association of Petroleum Geologists Bulletin*, 100(4), 683–689.
- Waples, D. W., Leonard, J. E., Coskey, R., Safwat, S., & Nagdy, R. (2010). *A new method for obtaining personalized kinetics from archived Rock-Eval data, applied to the Bakken Formation*. Williston Basin: AAPG Search and Discovery, Article #90108.
- Waples, D. W., & Marzi, R. W. (1998). The universality of the relationship between vitrinite reflectance and transformation ratio. *Organic Geochemistry*, 28(6), 383–388.
- Zumberger, J. (2013). *Re-invigorating the Permian Basin*. West Texas Geological Society Fall Symposium, Publication #13-126.



## Case Studies



# High-Resolution Palynostratigraphy and Palynofacies of the Upper Cretaceous and K/Pg Boundary, SE Sirt Basin, Libya: A Case Study

Ali Daw El-Mehdawi

## Abstract

Very rich, diverse and exquisitely preserved palynological material including dinocysts, sporomorphs, prasinophytes, acritarchs and freshwater algae have been recognised from the study of Upper Cretaceous-early Paleocene section in the C3-65 Well, southeast Sirt Basin, Libya. Tens of well-preserved new varieties of dinocysts have been recorded and kept in open nomenclatures for the time being. Reworked Palaeozoic acritarchs and miospores are also recorded. Twenty-five stratigraphically and environmentally controlled palynomorph associations are recognised and range in age from late Cenomanian to late Danian. Age determinations were based solely on palynomorph content for the earliest sixteen associations and on integrated palynomorphs and calcareous nannofossils data for the late associations. Based on integration of the recorded palynological components, the Etel Formation has been assigned to Late Cretaceous, late Cenomanian–Turonian; Rachmat Formation to late Turonian-late Campanian; Tagrift Formation to late Campanian-early Maastrichtian; Sirte Shale Formation to late Maastrichtian, and the lower part of the Hagfa Shale to Early Palaeocene, late Danian age. Eleven main palaeo-environmentally, controlled palynofacies including brackish swamp, estuarine, aerobic and dysaerobic marine, very restricted marine, and fully open-marine conditions are recognised based on integration between the different types of organic matter components and their preservation on one hand, and on available nannofossil data across the K/Pg boundary on the other. The investigated organic matters are of good

quality and quantity, but it is proved to be immature to marginally mature, whereas in the deeper part of the basin to the north of the study area is known to be mature to over mature and is thus a good source rock.

## 1 Introduction

This study is concerned with the palynostratigraphy and palynofacies investigation of the Upper Cretaceous with particular emphasis on the Cretaceous/Tertiary (K/Pg) boundary in the C3-65 Well, SE Sirt Basin, Libya (Fig. 1). The main thrust of this study has been placed on the value of dinocysts, spores, pollen and associated organic debris as palynostratigraphical and palaeoenvironmental indicators.

The current study aims to re-address this imbalance, which significantly impacts petroleum exploration using the following means to: (1) establish a refined local palynostratigraphical zonation scheme for the Upper Cretaceous and K/Pg boundary sediments; (2) compare the locally established zonation scheme with those recorded from other areas in order to construct a reliable chronostratigraphic scheme to be used in the future for regional correlation within the Sirt Basin and neighbouring areas; (3) identify changes in the palynomorph assemblages across the K/Pg boundary to recognise any ecological and/or environmental changes; (4) correlate palynostratigraphical data with other biostratigraphical data wherever possible and (5) establish a depositional scenario for the study section by integrating recovered palynological organic components and palynomorphs.

The present study is of particular importance since palynostratigraphical data have previously been little used for age determination in the Sirt Basin. In consequence, there is very little in the way of detailed taxonomic and palynostratigraphical data covering the Cenomanian-Danian period in Libya in general.

A. D. El-Mehdawi (✉)  
Exploration Department, National Oil Corporation, Tripoli, Libya  
e-mail: [amehdawi@noc.ly](mailto:amehdawi@noc.ly)

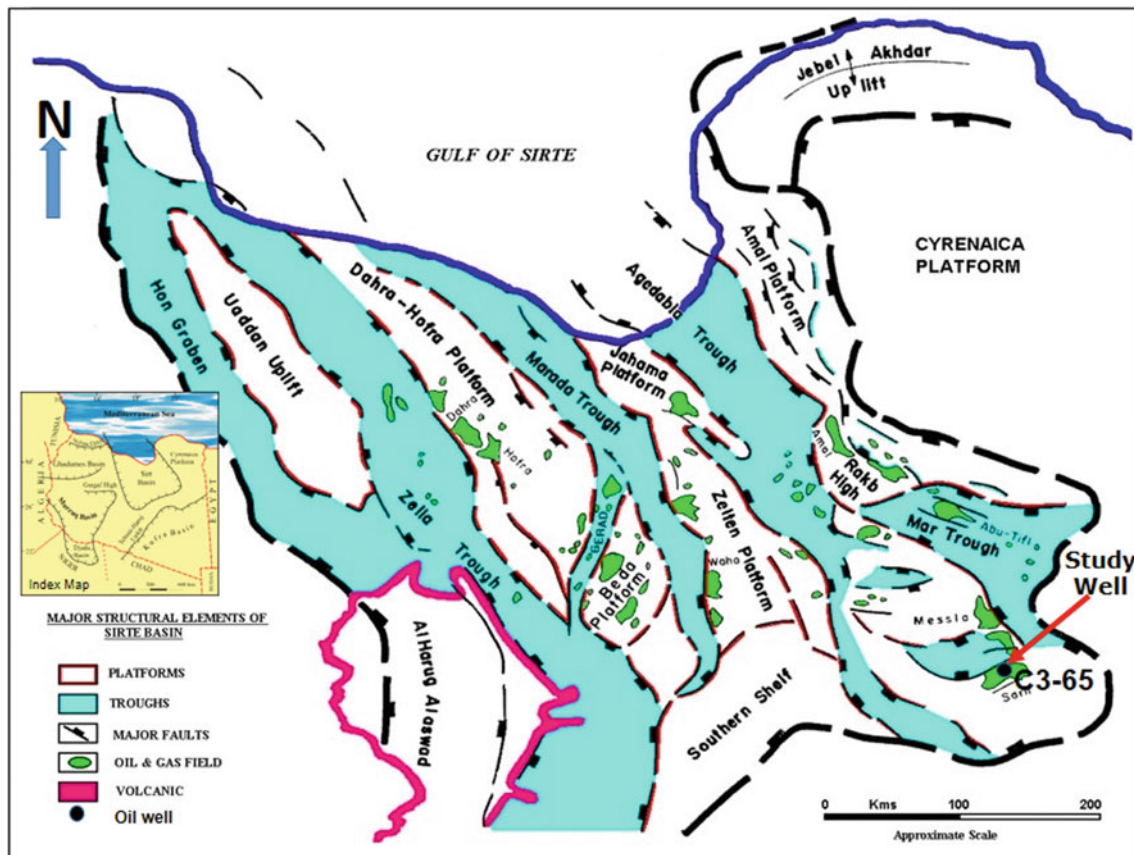


**Fig. 1** Generalized map of the main tectonic elements of the Sirt Basin and location of the study well; after Rusk (2001)

There are limited published data on the Upper Cretaceous and Paleogene palynology of Libya. Of these are Baair et al. 2003, Bu-Argoub 1996, Muftah et al. 2004, El-Mehdawi 1991, 1998, 2008, Keegan and Stead 2007. In comparison, more Upper Cretaceous data are available from other regions in North, East and West Africa, but either they are stratigraphically limited or focussing on non-marine sections such as in Aboul Ela et al. (2019), Below (1984), Boltenhagen (1977), Brinkhuis and Leereveld (1988), Brinkhuis and Zachariasse (1988), El Atfy et al., (2017a), Jain and Mill-epied (1975), Salard-Cheboldaeff (1990), Schrank (1987, 1994), Schrank and Ibrahim (1995) and Schrank and Perch Nielsen (1985). These factors have prevented a complete comparison with the present study. The most important palynostratigraphical data regarding the K/Pg boundary in North Africa come from the El Haria and El Kef sections, Tunisia by Brinkhuis and Zachariasse (1988), Brinkhuis and Leereveld (1988).

However, voluminous body of data exists concerning the stratigraphic distribution of dinocysts from North America, Western Europe, Australia and the surrounding continental margins. The data from these publications have been utilised to help validate the established palynological zonation scheme.

## 2 Geological Setting

The Sirt Basin forms the south to south-eastward extension of the Gulf of Sirt (Fig. 1), with an aerial extent of approximately 500,000 km<sup>2</sup>. To the North-East, it is bounded by the Cyrenaica Platform and to the south and west by the the Palaeozoic basins of the Al Kufrah, Murzuq and Al Hamada Al Hamarh. The Sirt Basin contains about 15 giant oil and gas fields. It is an intracratonic basin (Gumati & Nairn, 1991) situated at the northern margin of the African continent. It is developed as a result of Suez-type crustal extensions of an old eroded basement and subsequent Palaeozoic uplift. It became a site of major geotectonic activity beginning with an Upper Cretaceous transgression and ending with a Miocene regression (Hecht et al., 1964). The structural features of the Sirt Basin have been classified as extensional fault blocks (Harding & Lowell, 1979). Two regions have similar structural styles, the North Sea and Gulf of Suez, and the dominant fault movement has been considered as dip slip. In the former, horsts, grabens, and tilted fault blocks developed during gravity (normal) faulting modified by erosion prior to several Upper Jurassic and Cretaceous transgressions. The intensive block faulting of a broad structural arch or dome, formed

during the late Hercynian, was subsequently eroded, resulting in the development of platforms and five main troughs trending north-west and southeast (Fig. 1). More than 8333 m (25,000 ft.) of predominantly marine Upper Mesozoic and Cenozoic sediments have accumulated in the deeper part of the basin, and thin sequences of Palaeozoic, which survived the erosion of the Hercynian Orogeny, are generally widespread along the margin of the basin. As a result of this orogeny, most of the Palaeozoic deposits were removed by erosion whereas the Sirt area remained a topographic high until Late Mesozoic, at which time movement and deformation took place (Gumati & Nairn, 1991, p. 95). Many workers have erroneously designated the Upper Cretaceous (Cenomanian to Santonian) as the time when the collapse of the Sirt anticlinorium was initiated.

The multicoloured shale of the so-called Nubian/Sarir Sandstone (Jurassic-Lower Cretaceous) in the eastern part of the Sirt Basin, particularly from concession 82, yielded dinocyst assemblages dominated by *Phoberocysta*, *Mud-erongia* and *Oligosphaeridium* species (Thusu et al., 1988). Furthermore, Vitebro (1969) reported the presence of Charophytes in association with brackish water ostracods, and concluded that the multicoloured shales in concession 82 (NE of the study area) were deposited in a brackish-lagoonal environment. However, from this evidence, and keeping in mind other tectonic events in North Africa, the collapse of the Sirt anticlinorium may have commenced as early as the Late Jurassic. There is, however, no doubt that the major collapse of the Sirt anticlinorium occurred during Late Cretaceous. This is supported by the presence of basal Upper Cretaceous sandstones, thick marine shales and carbonate deposits on basement rocks in the grabens or draped over basement highs (horsts), resulting from the collapse of the anticlinorium. Some workers (Barsotti, 1963; Reymont, 1980) believe that a connection may have existed between the ancient Tethys and the Gulf of Guinea, via the Sirt Basin, Chad and Nigeria, during the early Late Cretaceous (late Cenomanian–Turonian) and Late Cretaceous-Paleocene (Maastrichtian-Paleocene) transgression. The existence of the early Late Cretaceous connection has been postulated, but this claim is disputed by Barr (1972) and Rebelle (1990).

The important oil reserves in the Sirt Basin have accumulated in different types of sedimentary rocks ranging from Cambro-Ordovician to Eocene and also in a fractured and weathered granitic basement. The Cambrian to Lower Cretaceous pre-rift accounts for 36% of the ultimate oil reserves and 24% of the ultimate gas reserves (Chatellier & Slevin, 1988). A large number of these fields in the SE Sirt Basin produces oil from the Nubian/Sarir Sandstone.

It is reported that the whole of the Upper Cretaceous and the lower part of the Paleocene sequence form a thick cap and potential source rocks in much of the SE Sirt Basin.

### 3 Stratigraphy

The stratigraphy of the study area is given in Fig. 2. It consists of a flat gravel, and sand plain-surface outcrops are therefore absent. The carbonate (reservoir) build-ups in the study area are minor, and the Nubian/Sarir Sandstone (pre-Upper Cretaceous) is the only significant sandstone deposit. This sandstone constitutes the primary reservoir rock, and so, the pre-Upper Cretaceous is the only reasonable petroleum prospect.

The following is a stratigraphic summary of the study area from bottom to top in ascending order.

#### 3.1 Basement

The basement in the study area ranges from granite, granodiorites and, rarely, diorites to metamorphic rocks of low-grade meta-sediments to quartzite, phyllite and schist. The K/Ar radiometric dating of the granite indicates a Late Precambrian to Early Cambrian age (AGOCO, 1980).

##### 3.1.1 Upper Jurassic-Lower Cretaceous

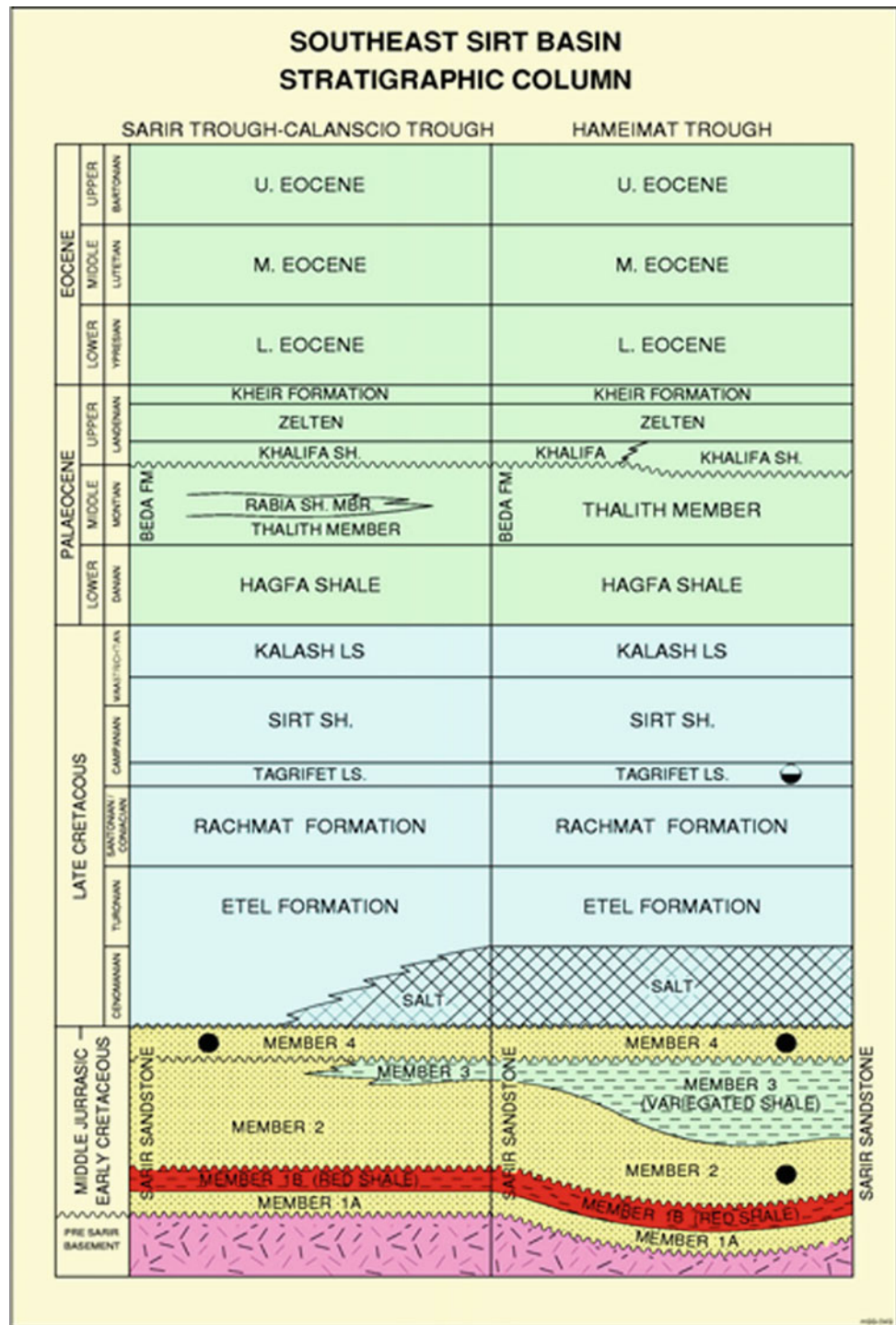
###### Sarir/Nubian Sandstone

The Sarir Sandstone, which is known as Nubian Sandstone in other parts of the basin, consists of sandstone-dominated section overlain unconformably by a transgressive sequence of Upper Cretaceous age. It directly overlies an erosional surface of mostly Pre-Cambrian plutonic and metamorphic rocks, and in some areas outside the study area, overlies erosional remnants of either Triassic or Cambro-Ordovician sediments.

The Sarir Sandstone is up to 6000 ft. thick (Hea, 1971), usually pinching-out towards the south. It is generally of continental origin as supported by the complete lack of marine fauna and the presence of strongly oxidised red sandstones and shales. The presence of gymnosperm pollen, *Classopollis* in the sands, indicates an arid to semiarid subaerial setting. However, several wells to the north-east of the study area contain greenish to grey shales that have been dated as Middle Triassic to Early Cretaceous age (Thusu et al., 1988).

In concession 82, north-east of the study area, the Sarir/Nubian shales, yielded Lower Cretaceous dinocyst assemblages dominated by *Phoberocysta neocomica*, *Mud-erongia simplex* and *Oligosphaeridium perforatum* (Thusu et al., 1988). Vitebro (1969) reported the presence of charophyte *Clavator harrisi* in association with brackish water ostracoda including *Therioisynoecum* spp., *Cytherella* spp. and *Bisulcocypsis* spp. He concluded that the multicoloured shales in concession 82 were deposited in a brackish-lagoonal environment.

**Fig. 2** Stratigraphic section of the study area (Agoco File unpublished)



The Sarir Sandstone in the study area falls into three lithological units, a lower shaley sandstone, a middle clean sandstone and an upper shaley, silty sandstone. These units can be further subdivided into five members, numbered 1–5 from oldest to youngest. Porous intervals occur in member 3 which forms good petroleum reservoirs. This stratigraphic

unit lacks any organic-source content in the study area (Sarir Trough), whereas in the Faregh Trough and eastern Hameimat Trough to the north and north east of the study area, the middle Nubian Shale is highly radioactive and organic rich with good source quality containing over 1% by weight (rich), and  $S_2$  values are good (greater than 5 mg/g) (Sikander et al., 2013).

### 3.1.2 Upper Cretaceous

#### Etel Formation

This formation consists mainly of variegated, sandy, silty and anhydritic shales and mudstones which are non-calcareous, barren of any planktonic foraminifera, with only a few benthonic forams present. There is a marked variation in thickness, from 68 ft. in the C3–65 Well to more than 170 ft. to the North of the study area and reaches up to more than 2000 ft. in the Hameimat Trough. Its contact with the underlying Sarir Sandstone is unconformable and usually marked by a thick anhydrite bed, reaching a thickness of more than 9 ft.

Locally, a transgressive sandstone unit marks the base of this formation. This is better developed in Concession 65, particularly in the vicinity of the “C” main field (Sanford, 1970), but missing in the study well. These sandstones are typically fine-grained, moderately sorted and frequently glauconitic, subrounded and contain clay, silica and cements, as well as anhydrite cements, lenses and nodules. These sandstones appear to be generally lenticular in nature and of marginal marine to marine origin. The transgressive sandstones are barren of any planktonic foraminifera, and only, a few benthonic forams occur.

The Etel shales, which are highly radioactive, are proved to be lean source rock in most of the troughs, with exceptions in the Hameimat and Kotla troughs to the north-east and north-west of the study area. In terms of source quality, geochemistry revealed that the shales are poor to fair (El Alami, 1996; Sikander et al., 2013).

#### Rachmat Formation

The Rachmat Formation consists of a uniform thickness of grey and grey brown, fissile shales interbedded with some silty shales and glauconitic sandstones of green, grey and pink colour. Sandy limestones and dolomites are locally present. Core 2 of the study C3-65 Well yielded abundant agglutinated and calcareous benthonic forams, ostracoda, echinoderm and fish debris. Benthonic forams are represented by *Ammonarginulina khargensis*, *Gavelinella* spp., *Trochammina* sp. and *Haplophragmoides* spp. and ostracoda represented by *Cythereis* spp. Planktonic foraminifera are very rare and include *Heterohelix* sp., *Pseudogumbelina* sp. and rotalides indet. This assemblage is suggested to indicate a Campanian–Maastrichtian age (AGOCO unpublished internal report).

#### Tagrifet Formation

This formation consists of white, light- to dark-grey, slightly glauconitic, argillaceous limestones, grading downwards into dark grey to black, fissile shales. This unit attains a thickness of 196 ft. in the C3-65 Well and increases in

thickness northwards. Abundant agglutinated forams including *Haplophragmoides* sp. and *Rotalia algeriana*, fish debris (scales, teeth, and spines), Lamellibranchia indet. (Bivalve fragments) and echinoderm fragments characterise the basal part of this formation in the study well. This assemblage has been interpreted as Campanian–Maastrichtian, deposited in shallow marine environment (AGOCO unpublished internal report). The argillaceous limestones of the Tagrifet and Rachmat formations have variable to low porosity and contain hydrocarbon shows in several wells. These are referred to as the “Tagrifet Limestone” in the Augila and Nafoora fields, north of the study area.

#### Sirte Formation

Sirte Formation is also known Sirte Shale. This stratigraphic horizon is about 400 ft. thick in the study C3-65 Well and is generally characterised by black, dark-grey and grey-brown calcareous shales with scattered thin beds and laminae of marl and argillaceous limestones, which are more highly fossiliferous than the lower formations.

The Upper Cretaceous/Paleocene boundary (K/Pg boundary) is characterised by high gamma ray reading and was recognised and cored only in the middle of the shale sequence of this formation at the C3-65 Well (Fig. 3). This core yielded abundant agglutinated foraminifera, bivalves, gastropods and fish remains (bones and teeth), which indicate a shallow marine environment of deposition.

#### Kalash Formation

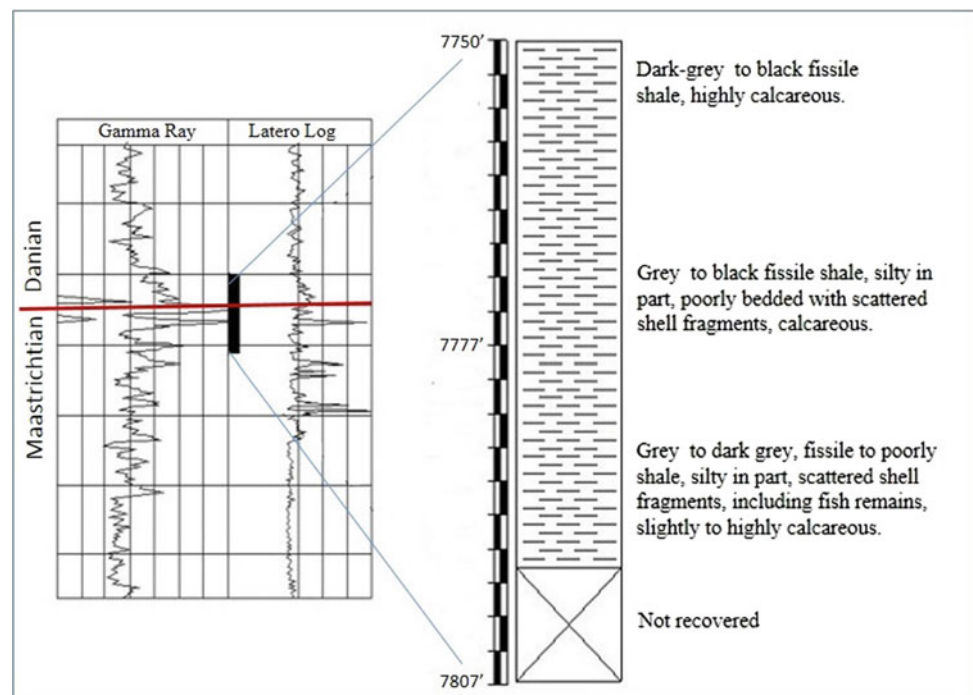
This unit is composed of argillaceous and dense limestones. It is a diachronous unit, deposited during a marine transgression in the Late Cretaceous/Paleogene period (Field, 1969). It is of variable thickness reaching up to 317 ft. in some wells within the study area but is absent in the study C3-65 Well. Generally, it is well developed and increases in thickness towards the north and north-west of the study area. However, south of the study area the Upper Cretaceous limestone grades laterally into sandstones indicating shallowing conditions.

### 3.1.3 Paleogene

#### Paleocene

The Paleocene section in the study area consists of 1500 to more than 1900 ft. of carbonates which lies on a lower shaley unit of the Hagfa Shale. The carbonate unit consists mainly of porous dolomites with some limestone and shales and rare streaks of anhydrite. The dolomites are mainly secondary. The limestone intercalations carry a Paleocene marine fauna, including *Miscellanea miscella*, *Alveolina ovoidea* and *Operculina patelensis*.

**Fig. 3** Gamma ray (GR) responses of the K/Pg boundary and generalised lithological description of the study Core 1, C3-65 Well



The shales are dark grey to black in colour and sometimes represent continuous deposition of the Sirte Shale as in the study C3-65 Well (Fig. 3). They carry marine fauna including *Globorotalia pseudoloides* and *G. trinidadensis*.

### Eocene

The Eocene section in the C3-65 Well is about 3338 ft. thick and can be subdivided into three lithostratigraphic units, characterised by relatively constant lithology and thickness across the study area.

**Lower Eocene:** This sequence is composed of evaporites succession, ranging from shales to marl and limestones, which develop into a dolomite facies, interbedded with anhydritic dolomites and anhydrites. This succession is broadly equivalent to the Kheir Marl or the Kheir Formation (Barr & Weegar, 1972). However, this evaporites sequence is unfossiliferous (Sanford, 1970). The Kheir Formation contains common microfossils including *Operculina* and other smaller benthonic and planktonic foraminifera. *Globorotalia velascoensis* has been recovered from the lower Kheir Formation, whereas *G. subbotinae* occurs in the uppermost part. These fossils suggest that the Kheir Formation straddles the Paleocene-Eocene (Thanetian-Ypresian) boundary; the lower Kheir Formation being upper Paleocene and the upper part being lower Eocene (Barr & Weegar, 1972; Sanford, 1970).

**Middle Eocene:** The middle Eocene known as the Gialo Limestone (Barr & Weegar, 1972), in the northern part of the Sirt Basin, is typically a nummulitic calcilutite, occasionally grading into a nummulitic calcarenite. Beds of shale

and lignite are sometimes present. The Gialo Limestone is better developed in other concessions of the Sirt Basin north of the study area, where it develops into a nummulitic and skeletal calcarenite facies, the upper part of which forms the principal reservoir in the Gialo Field (Barr & Weegar, 1972). The middle Eocene beds are very fossiliferous and are characterised by the presence of several species of *Nummulites*, such as *N. curvispira*, *N. subbeaumonti*, *N. perforatus* and *N. bacthisariensis*, and other forams including *Coskinolina* and *Dictyoconoides* (Sanford, 1970).

**Upper Eocene:** The upper Eocene in the study area consists primarily of sandy dolomites interbedded with dolomitic sandstone, becoming predominantly shaley and marly towards the bottom of the sequence. This represents the transitional sequence between the middle Eocene Limestone below and the epicontinental, detrital, post-Eocene beds above. Dating of the sequence is based on the presence of the late Eocene *Nummulites fabianii* and *N. striatus* (Sanford, 1970).

### Oligocene-Recent

This section is about 2910 ft. thick in the study C3-65 Well and is subdivided into three lithological units (Sanford, 1970). The upper unit consists of unconsolidated, slightly feldspathic sand; a middle unit consists of grey-green and red-brown shale and claystone with dolomite and sandstone partings, and the lower unit consists of fine to coarse-grained sandstone with some claystone partings and dolomites. These beds are mostly unfossiliferous. Miocene rocks are not recognised in the area. The Oligocene to recent

sediments crop out on the surface and appear to have been deposited in a continental to marginal marine environment, representing the last major regressive phase in the area.

## 4 Materials and Processing Procedure

The database of this study consists of 59 cores and ditch cuttings samples collected from the Arabian Gulf Oil Company (AGOCO), C3-65 Well. This well was chosen because it contains the largest number of the Upper Cretaceous-cored intervals in the Sirt Basin and is the only in the area that straddles the K/Pg Boundary.

The preparation palynological procedure includes the following steps:

**Cleaning samples:** Washing the samples under running tap water to ensure they are free from contamination such as drilling mud and soil, which may adhere to the ditch cuttings.

**Crushing samples:** The aim of this step is to produce particles with an average size from 1 to 2 mm. The aim is to present a larger surface area for acid digestion.

**Amounts of samples required:** Shale: 5–15 g, calcareous or siliceous shale and argillaceous sandstone: 25–30 g and sandstones and argillaceous limestone: 35–50 g proved to be satisfactory:

### 4.1 Demineralisation

**Testing for carbonates:** This is done in order to determine if there is any presence of carbonate material in the samples by adding a few drops of 10% HCL. If the test proves positive, the rock will require pre-treatment with HCL as in the following step:

**Removal of carbonate material:** The removal of calcium and magnesium carbonate material is necessary prior to HF treatment, to avoid any precipitation of secondary fluorides (CaF<sub>2</sub>, MgF<sub>2</sub>). This is achieved by dissolving the rock samples in 35–37% HCL (hydrochloric) acid.

**Removal of the silicate material:** After the carbonate material has been removed, 40% HF (hydrofluoric) acid is added with great care to remove silicates. This is achieved by leaving the samples in HF for not less than 24 h and stirring from time to time in order to accelerate reaction.

**Concentration of organic matter:** This is achieved by washing the neutralised residue under tap water and through 10 µm nylon mesh to remove fine particles.

**Oxidation:** The carbonate and silicate free residue is divided into two parts: one is further treated (oxidised), and the other is left unoxidised. One or two slides are prepared from the unoxidised portion in order to investigate palynofacies and particulate organic matter (POM) prior to oxidation, and the second part was subjected to oxidation to

remove the unwanted organic or inorganic materials and generally to clean up the sample. This step is performed by adding nitric acid (HNO<sub>3</sub>) or Schultze's solution (KClO<sub>3</sub>: 3 HNO<sub>3</sub>) to the residue. The reaction time varies between 5 and 15 min, and in order to avoid over oxidation, the sample is continually assessed by pipetting and viewing the residue under a microscope.

Once the proper oxidation level is achieved, the residue is washed through a 10 µm sieve until neutral PH is achieved. 2% potassium hydroxide solution is then added to remove the humic acid that is a product of oxidation.

**Heavy mineral separation:** This is used to separate the heavy particles from the light ones. Zinc bromide (ZnBr) of a specific gravity (1.9–2.0), greater than that of the organic matter, is added to the residue and centrifuged for 10 min so that the organic material in the sample floats, whilst the inorganic material sinks to the bottom. The suspended material containing the palynomorphs is pipetted out and washed through a 10 µm sieve until neutral PH is achieved and then decanted from water to be ready for the next step.

**Ultrasonic treatment:** Ultrasonic treatment was used sparingly to disaggregate clumps of organic matter, particularly for samples rich in amorphous debris.

**Slide preparation:** The cleaned and neutralised residue is mixed with a small drop of the dispersing solution polyvinyl alcohol (PVA) to prevent coagulation of the organic residue on the slide. This mixture is spread onto a 32 × 22 mm cover slip using well labelled pipettes and allowed to dry on a hot plate (25°C) under a dust cover. A clean glass slide (size 75 × 25 mm) is warmed on a hot plate (120°C), and a few drops of Petropoxy-154 (Petropoxy-154 resin and Petropoxy-154 curing agent mixed at a ratio 10:1) smeared across its surface. This is heated to expel any air bubbles, after which the cover slip is inverted and dropped onto the slide. Care must be taken so as to prevent the formation of small air bubbles. Both the coverslip and glass slide are left on the hot plate (5–10 min) until the Petropoxy is hard.

**Photography:** Photomicrographs for most age diagnostic taxa were taken using a Polyvr PhotoMicroscope. The plate description provides the taxon name, core number, sample depth, slide number and England's Finder reference coordinates. The magnification of displayed taxa is ×230, unless otherwise stated in the figure caption.

## 5 Palynostratigraphy

The investigated samples have yielded very rich, diverse (Figs. 4 and 5) and exquisitely preserved palynomorph assemblages in which more than 700 *in-situ* taxa have been reported including more than 450 species assignable to 111 genera of peridinioid and gonyaulacoid dinocysts and more than 150 species of sporomorphs prasinophytes, acritarchs



and freshwater alga, scolecodonts, microforminiferal test linings and diatoms tests were also recognised. More than 55 species of reworked Early Paleozoic acritarchs and miospores were also reported. Tens of well-preserved new species and varieties of dinocysts were recorded during this study were kept in open nomenclatures for the time being.

The palynostratigraphical results of this study are presented in the form of palynological associations. This is achieved using the combined evidence of dinocysts and miospores.

“The term “association” is here used to identify groups of successive assemblages (phytoplankton, pollen, spores or both) with shared characteristics of composition, and controlled by the range of taxa. It was also necessary to identify single assemblages as new associations. This was done only where a significant change in the composition of taxa present in a single assemblage was identified relative to those preceding and succeeding it (Jolley, 1992). The identified associations were given sequential numbers in ascending stratigraphic order; however, several taxa make their first or last occurrence or have restricted ranges, within these associations. The first occurrence of some palynomorphs has been taken as datum events for some associations. The recovered palynomorphs were analysed using ‘Tilia’ software. The raw numerical counted data were converted into percentages using the analysis facility, and the sum of the different groups and complexes of palynomorphs were calculated. The percentage of taxa was analysed in the “Tilia” package, using the stratigraphically constrained cluster analysis. The latter compares the assemblage similarities with those of adjacent samples. Assemblages falling within a cluster on the Tilia graph dendrogram (that have a total sum of squares of approximately less than three) are here considered to be a potential “association.” For more details regarding cluster and dendrogram analysis, please see Grimm, 1987.

The present study has more advantages over the other known studies of similar stratigraphic level either from Libya or neighboring area that relied on successive cored intervals and yielded very rich stratigraphically important species of marine and non-marine palynomorph assemblages incorporated in a most detailed Upper Cretaceous and Danian palynostratigraphical zonation scheme. The age synthesis presented herein is based mainly on correlation with the only available local studies from the Sirt Basin and NE Libya (Bu-Argoub, 1996, and Keegan & Stead, 2007) and similar studies from North, East, and West Africa, Middle East, Europe, Australia and North America. The K/Pg boundary section is supplemented with a nannofossil study by El-Mehdawi (1996).

Twenty-five palynomorph associations range in age from Late Cretaceous, late Cenomanian to early Paleocene, late Danian have been recognised. These associations are described below, from bottom to top in an ascending

stratigraphic order. The stratigraphic distribution of some of the recorded dinocysts, miospores and their bioevents, and the inferred palynostratigraphic succession are shown in Figs. 6, 7, 8 and 9.

For expressing the relative abundances of palynomorphs groups and complexes in the description below, the following terms have been used: abundant >15%, common 5–15%, present 2–5%, rare <1% (Figs. 10, 11, 12 and 13).

Figures 6a, b and 7 show the stratigraphic distribution of significant age diagnostic dinocysts and miospore taxa across the Upper Cretaceous and K/Pg boundary sections, whereas Plates 1, 2, 3, 4, 5, 6, 7, 8, 9, 10, 11, 12, 13, 14, 15, 16, 17, 18, 19, 20, 21 and 22 illustrate some of the encountered age diagnostic taxa.

Figures 8 and 9 summarise the palynostratigraphy and palynofacies successions and some of the dinocysts and miospores distribution events across the study section.

The majority of the dinocysts taxa recorded during the course of this study and mentioned in this chapter are fully referenced in Williams et al. (2017): “The Lentin and Williams’s index of fossil dinoflagellates.”

### Association 1

**Age:** late Cenomanian–Turonian.

**Interval:** 8614’–8617’.

This association is characterised mainly by non-marine taxa including abundant pteridophyte spores (32%), angiosperm pollen (25%) and other sphaeromorphic acritarchs. This association is dominated by undetermined tricolporate and tricolpate forms. Common species of *Gabonispuris* occur including *Gabonispuris bacaricumulus*, *G. pseudoreticulatus* and species usually present in the tetrad form, identified as *Gabonispuris* sp. A. Other taxa include *Cyathidites australis* and *Araucariacites australis*.

Stratigraphically, most important sporomorphs present in this association are rare specimens of *Nyssapollenites albertensis*, *N. triangulus* and *Nyssapollenites* sp. This association is not analogous to any published one in the literature; however, some sporomorph assemblages including *Nyssapollenites albertensis* have been recognised from the late Albian-early Cenomanian of North America (Singh, 1971), the alleged Albian of Egypt (Abdel Mohsen 1986), the Cenomanian of USA and Egypt (Bebout, 1980; Schrank, 1987) and Albian-Cenomanian, N. Sudan (Schrank, 1991). Assemblages including *N. triangulus* have been recorded from the Cenomanian of USA (Groot et al., 1961; Brenner, 1967; Canright & Carter, 1980), Egypt (Schrank, 1987), the late Albian-Turonian of the Atlantic Coastal Plain (Doyle & Robbins, 1977) and the Turonian of Portugal and southern France (Medus et al., 1980). Thus and van der Eem (1985) recorded *Nyssapollenites* sp. from the late Albian-early

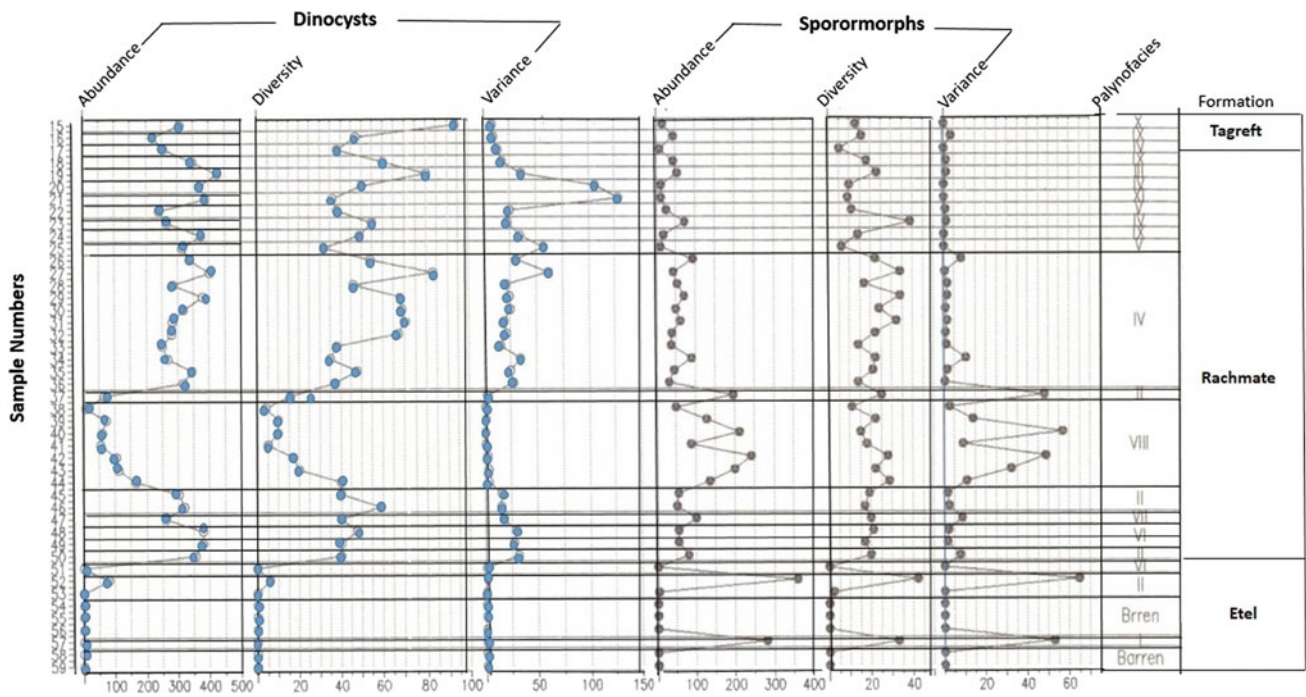


**Fig. 4** Abundance, diversity and variance distribution graphs for dinocysts and sporomorphs across the study Upper Cretaceous section

Cenomanian of NE Libya. Species of *Gabonisporis* have been recorded world-wide, with their first occurrence in the Cenomanian. *Gabonisporis pseudoreticulatus* is known from the late Albian-basal Turonian of Gabon (Boltenhagen, 1975), and *Gabonisporis bacaricumulus* has a recorded stratigraphic range spanning the Turonian to Danian (Srivastava 1972; Wang and Zhao 1980). However, based on the presence of species of *Nyssapollenites* and *G. bacaricumulus*, an amended late Cenomanian–Turonian age is suggested.

Albian to early Cenomanian age is not supported herein due the absence of typical components such as elaterate pollen (*Elaterosporites*, *Elaterocolpites* and *Elateroplicites*) and species of *Afropollis*, *Cretacaeiporites*, *Sofrepites* and *Galeacornea* and the triporate and *Classopollis* assemblages which have been reported by Thusu and van der Eem (1985) and Keegan and Stead (2007) from the early Cenomanian of NE Libya and neither reported by Bu-Argoub (1996) from SE Sirt Basin. However, the absence of elaterates in the studied samples possibly could be due to an unknown ecological factor (El Atfy, 2021).

### Association 2

**Age:** late Cenomanian–Turonian.

**Interval:** 8588'–8591'.

This association is characterised by impoverished terrestrial and marine taxa and differs from the preceding and succeeding associations by its poor recovery and lack of angiosperm pollen. The terrestrial assemblage consists mainly of *Gabonisporis bacaricumulus* and *Gabonisporis*

spp., and the marine taxa include *Palaeohystrichophora infusorioides* and *Alterbidinium ?acutulum*.

The poor recovery of this association necessitates a tentative age assignment based on its stratigraphic position between Association 1 and Association 3, as late Cenomanian–Turonian.

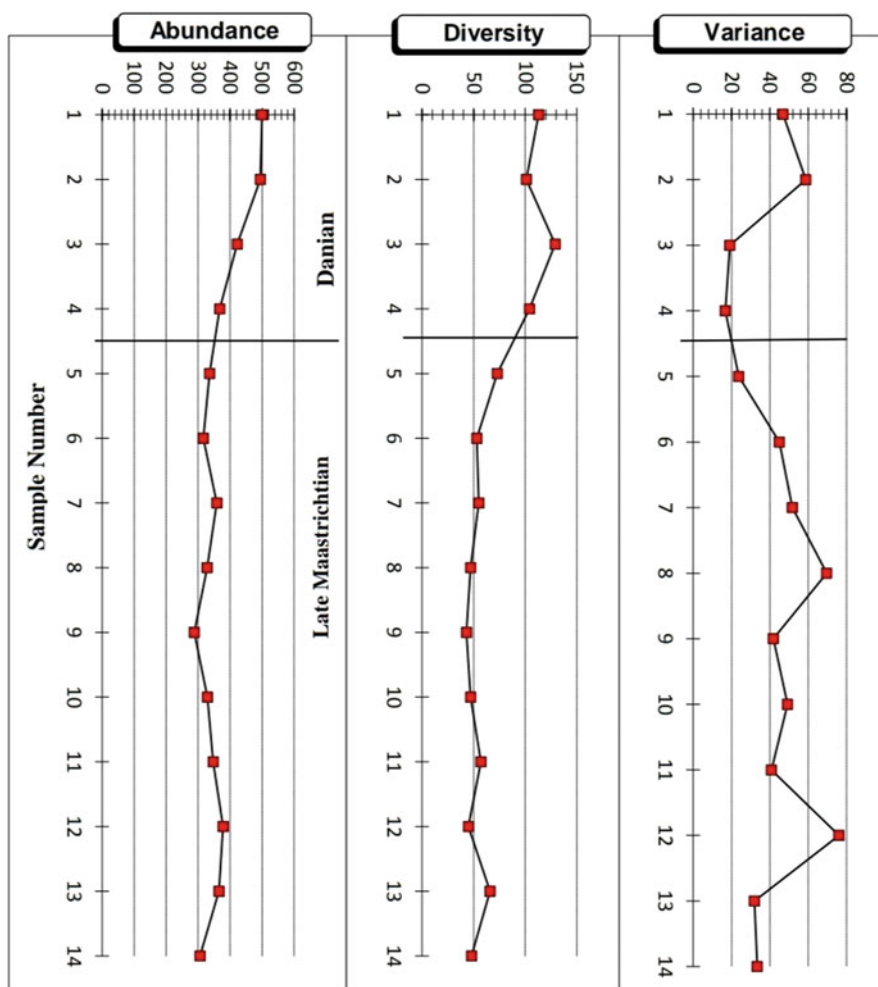
### Association 3

**Age:** late Cenomanian–Turonian.

**Interval:** 8584'–8588'6".

This association is characterised by an overwhelming predominance of pteridophyte spores (52%), including common *Cyathidites minor* and *C. australis*, common *Triporoletes* spp. The association includes the first occurrence of the water fern *Ariadnaesporites verrucatus* (common), which is generally known from Coniacian to Campanian sediments. Angiosperm and gymnosperm pollen are also common and are represented by common appearance of *Ephedripites*, including *E. montanaensis* and *E. ovalis* and *Araucariacites australis*, respectively. Other characteristic events include the first occurrence of *Foveotriletes* cf. *subtriangularis* (*F. subtriangularis*, Albian–Cenomanian, USA), *Perotriletes pannuceus* (Albian–Cenomanian, Senegal, Tunisia, Peru, Brazil, Egypt, NE Libya, Sudan) and *Stellatopollis* spp. (mainly known from Early Cretaceous) and the occurrence of *Gabonisporis pseudoreticulatus* (late Albian–basal Turonian, Gabon). The dinocysts represent 7.2% of the total palynomorph assemblages. They are characterised by rare assemblages of *Palaeohystrichophora infusorioides*,

**Fig. 5** Abundance, diversity and variance distribution graphs for dinocysts across the study K/Pg boundary section



*Exochosphaeridium phragmites*, *Coronifera oceanica* and presence of new peridinioid forms, which are kept in open nomenclature for the time being.

Based on the sporomorph content, a late Cenomanian–Turonian age has been suggested for this association. The Albian and early Cenomanian are not considered to be represented herein, due to the absence of the index taxa mentioned under Association 1. The presence of *A. verrucatus* in this horizon may extend its range down to the late Cenomanian. The absence of Coniacian index taxa such as *Droseridites senonicus* and *Longapertites marginatus*, which are present in the subsequent association precludes a Coniacian age being considered for this association.

#### Association 4

**Age:** late Cenomanian–Turonian.

**Interval:** 8580'–8581'6".

This association is characterised by up to 75% of dinocysts including abundant *Canningia reticulata*, common *Florentinia* spp., species of *Exochosphaeridium* (including *E. bifidum*, *E. phragmites*) and present to common

*Florentinia laciniata* var. A. The dinocysts marker event for this association includes the first occurrences of new varieties of peridinioid dinocysts. Characteristic sporomorphs in this association include excessive percentages of *Ariadnaesporites verrucatus*, the first occurrence of *Lycopodiumsporites* sp. A and decline in *Ephedripites* species. Stratigraphically important dinocyst events include the first occurrence of *Eurydinium ingramii*, which is mainly recorded from the Albian to Cenomanian of western Australia (Cookson & Eisenack, 1971) and the Turonian of offshore SW Africa (Davey, 1978); the first occurrence of *Odontochitina cribropoda*, which is known from the Early Cretaceous of India (Jain & Taugourdeau-Lantz, 1973), the Senonian of Australia (Deflandre & Cookson, 1955) and offshore SW Africa (Davey, 1978) and the Coniacian of France (Foucher, 1979); the first occurrence of *O. costata*, known from the Aptian to Maastrichtian world-wide, and the first occurrence of *Xenascus plotei* is known from the Albian to early Cenomanian of Libya (Uwins & Batten, 1988) and the Aptian to Cenomanian of Morocco (Below, 1981).

Occurrence of *O. costata*, *X. plotei* and *E. phragmites* in this association together with *Eurydinium ingramii* all

Late Cretaceous						Paleocene	Age	Selected Dinocysts
Cenomanian	Turonian	Coniacian	Santonian	Campanian	Maastricht.	Danian		
Etel	Rachmat			Tagrifet.	Sirt	Hagfa	Formation	
							<i>Ascodinium serratum</i>	
							<i>Dapsilidinium ? pumilum</i>	
							<i>Formea granulata</i>	
							<i>Litosphaeridium arundum</i>	
							<i>Trithyrodinium suspectum</i>	
							<i>Heterosphaeridium heteracanthum</i>	
							<i>Eurydinium ingramii</i>	
							<i>Dapsilidinium pumilum</i>	
							<i>Pseudoceratium polymorpha</i>	
							<i>Dinogymnium digitus</i> subsp. <i>Crassum</i>	
							<i>Dinogymnium vozhenikovae</i>	
							<i>Pseudoalterbia concinna</i>	
							<i>Trithyrodinium rhomboideum</i>	
							<i>Odontochitina cribropoda</i>	
							<i>Canningia kukebaiensis</i>	
							<i>Aiora fenestrata</i>	
							<i>Alterbidinium acutulum</i>	
							<i>Palaeocystodinium denticulatum</i>	
							<i>Xenascus australensis</i>	
							<i>Xenascus plotei</i>	
							<i>Dinogymnium acuminatum</i>	
							<i>Isabelidinium acuminatum</i>	
							<i>Spinidinium echinoideum</i>	
							<i>Spiniferites supparus</i>	
							<i>Nematosphaeropsis</i> sp. A var. nov.	
							<i>Nematosphaeropsis</i> sp. B var. nov.	
							<i>Isabelidinium glabrum</i>	
							<i>Eurydinium</i> var. A. nov.	
							<i>Eurydinium tempestivum</i>	
							<i>Nematosphaeropsis</i> var. D. nov.	
							<i>Dinogymnium microgranulosum</i>	
							<i>Dinogymnium sphaerosphalum</i>	
							<i>Hystrichosphaeridium recurvatum recurvatum</i>	
							<i>Xenascus gochtii</i>	
							<i>Xenascus sarjeantii</i>	
							<i>Xenascus serpaglii</i>	
							<i>Alterbidinium emulatum</i>	
							<i>Cerodinium boloniense</i>	
							<i>Senegalinium laevigatum</i>	
							<i>Spiniferites ramosus granomembranaceus</i>	
							<i>Chatangiella madura</i>	
							<i>Chatangiella specabilis</i>	
							<i>Eucladinium madurensis</i>	
							<i>Dinogymnium albertii</i>	
							<i>Alterbidinium minus</i>	
							<i>Chatangiella microcantha</i>	
							<i>Chatangiella verrucosa</i>	
							<i>Fromea chytra</i>	
							<i>Senegalinium bicavatum</i>	
							<i>Senegalinium laevigatum</i>	
							<i>Heslertonia cylindrata</i>	
							<i>Rottnestia borussica</i>	
							<i>Spiniferites pseudofurcatus</i>	
							<i>Spiniferites wetzelii</i>	
							<i>Odontochitina tabulata</i>	
							<i>Manumiella lata</i>	
							<i>Nelsoniella aceras</i>	
							<i>Nelsoniella tuberculata</i>	
							<i>Dinogymnium cooksoniae</i>	
							<i>Nematosphaeropsis grande</i>	
							<i>Xenascus</i> sp. A var. nov.	
							<i>Amphorosphaeridium fenestratum fenestratum</i>	
							<i>Amphorosphaeridium multibrevum</i>	
							<i>Andalusiella gabonensis</i>	

Fig. 6 a, b Stratigraphic ranges of selected important dinocysts through the study section.

Late Cretaceous						Paleocene		Age	Selected Dinocysts
Cenomanian	Turonian	Coniacian	Santonian	Campanian	Maastricht	Danian	Formation		
								<i>Andalusiella polymorpha polymorpha</i>	
								<i>Areoligera coronata</i>	
								<i>Dinogymnium decorum</i>	
								<i>Dinogymnium digitus digitus</i>	
								<i>Dinogymnium nelsonense</i>	
								<i>Dinogymnium westralium</i>	
								<i>Senegalinium bicavatum</i>	
								<i>Chatangiella? Biapertura</i>	
								<i>Diphyes colligerum</i>	
								<i>Andalusiella polymorpha aegyptica</i>	
								<i>Andalusiella polymorpha</i> subsp. A var. nov.	
								<i>Senonisphaera</i> sp. A var. nov.	
								<i>Andalusiella ?Dubia</i>	
								<i>Spinidinium ornatum</i>	
								<i>Yolkinigymnium elongatum</i>	
								<i>Cerodinium diebelii</i>	
								<i>Cerodinium granulostriatum</i>	
								<i>Cerodinium leptodermum</i>	
								<i>Cerodinium pannuceum</i>	
								<i>Manumiella</i> sp. A var. nov. □	
								<i>Cordosphaeridium fibrospinosum</i>	
								<i>Phelodinium magnificum</i>	
								<i>Phelodinium trispis</i>	
								<i>Senegalinium microgranulatum</i>	
								<i>Trithyrodinium evittii</i>	
								<i>Andalusiella ivorensis</i>	
								<i>Dinogymnium avellana</i>	
								<i>Pierceites pentagona</i>	
								<i>Ammphorosphaeridium multibrevum</i>	
								<i>Apteodinium australense</i>	
								<i>Areoligera volata</i>	
								<i>Cerodinium striatum</i>	
								<i>Cordosphaeridium gracile</i>	
								<i>Cordosphaeridium inodes</i>	
								<i>Dissphaerogena carposphaeropsis</i>	
								<i>Fibradinium annetorpense</i>	
								<i>Fibrocysta licia</i>	
								<i>Glaphyrocysta reticulosa</i>	
								<i>Heteralacysta granulata</i>	
								<i>Impagidinium dispersitum</i>	
								<i>Palynodinium spongiosum</i>	
								<i>Rendinium gracile</i>	
								<i>Palaeocystodinium australinum</i>	
								<i>Palaeocystodinium golzowense</i>	
								<i>Palaeocystodinium lidiae</i>	
								<i>Spiniferites hylospinosus</i>	
								<i>Spiniferites hyperacanthus</i>	
								<i>Turbiosphaera filosa</i>	
								<i>Carpatella cornuta</i>	
								<i>Hystrichokolpoma granulatum</i>	
								<i>Hystrichostrogylon membraniphorum</i>	
								<i>Kenleyia lophophora</i>	
								<i>Kenleyia pachycerata</i>	
								<i>Lejeuncysta globosa</i>	
								<i>Manumiella conorata</i>	
								<i>Manumiella seelandica</i>	
								<i>Nematosphaeropsis</i> sp. C var. nov.	
								<i>Phelodinium boldii</i>	
								<i>Pyxidopsis ardonensis</i>	
								<i>Alisocysta circumtabulata</i>	
								<i>Cordosphaeridium cantharellum</i>	
								<i>Cordosphaeridium exilimurum</i>	
								<i>Cribroperidinium intricatum</i>	
								<i>Danea californica</i>	
								<i>Danea impages</i>	
								<i>Danea manicata</i>	
								<i>Fibrocysta axialis</i>	
								<i>Fibrocysta furcata</i>	
								<i>Fibrocysta lappacea</i>	
								<i>Fibrocysta radiata</i>	
								<i>Fibrocysta vectensis</i>	
								<i>Hystrichostrogylon holoyemium</i>	
								<i>Hystrichokolpoma cinctum</i>	
								<i>Impagidinium maculatum</i>	
								<i>Impagidinium parvireticulatum</i>	
								<i>Kallosphaeridium capulatum</i>	
								<i>Lingulodinium machaerophorum</i>	
								<i>Spinidinium pilatum</i>	
								<i>Tenua formosa</i>	
								<i>Xuidinium laevigatum</i>	
								<i>Muratodinium fimbriatum</i>	

Fig. 6 (continued)

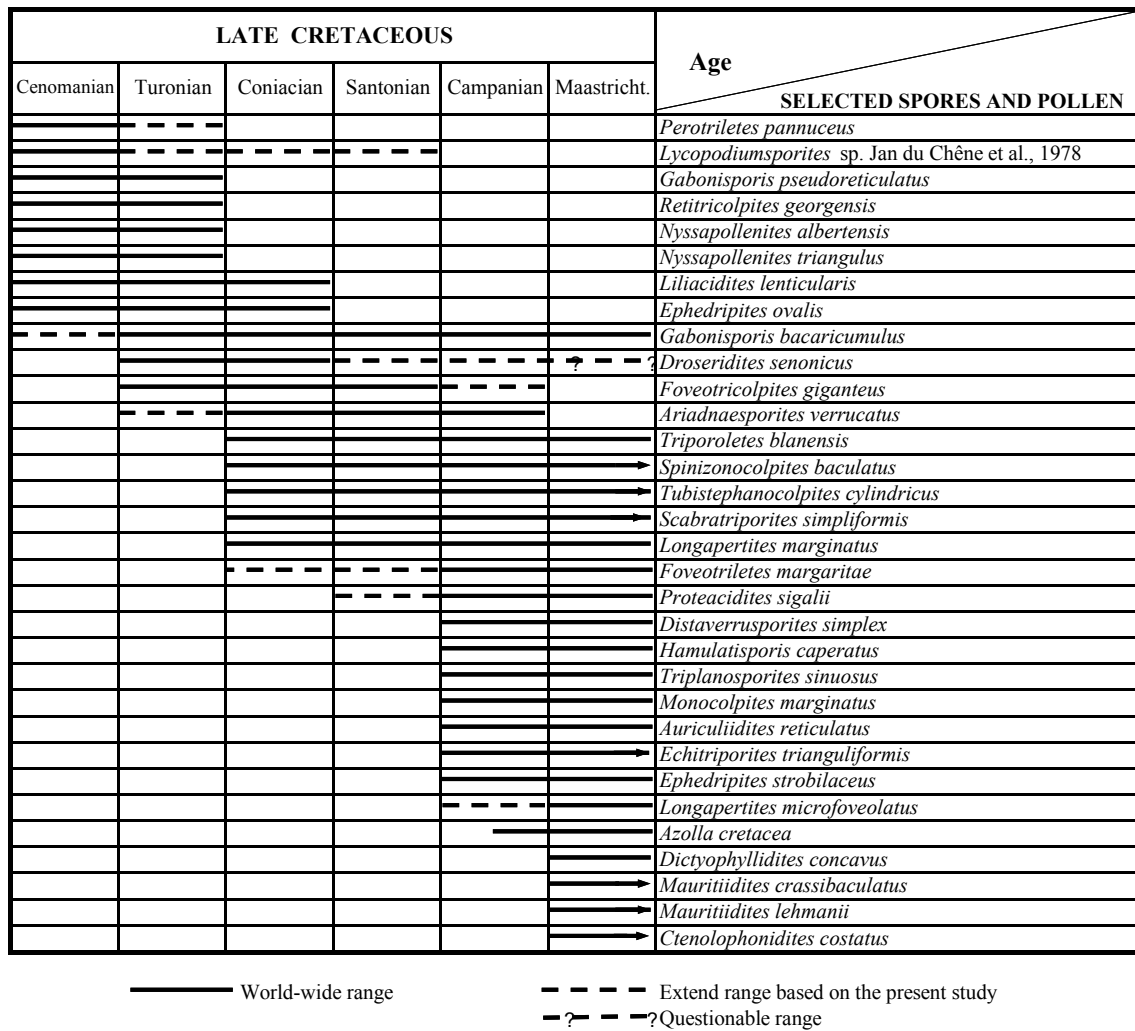


**Fig. 7** Stratigraphic ranges of selected important spores and pollen grains through the study section

support a late Cenomanian–Turonian. A younger Coniacian age is not considered likely due to the absence of *Droseridites senonicus* and *Longapertites marginatus*, which have their first appearance in the succeeding Association 6.

#### Association 5

**Age:** Coniacian-Santonian

**Interval:** 8562'–8578'6"

This association is marked by a decline in the frequency of two dinocysts which are dominated the preceding association: *Canningia reticulata* and *Florentinia* spp. It is also characterized by an influx of *Exochosphaeridium phragmites* (10.4 at the base), *Subtilisphaera cheit* (9.3 at the base) and the angiosperm pollen *Monocolpopollenites* sp. (2% at the base and 5.9 at the top) and the first occurrence and influx of *Nematosphaeropsis* species (7.8% at the base), including *N. fragilis*, and other two new varieties *Nematosphaeropsis* sp. A var. nov. and *Nematosphaeropsis* sp. B var. nov. (Plate 8, Figs. 1, 2, 5 and 6).

Few sporomorphs make their first occurrences in this association include the important Coniacian-Santonian angiosperm pollen *Droseridites senonicus* which is known from Senegal, the Ivory Coast (Jardiné & Magloire, 1965), Nigeria (Mebradu, 1982; Lawal & Moullade, 1986; Odébodé, 1987), Sudan (Kaska, 1989); *Longapertites marginatus* has been reported from the Santonian to Maastrichtian of SE Nigeria (Lawal & Moullade, 1986). The trilete spore *Triporoletes blanensis*, known from the Early Senonian of Czechoslovakia (Pacltovà, 1961), the Senonian of Nigeria (Lawal & Moullade, 1986; Jan du Chêne et al., 1978), also shows its first occurrence in this association together with *Foveotriletes margaritae*. The latter known from the Campanian to Maastrichtian of Nigeria (Van Hoeken-Klinkenberg, 1966, Jan du Chêne, 1980, Salami, 1990) and the Maastrichtian of Tunisia (Méon, 1990).

This association assigned to a Coniacian-Santonian age based on the first occurrences of *D. senonicus*, *L. marginatus* and *T. blanensis*, all of which make their first appearance in

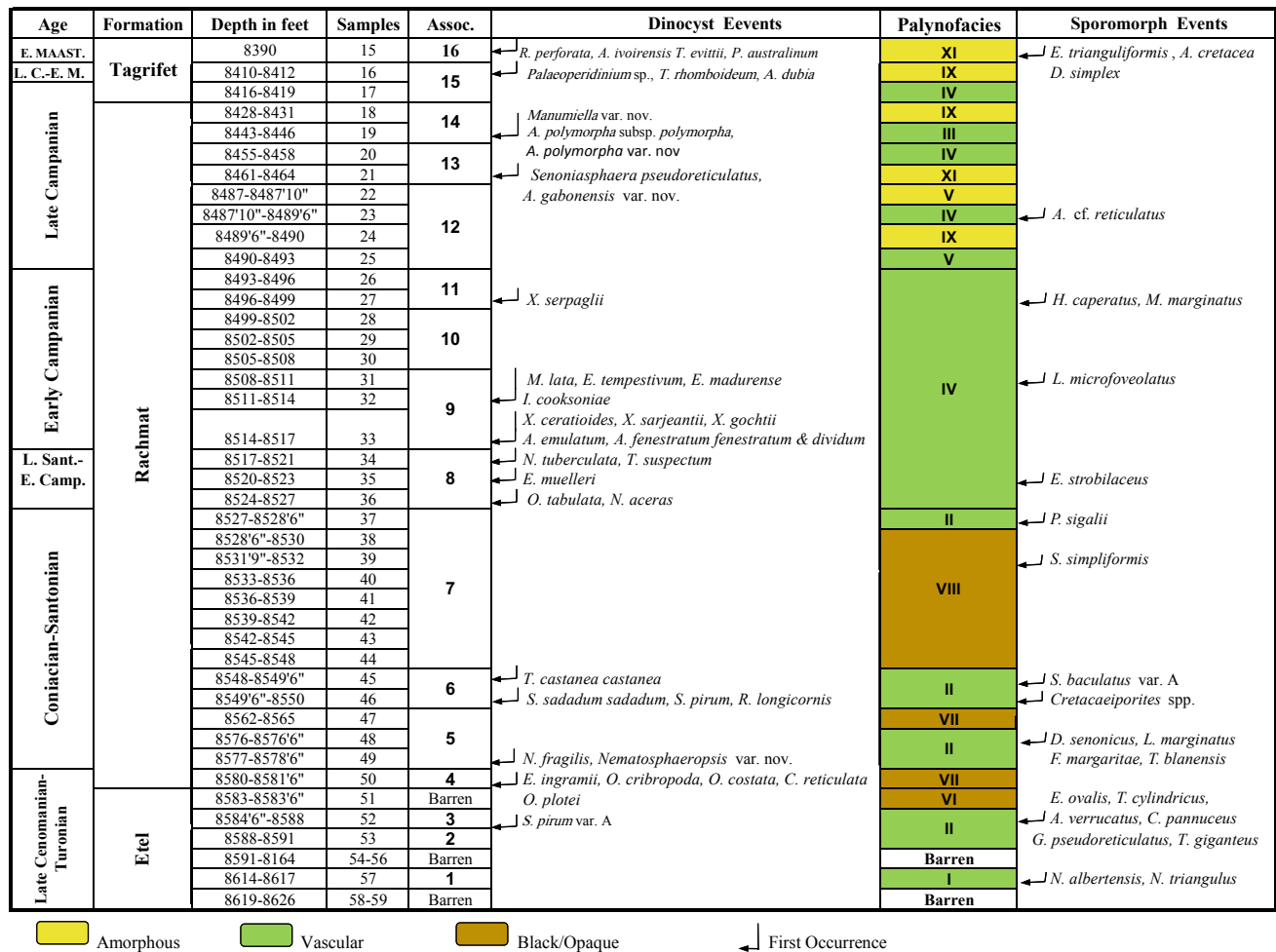


**Fig. 8** Summarized palynostratigraphy, palynofacies and palynomorph events recorded in the study Upper Cretaceous section

the Coniacian. This supported by the absence of the index Campanian-Maastrichtian dinocyst assemblage, which make their first occurrence in the succeeding Association 6.

The first occurrence of the chorate dinoflagellate cysts *Nematosphaeropsis* spp. at the base, and the angiosperm pollen *Droseridites senonicus* and *Longapertites marginatus* at the top considered as a datum event for this association.

#### Association 6

**Age:** Coniacian-Santonian.

**Interval:** 8548'-8550'.

This association is marked by a decline in some of the taxa which are typical of Association 5. These include species of *Nematosphaeropsis* spp., *Exochosphaeridium phragmites*, *Subtilisphaera cheit* and the angiosperm pollen *Monocolpopollenites* sp. An influx of *Coronifera minus* (7.6–10.5%), *Palaeohystrichophora infusorioides* (6.7–9.1), *Hystrichodinium pulchrum* (2.7%) is also notable. This association also contains an influx of sporomorphs including

*Cyathidites australis*, *Todisporites major*. The most characteristic dinocyst events of this association are the first occurrences of *Trichodinium castanea* subsp. *castanea*. Rare specimens of the angiosperm pollen *Droseridites senonicus* are also identified in this association.

The age of this association is suggested to be Coniacian-Santonian based on the presence of *D. senonicus*.

#### Association 7

**Age:** Coniacian-Santonian.

**Interval:** 8527'-8548'.

This association is marked by a decline in most of the dinocyst assemblages encountered in the former associations. Association 7 is characterised by an overwhelming predominance of pteridophyte spores (21.9–59.8%), including *Cyathidites minor*, *C. australis*, *Todisporites minor*, *T. major* and *Cyathidites* sp. A, and an influx of Trilete spore form D (12.1%) and the water fern *Ariadnaesporites verrucatus* (9.6%) which characterise the base and the top of this

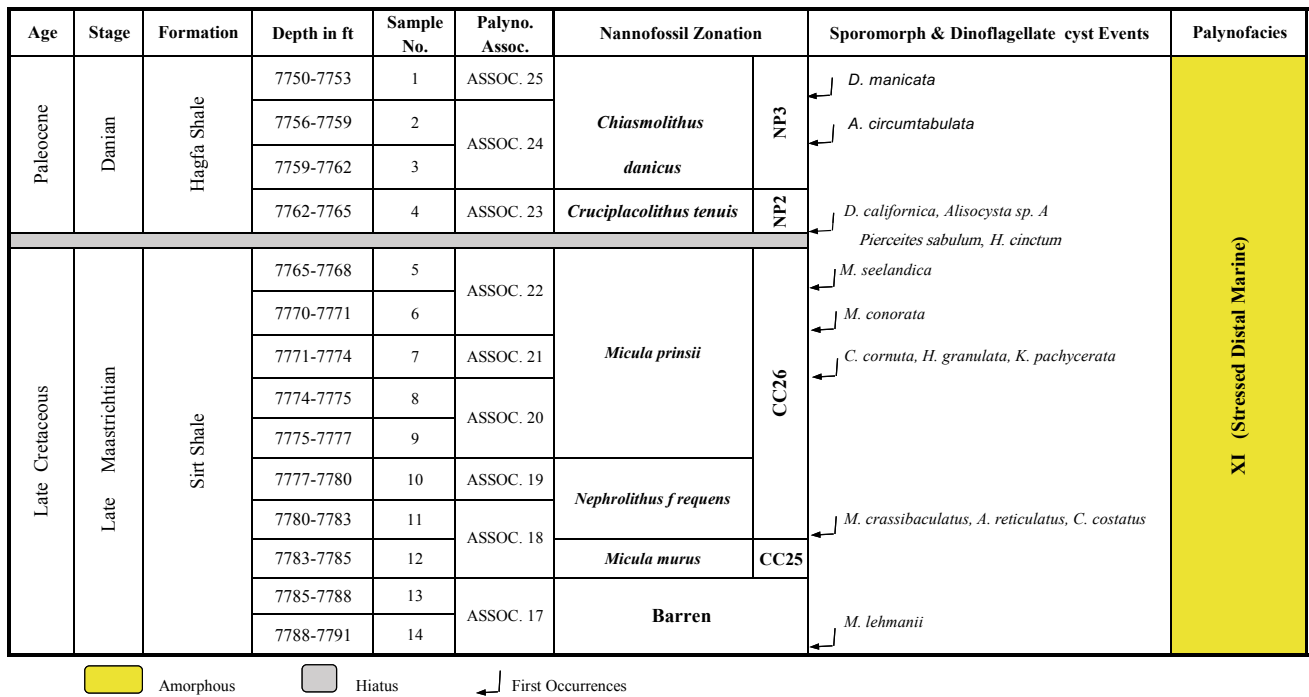
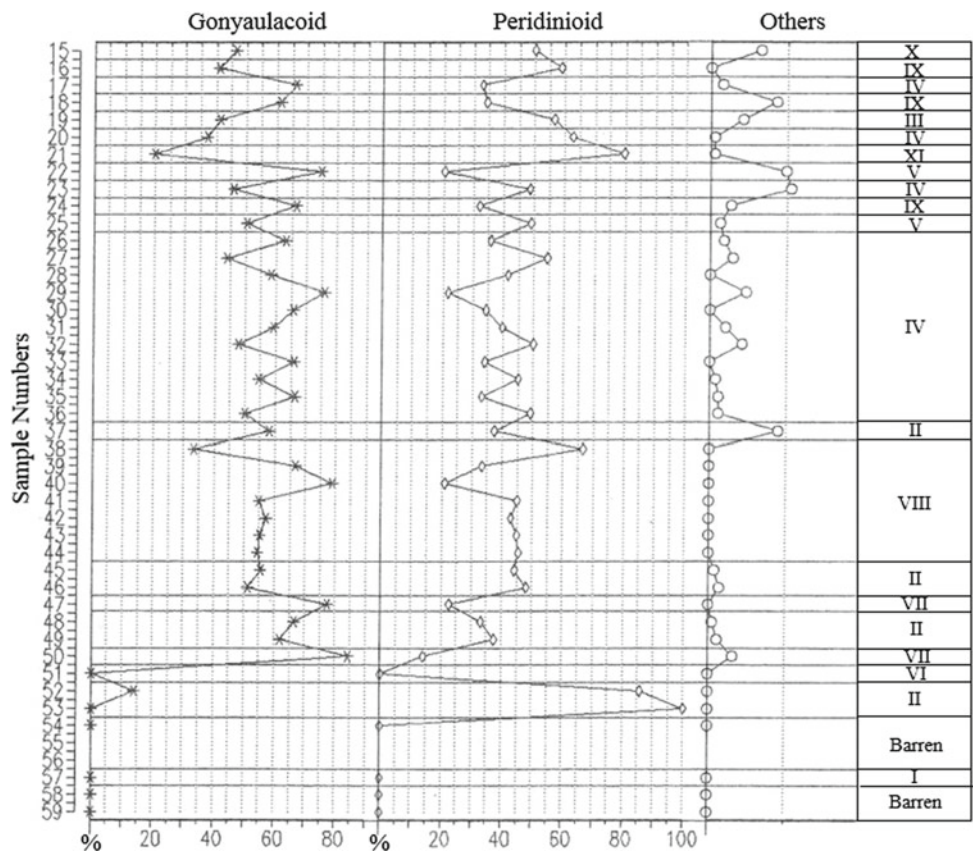


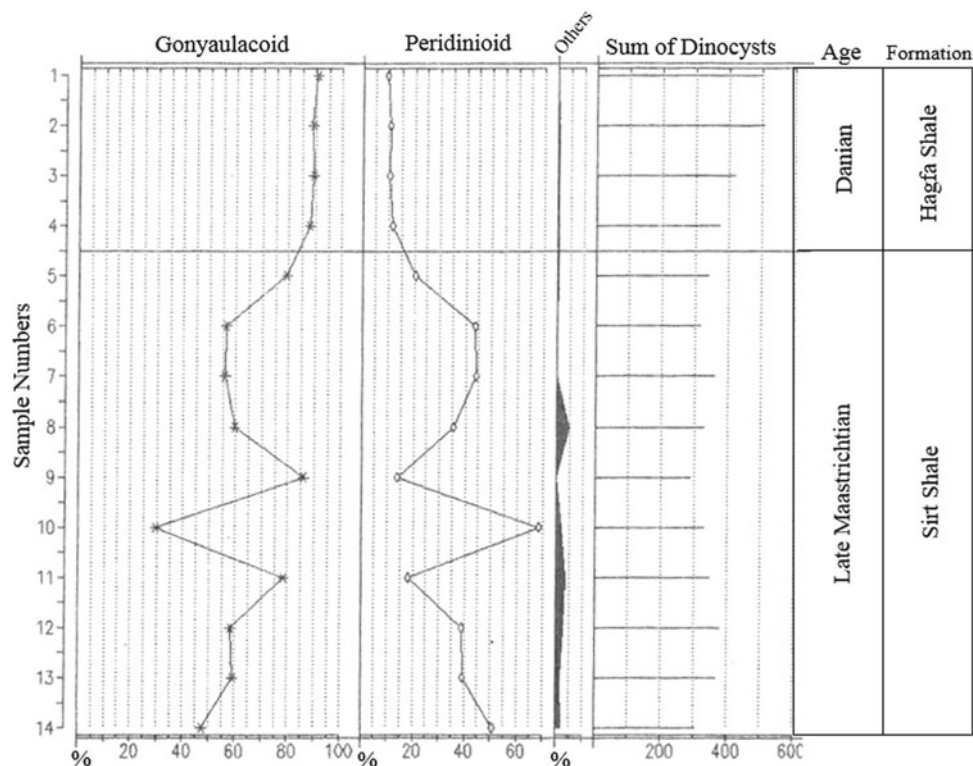
Fig. 9 Summarized palynostratigraphy, palynofacies and palynomorph events across the study K/Pg boundary section

Fig. 10 Frequency distribution of the gonyaulacoid and peridinioid dinocysts in the Upper Cretaceous section





**Fig. 11** Frequency distribution of the gonyaulacoid and peridinioid dinocysts across the K/Pg boundary section



association, respectively. *Droseridites senonicus* shows a rare percentage at the base of this association (interval 8545'–8548'). The most characteristic dinocysts include *Eurydinium ovatum* which makes its first occurrence 3 ft above the base of this association (interval 8542'–8545'). The top is characterised by the first occurrence of the angiosperm pollen *Scabratrporites simpliformis*, which occurs at 8531' 9"–8532'; this pollen is known from the Senonian of Senegal, Ivory Coast (Jardiné & Magloire, 1965) and the Maastrichtian of Nigeria and Egypt (Jan du Chêne et al., 1978; Schrank, 1987, respectively) and the Paleocene of Nigeria (Van Hoeken-Klinkenberg, 1966). A single grain of the angiosperm pollen *Proteacidites sigalii* is recorded from the uppermost sample interval 8527'–8528'6"; this type of pollen is known from the Campanian to Maastrichtian of Egypt (Schrank, 1987; Sultan, 1985), NE Nigeria (Lawal & Moullade, 1986) and Gabon (Boltenhagen, 1978).

This association is dated as Coniacian-Santonian based on its relative stratigraphic position between Association 6 (Coniacian-Santonian) and Association 8 (Santonian-early Campanian). The presence of a single specimen of *P. sigalii* (Campanian–Maastrichtian), if not due to contamination, extends its range down to the Coniacian.

This association is characterised by a distinctive "High-Energy Distal Marine, Black/Opaque Palynofacies," which represents a major regression in the study section during the Coniacian-Santonian time. For more details on this interval, see the discussion in the palynofacies section below.

#### Association 8

**Age:** late Santonian-early Campanian.

**Interval:** 8517'–8527'.

By comparison with Association 7, this association is dominated by dinocysts and is characterised by an influx of *Palaeohystrichophora infusorioides* (12.3–21.9%), *Subtilisphaera cheit* (4.4–8.2%), *Canningia reticulata*, *Cyclonephelium chabaca*, *Florentinia mantellii* and species of *Nematosphaeropsis* spp. (1.9–5%). New varieties of *Nematosphaeropsis* also have been recorded from this association. This association is marked by a decline in sporomorphs characteristic of the preceding association.

The most important stratigraphic events to occur in this association include the first occurrence of *Nelsoniella aceras* and *Odontochitina tabulata* at the basal part; the middle part is distinguished by first occurrence of *Nematosphaeropsis grande* and *Exochosphaeridium muelleri*, whereas the top part is noted by the first occurrence of *Nelsoniella tuberculata* and *Trithyrodinium suspectum* (8517'–8521'). *N. aceras* and *N. tuberculata* have previously been recorded from the late Santonian to early Campanian of Australia (Cookson & Eisenack, 1960, 1982; Ingram, 1982; Helby et al., 1987); *N. aceras* has been recorded by Keegan and Stead (2007) from Cyrenaica Platform, NE Libya (T1-41 Well) but did not show its stratigraphic range or interval. Recently, Mansour et al. (2020) have reported *N. aceras*, *N. tuberculata* and *Trithyrodinium suspectum* from their newly established *Dinogymnium acuminatum-Nelsoniella aceras-*

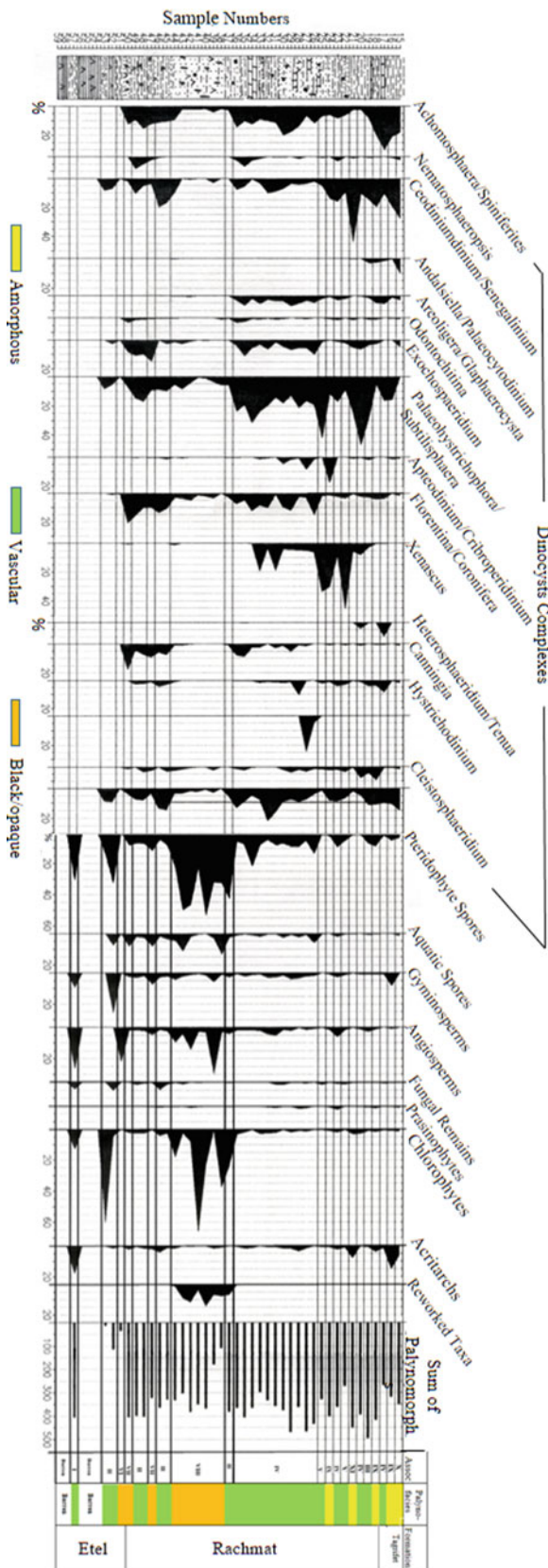


**Fig. 12** Frequency distribution of the dinocyst complexes, miospore and other palynomorph groups in the Upper Cretaceous section

*Odontochitina porifera* assemblage zone, which has been assigned to a Santonian age. *E. muelleri* has been recorded from the early Senonian of Germany (Yun, 1981) and early Campanian of Australia (Marshall, 1984). *N. grande* is known from the Campanian of Ghana (Davey, 1975) and is recorded as “*Unipontidium*” *grande* from the Late Santonian-Early Campanian of NE Libya (Keegan & Stead, 2007). Sporomorphs that first occur in this association include *Ephedripites strobilaceus*, known from the Campanian to Paleogene of Nigeria (Salami, 1984, 1990).

Consistent with the present finding, Helby et al. (1987) examined the palynomorphs from Albian to Danian sediments from Australia and established several range zones, one of which is *Nelsoniella aceras* zone, of late Santonian-early Campanian age. This zone is considered herein to equate with Association 8. This is supported by the mutual occurrences of *N. aceras*, *N. tuberculata*, *Palaeohystrichophora infusorioides* and *Isabelidium* spp. Also, Mao Shaozhi and Mohr (1992) documented the first occurrence of *N. aceras* from the Dinocyst Zone A in the ?late Santonian-early Campanian of the Southern Indian Ocean.

The tabulated certioide *Odontochitina tabulata* El-Mehdawi, 1998, with the epicavate peridioid cysts listed above is considered as a marker species for this association.

From the above discussion, this association is ascribed to the late Santonian-early Campanian age.

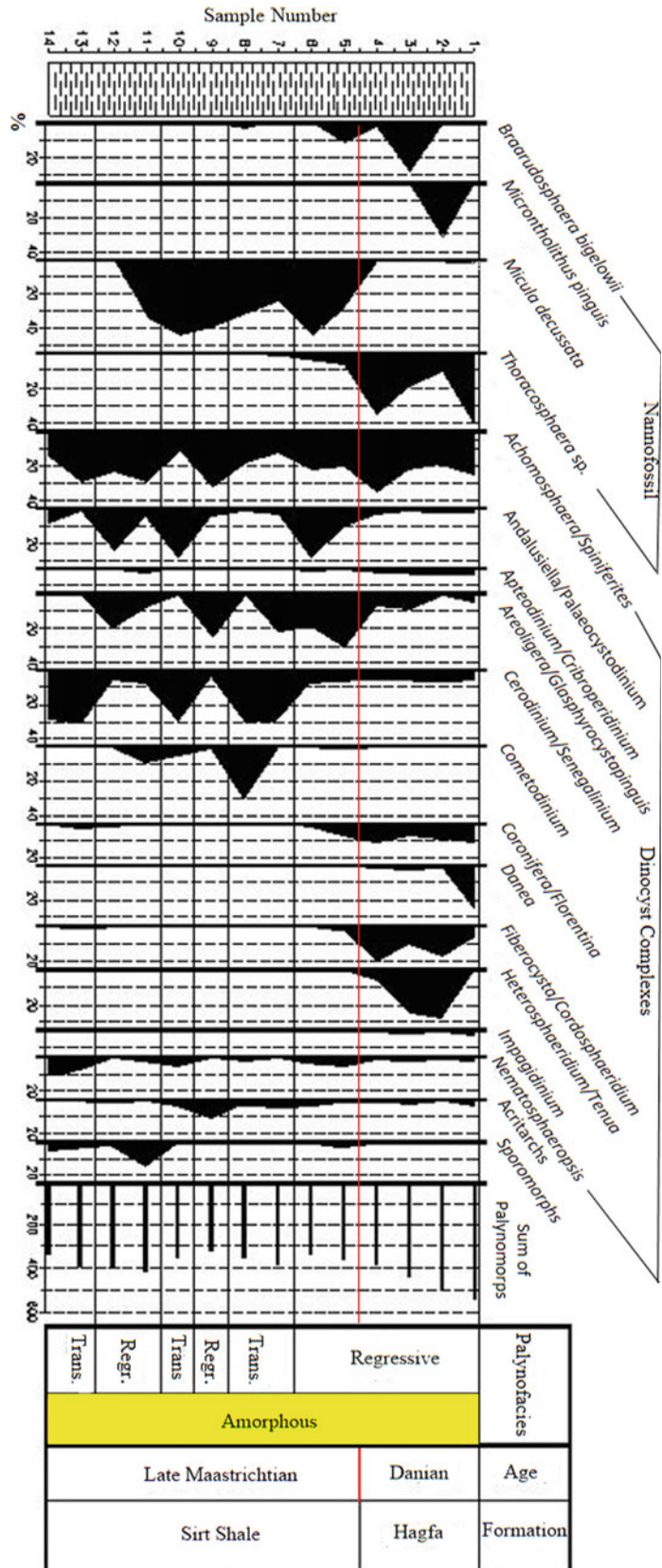
**Association 9**

**Age:** early Campanian.

**Interval:** 8508’-8517’.

This association is characterised by a decline in *Nelsoniella aceras*, *N. tuberculata*, *Florentinia mantellii*, *Nematosphaeropsis* species, *Palaeohystrichophora infusorioides*, the absence of *Odontochitina tabulata* and *Eurydinium ovatum* and an influx of *Cyclonephelium chabaca*. Important stratigraphic events that occur in this association include the first occurrence of dinocysts *Alterbidinium emulatum* (common), *Amphorosphaeridium fenestratum* subsp. *fenestratum*, *A. fenestratum* subsp. *dividum* (present), *Cribroperidinium cooksoniae* (rare), *Eucladinium madurense* (rare), *Eucladinium* sp. A and *Eucladinium* sp. B (rare), *Eurydinium tempestivum* (present), *Isabelidium acuminatum* (present), *I. cooksoniae* (present), *Manumiella lata* (rare), *Palaeohystrichophora granulata* (rare), *Pseudoalterbia concinna* (rare), *Xenascus ceratioides* (common), *X. gochtii* (present) and *X. sarjeantii* (common). The sporomorph *Longaperites microfoveolatus* first occurs at the top of this association (interval 8508’-8511’). *A. fenestratum* subsp. *fenestratum* and *A. fenestratum* subsp. *dividum* have previously been reported from the Campanian to Maastrichtian of South Africa in association with *Exochosphaeridium bifidum*,

**Fig. 13** Frequency distribution of the dinocysts complexes, miospores groups and nannofossil blooms across the K/Pg boundary blooms across the K/Pg boundary section. Nannofossil data after El-Mehaghag (1996)



Depth in ft.	Sample No.	Formation	Age	Palynofacies	Deposition Environment	Characteristic Features
5550-7765	1 to 4	Hagfa Shale	Danian	(Palynofacies XI) Distal Marine	Stressed marine with variable salinities	High diversity and abundance of gonyaulacoid cysts; presence of distinctive blooms of calcareous nannofossils & dinoflagellate cyst complexes.
7765-7791	5 to 14	Sirt Shale	Maastrichtian	(Palynofacies X) Distal Marine	Normal marine, dysaerobic-anoxic	High diversity and abundance of peridinioid cysts, blooms of nannofossils and dinocyst complexes are distinctive.
8390	15	Tagrifi	L. Camp.- E. Maastrichtian	(Palynofacies IX) Proximal Marine	Normal salinity, oxygenated	Diverse palynomorphs. Diatoms and diatom fragments present.
8410-8412	16			(Palynofacies IV) Distal Marine	Normal marine with high terrestrial supply	Common acritarchs, with presence of reasonable amount of fine black/opaque and vascular debris.
8416-8419	17	Rachmat	Cenomanian-Campanian	(Palynofacies IX) Proximal Marine	High energy Aerobic to dysaerobic	Dominated by large vascular debris but with rare sporomorphs.
8428-8431	18			(Palynofacies III) Proximal Marine	Reduced salinity & high energy	High percentages of <i>Senegalinium/Cerodinium</i> and <i>Achomphaera/Spiniferites</i> complexes. Diatoms are recognised.
8443-8446	19			(Palynofacies IV) Distal Marine	Probably normal marine Low energy	High sporomorph and peridinioid content.
8455-8458	20			(Palynofacies XI) Distal Marine	Stressed anoxic	Low sporomorphs and high <i>Palaeohystrichophora/Subtilisphaera</i> Complex, presence of prasinophytes and acritarchs.
8461-8464	21			(Palynofacies V) Distal Marine	Aerobic to dysaerobic	<i>Cerodinium granulostriatum</i> 48% of total dinoflagellate cysts
8487-848710"	22			(Palynofacies IV) Distal Marine	Reduced salinity and high energy	Biodegraded vascular debris and abundant <i>Xenascus</i> Complex.
848710"-84896"	23			(Palynofacies IX) Proximal Marine	Marine, aerobic to dysaerobic with high bioactivity.	Dominated by ceratioid and peridinioid cysts, and miospores
848910"-8490	24			(Palynofacies V) Distal Marine	Aerobic to dysaerobic	Common biodegraded <i>Xenascus</i> and <i>Cribroperidinium</i> , amorphous and vascular debris.
8490-8493	25			(Palynofacies IV) Distal Marine	Low energy & occasionally with stressed and reduced salinity.	Dominated by peridinioid and ceratioid cysts.
8493-8527	26 to 36			(Palynofacies II) Proximal Marine	Low energy restricted marine	Finer vascular debris, high sporomorph contents, high percentages of <i>Palaeohystrichophora</i> and <i>Achomphaera/Spiniferites</i> complexes.
8527-85287"	37			(Palynofacies VIII) Distal Marine	High energy	Large vascular debris, with high sporomorphs
85286"-8548	38 to 44			(Palynofacies II) Proximal Marine	Normal marine, low energy	Dominated by equidimensional-shaped black/opaque debris.
8548-85496"	45 to 46			(Palynofacies VII) Proximal Marine	High energy	High terrestrial supply.
8562-8565	47			(Palynofacies II) Proximal Marine	Normal marine, low energy	Large vascular and lath-shaped black/opaque debris.
8576-85786"	48 to 49			(Palynofacies VII) Proximal Marine	Marine, high energy	High terrestrial supply.
8580-85816"	50	(Palynofacies VI) Distal Non-marine	Non- marine, high energy	Large vascular and lath-shaped black/opaque debris.		
8583-85836"	51	(Palynofacies IV) Proximal Marine	Low energy	Common black/opaque debris with fine vascular debris.		
85846"-8591	52-53	Etel	Late Cenomanian-Turonian	(Palynofacies I) Proximal Non-marine	Low energy, ?swamp environm. with stagnant conditions	Large size vascular debris
8591-8614	53 to 56			Barren		
8614-8617	57			Barren		
8619-8626	58 to 59			Barren		

● Vascular ● Black/opaque ● Amorphous

**Fig. 14** Summary of organic palynofacies in the studied Upper Cretaceous and K/Pg boundary sections

*Hystrichodinium pulchrum*, *P. infusorioides* and *Areoligera* sp. (Davey, 1969b); *E. tempestivum* has been recorded from the Turonian to Santonian of the Tarim Basin, China (Mao & Norris, 1988) in association with *A. emulatum*, *P. concinna* and *Eucladinium gambangense*; *E. madurense* from the Senonian strata of the Eucla Basin, W. Australia (Cookson & Eisenack, 1970), and from the Campanian of the S. Dakota, USA (Lentin & Williams, 1980); *I. acuminatum*, *I. cooksoniae*, *E. gambangense* and *E. madurense* from NE Libya (El-Mehdawi, 2008); *M. lata* from the Santonian-Early Campanian of W. Australia (Cookson & Eisenack, 1968) and the Santonian to Campanian of Argentina (Pöthe and Baldis, 1986); the majority of *Xenascus* species are known mainly from Senonian sediments world-wide (Corradini, 1973; Deflandre, 1937; Ioannides, 1986; Yun, 1981; Zaitzeff & Cross, 1971) and the angiosperm pollen *L. microfoveolatus* from the Maastrichtian strata of Nigeria (Lawal & Moullade, 1986). *Isabelidinium acuminatum* and *I. cooksoniae* are important and diagnostic marker species for this association. The former was identified from the ammonite-dated Late Santonian of the Isle of Wight (Clarke & Verdier, 1967).

This association is partially equivalent to the *Satyrodinium haumuriense-Isabelidinium belfastense-Odontochitina operculata* Assemblage Zone established by Mansour et al. (2020) from Egypt and have species in common such as *Eucladinium* sp., *Isabelidinium acuminatum* and *Palaeohystrichophora infusorioides*.

Based on the evidence cited above, an early Campanian age is considered as appropriate for this association.

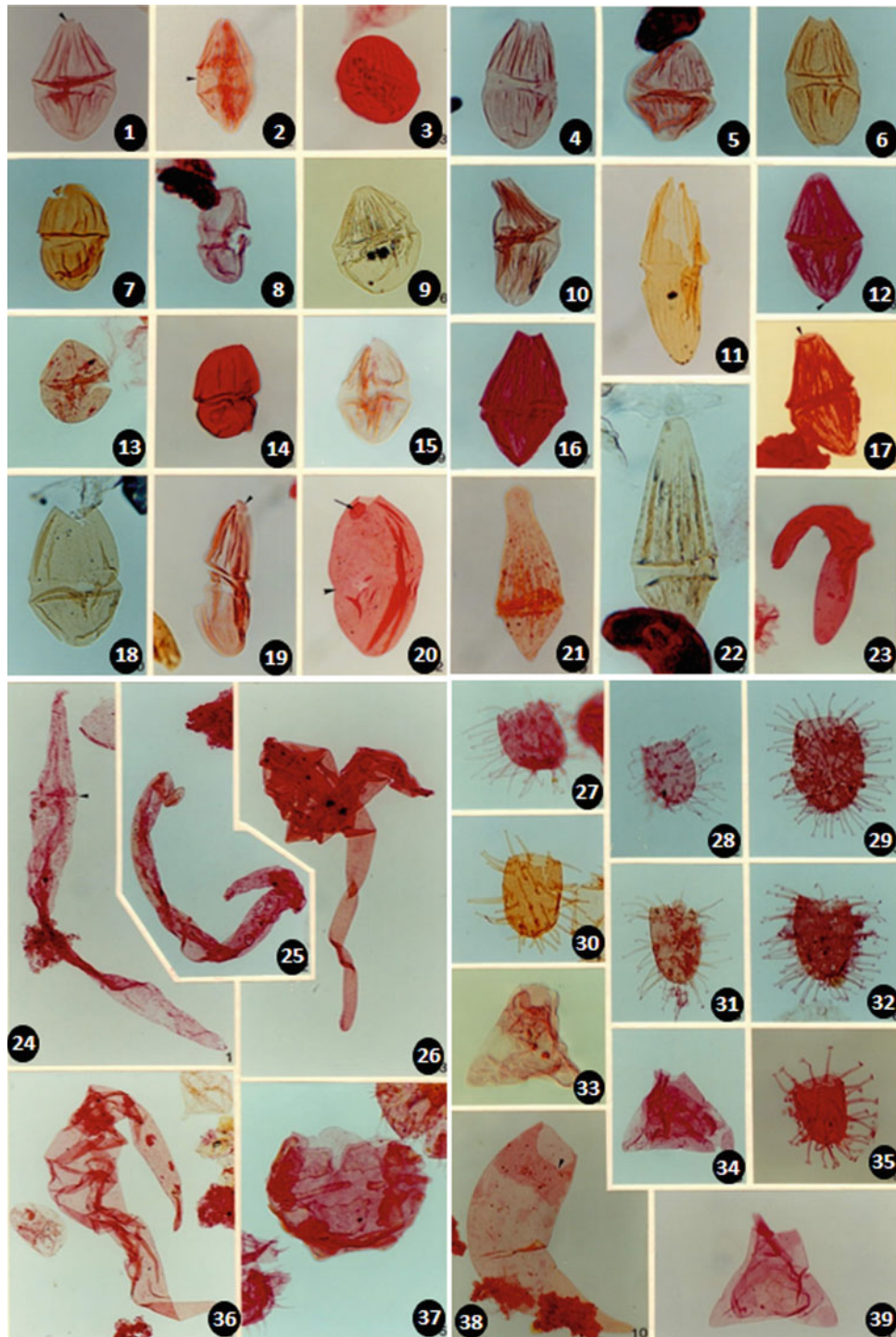
#### Association 10

**Age:** early Campanian.

**Interval:** 8499'-8508'.

This association is marked by a dinocysts decline that were dominant in the preceding association. These include *Alterbidinium emulatum*, *Eurydinium tempestivum*, *Isabelidinium acuminatum*, *I. cooksoniae*, *Xenascus ceratioides*, *X. gochtii*, *X. jolleyi* and *X. sarjeantii*. There is also a complete disappearance of *Amphorosphaeridium* species and an absence of *Eucladinium* species and *Pseudoalterbia concinna*. The association is also characterised by high influx of *Florentinia mantellii*, *F. radiculata*, *Hystrichodinium pulchrum*, *Spiniferites multibrevis*, *S. ramosus* subsp. *ramosus* and a high diversity of *Cribroperidinium* species. Other accessory taxa which make their first occurrence in this association include *Spiniferites mirabilis*, *Chatangiella micracantha*, *Spinidinium ornatum*, *Cribroperidinium intricatum* and *Cerodinium leptodermum*.

This association equates partially with the LPC3 Zone, early Campanian from NE Libya (Keegan & Stead, 2007) and has few species in common. Some of the peridinioid species that have been reported by Keegan and Stead (2007) from their zone (LPC3) including *Andalusiella gabonense*, *Cerodinium granulostriatum* and *Palaeocystodinium*



*australinum* are most probably caved from the younger horizons. In the present study, these are reported from the succeeding associations.

An early Campanian age is considered appropriate for this association based on its stratigraphic position between the well dated early Campanian Associations 9 and 11 and palynofloral

data supplemented by the rare occurrence of *C. micracantha*, which is known from the Campanian of Australia (Cookson and Eisenack 1960) and USSR (Vozzhennikova, 1967), and the high diversity of *Criboperidinium* species. A late Campanian or Maastrichtian age is unlikely due to the lack of important index taxa retrieved in the succeeding associations.

◀ **Plate 1** 1. *Dinogymnium acuminatum*; cuttings, 8390', 3(ox), Q35/0. Arrow points to the apical archeopyle with attached operculum. 2. *Dinogymnium decorum*; Core 1, 7780'-7783', 1(ox), X56/4. Specimen showing apical archeopyle with free operculum. Arrow points to the broad paracingulum. 3. *Dinogymnium avellana*; Core 1, 7777'-7780', 1(ox), U36/0. 4. *Dinogymnium nelsonense*; Core 5, 8577'-8578'6", 1(ox), L60/0. 5. *Dinogymnium vozzhennikovae*; Core 1, 7780'-7783', 1(ox), T33/1. 6. *Dinogymnium nelsonense*; Core 4, 8511'-8513', 1(ox), H58/2. 7. *Dinogymnium digitus* subsp. *crassum*; Core 4, 8511'-8514', 2(ox), G60/0. The fragmentation of the apex indicates presence of apical archeopyle. 8. *Dinogymnium digitus* subsp. *crassum*; Core 4, 8490'-8493', 1(ox), T32/3. 9. *Dinogymnium euclaensis*; Core 3, 8455'-8458', 5(unox), X38/1. 10. *Dinogymnium sphaerocephalum*; Core 4, 8549'6"-8550', 1(ox), O54/1. 11. *Dinogymnium digitus* subsp. *digitus*; Core 4, 8489'6"-8490', 1(ox), C47/0. 12. *Dinogymnium westralium*; Core 1, 7785'-7788', 1(ox), K35/0. Arrow points to the clear thorny antapex. 13. *Dinogymnium euclaensis*; Core 1, 7788'-7791', 1(ox), N34/0. 14. *Dinogymnium digitus* subsp. *crassum*; Core 4, 8496'-8499', 2(ox), N52/0. Specimen showing apical archeopyle with free operculum. 15. *Dinogymnium vozzhennikovae*; Core 1, 7780'-7783', 1(ox), U53/3. 16. *Dinogymnium westralium*; Core 1, 7785'-7788', 3(ox), N56/0. 17. *Dinogymnium westralium*; Core 1, 7785'-7788', 4(ox), N48/3. Arrow points to the clear apical archeopyle with attached an operculum. 18. *Dinogymnium albertii*; Core 4, 8493'-8499', 1(unox), K41/2. Specimen showing an apical archeopyle with a free operculum. 19. *Dinogymnium digitus* subsp. *digitus*; Core 3, 8443'-8446', 1(ox), X32/3. Arrow points to the apical archeopyle with attached operculum.

### Association 11

**Age:** early Campanian.

**Interval:** 8493'-8499'.

The dinocyst assemblages of this association are characterised by the first occurrence of new peridinoid dinocysts (24.4%) resembling *Apteodinium* Eisenack 1958 emend Sarjeant and Lucas-Clark 1987 and *Lagenorhytis* Duxbury 1979b but differs from both in having 3I/3I archeopyle rather than a precingular archeopyle and is comparable to *Chichaouadinium* below 1980 in having an 3I/3I archeopyle, but differs by its lacking of a cornucavate to circumcavate tabulated cyst. A decline in percentages of most of the species characteristic to the preceding associations is noted. There is a marked influx of the chorate species such as *Exochosphaeridium muelleri*, *Coronifera minus*, *C. oceanica*, *Cribroperidinium cooksoniae* and a high diversity of *Chatangiella* species, including ?*Chatangiella biapertura*, *C. madura*, *C. spectabilis*, *C. verrucosa* and *C. cf. williamsii*. Other characteristic dinocyst events include the first occurrence of *Litosphaeridium arundum*, *Pervosphaeridium brevispinum*, *P. cenomaniense*, *Xenascus serpaglii* and *Xenascus* sp. A var. nov. (Plate 3, Figs. 16 and 20). Sporomorph events include the first occurrence of *Hamulatisporis caperatus* and *Monocolpites marginatus*, together with an influx of *Gabonisporsis* spp. and *Ariadnaesporites verrucatus*.

Ioannides (1986) established a number of palynomorph intervals for the late Cretaceous and early Paleocene of the

20. *Dinogymnium cooksoniae*; Core 4, 8493'-8496', 1(ox), R45/2. Specimen showing apical archeopyle with detached operculum (large arrow) and paracingulum (small arrow). 21. *Dinogymnium longicornis*; Core 1, 7774'-7775', 1(ox), G61/4. 22. *Dinogymnium longicornis*; Core 1, 7780'-7783', 2(ox), H34/0. 23. *Dinogymnium digitus* subsp. *digitus*; cuttings, 8390', 1(ox), K34/0. 24. *Yolkinigymnium elongatum*; Core 1, 7774'-7775', 2(ox), G33/2; X150. 25. *Yolkinigymnium elongatum*; Core 1, 7774'-7775', 1(ox), D60/0; X150. Arrow points to the paracingulum. 26. *Yolkinigymnium* spp.; Core 1, 7774'-7775', 1(ox), J49/3. 27. *Tanyosphaeridium regulare*; Core 1, 7750'-7753', 2(ox), W45/2. 28. *Tanyosphaeridium regulare*; Core 1, 7750'-7753', 2(ox), D51/0. 29. *Tanyosphaeridium xanthiopyxides*; Core 5, 8577'-8578'6", 1(ox), S43/2. 30. *Tanyosphaeridium variecalamus*; Core 4, 8502'-8505', 1(ox), X51/0. 31. *Tanyosphaeridium variecalamus*; Core 4, 8499'-8502', 1(ox), K30/0. 32. *Tanyosphaeridium xanthiopyxides*; Core 5, 8577'-8578'6", 1(ox), P50/2. 33. *Trigonopyxidia ginella*; Core 1, 7756'-7759', 3(ox), H45/0. Specimen showing an endocyst filling pericoel. 34. *Trigonopyxidia ginella*; Core 1, 7785'-7788', 1(ox), G59/0. 35. *Tanyosphaeridium* spp.; Core 1, 7785'-7788', 1(ox), H42/3. Specimen showing an endocyst filling pericoel. 36. *Yolkinigymnium* spp.; Core 1, 7774'-7775', 2(ox), W46/2; X150. 37. Dinocyst type A.; Core 1, 7759'-7762', 1(ox), H48/3. 38. *Walloodinium angulicum*; Core 4, 7774'-7775', 7(ox), R40/3; X150. Specimen showing apical archeopyle with slightly zig-zag parasutures, reflecting precingular paraplates and probable parasulcal notch (arrow). 39. *Trigonopyxidia ginella*; Core 1, 7756'-7759', 1(ox), Q52/3

Arctic. His oldest palynomorph interval, which has been dated as Santonian-Campanian, bears some similarities to Association 11 including a high diversity of *Chatangiella* species such as *Chatangiella madura*, *C. verrucos*, and *C. spectabilis* and the occurrence of *Isabelidinium acuminatum*, *Palaeohystrichophora infusorioides* and *Xenascus ceratioides*. The Arctic assemblages are, however, lacking a number of species which are characteristic of Association 11, such as new variety of peridinoid species bearing an intercalary archeopyle type 3I/3I; opercula pieces free or attached, which could be endemic to the Sirt Basin. El-Mehdawi (2008) reported few peridinoid species from the upper part of Al Hilal Formation (Santonian-early campanian) exposed in Al Jabal al akhdar area, NE Libya in common with this association, including ?*C. biapertura*, *I. acuminatum* in association with other species include *X. ceratioides*, *X. arjeantii*, and presence of *Eucladinium gambangense* and *E. madurense* which are character for the Association 8 and 9.

The Association 11 has no counterpart either from the zonation scheme proposed by Bu-Argoub (1996) from SE Sirt Basin or from the Keegan and Stead (2007) from NE Libya.

This association has been assigned to an early Campanian based on high diversity of *Chatangiella* and *Cribroperidinium* species and its stratigraphic position between the early Campanian Association 10 and 12.

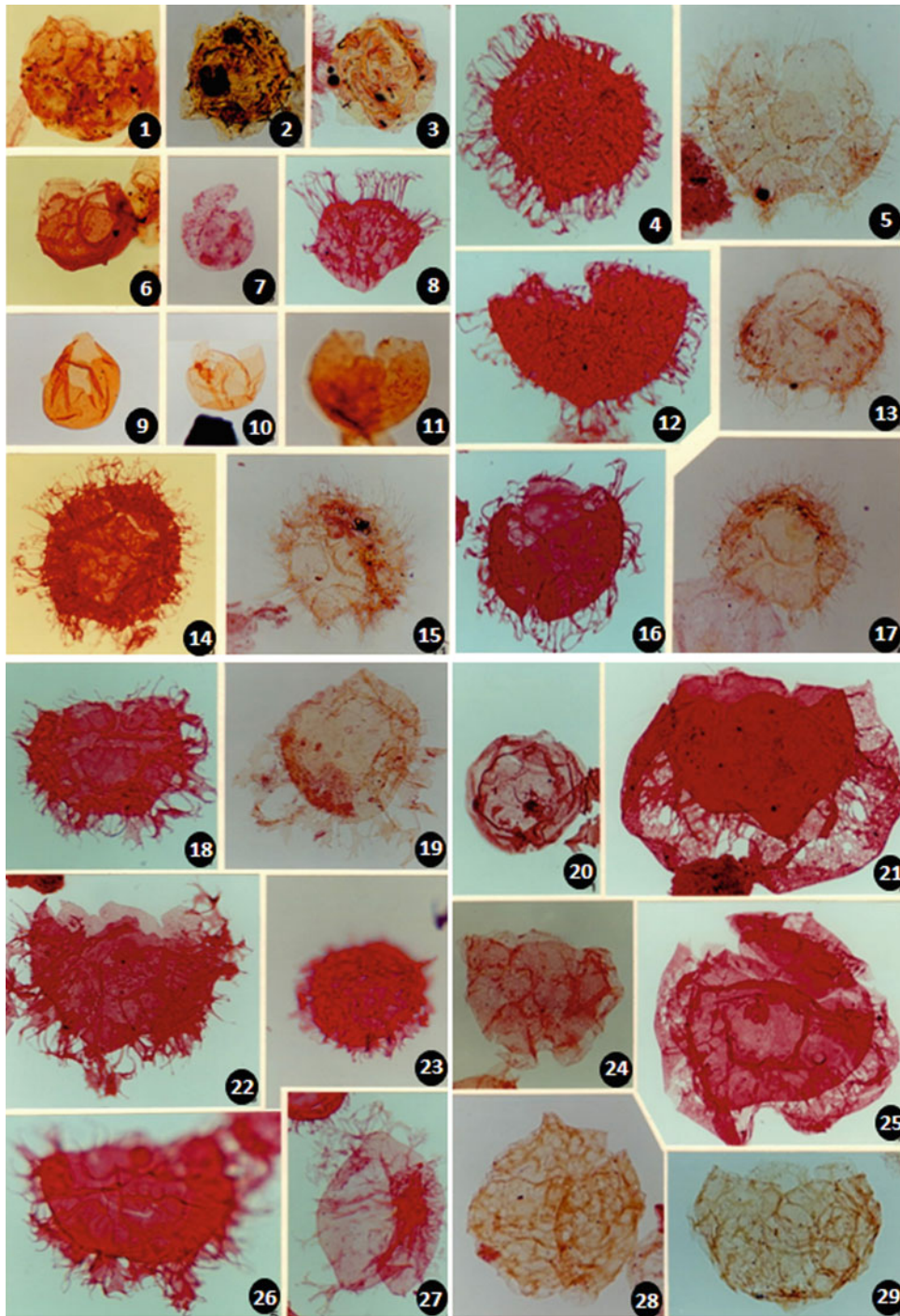


**Plate 2** 1. *Alisocysta circumtabulata*; Core 1, 7750'-7753', 1(ox), Q51/4. 2. *Alisocysta* sp. A; Core 1, 7762'-7765', 4(ox), O46/1. 3. *Alisocysta* sp. A; Core 1, 7750'-7753', 3(ox), P40/3. 4. *?Adnatosphaeridium* sp.; Core 1, 7762'-7765', 1(ox), G55/0. 5. *Areoligera* cf. *senonensis*; Core 1, 7783'-7785', 1(ox), T50/4; dorsal view. 6. *Alisocysta* sp. B; Core 1, 7750'-7753', 1(ox), E42/2. 7. *Batiacasphaera ?compta*; Core 1, 7762'-7765', 1(ox), M53/4. 8. Operculum; *?Adnatosphaeridium* sp.; Core 1, 7762'-7765', 1(ox), H36/0. 9. *Batiacasphaera* sp. A; Core 4, 8502'-8505', 1(ox), N53/4. 10. *Batiacasphaera* sp. A; Core 4, 8502'-8505', 1(ox), D43/3. 11. *Batiacasphaera* sp. B; Core 4, 8508'-8511', 1(ox), E39/0. 12. *?Adnatosphaeridium* sp.; Core 1, 7762'-7765', 1(ox), J56/2. 13. *Areoligera* cf. *senonensis*; Core 1, 7783'-7785', 1(ox), F56/1; ventral view. 14. *Adnatosphaeridium multispinosum*; Core 1, 7759'-7762', 1(ox), E51/4; dorsal view. 15. *Areoligera* cf. *senonensis*; Core 1, 7783'-7785', 2

(ox), L46/3; dorsal view. 16. *Areoligera* cf. *senonensis*; Core 1, 7765'-7768', 2(ox), F37/3. 17. *Areoligera* cf. *senonensis*; Core 1, 7783'-7785', 2(ox), L38/0. 18. *Areoligera* cf. *coronata*; Core 1, 7762'-7765', 1(ox), W56/1; dorsal view. 19. *Areoligera coronata*; Core 1, 7788'-7791', 1(ox), R45/0; ventral view. 20. *Senoniasphaera* spp.; Core 4, 8496'-8499', 1(ox), E36/3. 21. *Riculacysta perforata*; Core 1, 7765'-7768', 3(ox), Q50/4. 22. *Areoligera coronata*; Core 1, 7759'-7762', 1(ox), V57/2; dorsal view. 23. *Areoligera tauloma*; Core 1, 7762'-7765', 1(ox), B55/1; folded specimen. 24. *Senoniasphaera* sp. A; Core 3, 8443'-8446', 1(ox), X38/1. 25. *Riculacysta perforata*; Core 1, 7765'-7768', 1(ox), G33/0. 26. *Areoligera* cf. *coronata*; Core 1, 7759'-7762', 1(ox), B58/4; dorsal view. 27. *Areoligera* sp. B; Core 1, 7759'-7762', 1(ox), E43/0; ventral view. 28. *Senoniasphaera* sp. A. var. nov.; Core 3, 8461'-8464', 1(ox), H52/1. 29. *Senoniasphaera* sp. A. var. nov.; Core 3, 8461'-8464', 1(ox), L29/4

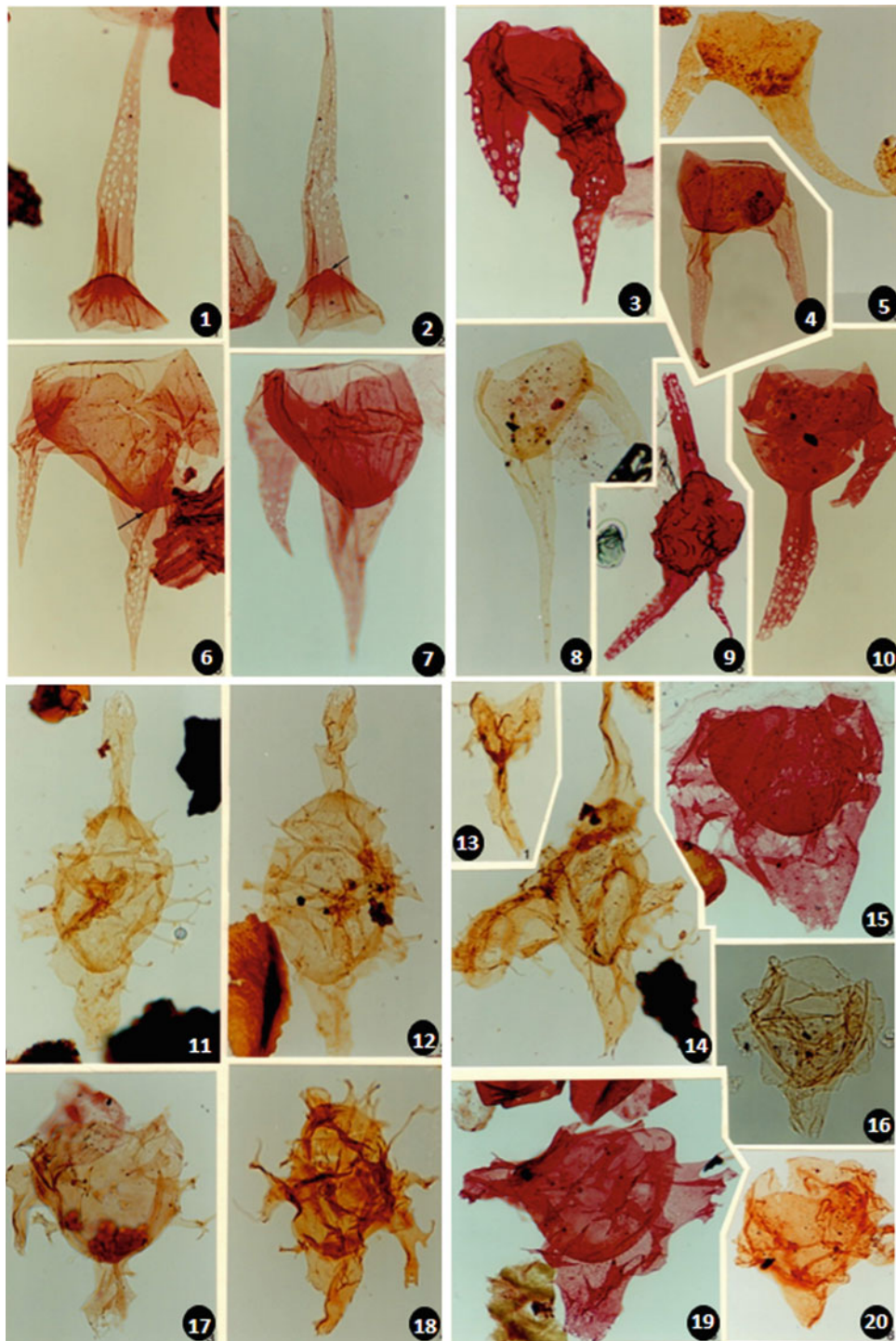
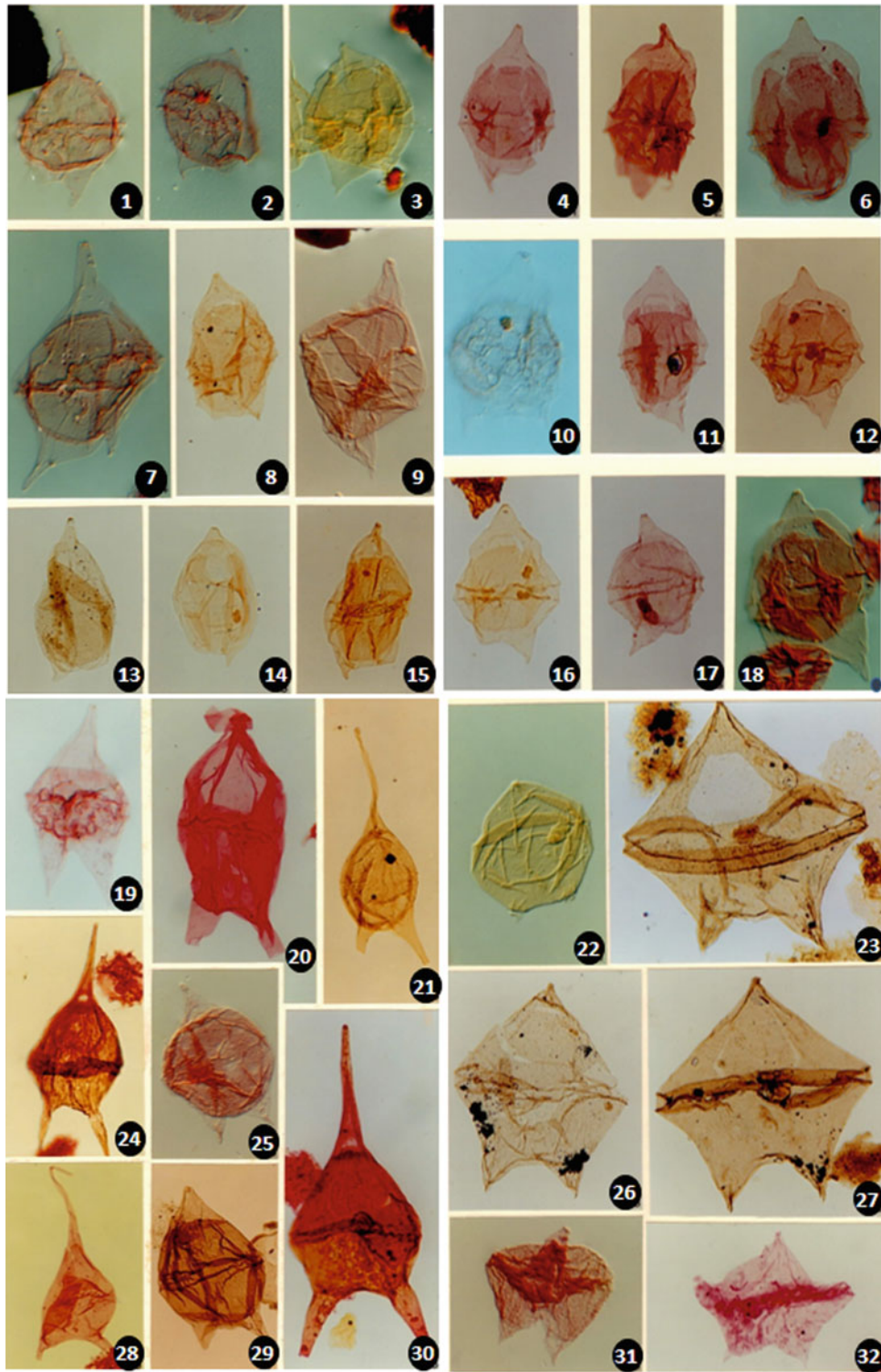


**Plate 3** 1 and 2. Opercula, *Odontochitina tabulata*; Core 4, 8520'-8523', 7(ox), P47/1 and 4(ox), F53/0 respectively. Note the apical nipple at the apex of the endo-operculum (arrow). 3. *Odontochitina cribropoda*; Core 5, 8580'-8581'6", 1(ox), M50/0. 4. *Odontochitina costata*; Core 4, 8487'10"-8489'6", 2(ox), U39/0; X150. 5. *Odontochitina costata*; Core 4, 8489'6"-8490', 1(ox), N58/1. 6. *Odontochitina tabulata*; Core 4, 8520'-8523', 7(ox), P44/4, ventral view. Note the antapical nipple at the antapex of the endocyst (arrow). 7. *Odontochitina tabulata*; Core 4, 8520'-8523', 4(ox), P31/0; ventral view. 8. *Odontochitina costataloperculata* complex; Core 3, 8461'-8464', 2(ox), M48/4; X190. 9. *Odontochitina cribropoda*; Core 5, 8580'-8581'6", 4(ox),

L38/1; X150. 10. *Odontochitina cribropoda*; Core 2, 8428'-8431', 2(ox), W41/2. 11. *Xenascus ceratioides*; Core 4, 8508'-8511', 1(ox), P61/3. 12. *Xenascus ceratioides*; Core 4, 8508'-8511', 1(ox), V61/4. 13. *Xenascus ceratioides*; Core 4, 8508'-8511', 1(ox), S51/0. 14. *Xenascus ceratioides*; Core 4, 8508'-8511', 1(ox), V60/0. 15. *Xenascus australensis*; Core 4, 8593'-8596', 1(ox), E49/0. 16. *Xenascus* sp. A var nov.; Core 3, 8455'-8458, 2(unox), M46/1. 17. *Xenascus sarjeantii*; Core 4, 8496'-8499', 1(ox), U52/0. 18. *Xenascus sarjeantii*; Core 4, 8511'-8514', 4(ox), G62/1. 19. *Xenascus australensis*; Core 4, 8493'-8496', 4(ox), F52/0. 20. *Xenascus* sp. A var. nov.; Core 4, 8487'-8487'10", 1(ox), H47/0





◀ **Plate 4** 1. *Alterbidinium acutulum*; Core 5, 8580'-8581'6", 2(ox), L45/0, IC. 2. *Alterbidinium acutulum*; Core 5, 8580'-8581'6", 1(ox), C35/0, IC. 3. *Alterbidinium* cf. *circulum*; Core 4, 8511'-8514', 2(ox), E59/4, IC. 4. ?*Chatangiella biapertura*; Core 4, 8496'-8499', 2(ox), K41/0; dorsal view. 5. *Chatangiella madura*; Core 4, 8493'-8496', 3(ox), R33/4; dorsal view. 6. *Chatangiella madura*; Core 4, 8496'-8499', 1(ox), S43/0; intermediate focus. 7. *Alterbidinium* cf. *distinctum*; Core 4, 8496'-8499', 2(ox), L41/0, IC. 8. *Alterbidinium emulatum*; Core 4, 8508'-8511', 1(ox), K54/1. 9. *Alterbidinium acutulum*; Core 5, 8577'-8578'6", 1(ox), C62/4, IC. 10. *Chatangiella micracantha*; Core 4, 8499'-8502', 3(ox), L36/4, IC. A badly preserved specimen. 11. *Chatangiella spectabilis*; Core 4, 8493'-8496', 1(ox), K42/0; ventral view. 12. *Chatangiella verrucosa*; Core 4, 8496'-8499', 1(ox), P39/3; intermediate focus. 13. *Alterbidinium emulatum*; Core 4, 8496'-8499', 3(unox), D34/2. 14. *Alterbidinium emulatum*; Core 4, 8514'-8517', 3(ox), C42/1. 15. *Alterbidinium emulatum*; Core 4, 8511'-8514', 4(ox), C51/0. 16. *Chatangiella* cf. *williamsii*; Core 4, 8511'-8514', 1(ox), J38/2; intermediate focus. 17. *Chatangiella* cf. *williamsii*; Core 4, 8496'-8499', 1(ox), E57/0; dorsal view. 18. *Chatangiella verrucosa*; Core 4, 8496'-8499', 3(ox), N38/0, IC; intermediate focus. 19. *Cerodinium depressum*; Core 1, 7780-

7783', 1(ox), O46/1, IC; intermediate focus. 20. *Cerodinium diebelii* var. A; Core 1, 7785'-7788', 2(ox), V44/0; intermediate focus. Specimen showing large intercalary archeopyle. 21. *Cerodinium diebelii*; Core 1, 7771'-7774', 1(unox), F34/1; ventral view. A specimen characterised by a globular ambitus and having more prominent tuberculae. 22. *Phelodinium* cf. *gaditanum*; Core 5, 8545'-8548', 3(unox), V51/0, IC; intermediate focus. 23. *Phelodinium magnificum*; Core 1, 7785'-7788', 1(unox), T60/0; dorsal view. Arrow points to the operculum inside the cyst. 24. *Cerodinium diebelii*; Core 1, 7774'-7775', 3(ox), N28/0; X550; intermediate focus. 25. *Cerodinium boloniense*; Core 5, 8549'6"-8550", 1(ox), L50/2, IC; intermediate focus. 26. *Phelodinium magnificum*; Core 1, 7785'-7788', 1(unox), W44/0; dorsal view. 27. *Phelodinium magnificum*; Core 1, 7785'-7788', 1(unox), F32/0; intermediate focus. 28. *Cerodinium diebelii* var. B; Core 1, 7762'-7765', 1(ox), K42/1; X150; ventral view. 29. *Cerodinium graulostriatum*; Core 3, 8455'-8458', 2(unox), H38/3; X150; intermediate focus. 30. *Cerodinium diebelii*; Core 1, 7785'-7788', 1(ox), D39/3; X190; intermediate focus. 31. *Phelodinium pachyceras*; Core 5, 8545'-8548', 4c(ox), U43/1, IC. Probably as a result of drilling mud contamination. 32. *Phelodinium tricuspis*; Core 1, 7759'-7762', 1(ox), E58/4; intermediate focus

## Association 12

**Age:** early late Campanian.

**Interval:** 8487'-8493'.

This association is characterised by the absence of *Chatangiella* species and the peridinoid dinocysts varieties with intercalary archeopyle type 3I/3I and a decline in the chorate species *Exochosphaeridium muelleri*, *Coronifera minus*, *C. oceanica*, *Cribopteridinium cooksoniae* and *Cyclonephelium chabaca*. The most important stratigraphic markers in this association include higher influx of *Palaeohystrichophora infusorioides* and *Xenascus* species (*X. ceratioides*, *X. sarjeantii* and *X. gochtii*). New varieties of peridinoid forms are identified in conjunction with the first occurrence of *Cerodinium granulostriatum* and the angiosperm pollen *Auriculiidites* cf. *reticulatus*.

Schrank (1987) and El Beialy (1995) investigated palynomorphs from the phosphatic strata of Egypt, which they dated as a Campanian–Maastrichtian. Their assemblage is considered younger than the present association and having only a few species in common, including *Cribopteridinium cooksoniae*, *Cerodinium obliquipes*, *Senegalinium bicavatum*, *S. laevigatum*, *C. granulostriatum*, *Hystrichodinium pulchrum*, *Spiniferites multibrevis* and *S. supparus*. Schrank's (ibid) and El Beialy's (ibid) dinocyst assemblage lacks two of the most abundant species recorded in Association 12: *P. infusorioides* and *Xenascus* species, which are known to range from the Albian to Maastrichtian, world-wide. Association 12 lacks typical late Campanian and Maastrichtian assemblages, some of which were recorded by Schrank (ibid.) and El Beialy (ibid) from Egypt and reported herein to occur in Associations 13–22. These include dinocysts such as *Cerodinium diebelii*, *Cerodinium obliquipes*, *Palaeocystodinium/Andalusiella* complex (Fig. 12), *Phelodinium magnificum*, *P. tricuspis*, *Cordosphaeridium*

*fibrospinosum*, *Dinogymnium euclaensis*, *Kenleyia lophophora*, *K. pachycerata* and the angiosperm pollen *Proteacidites dehaani*, *Echitriporites trianguliformis*, *Mauritiidites crassibaculatus* and *M. lehmanii*.

Based on the combination of the evidence cited, abundance of *P. infusorioides* and *Xenascus* species and the absence of typical uppermost late Campanian and Maastrichtian assemblages, Association 12 has been assigned to the late Campanian and most probably an early late Campanian.

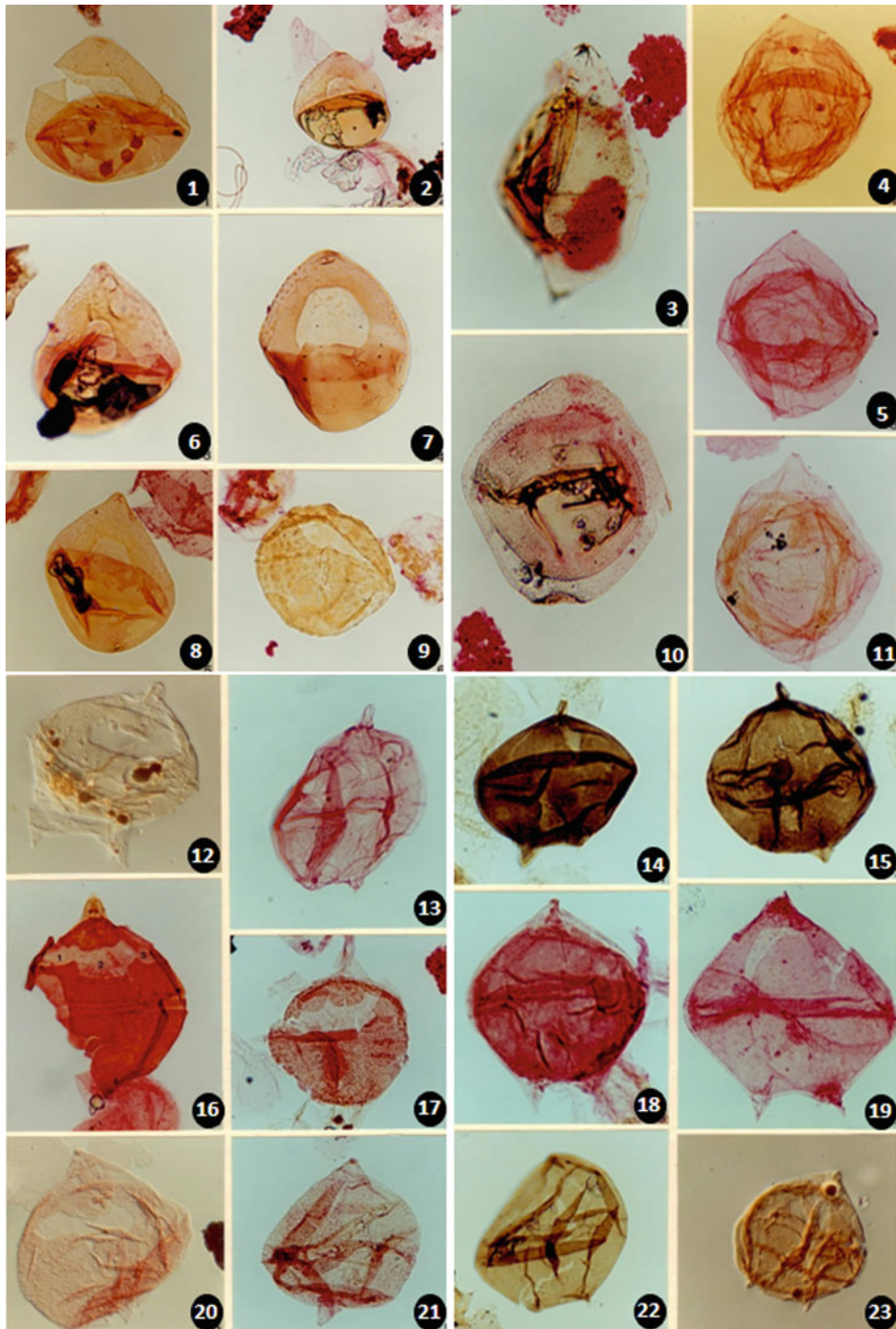
## Association 13

**Age:** late Campanian.

**Interval:** 8455'-8464'.

This association is marked by a decline in sporomorphs and an influx of peridinoid cysts. The base of the association is characterised by influxes of the peridinoid genus *Cerodinium granulostriatum* with some new variety of the genus and the top by influxes of the *Palaeohystrichophora infusorioides* and a new variety of the genus *Operculodinium* at its upper part. The base is also marked by presence of high percentages of *Senegalinium bicavatum*. A marked decline was noted for *Hystrichodinium pulchrum*, *Achomosphaera/Spiniferites* complex and *Xenascus* complex (Fig. 12). Taxa that make their first occurrence in this association include *Andalusiella gabonensis*, *Dinogymnium euclaensis*, *Operculodinium centrocarpum*, *Operculodinium* spp., *Palaeocystodinium denticulatum*, *Senoniasphaera* sp. A. var. nov. (Plate 2, Figs. 28 and 29), *Trithyrodinium evittii* and *Circulodinium brevispinatum*.

Abundance of *C. granulostriatum* is known from the Maastrichtian of Senegal (Jain & Millepied, 1973) and the Maastrichtian to Danian of NW Tunisia (Brinkhuis & Zachariasse, 1988). *A. gabonensis* is reported from the



Maastrichtian of Gabon (Malloy, 1972) and the Campanian–Maastrichtian of Egypt (Schrank, 1987), Sirt Basin, Libya (Bu-Argoub, 1996), NE Libya (Keegan & Stead, 2007). Extension of the range of the species down to the Santonian by Keegan and Stead (2007) is not accepted as most probably due to caving. The occurrence of these suggests a Campanian–Maastrichtian age for this association.

However, due to the occurrence of low percentages of members of the *Palaeocystodinium/Andalusiella* complex (which flourished in the late Campanian–Maastrichtian), the abundance of *P. infusorioides* (which does not range higher than Campanian) and the absence of *Cerodinium diebelii*, known mainly from Maastrichtian strata, in which its first occurrence has been used in different areas to indicate the

◀ **Plate 5** 1. *Nelsoniella aceras*; Core 4, 8517'-8520', 2(ox), P48/4; dorsal view. 2. *Nelsoniella aceras*; Core 4, 8517'-8521', 1(ox), H62/2; dorsal view. 3. *Manumiella conorata*; Core 1, 7770'-7771', 4(ox), D55/1; lateral view. 4. *Manumiella* sp. A var. nov.; Core 1, 7788'-7791', 2(ox), P44/3; lateral view. 5. *Manumiella* sp. A var. nov.; Core 1, 7788'-7791', 3(ox), E49/1; dorsal view. 6. *Nelsoniella tuberculata*; Core 4, 8517'-8521', 1(ox), W59/3; dorsal view. 7. *Nelsoniella aceras*; Core 4, 8499'-8502', 2(ox), V63/1; dorsal view. 8. *Nelsoniella tuberculata*; Core 4, 8517'-8520', 1(ox), P46/1; dorsal view. 9. *Nelsoniella* sp.; cuttings, 8390', 1(ox), G46/3; dorsal view. 10. *Manumiella seelandica*; Core 1, 7765'-7768', 1(ox), W47/0; intermediate focus. 11. *Manumiella* sp. A var. nov.; Core 1, 7783'-7785', 1(ox), S45/4; lateral view. 12. *Trithyrodinium evittii*; Core 3, 8455'-8458', 2(unox), V43/4, IC; dorsal view. Specimen showing clear bat-shaped 3I/3I archeopyle with free opercula. 13. *Trithyrodinium evittii*; Core 1, 7762'-7765', 1(ox), Q56/3; dorsal view. Specimen showing a bat-shaped 3I/3I archeopyle with attached opercula. 14. *Senegalinium bicavatum*; Core 2, 8428'-8431', 1

(unox), V30/1; intermediate focus. 15. *Senegalinium bicavatum*; Core 3, 8443'-8446', 1(unox), E53/0; intermediate focus. 16. *Trithyrodinium rhomboideum*; Core 2, 8410'-8412', 1(ox), D48/0; dorsal view. Specimen with clear bat-shaped 3I/3I archeopyle, free opercula and prominent paracingulum. 17. *Trithyrodinium suspectum*; Core 4, 8517'-8520', 1(ox), T63/3; dorsal view. Specimen showing a bat-shaped 3I/3I archeopyle with free opercula. 18. *Senegalinium bicavatum*; Core 3, 8443'-8446', 1(ox), K40/0; dorsal view. Specimen showing a circumcavate cyst due to the effect of the chemical processing. 19. *Senegalinium bicavatum*; Core 2, 8416'-8419', 4(ox), L55/2; dorsal view. Specimen showing a showing a circumcavate cysts due to the effect of chemical processing. 20. *Trithyrodinium* sp. A; Core 5, 8577'-8578'6", 1(ox), F56/0, IC; dorsal view. Specimen with bat-shaped 3I/3I archeopyle and free opercula. 21. *Trithyrodinium* sp. A; Core 5, 8577'-8578'6", 1(ox), C55/0; intermediate focus. 22. *Senegalinium laevigatum*; Core 2, 8416'-8419', 1(unox), E49/4; intermediate focus. 23. *Senegalinium laevigatum*; Core 3, 8455'-8458', 3(unox), J38/0, IC; intermediate focus

base of the Maastrichtian age (see discussion under Association 15), a Maastrichtian age is not considered likely.

The late Campanian-Maastrichtian Assemblage Zone III from SE Sirt Basin (Bu-Argoub, 1996) has some peridoid species in common with present association in which mixed with some index Maastrichtian species such as *Cerodinium diebii*, *Palaeocystodinium australinum* and *P. lidiae*, *Dinogymnium longicorne* which are most probably caved from the younger horizon. The late Campanian, LPC2 Zone from NE Libya (Keegan & Stead, 2007), has many common species with the present association; other than that, however, the *Palaeocystodinium australinum* and *P. golzowense* are considered as caved from the younger horizon.

Late Campanian age is considered appropriate for the present association.

#### Association 14

**Age:** late Campanian.

**Interval:** 8428'-8446'.

This association is marked by a decline in the dominant and characteristic assemblages of the preceding association, including *Cerodinium granulostriatum*, *Palaeohystrichophora infusorioides*, *Operculodinium* spp., *Xenascus* spp., and an increase of *Hystrichodinium pulchrum*, *Senegalinium bicavatum*, *S. laevigatum*, *Coronifera glaberla* and long-ranging trilete spores such *Cyathidites australis*, *Todisporites major* and indeterminate tetraporate pollen forms. The most important dinocyst events mark the base of this association is the first occurrence of *Andalusiella polymorpha* subsp. *polymorpha* and *Andalusiella polymorpha* subsp. var. nov. (Plate 6, Figs. 4, 6, 9 and 10), *Manumiella* sp. A var. nov. (Plate 5, Figs. 4, 5 and 11). Other important taxa showing their first occurrence in this association are *Trichodinium castanea* subsp. *bifurcatum*, *Cyclonephelium vannophorum*, *Dinopterygium cladoides* and *Spiniferites*

*wetzeli*. A high diversity of *Odontochitina* species is noted in this association.

*A. polymorpha* subsp. *polymorpha* is known from late Campanian-Maastrichtian strata world-wide (Malloy, 1972; Riegel, 1974; Lentin & Williams, 1980; Schrank, 1984, 1987; Brinkhuis & Zachariasse, 1988, Bu-Argoub, 1996, and Keegan & Stead, 2007). The high diversity, abundance and main stratigraphic records of *Odontochitina* species are known from pre-Maastrichtian strata world-wide (Bu-Argoub, 1996; Davey, 1978; Jain & Milleped, 1975; Keegan & Stead, 2007; Mansour et al., 2020; Schiøler, 1992; Srivastava, 1992). *C. vannophorum* is known to range from Early Cretaceous to Coniacian (Davey, 1969a; Williams, 1975, 1978; Norvick and Burger, 1967; Below, 1981; Singh, 1983; Batten & Uwins, 1985; Thusu & Van Der Eem, 1985; Sweet & McIntyre, 1988).

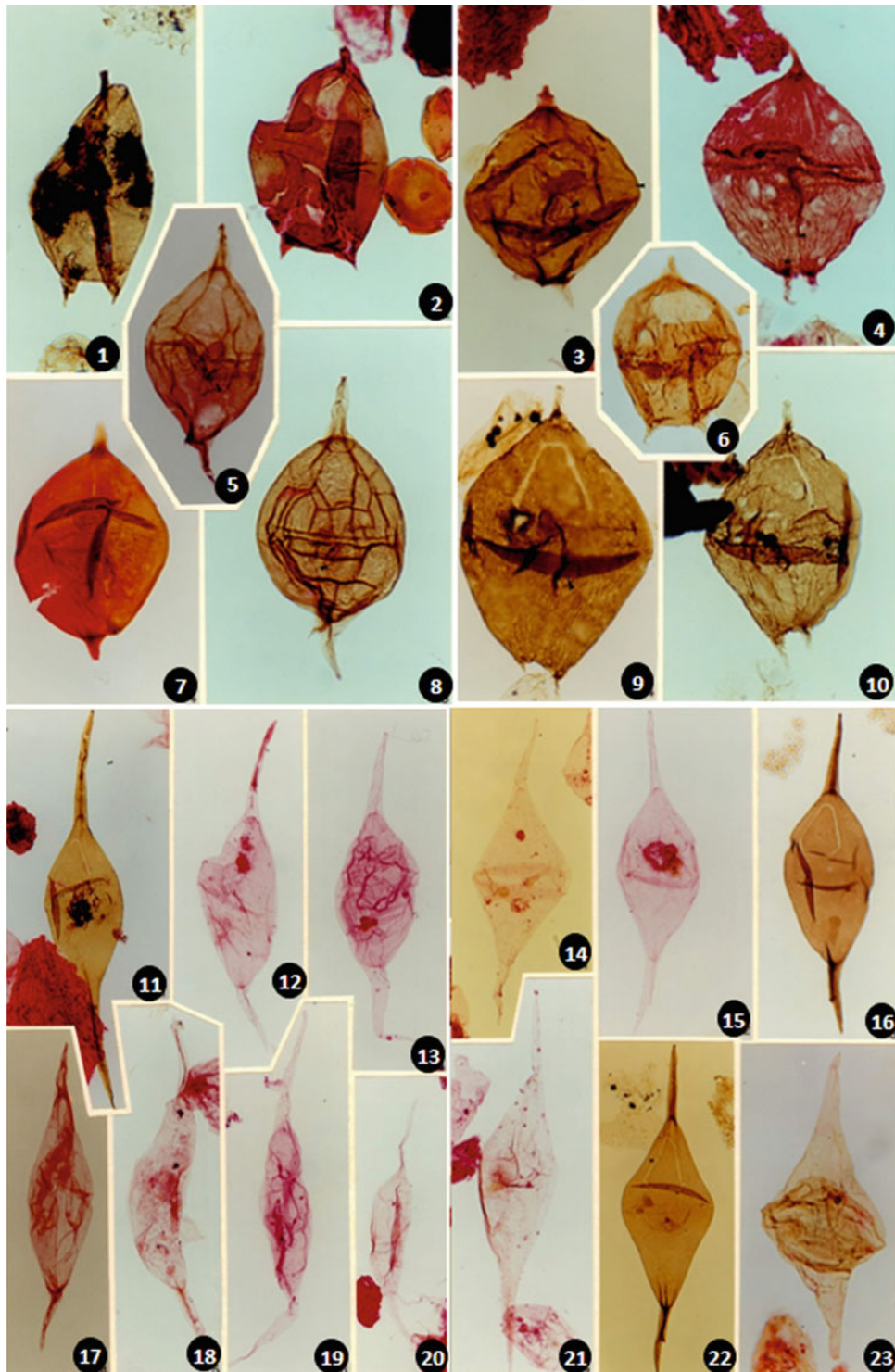
Based on the evidence cited above, a late Campanian age is considered appropriate for this association. The absence of *Cerodinium diebii*, which is known mainly from the Maastrichtian strata world-wide and has been reported herein in the succeeding associations, could also be in favour of a late Campanian age. The Campanian age is also supported by the presence of the nannofossil data for the interval 8422'-8425' (El-Mehaghag, 1996). The nannofossil assemblages are characterised by the co-occurrence of *Reinhardtites anthophorus* and *Aspidolithus parvus constrictus*, which are the zonal markers for the top of CC18C to CC22C (El-Mehaghag, 1996; Perch-Nielsen, 1979; Sissingin, 1977).

#### Association 15

**Age:** late Campanian-early Maastrichtian.

**Interval:** 8410'-8419'.

This association is characterised by an increase in the percentage of sporomorphs, including an influx of *Inaperturopollenites hiatus*. Dinocysts are marked by a decline in *Dinogymnium* species and *Cerodinium obliquipes* and an influx of *Achomospaera ramulifera*, *Spiniferites ramosus*



subsp. *ramosus* and *Subtilisphaera* species (including *S. cheit* and *S. senegalensis*). Species of *Senegalinium*, including *S. bicavatum* and *S. laevigatum*, continue to be common; and at the base of the association, there is an influx of *Hystri-chodinium pulchrum* and *Circulodinium distinctum*. At the top part of the association, *Cerodinium diebelii*, *C. striatum*,

*Palaeoperidinium* sp., *Trithyrodinium rhomboideum*, *Andalusiella dubia* and the triporate pollen grain *Proteacidites* sp. make their first occurrence. At the base of the association, *Cyclonephelium paucispinum* and *Thalassiphora* sp. B make their first occurrence. Furthermore, *Odontochitina costata*, *Manumiella lata*, *Andalusiella polymorpha* subsp. var. nov.

◀ **Plate 6** 1. *Andalusiella polymorpha* subsp. *polymorpha*; Core 2, 8428'-8431', 2(unox), Q42/0; intermediate focus. 2. *Andalusiella polymorpha* subsp. *polymorpha*; Core 3, 8443'-8446', 2(ox), J47/2; intermediate focus. 3. *Andalusiella polymorpha* subsp. *aegyptiaca*; cuttings, 8390', 3(ox), V52/2; intermediate focus. Specimen showing a faint paracingulum (small arrow) and a bean-shaped flagellar scar (large arrow). 4. *Andalusiella polymorpha* A sub sp. var. nov.; Core 3, 8443'-8446', 2(ox), O42/0; dorsal view. Specimen showing a clear paracingulum and archeopyle with operculum attached posteriorly and anteriorly, and a parasulcus (arrows) indicated by a shallow longitudinal depression. 5. *Andalusiella ivoirensis*; cuttings, 8390', 1(ox). K45/0; ventral view. Arrow points to the flagellar scar. 6. *Andalusiella polymorpha* subsp. var. nov.; Core 8489'6"-8490', 1(ox), G52/4; intermediate focus. Specimen showing an archeopyle with a free operculum. 7. *Andalusiella* sp. A; cuttings, 8390', 2(ox), C44/1; intermediate focus. 8. *Andalusiella ivoirensis*; cuttings, 8390', 5(ox), V51/0; intermediate focus. Arrow points to the flagellar scar. 9. *Andalusiella polymorpha* subsp. A var. nov.; Core 3, 8443'-8446', 6(unox), J47/0; intermediate focus. Specimen showing an archeopyle with an operculum attached

(Plate 6, Figs. 4, 6, 9 and 10), *Palaeohystrichophora infusorioides* complex and *Xenascus* complex have their last occurrence in this association (Fig. 12).

Taxa absent from this association, but present in the preceding and succeeding associations, include *Andalusiella polymorpha* subsp. *polymorpha*, *Coronifera glaberla* and *Senoniasphaera* sp. A. var. nov. Jain and Millepied (1975), proposed several assemblage zones for the Cretaceous sediments of Senegal. Four of which span the early Albian to Cenomanian, and two of which span the late Campanian to Maastrichtian. Their Zone-IV (late Campanian–Maastrichtian) is considered to be equivalent to associations 14–16; both contain *Trichodinium castanea* subsp. *castanea*, *T. castanea* subsp. *bifurcatum*, *Circulodinium distinctum* and species of *Dinogymnium* and *Senegalinium*. Fisher and Denison (1977 after Ioannides, 1986) considered *O. operculata* and *P. infusorioides* range no higher than the Campanian, whilst *Xenascus ceratioides* occurred throughout the middle Maastrichtian. May (1980) recorded diverse dinocyst assemblages from the Late Cretaceous sediments of the Monmouth Group, New Jersey, bearing features in common with Association 15. He suggested that the Campanian–Maastrichtian boundary was defined on the first occurrence of *Cerodinium diebelii*, which is similarly used to mark the base of Maastrichtian (interval 8410'–8412') in the studied well. The first occurrence of *C. diebelii* as a basal Maastrichtian marker has also been used by Ioannides (1986) from the Late Cretaceous of the Arctic Archipelago, and by Harker et al. (1990) from the Interior plains of Canada. Taxa disappearing with the appearance of *C. diebelii* include *Palaeohystrichophora infusorioides*, *Odontochitina costata* and the *Xenascus* complex. These species, which appear at or above the level of *C. diebelii*, include *Palaeocystodinium australinum*, *Pierceites pentagona*, *Dinogymnium westralium*, *Yolkinigymnium elongatum* and *Yolkinigymnium* spp.

posteriorly and a bean-shaped flagellar scar (arrow). 10. *Andalusiella polymorpha* subsp. A. var. nov.; Core 3, 8443'-8446', 1(unox), Q47/3; intermediate focus. 11. *Palaeocystodinium golzowense*; Core 1, 7777'-7780', 1(ox), M51/4. 12. *Palaeocystodinium golzowense*; Core 1, 7777'-7780', 1(ox), E57/3. 13. *Palaeocystodinium golzowense*; Core 1, 7756'-7759', 1(ox), G43/2. 14. *Palaeocystodinium australinum*; Core 1, 7777'-7780', 2(ox), S30/1; X150. Specimen showing circumcavate cyst as a result of oxidation effect. 15. *Palaeocystodinium australinum*; Core 1, 7777'-7780', 1(ox), C44/2; X150. 16. *Palaeocystodinium australinum*; Core 1, 7777'-7780', 1(unox), F28/1; X150. 17. *Palaeocystodinium lidiae*; cuttings, 3(ox), V43/3. A specimen with short apical and antapical horns. 18. *Palaeocystodinium lidiae*; Core 1, 7750'-7753', 1(ox), O29/4. 19. *Palaeocystodinium lidiae*; Core 1, 7756'-7759', 1(ox), H36/4. 20. *Palaeocystodinium lidiae*; Core 1, 7759'-7762', 1(ox), P35/0; X150. 21. *Palaeocystodinium australinum*; Core 1, 7777'-7780', 1(ox), E58/1; X150. 22. *Palaeocystodinium australinum*; Core 1, 7777'-7780', 1(unox), D37/0; X550. 23. *Palaeocystodinium denticulatum*; Core 3, 3(ox), 8461–8464', L33/3

The bottom part of this association (interval 8410'–8412') is characterised by the co-occurrence of *P. infusorioides* and *O. costata* with *C. diebelii* but does not appear above this level. Consequently, this association could be assigned to a late Campanian–early Maastrichtian age.

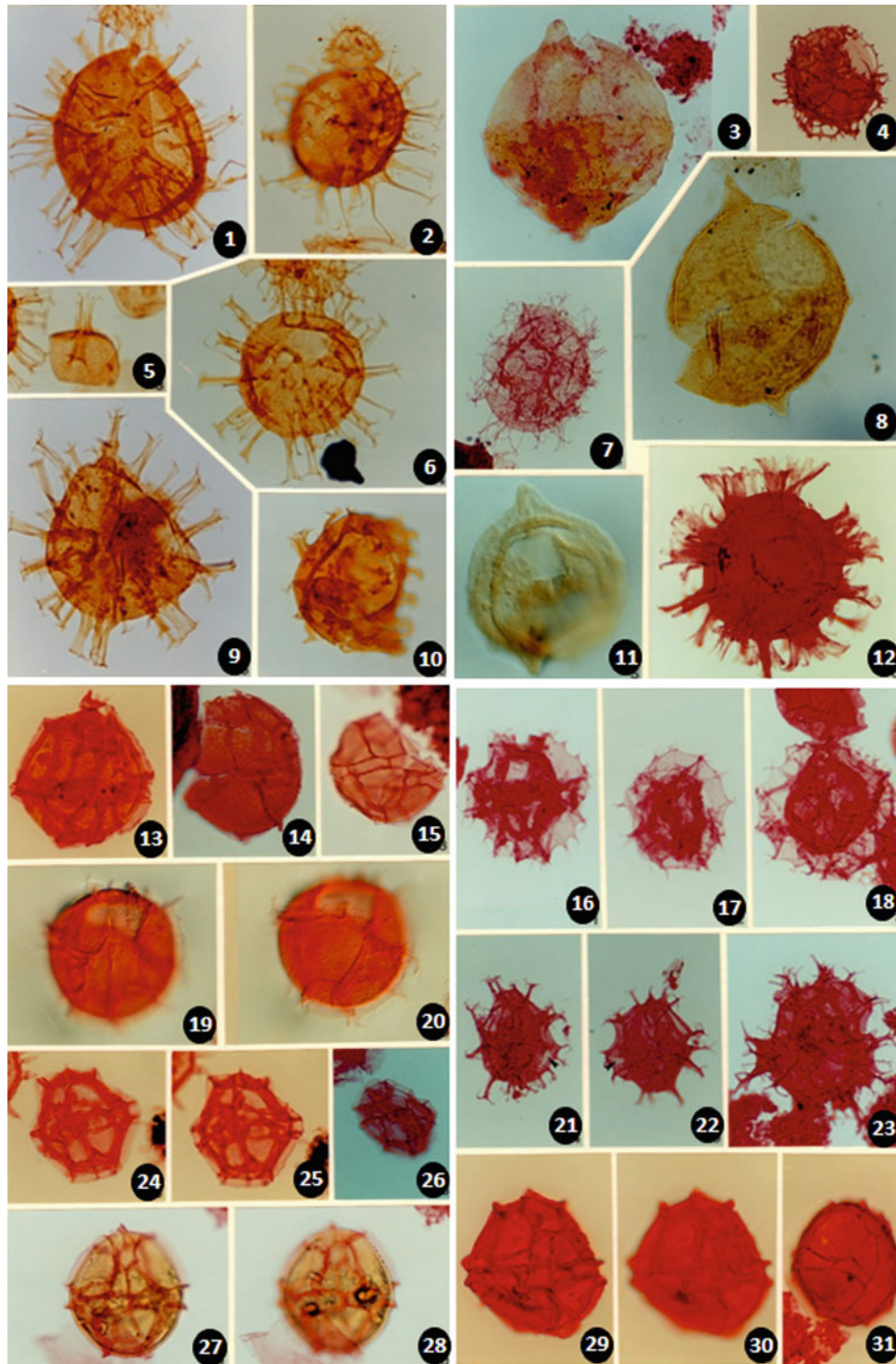
Data from the same interval contained very rare Late Cretaceous nannofossil assemblages that are characterised by three species: *Micula decussata* (late Coniacian–Palaeocene), *Micula concava* and *Watznaueria barnesae* (El-Mehaghag, 1996).

#### Association 16

**Age:** early Maastrichtian.

**Interval:** 8390'.

This association is represented by a single ditch cuttings sample and is characterised by a decline in sporomorphs and an increase of *Palaeocystodinium/Andalusiella* complex (Fig. 12). Important stratigraphic events occurring in this association include the introduction of typical Maastrichtian assemblages. These are marked by the first occurrence of *Andalusiella ivoirensis*, *A. mauthei*, *A. polymorpha* subsp. *aegyptiaca*, *Areoligera coronate* complex, *Areoligera* cf. *senonensis*, *Cerodinium diebelii*, *Dinogymnium westralium*, *Glaphyrocysta divaricata*, *Nematosphaeropsis* sp. C var. nov. (Plate 8, Figs. 9 and 10), *Riculacysta perforata*, *Pyxidinoopsis ardonensis*, *Palaeocystodinium australinum*, *Phelodinium magnificum*, *Senegalinium microgranulatum* and *Turbiosphaera filosa*. Sporomorphs, which make their first occurrence in this association, include *Ariadnaesporites spinosus*, *Azolla cretacea*, *Distaverrusporites simplex* and *Echitriporites trianguliformis*. These taxa are mainly known from the late Campanian–Maastrichtian of Nigeria and Egypt (Van Hoeken-Klinkenberg, 1966; Jan du Chêne et al., 1978; Jan du Chêne, 1980; Lawal & Moullade, 1986; Schrank, 1987).



However, it is worthy to mention that the present association has no counterpart neither from the zonation schemes of Bu-Argoub (1996) from SE Sirt Basin, nor of Keegan and Stead (2007) from NE Libya, or Mansour et al. (2020) from Egypt.

From the evidence cited above, Association 16 favoured to be of an early Maastrichtian age.

#### **Association 17**

**Age:** late Maastrichtian.

**Interval:** 7785'-7791'.

This association is marked by an influx of the dinocyst *Cerodinium/Senegalinium* complex, characterised by abundant *Cerodinium pannuceum* and *Phelodinium magnificum*

◀ **Plate 7** 1. *Amphorosphaeridium fenestratum* subsp. *dividum*; Core 4, 8511'-8514', 2(ox), F54/2. 2. *Amphorosphaeridium fenestratum* subsp. *dividum*; Core 4, 8514'-8517', 3(ox), B43/4. 3. *Carpatella cornuta*; Core 1, 7771'-7774', 1(ox), J49/4. 4. *Cannosphaeropsis* sp. B; Core 4, 8496'-8499', 2(ox), T47/2. 5. Operculum; *Amphorosphaeridium fenestratum* subsp. *fenestratum*; Core 4, 8514'-8517', 5(ox), O53/1. 6. *Amphorosphaeridium fenestratum* subsp. *fenestratum*; Core 4, 8514'-8517', 4(ox), G36/0. 7. *Cannosphaeropsis* sp. A; Core 5, 8549'6"-8550', 1(ox), E48/0. 8. *Carpatella cornuta*; Core 1, 7759'-7762', 1(unox), Y46/0. 9. *Amphorosphaeridium fenestratum* subsp. *fenestratum*; Core 4, 8514'-8517', 5(ox), K50/4. 10. *Amphorosphaeridium multibrevum*; Core 4, 8514'-8517', 4(ox), E57/0. 11. *Carpatella cornuta*; Core 1, 7771'-7774', 7(ox), D40/3, IC. 12. *Cordosphaeridium exilimurum*; Core 1, 7756'-7759', 3(ox), O47/1. 13. *Impagidinium maculatum*; Core 1, 7759'-7762', 1(ox), M51/0; intermediate view. 14. *Impagidinium maculatum*; Core 1, 7759'-7762', 1(ox), J41/0; lateral view. 15. *Impagidinium* sp. C; Core 1, 7750'-7753', 2(ox), D45/3; lateral view. 16. *Hystrichostrogylon holohymenium*; Core 1, 7756'-7759', 2(ox), C46/4. 17. *Hystrichostrogylon*

*holohymenium*; Core 1, 7756'-7759', 1(ox), D44/2. 18. *Hystrichostrogylon holohymenium*; Core 1, 7756'-7759', 1(ox), P33/3. 19. *Impagidinium parvireticulatum*; Core 1, 7750'-7753', 2(ox), V37/0; ventral view. 20. *Impagidinium parvireticulatum*; Core 1, 7750'-7753', 2(ox), V37/0; dorsal view. 21. *Hystrichostrogylon membraniphorum*; Core 1, 7762'-7765', 1(ox), J34/1. Arrow points to the opening in the posterior part of the periphagmal pericoel. 22. *Hystrichostrogylon membraniphorum*; Core 1, 7762'-7765', 1(ox), G52/4. 23. *Hystrichostrogylon membraniphorum*; Core 1, 7765'-7768', 1(ox), M42/3. 24. *Impagidinium* sp. 1 Heilmann-Clausen, 1985; Core 1, 7750'-7753', 2(ox), S45/0; ventral view. 25. *Impagidinium* sp. 1 Heilmann-Clausen, 1985; Core 1, 7750'-7753', 2(ox), S45/0; dorsal view. 26. *Impagidinium* sp. 1. Heilmann-Clausen, 1985; Core 1, 7750'-7753', 1(ox), L40/0; lateral view. 27. *Impagidinium* sp. A; Core 1, 7750'-7753', 3(ox), O62/0; ventral view. 28. *Impagidinium* sp. A; Core 1, 7750'-7753', 3(ox), O62/0; dorsal view. 29. *Impagidinium crassimuratum*; Core 1, 7759'-7762', 1(ox), S35/3; ventral view. 30. *Impagidinium crassimuratum*; Core 1, 7759'-7762', 1(ox), S35/3; dorsal view. 31. *Impagidinium dispersitum*; Core 1, 7759'-7762', 1(ox), D56/0

and an influx of *Achomosphaera/Spiniferites* complex at the top of the association (Fig. 12). Other abundant taxa include *Pxydinopsis ardonensis* and *Nematosphaeropsis* sp. var. nov. Accessory taxa include *Andalusiella gabonensis*, *Spiniferites wetzeli*, *S. mirabilis*, *S. ramosus* subsp. *ramosus*, *S. multibrevis*, *Manumiella* sp. var. nov., *Disphaerogena carposphaeropsis* and *Fromea fragilis*. The Dinocysts which have been recognised only from this association are *Aiora fenestrata* and *Pierceites pentagonus*. The former is long ranging (mid-Cretaceous-Maastrichtian), whereas the later is known from the Maastrichtian (Habib and Drugg, 1987, May, 1980) and Maastrichtian-Danian of Alabama, USA (Moshkovitz & Habib, 1993). Sporomorphs are dominated by the gymnosperm pollen grain *Inaperturopollenites hiatus*. Rare specimens of angiosperm pollen grains are also recognised including rare *Spinizonocolpites baculatus*, *Monocolpites marginatus* and *Mauritiidites lehmanii*, which represent < 1% of the total palynomorph assemblages. *Cerodinium pannuceum*, *Phelodinium magnificum* and *Disphaerogena carposphaeropsis* are mainly known from Maastrichtian and Palaeocene strata world-wide (e.g., Stanley, 1966; Zaitzeff & Cross, 1971; Benson, 1976; May, 1980; Brinkhuis & Leereveld, 1988; Brinkhuis & Zachariasse, 1988; Heilmann-Clausen, 1985; Firth, 1993; Jan du Chêne, 1988; Soncini & Rauscher, 1988). *P. ardonensis* has been reported only from the Danian sediments of Senegal (Jan du Chêne, 1988); *S. baculatus* is known from the late Maastrichtian sediments of Nigeria and Somalia (Jan du Chêne et al., 1980; Oloto, 1989; Edet & Nyong, 1994; Schrank, 1994), Senonian-Palaeocene of Sarawak (Muller, 1968) and Paleogene sediments (Palaeocene and Eocene) of India and Nigeria (Jan du Chêne et al., 1978; Mathur & Chopra, 1987); *M. lehmanii* is known from the Maastrichtian of Cameroon and Egypt (Salard-Chebouldaëff, 1978; Schrank, 1987) and Late Maastrichtian of Somalia (Schrank, 1994). *M. marginatus* has been reported mainly from the late

Maastrichtian-Eocene sediments of Nigeria (Adegoke et al., 1978; Edet & Nyong, 1994; Jan du Chêne, 1977).

Based on the stratigraphic range of the taxa cited above, a late Maastrichtian age is considered appropriate for this association.

There is no nannofossil data for these intervals, probably due to dissolution. The upper boundary coincides with the base of the nannofossil zone *Micula murus* (CC25) of El-Mehaghag (1996).

#### Association 18

Age: late Maastrichtian.

Interval: 7780'-7785'.

This association is marked by a decline in the main components of the preceding association and an influx of *Andalusiella gabonensis*, *Spiniferites wetzeli* and *Areoligera* cf. *senonensis*. Accessory taxa include *Cometodinium whitei*, *Cerodinium diebelii* and *Palaeocystodinium lidiae*. The latter species is known mainly from the late Maastrichtian sediments world-wide (Davey, 1969a; Erkmen & Sadek, 1981; Górka, 1963; Lindgren, 1984), and the former species (*C. whitei*) is known mainly from Aptian to Maastrichtian sediments world-wide (e.g. Aptian-Albian, Senegal; Vraconian-early Cenomanian, Libya; Coniacian, France; early Campanian, Iran; Maastrichtian, Nigeria). *S. wetzeli* is mainly known from the Senonian sediments of Baltic Region and France (Deflandre, 1935; Wetzel, 1933), Maastrichtian sediments of Arctic and Germany (Ioannides, 1986; Marheinecke, 1986). One of the most important stratigraphic events to occur in this association is the first occurrence of *Kenleyia lophophora* and new variety of *Glaphyrocysta* sp. var. nov. The former species was mainly known from the Paleocene strata of Australia and NW Tunisia (Brinkhuis & Zachariasse, 1988; Cookson & Eisenack, 1965, 1967), but the Libyan assemblage supports Oloto's (1989) findings from the late Maastrichtian of



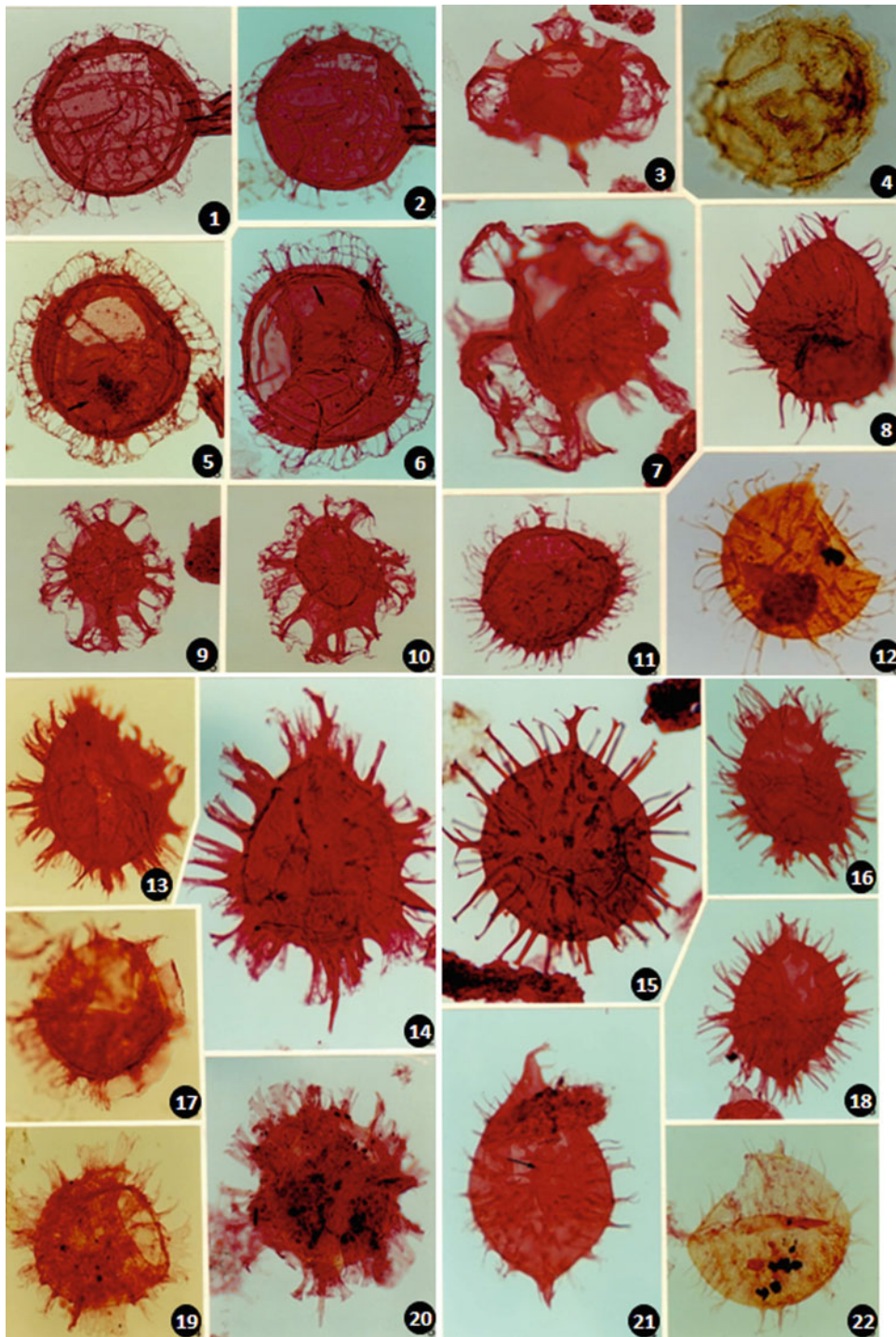


**Plate 8** 1. *Nematosphaeropsis* sp. A var. nov.; Core 5, 8562'-8565', 1 (ox), H50/2; ventral view. Focused on the ventral side to show the offset nature of the paracingulum and the intergonal processes. 2. *Nematosphaeropsis* sp. A var. nov.; Core 5, 8562'-8565', 1(ox), H50/2; dorsal view. Focused on the third dorsal paraplate to show the nature of the intergonal processes. 3. *Disphaerogenera carposphaeropsis*; Core 1, 7770'-7773', 4(ox), N51/0; X150; dorsal view. 4. *Danaea* spp.; Core 1, 7750'-7753', 1(unox), C32/4; antapical view. 5. *Nematosphaeropsis* sp. B var. nov.; Core 5, 8576'-8576'6", 1(ox), C41/3. Arrow points to the operculum inside the cyst. 6. *Nematosphaeropsis* sp. B var. nov.; Core 5, 8562'-8562', 1(ox), W59/2. 7. *Disphaerogenera carposphaeropsis*; Core 1, 7770'-7771', 1 (ox), S42/3; intermediate focus. 8. *Nematosphaeropsis* sp. var. B nov.; Core 5, 8562'-8565', 1(ox), W59/2. 9. *Exochosphaeridium bifidum*; Core 5, 8580'-8581'6", 1(ox), L58/0; lateral view.

*Nematosphaeropsis* sp. C var. nov.; Core 1, 7765'-7768', 1(ox), R55/0. 10. *Nematosphaeropsis* sp. C var. nov.; Core 1, 7765'-7768', 1 (ox), Q50/3. A densely granulate cyst with distally fenestrate processes. 11. *Exochosphaeridium bifidum*; Core 5, 8580'-8581'6", 1(ox), J59/2; dorsal view. 12. *Exochosphaeridium bifidum*; Core 4, 8511'-8514', 3 (ox), F38/3. 13. *Danaea californica*; Core 1, 7762'-7765', 1(ox), D58/0; lateral view. 14. *Danaea californica*; Core 1, 7756'-7759', 3(ox), O43/0; lateral view. 15. *Fibrocysta axiallis*; Core 1, 7785'-7788', 3(ox), M55/2. 16. *Fibrocysta radiata*; Core 1, 7762'-7765', 1(ox), D56/0. 17. *Danaea manicata*; Core 1, 7750'-7753', 1(ox), M49/0; dorsal view. 18. *Fibrocysta radiata*; Core 1, 7759'-7762', 1(ox), S39/2. 19. *Danaea manicata*; Core 1, 7750'-7753', 1(ox), C50/0; lateral view. 20. *Danaea californica*; Core 1, 7750'-7753', 2(ox), D48/4; dorso-lateral view. 21. *Fibrocysta lappacae*; Core 1, 7762'-7765', 1(ox), W58/3. Arrow points to the operculum inside the cyst

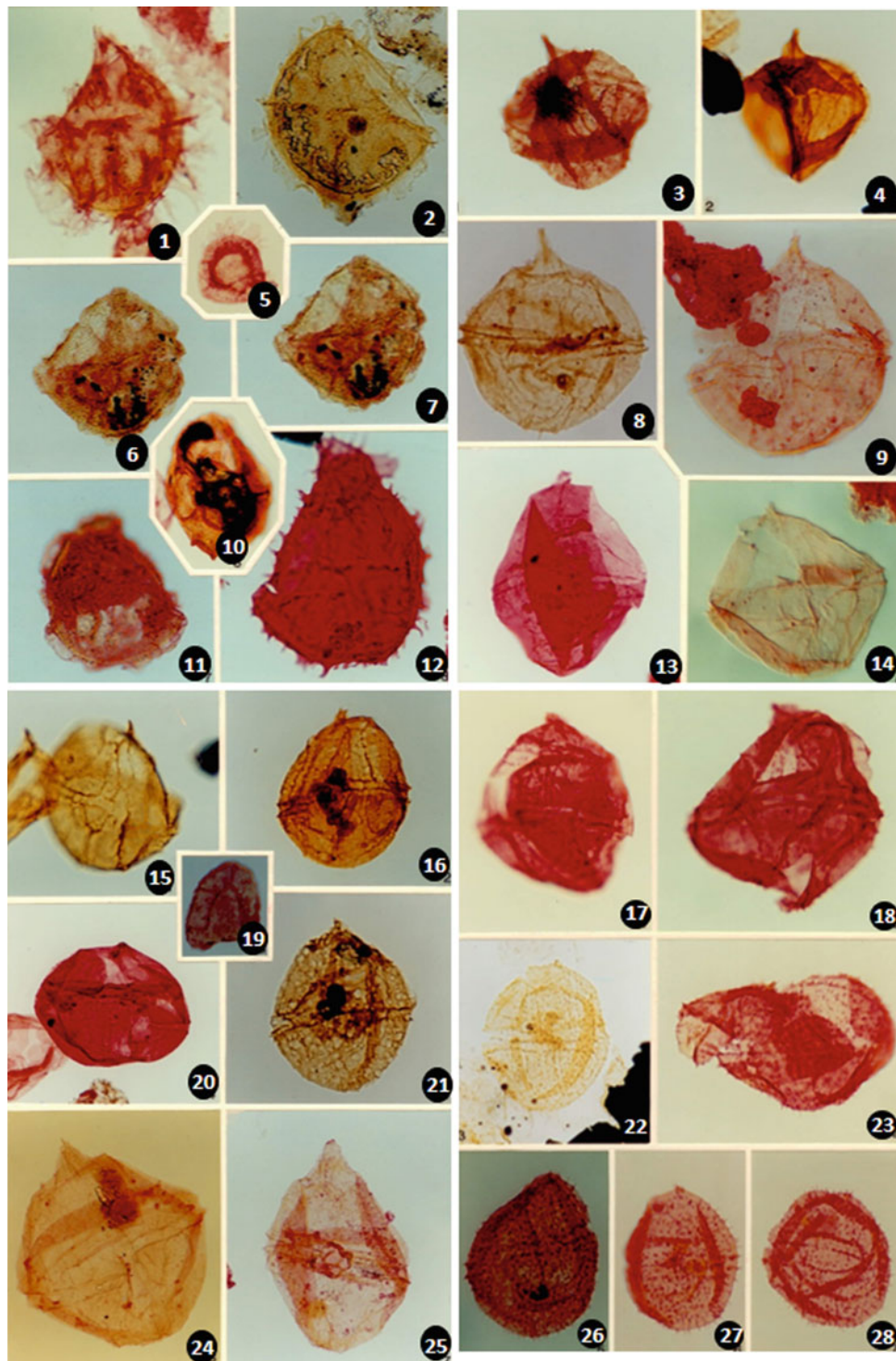
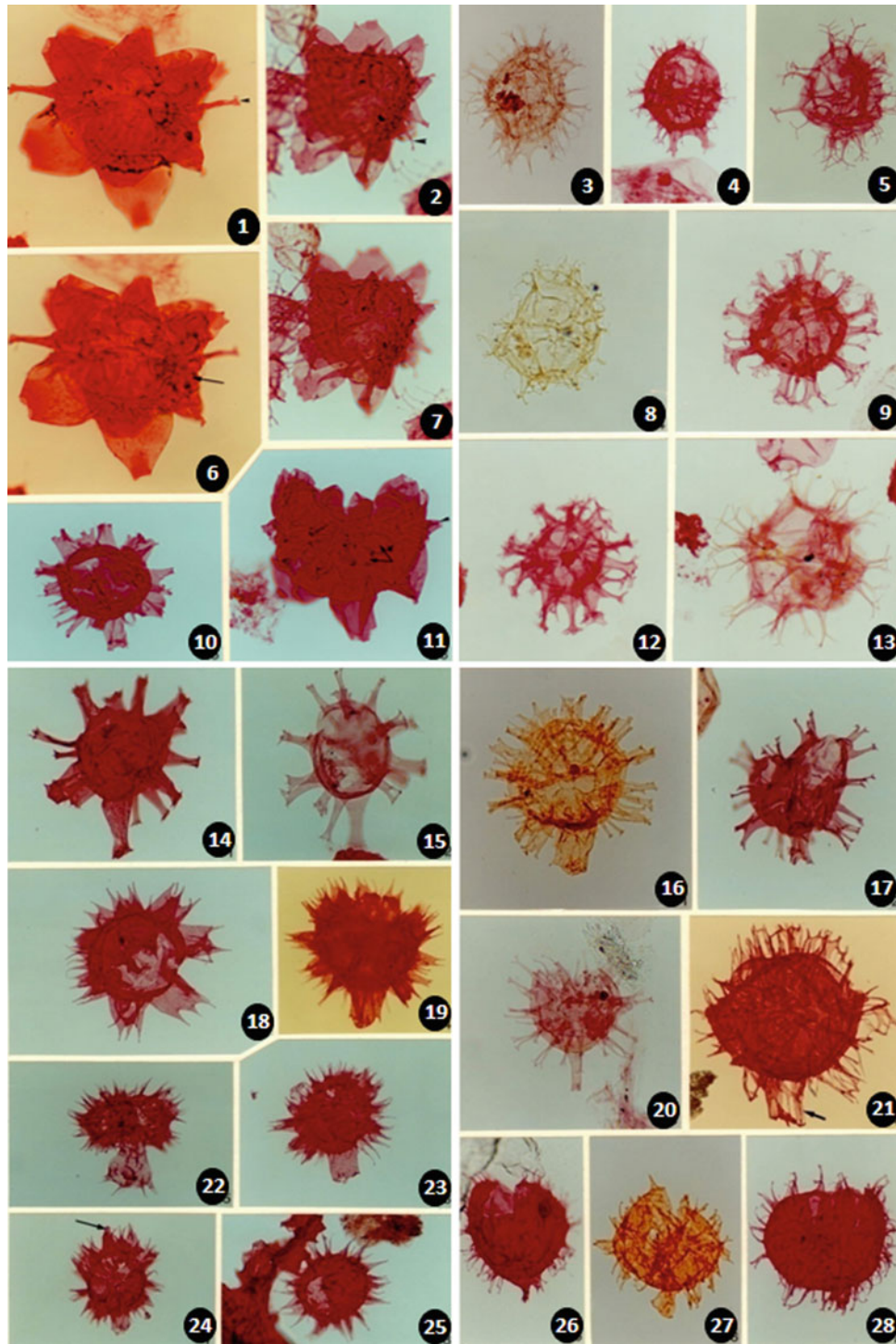


**Plate 9** 1. *Danea manicata*; Core 1, 7750'-7753', 2(ox), H39/2; high focus, lateral view. 2. *Danea abbreviata*; Core 1, 7750'-7753', 1(unox), F40/2; lateral view. 3. *Cribroperidinium intricatum*; Core 4, 8502'-8505', 1(ox), D61/0. 4. *Cribroperidinium intricatum*; Core 4, 8505'-8508', 1(ox), L40/0. 5. Operculum, *Danea manicata*; Core 1, 7750'-7753', 2(ox), E50/0. 6. *Danea impages*; Core 1, 7750'-7753', 2(ox), L51/4; low focus, lateral view. 7. *Danea impages*; Core 1, 7750'-7753', 2(ox), L51/4; high focus, lateral view. 8. *Cribroperidinium orthoceras*; Core 3, 8461'-8464', 3(ox), T34/1. 9. *Cribroperidinium wetzelii*; Core 1, 7780'-7783', 1(ox), C55/4. 10. *Danea* spp.; Core 1, 7750'-7753', 2(ox), E43/0; dorsal view. 11. *Danea impages*; Core 1, 7750'-7753', 2(ox), C49/2. 12. *Danea abbreviata*; Core 1, 7759'-7762', 1(ox), F58/2; lateral view. Specimen showing penitabular septa grading to intratabular processes. 13. *Cribroperidinium tenuitabulatum*; Core 1, 7759'-7762', 1(ox), P39/0, IC. 14. *Cribroperidinium wetzelii*; Core 1, 7750'-7753', 3

(ox), N57/0, IC. 15. *Cribroperidinium* sp. C; Core 4, 8489'6"-8490', 1(ox), N44/2; ventral view, low focus. 16. *Cribroperidinium* sp. C; Core 4, 8489'6"-8490', 1(ox), N50/0. 17. *Trichodinium castanea* var. A; Core 3, 8443'-8446', 1(ox), X32/3. 18. *Trichodinium castanea* var. A; Core 3, 8443'-8446', 2(ox), B28/4. 19. Operculum, *Cribroperidinium* sp.; Core 4, 8505'-8508', 1(ox), G47/2. 20. *Cribroperidinium* sp. E; 8496'-8499', 1(ox), O35/4. 21. *Cribroperidinium* sp. D; Core 4, 8496'-8499', 2(unox), L39/0. 22. *Trichodinium castanea* subsp. *castane*; Core 2, 8410'-8412', 1(unox), W40/3. 23. *Trichodinium castanea* subsp. *castane*; cuttings, 8390', 1(ox), W51/4. 24. *Cribroperidinium* spp.; Core 1, 7780'-7783', 1(ox), R56/4. 25. *Cribroperidinium* spp.; Core 1, 7780'-7783', 1(ox), W56/3. 26. *Trichodinium castanea* subsp. *bifurcatum*; cuttings, 8390', 3(ox), O35/0. 27. *Trichodinium castanea* subsp. *bifurcatum*; Core 2, 8410'-8412', 1(ox), E44/0. 28. *Trichodinium castanea* subsp. *bifurcatum*; Core 2, 8410'-8412', 1(ox), G44/4



Nigeria. This association has the highest percentage of sporomorphs of any of the other late Maastrichtian-Danian associations, including the gymnosperm pollen *Inaperturopollenites hiatus* (has a long stratigraphic range from Jurassic-Neogene) and the angiosperm pollen *Auriculiidites reticulatus* (known from the Campanian of Peru and Brazil;

the late Maastrichtian of Egypt, and Nigeria), *Mauritiidites lehmanii* (known from the Maastrichtian of Cameroon and Egypt), *Spinizonocolpites baculatus* (known from the late Maastrichtian of Nigeria and Somalia; Paleocene and Eocene of Sarawak, Nigeria, India and Brazil), *Ctenolophonidites costatus* (known from the late Maastrichtian of

◀ **Plate 10** 1. *Hystrichokolpoma cinctum*; Core 1, 7759'-7762', 1(ox), R49/4; high focus, latero-dorsal view, showing long slender paracingular processes (arrows) 2. *Hystrichokolpoma cinctum*; Core 1, 7759'-7762', 2(ox), M42/1. Specimen showing short tubules below the distal opening of the precingular and postcingular processes; low focus, latero-ventral view showing parasulcus processes (arrow). 3. *Spiniferites mirabilis*; Core 4, 8496'-8499', 1(ox), J37/3. 4. *Spiniferites multibrevis*; Core 1, 7785'-7788', 1(ox), S48/4. 5. *Spiniferites ramosus* subsp. *ramosus*; Core 2, 8428'-8431, 1(ox), D38/2. 6. *Hystrichokolpoma cinctum*; Core 1, 7759'-7762', 1(ox), R49/4; low focus, showing parasulcus (arrow) represented by about five thick processes, with clear striation on the postcingular ones. 7. *Hystrichokolpoma cinctum*; Core 1, 7759'-7762', 2(ox), M42/1. Specimen showing short tubules below the distal opening of the precingular and postcingular processes; high focus. 8. *Spiniferites multibrevis*; Core 3, 8455'-8458', 2(unox), T40/0. 9. *Spiniferites pseudofurcatus*; Core 1, 7774'-7775', 3(ox), U54/4. 10. *Hystrichokolpoma granulatum*; Core 1, 7759'-7762', 2(ox), V31/4; apical view. Specimen showing apical archeopyle with attached operculum. 11. *Hystrichokolpoma cinctum*; Core 1, 7759'-7762', 1(ox), K51/3; ventral view. Specimen showing short slender

paracingular processes (small arrow) and thick parasulcus processes (large arrow). 12. *Spiniferites pseudofurcatus*; cuttings, 8930', 1(ox), Q50/0. 13. *Spiniferites ramosus* subsp. *gracilis*; Core 2, 8410'-8412', 1(ox), G35/1. 14. *Florentinia deanei*; Core 1, 7762'-7765', 1(ox), H64/1. 15. *Florentinia deanei*; Core 1, 7750'-7753', 2(ox), C35/3. 16. *Florentinia radiculata*; Core 4, 8514'-8517', 3(ox), C50/0. 17. *Florentinia radiculata*; Core 4, 8496'-8499', 1(ox), F55/4. 18. *Florentinia ferox*; Core 1, 7762'-7765', 1(ox), K38/3; apical view. 19. *Florentinia ferox*; Core 1, 7756'-7759', 1(ox), U41/0. 20. *Florentinia radiculata*; Core 1, 7750'-7753', 2(ox), D40/2. 21. *Florentinia* sp. A; Core 5, 8580'-8581'6", 2(ox), P40/4. Arrow points to the fenestrate antapical process. 22. *Florentinia ferox*; Core 1, 7762'-7765', 1(ox), D37/1. Specimen showing broad figshaped antapical processes with short spines. 23. *Florentinia ferox*; Core 1, 7756'-7759', 1(ox), C43/3. 24. *Florentinia ferox*; Core 1, 7762'-7765', 1(ox), K55/0. Arrow points to the well developed apical nipple or "horn". 25. *Florentinia ferox*; Core 1, 7762'-7765', 1(ox), U54/0; apical view. 26. *Florentinia* spp.; Core 5, 8580'-8581'6", 1(ox), F60/1. 27. *Florentinia* spp.; Core 45, 8511'-8514', 2(ox), D62/1. 28. *Florentinia* spp.; Core 5, 8580'-8581'6", 1(ox), G57/1

Nigeria and Somalia; the early-middle Miocene of India), *Mauritiidites crassibaculatus* (known from the late Maastrichtian-Paleocene of Nigeria and the late Maastrichtian of Somalia) in addition to *Monocolpopollenites* sp. and other undifferentiated angiosperm pollen grains. The *C. costatus* and *M. crassibaculatus* make their first occurrence in this association.

Based on the stratigraphic range of the recovered taxa, a late Maastrichtian age was found appropriate for this association. The base of this association coincides with the lower boundary of the late Maastrichtian nannofossil *Micula murus* Zone (CC25), and the top coincides with the middle part of *Nephrolithus frequens* Zone (CC26) of El-Mehaghag (1996).

### Association 19

**Age:** late Maastrichtian.

**Interval:** 7777'-7780'.

This association is characterised by a decline in sporomorphs and some of the dinocysts which characterise the preceding association. These include *Spiniferites wetzelii*, *Areoligera* cf. *senonensis* and *A. coronata* complex, and an influx of *Cerodinium*/*Senegalinium* complex, characterised by a predominance of *Cerodinium pannuceum* (known from the Campanian–Maastrichtian of USA; Maastrichtian-Paleocene of Morocco and Tunisia) and *Palaeocystodinium*/*Andalusiella* complex (Fig. 12) which is characterised by abundant *Palaeocystodinium australinum* (known from the ?Campanian–Maastrichtian of USA; Maastrichtian of Morocco, Nigeria, Turkey; late Campanian, NE Libya). Other taxa which continue to be abundant include *Nematosphaeropsis* sp. var., nov. and *Andalusiella gabonensis* (mainly known from the Campanian–Maastrichtian of Egypt; Maastrichtian of Gabon). Accessory taxa include *Cometodinium whitei* (known mainly from Aptian to Maastrichtian strata world-wide) and *Senegalinium bicavatum* (Campanian–

Maastrichtian, NE Africa; Maastrichtian, Morocco, Nigeria; Maastrichtian-Danian, Tunisia) and *Trigonopyxidina ginella* (known mainly from early and Late Cretaceous sediments world-wide), and they show their first occurrence in this interval. They suggest late Maastrichtian-Danian age for this association, but the predominance of *Andalusiella gabonensis* (mainly known from the Campanian–Maastrichtian of Egypt; Maastrichtian of Gabon) suggests a late Maastrichtian age.

This association is also characterised by a peak of the nannofossil *Micula decussata*, second only to that in Association 22, and equates with the upper part of the late Maastrichtian nannofossil *Nephrolithus frequens* Zone (CC26) of El-Mehaghag (1996).

### Association 20

**Age:** late Maastrichtian.

**Interval:** 7774'-7777'.

The base of this association is characterised by a predominance of the dinocysts *Spiniferites* cf. *cornutus* subsp. *cornutus*, *Riculacysta perforata*, and *Kenleyia lophophora* and at its top by *Cometodinium whitei* and *Cerodinium pannuceum*. There is a decline in *Andalusiella gabonensis* and very rare sporomorphs are represented by *Mauritiidites lehmanii*. Accessory taxa include *Palaeocystodinium golzowense*, *Lejeunecysta hyalina*, *Cerodinium diebelii*, *C. obscurum*, *Spiniferites ramosus* subsp. *ramosus*, *S. multibrevis*, *Fromea chytra*, *Dinogymnium nelsonense* and *Dinogymnium* spp. The latter genus (*Dinogymnium*) has its last occurrence in Association 20, whereas *Dinogymnium avellana* has its last occurrence in Association 22. *R. perforata* is known only from the Maastrichtian-Danian of Tunisia (Brinkhuis & Leereveld, 1988; Brinkhuis & Zachariasse, 1988) and Paleocene-Oligocene world-wide (e.g. Stover, 1977; Mathur, 1986; El-Beialy, 1988 and 1990). *P. golzowense*, *L. hyalina* and *Cerodinium diebelii*

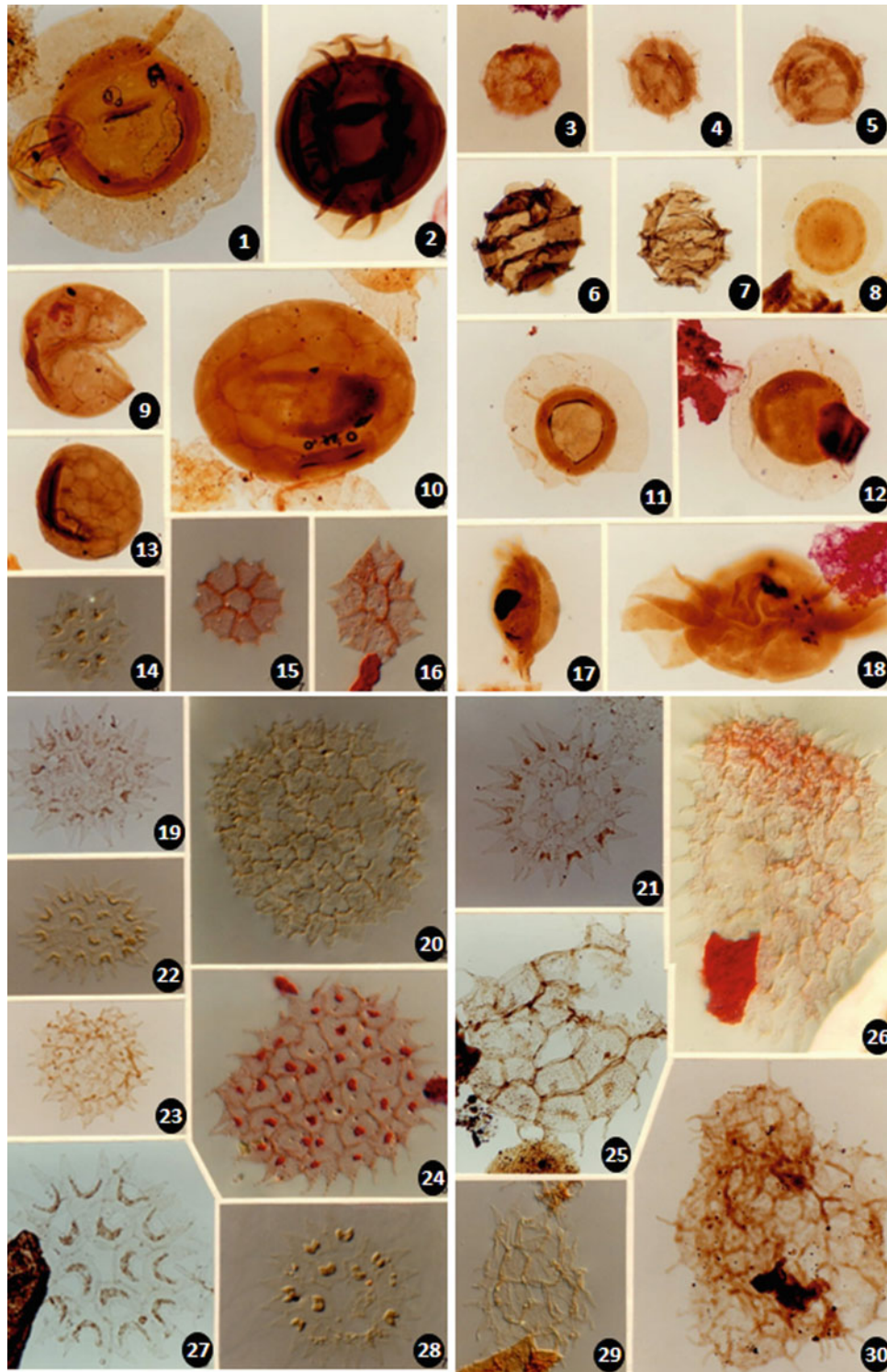


**Plate 11** 1. *Pterospermella* spp.; Core 4, 8461'-8464', 1(unox), N60/4. 2. *Pterospermella* spp.; Core 4, 8496'-8499', 1(ox), G33/4. 3. *Cymatiosphaera* spp.; Core 5, 8562'-8565', 1b(ox), J41/0. 4. *Cymatiosphaera* spp.; Core 4, 8499'-8502', 2(ox), J46/2. 5. *Cymatiosphaera* spp.; Core 4, 8496'-8499', 2(ox), F51/4. 6. *Cymatiosphaera* spp.; Core 4, 8487' 10'-8489'6", 1(unox), Q46/0. 7. *Cymatiosphaera* spp.; Core 4, 8487' 10'-8489'6", 1(unox), J35/4. 8. *Pterospermella* spp.; Core 4, 8487' 10'-8489'6", 1(unox), U59/0. 9. *Pterosphaeridia pachytheca*; Core 4, 8496'-8499', 1(ox), Q49/2. 10. *Pterosphaeridia pachytheca*; Core 4, 8502'-8505', 1(ox), M49/3. 11. *Pterospermella* spp.; Core 4, 8508'-8511', 1(ox), K60/1. 12. *Pterospermella* spp.; Core 4, 8487'10"-8489'6", 1a(ox), Y54/1. 13. *Pterosphaeridia pachytheca*; Core 4, 8496'-8499', 1(ox), Q49/2. 14. *Pediastrum angulatus*; Core 6, 8614'-8617', 2(ox), R52/4, IC. 15. *Pediastrum angulatus*; Core 4, 8536'-8539', 1(ox), R40/1,

IC. 16. *Pediastrum angulatus*; Core 4, 8536'-8539', 1(ox), D42/3, IC. 17. *Pterospermella* spp.; Core 4, 8502'-8505', 1(ox), Y54/2; equatorial view. 18. *Pterospermella* spp.; cuttings, 8390', 3(ox), R43/0; equatorial view. 19. *Pediastrum bifidites*; Core 6, 8614'-8617', 4(ox), V59/2. 20. *Pediastrum paleogeneites*; Core 5, 8584'-8588', 3(ox), K42/4, IC. 21. *Pediastrum* sp. A; Core 6, 8614'-8617', 2(ox), O61/3. 22. *Pediastrum bifidites*; Core 6, 8614'-8617', 6(ox), Q36/4, IC. 23. *Pediastrum bifidites*; Core 5, 8545'-8548', 1(unox), L55/1. 24. *Pediastrum paleogeneites*; Core 4, 8536'-8539', 1(ox), G46/0, IC. 25. *Pediastrum* sp. C; Core 5, 8545'-8548', 1(unox), M62/4; X150. 26. *Pediastrum* sp. B; Core 5, 8580'-8581' 6", 4(ox), X36/3, IC. 27. *Pediastrum* cf. *delicatites*; Core 6, 8614'-8617', 5(ox), M53/3. 28. *Pediastrum* sp. A; Core 6, 8614'-8617', 5(ox), X53/0, IC. 29. *Pediastrum* sp. A; Core 6, 8614'-8617', 4(ox), C51/4, IC. 30. *Pediastrum* sp. B; Core 6, 8614'-8617', 5(ox), X53/0

are known mainly from Maastrichtian-Palaeocene sediments world-wide, and *F. chytra* is known from the Santonian-Maastrichtian of Canada (McIntyre, 1974), Maastrichtian-Danian of USA and Australia (Cookson & Eisenack, 1970; Drugg, 1967; Helby et al., 1987).

The palynomorph assemblages present in this association suggest a late Maastrichtian. A Maastrichtian age is supported by presence of high diversity of *Dinogymnium* species which are known mainly from late Cretaceous strata world-wide and not crossing the K/Pg boundary. A Paleocene age is considered unlikely for this association due to the absence of Danian index taxa which begin to appear in Association 23.

This association equates with the base of the late Maastrichtian nannofossil *Micula prinsii* Zone of El-Mehaghag (1996).

### Association 21

**Age:** late Maastrichtian.

**Interval:** 7771'-7774'.

This association is characterised by the first occurrence of *Carpatella cornuta*, *Kenleyia pachycerata*, *Heteraulacacysta granulata*, *Phelodinium africanum* and *P. boldii*, a decline in the dominant elements of Association 20, and a higher influx of the *Areoligera/Glaphyrocysta* complex, predominated by the new variety *Glaphyrocysta* var. nov., and *Cerodinium/Senegalinium* complex (<30%), in *Senegalinium laevigatum* subsp. var. nov. was dominant (Fig. 12). Accessory taxa include *Kenleyia lophophora*, *Operculodinium* spp. *Spiniferites* cf. *cornutus* subsp. *cornutus*, *S. multibrevis*. *K. lophophora* is known from the late Maastrichtian of Nigeria (Oloto, 1989) and the Paleocene of Australia and Tunisia (Brinkhuis & Leereveld, 1988; Brinkhuis & Zachariasse, 1988; Cookson & Eisenack, 1967). *C. cornuta* is known from the uppermost Maastrichtian and Paleocene strata of Sweden (Damassa, unpubl. after Damassa, 1988), and Denmark (Hansen, 1977). *S. laevigatum* is known mainly from the Campanian-Maastrichtian of Egypt (Schrank, 1987), Nigeria (Edet & Nyong, 1994; Oloto, 1989), NW Africa (Jain & Millepied, 1973), USA (Habib & Miller, 1989), Sirt Basin (Bu-Argoub, 1996) and Maastrichtian-Danian of Tunisia (Brinkhuis & Zachariasse, 1988).

A late Maastrichtian age is most appropriate for this association as it similar to the preceding one. Paleocene age is not considered likely for this association due to the absence of Danian index taxa which show their first occurrence in Association 23.

This association equates with middle part of the late Maastrichtian nannofossil *Micula prinsii* Zone of El-Mehaghag (1996).

### Association 22

**Age:** late Maastrichtian.

**Interval:** 7765'-7771'.

This association represents the topmost part of the late Maastrichtian in the studied well. It is marked by a decline in the main elements of the preceding association and characterised by an influx of *Areoligera/Glaphyrocysta* complex dominated by *Riculacysta perforata*, and a higher influx of *Andalusiella/Palaeocystodinium* complex (Fig. 12) dominated by *Andalusiella gabonensis*. Accessory taxa include *Achomosphaera ramulifera*, *Areoligera coronata*, *Areoligera* cf. *senonensis*, *Disphaerogena carposphaeropsis* (Late Cretaceous, Baltic Region; Maastrichtian-Paleocene, Tunisia, USA; Early Paleocene, Denmark), *Florentinia ferox* (Albian-Danian, world-wide), *Hystrichokolpoma rigaudiae* (Albian-Pleistocene, world-wide), *Nematosphaeropsis* sp. C var. nov. (Plate 8, Figs. 9 and 10), *Phelodinium magnificentum* (Maastrichtian-Paleocene, world-wide), *Spiniferites* cf. *cornutus* subsp. *cornutus*, *S.* cf. *cornutus* subsp. *laevimurus* and *S. mirabilis*. *Manumiella conorata* (Paleocene, Australia, Romania, Tunisia) makes its first occurrence in the basal sample and *Manumiella seelandica* (late Maastrichtian, Morocco, Antarctica and USA; Maastrichtian-Danian, Morocco, Australia, Denmark, USA, Romania, New Zealand) in the uppermost sample. *R. perforata* is known mainly from Tertiary strata world-wide but also has been recorded from the Maastrichtian of Tunisia (Brinkhuis & Leereveld, 1988). These taxa suggest late Maastrichtian-Danian for this association but the high abundance of *Andalusiella gabonensis* (Mainly known from the Campanian-Maastrichtian of Egypt; Maastrichtian of Gabon). However, a late Maastrichtian age seems plausible for this interval. The last occurrence of *Dinogymnium* within this association and the first occurrence of the Danian index dinocyst taxa in the next association (Association 23) is also in favour of a late Maastrichtian age.

This association equates with the upper part of the late Maastrichtian nannofossil *Micula prinsii* Zone of El-Mehaghag (1996).

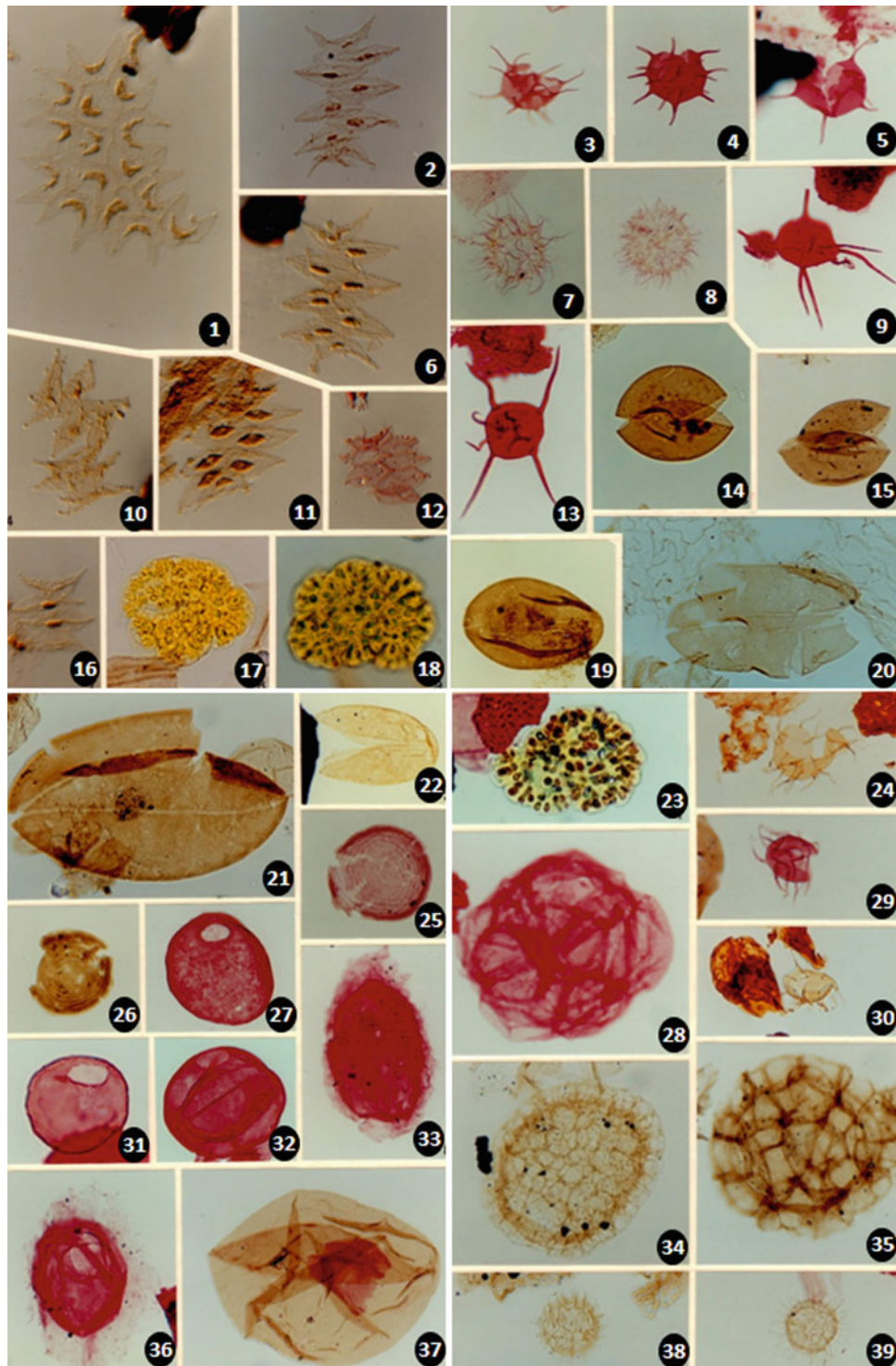
The Maastrichtian associations have no counterpart in the zonation scheme developed neither by Bu-Argoub (1996), nor by Keegan and Stead (2007).

### Association 23

**Age:** late early Danian.

**Interval:** 7762'-7765'.

This association represents the basal Danian in the studied well. It is marked by a decline in peridinioid cysts and an influx in gonyaulacoid cysts, including the *Achomosphaera*



◀ **Plate 12** 1. *Pediastrum* cf. *delicatites*; Core 6, 8614'-8617', 2(ox), F37/1, IC. 2. *Scenedesmus* spp.; Core 6, 8614'-8617', 4(ox), N45/1. 3. *Scenedesmus* spp.; Core 6, 8614'-8617', 6(ox), M56/0, IC. 4. *Veryhachium singulare*; Core 4, 8520'-8523', 1(ox), T63/1. 5. *Veryhachium singulare*; Core 5, 8580'-8581'6", 1(ox), X51/1. 6. *Veryhachium singulare*; Core 2, 8410'-8412', 1(ox), P42/0. 7. *Solisphaeridium* sp.; Core 2, 8410'-8412', 1(ox), D47/0. 8. *Solisphaeridium* sp.; Core 2, 8410'-8412', 1(ox), D57/2. 9. *Tubulospina oblongata*; Core 1, 7762'-7765', 1(ox), F57/4. 10. *Scenedesmus bifidus*; Core 6, 8614'-8617', 6(ox), V43/0, IC. 11. *Scenedesmus* spp.; Core 6, 8614'-8617', 1(unox), G41/0, IC. 12. *Scenedesmus* spp.; Core 4, 8536'-8539', 1(ox), G55/0, IC. 13. *Tubulospina oblongata*; Core 1, 7762'-7765', 1(ox), S58/2. 14. *Brazilea circularis*; Core 3, 8461'-8464', 1(unox), H52/0. 15. *Brazilea circularis*; Core 3, 8461'-8464', 1(unox), O59/4. 16. *Scenedesmus* spp.; Core 6, 8614'-8617', 5(ox), G45/4, IC. 17. *Botryococcus braunii*; Core 5, 8584'-8588', 2(ox), M55/0. 18. *Botryococcus braunii*; Core 6, 8511'-8514', 4(ox), K50/2. 19. *Brazilea parva*; Core 6, 8614'-8617', 2(ox), S37/3; X150. 20.

*Brazilea parva*; Core 3, 8584'-8588', 2(ox), R40/4. 21. *Brazilea parva*; Core 3, 8487'10"-8489'6", 1(unox), V39/2. 22. *Brazilea parva*; Core 3, 8584'-8588', 1(ox), E51/2. 23. *Botryococcus braunii*; Core 4, 8542'-8545', 1(ox), P57/0. 24. *Baltisphaeridium* sp. A; Core 4, 8487'-8487'10", 1(ox), Q51/1. 25. *Chomotriletes* spp.; Core 5, 8576'-8576'6", 1(ox), J46/3. 26. *Chomotriletes* spp.; Core 4, 8545'-8548', 1(unox), V39/2. 27. *Cyclopsiella* spp.; Core 4, 8496'-8499', 1(ox), S36/0. 28. *Palambages* spp.; Core 1, 7759'-7762', 1(ox), P36/4. 29. *Baltisphaeridium* sp. A; Core 4, 8490'-8493', 1(ox), Q31/2. 30. *Baltisphaeridium* sp. A; Core 4, 8487'-8487'10", 1(ox), G54/3. 31. *Cyclopsiella* spp.; Core 1, 7759'-7762', 1(ox), O52/4. 32. *Cyclopsiella* spp.; Core 1, 7756'-7759', 1(ox), M34/0. 33. *Eyrea nebulosa*; Core 5, 8580'-8581'6", 1(ox), W58/0. 34. *Palambages* spp.; Core 2, 8410'-8412', 1(unox), M44/3. 35. *Palambages* spp.; Core 4, 8487'10"-8489'6", 1(unox), J64/2. 36. *Eyrea nebulosa*; Core 5, 8549'6"-8550, 1(ox), G34/1. 37. *Leiosphaeridia* spp.; Core 4, 8496'-8499', 2(ox), V44/0; X150. 38. *Michrhystridium* spp.; Core 2, 8428'-8431', 1(unox), O46/3. 39. *Michrhystridium* spp.; cuttings, 8390', 1(ox), E39/0.

*Spiniferites* complex (up to 30%) (Fig. 13). ?*Adnatosphaeridium* sp. is the most characteristic taxon in this association, where it represents up to 10.6% of the total assemblage. The most characteristic events to occur in this association include the first occurrence of *Danea californica* and *Alisocysta* sp. A. The former species is known only from Paleocene strata world-wide and has been used in Danian zonation scheme from many different areas, such as Tunisia (Brinkhuis & Leereveld, 1988; Brinkhuis & Zachariasse, 1988), Denmark (Hansen, 1977; Kjellström & Hansen, 1981) and southern Sweden (Hultberg, 1985). This is the case in the current work where this species is herein considered a good stratigraphic marker for the early Paleocene. Accessory taxa include *Achomosphaera neptuni*, *Diphyes spinulum*, *Hystrichokolpoma rigaudiae*, *Spiniferites* cf. *cornutus* subsp. *cornutus*, *S. ramosus* subsp. *ramosus* and *Fibrocysta* spp. The latter is characterised by the occurrence of *F. furcata* and *F. radiata* which are known mainly from the Danian sediments of Senegal (Jan du Chêne, 1988) and the Eocene strata of Belgium, England, Germany (Bujak et al., 1980; Eaton, 1976; Islam, 1983; Morgenroth, 1966). Based on the evidence cited above, this association corresponds to the late early Danian.

Nannofossil assemblage is characterised by an influx of *Thoracosphaera* sp. (calcareous-walled dinoflagellate) and a decline of *Braarudosphaera bigelowii*. Association 23 equates with the upper part of the early Danian nannofossil zone *Cruciplacolithus tenuis* (NP2) of El-Mehaghag (1996).

However, the Danian associations have no counterpart in Libya. The available and published palynological studies on Libya include Bu-Argoub (1996), who studied the Upper Cretaceous in SE Sirt only, and the available Cenozoic study from NE Libya by Stead (2007) does not include the Paleocene sequence as the lithotypes are unfavourable for the preservation of palynomorphs.

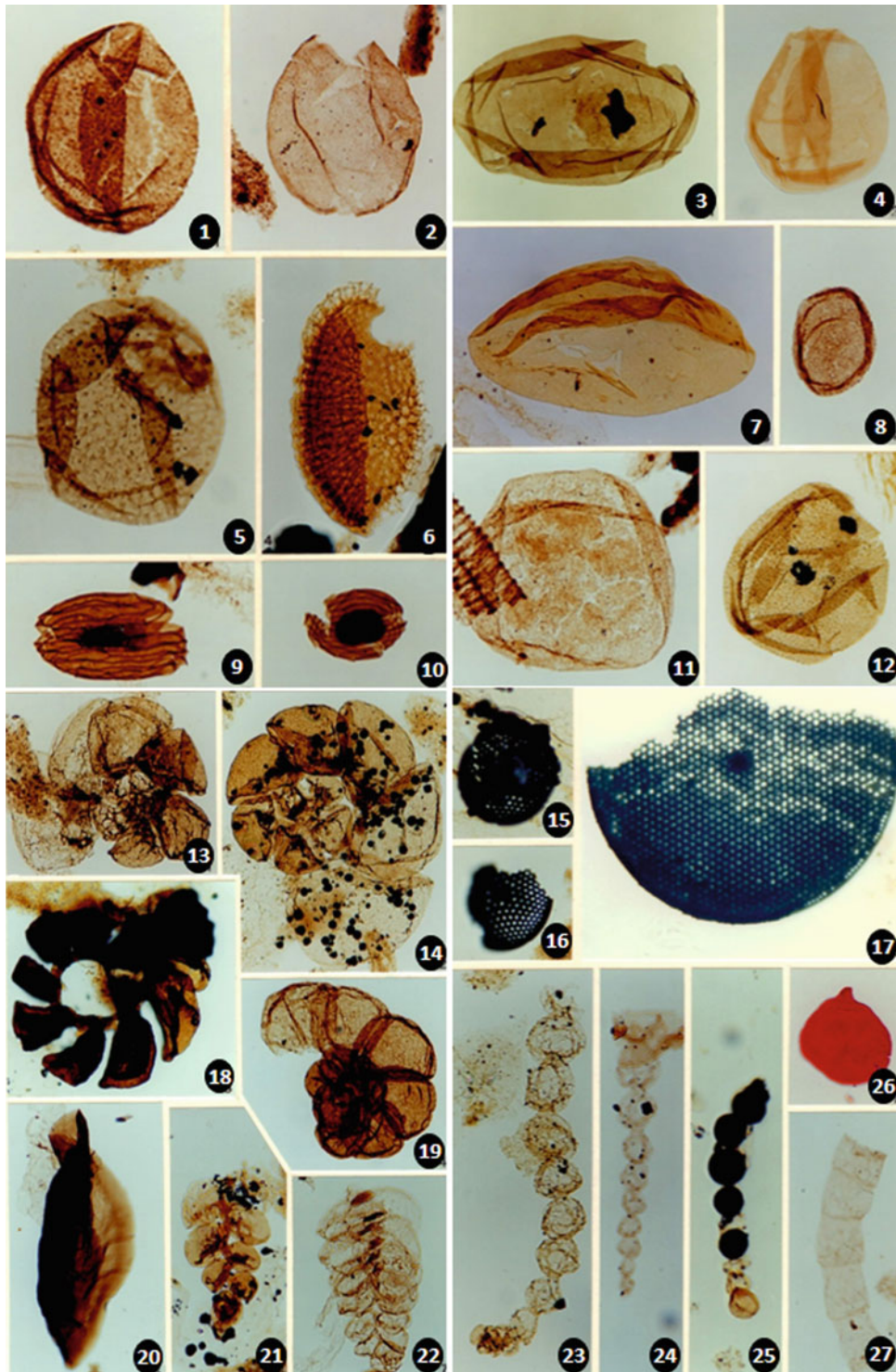
## Association 24

**Age:** early late Danian.

**Interval:** 7753'-7762'.

This association is marked by an influx of the *Tenua Heterosphaeridium* complex (24.8–27.4%) and *Fibrocysta Cordosphaeridium* complex (10.4–17.1% (Fig. 13)). Characteristic species include *Tenua formosa*, *Tenua* sp. C, *Fibrocysta furcata* and *Heterosphaeridium heteracanthum*, and there is a decline in the *Achomosphaera/Spiniferites* complex. Other accessory taxa include *Danea californica*, *Areoligera volata*, *Spiniferites* cf. *cornutus* subsp. *laevimurus*, *S. membranaceus*, *S. hyalospinosus*, *Canningia kukebaiensis* and *Apteodinium* cf. *reticulatum*. Taxa occurring for the first time in this association include *Alisocysta circumtabulata*, ?*Amphorosphaeridium multispinosum*, *Cerodinium* cf. *pentaradiatum*, and new varieties of the genera *Nematosphaeropsis* and *Rottnestia*. There is also a high diversity and high abundance of the genera *Impagidinium*, *Fibrocysta*, *Cordosphaeridium* and *Tenua*. *A. circumtabulata* is known mainly from Paleocene strata world-wide. In the El Haria and El Kef sections, NW Tunisia this species has been recorded from the interval 25 and 18 cm above the first occurrence of *Danea californica* (base of the K/Pg boundary) (Brinkhuis & Leereveld, 1988; Brinkhuis & Zachariasse, 1988). In contrast, this species has been recorded 6 ft. (2 m) above the first occurrence of *Danea californica* in this study. This observation may be taken as evidence to support a disturbance in the palynomorph succession across the studied K/Pg boundary section. *Areoligera volata* is mainly known from the Paleocene sediments of California and India (Drugg, 1967; Jain and Garg 1982). *Amphorosphaeridium multispinosum* is known from the Paleocene-Eocene (Belgium, England, France, Gabon, Nigeria, Senegal and Tunisia). *Cordosphaeridium*, *Fibrocysta* and *Impagidinium* have been





◀ **Plate 13** 1. *Lophosphaeridium* spp.; Core 6, 8614'-8617', 2(unox), M33/2. 2. *Lophosphaeridium* spp.; Core 6, 8614'-8617', 2(ox), J55/3. 3. *Leiosphaeridia* spp.; Core 6, 8614'-8617', 2(ox), W45/2; X445. 4. *Leiosphaeridia* spp.; cuttings, 8390', 1(ox), C44/2; X550. 5. *Lophosphaeridium* spp.; Core 3, 84,461'-8464', 1(unox), L52/4. 6. *Schizosporis reticulatus*; Core 3, 8443'-8446', 2(unox), K32/2; X150. 7. *Leiosphaeridia* spp.; Core 4, 8487'10"-8489'6", 3(unox), X45/4. 8. *Lophosphaeridium* spp.; Core 6, 8614'-8617', 5(ox), R34/0. 9. ? *Schizosporis* sp.; Core 6, 8614'-8617', 2(unox), R38/0. 10. ? *Schizosporis* sp.; Core 6, 8614'-8617', 2(ox), M60/0. 11. *Lophosphaeridium* spp.; Core 6, 8614'-8617', 4(ox), M37/3. 12. *Lophosphaeridium* spp.; Core 2, 8428'-8431', 1(unox), W41/1. 13. Microforaminiferal test lining, trochospiral form; Core 3, 8461'-8464', 1(unox), O55/0. 14. Microforaminiferal test lining, trochospiral form; Core 3, 8461'-8464', 1(unox), O48/4. 15. Diatom; Core 2, 8428'-8431', 1(unox), N39/3. 16. Diatom; Core 2, 8428'-8431', 1

(unox), O40/1. 17. Diatom; cuttings, 8390', 4(unox), M40/4. 18. Microforaminiferal test lining, planispiral form; Core 3, 8461'-8464', 1(unox), G51/1. 19. Microforaminiferal test lining, planispiral form; Core 6, 8614'-8617', 10(unox), V51/2; X550. 20. ?Microforaminiferal test lining; Core 6, 8614'-8617', 1(ox), T57/4; X550. 21. Microforaminiferal test lining; Core 1, 7750'-7753', 1(unox), F45/0. 22. Microforaminiferal Microforaminiferal lining, biserial form; Core 2, 8428'-8431', 1(unox), X52/3. 23. Microforaminiferal test lining, uniserial form; Core 6, 8461'-8464', 1(unox), M51/0; X150. 24. Microforaminiferal test lining, uniserial form; Core 4, 8487'10"-8489'10", 1(unox), T34/3; X150. 25. Microforaminiferal test lining, uniserial form; Core 1, 7750'-7753', 1(unox), X37/0; X150. Note that most of the chambers are pyritised. 26. Microforaminiferal test lining, single chamber; Core 1, 7750'-7753', 2(ox), B40/1. 27. Microforaminiferal test lining, uniserial form; Core 1, 8614'-8617', 11(ox), L52/4; X60

recorded with high diversity from this association. The most characteristic species include *C. exilimurum* (Danian, Senegal, Tunisia; Paleocene, Arctic Canada; Eocene, England), *F. lappacea* (Danian, Senegal; Paleocene, Morocco, Nigeria; Eocene, USA, Nigeria), *F. vectensis* (Paleocene, Arctic Canada, Morocco; Eocene, Belgium, England, Netherlands); *I. crassimuratum* is known only from the Early Eocene of New Zealand (Wilson, 1988), *I. dispertitum* (known from the Maastrichtian-Paleocene, Arctic Canada; Middle Eocene, New Zealand; late Eocene, Australia; Oligocene of Germany, USA) and *I. maculatum* (late Paleocene-Eocene, Australia, Belgium, New Zealand).

Based on the evidence cited above, a Danian age is appropriate for this association, but the majority of the discussed taxa is in favour of early late Danian age. This association is partly similar to Association 25 but differs in having very higher percentages of *Tenua* and *Heterosphaeridium* and low percentage of *Adnatosphaeridium* sp.

Nannofossils are characterised by a decline in *Thorasphaera* sp. and a higher influx of *Braarudosphaera bigelowii* and *Micrantholithus pinguis*. Association 24 equates with the lower part of the late Danian *Chiasmolithus danicus* Zone (NP3) of El-Mehaghag (1996).

### Association 25

Age: late Danian.

Interval: 7750'-7753'.

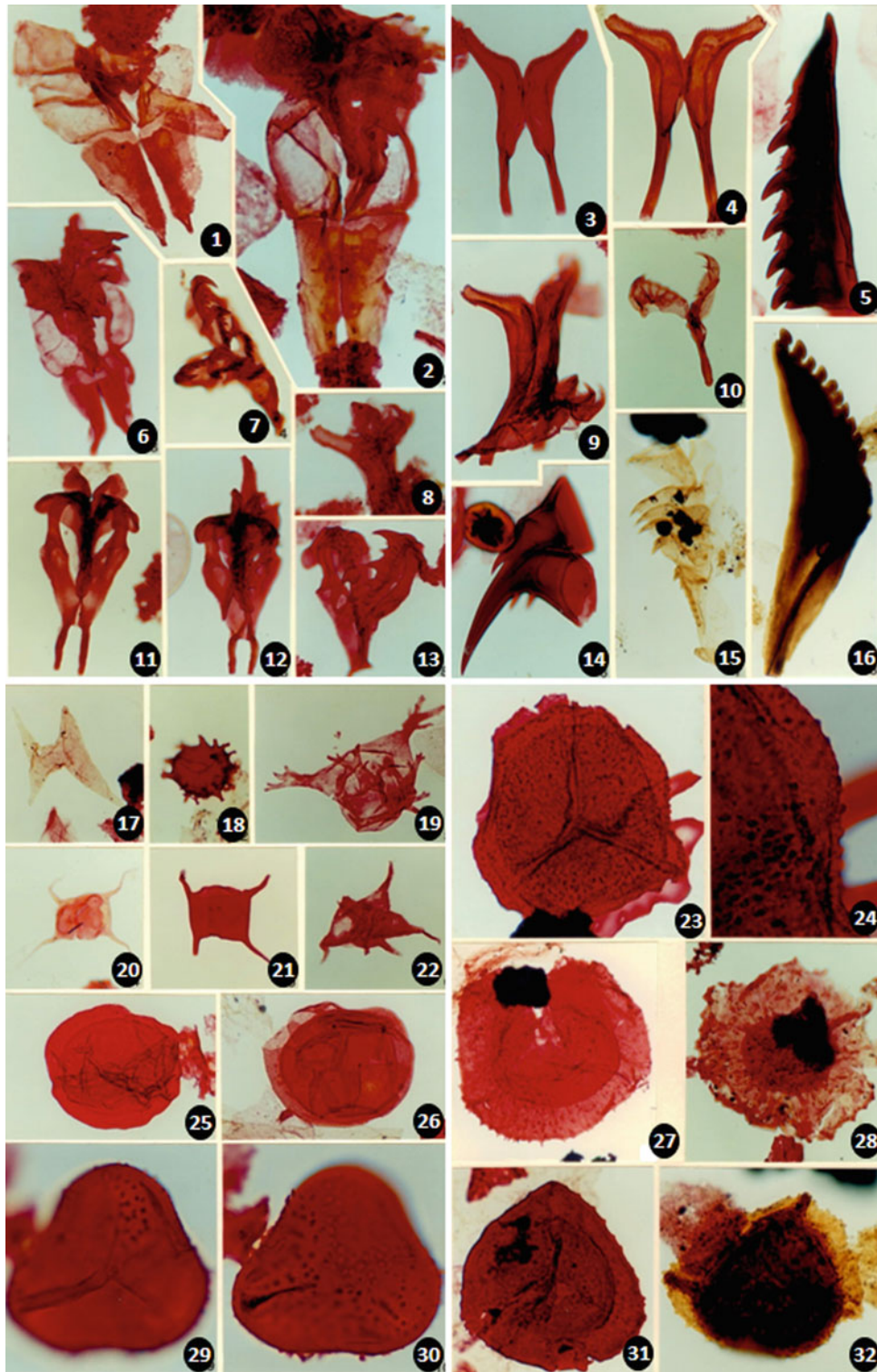
This association is marked by an influx of the *Danea* complex, including *Danea manicata*, *D. californica* and *D. impages* higher influx in the *Achomosphaera/Spiniferites* complex and a decline in the *Tenua/Heterosphaeridium* complex (Fig. 13). Accessory taxa include *Fibrocysta vectensis*, *Florentinia ferox*, *Rottnechia borussica*, *Disphaerogena carposphaeropsis*, *Apteodinium* cf. *reticulatum*, *Spiniferites ramosus* subsp. *ramosus*, *S. ramosus* subsp. *gracilis*, *S. mirabilis* and a new variety of *Nematosphaeropsis*. The most important events to occur in this association include the first occurrences of *D. manicata*

and *D. impages*. These two species are known from the early Eocene of California (Damassa, 1984). In the El Haria section, NW Tunisia, the first occurrence of *D. manicata* coincides with top of the *D. californica* Zone of Danian age. However, this suggests that this association could be younger in age than the *D. californica* zone of Brinkhuis and Zachariasse (1988) and Brinkhuis and Leereveld (1988). Other stratigraphically important taxa present in this association include *Impagidinium parvireticulatum*, which is known only from the Early Eocene of New Zealand (Wilson, 1988). Based on the dinocyst content, a late Danian age has been suggested for this association.

Association 25 equates with the upper part of the late Danian nannofossil *Chiasmolithus danicus* Zone (NP3) of El-Mehaghag (1996). However, it is worthy to mention that El-Mehaghag (ibid) has suggested a presence of a hiatus at the K/Pg boundary based on the absence of the nannofossil zone *Markalius inversus* and the lower part of the *Cruciplacolithus tenuis* Zone (Fig. 9). This was supported by his correlation of the calcareous nannofossil zonation scheme with the planktonic foraminiferal zonation of Berggren (1969).

## 6 Palynofacies Analysis

Palynofacies analysis is one of the tools that has been used to throw light on the depositional environment, thermal maturity and source rock potential of sediments. The concept of palynofacies was first defined by Combaz (1964) to include the total Particulate Organic Matter (POM) in an attempt to evaluate the depositional environment of sediments. The integration of palynofacies analysis with sedimentological, seismic and other geological data can contribute significantly to environmental reconstruction (e.g., the identification and differentiation of open marine, restricted marine, brackish and freshwater sediments) or to assess the transgressive/regressive trends and hence basin evaluation (Tyson, 1993).



- ◀ **Plate 14** 1. Scolecodonts; Core 1, 7774'-7775', 1(ox), D50/2. 2. Scolecodonts; Core 1, 7780'-7783', 3(ox), V41/4. 3. Scolecodonts; Core 1, 7770'-7773', 2(ox), V40/2. 4. Scolecodonts; Core 1, 7774'-7775', 9(ox), L63/1. 5. Scolecodonts; Core 1, 7777'-7780', 1(ox), Q49/1. 6. Scolecodonts; Core 1, 7785'-7788', 1(ox), V52/0. 7. Scolecodonts; Core 1, 7774'-7775', 1(ox), T60/0. 8. Scolecodonts; Core 1, 7774'-7775', 3(ox), D54/2. 9. Scolecodonts; Core 1, 7774'-7775', 9(ox), K37/3. 10. Scolecodonts; Core 1, 7774'-7775', 3(ox), G42/2. 11. Scolecodonts; Core 1, 7774'-7775', 7(ox), K41/0. 12. Scolecodonts; Core 1, 7780'-7783', 1(ox), W53/0. 13. Scolecodonts; Core 1, 7777'-7780', 1(ox), L45/3. 14. Scolecodonts; Core 1, 7750'-7753', 1(ox), H32/2. 15. Scolecodonts; Core 1, 7785'-7788', 1(unox), K59/0. 16. Scolecodonts; Core 3, 8461'-8464', 1(unox), V40/3. 17. *Horologinella quadrispina*; reworked, Core 4, 8527'-8528'6", 4(ox), V51/1. 18. *Multicisphaeridium ?cladum*; reworked, Core 4, 8542'-8545', 1(unox), P43/3. 19. *Multicisphaeridium* cf. *corallinum*; reworked, Core 4, 8539'-8542', 6(ox), J40/1. 20. *Veryhachium* sp.; reworked, Core 4, 8527'-8528'6", 5(ox), M57/0. 21. *Veryhachium* cf. *valiente*; reworked, Core 4, 8542'-8545', 3(ox), R49/3. 22. *Stellinium* sp.; reworked, Core 4, 8533'-8536', 1(ox), F48/0. 23. *Spelaeotriletes* sp. B; reworked, Core 4, 8539'-8542', 1(ox), K39/0. 24. *Spelaeotriletes* sp. B; reworked, Core 4, 8539'-8542', 1(ox), K39/0; X600. 25. *Auroraspora asperalla*; reworked, Core 4, 8527'-8528'6", 2(ox), M39/1. 26. *Auroraspora asperalla*; reworked, Core 4, 8527'-8528'6", 4(ox), Q43/4. 27. *Grandispora* sp. A; reworked, Core 4, 8539'-8542', 5(ox), E44/1. 28. *Grandispora libyensis*; Core 4, 8536'-8539'; 3(ox), R36/4; X550. 29. *Diatomozonotriletes* sp. Riegel, 1985; reworked, Core 4, 8527'-8528'6", 4(ox), F60/0; X600; distal and proximal view respectively. 30. *Diatomozonotriletes* sp. Riegel, 1985; reworked, Core 4, 8527'-8528'6", 4(ox), F60/0; X600; distal and proximal view respectively. 31. *Grandispora notensis*; reworked, Core 4, 8527'-8528'6", 2(ox), M42/0. 32. *Grandispora* sp. B; reworked, Core 5, 8545'-8548', 4(ox), K37/0.

Despite the voluminous palynofacies contributions published on this topic, there is still little agreement on the standard classification and nomenclature for P.O.M. This is largely because each of the published schemes treats P.O.M. from different angles (e.g. botanical, coal petrographical, chemical, sedimentological) and in some cases mixing terms. Well-known schemes include those of Combaz (1964, 1980), Staplin (1969), Burgers (1974), Fisher (1980), Habib (1982), Tyson (1984), Hart (1986) and Boulter and Riddick (1986).

Study of the palynological residues (unoxidised and oxidised) of the Upper Cretaceous sediments of the SE Sirt Basin has revealed abundant and well-preserved POM. For the purpose of this study, a simple classification has been used to establish generalised organic facies. The scheme follows that used by Habib and Miller (1989) to some extent. The most significant groups of POM recovered are attributed to four main categories: vascular, black/opaque, amorphous debris and palynomorphs. These categories are described below with some remarks on their importance in palaeoenvironmental interpretation.

## 6.1 Particulate Organic Matter Composition

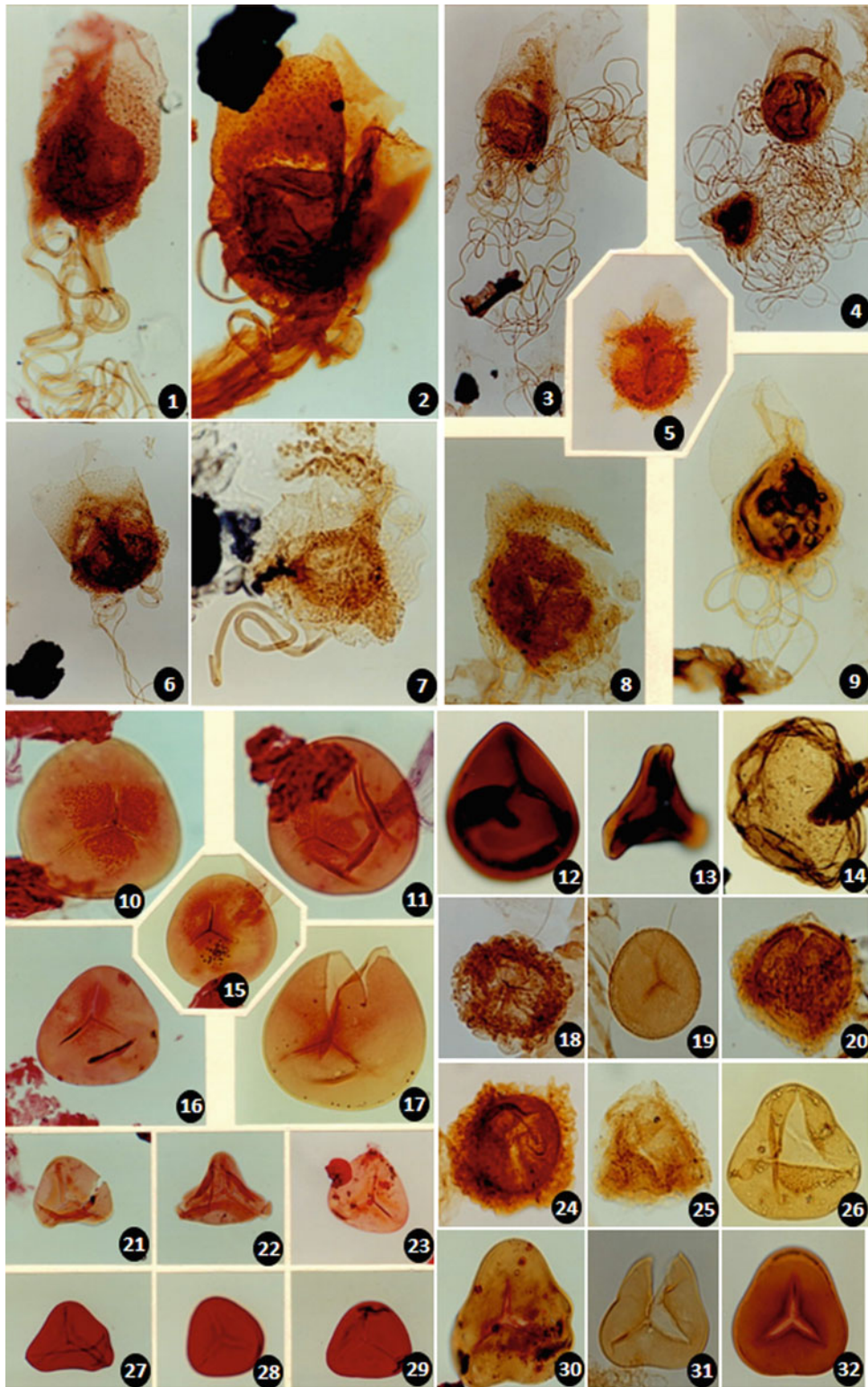
### Vascular Debris (Phytoclasts)

The most dominant POM type in the studied material, especially in the Etel, Rachmat and part of the Tagireft formations, is the vascular palynodebris. This category includes all plant tissues (epidermal tissues, plant hairs, tracheids, well preserved and biodegraded wood fragments). The epidermal tissues represent the outer waxy layer of the epidermal cell of leaves or stems and show the clear structure of epidermal cell outlines. It is possible to distinguish the lower leaf epidermis from the upper, the former being characterised by the presence of stomata, and between angiosperms and gymnosperms, the former being characterised by smaller cells with irregular outlines and smaller

randomly distributed stomata, whereas the latter is characterised by large cells with more or less rectangular cell outlines and stomata usually arranged in rows (Boulter & Riddick, 1986, p. 880). Boulter and Riddick (ibid.) demonstrated that leaf cuticles were most abundant in high-energy systems of deposition and are regularly present in sandstones although they are not restricted to them. The size of vascular debris has been observed to decrease in an offshore direction (Habib, 1982). The high abundance of the vascular debris in the study section, especially the presence of huge plant tissues and wood fragments suggests close proximity to the parent flora and an active fluvio-deltaic source (Tyson, 1993). Biodegraded vascular debris has also been noted to be characteristic of some of the Campanian intervals (see Palynofacies V). However, the nature of the biodegradation is difficult to specify. Hart (1986) suggested that degradation of organic matter by fungi is confined to oxygenated condition. The size of the vascular debris has been considered in order to assess the polarity of depositional sites. For details, please refer to Palynofacies I–V. The vascular debris from the present study equates with the vascular debris of Habib and Miller (1989) and the hylogen organic particles of Bujak et al. (1977).

### Black/Opaque Debris

This type of POM includes black/opaque debris which does not show any internal structure. It has been recognised mainly in association with coarse-grained sediments (Boulter & Riddick, 1986; Fisher, 1980) and is characterised by angular, equidimensional or lath-like shapes. Denison and Fowler (1980) suggested that the roundness of black/opaque debris increases with transportation. They observed that fragments deposited in a proximal deltaic environment are angular, whilst those deposited offshore, further away from the source area, are often rounded. This kind of debris has been interpreted by several workers to be the result of palaeoforest fires (Patterson et al., 1987), and/or biodegradation of structured woody material (Parry et al., 1981), and



◀ **Plate 15** 1. *Ariadnaesporites verrucatus*; Core 4, 8520'-8523', 4(ox), O36/0. 2. *Ariadnaesporites verrucatus*; Core 4, 8502'-8505', 1(ox), J38/0. 3. *Ariadnaesporites verrucatus*; Core 5, 8584'-8588', 2(ox), F53/2; X150. 4. *Ariadnaesporites* sp. B; Core 5, 8584'-8588', 1(ox), E40/0; X150. 5. *Ariadnaesporites spinosus*; Core 1, 7780'-7783', 1(ox), J37/2. 6. *Ariadnaesporites verrucatus*; Core 5, 8584'-8588', 1(ox), F50/0; X150. 7. *Ariadnaesporites* sp. A; Core 5, 8584'-8588', 1(ox), C50/3. 8. *Ariadnaesporites* sp. B; Core 5, 8584'-8588', 1(ox), H52/0. 9. *Ariadnaesporites* spp.; Core 5, 8584'-8588', 1(ox), S53/3. 10. *Cyathidites* sp. A; Core 4, 8542'-8545', 1(ox), J38/2. 11. *Cyathidites* sp. A; Core 4, 8542'-8545', 1(ox), E38/0. 12. *Biretisporites spectabilis*; Core 4, 8496'-8499', 1(ox), M61/1. 13. *Concavisporites* sp.; Core 4, 8487'10"-8489'10", 2a(ox), O46/3. 14. *Calamospora* sp.; Core 6, 8614'-8617', 1(unox), V33/4. 15. *Cyathidites* sp. A; Core 4, 8542'-8545', 1(ox), V54/0; X150. 16. *Cyathidites* sp. A; Core 4, 8533'-8536', 1(ox), N36/1. 17. *Cyathidites*

sp. A; Core 4, 8527'-8528'6", 4(ox), R62/0. 18. *Perotrilites pannuceus*; Core 5, 8584'-8588', 1(unox), N55/1. 19. ?*Cicatricosisporites* sp.; Core 5, 8584'-8588', 1(ox), E44/0. 20. *Perotrilites pannuceus*; Core 5, 8584'-8588', 2(ox), M38/0. 21. *Dictyophyllidites concavus*; Core 1, 7780'-7783', 1(ox), Q40/4. 22. *Dictyophyllidites concavus*; Core 1, 7785'-7788', 2(ox), O47/0. 23. *Dictyophyllidites concavus*; Core 1, 7785'-7788', 2(ox), O47/0. 24. *Perotrilites pannuceus*; Core 5, 8584'-8588', 1(ox), R51/3. 25. *Perotrilites pannuceus*; 8584'-8588', 1(ox), Q61/4. 26. *Cyathidites australis*; Core 6, 8614'-8617, 9(ox), Q52/2. 27. *Dictyophyllidites harrisii*; Core 4, 8542'-8545', 1(ox), M38/0. 28. *Dictyophyllidites* sp. A; Core 4, 8542'-8545', 1(ox), K49/0. 29. *Dictyophyllidites* sp. A; Core 4, 8542'-8545', 1(ox), G63/0. 30. *Cyathidites australis*; Core 4, 8499'-8502', 2(ox), M52/0. 31. *Cyathidites australis*; Core 5, 8584'-8588', 1(ox), C47/2. 32. *Cyathidites australis*; Core 4, 7496'-8499', 1(ox), W32/2

is associated with deposits of high-energy environments (Fisher, 1980).

In the studied section, this type of debris characterises some intervals of the Rachmat and Etel formations (Plate 22, Figs. 2, 3 and 6), with high abundance mainly from the sandstone intervals of the Rachmat Formation (e.g. interval 8528'6"-8548' and 8580-8581'6"). Its presence in huge amounts has been suggested to indicate deposition in a high-energy condition, and its shape and size are good indicators of the polarity of depositional sites (see Palynofacies VI-VII). This type of palynodebris equates to the inertinite debris of Habib and Miller (1989) and melanogen organic particles of Bujak et al. (1977).

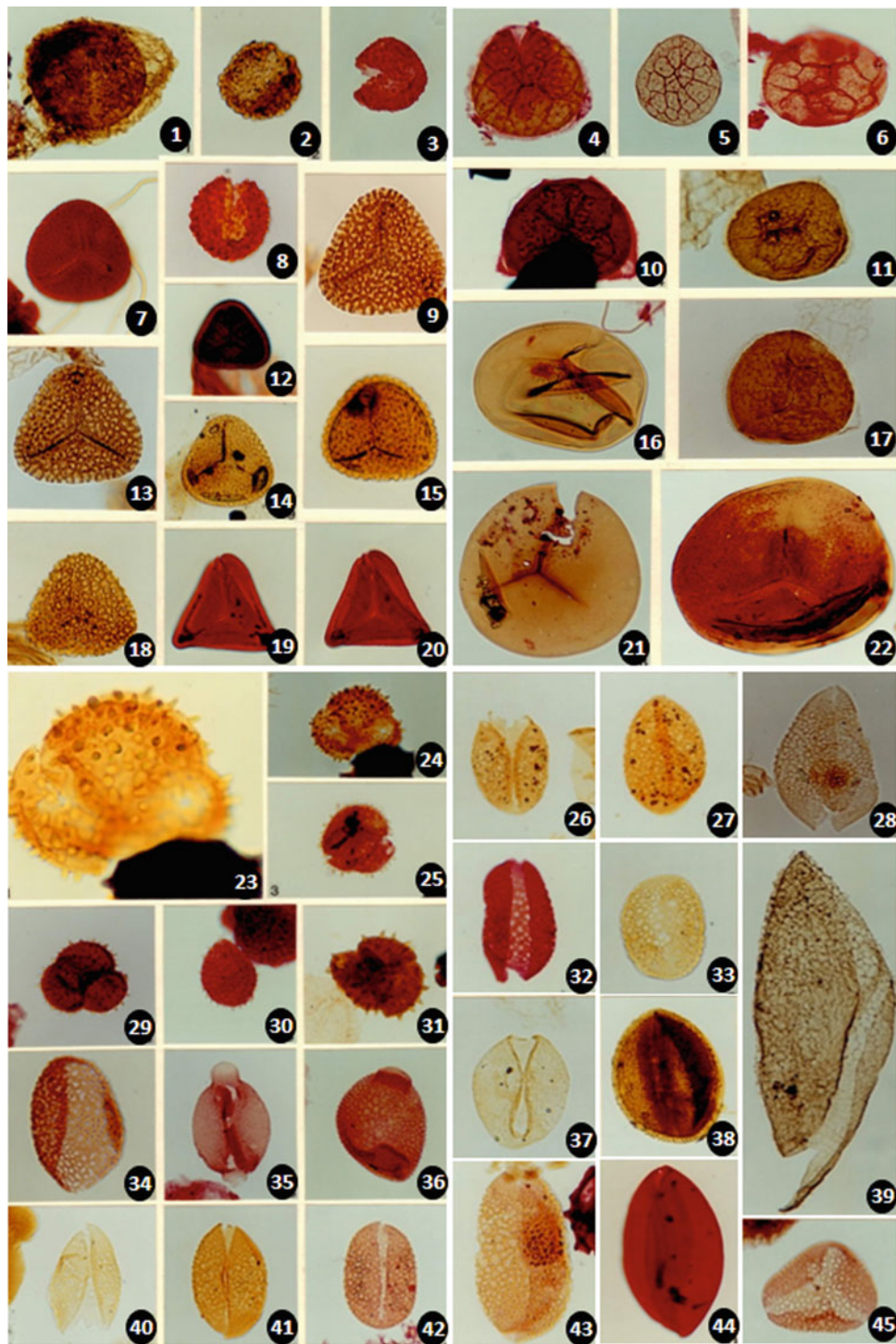
### Amorphous Organic Matter (AOM)

AOM is characterised by its aggregated or colloidal structure. Its appearance is dependent upon its source and environment of deposition (Masran & Pocock, 1981). This kind of palynodebris can be produced as organic aggregates derived from dissolved organic matter (Riley, 1970) or as concentrations of faecal pellet material (Porter & Robbins, 1981). Carbon isotopic evidence indicates that all typical marine AOM is ultimately phytoplankton derived (Lewan 1986, after Tyson, 1993). Combaz (1980) recognised four stages in the production of amorphous debris. These are the degradation and sapropelization of former structured material, the transformation of cell contents such as lipids, pigments, resins and waxes, the reorganisation of dead organic compound to other structurally different compounds and catagenetic changes. He recognised five types of amorphous organic matter based on its optical appearance and related these types to different lithologies and environments of deposition. These types are aggregate, granulate, sub-colloidal, flaky or jellified (for more details, see Combaz, 1980, p. 75-77). For the purpose of this study, these types are collectively termed amorphous debris. The origin of AOM cannot be determined under the transmitted light microscope, but, as Venkatachala (1984, p. 22) stated, a terrestrial origin can be attributed when AOM is associated

with biodegraded terrestrial matter and structured woody or epidermal tissues. A terrestrial origin for amorphous debris has also been proven by several other workers (Ioannides et al., 1976). Ioannides et al. (ibid.) suggested that the abundant AOM in the Kimmeridge oil shale has its origin in influxes of terrestrial swamp debris following the rise in sea level and coincides with an increase in sporomorph content. High concentration of AOM is considered to indicate deposition in reducing, dysaerobic to anoxic conditions (Tyson, 1993). This would also suggest that sedimentation shifted basin-ward, as such environments are more likely to occur on the outer shelf, basin slope and in restricted and starved basins. Well-preserved amorphous debris of marine algal origin is recognised from one sample in the Rachmat and Tagrifet formations (8461'-8464', sample 21 and 8390', sample 15; Fig. 14) and 14 samples from the K/Pg boundary Sect. (7750'-7791', samples 1-14, Fig. 13) associated mainly with marine and with rare or missing terrestrial taxa (Pl. 22; Figs. 11 and 12). See the normal and stressed distal marine amorphous palynofacies (Palynofacies X and XI; Figs. 12 and 13). The amorphous debris recorded from two samples of Rachmat Formation (8428'-8431', sample 18 and 8489'10"-8490', sample 24) and one sample from Tagrifet Formation (8410'-8412', sample 16; Fig. 14) has been considered to be the result of biodegradation of vascular debris and marine algae (see Palynofacies IX; Plate 22, Figs. 9 and 10). This type of palynodebris equates to amorphous debris of Habib and Miller (1989) and amorphogen organic particles of Bujak et al. (1977).

### Palynomorphs

This category includes all marine and non-marine palynomorphs such as dinocysts, acritarchs, prasinophytes, chlorophytes, spores, pollen and fungi. It also includes animal debris such as scolecodonts, microforaminiferal test linings and insect tissues. Most of the studied samples yielded rich and well-preserved palynomorphs assemblages suitable for quantitative analysis, with the exception of the Etel Formation, in which 3 samples out of 9 are productive.



- ◀ **Plate 16** 1. *Perotriletes* cf. *pannuceus*; Core 5, 8545'-8548', 5(ox), N54/2. 2. *Distaverrusporites simplex*; Core 1, 7780'-7783', 1(unox), V55/3. 3. *Distaverrusporites simplex*; cuttings, 8390', 1(ox), G46/1. 4. *Triporoletes blanensis*; Core 4, 8487'10"-8489'6", 4a(ox), F47/2. 5. *Triporoletes blanensis*; Core 4, 8577'-8578'6", 1(ox), G36/3. 6. *Triporoletes blanensis*; Core 4, 8531'9"-8532', 4(ox), M46/3. 7. *Foveotriletes margaritae*; Core 4, 8496'-8499', 3(ox), P57/2. 8. *Distaverrusporites simplex*; Core 1, 7780'-7783', 1(ox), O56/0. 9. *Foveotriletes* cf. *subtriangularis*; Core 5, 8584'-8588', 2(ox), S54/2. 10. *Triporoletes* spp.; Core 5, 8562'-8565', 1(ox), M44/2. 11. *Triporoletes* spp.; Core 5, 8584'-8588', 3(ox), H52/0. 12. *Foveotriletes margaritae*; Core 4, 8499'-8502', 2(ox), K41/2. 13. *Foveotriletes* cf. *subtriangularis*; Core 5, 8584'-8588', 2(ox), S54/2. 14. *Foveotriletes margaritae*; Core 2, 8410'-8412', 3(unox), O36/4. 15. *Foveotriletes* cf. *subtriangularis*; Core 5, 8584'-8588', 1(ox), M56/2. 16. *Todisporites major*; Core 4, 8542'-8545', 1b(ox), Q58/0. 17. *Triporoletes* spp.; Core 5, 8584'-8588', 2(ox), V48/0. 18. *Foveotriletes* cf. *subtriangularis*; Core 5, 8584'-8588', 2(ox), P44/2. 19. *Foveotriletes* sp.; Core 2, Core 4, 8428'7"-8430', 1(ox), K51/0; proximal view. 20. *Foveotriletes* sp.; Core 2, Core 4, 8428'7"-8430', 1(ox), K51/0; distal view. 21. *Todisporites major*; Core 4, 8493'-8499', 1(ox), L34/0. 22. *Todisporites scabratus*; Core 4, 8505'-8508', 1(ox), K44/2. 23. *Droseridites senonicus*; Core 4, 8514'-8517', 3(ox), D45/0. 24. *Droseridites senonicus*; Core 4, 8514'-8517', 3(ox), D45/0. 25. *Droseridites senonicus*; Core 5, 8562'-8565', 1(ox), H57/0. 26. *Liliacidites lenticularis*; Core 4, 8508'-8511', 1(ox), E36/3. 27. *Liliacidites lenticularis*; Core 4, 8502'-8505', 1(ox), E48/0. 28. *Liliacidites ?katitangataensis*; Core 5, 8584'-8588', 1(ox), P51/0. 29. *Droseridites senonicus*; Core 4, 8496'-8499', 1(ox), J57/3. 30. *Droseridites senonicus*; Core 1, 7780'-7783', 1(ox), N434/0. 31. *Droseridites senonicus*; Core 4, 8508'-8511', 1(ox), N47/1. 32. *Liliacidites variegatus*; Core 5, 8580'-8581'6", 1(ox), G56/2. 33. *Liliacidites variegatus*; Core 5, 8584'-8588', 2(ox), O40/3. 34. *Arecipites* sp.; Core 4, 8496'-8499', 1(ox), A38/4. 35. *Auriculiidites* cf. *reticulatus*; Core 4, 8487'10"-8489'6", 1a(ox), N58/3. 36. *Auriculiidites* cf. *reticulatus*; Core 1, 7780'-7783', 3(ox), W38/0. 37. *Liliacidites* sp. B; Core 5, 8584'-8588', 1(ox), K38/3. 38. *Liliacidites* spp.; Core 6, 8614'-8617', 4(ox), D48/0. 39. *Liliacidites* sp. C; Core 6, 8614'-8617', 4(ox), B32/0. 40. *Liliacidites intermedius*; Core 5, 8584'-8588', 1(ox), J58/3. 41. *Liliacidites intermedius*; Core 4, 8487'10"-8489'6", 4a(ox), J43/0. 42. *Liliacidites intermedius*; Core 4, 8511'-8514', 2(ox), V41/4. 43. *Liliacidites katitangataensis*; Core 5, 8577'-8578'6", 4(ox), D42/1. 44. *Monocolpites marginatus*; Core 4, 8496'-8499', 2(ox), F56/0. 45. *Liliacidites* sp. A; Core 5, 8577'-8578'6", 1(ox), D49/3.

The samples yielded mainly non-marine taxa. The Sirt Shale, Tagrifet and Rachmat formations, and the lower part of the Hagfa section are represented by 34, 3, 10 and 4 samples, respectively, all of which are productive, yielding rich and diverse marine and non-marine palynomorph assemblages.

### Dinocysts

Dinocysts are the most abundant and diverse palynomorphs group across the studied section with the exception of the Etel Formation, in which they are rare to absent. In order to interpret the depositional environments in the studied well, it has been necessary to establish a palaeoecological model for the identified dinocyst complexes. This has been achieved by comparing the distribution of taxa or complexes of morphologically closely related taxa with recent distribution patterns of their modern counterparts.

### Proportion of Gonyaulacoid to Peridinioid Cysts:

Gonyaulacoid and Peridinioid cysts are the two main groups which form the dinocyst community in the studied section. These two groups have been used by several workers to determine environmental trends and water salinity. Harland (1973), studying Campanian dinocysts from Alberta, Canada, attempted to interpret depositional environment in terms of the ratio of gonyaulacacean to peridiniacean assemblages. He found that the ratio was highest in open-marine deposits and became lower in nearshore environments. Downie et al. (1971) recognised that the peridinioid form *Wetzeliella* proliferated in estuarine conditions. This view has been supported by studies of quaternary sediments. High concentrations of peridinioids are characteristic of areas with high primary productivity related to increased nutrient availability in upwelling areas and river mouths (Bradford & Wall, 1984; Brinkhuis, 1994; Tyson,

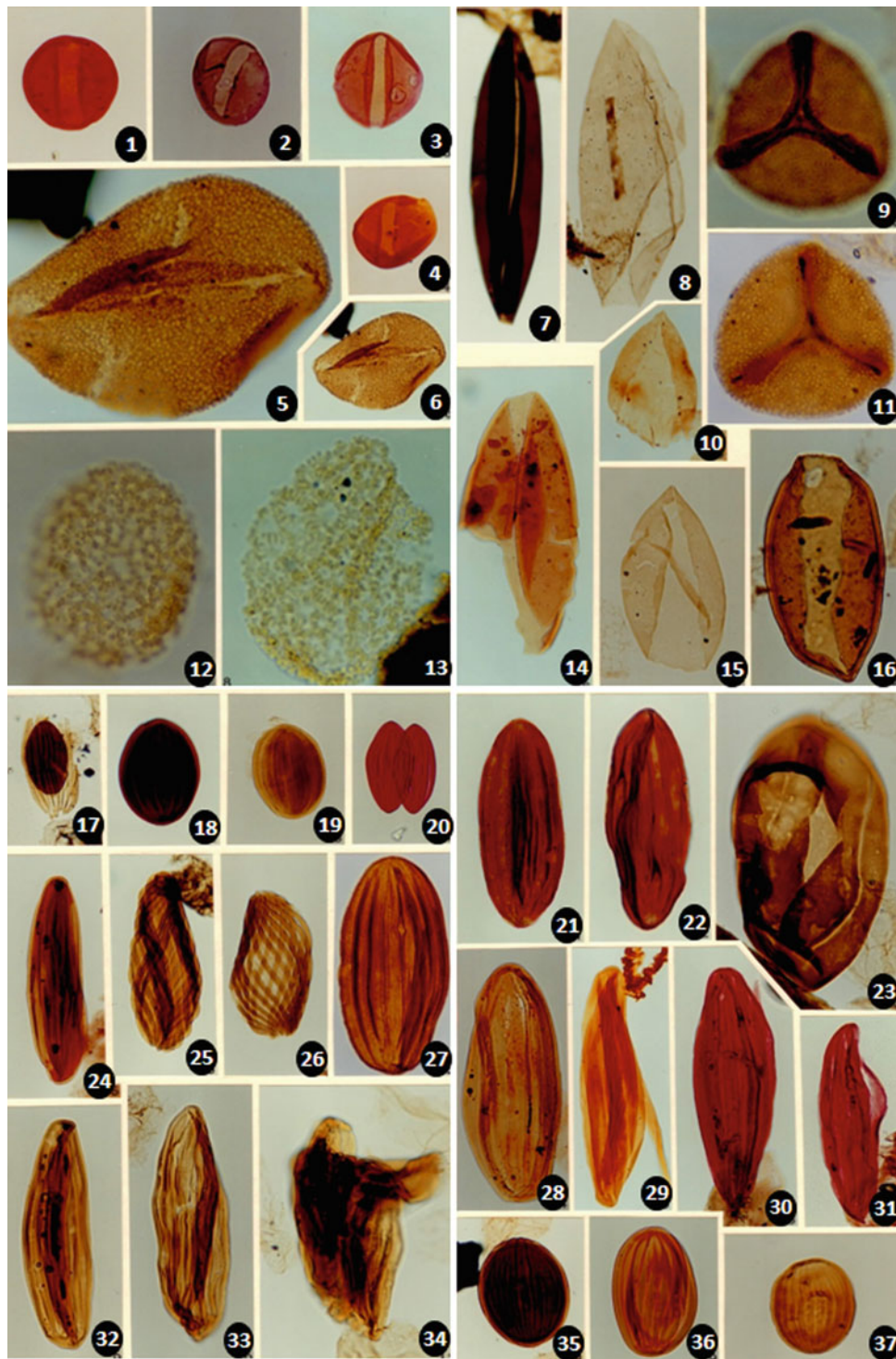
1993; Wall et al., 1977). A decrease in gonyaulacoid cysts has been suggested by Bradford and Wall (1984) as an indication of reduction of oceanic influence, greater water depth and lower salinity. These views are clearly shown across the Upper Cretaceous and the K/Pg boundary in the studied section, which is characterised by several blooms of peridinioid and gonyaulacoid cysts (Figs. 10 and 11), suggesting fluctuation between near shore and offshore trends and low and high salinities (e.g., see Palynofacies XI).

### Dinocyst Complexes

In the studied section, fourteen morphological dinocyst complexes have been recognised, but only a few complexes are considered important as environment indicators (Figs. 12 and 13), having counterparts in the literature. Nannofossil blooms from the studied K/Pg boundary (El-Mehaghag, 1996) have been also used and integrated with dinocyst complexes to assess the environmental trends of the recognised complexes across the K/Pg boundary.

**Achomosphaera/Spiniferites Complex:** This complex is composed of species of *Achomosphaera*, *Hystrihostrogylon*, *Rottnestia* and *Spiniferites*. Davey (1971) suggested that modern *Spiniferites* spp. flourish in nearshore shallow water conditions and decline in an offshore direction. The motile stage of these taxa (*Gonyaulax spinifera* group) is mainly restricted to shelf areas (estuarine to neritic), and the cysts can be abundant in these settings. High offshore frequencies are probably due to transportation (Davey & Rogers, 1975; Brinkhuis, 1994, after Wall et al., 1977). Islam (1984) found that the *Achomosphaera/Spiniferites* group has a versatile environmental tolerance. He suggested that this assemblage abounds in open-marine shelf environments. Brinkhuis and





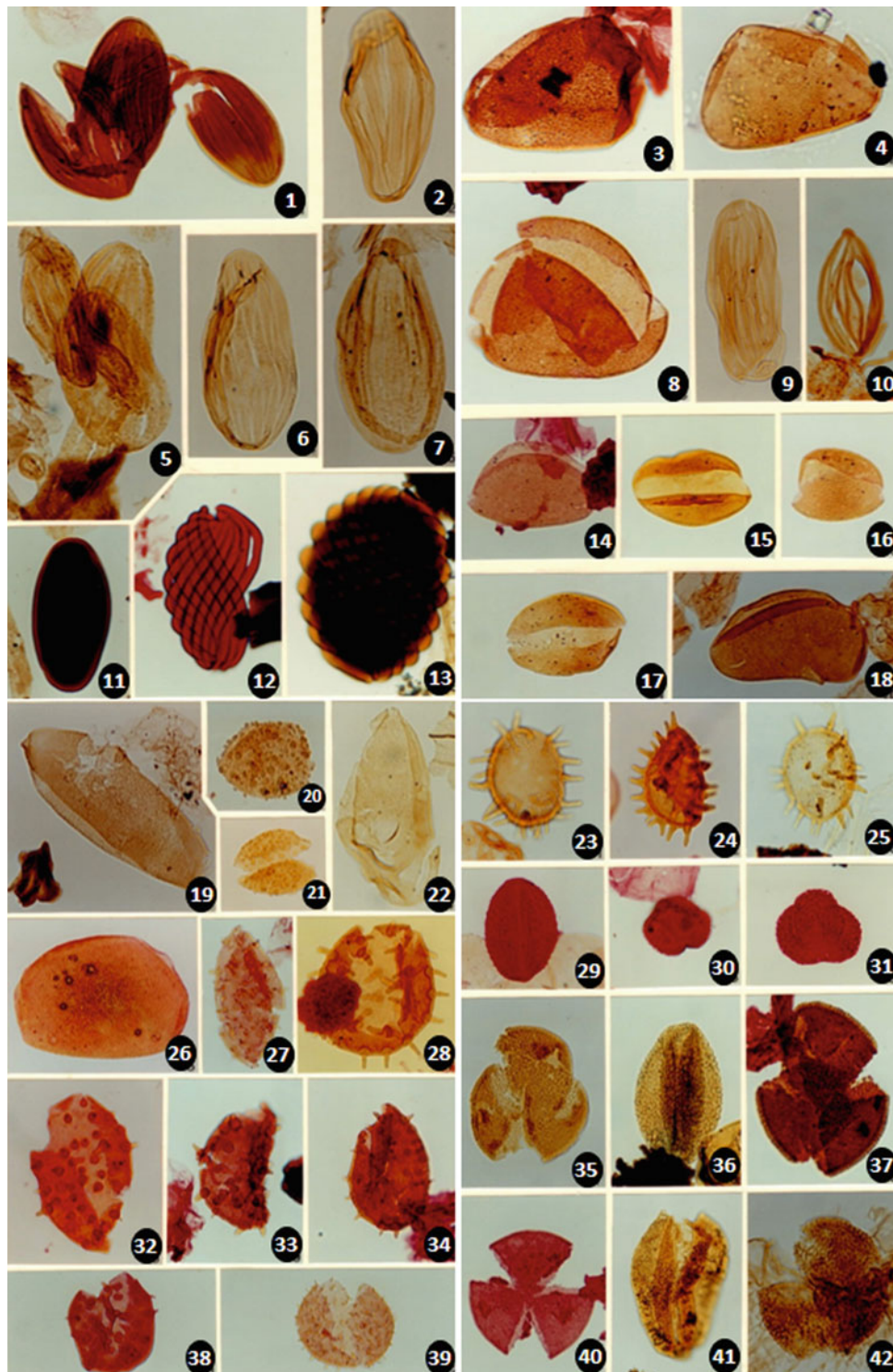
- ◀ **Plate 17** 1. *Monocolpopollenites* sp.; Core 4, 8496'-8499', 1(ox), L47/0. 2. *Monocolpopollenites* sp.; Core 5, 8576'-8576'6", 1(ox), E33/2. 3. *Monocolpopollenites* sp.; Core 1, 7788'-7791', 1(ox), R39/2. 4. *Monocolpopollenites* sp.; Core 4, 8502'-8505', 1(ox), J54/0. 5. *Retimonocolpites* spp.; Core 5, 8545'-8548', 5(ox), K43/0; X600. 6. *Retimonocolpites* spp.; Core 5, 8545'-8548', 5(ox), K43/0. 7. *Cycadopites* spp.; Core 6, 8614'-8617', 11(ox), V49/1. 8. *Cycadopites* spp.; Core 6, 8614'-8617', 4(ox), B41/4. 9. Trichotomosulcate form A; Core 4, 8487'10"-8489'6", 1(unox), P51/4; X600; distal view. 10. *Cycadopites* spp.; Core 4, 8508'-8511', 1(ox), O55/4. 11. Trichotomosulcate form A; Core 4, 8487'10"-8489'6", 1(unox), P51/4; X600; proximal view. 12. *Stellatopollis* sp.; Core 5, 8584'-8588', 1(ox), C55/0; X600. 13. *Stellatopollis* sp.; Core 5, 8584'-8588', 2(ox), J61/4; X600. 14. *Cycadopites* spp.; Core 1, 7780'-7783', 1(ox), W60/0. 15. *Cycadopites* spp.; Core 5, 8584'-8588', 1(ox), P37/0. 16. *Cycadopites* spp.; Core 1, 7780'-7783', 1(unox), L52/0. 17. *Ephedripites ambiguus*; Core 4, 8505'-8508', 1(unox), L51/3. 18. *Ephedripites ovalis*; Core 4, 8496'-8499', 1(ox), K37/0. 19. *Ephedripites ovalis*; Core 5, 8584'-8588'6", 1(ox), V37/0. 20. *Ephedripites virginiaensis*; Core 4, 8542'-8545', 1(ox), G66/3. 21. *Ephedripites strobilaceus*; Core 4, 8496'-8499', 1(ox), X61/2. 22. *Ephedripites strobilaceus*; Core 4, 8496'-8499', 2(ox), W35/4. 23. *Ephedripites* spp.; Core 5, 8584'-8588', 2(ox), L58/0. 24. *Ephedripites montanaensis*; Core 5, 8577'-8578'6", 1(ox), D41/4. 25. *Ephedripites jansonii*; Core 6, 8614'-8617', 1(unox), K53/2. 26. *Ephedripites jansonii*; Core 5, 8614'-8617', 4(ox), E47/0. 27. *Ephedripites strobilaceus*; Core 4, 8502'-8505', 2(ox), M46/4. 28. *Ephedripites strobilaceus*; Core 4, 8514'-8517', 3(ox), P62/2. 29. *Ephedripites* spp.; Core 4, 8511'-8514', 1(ox), U62/4. 30. *Ephedripites* spp.; Core 5, 8580'-8581'6", 2(ox), O47/0. 31. *Ephedripites* spp.; Core 5, 8580'-8581'6", 2(ox), E37/0. 32. Core 5, 8584'-8588'6", 3(ox), T53/3. 33. *Ephedripites montanaensis*; Core 5, 8584'-8588'6", 1(ox), H56/0. 34. *Ephedripites montanaensis*; Core 5, 8584'-8588'6", 1(ox), W56/1. 35. *Ephedripites* sp. 3. Salami, 1984; Core 4, 8508'-8511', 1(ox), E42/1. 36. *Ephedripites* spp.; Core 3, 8443'-8446, 1(ox), Q31/4. 37. *Ephedripites* spp.; Core 6, 8614'-8617', 4(ox), R48/0.

Zachariasse (1988) and Firth (1993) suggest that the blooms of *Achomosphaera-Spiniferites* cysts are indicative of drop in sea-level and basin-ward movement of facies through the late Maastrichtian and Danian. This view is supported by Hultberg and Malmgren (1986) who found that an increase in the abundance of *Spiniferites ramosus* indicates a shoreward shift in depositional environment, from outer to inner shelf facies. This group is the only major component throughout the studied stratigraphical succession. It is regarded as tolerant of nearshore (neritic) environment with different salinities, but flourishing in high salinity conditions. The high salinity preference of this complex is substantiated in the studied Danian section by correlation with blooms of the calcareous nannofossil *Thoracosphaera* sp. (Fig. 13). *Thoracosphaera* flourishes in harsh environments and high salinity conditions (Eshet et al., 1992; Jafar, 1979; Percival & Fischer, 1977). Moreover, the *Achomosphaera/Spiniferites* complex is found to decline and become characterised by short processes in anoxic and high-energy conditions, showing low percentages in palynofacies dominated with the *Xenascus* and *Areoligera/Glaphyrocysta* Complexes (low salinity indicators, see discussion below in the following complex). These conditions are probably unfavourable for the *Achomosphaera/Spiniferites* complex to flourish.

***Areoligera/Glaphyrocysta* Complex and *Heterosphaeridium/Tenua* Complex:** The *Areoligera/Glaphyrocysta* complex is composed of species of *Adnatosphaeridium*, *Areoligera*, *Cyclonephelium*, *Glaphyrocysta*, *Palynodinium* and *Riculacysta* species and has been found in abundance across the K/Pg boundary (Fig. 13). The *Heterosphaeridium/Tenua* complex is composed of species of *Circulodinium*, *Heterosphaeridium* and *Tenua* and has been found in abundance in the carbonates of the Tagrifet Formation as well as in the Danian mudstones. Downie et al. (1971) suggested that "*Areoligera* association" (which includes species of *Glaphyrocysta* and *Cyclonephelium*) is most

abundant in an open nearshore environment. Liengjarene et al. (1980) suggested that species of *Glaphyrocysta* flourish in estuarine water. Islam (1984) suggested that *Adnatosphaeridium-Areoligera-Glaphyrocysta* assemblages favour open-marine conditions but are thought to prefer high-energy environments. In the Lower Cretaceous sediments of southern Spain, *Cyclonephelium* was found to proliferate in nearshore environments (Brinkhuis & Zachariasse, 1988, after Brinkhuis, 1986). Brinkhuis and Zachariasse (1988) suggest that influx of *Cyclonephelium* group (*Cyclonephelium*, *Glaphyrocysta* and *Riculacysta*) across the K/Pg boundary of El Haria, NW Tunisia, represents a drop in the sea level. These are accompanied by increases in *Spiniferites* group and decline in *Senegalinium* group. The *Heterosphaeridium/Tenua* complex has no analogues in the literature, but it behaves similarly like the *Areoligera/Glaphyrocysta* complex. In general, these complexes flourish in nearshore (inner neritic) environments of low to mid-latitudes, often in association with carbonate build-up (Downie et al., 1971; May, 1980, Brinkhuis & Zachariasse, 1988; Brinkhuis, 1994, after Brinkhuis et al., 1992). The tolerance and adaptation to reduced salinity conditions is supported by correlation of these complexes with the abundances of the nearshore and brackish calcareous nannofossils *Braarudosphaera* and *Micrantholithus* (Houghton, 1993; Martini, 1971; Percival & Fischer, 1977) and decline of the nannofossil *Thoracosphaera* sp. (Fig. 13). Living *B. bigelowii* can tolerate relatively low salinities; the species is present in the Black Sea at 17–18% salinity (Bukry, 1974). However, the species is probably not so tolerant of elevated salinities. *B. bigelowii* is not found in the Red Sea which has salinity of 37–41% (Houghton, 1993, p. 30).

***Xenascus/Odontochitina* Complex:** This complex is only composed of the ceratioid cysts *Xenascus* and *Odontochitina* species. One of the extant representatives of the ceratioid cysts is the genus *Ceratium*. This living taxon usually



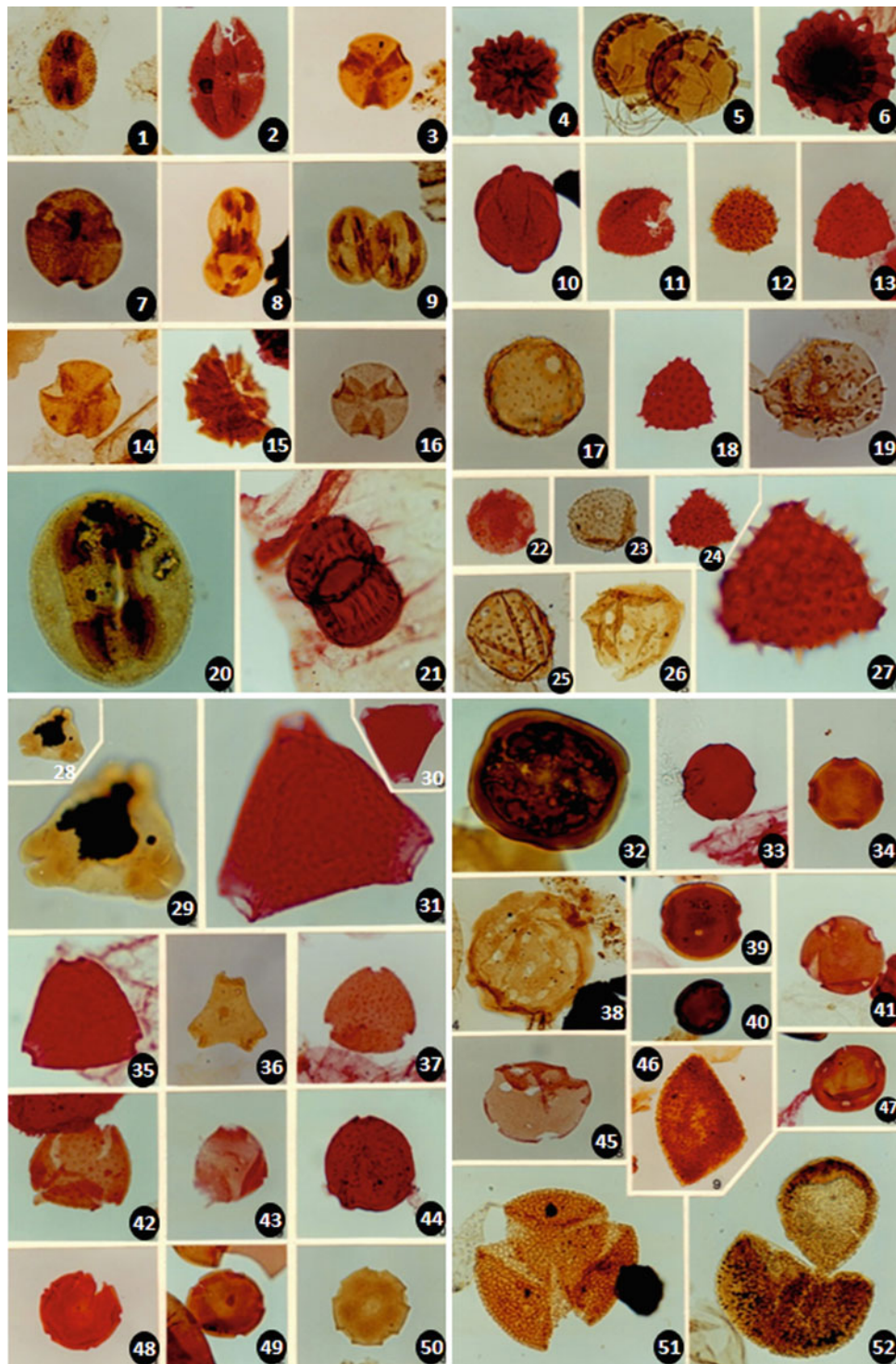
- ◀ **Plate 18** 1. *Ephedripites* sp. D; Core 4, 8531'9"-8532, 4(ox), G35/4. 2. *Ephedripites* sp. C; Core 5, 8584'-8588', 3(ox), H51/1. 3. *Longapertites marginatus*; Core 4, 8505'-8508', 3(ox), N56/4. 4. *Longapertites marginatus*; Core 5, 8576'-8576'6", 2(ox), C63/1. 5. *Ephedripites* sp. B; Core 5, 8584'-8588', 3(ox), N51/2. 6. *Ephedripites* sp. B; 8584'-8588', 3(ox), C49/4. 7. *Ephedripites* sp. B; Core 5, 8584'-8588', 2(ox), E36/2. 8. *Longapertites marginatus*; Core 5, 8576'-8576'6", 3(ox), Q41/1. 9. *Ephedripites* sp. C; Core 5, 8584'-8588', 2(ox), R48/3. 10. *Steevesipollenites* spp.; Core 4, 8511'-8514', 2(ox), P47/0. 11. *Ephedripites* sp. H; Core 4, 8508'-8511', 2(ox), T62/4. 12. *Ephedripites* sp. J; Core 4, 8531'9"-8532, 4(ox), P50/0. 13. *Ephedripites* sp. F; Core 4, 8527'-8528'6", 1(unox), W50/2. 14. *Longapertites microfoveolatus*; Core 4, 8487'10"-8489'6", 1a(ox), O41/1. 15. *Longapertites microfoveolatus*; Core 4, 8502'-8505', 1(ox), S49/0. 16. *Longapertites microfoveolatus*; Core 4, 8487'10"-8489'6", 2a(ox), S46/4. 17. *Longapertites microfoveolatus*; Core 4, 8499'-8502', 1(ox), P57/0. 18. *Longapertites* sp. C; Core 4, 8508'-85,011', 1(ox), S35/3. 19. *Longapertites* sp. A; Core 5, 8584'-8588', 1(ox), P52/4. 20. ?*Longapertites* sp. D; Core 4, 8508'-8511', 2(ox), P50/0. 21. ?*Longapertites* sp. D; Core 3, 8443'-8446', 1(unox), P33/3. 22. *Longapertites* sp. B; Core 5, 8584'-8588', 1(ox), G55/4. 23. *Spinizonocolpites baculatus* var. C; Core 1, 7788'-7791', 4(ox), E40/3. 24. *Spinizonocolpites baculatus* var. B; Core 1, 7788'-7791', 1(ox), V38/3. 25. *Spinizonocolpites baculatus* var. A; 8545'-8548', 1(unox), P41/2. 26. *Longapertites* sp. E; Core 1, 7780'-7783', 1(ox), L38/4. 27. *Mauritiidites lehmani*; Core 1, 7780'-7783', 1(ox), O42/0. 28. *Mauritiidites crassibaculatus*; Core 1, 7780'-7783', 2(ox), N47/0. 29. *Retitricolpites georgensis*; Core 4, 8539'-8542', 5(ox), G40/0. 30. *Retitricolpites georgensis*; Core 4, 8542'-8545', 1(ox), N49/0. 31. *Retitricolpites georgensis*; Core 4, 8542'-8545', 1(ox), M61/0. 32. *Mauritiidites crassibaculatus*; Core 1, 7788'-7791', 1(ox), G31/0. 33. *Mauritiidites crassibaculatus*; Core 1, 7780'-7783', 1(ox), S41/4. 34. *Mauritiidites crassibaculatus*; Core 1, 7777'-7780', 1(ox), K34/4. 35. *Tricolpites maximus*; Core 5, 8584'-8588', 1(ox), K53/0. 36. *Foveotricolpites giganteus*; Core 5, 8577'-8578'6", 1(unox), H37/0. 37. *Tricolpites ?maximus*; Core 4, 8505'-8508', 3(ox), P39/4. 38. *Mauritiidites* sp.; Core 1, 7780'-7783', 1(ox), T33/1. 39. *Mauritiidites lehmanii*; Core 1, 7780'-7783', 1(ox), M58/2. 40. *Tricolpites ?maximus*; Core 5, 8549'6"-8550', 1(ox), H58/0. 41. *Foveotricolpites giganteus*; Core 5, 8545'-8548', 3(unox), H45/0. 42. *Foveotricolpites giganteus*; Core 5, 8584'-8588', 1(ox), V52/3

inhabits freshwater and brackish lakes and ponds and has been considered as cosmopolitan in these environments (Taylor, 1987). Some species of the genus (e.g., *C. furca* and *C. fucus*) live in water with salinities as low as 6–10‰ in Cochin Backwater, India, and form the main community in Bardawil Lagoon, northern Sinai, Egypt where the salinity exceeds 70‰ (Taylor, 1987). In the fossil record, the presence of blooms of the ceratioid dinocysts is an indication of deposition in marginal marine environments with low salinity. Batten and Eaton (1980) recorded floods of the ceratioid dinocyst (*Muderongia*) from the brackish interval of the Wealden Beds, England. Wightman et al. (1987) reported floods of the same dinocyst from the brackish, marginal marine sediments of Alberta, Canada. They suggested that the sediments were deposited under very low salinity conditions, and postulated that the ceratioid dinocysts can adapt to the very low salinity conditions which occur in upper delta plain sediments. Leckie and Singh (1991) reported blooms of ceratioid dinocysts (*Nyctericysta davisii*) from the Albian sediments of Alberta, associated with low species diversity, indicative of a restricted, brackish water, estuarine environment. In the present study, some Campanian intervals of the Rachmat Formation are characterised by dominance of ceratioid dinocysts (*Xenascus*) in association with low diversity of dinocyst assemblages and degraded fine vascular debris (Fig. 12). This has been interpreted as indicative of stressed brackish or low saline conditions. See Plate 22, and discussion under Palynofacies V (high-energy (high bioactivity) distal marine vascular palynofacies) in this chapter.

**Cerodinium/Senegalinium Complex:** This complex includes species of the genera *Alterbidinium*, *Cerodinium*, *Deflandrea*, *Phelodinium*, and *Senegalinium*. Brinkhuis and Zachariasse (1988) suggest that the high percentage of *Senegalinium* group (which includes *S. bicavatum*, *S.*

*laevigatum*, *Phelodinium magnificum* and *Andalusiella dubia*) across the K/Pg boundary of the El Haria, NW Tunisia, represents rise in sea level. Firth (1993) studied Maastrichtian dinocysts of the SW Georgia, USA. By grouping several dinocyst taxa into complexes, he was able to recognise alternations between transgressive and regressive periods. Transgressive conditions were characterised by peridoid species such as *Senegalinium obscurum* and *Cerodinium pannuceum*. Assemblages characterised by decrease in both dinoflagellate species abundance and absolute abundances of marine phytoplankton, with a concurrent increase in relative abundance of gonyaulacoid *Achomosphaera-Spiniferites* cysts indicative of regression and basin-ward movement of facies. Similar patterns were observed in the present study in some of the late Campanian and latest Maastrichtian intervals (Figs. 12 and 13). The interval 8461'-8464' (sample 21) from the top part of the Rachmat Formation is also considered to represent a transgressive phase, with deposition in a stressful restricted anoxic distal marine condition. The assemblage from this sample is characterised by the highest percentage of the *Cerodinium/Senegalinium* complex (up to 48% of the total dinocyst assemblage), associated with less than 5% *Achomosphaera/Spiniferites* complex and absence of the *Areoligera/Glaphyrocysta* complex. See details under Palynofacies XI (stressed distal marine amorphous palynofacies) in the discussion below. Based on the evidence cited above, the influx of the *Cerodinium/Senegalinium* complex and predominance of the peridinioid cysts accompanied by decline in *Achomosphaera/Spiniferites* and *Areoligera/Glaphyrocysta* complexes is taken as a reliable indication of transgressive and anoxic phases with stressful conditions during the deposition of the Campanian and late Maastrichtian intervals in the studied section.

**Andalusiella/Palaeocystodinium Complex:** This complex is also stratigraphically restricted and has been



◀ **Plate 19** 1. *Retitricolporites* spp.; Core 6, 8614'-8617', 2(ox), X50/2. 2. *Retitricolporites* spp.; Core 6, 8614'-8617', 1(ox), Q61/0. 3. Tricolporate form indet.; Core 6, 8614'-8617', 2(ox), E53/0. 4. *Ctenolophonidites costatus*; Core 1, 7780'-7783', 1(ox), R50/0. 5. *Tubistephanocolpites cylindricus*; Core 5, 8577'-8578'6", 1(unox), L62/0. 6. *Tubistephanocolpites cylindricus*; Core 4, 8496'-8499', 3(ox), T50/2. 7. Tricolporate form indet.; Core 6, 8614'-8617', 4(ox), H48/0. 8. Tricolporate form indet.; Core 6, 8614'-8617', 5(ox), G59/0. 9. Tricolporate form indet.; Core 6, 8614'-8617', 4(ox), O43/2. 10. *Polycolpites* sp.; Core 4, 8539'-8542', 5(ox), N46/0. 11. *Echitriporites trianguliformis*; Core 1, 7783'-7785', 1(ox), S57/1. 12. *Echitriporites trianguliformis*; Core 1, 7785'-7788', 1(ox), O55/1. 13. *Echitriporites trianguliformis*; Core 1, 7780'-7783', 1(ox), V42/0. 14. Tricolporate form indet.; Core 6, 8614'-8617', 5(ox), U50/0. 15. *Ctenolophonidites costatus*; Core 1, 7780'-7783', 3(ox), O52/1. 16. Tricolporate form indet.; Core 6, 8614'-8617', 1(unox), P48/0. 17. *Echitriporites* sp. A; Core 5, 8548'6"-8588', 3(ox), U51/2. 18. *Echitriporites trianguliformis*; cuttings, 8390', 1(ox), Q57/2. 19. *Echitriporites* sp. B; Core 5, 8584'-8588', 1(ox), F62/0. 20. Tricolporate form indet.; Core 6, 8614'-8617', 4(ox), S44/0; X600. 21. *Tubistephanocolpites cylindricus*; Core 4, 8539'-8542', 5(ox), Q49/0. 22. *Echitriporites* sp. C; Core 1, 7780'-7783', 1(ox), X58/1. 23. *Echitriporites* sp. C; Core 4, 8443'-8446', 2(unox), R31/0. 24. *Echitriporites trianguliformis*; Core 1, 7780'-7783', 1(ox), N62/4. 25. *Echitriporites* sp. B; Core 5, 8584'-8588', 2(ox), G33/0. 26. *Echitriporites* sp. B; Core 5, 8548'-8588', 3(ox), U37/0. 27. *Echitriporites trianguliformis*; Core 1, 7780'-7783', 1(ox), N62/4;

X600. 28. ?*Nudopollis* sp.; Core 1, 7759'-7762', 1(unox), D63/1. 29. ?*Nudopollis* sp.; Core 1, 7759'-7762', 1(unox), D63/1; X600. 30. *Proteacidites sigalii*; Core 4, 8527'-8528'6", 2(ox), P40/4. 31. *Proteacidites sigalii*; Core 4, 8527'-8528'6", 2(ox), P40/4; X600. 32. Tetraporate form indet.; Core 4, 8508'-8511', 1(ox), V33/3; X600. 33. Tetraporate form indet.; Core 4, 8542'-8545', 1(ox), V62/0. 34. Tetraporate form indet.; Core 4, 8511'-8514', 2(ox), D41/1. 35. *Scabratriporites simpliformis*; Core 4, 8531'9"-8532', 4(ox), K36/0; X600. 36. *Proteacidites* sp.; Core 2, 8410'-8412', 1(unox), Q50/3. 37. *Scabratriporites* sp.; Core 4, 8487'6"-8489'6", 1a(ox), F39/0. 38. *Cretacaeiporites* spp.; Core 5, 8549'6"-8550', 1(unox), F52/0. 39. Tetraporate form indet.; Core 4, 8496'-8499', 2(ox), C52/4. 40. Tetraporate form indet.; Core 4, 8502'-8505', 1(ox), Q41/4. 41. ?*Caryapollenites* sp.; Core 3, 8443'-8446', 1(ox), J40/0. 42. *Scabratriporites* sp.; Core 4, 8587'10"-8489'6", 2a(ox), L62/2. 43. Triporate forms indet.; Core 3, 8443'-8446', 2(ox), M40/2. 44. Triporate forms indet.; Core 4, 8542'-8545', 1(ox), R55/0. Probably contamination. 45. *Cretacaeiporites* spp.; Core 4, 8493'-8496', 1(ox), V47/4. 46. *Periretisyncolpites* spp.; Core 4, 8508'-8511', 2(ox), E50/0. 47. ?*Caryapollenites* sp.; Core 5, 8580'-8581'6", 1(ox), D51/4. 48. Pentazonoporate form A indet.; Core 3, 8443'-8446', 1(ox), K31/2. 49. Pentazonoporate form A indet.; Core 3, 8443'-8446', 2(ox), J47/2. 50. Pentazonoporate form A indet.; Core 2, 8428'-8431', 1(unox), O47/2. 51. *Periretisyncolpites* spp.; Core 4, 8508'-8511', 1(ox), W62/1. 52. *Periretisyncolpites* spp.; Core 4, 8487'10"-8489'6", 1(unox), H50/1

recognised in the studied section from late Campanian to Danian sediments (Figs. 12 and 13). It is composed of the closely related genera *Andalusiella* and *Palaeocystodinium* and other new varieties of peridinioid forms. The species *Palaeocystodinium australinum* and *Andalusiella polymorpha*, which is the main constituent of this complex, are together considered to represent deposition in a littoral environment (Edet & Nyong, 1993). This complex is similar to the *Cerodinium/Senegalinium* Complex, which usually flourishes when the *Achomospaera/Spiniferites* and *Areoligera/Glaphyrocysta* complexes decline (Fig. 13).

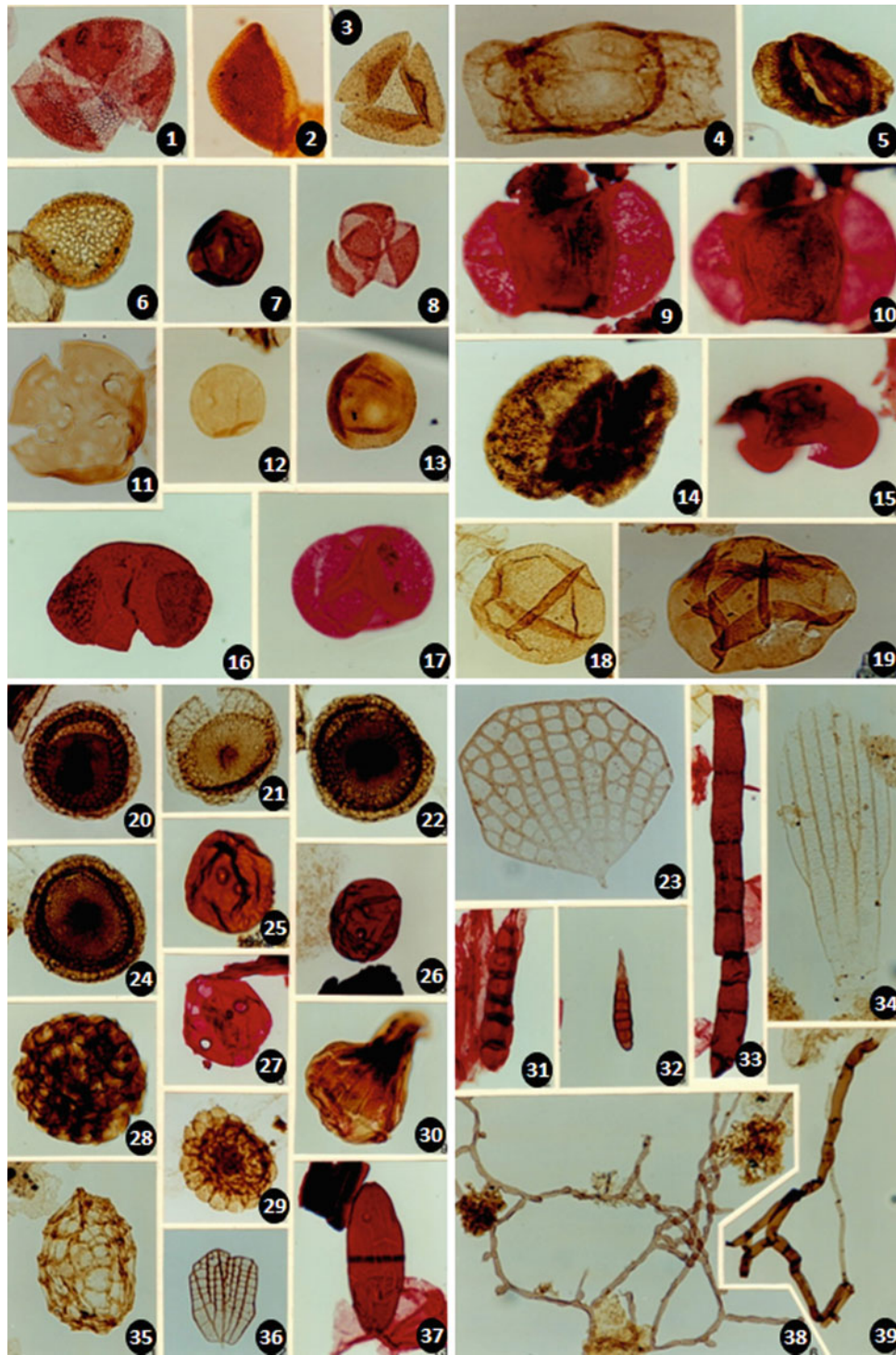
**Exochosphaeridium Complex:** This complex includes species of *Exochosphaeridium*, *Pervosphaeridium* and *Operculodinium*. *Exochosphaeridium* and *Pervosphaeridium* are closely related genera which differ only in the nature of the archeopyle. *Exochosphaeridium* and *Pervosphaeridium* are also comparable to *Operculodinium* differing in having a fibrous wall and processes. Some of the extant representative of this complex (e.g. *O. centrocarpum*, *O. psilatum*) are known to occur in a wide variety of environments ranging from oceanic to restricted marine (Brinkhuis, 1994). Offshore occurrences have been related to transportation (Harland, 1983; Wall et al., 1977). In the studied section, this complex forms high percentages of the dinocyst assemblages in some of the pre-Maastrichtian sediments but forms only minor elements of the latest Maastrichtian and Danian cyst assemblages. *Operculodinium* spp. has been recognised from the top of Rachmat Formation. *Exochosphaeridium* spp., which is the only representative of this complex in the studied pre-late Campanian sediments, has

been recognised in all marine palynofacies but in low percentages in the marine black/opaque palynofacies (Fig. 12).

**Palaeohystrichophora/Subtilisphaera Complex:** This complex includes all cosmopolitan species of the genera *Palaeohystrichophora* and *Subtilisphaera*. In the studied section, this group has been recognised in different depositional environments and in association with different types of palynofacies. In general, this complex does not show clear environmental trends, and it is suggested that it may survive and endure any depositional marine environment. However, it has been recognised as flourishing when the *Achomospaera/Spiniferites* and *Areoligera/Glaphyrocysta* complexes decline.

**Fibrocysta/Cordosphaeridium Complex and Danea Complex:** These complexes are stratigraphically limited to the late Maastrichtian and Danian (Fig. 13). The former complex includes species of the genera *Amphorosphaeridium*, *Fibrocysta* and *Cordosphaeridium*, and the latter is composed of *Danea* spp. only. These complexes haven't been documented in the literature, and their environmental trends are not well established. In the present study, these complexes appear to flourish in nearshore marine conditions. The *Fibrocysta/Cordosphaeridium* complex shows two distinct blooms in the Danian (interval 7756'-7759', sample 2), and the *Danea* complex, which appears in the early Danian, has one distinct bloom at the top most sample of the K/Pg boundary section (interval 7750'-7753', sample 1; Fig. 13).

**Coronifera/Florentinia Complex:** This complex includes species of the genera *Coronifera*, *Florentinia*,



◀ **Plate 20** 1. Syncolpate form indet.; Core 5, 8549'6"-8550', 1(ox), M61/0. 2. *Periretisyncolpites* spp.; Core 4, 8502'-8505', 1(ox), K34/2. 3. Syncolpate form indet.; Core 4, 85,216"-8523', 1(unox), N57/0. 4. Bisaccate form indet.; Core 6, 8614'-8617', 1(unox), S50/2. 5. Bisaccate form indet.; Core 4, 8520'-8523', 1(ox), M36/0. 6. *Periretisyncolpites* spp.; Core 4, 8487'10"-8489'6", 3(unox), N62/0. 7. *Spheripollenites* spp.; Core 6, 8614'-8617', 4(ox), B43/3. 8. Syncolpate form indet.; Core 4, 8487'10"-8489'6", 1a(ox), L59/1. 9. Bisaccate form indet.; Core 4, 8533'-8536', 1(ox), E47/0; distal view. 10. Bisaccate form indet.; Core 4, 8533'-8536', 1(ox), E47/0; proximal view. 11. *Spheripollenites* spp.; Core 5, 8584'-8588', 1(ox), Q45/3; X150. 12. *Exesipollenites* spp.; Core 6, 8614'-8617', 9(ox), Q40/4. 13. *Spheripollenites* spp.; Core 5, 8455'-8458', 1(unox), T42/1. 14. Bisaccate form indet.; Core 4, 8520'-8523', 4(ox), U53/0. 15. Bisaccate form indet.; Core 4, 8533'-8536', 4(ox), O37/1. 16. *Podocarpidites otagoensis*; Core 4, 8542'-8545', 1(ox), T61/0. 17. *Podocarpidites* sp.; Core 4, 8542'-8545', 4(ox), P59/0. 18. *Araucariacites australis*; Core 6, 8514'-8517', 1(ox), P52/2; X150. 19. *Araucariacites australis*; Core 5, 8584'-8588', 3(ox), K52/4. 20.

Fungal spore form A; Core 6, 8614'-8617', 4(ox), J47/1. 21. Fungal spore form A; Core 6, 8614'-8617', 6(ox), K31/4. 22. Fungal spore form A; Core 6, 8614'-8617', 1a(unox), E50/4. 23. Fruit fungal spore; Core 6, 8614'-8617', 2(ox), C46/0. 24. Fungal spore form A; Core 6, 8614'-8617', 2(ox), M41/0. 25. Fungal spore form B; Core 4, 8508'-8011', 1(ox), X39/1. 26. Fungal spore form B; Core 5, 8562'-8565', 1(ox), F50/3. 27. Fungal spore form B; Core 5, 8576'-8576'6", 1(ox), K43/0. 28. Fungal spore indet.; Core 5, 8584'-8588', 1(ox), N45/4. 29. Fungal spore indet.; Core 4, 8416'-8419', 1(ox), S57/4. 30. Fungal spore indet.; Core 6, 8614'-8617', 5(ox), U35/4. 31. Fungal spore indet.; Core 4, 8527'-8528'6", 2(ox), D49/0. 32. *Pluricellaesporites* sp.; Core 1, 7759'-7762', 1(ox), U59/1. 33. Fungal spore indet.; Core 4, 8523'-8527', 1(ox), P39/4; X150. 34. Fruit fungal spore; Core 3, 8461'-8464', 1(unox), M41/0. 35. Fungal spore indet.; Core 2, 8428'-8431', 1(unox), V34/0. 36. Fruit fungal spore; Core 6, 8614'-8617', 5(ox), J45/0. 37. Fungal spore indet. (diporate form); Core 5, 8549'6"-8550', F48/0. 38. Hypha; Core 4, 8489'6"-8490', 2(unox), S52/2. 39. Hypha; Core 6, 8614'-8617', 1b(unox), S44/4

*Hystrichokolpoma* and *Diphyes*. Published data show that the species of these genera may occur in virtually all marine environments (Figs. 12 and 13).

**Apteodinium/Cribroperidinium Complex:** This complex includes species of the genera *Apteodinium* and *Cribroperidinium* and appears to behave similarly as the *Xenascus/odontochitina* complex in the late Campanian sediments (e.g. interval 8489'10"-8490', sample 24; Fig. 12). It probably blooms and flourishes in low salinity environments.

**Impagidinium and Nematosphaeropsis Complexes:** The *Impagidinium* complex is composed of the genera such as *Impagidinium*, *Pterodinium* and *Dinopterygium*, whereas the latter *Nematosphaeropsis* complex is composed of *Nematosphaeropsis* and *Cannosphaeropsis* spp. McMinn (1993) based on a study of Quaternary dinocysts from SE Australia, noted that modern outer shelf and slope sediments contain significant numbers of *Impagidinium* and *Nematosphaeropsis* spp. He suggested that the abundance of these taxa provides a useful signature for interpreting sea-level change within late quaternary sequences. Brinkhuis (1994) suggests that *Nematosphaeropsis-Cannosphaeropsis* group characterises the outer neritic to continental slope environments of the upper Eocene to lower Oligocene of NE Italy. In the present study, *Impagidinium* complex has been recognised in high proportions in the Danian sediments in association with high abundances of the nannofossil *Thoracosphaera* sp., the *Achomosphaera/Spiniferites* and *Danea* complexes, in association with a reduced number of the *Areoligera/Glaphyrocysta* Complex (interval 7750'-7753', sample 1; Fig. 13), which may prefer high salinity conditions. The *Nematosphaeropsis* complex has been recorded in high numbers from the latest Maastrichtian (Fig. 13) and from some Campanian and pre-Campanian sediments (Fig. 12). Its late Maastrichtian trends show that these

blooms of this complex are associated with the blooms of the *Cerodinium/Senegalinium* complex (intervals 7774'-7775', 7777'-7780', 7785'-7788', samples 8, 10, 13) but also correlate with the influx of the *Areoligera/Glaphyrocysta* complex and decline of the *Impagidinium* complex below the K/Pg boundary (interval 7765'-7768', sample 5; Fig. 13).

### Algae, Prasinophytes and Acritarchs

**Algae:** The main components of the Chlorococcales in the studied section are *Pediastrum* and *Scenedesmus*. Modern *Pediastrum* and *Scenedesmus* are restricted to freshwater habitats (e.g., Round, 1973; Trainor, 1971), and so, fossil *Pediastrum* and *Scenedesmus* are considered to be reliable indicator of freshwater paleoenvironments (e.g., Batten & Lister, 1988; Ediger & Bati, 1988; El Atfy et al., 2017b; Fleming, 1989). Evitt (1963b) reported *Pediastrum* from marine strata, but considered them to have been transported from freshwater habitats into marine sediments. Most of the studied pre-Maastrichtian sediments contain freshwater algae (Fig. 12). Great freshwater influence is seen through the lower part of the studied section. These are related to the continuous influence of a fluvial system. Two types of *Pediastrum* have been recovered in this study, perforate types (Plates 11 and 12), which have been recognised with high abundance and good preservation mainly from the non-marine sediments of the Etel Formation (interval 8614'-8617', sample 57) and with compact type and in association of *Scenedesmus* (Plate 11, Figs. 14 to 16, 19 to 30; Plate 12, Figs. 1, 2, 6 and 10 to 12), which have been recorded from most marine and non-marine sediments of the Rachmat, Tagrifet and Etel formations. It is apparent that *Scenedesmus*, and the perforate forms of *Pediastrum* are indicative of a freshwater environment and more susceptible to changes in ecological conditions than the compact type.



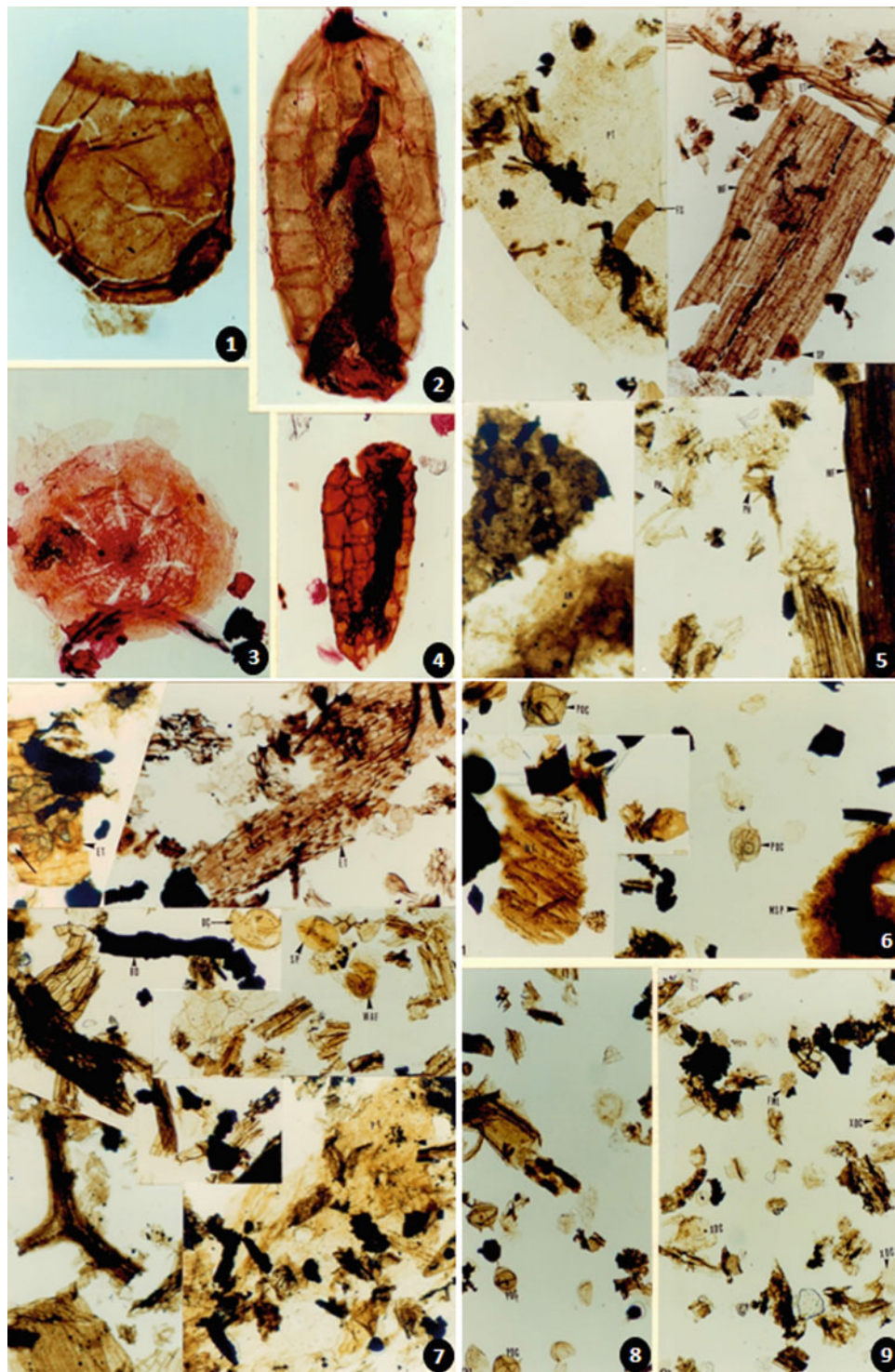


**Plate 21** 1. Fungal spore indet.; Core 6, 8614'-8617', 12 (ox), M43/0. 2. *Spermatites* spp.; Core 5, 8580'-8581'6", 4(ox), D34/2. 3. Scutate fruit fungal body; Core 4, 8539'-8542', 5(ox), G48/0; X240. 4. *Spermatites* spp.; Core 5, 8580'-8581'6", 4(ox), P36/1; X190. 5. Palynofacies I (Low Energy Proximal Non-marine Vascular Palynofacies). Late Cretaceous (late Cenomanian-Turonian), Core 6, 8614'-8617'; X60. Mosaic plate showing large size brown to dark brown wood fragments (WF), large size plant tissues (PT), epidermal tissues (ET), plant hairs (PH), fungal spores (FS), amorphous debris (AM) and spore (SP). 6. Palynofacies II (Low Energy Proximal Marine Vascular palynofacies). Late Cretaceous (late Cenomanian-Coniacian), Core 5, 8548'-8591'; X210. Mosaic plate showing abundant large epidermal tissues (ET) with wide clear stomata, and appreciable amount of large elongate wood fragments (WF), plant

tissue (PT), and lath-shaped black/opaque debris (BD). Chorate dinoflagellate cyst (DC), spore (SP), water fern (WAF). 7. Palynofacies III (High Energy Proximal Marine Vascular Palynofacies). Late Cretaceous (Campanian), Core 3, 8443'-8446'; X60. Note the presence of structured and equidimensional black and opaque debris. Salviniaceae megaspore (MSP), peridinioid dinoflagellate cysts (PDC). 8 Palynofacies IV (Low Energy Distal Marine Vascular Palynofacies). Late Cretaceous (late Santonian-Campanian); Core 4, 8487'10'-8489'6"; X60. 9. Palynofacies IV (Low Energy Distal Marine Vascular Palynofacies). Late Cretaceous (late Santonian-Campanian); Core 4, 8514'-8517'; X60. Abundant fine-grained structured debris, rare black/opaque debris, common dinoflagellate cysts. Ceratioid dinoflagellate cysts (XCD); microforaminiferal test lining (FML)

*Botryococcus* (Plate 12, Figs. 17, 18 and 23) is also a colonial green alga common in freshwater lakes and ponds. Cookson (1953) found living *Botryococcus* in salt and brackish water lagoons of The Coorong, S. Australia, and considered it as less useful as a paleoenvironment indicator. *Botryococcus* was found in very low percentages in certain intervals of the studied section. Its presence can be taken to indicate freshwater influence in a section barren of any other type of palynomorphs (see Palynofacies VI).

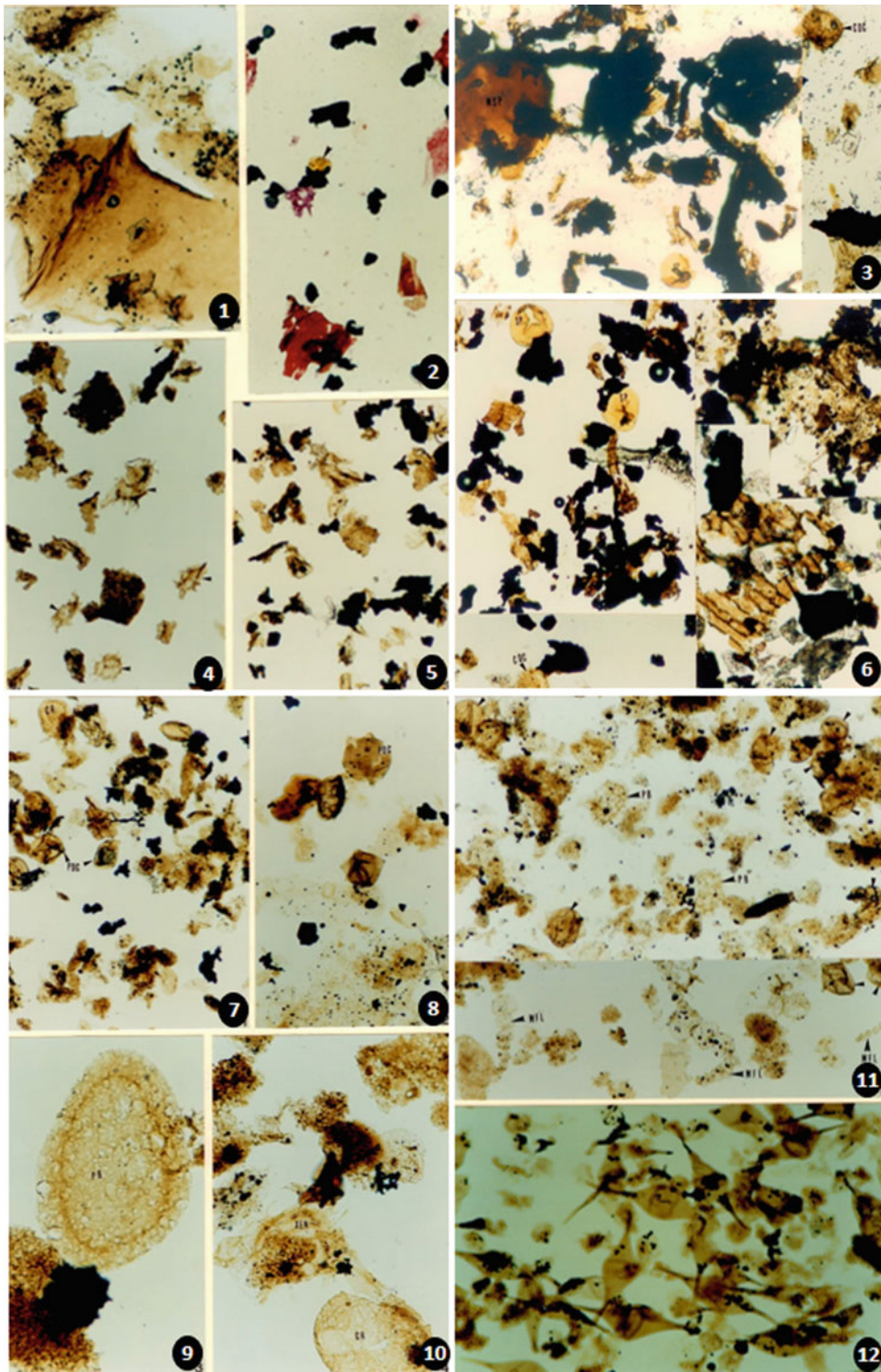
**Prasinophytes:** A few genera of prasinophytes have been recognised during the present study, including *Cymatiosphaera*, *Pterospermella* and *Pterosphaeridia*. Some species of *Cymatiosphaera* and *Pterospermella* (Plate 11, Figs. 1 to 13 and 17, 18), recorded in association with amorphous palynofacies, are characterised by their large size (>100 µm diameter). This group may be planktonic or benthonic, marine or freshwater. One genus, *Platymonas*, is known to be symbiotic with the marine worm *Convoluta* (Elsik, 1993). The prasinophytes are considered by Tappan (1980) as “disaster species,” surviving and flourishing at times when other phytoplankton undergo decline.

**Acritarchs:** Their role as paleoenvironment indicators was suggested by Staplin (1961). He recognised three acritarch associations from the Devonian sediments of Alberta (Canada), reflecting three types of depositional environment. The first association represented inshore facies and was characterised by simple spherical forms. 1.6 km from the reef, diversity rose and spined acanthomorphs appeared. 6.5 km from the reef, thick-spined and polyhedral forms appeared, with diversity remaining high. Wall (1965) and El-Mehdawi (2004) reached similar conclusions when working on acritarchs of the Early Jurassic of England and Late Silurian, Lower Acacus Member, Ghadāmis Basin, NW Libya. They found that diversity and abundance were low in the early stages of a transgression, high when open-marine and offshore conditions were established and low when regression took place and nearshore condition is prevailing. Smooth cysts are usually taken as indication of a near shore, high energy, turbid environment, whereas spiny cysts are indicative of deeper, low energy and cleaner water. This group has been recovered in very low percentages relative to other groups (Figs. 12 and 13).

The most representative is the spherical form *Eyrea nobulosa*, which characterises the lower part of the studied pre-Campanian section. A few numbers of spiny forms have been recognised from the Campanian and the K/Pg boundary sections.

**Sporomorphs:** This group includes all palynomorphs produced by terrestrial vegetation and includes spores, pollen and fungal remains. The percentage of sporomorphs to other palynomorphs (especially phytoplankton) has been taken as an indicator of proximity to shore. Sporomorph abundance declines with increasing distance from the parent

flora (Williams & Sarjeant, 1967). Spores and pollen have been recorded in high percentages from the Rachmat and Etel formations and in low percentages from the Sirt Shale, Tagrifet Limestone and Hagfa Shale formations (Figs. 12 and 13). The high percentage of this group is produced by the common appearance of pteridophyte and aquatic spores in the pre-Maastrichtian succession (Fig. 12). The latter group is mainly produced in low-lying, swampy deltaic areas, and their dominance indicates humid condition (Schrank & Nesterova, 1993; Tyson, 1993). In the studied area, this observation is supported by the common appearance of freshwater mire water spores represented by the *Ariadnaesporites* (Elsik, 1966; Odébodé and Skarby, 1980; Parry et al., 1981; Edet & Nyong, 1993). The influence of a fluvial system in the lower part of the studied section is substantiated by the common appearance of freshwater algae *Pediastrum* and *Scenedesmus*. The palynoflora of the family Hydrodictyceae could have been transported to marginal marine sites of deposition (Edet & Nyong, 1993; Evitt, 1963; Schrank, 1987). The presence of elevated open forest communities during the Campanian time is suggested by the presence of rare miospores, thought to be related to the modern taxon “*Elaeis*” type (e.g. *Trichotomosulcate* form A indet. (Plate 17, Fig. 9) and *Illiciaceae* (e.g. *Periretisyncolpites* spp.; Plate 19, Figs. 51 and 52) (Edet & Nyong, 1993). A few species of the miospore *Proteacidites sigalii* and *Proteacidites* sp., which were probably sourced from plants of the Proteaceae, have also been recognised. Schrank (1987) and Edet and Nyong (1993) claimed that the presence of these taxa in the Campanian–Maastrichtian sediments of Egypt and Nigeria indicate presence of rain forest during the Campanian–Maastrichtian time. The Maastrichtian succession is characterised by the rare occurrence of other sporomorphs of freshwater swamp communities, including the aquatic spore *Azolla cretacea* and the “*Mauritia*-type” pollen such as *Mauritiidites crassibaculatus* and *M. lehmanii* (Edet & Nyong, 1993). A mangrove swamp community is represented by the rare occurrence of *Spinizonocolpites* spp. (which are morphologically similar to the extant pollen *Nypa*) and the presence of the semi-mangrove *Echitriporites*, which is thought to be sourced from semi-mangrove plants (Adegoke et al., 1978; Edet & Nyong, 1993; Germeraad et al., 1968; Muller, 1968; Schrank, 1987, 1994). The rare occurrence of these taxa is probably related to the poor pollen production of the parent flora (Poumot, 1989; Schrank, 1987). However, their presence in low percentages may suggest the continued presence of mangrove and semi-mangrove communities along the coast during the Maastrichtian. In modern tropical regions, *Nypa* palms grow naturally in estuarine or swampy mud of fresh, brackish or salt water of South East Asia and *Mauritia* palms from swamp and marsh vegetation in Columbia (Gonzalez-Gonzman, 1967 after Edet & Nyong, 1993). These



◀ **Plate 22** 1. Palynofacies IV (Low Energy Distal Marine Vascular Palynofacies). Late Cretaceous (Campanian), Core 2, 8416'-8419', 1 (unox), Q47/1; X60. Coarse grained plant tissues. Palynomorphs are invisible because have been embedded in a coarse-grained structured debris. 2. Palynofacies VI (High Energy Distal Non-marine Black/Opaque Palynofacies). Late Cretaceous (late Cenomanian-Turonian), Core 5, 8583'-8583'6"; X150. Note the dominance of equidimensional, mostly rounded black/opaque debris, and fine rare corroded structured debris. Palynomorphs are absent except for a few specimens of *Botryococcus* (arrow), probably represents contamination. 3. Palynofacies VII (High Energy Proximal Marine Black/Opaque Palynofacies). Late Cretaceous (late Cenomanian-Turonian); Core 5, 8580'-8581'6"; X60. Abundant coarse-grained lath-shaped brown to black wood fragments, black/opaque debris and finer tissues. Salviniaceae megaspore (MSP), chorate dinoflagellate cyst (CDC). 4 & 5. Palynofacies V (High Energy Distal Marine Vascular Palynofacies (aerobic-dysaerobic). Late Cretaceous (late Campanian); Core 4, 8487'-8487'10" and 8490'-8493'; X60. Abundant fine-grained degraded structured debris and common ceratioid dinoflagellate *Xenascus* spp. (arrows). Black/opaque debris also present in appreciable amounts. 6. Palynofacies VIII (High Energy Distal Marine Black/Opaque Palynofacies). Late Cretaceous (Coniacian-Santonian); Core 4, 8528'6"-8548'; X60. Mosaic plate, showing the dominance of the fine-grained equidimensional black/opaque debris, degraded finer and coarse-grained

communities are generally well established during high-stand phases and have been considered as being very sensitive to sea-level variations (Poumot, 1989 after Fredoux & Tastet, 1976). The interpretation of a wet tropical lowland environment during the late Cretaceous is supported by the rare presence of bisaccate pollen. These taxa are indicators of dry upland areas and generally preferring cold climates. The poor preservation and rare occurrence (one specimen from the late Cenomanian-Turonian and few specimens from the Santonian-early Campanian sediments) of the recorded specimens in the studied section probably suggest reworking. The scarcity of these taxa could also be attributed to the absence of an upland flora around the studied area during the Late Cretaceous. The rare occurrence of ephedroid pollen in comparison to the high percentages of pteridophytic spores and the absence of *Classopollis* spp. (which are xerophytes (Schrank & Nesterova, 1993)) also supports the prevalence of humid wet conditions. These results are in accordance with Herengreen and Chlonova (1981), who postulated tropical-subtropical conditions in N. Africa during the Late Cretaceous time.

Fungal remains include spores, fruiting bodies and other microscopic parts. The spores are produced and shed in large numbers, a single body of *Pisolithus tinctorius*, can produce more than 5 billion spores (Elsik, 1993, after Benninghoff, 1965). Fungi have been found living in marine and non-marine environments (Elsik, 1993, p. 163). In the present study, various types of fungal remains are recognised in variable percentages, especially from the Etel Formation and the lower and upper part of the Rachmat Formation (Fig. 12). The recorded types include hyphae, fruiting bodies, scutates fruit bodies and other newly described forms.

The amorphous debris is probably a product of degradation of structured debris. Spores (SP) dominated by *Todisporites/Cyathidites* spp.; chorate dinoflagellate cyst (DC). 7, 8, 9 & 10. Palynofacies IX (High Energy Proximal Marine Amorphous Palynofacies, high bioactivity (aerobic-dysaerobic)). Late Cretaceous (late Campanian-early Maastrichtian); 7. Core 4, 8428'-8431'; X60. 8. Core 2, 8410'-8412'; X60; 9. Core 4, 8489'10"-8490'; X65; 10. Core 4, 8489'10"-8490'; X150. Dominant granulated amorphous debris, product of degraded and altered structured debris and palynomorphs. This facies as also dominated by the ceratioid dinoflagellate cysts (XCD) *Xenascus* spp. together with *Cribroperidinium* spp. (CR) and peridinioid forms (PDC) *Cerodinium/Senegalinium* spp. An appreciable amount of fine structured, black/opaque debris. Altered and degraded Palambages (PB), *Cribroperidinium* (CP) and vascular debris (SD) are also noted. 11. Palynofacies XI (Stressed Distal Marine Amorphous palynofacies (Anoxic)). Late Cretaceous (Campanian); Core 4, 8461'-8464', X60. Note the dominance of the monospecific dinoflagellate cysts, *Cerodinium/Senegalinium* Complex (arrows), Palambages (PB) and the uniserial microforaminiferal test linings (MFL). 12. Palynofacies XI (Stressed Distal Marine Amorphous palynofacies (Anoxic)). Late Cretaceous (latest Maastrichtian); Core 1, 7777'-7780', X60. Note the dominance of the dinoflagellate cyst *Andalusiella/Palaecystodinium* Complex.

Their presence generally indicates oxygenated conditions. This is probably the case in some Campanian sediments of the Rachmat Formation (intervals 8528'-8431', 8487'-8487'10", 8489'-8490' and 8490'-8493', samples 18, 22, 24 and 25), which are characterised by vascular and amorphous palynofacies (Plate 21, Figs. 3A and B; Plate 22, Figs. 1-4). Fungi have been found living in marine and non-marine environments (Elsik, 1993, p. 163). In the present study, various types of fungal remains are recognised in variable percentages, especially from the Etel and the lower and upper part of the Rachmat formations (Fig. 12; Pl. 20, Figs. 20 to 39; Pl. 21, Figs. 1 to 4). The recorded types include hyphae, fruiting bodies, scutate fruit bodies and other newly described forms. The effects of fungi on algae and vascular debris have been recognised throughout the geological record. Some produce enzymes which penetrate organic matter and digest polysaccharides. This action provides an easy path for bacterial attack, which can alter the organic matter (Venkatachala, 1981, p. 81). The presence of fungi generally indicates oxygenated conditions.

### 6.1.1 Results and Interpretation

Three main organic palynofacies are characterised by three, main non-palynomorph debris described above (vascular, black/opaque and AOM). These are deposited under varying environmental conditions (non-marine to open marine). Each depositional environment has reproduced its own lithology, composition and preservation of the palynodebris. Polarity (proximal or distal to source), salinity and energy (low or high) have been assessed using the palynomorph groups, complexes, preservation and size of the palynodebris. Data on nanofossils blooms and dinocyst complexes have been

integrated to interpret the depositional conditions across the K/Pg boundary. The recognised palynofacies and subdivisions are described below and summarised in Fig. 14.

**Palynofacies I (Low Energy Proximal Marine); Plate 21, Fig. 5**

**Depth:** 8614'-8617' (sample 57).

**Occurrence:** Etel Formation.

**Discussion:** This facies is represented by a dark-grey shale sample from Core 6, in the Etel Formation. It is characterised by abundant vascular debris dominated by large, brown to dark brown (occasionally yellow and pale yellow to brown) well preserved and biodegraded wood fragments. Plant hairs and tracheids are also present. Appreciable amounts of AOM (probably produced from degradation and alteration of terrestrial matter) were noted. Structureless tissues with spines, which may be animal remains, are also recognised. Sporomorphs divers and abundant. Pteridophyte spores and angiosperm pollen are the most abundant taxa. Freshwater algae *Pediastrum* and *Scenedesmus* are the main aquatic components of this palynofacies. Fungal remains including spores, fruits and hyphae. Acritarchs are abundant and dominated by large size leiosphere and lophosphere forms, and rare microforaminiferal test linings are also recognised. Scolecodonts are common, and marine dinocysts are absent. The Etel Formation in the studied well is mainly composed of an anhydritic claystone sequence, interbedded with anhydritic green to purple mudstones. The dominance of the large vascular debris, abundance of miospores and abundant presence of the sphaeromorph acritarchs and microforaminiferal test linings would indicate deposition in a very shallow marginal marine of a very restricted condition proximal to the terrestrial supply. Freshwater alga *Pediastrum* is dominated by the perforate type; *Scenedesmus* is also present with better preservation than those recorded from the marine intervals. The presence of these algae in association with the fungal remains, animal tissues and scolecodonts would suggest deposition probably in a brackish swamp, pond or lake with quiet and stagnant conditions close to shore line.

**Palynofacies II (Low Energy Proximal Marine); Plate 21, Fig. 7**

**Depth:** 8584'-8591'; 8576'-8578'6"; 8548'-8550'; 8527'-8528'6" (samples 37, 45, 46, 48, 49, 52, 53).

**Occurrence:** Top most part of the Etel and the lower part of the Rachmat formations.

**Discussion:** This palynofacies dominates by large vascular debris consisting of well-preserved, brown wood fragments and yellow to brown plant tissues showing well-preserved stomata. An appreciable amount of lath-shaped black and opaque debris is present. Rare amount of AOM and degraded

structured debris is also recognised. Dinocysts are abundant and diverse, and sporomorphs are common, except at the lower part of this facies interval 8584-8588'6" (sample 52), where they are abundant. Gonyaulacoid cysts are abundant throughout this facies, except in the lower interval (8584'-8591') in which the gonyaulacoid cysts are absent or present (sample 52, 53) and peridinioid cysts are abundant. The dinocysts are dominated by the *Cerodinium/Senegalinium* and *Palaeohystrichophora/Subtilisphaera* complexes which are more pronounced across this facies and become diluted in its upper, with presence of the *Achomosphaera/Spiniferites* and *Florentinia/Coronifera* complexes. The sporomorphs are dominated by the pteridophyte spores, but the aquatic fern spores (*Ariadnaesporites*) are also rare to common and show their first occurrence at the interval 8584'6'-8588' (sample 52). *Pediastrum* is present to common except in the lowermost sample, where they are abundant. Fungal remains and *Botryococcus* are also recognised. The bulk composition of this palynofacies suggests deposition in a shallow marginal marine environment proximal to the terrestrial supply. The lowermost two samples of this facies at interval 8584-8591' (sample 52 and 53) have the lowest percentage of dinocyst assemblages and are characterised by an abundance of *Palaeohystrichophora/Subtilisphaera* and *Cerodinium/Senegalinium* complexes and low percentages of the *Achomosphaera/Spiniferites*. The abundance of large vascular debris, present to common water ferns through this palynofacies, would suggest near shore with prevalence of fluvial conditions. Stagnant and restricted marginal marine conditions are suggested for the lower part, which represents the first prominent marine conditions in the study well. In summary, this palynofacies is considered to represent a transgressive phase.

**Palynofacies III (High-Energy Proximal Marine); Plate 21, Fig. 6**

**Depth:** 8443'-8446' (sample 19).

**Occurrence:** Top most part of the Rachmat Formation.

**Discussion:** This facies is dominated by smaller size of vascular debris and a large amount of lath-shaped black/opaque debris. Dinocysts are abundant and distinctive and represented by *Palaeohystrichophora/Subtilisphaera* and *Cerodinium/Senegalinium* complexes. Gonyaulacoid cysts are also abundant and include common *Achomosphaera/Spiniferites* complex. Sporomorphs are common. Aquatic fern spores (*Ariadnaesporites* spp.) are present to rare. Freshwater algae and acritarchs are rare. The common dinocysts suggest deposition in marine conditions. The common sporomorphs including rare water ferns indicate proximity to land. The predominance of peridinioid cysts suggests reduced salinity (Harker et al., 1990), and the high percentages of the *Cerodinium/Senegalinium* complex, and low percentage of

the *Achomospaera/Spiniferites* complex suggests a transgressive state. The high amounts of lath-shaped black/opaque debris and the fine size of the vascular debris suggest deposition under high-energy conditions, not far from the terrestrial supply (Keating, 1991, after Denison & Fowler, 1980). Rare aquatic spores and freshwater algae indicate minor effect of the fluvial condition.

**Palynofacies IV (Low Energy Distal Marine); Plate 21, Figs. 8, 9, Plate 22, Fig. 1**

**Depth:** 8493'-8527'7", 8455'-8458', 8416'-8419' (samples 17, 20, 23, 26-36).

**Occurrence:** Middle part of the Rachmat Formation and the lower part of the Tagrifet Formation.

**Discussion:** This facies is characterised by abundant and well preserved, fine vascular debris. Equidimensional black/opaque debris is present to rare; traces of AOM are also recognised. Dinocysts are abundant and diverse, and the gonyaulacoid cysts are more abundant than the peridinioid. The *Achomospaera/Spiniferites*, *Palaeohystrichophora/Subtilisphaera*, and *Xenascus* complexes characterise the middle part of the Rachmat Formation (Samples 26-36). Miospores are abundant. Angiosperm pollen is present in relatively high percentages in the middle part (samples 31 and 32) of this association. Acritarchs, prasinophytes and *Palmabages* are rare to present. Microforaminiferal test linings are recognised throughout this interval. Freshwater algae (*Pediastrum*) are present to rare. The abundance and the high diversity of dinocysts suggest a fully marine environment. This directly follows a period of regression characterised by high terrestrial content and low abundance and diversity of marine algae. Fluctuations in depositional conditions are recognised in this facies and are reflected in the presence of dinocyst complexes in the interval 8493'-8527'7" (sample 26-36). The lowermost samples of this interval are characterised by a high diversity of dinocysts (38-45 species in comparison with 16 species in the Palynofacies VIII, below). Moreover, this interval is characterised by an influx of the *Odontochitina*, *Cerodinium/Senegalinium* and *Nematosphaeropsis* complexes. The presence of *Nematosphaeropsis* spp. in significant numbers has been suggested to indicate oceanic phase and outer self-conditions (McMinn, 1993). The *Cerodinium/Senegalinium* complex also flourishes in transgressive phase (Firth, 1993). The proliferation of ceratioid dinocysts at the interval 8508'-8511' and 8514'-8517' (samples 31 and 33) probably represents deposition in low salinity conditions. The maximum diversity in dinocysts was recognised at interval 8496'-8499' (sample 27). The interval 8416'-8419' (sample 17) in the Tagrifet Formation is characterised by larger vascular debris (> 500 µm), low diversity (38 species) and high abundance of dinocysts (Plate 22, Fig. 1). The vascular debris is dominated by large plant tissues associated with pyrite

framboids and rare black/opaque debris. Acritarchs and freshwater algae are rare. Sporomorphs are rare, and dinocysts are characterised by the highest percentage of the *Achomospaera/Spiniferites* and *Heterosphaeridium/Tenua* complexes. Fish remains (scales, spines, teeth etc.), rare planktonic and agglutinated microforaminifera and echinoderm fragments have been also reported from this interval. These would suggest deposition in shallow marine conditions. This is supported by the presence of high percentages of the *Achomospaera/Spiniferites* complex which flourish in nearshore environment (Brinkhuis & Zachariasse, 1988; Downie et al., 1971; Hultberg & Malmgren, 1986) and the *Heterosphaeridium/Tenua* complex (considered as equivalent to the *Areoligera/Glaphyrocysta* Complex), which also flourishes in nearshore environments with reduced salinity (Brinkhuis 1986 after Brinkhuis & Zachariasse, 1988). The dominance of vascular debris (mainly plant tissues), rare to absent black/opaque debris, abundance of dinocysts and rare sporomorphs indicate that the shallow marine environment with low energy and distal to source.

**Palynofacies V (High-Energy (High Bioactivity) Distal Marine); Plate 22, Figs. 4, 5**

**Depth:** 8487'-8487'10" and 8490'-8493' (samples 22, 25).

**Occurrence:** Top of the Rachmat Formation.

**Discussion:** This facies is characterised by abundant, fine biodegraded and badly preserved vascular debris. The black/opaque debris is present to common, and the AOM is rare. Sporomorphs are present to common, and dinocysts are abundant, but with low diversity. Two dinocyst complexes dominate this palynofacies including the *Xenascus* and *Palaeohystrichophora/Subtilisphaera* complexes (Fig. 12). The *Achomospaera/Spiniferites* and *Cerodinium/Senegalinium* complexes are common. Acritarchs are rare, and freshwater algae are absent.

Floods of ceratioid dinocysts (*Xenascus*) indicate deposition under very low salinity conditions. Abundance of fine-biodegraded vascular debris and black/opaque debris would suggest deposition in a distal, high-energy environment with aerobic to dysaerobic prevailing conditions favourable for fungal development (Hart, 1986; Tyson, 1993). The finer organic components and the rarity of sporomorphs would suggest a distal depositional site. Tyson (1993) noted that only a minority of highly adaptive species are able to cope with high energy, stressed inshore environments, by comparison to offshore environment where a decrease in energy allows more diversification with no single taxon dominating the system. This can be seen in this palynofacies in which the dinocysts are dominated by ceratioid species of *Xenascus* and the peridinioid species of *P. infusorioides*, suggesting that deposition probably took place in a shallow marine environment, in which strenuous

conditions prevailed. This palynofacies represents a regressive phase at the top of Rachmat Formation.

**Palynofacies VI (High-Energy Distal Non-Marine); Plate 22, Fig. 2**

**Depth:** 8583'-8583'6" (sample 51).

**Occurrence:** Upper part of the Etel Formation.

**Discussion:** This palynofacies is characterised by poor recovery of POM in comparison to the other recognised palynofacies and presence of finer equidimensional black/opaque debris. Phytoclasts are common and are represented by fine-degraded epidermal plant tissues. Amorphous debris is absent. Palynomorphs are generally absent except for the presence of a few specimens of *Botryococcus* that were recognised (Fig. 12). The POM in this facies was recovered from anhydritic grey to greenish-grey mudstone with bands of green to grey anhydritic siltstone. The palynological component and the lithological content of this palynofacies would suggest deposition in a non-marine environment at a distal site and with high-energy conditions. The presence of the rare specimens of *Botryococcus* (if not contaminants or reworked) indicates the presence of source of brackish water close to the depositional site. This palynofacies probably represents a regressive phase at the uppermost part of the Etel Formation.

**Palynofacies VII (High-Energy Proximal Marine); Plate 22, Fig. 3**

**Depth:** 8562'-8565' and 8580'-8581'6" (samples 47 and 50).

**Occurrence:** Lower part of the Rachmat Formation.

**Discussion:** These intervals are composed of green and purple glauconitic and pyritic sandstones and siltstones with purple mudstone pebbles. Samples yielded abundant lath-shaped black/opaque debris. Vascular debris is present to common and is generally represented by finer, badly preserved and degraded epidermal tissues and brown wood fragments. Dinocysts are abundant, but with low diversity in comparison to samples above and below this palynofacies. The gonyaulacoid cysts are predominant, include common to abundant *Florentinial/Coronifera* and *Canningia* and common *Exochosphaeridium* and *Achomosphaera/Spiniferites* complexes. Peridinioid cysts are represented by common *Cerodinium/Senegalinium* and *Palaeohystrichophora/Subtilisphaera* complexes (Fig. 12). Sporomorphs are common to abundant and are represented by common aquatic fern spores (*Ariadnaesporites* spp.). Acritarchs (*Eyrea*), *Pediasstrum* and *Botryococcus* are present. Microforaminiferal test linings are also recognised. The abundance of dinocysts indicates deposition in a marine environment. Both *Florentinial/Coronifera* and *Achomosphaera/Spiniferites* complexes are characterised by species with short and reduced processes

comparable to those species of the same complexes recognised from open-marine conditions of the Danian intervals. These occur in association with common *Canningia* Complex, which may suggest nearshore environmental conditions. The black/opaque debris is lath-shaped indicating a proximal, high-energy environment. The lithological content and the predominance of a few dinocyst genera with low species diversity would suggest deposition in proximal high-energy stressed conditions. The interpretation of proximity of the depositional site to the terrestrial vegetation supply is substantiated by the presence of common aquatic fern spores, indicating the prevalence of a fluvial system during the deposition of this facies. This palynofacies probably indicates a regressive phase at the lower part of Rachmat Formation.

**Palynofacies VIII (High-Energy Distal Marine); Plate 22, Fig. 6**

**Depth:** 8527'-8548' (sample 37-44).

**Occurrence:** Middle part of the Rachmat Formation.

**Discussion:** These intervals are composed mainly of slightly micaceous fine to very fine-grained, dirty glauconitic silty sandstones with black mudstone bands and bearing purple and grey mudstone pellets. The most characteristic POM of this palynofacies is the abundance of small, equidimensional, and rarely lath-shaped black/opaque debris. Rare amounts of fine and large degraded structured debris are also recognised. Amorphous debris is also present. Sporomorphs are abundant and are dominated by pteridophyte spores of *Todisporites/Cyathidites* spp. (Fig. 12). Aquatic fern spores (*Ariadnaesporites* spp.) are common at the top and the bottom parts and rare to absent in the middle part. Angiosperms are present to common (the number probably effected by contamination of Paleogene pollen). Dinocysts are common but generally with low diversity. Both gonyaulacoid and peridinioid cysts are abundant (Fig. 10). *Achomosphaera/Spiniferites* and *Palaeohystrichophora/Subtilisphaera* complexes are the common taxa in this palynofacies. The *Cerodinium/Senegalinium* complex is generally absent, except at the bottom where it is common. Freshwater algae are abundant and are represented mainly by the compact type of *Pediasstrum*. Acritarchs and prasinophytes are rare to absent. Reworked Palaeozoic, mainly Devonian miospores and acritarchs are recognised (Plate 14, Figs. 17 to 32) and represent up to 13.9% of the total palynomorph. Lithological content, type of palynodebris, predominance of terrestrial taxa over the marine taxa in comparison to the palynofacies above and below this facies, and presence of high percentages of reworked Palaeozoic taxa indicate deposition in shallow marginal marine condition representing a major drop in the sea level. The abundance of pteridophyte spores, aquatic spores and freshwater algae suggests continuous

fluvial influence. The paucity of well-preserved vascular debris and the abundance of equidimensional black/opaque debris suggests a distal depositional site with high-energy conditions.

This palynofacies represents a major regression phase at the middle part of Rachmat Formation during the Coniacian-Santonian time.

**Palynofacies IX (High-Energy (High Bioactivity) Proximal Marine); Plate 22, Figs. 7 to 10**

**Depth:** 8410'-8412', 8528'-8431' and 8489'6"-8490' (samples 16, 18 and 24).

**Occurrence:** Top part of Rachmat and the base of Tagrifet formations.

**Discussion:** This palynofacies is composed of abundant light yellow to dark brown amorphous debris and present to common vascular debris (including wood fragments, epidermal tissues and tracheids). The equidimensional black/opaque debris is rare to present. The dinocysts are abundant and highly diverse where sporomorphs are present to common with low to high diversity. The lower interval (8489'6"-8490', sample 24) of this palynofacies is characterised by abundant *Xenascus* and *Apteodinium/Cribroperidinium* complexes, common *Cerodinium/Senegalinium* and *Palaeohystrichophora/Subtilisphaera* complexes, whilst the upper two samples are characterised by abundant *Cerodinium/Senegalinium*, *Palaeohystrichophora/Subtilisphaera* and *Achomospaera/Spiniferites* complexes, rare *Xenascus* complex and rare to present *Apteodinium/Cribroperidinium* complex. Acritarchs are rare in the lower sample and present to common in the upper two samples, in which they are represented by *Leiosphaeridial Lophosphaeridium* spp. and other indeterminate spherical forms bearing short spines. Freshwater algae are rare, and microforaminiferal test linings, prasinophytes and *Palambages* are present. In this facies, the amorphous debris is associated with biodegraded vascular debris, degraded and altered marine algae; common sporomorphs and presence of a high amount of fungal remain particularly in the lower sample. Components of this palynofacies indicate deposition in a shallow marine environment with aerobic to dysaerobic stressed conditions and high bioactivity. Dominance of *Cerodinium/Senegalinium* complex probably suggests a transgressive phase following the regression period in the preceding interval at 8490-8493' (sample 25, Palynofacies V). Abundance of the *Cribroperidinium* and *Xenascus* spp. suggests reduced salinity in the lower sample (sample 24), whereas rarity of these forms in the upper two samples and presence to common acritarchs and *Achomospaera/Spiniferites* complex in association of common sporomorphs would probably suggest deposition in more offshore environment with slightly higher salinity, proximal to the terrestrial supply.

**Palynofacies X (Normal Distal Marine)**

**Depth:** 8390' (sample 15).

**Occurrence:** Sirt Shale.

**Discussion:** This palynofacies is represented by single ditch cutting sample composed of dark grey to black fissile mudstones. It yielded abundant pale yellow to dark-brown amorphous debris associated with pyrite framboids. Vascular debris is rare. The dinocysts are highly diverse (Fig. 4). Gonyaulacoid and peridinioid cysts are present with about equal percentages. *Cerodinium/Senegalinium* and *Achomospaera/Spiniferites* complexes are abundant, and *Andalusiella/Palaeocystodinium* complex is common. Sporomorphs present include rare aquatic fern spores (*Azolla cretaceae* and *Ariadnaesporites spinosus*) and rare specimens of the mangrove pollen *Echitriporites trianguliformis*. Acritarchs are present to common and are characterised by acanthomorph types, with spherical bodies bearing short spines. The chlorophytes (*Palambages*) are present, and the prasinophytes are rare, represented by large-sized (up 100 µm in diameter) of *Pterospermella* spp. The microforaminiferal test linings (mainly uniserial), Scolecodonts and diatom tests are present, and the freshwater algae are absent. Based on the dominance of AOM, rare phytoclast and black/opaque debris, rare sporomorphs, high abundance and diversity of dinocysts, and absence of freshwater algae, deposition in a distal normal marine environment is suggested. Abundance of *Cerodinium/Senegalinium* probably would suggest a transgressive phase. The rare aquatic spores and angiosperm pollen *Echitriporites* suggests the presence of a coastal freshwater swamp and mangrove communities in the area during the deposition of this palynofacies.

**Palynofacies XI (Stressed Distal Marine); Plate 22, Figs. 11, 12**

**Depth:** 8461'-8464' (Core 4, sample 21) and 7750'-7791' (Core 1, K/Pg boundary, sample 1-14).

**Occurrence:** Upper part of the Rachmat, top most part of the Sirt, and the lower most part of the Hagfa formations.

**Discussion:** This palynofacies is recovered from dark-grey to black fissile mudstones, silty in part and characterises by light yellow to dark-brown amorphous debris associated with abundant pyrite framboids. The vascular and black/opaque debris are rare to absent. The dinocysts are pervasive and with low diversity in the late Campanian and latest Maastrichtian samples, highly diverse in the Danian. The peridinioid dinocysts are predominant in late Campanian and latest Maastrichtian, in contrast to the Danian intervals, where the gonyaulacoid cysts are dominant. Sporomorphs are rare to present in the late Campanian (sample 21) and Danian (samples 1-4) but rare to common in the latest Maastrichtian (samples 5-14). Acritarchs are rare to common (dominated by *Leiosphaeridial*



*Lophosphaeridium* spp. and other indeterminate acanthomorph types characterised by forms bearing short spines). *Palambages* spp. are present to common. The prasinophytes represented by presence of large (up to >100 µm in diameter) *Pterospermella* spp. The scolecodonts and microforaminiferal test linings (uniserial, large planispiral and trochospiral forms) are present. Some zooclasts (structureless animal debris associated with scolecodonts) are recorded mainly from the earliest Danian interval 7762'-7765' (sample 4). The vascular debris and sporomorphs are generally rare. The late Campanian interval 8461'-8464' (Core 4, sample 21) of the Rachmat Formation is characterised by abundances of *Cerodinium/Senegalinium* and *Palaeohystrichophora/Subtilisphaera* complexes. Microforaminiferal test linings of uniserial forms are abundant. *Palambages* spp. are common.

The low percentage of the *Achomosphaera/Spiniferites* complex, the predominance *Cerodinium/Senegalinium* and *Palaeohystrichophora/Subtilisphaera* complexes, the predominance of the AOM, and scarcity of the terrestrial debris all would indicate deposition in a stressed and starved, restricted anoxic marine conditions. Characteristic sporomorph assemblages include rare occurrences of the mangrove pollen *Spinizonocolpites baculatus* and the semi-mangrove pollen (e.g., *Echitriporites trianguliformis*). Presence of coastal freshwater swamp and mangrove communities in the area during the deposition of this palynofacies is suggested by rare occurrences of the aquatic spores (*Azolla cretacea*) and the angiosperm pollen (e.g., *Echitriporites trianguliformis*, palms of *Mauritiidites crassibaculatus* and *M. lehmanii*). Low salinity in the top most samples (interval 7765'-7771', Core 1, samples 5 and 6) of the latest Maastrichtian is indicated by correlation of the *Areoligera/Glaphyrocysta* complex with the blooming of *Braarudosphaera bigelowii* (near shore, brackish water). In Danian intervals (7750'-7765'; Core 1, samples 1-4), dinocyst assemblages are diverse and abundant. They are characterised by a predominance of gonyaulacoid cysts, three dinocyst complexes and calcareous nannofossil blooms. The first and the fourth Danian samples (intervals 7750'-7753' and 7762'-7765', samples 1 and 4) are characterised by abundance of *Achomosphaera/Spiniferites* and *Danea* complexes and calcareous nannofossil *Thorasphaera* sp. (high salinity) blooms. The middle two samples (intervals 7756'-7759' and 7759'-7762', samples 2 and 3) are characterised by an influx of *Heterosphaeridium/Tenua* complex and by *Braarudosphaera bigelowii* (near shore, brackish water) and *Micrantholithus pinguis* (near shore) blooms at interval 7756'-7759' (Fig. 13). Integration of dinocyst complexes and nannofossil blooms indicates deposition in a nearshore marine environment, with probably high and low salinities. In conclusion, the studied K/Pg boundary section was deposited under three marine

transgressive and regressive phases (Fig. 13). The three transgressive phases (intervals 7785'-7791', 7777'-7780' and 7771'-7775'; samples 14, 13, 10, 7 and 8) are characterised by influxes of the *Cerodinium/Senegalinium* and *Andalusiella/Palaeocystodinium* complexes and decline in the *Areoligera/Glaphyrocysta* and *Achomosphaera/Spiniferites* complexes. The three regressive phases (intervals 7780'-7785', 7777'-7780' and 7750'-7771', samples 1-6, 9 and 10) are characterised by influxes of the *Areoligera/Glaphyrocysta*, *Achomosphaera/Spiniferites* and *Heterosphaeridium/Tenua* complexes and decline of the *Cerodinium/Senegalinium* and *Andalusiella/Palaeocystodinium* complexes.

However, these six transgression and regression phases and their dinocyst complexes and blooms are correlated with the calcareous nannofossil blooms across the K/Pg boundary (Fig. 13) and are in favour of an oscillation and a drop in sea-level at the end of late Maastrichtian and in accordance with the global event suggested by Vail et al. (1977) and Haq et al. (1987).

## 7 Petroleum Source Potential

Sirte Shale is the main source rock in Sirt Basin, but these mudstones are only mature enough to produce oil exclusively in the deeper part of the basin to the north of the study area. Sirte Shales in the study area are above or at the marginal limits of depth necessary to initiate maturation. In order to mature these mudstones, an additional 2743 m (9000 ft) of depth has been calculated (AGOCO file unpublished), a view supported herein, as the Upper Cretaceous and the earlier part of the Palaeocene mudstone is immature to marginally mature with low Thermal Alteration Index (TAI) values. The Upper Jurassic-Lower Cretaceous variegated shales in the Sarir Sandstone have also been considered as being secondary source rock in the basin (AGOCO file unpublished). The POM components of most of the study section are ideal as a potential source for hydrocarbon generation. TAI values were measured using the *Todisporites/Cyathidites* spp. as *in-situ* taxa. The TAI readings are found to range in between 1 and 3 for the *in-situ* taxa. Reworked Palaeozoic taxa show TAI values up to 4. These values would suggest immature to marginal mature for *in-situ* material and mature for the reworked material. Partially, mature to immature samples are generally associated with 'high energy distal marine palynofacies' (samples 8490'-8493' and 8487'-8487'10" of Core 4), which represents degraded vascular palynofacies. K/Pg boundary mudstones of Core 1, characterised by AOM, yielded high TOC values ranging in between 1.4 and 4.4%. This indicates good

source rock potential, but inadequate maturity of these mudstones and the remainder of Upper Cretaceous sediments to low potential. In contrast, these sediments are mature to the north, north-east and north-west of the study area (Burwood et al., 2003; El Atfy et al., 2017a, 2017b).

There is general relationship between oil gravity and the degree of thermal maturation of source rocks. The lowest gravity oil which can be sourced by marine AOM at an early stage of maturity is about 28° API. The range in this early stage is up to 35° API. Oil with gravity between API 35° and 42° is sourced during the middle stage of maturity, whereas those greater than 42° API at the late stage of source rock maturity (Barnard & Cooper, 1981, p. 172). In the study area (Sarir Field), the mean of the API is 37°, and in the Messlah Field to the north, it is 39° (AGOCO, 1980) indicating sourcing during the middle stage of maturity. A Trissic source shale is suggested in the Maragh trough to the north-east of the study area where it characterised by type I and II organic facies deposited in freshwater lacustrine-lagoonal environment. These are considered late mature and prone to generating high quality waxy crudes (Sikander et al., 2013).

The petroleum prospect in the study area and surrounding areas is the sandstones underlying the marine Upper Cretaceous mudstones and carbonates and overlying either the Precambrian or Lower Palaeozoic basement. These sandstones have several names in the Sirt Basin (e.g. pre-Upper Cretaceous, Calanscio Sandstone, Basal Sandstone, Nubian Sandstone or Sarir Sandstone). They are traditionally considered to be Late Jurassic-Early Cretaceous and are thought to be largely of non-marine origin with occasional marine influence (Thusu et al., 1988). The transgressive sandstone which sometimes appears in the Rachmat Formation in the study area is considered to represent a minor oil producer (AGOCO unpublished internal report).

## 8 Conclusions

The studied Upper Cretaceous and the K/Pg sections have yielded well preserved, highly diverse and abundant marine and non-marine palynomorphs, including varieties and species to be recorded for the first time from Libya.

1. Based on the integration of the recorded palynomorph components, 25 high-resolution stratigraphically and environmentally controlled palynomorph association spanning the Upper Cretaceous and early Palaeocene sequences have been proposed.
2. Integration between the recorded palynomorph association and nannofossil zones of El-Mehaghag (1996) has enabled us to assign the studied rock units to reliable

and highly confident age dates. The Etel Formation yielded impoverished organic remains and palynomorphs, indicating a late Cenomanian–Turonian age. The Rachmat Formation is dated as a late Turonian to late Campanian. It is characterised by short-ranging dinocysts, some of which are used in the zonation schemes in the neighbouring area, North Africa, Western Europe and Australia. The Tagrifet Formation is assigned to late Campanian to early Maastrichtian. The Sirte Shale Formation is assigned to the late Maastrichtian, and the studied lower part of the Hagfah Shale Formation is assigned to the early Paleocene, late early Danian-late Danian age.

3. Eleven organic palynofacies characterised by designative fourteen dinocyst complexes and blooms are recognised, reflecting a wide range of depositional palaeoenvironments. Transgressive and regressive pulses and high to low salinity events have been recognised throughout the study sequence. These interpretations have been supported by correlation of the recognised dinocyst complexes with the established nannofossil blooms from the K/Pg section.
4. The recognised latest Maastrichtian regressive phase corresponds with the global regressive phenomenon (Haq et al., 1987; Vail et al., 1977).

**Acknowledgements** The author would like to express sincerest gratitude to Prof. David W. Jolley, Head of Geosciences School, Aberdeen University, UK for his support and assistance throughout the course of my research. My gratitude to the National Oil Company (NOC) for their permission to publish this work. The author is deeply indebted to Prof. Rajab Elkhazmi, Prof. Salah El Beialy and Dr. Haytham El Atfy for their reviewing, fruitful comments and suggestions that improved the quality of this work.

## References

- Abdel, M. S. (1986). Albian microflora from the Nubian Sandstone east of Aswan, Egypt, Neues Jahrbuch für Geologie und Paläontologie. *Monatsh.*, 6, 357–370.
- Abou Ela, N. M., Tahouna, S. S., & Raafat, A. (2019). The Cretaceous (Barremian-Maastrichtian) palynostratigraphy and palynofacies of the Drazia-I well North Egypt. *Palynology*, 44(1), 94–113.
- Adegoke, O. S., Jan du Chêne, R. E., Agumanu, A. E., & Ajayi, P. O. (1978). Palynology and age of the Kerri-Kerri formation Nigeria. *Revista Española De Micropaleontología*, 10(2), 267–283.
- AGOCO. (1980). Geology of a stratigraphic giant—the messlah oil field. In M. J. Salem & M. T. Busreuil (Eds.), *The geology of Libya* (Vol. II, pp. 521–536). Academic press.
- Baair, M. Y., Rabti, I., Johnson, B., Miladi, N., & Swire, P. (2003). The regional geology of the Northwestern edge of the Sirt Basin. In M. J. Salem & K.M. Oun (Eds.), *The Geology of Northwest Libya Second Symposium* (pp. 3–37), Elsevier.
- Barnard, P. C., & Cooper, B. S. (1981). Oil and source rock of the North Sea Area. In L. V. Illing & G. D. Hobson (Eds.), *Petroleum*

- geology of the continental shelf of North–West Europe (pp. 169–175). Heyden.
- Barr, F. T. (1972). Cretaceous biostratigraphy and planktonic foraminifera of Libya. *Micropalaeontology*, 18(1), 1–6.
- Barr, F. T., & Weegar, A. A. (1972). *Stratigraphic nomenclature of the Sirte Basin* (pp. 1–197). Petroleum Exploration Society.
- Barsotti, G. (1963). Paleocene Ostracods of Libya (Sirte Basin) and their wide African distribution. *Revue De L'institut Français Du Pétrole*, 18(11), 1520–1535.
- Batten, D. J., & Eaton. (1980). Dinoflagellates and salinity variation in the Wealden (Lower Cretaceous) of southern England. Abstract (p. 32), V Int. Palynol. Conf.
- Batten, D. J., & Lister, J. K. (1988). Evidence of freshwater dinoflagellates and other algae in the English Wealden (Early Cretaceous). *Cretaceous Research*, 9, 171–179.
- Batten, D. J., & Uwins, P. J. R. (1985). Early to Late cretaceous (Aptian–Cenomanian) palynomorphs. In B. Thusu & B. Uwins (Eds.), *Palynostratigraphy of Northeast Libya* (Vol. 4, pp. 151–168), *Journal of Micropalaeontology*.
- Bebout, J. W. (1980). Observed stratigraphic distribution of spores, pollen and “incertae sedis” palynomorphs in the Tertiary section of the Cost no. B-2 well Baltimore Canyon. *Atlantic Outer Continental Shelf, Palynology*, 4, 181–196.
- Below, R. (1981). Dinoflagellaten-Zysten aus dem oberen Hauterive bis unteren Cenoman Sud-West-Marokkos. *Palaeontographica B*, 176, 1–145.
- Below, R. (1984). Aptian to Cenomanian dinoflagellate cysts from the Mazagan Plateau, northwest Africa (site 545 and 547, Deep Sea Drilling Project Leg 79, Initial Reports of the Deep Sea Drilling Project, 79, pp. 621–649.
- Benson, D. G. (1976). Dinoflagellate taxonomy and biostratigraphy at Cretaceous-Tertiary boundary, Round Bay, Maryland. *Tulane Studies in Geology and Paleontology*, 12, 169–233.
- Boltenhagen, E. (1975). Quelques spores du Crétacé Supérieur du Gabon. *Revue De Micropaléontologie*, 18, 69–80.
- Boltenhagen, E. (1977). Microplancton du Crétacé Supérieur du Gabon, Cahiers de Paléontologie, CRNS, pp. 1–150
- Boltenhagen, E. (1978). *Proteacidites sigalii* espèce nouvelle de pollen Protéacéïde du Sénomien du Gabon. *Revue De Micropaléontologie*, 21(1), 13–15.
- Boulter, M. C., & Riddick, A. (1986). Classification and analysis of palynodebris from the Palaeocene sediments of the Forties Field. *Sedimentology*, 33, 871–886.
- Bradford, M. R., & Wall, D. A. (1984). The distribution of Recent organic-walled dinoflagellate cysts in the Persian Gulf, Gulf of Oman, and northwestern Arabian Sea. *Palaeontographica Abt. B*, 192, 16–84.
- Brenner, G. J. (1967). Early angiosperms pollen differentiation in the Albian to Cenomanian deposits of Delaware (USA). *Review of Palaeobotany and Palynology*, 1, 219–227.
- Brinkhuis, H. (1994). Late Eocene to Early Oligocene dinoflagellate cysts from the Priabonian type-area (Northeast Italy): Biostratigraphy and palaeoenvironment interpretation. *Palaeogeography, Palaeoclimatology and Palaeoecology*, 107, 121–163.
- Brinkhuis, H., & Leereveld, H. (1988). Dinoflagellate cysts from the cretaceous/tertiary boundary sequence of El Kef, northwest Tunisia. *Review of Palaeobotany and Palynology*, 56, 5–19.
- Brinkhuis, H., & Zachariasse, W. J. (1988). Dinoflagellate cysts, sea level changes and planktonic foraminifers across the cretaceous/tertiary boundary at El Haria NW. Tunisia. *Marine Micropalaeontology*, 13(2), 153–191.
- Bu-Argoub, F. M. (1996). Palynological and palynofacies studies of the upper cretaceous sequence in well C275–65, Sirte Basin, NE Libya; Geology of Sirte Basin, Geology of Sirte Basin. In M. J. Salem, A. J. Mouzoughi, & O. S. Hammuda (Eds.), *Geology of Sirte Basin, Second Symposium*, I, pp. 419–453.
- Bujak, J. P., Barss, M. S., & Williams, G. L. (1977). Offshore East Canada organic type and color and hydrocarbon potential. *Oil and Gas Journal*, 75, 198–201.
- Bujak, J. P., Downie, C., Eaton, G. L., & Williams, G. L. (1980). Dinoflagellate cysts and acritarchs from the Eocene of southern England. *Special Papers in Palaeontology*, 24, 1–100.
- Bukry, D. (1974). Coccoliths as paleosalinity indicators, evidence from Black Sea. *American Petroleum Geologist, Memoir*, 20, 353–363.
- Burgess, J. D. (1974). Microscopic examination of kerogen (Dispersed organic matter) in petroleum exploration. *Geological Society of America, Special Paper*, 153, 19–30.
- Burwood, R., Redfern, J., & Cope, M. J. (2003). Geochemical evaluation of East Sirte Basin (Libya) petroleum systems and provenance. *Macgregor DS and Cameron NR, Petroleum geology of Africa: New bThemes and Developing Technologies* (pp. 203–240). Geol. Soc.
- Canright, J. E., & Carter, F. J. (1980). Biostratigraphy of some Cretaceous microfloras from Arizona. *Proceedings of the 4th International Palynological Conference, Lucknow (1976–1977)*, 2, 805–810.
- Chatellier, J., & Slevin, A. (1988). Review of African petroleum and gas deposits. *Journal of Africa Earth Sciences*, 7(3), 561–578.
- Clarke, R. F. A., & Verdier, J. P. (1967). An investigation of microplankton assemblages from the Chalk of the Isle of Wight, England. *Verhandelingen Der Koninklijke Nederlandse Akademie Van Wetenschappen, Afdeling Natuurkunde, Eerste Reeks*, 24, 1–96.
- Combaz, A. (1964). Les Palynofaciés. *Revue De Micropaléontologie*, 7, 205–218.
- Combaz, A. (1980). Les kérogènes vus au microscope. In B. Durand (Ed.), *Kerogen Insoluble organic matter from sedimentary rocks* (pp. 55–111), Imprimerie Bayeusaune.
- Cookson, I. C. (1953). Records of the occurrence of *Botryococcus braunii*, Pediastrum and the Hystrichosphaeidae in Cenozoic deposits of Australia. *National Museum Victoria, Melbourne*, 18, 107–123.
- Cookson, I. C., & Eisenack, A. (1960). Microplankton from Australian Cretaceous sediments. *Micropaleontology*, 6(1), 1–18.
- Cookson, I. C., & Eisenack, A. (1965). Microplankton from the Dartmoor Formation, SW. Victoria. *Proceedings of the Royal Society of Victoria*, 79, 133–137.
- Cookson, I. C., & Eisenack, A. (1967). Some Early Tertiary microplankton and pollen grain from a deposit near Strahan, western Tasmania. *Proceedings of the Royal Society of Victoria*, 79, 139–146.
- Cookson, I. C., & Eisenack, A. (1968). Microplankton from two samples from Gingin 1369 Brook No. 4 Borehole, Western Australia. *Journal of the Royal Society of Western Australia*, 51, 110–122.
- Cookson, I. C., & Eisenack, A. (1970). Cretaceous microplankton from the Eucla Basin, Western Australia. *Proceedings of the Royal Society of Victoria*, 83(2), 137–157.
- Cookson, I. C., & Eisenack, A. (1971). Cretaceous microplankton from Eyre No.1 Bore Core 20, Western Australia. *Proceedings of the Royal Society of Victoria*, 84(2), 217–225.
- Cookson, I. C., & Eisenack, A. (1982). Mikrofossilien aus australischen Mesozoischen und Tertiären sedimenten Zweiter Teil. *Palaeontographica, Abt.B.*, 184, 23–63.
- Corradini, D. (1973). Noncalcareous microplankton from the Upper Cretaceous of the Northern Apennines. *Bollettino Della Società Paleontologica Italiana*, 11(2), 119–197.
- Damassa, S. P. (1984). Morphological variability and paraplate configuration of the dinoflagellate genus *Danea* Morgenroth 1968. *Palynology*, 8, 51–69.

- Damassa, S. P. (1988). *Carpatella cornuta* Grigorovich 1969 (Dinophyceae)—A member of the Aptiana-Ventriosum Complex. *Palynology*, 12, 167–177.
- Davey, R. J. (1969a). Non-calcareous microplankton from the Cenomanian of England northern France, and North America, Part 1. *Bulletin of the British Museum (Natural History) Geology*, 17, 103–180.
- Davey, R. J. (1969b). Some dinoflagellate cysts from the Upper Cretaceous of northern Natal, South Africa. *Palaeontologia Africana*, 12, 1–23.
- Davey, R. J. (1971). Palynology and palaeoenvironmental studies with special reference to the continental shelf sediments of South Africa. In A. Farinacci (Ed.), *Proceedings of the 2nd Planktonic Conference Roma*, 1970, 1. Edizioni Technoscienza.
- Davey, R. J. (1975). A dinoflagellate cyst assemblage from the Late Cretaceous of Ghana. *Proceedings of the 5th West African Colloquium on Micropaleontology*, 7(5), 150–173.
- Davey, R. J. (1978). Marine cretaceous palynology of Site 361, D.S.D. P Leg 40, off southwestern Africa. In H. M. Bolli, & W. B. F. Ryan, et al. (Eds.), *Initial Reports of the Deep Sea Drilling Project* (Vol. XL, pp. 883–913).
- Davey, R. J., & Rogers, J. (1975). Palynomorph distribution in recent offshore sediments along two traverses off Southwest Africa. *Marine Geology*, 18, 213–225.
- Deflandre, G. (1935). Considérations biologiques sur les microorganismes d'origine planctonique conservés dans les silex de la craie. *Bulletin Biologique De La France Et De La Belgique*, 69, 213–244.
- Deflandre, G. (1937). Microfossiles des siles crétacés. Deuxième partie. Flagellés incertae sedis. *Hystrichosphaeridés*, 26, 51–103.
- Deflandre, G., & Cookson, I. C. (1955). Fossil microplankton from Australian Late Mesozoic and Tertiary sediments. *Australian Journal of Marine and Freshwater Research*, 6, 242–313.
- Denison, C., & Fowler, R. M. (1980). Palynological identification of facies in a deltaic environment. In *Proceedings of the Meeting on the sedimentation of North Sea Reservoir Rocks* (Vol. XII, pp. 1–22). Norsk Petroleumforening.
- Downie, C., Hussain, M. A., & Williams, G. L. (1971). Dinoflagellate cysts and acritarchs association in the Palaeogene of southeast England. *Geoscience and Man*, 3, 35–39.
- Doyle, J. A., & Robbins, E. I. (1977). Angiosperm pollen zonation of the continental Cretaceous of the Atlantic Coastal Plain and its application to deep wells in the Salisbury Embayment. *Palynology*, 1, 43–78.
- Drugg, W. S. (1967). Palynology of the Upper Moreno Formation (Late Cretaceous-Paleocene). *Palaeontographica, Abt.B.*, 120, 1–71.
- Eaton, G. L. (1976). Dinoflagellate cysts from the Bracksham Beds (Eocene) of the Isle of Wight, Southern England. *Bulletin of the British Museum (Natural History) Geology*, 26, 227–332.
- Edet, J. J., & Nyong, E. E. (1993). Depositional environments, sea-level history and palaeobiogeography of the late Campanian-Maastrichtian on the Calabar flank, SE Nigeria. *Palaeogeography, Palaeoclimatology and Palaeoecology*, 102, 161–175.
- Edet, J. J., & Nyong, E. E. (1994). Palynostratigraphy of Nkporo Shale exposures (late Campanian-Maastrichtian) on the Calabar Flank, SE Nigeria. *Review of Palaeobotany and Palynology*, 80, 131–147.
- Ediger, V. S., & Bati, Z. (1988). Morphological examination of the *Pediastrum* (Chlorophyta) from the Tertiary strata of the Thrace Basin (N.W. Turkey). *Pollen Et Spores*, 30, 203–222.
- El Alami, M. A. (1996). Habitat of oil in Abu Attifel area, Sirt Basin, Libya. In M. J. Salem, A. S. El Hawat, & A. M. Sbeta (Eds.), *The geology of Sirt Basin* (Vol. II, pp. 337–348). Elsevier.
- El Atfy, H. (2021). Palynofacies as a paleoenvironment and hydrocarbon source potential assessment tool: An example from the Cretaceous of north Western Desert Egypt. *Palaeobiodiversity and Palaeoenvironments*, 101, 35–50.
- El Atfy, H., El Diasty, W. S., & El Beialy, S. Y., et al. (2017a). Palynofacies and geochemical analyses of the Upper Cretaceous–Eocene succession, western Sirte Basin, Libya. Palaeoenvironmental interpretation and implications for hydrocarbon generation potential. *Journal of Petroleum Science and Engineering*, 157, 48–163.
- El Atfy, H., Anan, T., & El-Soughier, M. I. (2017b). Paleocologic and stratigraphic significance of the freshwater algae *Pediastrum* in the Upper Cretaceous (Turonian) marine deposits, north Western Desert Egypt. *Paläontologische Zeitschrift*, 91, 273–281.
- El-Beialy, S. Y. (1988). Neogene palynostratigraphy of the El Qawasim No. 1 well, Nile Delta Egypt. *Neues Jahrbuch Für Geologie Und Paläontologie, Mh*, 8, 453–463.
- El-Beialy, S. Y. (1990). Tertiary dinoflagellate cysts from the Mit Ghamr-1 well, Nile Delta Egypt. *Review Palaeobotany and Palynology*, 63, 259–267.
- Elsik, W. C. (1966). New sporomorph genera from the cretaceous of Peru. *Pollen Et Spores*, 8(3), 553–564.
- El Beialy, S. Y. (1995). Campanian-Maastrichtian palynomorphs from the Duwi (Phosphate) Formation of the Hamrawein and Umm El Hueitat mines, Red Sea Coast, Egypt. *Review of Palaeobotany and Palynology*, 85, 303–317.
- El-Mehaghag, A. A. (1996). Cretaceous and Tertiary calcareous nannofossils biostratigraphy of North and Northeast Libya. In M. J. Salem, A. J. Mouzoughi, & O. S. Hammuda (Eds.), *Sedimentary Basins of Libya, 1st symposium, Geology of Sirt Basin*, (Vol. I, pp. 475–512). Elsevier.
- El-Mehdawi, A. D. (1991). Preliminary palynological study of the upper cretaceous Al Hilal Formation, Ra's Al Hilal Area, NE Libya. In M. J. Salem, O. S. Hammuda, & B. A. Eliagoubi (Eds.), *Geology of Libya*, (Vol. IV, pp. 1351–1355). Elsevier.
- El-Mehdawi, A. D. (1998). *Odontochitina tabulata* sp. nov. A Late Santonian-Early Campanian Dinoflagellate cyst from SE Sirte Basin, Libya. *Journal of Micropalaeontology*, 17(2), 173–178.
- El-Mehdawi, A. D. (2004). Palynological Analysis of the Lower Acacus Member in Wells A1-NC1 and A1-NC3A, Ghadamis Basin, NW Libya. In M. J. Salem, & K. M. Oun(Eds), *Sedimentary Basins of Libya, 2nd Symposium, The Geology of West Libya* (Vol. I, pp. 225–236). Elsevier.
- El-Mehdawi, A. D. (2008). Palynological analysis of the upper cretaceous Al Hilal Formation, Ra's Al Hilal area, Al Jabal Al Akhdar, NE Libya. In M. J. Salem, A. El-Arnauti, A. S. El Sogher (Eds.), *Sedimentary Basin of Libya, 3rd Symposium, The Geology of East Libya*, (Vol. III, pp. 143–162), Elsevier.
- Elsik, W. C. (1993). The morphology, taxonomy, classification and geological occurrences of fungal Palynomorphs. A Short Course, presented by AASP Inc., Louisiana State University (pp. 23–24), October 1993, unpublished.
- Erkmen, U., & Sadek, A. (1981). Contribution to the stratigraphy of the German Formation (Late Cretaceous-Early Tertiary) in SE Turkey by means of dinoflagellate and nannoplankton. *Neues Jahrbuch Für Geologie Und Paläontologie, Abhandlungen*, 1901(3), 129–140.
- Evitt, W. R. (1963). Occurrence of freshwater alga *Pediastrum* in Cretaceous marine sediments. *American Journal of Sciences*, 261, 890–893.
- Field, R. A. (1969). The Cretaceous/Tertiary boundary in the area of concession 65 and 80, Cyrenaica. London Palaeontological Note, CPR/PLN 3557, BP., Exploration and Production Research Division: P9, unpublished.
- Firth, J. V. (1993). Dinoflagellate assemblages and sea level fluctuation in the Maastrichtian of southwest Georgia. *Review of Palaeobotany and Palynology*, 79, 179–204.
- Fisher, M. J. (1980). Kerogen distribution and depositional environment in the Middle Jurassic of Yorkshire, UK. *Fourth International Palynological Conference, Lucknow, 1976–1977(2)*, 574–580.

- Fisher, M. J., & Denison, C. N. (1977). Stratigraphic range charts of diagnostic dinocysts: Late Cretaceous. In *Distribution of biostratigraphic diagnostic dinocysts and miospores from the northwestern European Continental Shelf and adjacent areas* (pp. 17–21). International Palynological Colloquium; Institut Kontinental Sokkelundersøkset.
- Fleming, R. F. (1989). Fossil scenedesmus (Chlorococcales) from the Ranton Formation, Colorado and New Mexico, U.S.A. *Review of Palaeobotany and Palynology*, 59, 1–6.
- Foucher, J. C. (1979). Distribution stratigraphique des kystes de dinoflagelles et des Acritarches dans le Cretace superieur du Bassin de Paris et de L'Europe septentrional. *Palaeontographica, Abt.B.*, 169, 78–105.
- Fredoux, A., & Tastet, J. P. (1976). Apport de la palynologie à la connaissance paléogéographique du littoral ivoirien entre 8.000 et 12.000 ans B. P. 7th African Micropaleontological Colloquium, Dep. Geol. Univ. Ile-Ife, (abstract)
- Germeraad, J. H., Hopping, C. A., & Muller, J. (1968). Palynology of Tertiary sediments from tropical areas. *Review of Palaeobotany and Palynology*, 6, 189–348.
- Górka, H. (1963). Coccolithophoridés, Dinoflagellés, Hystrichosphaeridés et microfossiles incertae sedis du Crétacé supérieur de Pologne. *Acta Palaeontologica Polonica*, 8, 1–83.
- Grimm, E. C. (1987). Coniss: A FORTRAN 77 program for stratigraphically constrained cluster analysis by the method of incremental sum of squares. *Computers and Geosciences*, 13(1), 13–35.
- Groot, J. J., Penny, J. S., & Groot, C. R. (1961). Plant microfossils and age of the Raritan, Tuscaloosa and Magothy Formation of the eastern United States. *Palaeontographica B*, 108, 121–140.
- Gumati, Y. D., & Nairn, A. E. M. (1991). Tectonic subsidence of the Sirte Basin Libya. *Journal of Petroleum Geology*, 14(1), 93–102.
- Habib, D. (1982). Sedimentation of black clay organic facies in a Mesozoic oxic North Atlantic. *Proceedings of the Third North American Convention*, 1, 217–220.
- Habib, D., & Miller, J. A. (1989). Dinoflagellate species and organic facies evidence of marine transgression and regression in the Atlantic Coastal Plain. *Palaeogeography, Palaeoclimatology, Palaeoecology*, 74, 23–47.
- Hansen, J. M. (1977). Dinoflagellate stratigraphy and echinoid distribution in Upper Maastrichtian and Danian deposits from Denmark. *Bulletin of the Geological Society of Denmark*, 26, 1–26.
- Harding, T. P. & Lowell, J. D. (1979). Structural styles, their plate-tectonic habitats and hydrocarbon traps in petroleum provinces. *AAPG Bulletin*, 63, 1016–1058.
- Haq, B. U., Hardenbol, J., & Vail, P. R. (1987). Chronology of fluctuating sea levels since the Triassic. *Science*, 235, 1156–1167.
- Harker, S. D., Sarjeant, W. A. S., & Caldwell, W. G. (1990). Late cretaceous (Campa Vozhenikova nian) organic-wall microplankton from the interior plains of Canada, Wyoming and Texas: Biostratigraphy, Palaeontology and Palaeoenvironment interpretation. *Palaeontographica, Abt.B.*, 219, 1–243.
- Harland, R. (1973). Dinoflagellate cysts and acritarchs from the Bearpaw Formation (Upper Campanian) of South Alberta, Canada. *Palaeontology*, 16, 665–706.
- Harland, R. (1983). Distribution maps of recent dinoflagellate cysts in bottom sediments from North Atlantic Ocean and adjacent seas. *Palaeontology*, 26, 321–387.
- Hart, G. F. (1986). Origin and classification of organic matter in clastic systems. *Palynology*, 10, 1–23.
- Hea, J. P. (1971). Petrography of the Paleozoic-Mesozoic sandstones of the southern Sirte Basin, Libya. In C. Gray (Ed.), *1st symposium on the geology of Libya* (pp. 107–126). Faculty of Science, University of Libya.
- Hecht, F., Furst, M., & Klitzsch, E. (1964). Zur geologic Von Libyen, *Geol. Rundschau*, 53, 413–470.
- Heilmann-Clausen, C. (1985). Dinoflagellate stratigraphy of the uppermost Danian to Ypresian in the Viborg I borehole, central Jylland, Denmark. *Danmarks Geologiske Undersøgelse, A(7)*, 1–69.
- Helby, R., Morgan, R., & Partridge, A. D. (1987). A palynological zonation of the Australian Mesozoic. In P. A. Jell (Ed.), *Studies in Australian Mesozoic Palynology, Association of Australian Palaeontologists* (Vol. 4, pp. 1–94).
- Hengreen, G. F. W., & Chlonova, A. F. (1981). Cretaceous microfloral provinces. *Pollen Et Spores*, 23, 441–555.
- Houghton, S. D. (1993). Recent coccolith sediment patterns and transport in the North Sea: Implication for palaeoceanographic studies of marginal and continental shelf seas. In D. G. Jenkins (Ed.), *Applied micropaleontology* (pp. 1–38). Kluwer Academic Publisher.
- Hultberg, S. U. (1985). Danian Dinoflagellate zonation, C-T boundary, and the stratigraphical position of the Fish Clay in southern Scandinavia. In S. U. Hultberg (Ed.), *Dinoflagellate studies of the Upper Maastrichtian and Danian in southern Scandinavia* (pp. 56–82). University of Stockholm.
- Hultberg, S. U., & Malmgren, B. A. (1986). Quantitative biostratigraphy based on late Maastrichtian dinoflagellate and planktonic foraminifera from southern Scandinavia. *Cretaceous Research*, 8, 211–228.
- Ioannides, N. S. (1986). Dinoflagellate cysts from Upper Cretaceous-Lower Tertiary sections, Bylot and Devon Islands, Arctic Archipelago. *Geological Survey of Canada, Bulletin*, 371, 1–99.
- Ioannides, N. S., Stavrinou, G. N., & Downie, C. (1976). Kimmeridgian microplankton from Clavell's Hard, Dorset, England. *Micropalaeontology*, 22, 443–478.
- Islam, M. A. (1983). Dinoflagellate cysts from the Eocene Cliff section of the Isle of Sheppey southeast England. *Revue De Micropaléontologie*, 25(4), 231–150.
- Islam, M. A. (1984). A study of early Eocene palaeoenvironment in the Isle of Sheppey as determined from microplankton assemblage's composition. *Tertiary Research*, 6(1), 11–21.
- Jafar, S. A. (1979). Taxonomy, stratigraphy and affinities of calcareous nannoplankton genus *Thoracosphaera* Kamaaptner. 4th International Palynological Conference. *Lucknow*, 2, 1–21.
- Jain, K. P., & Carg, R. (1982). Revision of some dinoflagellate cysts from Meghalaya, India. *Journal of the Palaeontological Society of India*, VB.27, 68–70.
- Jain, K. P., & Millepied, P. (1973). Cretaceous microplankton from Senegal Basin, W. Africa. 1. Some new genera species and combination of dinoflagellates. *Palaeobotanist*, 20, 22–32.
- Jain, K. P., & Millepied, P. (1975). Cretaceous microplankton from Senegal Basin, W. Africa. Pt. II. *Systematics and Biostratigraphy*. *Geophytology*, 5, 126–171.
- Jain, K. P., & Taugourdeau-Lantz, J. (1973). Palynology of Dalmiapuram grey shale Dalmiapuram Formation, District Trichinopoly, South India-1. *Taxonomy. Geophytology*, 3, 52–68.
- Jan du Chêne, R. (1977). Palynostratigraphie (Maastrichtien-Eocène inférieur) des Flyschs du Schlieren (Canton d'Obwald, Suisse centrale). *Revue De Micropaléontologie*, 20, 147–156.
- Jan du Chêne, R. (1980). Palynological study of the Tar Sand. Upper Maastrichtian of southwest Nigeria. In *Proceedings of IV International Palynological conference Lucknow, (1976–77)* (Vol. 2, pp. 794–799).
- Jan du Chêne, R. (1988). Etude Systematique des kystes de dinoflagellatés de la Formation des Madelenines (Danien du Sénégal). *Cahiers de Micropaléontologie, C.N.R.S.*, 2, 147–174.
- Jan du Chêne, R., Adegoke, O. S., Adediran, S. A., et al. (1978). Palynology and foraminifera of the Lokoja Sandstone

- (Maastrichtian) Bida Basin, Nigeria. *Revue De Micropaléontologie*, 10, 379–393.
- Jardiné, S., & Magloire, L. (1965). Palynologie et stratigraphie du Cretace des bassins du Senegal et de Côte d'Ivoire. *Mém. Bur. Rech. Géol. Min.*, 32, 187–245.
- Jolley, D. W. (1992). Palynofloral association sequence stratigraphy of the Palaeocene Thanet Beds and equivalent sediments in eastern England. *Review of Palaeobotany and Palynology*, 74(1), 207–237.
- Kaska, H. V. (1989). A spores and pollen zonation of Early Cretaceous to Tertiary nonmarine sediments of central Sudan. *Palynology*, 13, 79–90.
- Keating, J. M. (1991). A palynological study of the Jurassic (Pliensbackian to Oxfordian) strata of the North West Hutton Field, Northern North Sea. Ph.D. Thesis, Sheffield University, Centre for Palynological Studies, (p. 606), unpublished.
- Keegan, J. B., & Stead, D. T. (2007). Late cretaceous palynofloras of Northeast Libya. In J. B. Keegan, & A. L. Mansouri (Eds.), *Subsurface Biostratigraphy of the Cretaceous to Cenozoic of Northeast Libya* (pp. 85–117), Wellstrat Service Limited.
- Kjellström, G., & Hansen, J. M. (1981). Dinoflagellate biostratigraphy of the Cretaceous-Tertiary boundary in Southern Scandinavia. *Geologiska Föreningens i Stockholm Förhandlingar*, 103, 271–278.
- Lawal, O., & Moullade, M. (1986). Palynological biostratigraphy of Cretaceous sediments in the Upper Benue Basin, NE Nigeria. *Revue De Micropaléontologie*, 29, 61–83.
- Leckie, D. A., & Singh, C. (1991). Estuarine deposits of the Albian Paddy Member (Peace River Formation) and lowermost Shaffsbury Formation, Alberta Canada. *Journal of Sedimentary Petrology*, 61(5), 825–849.
- Lentin, J. K., & Williams, G. L. (1980). Dinoflagellate provincialism, with emphasis on Campanian Peridiniaceans. American Association of stratigraphic palynologists. *Contr. Series*, 7, 1–47.
- Liengjærn, M., Costa, L., & Downie, C. (1980). Dinoflagellate cysts from the Upper Eocene-Lower Oligocene of the Isle of Wight. *Palaeontology*, 23, 475–499.
- Lindgren, S. (1984). Acid resistant peridinioid dinoflagellates from the Maastrichtian of Trelleborg, southern Sweden. *Acta Universitatis Stockholmiensis, Stockholm Contributions in Geology*, 39(6), 45–201.
- Malloy, R. E. (1972). An Upper Cretaceous dinoflagellate cyst lineage from Gabon, West Africa. *Geoscience and Man*, 4, 49–56.
- Mansour, A., Tahoun, S. S., Gentzisc, T., et al. (2020). The marine palynology of the Upper Cretaceous Abu Roash 'A' Member in the BED 2–3 borehole, Abu Gharadig Basin. *Egypt. Palynology*, 44(1), 167–186.
- Mao, S., & Mohr, B. A. R. (1992). Late Cretaceous dinoflagellate cysts (?Santonian-Maastrichtian) from the Southern Indian Ocean (Hole 748C). *Proceeding of the Ocean Drilling Program, Scientific Results*, 120, 307–341.
- Mao, S., & Norris, G. (1988). Late cretaceous-early tertiary dinoflagellate and acritarchs from the Kashi Area, Tarim Basin, Xinjiang Province, China. (*Royal Ontario Museum, Life Sciences Contributions*, 150, 93.
- Marheinecke, U. (1986). Dinoflagellaten des Maastrichtium der Grubs Hemmoor (Niedersachsen) [Dinoflagellates from the Maastrichtian of Hemmoor, Lower Saxony]. *Geologie Jahrbuch*, A39, 3–93.
- Marshall, N. G. (1984). Late Cretaceous dinoflagellates from the Perth Basin, Western Australia. Ph.D. Thesis, University of Western Australia, p. 297, unpublished.
- Martini, E. (1971). Standard Tertiary and Quaternary calcareous nannoplankton zonation. In A. Farinacci (Ed.), *Proceedings II Planktonic Conference, 1970*, pp. 739–785.
- Masran, T. C., & Pocock, S. J. (1981). The classification of plant derived particulate organic matter in sedimentary rocks. In J. Brooks (Ed.), *Organic Maturation Studies and Fossils Fuel Exploration* (pp. 145–159), Academic Press.
- Mathur, Y. K. (1986). Dinoflagellate cyst biostratigraphy and age of the Middle Eocene Kalol Formation in the Kalol-109 well, north Cambay Basin, western India. *Review of Palaeobotany and Palynology*, 47, 193–202.
- Mathur, Y. K., & Chopra, A. S. (1987). Palynofossils from the Cenozoic subsurface sediments of the Bengal Basin. *Geoscience Journal*, 8, 109–152.
- May, F. E. (1980). Dinoflagellate cysts of the gymnodiniaceae, peridiniaceae, and gonyaulacaceae from the upper cretaceous monmouth group, Atlantic Highlands, New Jersey. *Palaeontographica, Abt.B.*, 172, 10–116.
- McMinn, A. (1993). Neogene dinoflagellate cyst biostratigraphy from Sites 815 and 823, Leg 133, northeastern Australian Margin. In J. A. Mckenzi, P. J. Davies, & A. Palmer-Julson, et al. (Eds.), *Drilling Program, Scientific Results, College Program* (Vol. 133, pp. 97–105).
- McIntyre, D. J. (1974). Two new Paleocene dinoflagellates from Virginia and Maryland. *Palaeontology*, 17, 65–70.
- Mebradu, S. (1982). Stratigraphic palynology of Obi (Lafia), Plateau State of Nigeria. *Review of Palaeobotany and Palynology*, 36, 317–323.
- Medus, J., Boch, A., Parron, C., Lauerjat, J., & Triat, J. M. (1980). Turonian Normapolles from Portugal and southern France: Correlations. *Review of Palaeobotany and Palynology*, 31, 105–153.
- Méon, H. (1990). Palynologic studies of the Cretaceous-Tertiary boundary interval at EL Kef outcrop, northwestern Tunisia: Paleogeographic implications. *Review of Palaeobotany and Palynology*, 65, 85–94.
- Morgenroth, P. (1966). Mikrofossilien und Konkretionen des nordwesteuro-päisichen untereoziäns. *Palaeontographica B*, 119, 1–53.
- Moshkovitz, S., & Habib, D. (1993). Calcareous nannofossil and dinoflagellate stratigraphy of the cretaceous-tertiary boundary, Alabama and Georgia. *Micropaleontology*, 39, 167–191.
- Muftah, A., Addalouh, A., El-Mehdawi, A. D., & Daniels, H. J. (2004). Biostratigraphic indicators and paleoenvironment of Lidam formation, North Sirt Basin, Libya. In E. A. A. Youssef (Ed.), *Proceedings of 7th international conference on the geology of the Arab World (GAW7)* (pp. 203–208), Cairo University.
- Muller, J. (1968). Palynology of the Pedawan and Plateau Sandstone Formation (Cretaceous-Eocene) in Sarawak, Malaysia. *Micropaleontology*, 14, 1–37.
- Norvick, M. S., & Burger, D. (1976). Palynology of the cenomanian of Bathurst Island, Northern Territory, Australia. *Bureau of Mineral Resources Bulletin*, 151, 1–169.
- Odébodé, M. O. (1987). Palynological dating of the Lamja Sandstone (Benué Basin, Nigeria) and its geological significance. *Journal of African Earth Sciences*, 6, 421–426.
- Odébodé, M. O., & Skarby, A. (1980). Ariadnaesporites (Salviniaceae) from the Cretaceous of Nigeria. *Grana*, 19, 197–209.
- Olot, I. N. (1989). Maastrichtian dinoflagellate cyst assemblage from the Nkporo Shale on the Benin Flank of the Niger Delta. *Review of Palaeobotany and Palynology*, 57, 173–186.
- Pacltová, B. (1961). On some plant microfossils from freshwater sediments of the Upper Cretaceous (Senonian) in the Bohemian Basins. *Shorn. Ustredniho Ustavu Geol., Paleont. (Prahu)*, 26, 47–102.
- Parry, C. C., Whitley, P. K. J., & Simpson, R. D. H. (1981). Integration of palynology and sedimentological methods in facies analysis of the Brent Formation. In L. V. Illing & G. D. Hobson (Eds.), *Petroleum geology of the continental shelf of North West Europe* (pp. 205–215). Heyden.

- Patterson, I. I. I., W. A., Edwards, K. J., & Maguire, D. J. (1987). Microscopic charcoal as a fossil indicator of fire. *Quaternary Science Reviews*, 6, 3–23.
- Perch-Nielsen, K. (1979). Calcareous nannofossils from the Cretaceous between the North Sea and the Mediterranean. *IUGS Series A*, 6, 223–272.
- Percival, S. F., & Fischer, A. G. (1977). Changes in calcareous nannoplankton in the Cretaceous Tertiary biotic crisis at Zumaya, Spain. *Evolution Theory*, 2, 1–35.
- Porter, K. G., & Robbins, E. I. (1981). Zooplankton faecal pellets link fossil fuel and phosphate deposits. *Science*, 212, 931–933.
- Pöthe de Baldi, E. D. (1986). Dinoflagellos de la facies de mar abierto del Santoniano-Campaniano del sur de Lago Viedma, Provincia de Santa Cruz, Argentina. *Ameghiniana*, 23, 167–183.
- Poumot, C. (1989). Palynological evidence for eustatic events in the tropical Neogene. *Bulletin Des Centres De Recherches Exploration-Production Elf-Aquitaine*, 13(2), 437–453.
- Rebelle, M. (1990). The marine transgression in the Benue Trough (NE Nigeria): A palaeogeographic interpretation of the Gongila Formation. *Journal of African Earth Sciences*, 10, 643–655.
- Reyment, R. A. (1980). Biogeography of the Saharan Cretaceous and Paleocene Epicontinental Transgressions. *Cretaceous Research*, 1, 299–327.
- Riegel, W. (1974). New forms of organic-walled microplankton from an Upper Cretaceous assemblage in Southern Spain. *Revista Española De Micropaleontología*, 6(3), 347–366.
- Riley, G. A. (1970). Particulate organic matter in sea water. *Advanced in Marine Biology*, 8, 1–118.
- Round, F. E. (1973). *The biology of the algae* (2nd ed., p. 278p). Edward Arnold.
- Rusk, D. C. (2001). Libya: Petroleum potential of the under explored basin centers- A twenty-first-century challenge. In M. W. Downey & J. C. Threet, et al. (Eds.), *Petroleum provinces of the twenty-first century* (Vol. 74, pp. 429–452), AAPG Memoir.
- Salami, M. B. (1984). Ephedripites strobilaceus nov. comb. and polymorphism within Ephedroid pollen grains of the Late Cretaceous and Early Tertiary of Southern Nigeria. *Revista Española De Micropaleontología*, 16, 425–430.
- Salami, M. B. (1990). Palynomorph taxa from the 'Lower Coal Measures deposits (?Campanian-Maastrichtian) of Anambra Trough southeastern Nigeria. *Journal of African Earth Sciences*, 11, 135–150.
- Salard-Chebodaëff, M. (1978). Sur la palynoflore maestrichtienne et tertiaire du bassin sédimentaire littoral du Cameroun. *Pollen Et Spores*, 20, 215–256.
- Sanford, R. M. (1970). Sarir oil field, Libya; Desert Surprise. In M. T. Halbouty (Ed.), *Geology of giant petroleum field*. Mem. Am. Assoc. Petrol. Geol., Memoir 14, 449–476.
- Schiøler, P. (1992). Dinoflagellate cysts from the Arnager Limestone Formation (Coniacian, Late Cretaceous), Bornholm, Denmark. *Review of Palaeobotany and Palynology*, 72, 1–25.
- Schrank, E. (1984). Organic-walled microfossils and sedimentary facies in the Abu Tartur Phosphates (Late Cretaceous, Egypt). *Berliner Geowiss. Abh. A*, 50, 177–187.
- Schrank, E. (1987). Palaeozoic and Mesozoic Palynomorphs from northeast Africa (Egypt and Sudan) with special reference to Late Cretaceous pollen and dinoflagellates. *Berliner Geowiss. Abh. a.*, 75 (1), 249–310.
- Schrank, E. (1991). Mesozoic palynology and continental sediments in NE Africa (Egypt and Sudan)—A review. *Journal of African Earth Science*, 12(1), 363–373.
- Schrank, E. (1994). Palynology of the Yesomma Formation in northern Somalia: Study of pollen, spores and associated phytoplankton from the Late Cretaceous Palmae Province. *Palaeontographica Abt. B*, 231, 63–112.
- Schrank, E., & Ibrahim, M. I. A. (1995). Cretaceous (Aptian-Maastrichtian) Palynology of Foraminifera-Dated Wells (KRM-1, AG-18) in Northwestern Egypt. *Berliner Geowissenschaftliche Abhandlungen (A)*, 177, 1–44.
- Schrank, E., & Nesterova, E. (1993). Palynofloristic changes and Cretaceous climates in northern Gondwana (NE Africa) and southern Laurasia (Kazakhstan). In U. Thorweihe & H. Schandelmeier (Eds.), *Geoscientific research in Northeast Africa* (pp. 381–389). Balkema.
- Schrank, E., & Perch-Nielsen, K. (1985). Late Cretaceous palynostratigraphy in Egypt with comments on Maastrichtian and Early Tertiary calcareous nannofossils. *Newsletters on Stratigraphy*, 15 (2), 81–99.
- Sikander, A. H., Basu, S., & Wafa, F., et al. (2013). Atlas of petroleum geology and geochemistry of source rocks and hydrocarbons in Sirt Basin, Libya. In A. S. El-Hawat (Ed.), (Vol. 6, p. 340). Benghazi University, Special Publication.
- Singh, C. (1971). Lower cretaceous microfloras of the Peace River area, North Western Alberta. *Alberta Research Council*, 28, 301–542.
- Singh, C. (1983). Cenomanian microfloras of the Peace River area, northwestern Alberta. *Alberta Research Council*, 44, 1–322.
- Sissingin, W. (1977). Biostratigraphy of Cretaceous calcareous nannoplankton. *Geologie En Mijnbouw*, 56(1), 37–65.
- Soncini, M., & Rauscher, R. (1988). Associations de dinokystes du Maastrichtien- Paleocene Phosphate Au Maroc. *Soc. Nat. Elf Aquitaine*, 12, 427–450.
- Srivastava, S. K. (1992). Dinocyst biostratigraphy of Cenomanian strata of the western Gulf Coastal Plain. *Southern United States. Palaeobotanist*, 39(2), 155–235.
- Stanley, E. A. (1966). The problem of reworked pollen and spores in marine sediments. *Marine Geology*, 4, 397–408.
- Staplin, F. L. (1961). Reef-controlled distribution of Devonian microplankton in Alberta. *Palaeontology*, 4(3), 392–424.
- Staplin, F. L. (1969). Sedimentary organic matter, organic metamorphism and oil and gas occurrences. *Bulletin of Canadian Petroleum Geology*, 17(1), 47–66.
- Stead, D. T. (2007). Cenozoic palynofloras of Northeast Libya. In J. B. Keegan, & A. L. Mansouri (Eds.), *Subsurface Biostratigraphy of the cretaceous to Cenozoic of Northeast Libya* (pp. 183–228), Wellstrat Service Limited, United Kingdom
- Stover, L. E. (1977). Oligocene and Early Miocene dinoflagellate from Atlantic Core hole 5/5B, Blake Plateau. *American Association of Stratigraphic Palynologists, Contributions Series*, 5A, 66–88.
- Sultan, I. Z. (1985). Maastrichtian plant microfossils from El Mahamid area, Nile Valley, southern Egypt. *Revue De Micropaléontologie*, 28, 213–222.
- Sweet, A. R., & McIntyre, D. J. (1988). Late Turonian marine and nonmarine palynomorphs from the Cardium Formation, north central Alberta foothills, Canada. *Mem. Can. Soc. Petrol. Geol.*, 15, 499–516.
- Tappan, H. (1980). The palaeobiology of plant Protists; W. H. Freeman.
- Taylor, F. J. R. (1987). Dinoflagellate morphology. In F. J. R. Taylor (Ed.), *The biology of dinoflagellates* (pp. 24–91). Botanical Monographs, Blackwell.
- Thusu, B., & van der Eem, J. G. L. A. (1985). Early Cretaceous (Neocomian-Cenomanian) palynomorphs. *Journal of Micropalaeontology*, 4(1), 131–150.
- Thusu, B., van der Eem, J. G. L. A., El-Mehdawi, A. D., et al. (1988). Jurassic-Early Cretaceous palynostratigraphy in northeast Libya. In A. El-Arnauti, B. Owens, & B. Thusu (Eds.), *Subsurface palynostratigraphy of Northeast Libya* (pp. 171–213). Garyounis University Publications, Benghazi.
- Trainor, F. R. (1971). Development of form in Scenedesmus. In B. C. Parker, & R. M. Jr. Brown (Eds.), *Contribution in Phycology* (pp. 81–92), Allen Press.

- Tyson, R. V. (1984). Palynofacies investigation of Callovian (Middle Jurassic) sediments from DSDP Site 543, Blake-Bahama Basin, Western Central Atlantic. *Marine and Petroleum Geology*, 1, 3–13.
- Tyson, R. V. (1993). Palynofacies analysis. In D. G. Jenkins (Ed.), *Applied Micropaleontology* (pp. 153–191), Kluwer Academic Publisher.
- Uwins, P. J. R., & Batten, D. J. (1988). Early to mid-Cretaceous palynology of northeast Libya. In A. EL-Arnauti, B. Owens, & B. Thusu (Eds.), *Subsurface Palynostratigraphy of Northeast Libya* (pp. 215–231). Garyounis University Publication.
- Vail, P. R., Mitchum, Jr. R. M., & Thompson, I. I. S. (1977). Seismic stratigraphy and global changes of sea level, Part 4: global cycles of relative changes of sea level. In C. E. Payton (Ed.), *Seismic Stratigraphy-Application to Hydrocarbon Exploration*, Am. Ass. Petrol. Geol., 26, 83–97.
- Van Hoeken Klinkenberg, P. J. (1966). Maastrichtian, Paleocene and Eocene pollen and spores from Nigeria. *Leidse Geologische Mededelingen*, 38, 37–48.
- Venkatachala, B. S. (1981). Hydrocarbon source rock evaluation. A *New Palynological Approach: Petrol Asia Journal*, 4, 80–93.
- Venkatachala, B. S. (1984). Finely divided organic matter, its origin and significance as hydrocarbon source material. *Bulletin ONGC*, 21(1), 23–45.
- Viterbro, I. (1969). Lower cretaceous charophytes from the subsurface “Nubian Complex” of the Sirte Basin (Libya). In *3rd African Micropalaeontology Colloquium, Proceedings*, pp. 393–402.
- Vozzhennikova, T. F. (1967). Fossilized peridinioid algae in the Jurassic, Cretaceous and Paleogene deposits of the USSR. In W. A. S. Sarjeant (Ed.), *Boston Spa, Yorkshire, England, National Lending Library for Science and Technology*, 1971, (1–2), p. 453.
- Wall, D. (1965). Microplankton, pollen, and spores from the Lower Jurassic in Britain. *Micropaleontology*, 11(2), 151–190.
- Wall, D., Dale, B., Lohmann, G. P., & Smith, W. K. (1977). The environmental and climatic distribution of dinoflagellate cysts in modern marine sediments from regions in the North and South Atlantic oceans and adjacent seas. *Marine Micropalaeontology*, pp. 121–200.
- Wetzel, O. (1933). Die in organischer Substanz erhaltenen Mikrofossilien des baltischen Kreide-Freuersteins mit einem sediment-petrographischen und stratigraphischen Anhang. *Palaeontographica, Abt.A.*, 77, pp. 141–188.
- Wightman, D. M., Pemberton, S. G., & Singh, C. (1987). Depositional modelling of the Upper Mannville (Lower Cretaceous), east central Alberta: Implication for the recognition of brackish water deposits. *Society of Economic Paleontologist and Mineralogist, Special Publication*, 40, 189–220.
- Williams, G. L. (1975). Dinoflagellate and spore stratigraphy of Mesozoic-Cenozoic offshore Eastern Canada. *Geological Survey of Canada, Paper*, 74–30(2), 107–161.
- Williams, G. L. (1978). Palynological biostratigraphy; Deep Sea Drilling Project sites 367 and 370. Initial Reports of the Deep Sea Drilling Project, Washington, Vol. XLI, pp. 783–815.
- Williams, G. L., & Sarjeant, W. A. S. (1967). Organic-walled microfossils as depth and shoreline indicators. *Marine Geology*, 5, 389–412.
- Williams, G. L., Fensome, R. A., & MacRae, R. A. (2017). The Lentin and Williams index of fossil dinoflagellates 2017 edition, Geological Survey of Canada (Atlantic), AASP Contributions Series Number 48, p. 1097.
- Wilson, G. J. (1988). Paleocene and Eocene dinoflagellate cysts from Waipawa, Hawkes Bay, New Zealand. *New Zealand Geological Survey Paleontological, Bulletin*, 57, 1–96.
- Wilson, L. R., & Hoffmeister, W. S. (1953). Four new species of fossil Pediastrum. *American Journal of Sciences*, 251, 753–760.
- Yun, H. S. (1981). Dinoflagellaten aus der Oberkreide (Santon) von Westfalen. *Palaeontographica, Abt.B.*, 177, 1–89.
- Zaitzeff, J. B., & Cross, A. T. (1971). The use of the dinoflagellate and acritarchs for zonation and correlation of the Navarro Group (Maastrichtian) of Texas. *Geological Society of America, Special Paper*, 127, 341–377.





# Viability of the Upper Member of the Mississippian Lodgepole Formation as an Economic Source Rock in the Williston Basin

Murray Dighans and Mohamed K. Zobia

## Abstract

This study demonstrates a successful first attempt to combine palynofacies and organic geochemical data (programed pyrolysis and oil extracts) to appraise the hydrocarbon source potential of the upper marker bed of the Mississippian Lodgepole Formation (herein referred to as the Upper Lodgepole) in the Williston Basin. The study area covers the southeast corner of Saskatchewan, Canada, and northwest corner of North Dakota, USA. In this area, the Upper Lodgepole is a primarily organic-rich carbonate source rock that reaches a maximum thickness of roughly 30 m with TOC reaching a maximum of 9.06 wt%, and vitrinite reflectance equivalence values ranging from 0.76 to 0.87%. Palynofacies analysis of both core and cuttings unequivocally confirms that the organic material is indeed highly oxidized and degraded. A detailed point count of organic matter particles shows the interval to contain 100% degraded terrestrial phytoclasts, a predominantly gas-prone, type-III kerogen. However, the combined core extract, pyrolysis, and palynological data indicate a mixed type-II/III source rock. The absence of type-II kerogen material in palynological samples is believed to be a result of both diagenetic oxidation and thermal cracking and dissociation during maturation.

## Keywords

Palynofacies • Lodgepole • Pyrolysis • Williston Basin • Vitrinite Reflectance • TOC

M. Dighans  
Endeavor Energy Resources, LP, Midland, Texas, USA

M. K. Zobia (✉)  
Department of Geosciences, The University of Texas Permian Basin, Odessa, Texas, USA  
e-mail: [zobaa\\_m@utpb.edu](mailto:zobaa_m@utpb.edu)

## 1 Introduction

The present study focuses on the Upper Lodgepole Formation in the southeast corner of Saskatchewan, Canada, and northwest corner of North Dakota, USA (Fig. 1). The Upper Lodgepole Formation has long been speculated as a significant source rock in the Williston Basin. Osadetz and Snowdon (1995) claimed that the samples analyzed in the Lodgepole have “consistently higher hydrocarbon yields suggesting marginal to excellent potential, better than other sources at comparable maturities.” They also reported the Upper Lodgepole to have up to 14.47 wt% TOC with upwards of 444 °C  $T_{max}$  northwest and up-dip of the present study area (Fig. 2, Geological Survey Canada data points). Numerous penetrations while exploiting the underlying Bakken shales show significant gas shows and solvent ultraviolet cuts on mud logs adding to the assumption that this could be a significant oil play worthy of being exploited.

Published  $T_{max}$  values from the underlying Bakken shales tend to be on the magnitude of roughly 10 °C lower than samples from the overlying Lodgepole Formation (e.g., Osadetz & Snowdon, 1995). In addition, core extract data collected through this study show a marine source with a vitrinite reflectance equivalent (VRO-eq) of 0.7% and 0.75% in the Oungre and Sparks wells, respectively. Therefore, to further understand the thermal maturity of the Upper Lodgepole in our focus area, we must understand the drivers behind the different thermal maturity values. This study not only incorporates new pyrolysis data from the Sparks and Oungre cores to previously published datasets, but also utilizes palynological data from the Oungre core as well as cuttings from the Gulbranson 1-1H, Gulbranson 2-1H, and Wolter 15-8H wells (Fig. 2) to help resolve the elevated thermal maturities seen from pyrolysis. Therefore, the objectives of this study are to: (1) complete pyrolysis on the two cores, the Oungre and Sparks, to compare data to understand thermal maturity in northwestern North Dakota compared to published information from up-dip, (2) collect



**Fig. 1** Location map of the Williston Basin shows the focus area for this study boxed in red

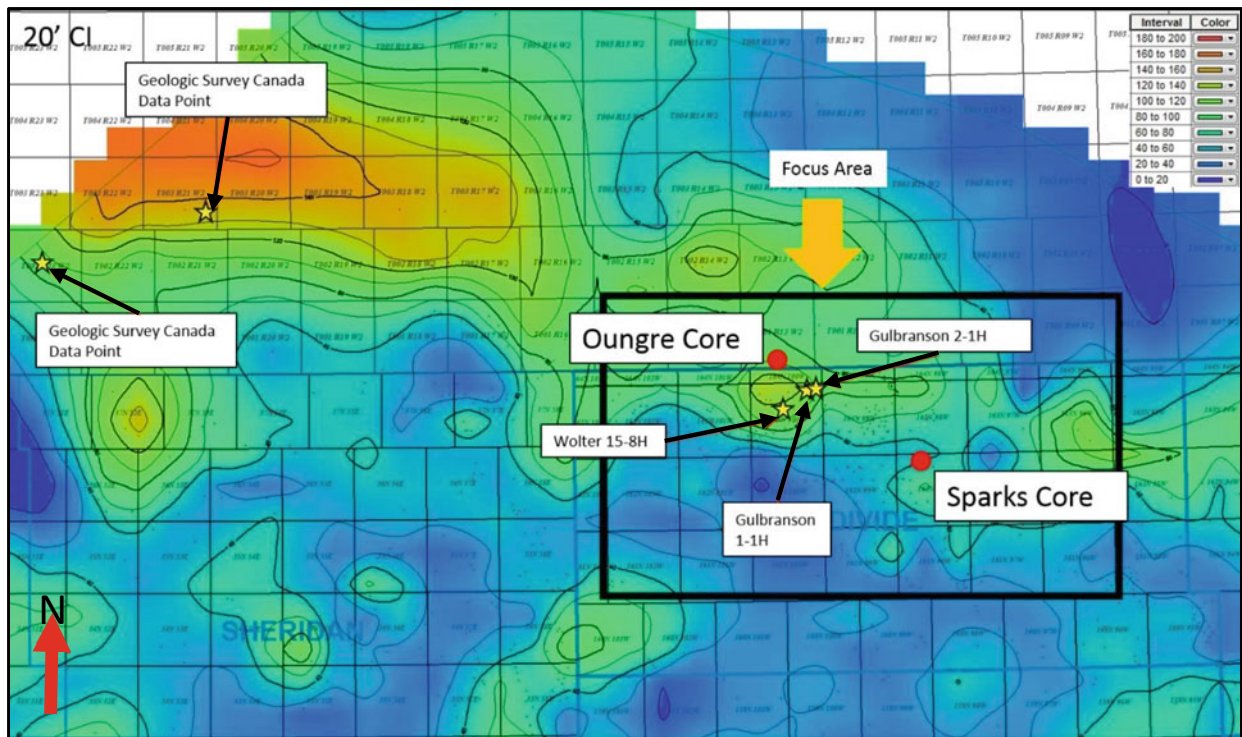


**Fig. 2** Isopach map of the Upper Lodgepole in the Williston Basin with locations of key wells discussed in the present study

oil extract information to gain a baseline of the type of oils that will be produced and the equivalent maturity of said oils, (3) analyze palynological sedimentary organic matter from the cores and cuttings in the area to provide support to the maturation and type of organics and the type of hydrocarbon they will produce.

Understanding the thermal maturity of the Upper Lodgepole is paramount to the ability of exploiting this interval as a successful unconventional play. While a large regional study is yet to be done, several snippets offer clues to the thermal maturity. Osadetz and Snowdon (1995) did a comprehensive study of petroleum source rocks of the Canadian Williston Basin. According to their analysis most of the Lodgepole carries little source rock potential except for the Upper and Roncott (middle marker bed) members of the Lodgepole. Their analysis looked at three wells in the Upper Lodgepole of Saskatchewan, northwest, and up-dip of the locality focused on by this study. Rock-Eval pyrolysis of the three wells yielded  $T_{\max}$  values ranging from 415 to 444 °C and total organic carbon (TOC) values as great as 14.46 wt%. This would place the Upper Lodgepole as marginally mature to low oil window with an outstanding TOC content (Peters, 1986). Their work also cites a greater hydrocarbon potential than the underlying Bakken shales; “Rich source rocks in Bakken shales yield no more than 42 mg/g TOC in the deepest well drilled in the Canadian Williston Basin and have hydrocarbon yield not exceeding 25.4 mg/g TOC. In the same well, all Lodgepole yields exceed 45 mg/g TOC, yet both formations have comparable hydrogen index.” However, none of the solvent extract samples from their study suggests that the formation has entered hydrocarbon generation. This introduces the conundrum this paper tries to resolve, that the Upper Lodgepole shows to be mature in pyrolysis in contradiction to other datasets. Osadetz and Snowdon (1995) conclude that the limited samples and analysis cannot define the depth of the onset of the oil window, but that based on the Bakken and Winnipegosis analysis that it must lie near a true vertical depth (TVD) of 7546 ft (2300 m). The analysis outlined in this paper lies in an area of 7000–8000 ft TVD (2133–2438 m).

## 2 Geologic Setting

The Williston Basin is an intracratonic basin centered in northwestern North Dakota with portions reaching into southern Saskatchewan, southwestern Manitoba, and eastern Montana (Fig. 1). The basin reaches a maximum depth of approximately 4877 m (16,000 ft) in McKenzie County, North Dakota, with structural trends associated with a wrench fault system (Sonnenberg et al., 2011). Intermittent subsidence started during the Ordovician and through the

Phanerozoic due to the interaction of two Archean shear zones, the Brockton–Froid–Frombert Fault Zone and the Transcontinental Arch (Gaswirth et al., 2010). The Lodgepole Formation is Mississippian in age and is the lowest member of the Madison Group (Fig. 3). In order of deposition, the Lodgepole is overlain in the Madison by the Mission Canyon and Charles formations. The Lodgepole Formation overlies the Upper Bakken Shale, a prolific source rock in the Williston Basin. The Lodgepole sediments were sourced from the Elk Point Basin in southern Saskatchewan, Canada, and transitioned to the Central Montana Trough by the Mission Canyon (Gaswirth et al., 2010). Sediments were deposited during cycles of rapid transgression and slow regression. At least three cycles of rapid transgression and episodic progradation of low angle clinoforms occurred during the Lodgepole deposition (Kent, 1984). Each cycle contains a dark gray mudstone that coarsens upward to grainstone and wackestone deposits with progressively coarser deposits moving away from the basin center.

The Lodgepole contains three organic-rich marker beds in the northern Williston Basin, each of which unconformably lies atop shelf carbonates. The uppermost interval, the Upper Lodgepole, is a thinly laminated organic-rich mudstone. Deposition follows the hummingbird trough trend, a multi-stage salt dissolution feature driven by the dissolution of the underlying Prairie salts. This dissolution is driven by fractures associated with Precambrian basement faulting, allowing the permeation of meteoric waters. Underlying dissolution drove increased sedimentation on an already silled shelf leading to an increase in water column stratification (MacKnight & Bend, 2015). The silled shelf sheltered the sub-basin from waves creating an anoxic to dysoxic environment and allowed for the deposition of the sub-basin reaching a maximum thickness of 52 m in southeastern

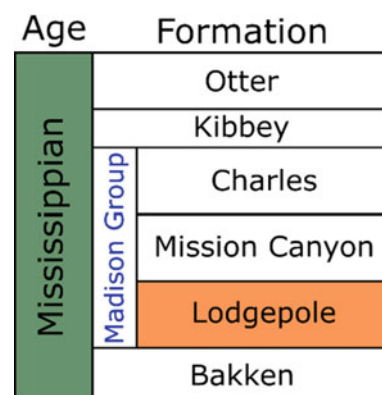


**Fig. 3** Mississippian system in the Williston Basin. The Lodgepole represents the base of the Madison Group and is of early Mississippian age. Except for the Otter, all units are oil producing zones. The base of the Bakken occurs within the uppermost Devonian System, not shown

Saskatchewan. Later dissolution of salts surrounding the area allowed for a thickening on a structural high.

### 3 Materials and Methods

Samples for palynological analysis from the Oungre core were taken from the same core plugs that were taken to perform programmed pyrolysis, allowing for accurate data correlation. Cuttings were collected from the Upper Lodgepole as dictated on mud logs. Sample thicknesses varied based on the amount and availability of samples. Palynological organic matter extraction was conducted following the standard technique outlined in Traverse (2007). A total of 10 microscopic slides were examined in transmitted light. Seven of the slides represent different intervals in the Oungre core as well as one slide from each of the Gulbranson 1-1H, Gulbranson 2-1H, and Wolter 15-8H wells (Table 1). Three hundred sedimentary organic matter (SOM) particles were point counted from each slide. These particles were separated into categories to determine the kerogen type as well as the overall level of organic matter degradation (Table 2). Rock-Eval pyrolysis was initially performed on two samples from the Sparks core and seven samples from the Oungre core. Initial pyrolysis of samples through commercial lab 1 were cleaned first with an azeotropic mixture of chloroform-methanol (89:11 v/v) for 24 h.

Samples were then Soxhlet extracted for 48 h with an azeotropic mixture of DCM-methanol (87:13 v/v). After that, samples were run through a Rock-Eval 6. Samples from the Oungre core were then rerun through commercial lab 2 utilizing a Hawk pyrolysis and two different preparation methods. Method A involved cleaning the samples in DCM after they were crushed with a ball mill. The samples were agitated three times at a 10-min interval between each agitation. After all agitations, samples were air dried and then

**Table 1** Each of the studied 10 samples, their respective well name and depth

Sample number, well name	Depth (ft)	Depth (m)
LP1, Oungre	7350.3	2240.37
LP2, Oungre	7360.17	2243.38
LP3, Oungre	7363.55	2244.41
LP4, Oungre	7373.39	2247.41
LP5, Oungre	7380.91	2249.7
LP6, Oungre	7387.53	2251.72
LP7, Oungre	7392.78	2253.32
LP8, Gulbranson 1-1H	7370–7460	2246.38–2273.81
LP9, Gulbranson 2-1H	7340–7430	2237.23–2264.66
LP10, Wolter 15-8H	7580–7610	2310.38–2289.05

run through Hawk pyrolysis. If *S1* carryover was seen to the *S2* peak, the process was repeated. Method A was run on only two samples from the Oungre core. Method B involved the samples being homogenized through the same ball mill process but then loaded immediately to the Hawk pyrolysis without cleaning.

In addition to the above analyses, samples were also subject to core extract analysis at a consulting commercial laboratory.

## 4 Results

### 4.1 Contracted Data

Programed pyrolysis was conducted to assess the amount of organic matter present, and their quality and potential, as well as thermal maturity. Due to both the Oungre and Sparks cores being drilled with oil-based mud, samples were cleaned prior to running pyrolysis on the first set of samples from commercial lab 1. Commercial lab 2, Method A used a lighter solvent for a shorter time frame and commercial lab 2, Method B did not use a solvent to prepare. Pyrolysis values were significantly impacted by the change in sample preparation methods. It is evident that *S2* values increased with the less aggressive cleaning on five out of seven samples (Fig. 4). Additionally, VRo-eq decreased on all but one sample bringing the range of values from 0.76 to 0.87 (average 0.81) from commercial lab 1 to 0.73–0.83 (average 0.78) from commercial lab 2, Method B (Fig. 5). TOC showed an increase on all but one sample (Fig. 6).

Due to concerns around thermal maturity and subsequent mobility of the hydrocarbons two samples underwent hydrocarbon extraction to resolve some of these questions. One sample was taken from the Oungre and one from the Sparks core. Close to half of the overall extract from both wells was asphaltenes while a low constituent was saturates (Fig. 7). Thermal maturity was estimated to be at 0.7% VRo-eq on the Oungre and 0.75% VRo-eq on the Sparks samples. A marine green algae source was postulated from the contracted lab due to elevated levels of C27 and C29.

### 4.2 Palynofacies Analysis

Ten samples were evaluated for their sedimentary organic matter content. Seven samples were from the Oungre core. Cuttings were also collected from three offsetting wells to use as a control group to confirm findings from the Oungre core. Palynofacies analysis yielded predominantly degraded terrestrial phytoclasts with lesser percentages of opaque phytoclasts (Table 2; Plate 1). An initial concern in using

**Table 2** Palynofacies point counting results

Well	Depth		Weight (g)	Phytoclasts								Pollen spore	Total particles counted		
				Opaque phytoclasts				Translucent phytoclasts						Total phytoclasts	
	Equant			Lath-shaped		Cuticle		Others							
	Meters	Feet		Deg	U-Deg	□eg	U-Deg	Deg	U-Deg	Deg	U-Deg				
Gulbranson 1-1H	2310.38–2319.53	7580–7610	8	9							291		300		300
Wolter	2246.38–2255.52	7370–7400	4	25					1				274		300
Gulbranson 2-1H	2237.23–2264.66	7340–7430	4	22								2	275	1	299
Oungre	2240.37	7350.30	22	12			3						284	1	300
Oungre	2243.38	7360.17	19	4	1		1						292	2	300
Oungre	2244.41	7363.55	20	5									294	1	300
Oungre	2247.22	7372.77	14	8									292		300
Oungre	2243.70	7380.91	20	1	3								296		300
Oungre	2251.72	7387.53	11	5	1								294		300
Oungre	2253.32	7392.78	11	6									293	1	300

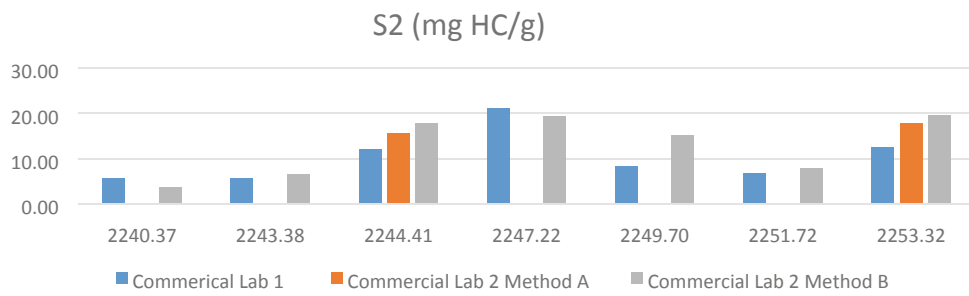
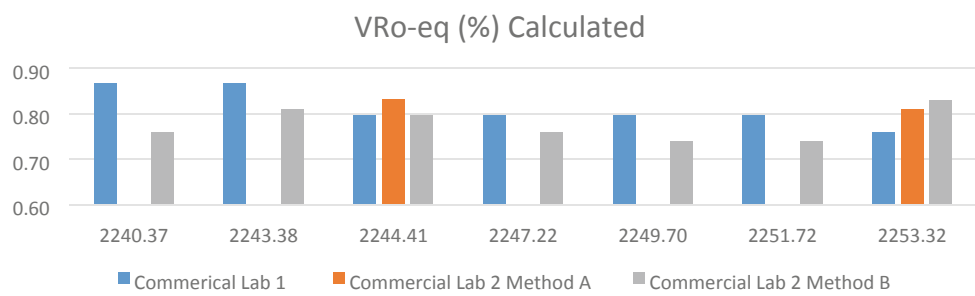


**Fig. 4** Comparison of S2 values of the Oungre core samples obtained from the two commercial labs using variable cleaning methods. The most aggressive cleaning method was used in commercial lab 1, a less aggressive cleaning was used in commercial lab 2, Method A, and no cleaning was applied in commercial lab 2, Method B

**Fig. 5** Comparison of VRo-eq values of the Oungre core samples obtained from the two commercial labs using variable preparation methods



cuttings was the potential for caving and/or uphole mixing. However, confidence is high that cutting samples were representative of the interval since the range of point counts was within the range of what was witnessed on the core samples.

Crushing samples produced a very pronounced oil smell with every sample. Overwhelmingly identified in the point count exercise was heavily degraded “amorphous” phytoclasts. Opaques account for the heavily oxidized component of phytoclasts. The percentage of opaque phytoclasts (black

**Fig. 6** Comparison of TOC values of the Oungre core samples obtained from the two commercial labs using variable preparation methods

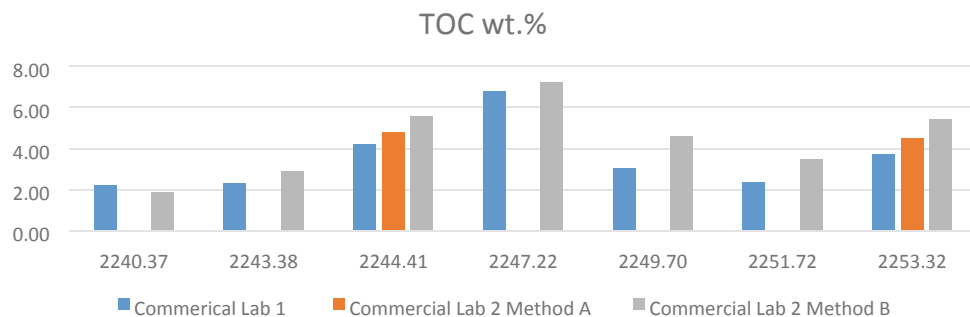
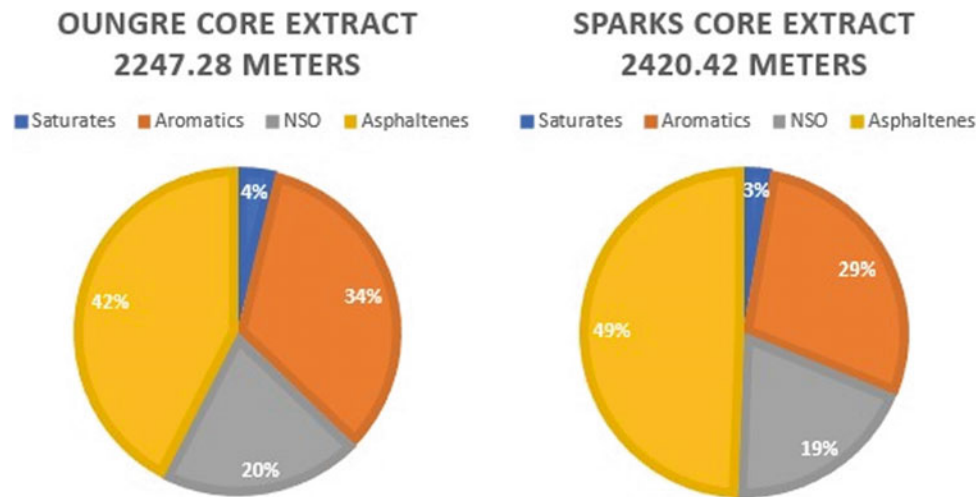


**Fig. 7** Core extract analysis of Sparks core sample and Oungre core sample shows high percentage of asphaltenes over other components



debris) ranged from 1 to 9%. Chitinozoans were seen in several samples both from core and cuttings. Since chitinozoans are not known to exist beyond the Devonian Period (Traverse, 2007), their presence here, in Mississippian strata, is especially interesting. However, this requires further careful investigation, which will be carried out independently later.

## 5 Discussion

Although maturation of the Lodgepole appears to be questionable, several studies tie overlying production in the Mission Canyon to be sourced from the Lodgepole. Burrus et al. (1996) suggested through modeling efforts and oil typing that thermally mature oils near the North American Central Plains Conductivity Anomaly were migrated up-dip to the Madison subcrop in eastern Saskatchewan and western Manitoba where the Lodgepole has been produced along a stratigraphic trap (Fig. 8). The down-dip origin of these oils, being sourced from our area of focus, suggests a mature Lodgepole source at our locality (Burrus et al., 1996). Chen et al. (2009) suggested in their oil fingerprinting analysis that lower maturity, Lodgepole sourced oils, were present in the

stratigraphically younger Mission Canyon (Midale in Saskatchewan) intervals in the Midale Central and Weyburn fields directly north of this study area. Lodgepole oils were identified by “low oil maturity, high sulfur content, and low API gravity” (Chen et al., 2009, p. 850).

Based on these studies, it is logical to think of the Lodgepole in our study area as being within the oil generation window. Somewhat surprisingly, operators have had poor luck producing economical amounts of oil, if at all. The Oungre 2-3-13 only produced 307.7 bbls of commingled production with a set of vertical perforations in the Upper Lodgepole. The Wehrman 1-19 perforated the Upper Lodgepole with a cumulative oil production of 688 bbls (North Dakota DMR, 2016). The Holm State 16-162-98H targeted the Upper Lodgepole on the fringe of the play area, down-dip, and to the southeast of the play area. Around 250 units of gas were encountered through the lateral. Once the stage was completed, a subsequent split in the production casing left the well shut in. A permit was placed to recomplate the Holm State, but it was never recompleted. Eventually, the well was shut in (North Dakota DMR, 2016).

All of the aforementioned present us with two different scenarios: The Upper Lodgepole is a mature source rock viable of producing significant oil, or the Upper Lodgepole

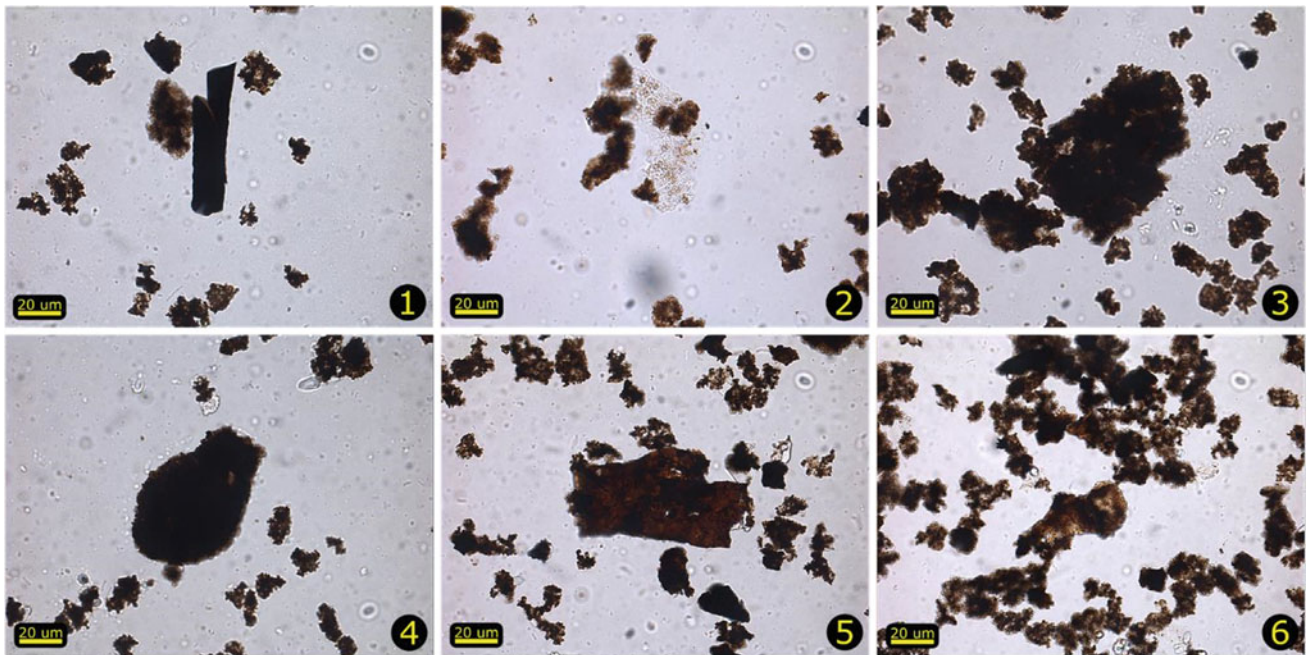


**Plate 1** Sedimentary organic matter from the Upper Lodgepole in the Oungre Core. **1** Lath-shaped opaque phytoclast, depth: 2244.41 m (7360.17 ft). **2** The one example of amorphous marine organic matter, possibly algal, that was recorded, depth: 2249.7 m (7380.91 ft). **3**

Degraded phytoclast, depth: 2249.7 m (7380.91 ft). **4** Chitinozoan? Depth: 2240.37 m (7350.3 ft). **5** Chitinozoan, depth 2249.7 m (7380.91 ft). **6** Degraded terrestrial phytoclast facies, depth 2249.7 m (7380.91 ft).

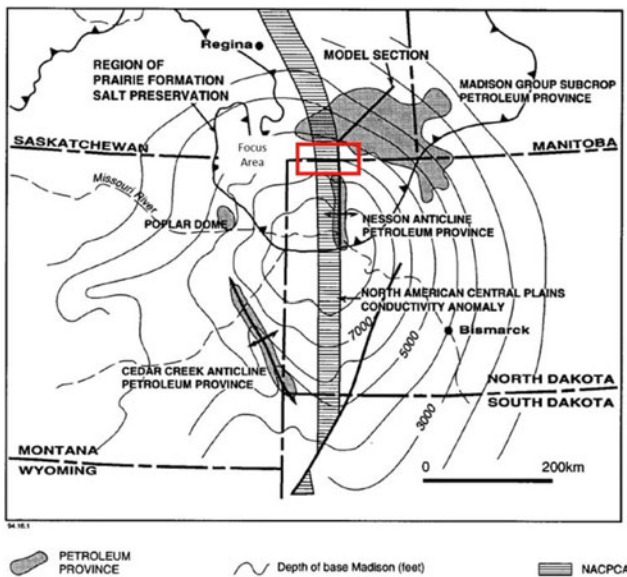


**Fig. 8** Locality of North American Central Plains Conductivity Anomaly (NACPCA) along the Nesson Anticline. The focus area of this study is outlined by a red box and in line with the NACPCA (After Burrus et al., 1996).

is a marginally mature to immature source rock unlikely to be a significant source rock in the study area. A detailed account will be given on both scenarios including their shortcomings, how they fit with data from the more

researched underlying Bakken Formation, and a plausible explanatory hypothesis.

## 5.1 Pyrolysis Analysis (Prior Work)

$T_{max}$  values near the CPEC Minton well, or the thicker portion of the Upper Lodgepole, were on the order of  $\sim 438$  °C with TOC values reaching up to 14.46 wt% (Osadetz and Snowdon, 1995). This is above the bottom of oil window indicator of 435 °C (Peters, 1986). Osadetz and Snowdon (1995) further indicated that the Lodgepole was a type-II source rock that had a very high hydrocarbon yield on the order of 45.62–118.6 mg/g TOC. This is significant compared to the underlying Bakken Formation, which did not exceed 25.4 mg/g TOC in their analysis. Their research concluded that while the Lodgepole is a significant source rock, maturity was at best immature to marginally mature.

## 5.2 Pyrolysis Analysis (This Study)

TOC values from the Oungre core ranged from 2 to 7 wt% with  $T_{max}$  values ranging from 440 to 446 °C. The Sparks core contained TOC values ranging from 1.4 to 9.06 wt% with  $T_{max}$  values of 444–446 °C. Hydrogen index values from both samples ranged from 252.61 to 338 mg HC/g. For

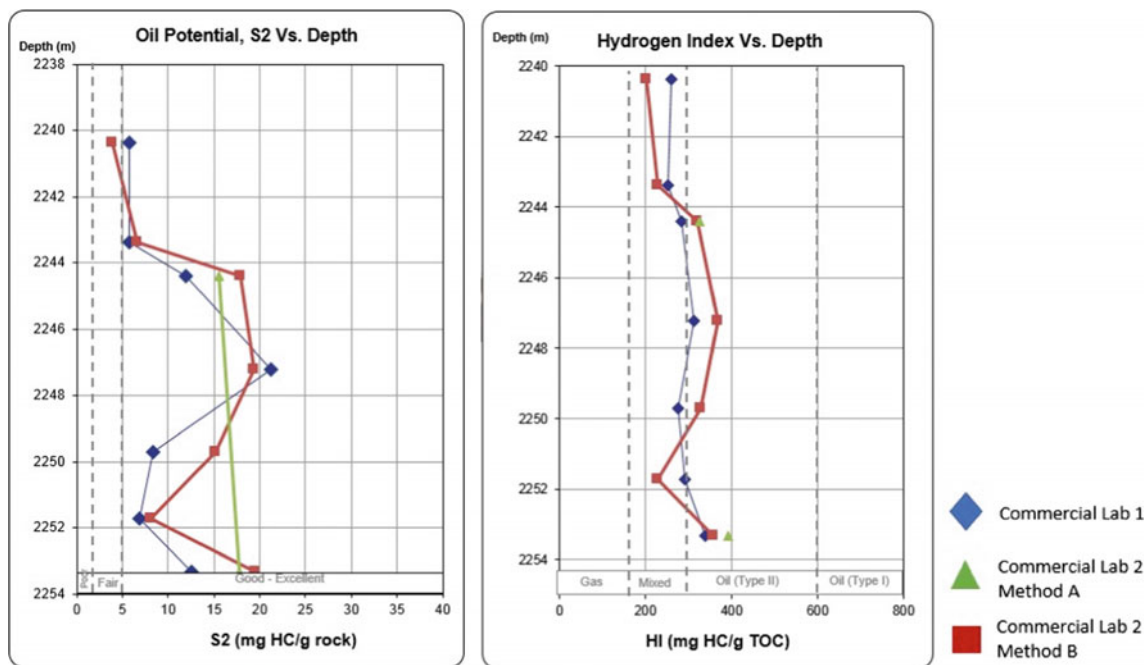


**Fig. 9** Observed  $S_2$  and HI values for the Oungre samples.  $S_2$  values increased as lighter cleaning methods were utilized. This translates to a greater HI and places samples further away from a mixed source toward an oil-prone source rock

comparison, the CPEC Minton is roughly 450 m (true vertical depth) up-dip to the Oungre and Sparks and yielding a  $T_{\max}$  gradient of 0.005 °C/ft. The analysis from the Sparks and Oungre cores initially shows a significantly mature source rock. Using the determined hydrogen index values, the type of hydrocarbon produced in the source rock can be estimated as a mixed type-II/III. Hydrogen index values ranging from 0 to 150 yield gas, 150–300 return gas and oil, and above 300 produces oil.  $T_{\max}$  values for the oil producing window are estimated to be between 435 and 470 °C (Peters, 1986). Using these outlines, the Upper Lodgepole would indeed be a mature source rock that would produce oil at the Oungre and Sparks locations.

Pyrolysis analysis was rerun on samples from the Oungre core using lighter cleaning methods (commercial lab 2, methods A and B) resulting in a shift in several of the measured parameters. An expected increase in  $S_1$  and TOC was noted. More interesting though, was an increase in the  $S_2$  peak. This in turn influences the HI calculation moving it further into the type-II oil-prone range (Fig. 9).

Comparing HI to  $T_{\max}$  (Fig. 10a), the rerun samples dominantly shifted upward toward the type-II boundary and away from a type-III source rock. Parameters for the different source types are the Green River Shale (type-I), Liassic Shale (type-II), and Cambay Basin Coal (type-III). Finally, comparing the kerogen quality by plotting the  $S_2$  versus TOC, it was found that with an increase in TOC, samples begin to generally cross into type-II, oil-prone kerogen (Fig. 10b).

### 5.3 Comparison with the Bakken Formation

The results of the analysis within the study area further illuminate the previously mentioned conundrum: the underlying Bakken shales have a  $T_{\max}$  of ~435 °C, which is 10 °C lower than the Upper Lodgepole source rocks from the original analysis (Fig. 11; Jin & Sonnenberg, 2012). While comparing source rocks from different formations is generally problematic, it is counterintuitive that shallow source rocks would have a higher thermal maturity than deeper source rocks. This phenomenon is also observed in the data collected by the Geological Survey of Canada from four different wells each of which shows an approximate decrease in  $T_{\max}$  of 10 °C between the Upper Lodgepole and Bakken shales (Osadetz & Snowdon, 1995).

### 5.4 Core Extract Analysis

Core extract analysis tells a story more in line with what would be expected of a carbonate source rock and demonstrates thermal maturity in line with the underlying Bakken shales. Analysis and interpretation were done through a consulting commercial laboratory which showed elevated C27 and C29 values indicative of a non-degraded green algae source. The vitrinite reflectance equivalence was 0.7% in the Oungre core and 0.75% in the Sparks core.



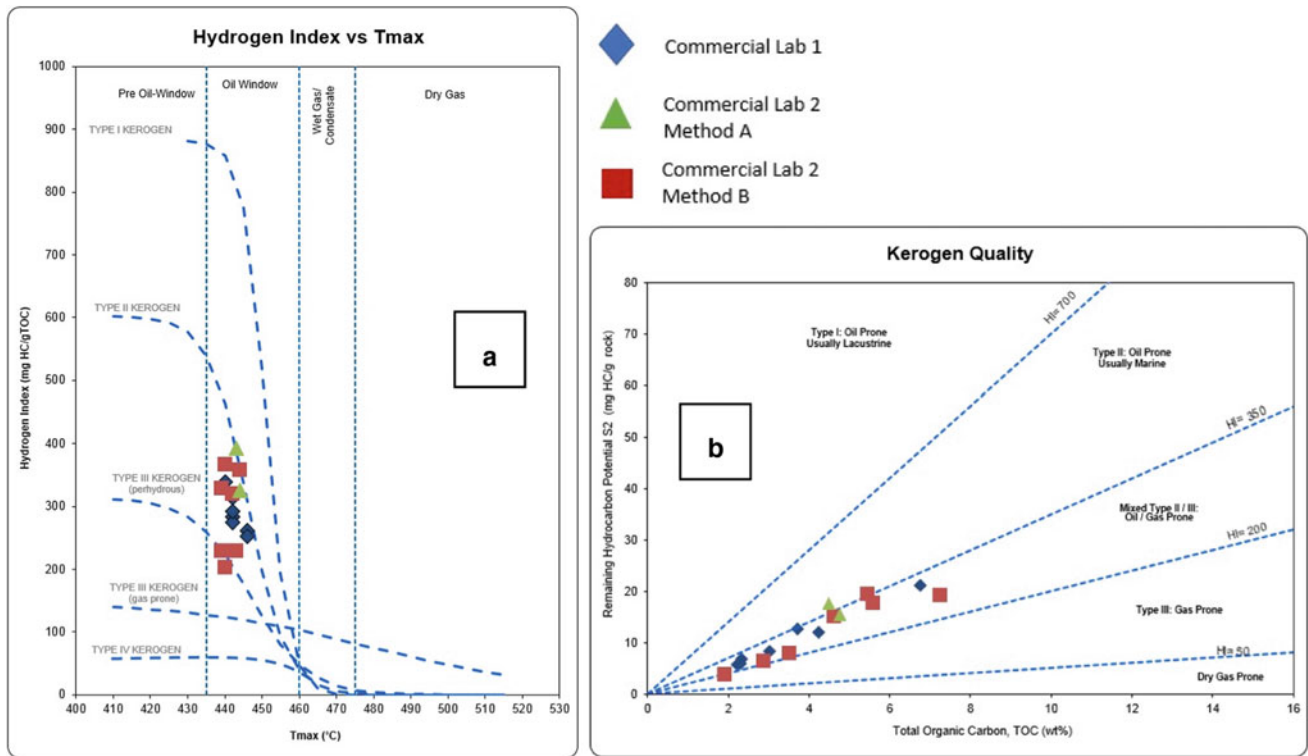


**Fig. 10** a HI versus  $T_{max}$  values of the Oungre core. Parameters for organic types were derived from Green River Shale (type-I), Liassic Shale (type-II), and Cambay Basin Coal (type-III). **b** Kerogen Quality ( $S_2$  vs. TOC) for the Oungre samples. An increase in TOC results in samples crowding closer to type-II kerogen

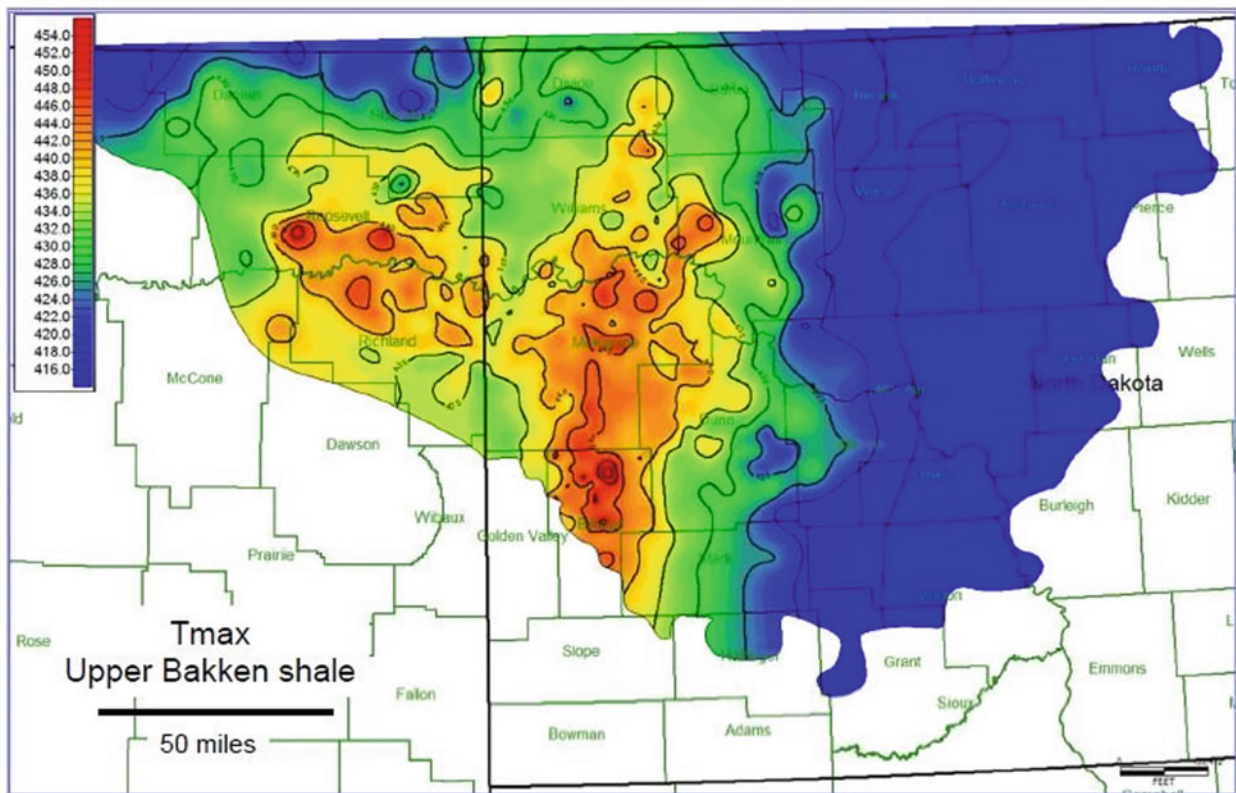


**Fig. 11**  $T_{max}$  values from the Upper Bakken Shale (After Jin & Sonnenberg, 2012)

## 5.5 Palynofacies Analysis

Osadetz and Snowdon (1995, p. 30) hint at the only previous comments on palynomorph identification through a few short sentences citing a personal communication with peers J. Utting in 1986 and L. D. Stasiuk in 1989. Organic matter in this communication was described as “an orange-brown fluorescing, mesh like matrix bituminated network and lesser marine algalite” with “amorphous kerogen dominating the organic material on slides prepared for palynomorph identifications.” As stated by Zobaa et al. (2015), simply describing organic material as amorphous organic material (AOM) yields little significance to origin, depositional environment, or kerogen typing. Instead, amorphous organic material needs to be separated between terrestrial and marine.

Palynofacies analysis initially was envisioned to be a “tie breaker” to discern if the source rock was indeed thermally mature or if it is in fact immature. What was not expected was that nearly all organic material was found to be terrestrial phytoclasts. Since this is a carbonate source rock, it is puzzling as to how phytoclasts could be present in such overwhelmingly high abundance. Nevertheless, they are and the abundance of them would indicate a strong terrestrial influence leading to type-III source rock. Although heavily degraded they are also equant in shape, indicative of long distance of transportation. Opaques accounted for 1–9% of the overall pytyoclasts counted and further support heavy oxidation and degradation. Silt lenses are common in the core likely from storm deposits. Periodic storms could have further allowed oxygenation of dysoxic waters allowing for further breakdown of the phytoclast material.

## 5.6 Data Integration

One explanation for the disparity between data points could be derived from  $T_{\max}$  suppression due to varying HI values

at lower  $T_{\max}$  values. As an example, Snowdon (1995) documented the influence of HI on  $T_{\max}$  suppression in the second white speckled shale of the Upper Cretaceous in the Alberta Basin. His work showed that reworked organic material yielded a lower HI which correlated to an increased  $T_{\max}$ . Organic reworking causes a slower release of hydrocarbons during pyrolysis which creates a higher  $S_2$  peak, producing a false increase in derived  $T_{\max}$  values. At  $T_{\max}$  values greater than 450 °C, the correlation between HI and  $T_{\max}$  is insignificant, and as maturity increases, the HI decreases and the suppression effect disappears (Snowdon, 1995). This phenomenon was observed within the Upper Lodgepole in the Oungre well (Fig. 12), in which  $T_{\max}$  values decreased with depth, again counterintuitive. Plotting  $T_{\max}$  values versus HI (Fig. 12) also illustrates the expected phenomenon, increasing HI values as  $T_{\max}$  values decrease. HI values from the Bakken are typically on the order of 550–600 °C in the area.

Visual analysis of the phytoclasts revealed that the organic material is heavily degraded and no doubt plays a role in the calculated HI values. However, the large difference in HI values in the Bakken shales and the Upper Lodgepole could be more accurately differentiated by the type of organics found. Gas-prone source rocks will have an HI value of 0–150, mixed gas and oil source rocks have an HI of 150–300, and oil rocks will have an HI above 300 (Peters, 1986). Due to the presence of phytoclasts, a type-III, predominantly gas-prone source, an anticipated HI value would be considerably lower. This leads to an accord between both the pyrolysis information and the visual confirmation of phytoclasts.

Although the phytoclasts and pyrolysis data seem to agree, there are still two questions that need to be resolved. First, this is a carbonate source rock and there must have been some marine organic material deposited initially; if so, where is it now? Second, core extract analysis indicates a non-degraded marine green algae source material, which was not observed during visual palynological analysis.

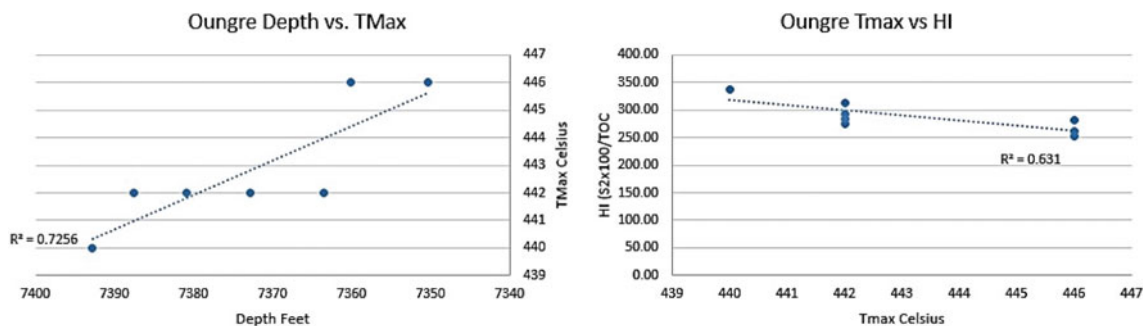


**Fig. 12** Left: Plot of  $T_{\max}$  versus true vertical depth from Oungre core pyrolysis data (commercial lab 1). This shows an inverse correlation between temperature and depth which is contrary to what is expected. Right: Plot of  $T_{\max}$  versus HI from the Oungre core pyrolysis data

(commercial lab 1). This shows an inverse correlation between  $T_{\max}$  and HI similar to what Snowdon (1995) found in his analysis and subsequent interpretation of HI suppression

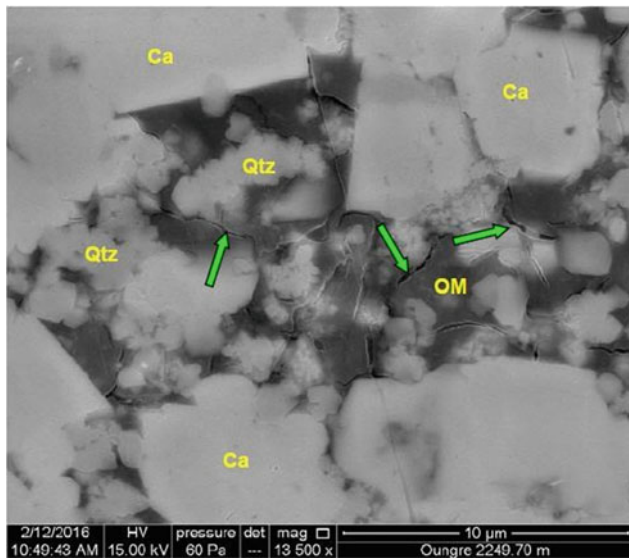


**Fig. 13** SEM image of fractures within the Upper Lodgepole organics, indicative of being within the gas/oil window

A plausible answer is found in the preferential conversion to bitumen. At early maturation stages, type-I/II kerogen will preferentially convert to bitumen and oil leaving type-III/IV sources behind (Hackley & Cardott, 2016). This would resolve the paucity of marine organic particles present through standard palynofacies analysis. As for the pyrolysis analysis, a theory stands that since samples were cleaned prior to analysis that the mobile hydrocarbons were stripped. However, it is likely that a portion of the bitumen was also extracted during cleaning, artificially lowering the type-II source constituents, and biasing the analysis toward the remaining phytoclasts. All organics equal a type-III source through pyrolysis should show a higher thermal maturity due to its lower hydrogen content. Furthermore, since the phytoclasts showed heavy degradation, the amount of hydrogen available is even lower.

SEM imaging (Fig. 13) shows the bitumen present within the pore space. Fractures within the bitumen are also indicative of the samples being within the gas/oil window (Hackley & Cardott, 2016). This is consistent with results of rerunning samples through commercial lab 2 which utilizes lighter cleaning solvent. These results came back showing a higher  $S_2$  peak, proof that the more invasive cleaning from commercial lab 1 did indeed strip some of the organics. Furthermore, an increase in the HI pushed samples toward more a type-II/III source rock. VRo-eq also dropped to around 0.73–0.83% bringing the thermal maturity of the Oungre samples lower and closer to the range of the core extract and the underlying Bakken Shale.

## 6 Conclusions

The studied Upper Lodgepole samples contain type-II/III source materials. This is drawn from the combined identification of degraded phytoclasts from palynofacies analysis as well as the pyrolysis and core extract data. Thermal maturity in the analysis through commercial lab 1 was high due to their invasive cleaning method that stripped type-II daughter materials from the analysis. Values from commercial lab 2 with less invasive preparation methods place the thermal maturity in line with maturity values from both the underlying Bakken shales as well as the core extract values. No signs of marine organisms were observed through microscopic work, which is likely because type-II organic materials were preferentially converted to hydrocarbons leaving only the degraded phytoclasts behind. A greater concentration of low-hydrogen terrestrial material in extracted Lodgepole samples drove the apparent VRo-eq maturity higher relative to less- or unextracted samples. Extracted pyrolysis also made the Lodgepole appear more mature than that of the underlying Bakken Shale when maturity for both is calculated using the same VRo-eq equation. The discrepancy is explainable as a difference in the organic matter type, its starting hydrogen content, and its kinetic pathway during catagenesis.

The Upper Lodgepole is an economically viable source rock for both oil and gas in the study area based on its organic matter, type, richness, and maturity.

**Acknowledgements** Deep gratitude is expressed to the following colleagues for their guidance and support: Dr. Cory Hoffman, Mr. Bob Bachman, Mr. John McLeod, Ms. Chantel Lines, and Mr. Riley Brinkerhoff.

## References

- Burrus, J., Wolf, S., Osadetz, K., & Visser, K. (1996). Physical and numerical modelling constraints on oil expulsion and accumulation in the Bakken and Lodgepole petroleum systems of the Williston Basin (Canada-USA). *Bulletin of Canadian Petroleum Geology*, 44 (3), 429–445.
- Chen, Z., Osadetz, K. G., Jiang, C., & Li, M. (2009). Spatial variation of Bakken or Lodgepole oils in the Canadian Williston Basin. *AAPG Bulletin*, 93(6), 829–851.
- Gaswirth, S. B., Lillis, P. G., Pollastro, R. M., & Anna, L. O. (2010). Geology and undiscovered oil and gas resources in the Madison Group, Williston Basin, North Dakota and Montana. *The Mountain Geologist*, 47(3), 71–90.
- Hackley, P. C., & Cardott, B. J. (2016). Application of organic petrography in North American shale petroleum systems: A review. *International Journal of Coal Geology*, 163, 8–51.

- Jin, H., & Sonnenberg, S. A. (2012). Source rock potential of the Bakken shales in the Williston Basin, North Dakota and Montana. AAPG Search and Discovery Article No. 20156: 5 pp
- Kent, D. (1984). Depositional setting of Mississippian strata in southeastern Saskatchewan: A conceptual model for hydrocarbon accumulation. *Saskatchewan Geological Society Special Publication*, 7, 19–30.
- MacKnight, S. G., & Bend, S. L. (2015). Internal stratigraphy review and petroleum potential of the Lower Mississippian Lodgepole Formation Souris Valley Beds, southern Saskatchewan. In *23rd Williston Basin Petroleum Conference Core Workshop, 2015* (pp. 51–66)
- North Dakota DMR. (2016). *North Dakota Department of Mineral Resources Well Data Website*. <https://www.dmr.nd.gov/oilgas/findwellsvw.asp>. Accessed May 2016.
- Osadetz, K. G., & Snowdon, L. R. (1995). Significant Paleozoic petroleum source rocks in the Canadian Williston Basin: Their distribution, richness and thermal maturity (southeastern Saskatchewan and southwestern Manitoba). *Geological Survey of Canada Bulletin*, 487, 1–60.
- Peters, K. (1986). Guidelines for evaluating petroleum source rock using programmed pyrolysis. *AAPG Bulletin*, 70(3), 318–329.
- Snowdon, L. R. (1995). Rock-Eval  $T_{max}$  suppression: Documentation and amelioration. *AAPG Bulletin*, 79(9), 1337–1348.
- Sonnenberg, S. A., LeFever, J. A., & Hill, R. J. (2011). Fracturing in the Bakken petroleum system, Williston Basin. In J. W. Robinson, J. A. LeFever, S. B. Gaswirth (Eds.), *The Bakken-three forks petroleum system in the Williston Basin* (pp. 393–417). Rocky Mountain Association of Geologists, Denver, Colorado.
- Traverse, A. (2007). *Paleopalynology: Topics in Geobiology 28* (2nd ed.). Springer.
- Zobaa, M. K., El Beialy, S. Y., Taha, A. A., & Oboh-Ikuenobe, F. E. (2015). Improved graphical representation of sedimentary organic matter as paleoenvironmental parameters. *Geological Society of America Abstracts with Programs*, 47(7), 365.



# Integration of Palynological and Foraminiferal Analyses Toward Evaluation of the Paleoenvironment and Hydrocarbon Potential in the Orange Basin, SW Africa

Marissa K. Spencer, Damián Cárdenas, Francisca E. Oboh-Ikuenobe, and Tapas Chatterjee

## Abstract

Changes in the paleogeography during the Gondwana breakup and the proto-South Atlantic development have been of enduring significance to scientists. The realignment of these landmasses during the Mesozoic, which includes the Orange Basin formation in southern Africa, had a substantial effect on the environment. These paleoenvironmental differences likely affected fossil preservation and hydrocarbon maturation. Palynology is an invaluable tool for inferring paleoenvironmental conditions and hydrocarbon potential, and therefore, is used in this study to evaluate this key offshore South African area. A total of forty-three samples from six conventional cores from four exploration wells (K-A2, K-A3, K-H1, and K-E1) within three blocks were analyzed for their palynomorph, particulate organic matter (kerogen), and foraminiferal contents. Integration of the palynomorph, palynofacies, and foraminiferal data has provided information that suggest the sediments are early Cenomanian in age and deposited in a shallow marine (inner-middle shelf) setting. Moreover, they are characterized primarily by gas-prone Type-III with some oil-prone Type-II kerogen in this frontier basin. The integrated approach revealed significant information that can be used to calibrate basin models and improve the understanding of the petroleum potential of the basin.

## Keywords

Orange basin • Frontier basin • Biostratigraphy • Palynology • Hydrocarbon potential • Paleoenvironment

## 1 Introduction

The Orange Basin, located in the western passive margin of southern Africa, is considered one of the major sedimentary basins in the South Atlantic. It is geographically located near the international border of South Africa and Namibia. The basin covers an area of around 160,000 mi<sup>2</sup> (Kuhlmann et al., 2010) between the Walvis and Agulhas Ridges along the coast offshore of the western portion of Southern Africa (Fig. 1). Sedimentation in the Orange Basin is Late Jurassic to Quaternary age and consists of lacustrine sediments overlying basic and alkaline volcanic rocks added from rift flood basalts, and fluvio-deltaic sandstones and conglomerates contributed by the Orange River (Adekola et al., 2012; Brownfield, 2016; Jungslager, 1999; Muntingh, 1993; Van der Spuy, 2003). During the Early Cretaceous (Barremian–Aptian), fluvial deposits and marine interbedded sandstones and shales have been deposited in response to transgressive–regressive cycles. In addition, a major flooding event is recorded in the early Aptian which resulted in the progradation of additional siliciclastic material (Van der Spuy, 2003) and sedimentation reaching a thickness of more than 7 km in the north and approximately 3 km in the southern parts of the basin (Fig. 2; Brown et al., 1996; Muntingh, 1993).

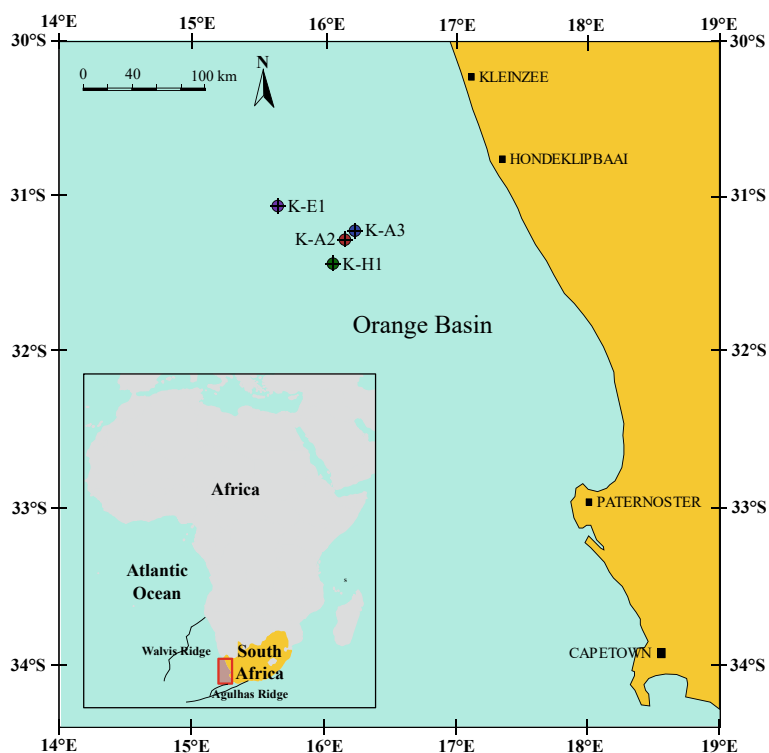
The Orange Basin has not been well explored in spite of its proven hydrocarbon reserves, and little is known of its potential. Studies by Jungslager (1999), Kuhlmann et al. (2010), Paton et al. (2007), Van der Spuy (2003), and have considered various aspects of the basin's hydrocarbon systems. Biostratigraphic information for the basin is mostly limited to palynology (Adekola et al., 2014; Benson, 1990; Bamford & Corbett, 1994, 1995; Davey, 1978; Davey &

M. K. Spencer (✉) · D. Cárdenas · F. E. Oboh-Ikuenobe  
Geosciences and Geological and Petroleum Engineering, Missouri  
University of Science and Technology, Rolla, MO, USA  
e-mail: [mksb7d@mst.edu](mailto:mksb7d@mst.edu)

D. Cárdenas  
Smithsonian Tropical Research Institute, Panamá, Panamá

T. Chatterjee  
Department of Earth Sciences, University of the Western Cape,  
Cape Town, South Africa

**Fig. 1** Map of the Orange Basin, off South Africa, showing the locations of the four studied wells (K-A2, K-A3, K-E1, and K-H1)



Rogers, 1975; De Villiers & Cadman, 2001; McLachlan & Pieterse, 1978, Oboh-Ikuenobe & De Villiers, 2003; Sandersen et al., 2011; Zavada, 2004) and foraminifera (McMillan, 2003, 2008; Stevenson & McMillan, 2004).

This study focuses on the lithology, palynomorphs, particulate organic matter, and foraminifera in wells K-A2, K-A3, K-H1, and K-E1 (Fig. 1) located between 15° and 17° latitude and around 31° longitude within blocks 3A and 2C of the Orange Basin. The aim of the study of these Cretaceous strata is to provide information about the paleoenvironment and hydrocarbon potential of a previously understudied area of the basin. Palynofacies analysis is very useful in discerning paleoenvironmental conditions and proximity to paleoshoreline, particularly when the paucity of microfossils limits interpretations. The characteristics of phytoclasts, such as their sizes, shapes, and oxidation levels, are used to infer their distance from source and the paleoshoreline (Tyson & Follows, 2000). Additional valuable biostratigraphic information provided by foraminifera is integrated with palynological data to better constrain the paleoenvironmental reconstruction, age, and hydrocarbon potential of the sediments.

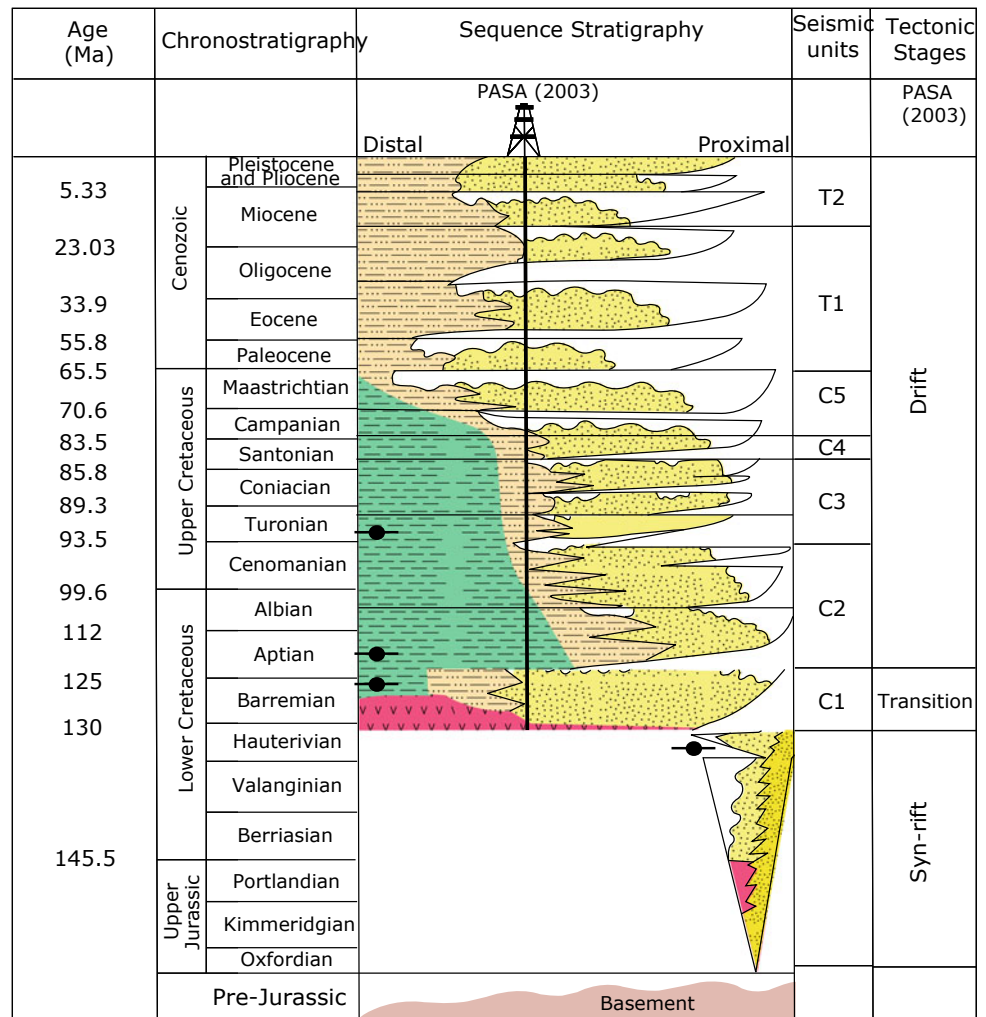
## 2 Geologic Setting

The Orange Basin developed as part of a rift-drift sequence during the breakup of the supercontinent Gondwana, which resulted in the separation of South America and Africa in the

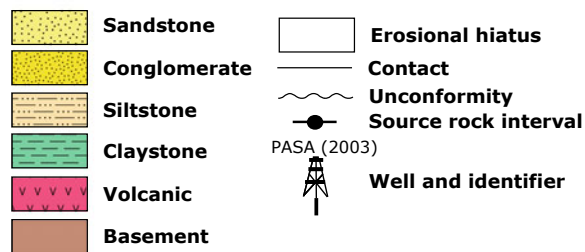
Late Jurassic, and the development of the South Atlantic in the Early Cretaceous (Brownfield, 2016; Brown et al., 1996; Muntigh 1993; Muntigh & Brown, 1993). This breakup created the space in the basin (Campher, 2009) for diverse and thick Upper Jurassic to Lower Cretaceous siliciclastic marine, lacustrine, and volcanic sediments (Brownfield, 2016; Muntigh and Brown 1993; Paton et al., 2007). The development of the structure of the basin involved two major phases consisting of rifting and then later drift phases (Brownfield, 2016; Campher et al., 2009). The rifting commenced in the Jurassic and continued into the Early Cretaceous, forming north–south trending grabens and half-grabens, and ceased in the late Hauterivian (Brownfield, 2016). An injection of basalt and unconformity occurred at the margin sometime in the Early Cretaceous, followed by marine ingression and flooding in the mid-Cretaceous resulting from thermal subsidence and eustasy along the margin; this culminated in the Atlantic being fully open by the Late Cretaceous (Kuhlmann et al., 2010).

A major uplift occurred along the margin during this time as the continent moved over the Africa Superplume, resulting in at least one kilometer of uplift in the Orange Basin that created a shelf-slope topography documented by deltaic progradation of Albian age in the basin (Baby et al., 2020). The development of canyons and normal faults, as well as listric faults and toe thrusts, was prevalent along the shelf edge. The movement of the tectonic plates resulted in the movement of Africa northward. This position change

**Fig. 2** Lithologic column of the well K-A2 showing the core sample locations and key foraminiferal and palynomorph taxa



**EXPLANATION**



resulted in climate fluctuations in the southern portion of the basin, from arid to temperate, tropical, and then back to temperate conditions (Boucot et al., 2013; Scotese 2002). This was controlled in part by the changes in the equatorial distance and the development of ocean currents (Benguela, Mozambique, and Antarctic Subpolar gyres) once the continents were far enough apart (Fischer & Uenzelmann-Neben, 2018; Gordon, 1973).

**3 Materials and Methods**

**3.1 Palynology**

Thirty-seven core samples from six conventional cores of the four wells (one each from K-E1 and K-H1; two cores each from K-A2 and K-A3) were analyzed for their palynomorph

**Table 1** Particulate organic matter (POM) components identified in this study

<i>Palynomorphs</i>			
Terrestrial	Sporomorphs		Fungal remains
	Pollen	Spores	Filamentous hyphae (C), spores, or mycelia, of brown color and ranging from 5 $\mu\text{m}$ to more than 100 $\mu\text{m}$ in size
	Yellow grains (A) of terrestrial plant origin (gymnosperm and angiosperm)	Pale yellow to orange-brown grains (B) of terrestrial plant origin (bryophytes and pteridophytes)	
Nonmarine aquatic	Micro- and megaspores		Algae
	Spores (D) produced by heterosporous embryophytic plants (water ferns)		Cysts, zygospores, or coenobia (E) of orange-brown to brown color produced by algae
Marine	Dinoflagellate cysts		Palynomorphs
	Cysts (F) produced by dinoflagellates which may be smooth or ornamented with tabulation and/or processes		Palynomorph of animal-like protists, microflora, and foraminiferal test lining (G)
<i>Palynodebris</i>			
Structured organic material	Phytoclasts		Zooclasts
	Degraded	Structured	Fragment of animal origin (i.e., insect) and may be yellow or brown (O & P)
	Broken-down plant material that is nearly structureless and may be yellow to brown in color (H)	Translucent angular material of terrestrial plant origin with internal structure (I)	
	Opaques		Black particles (J-L) which may be phytoclasts including woody material such as cuticles, tracheids (M), parenchyma (N), or palynomorphs oxidized or affected by diagenesis
	Black particles (J-L) which may be phytoclasts including woody material such as cuticles, tracheids (M), parenchyma (N), or palynomorphs oxidized or affected by diagenesis		
Structureless organic material	Amorphous organic matter (AOM)		Resin
	Diaphanous or translucent kerogen particles (Q & R) of marine origin including dinoflagellates and acritarchs with variable texture (fluffy, clotted, or granular) and colors including clear, gray, and brown (S)		Yellow to brown translucent and structureless angular particles (T), sometimes with conchoidal fracture along edges, produced from tree sap

Examples of the different types of components (A-S) are shown in Fig. 3

and particulate organic matter (kerogen) contents. Fifteen grams of each sample were digested in hydrochloric and hydrofluoric acids to dissolve carbonates and silicates, respectively (Traverse, 2007). A portion of the organic residue was oxidized with Schultze solution ( $\text{KClO}_3$  plus  $\text{HNO}_3$ ) and sieved using a 10  $\mu\text{m}$  mesh. The oxidized and unoxidized (kerogen) organic residues were strewn-mounted on glass slides that were used for palynomorph identification and palynofacies analysis, respectively, under transmitted light microscopy. The slides of the sieved residues were scanned for routine identification of palynomorphs (to the species level whenever possible) based on existing literature, reference indices, and palynological databases (Ibrahim et al., 2015; Jansonius & Hills, 1976 and supplements, Fensome et al., 2019; Frederiksen et al., 1982; Jaramillo & Rueda, 2019; Slimani et al., 2010). Additionally, the chronostratigraphic ranges of taxa were confirmed using Palynodata and White (2008), Fossilworks, the Paleobiology Database, and AlgaeBase (Guiry and Guiry, 2021).

For palynofacies analysis, 300 particles of particulate organic matter components were counted in each kerogen

slide. Eight types of particulate organic matter components were identified (Table 1, Fig. 3), following the classification schemes of Tyson (1993, 1995) and Oboh-Ikuenobe et al. (2005). An additional 300 point-counts per slide of phytoclasts and opaques were obtained separately to generate data for lath-shaped and equidimensional particles. Ternary plots with AOM—Phytoclasts—Palynomorphs (Tyson, 1995) and marine amorphous organic matter (MAOM)—Phytoclasts/nonmarine Palynomorphs—marine Palynomorphs (modified from El Beialy et al., 2016) as end members (Fig. 4) were used to characterize the kerogen and interpret the paleoenvironmental conditions. The particulate organic matter data were used for cluster analysis (Wards, stratigraphic constraints) using the Paleontological Statistics Software Package for Education and Data Analysis (PAST© 2001) to identify palynofacies assemblages. Cluster analysis was used to compare the distances between the measured parameters (Sokal & Michener, 1958). Sample distances are represented on the left side (Q-mode) of the cluster dendrogram, while component abundances are on the right.



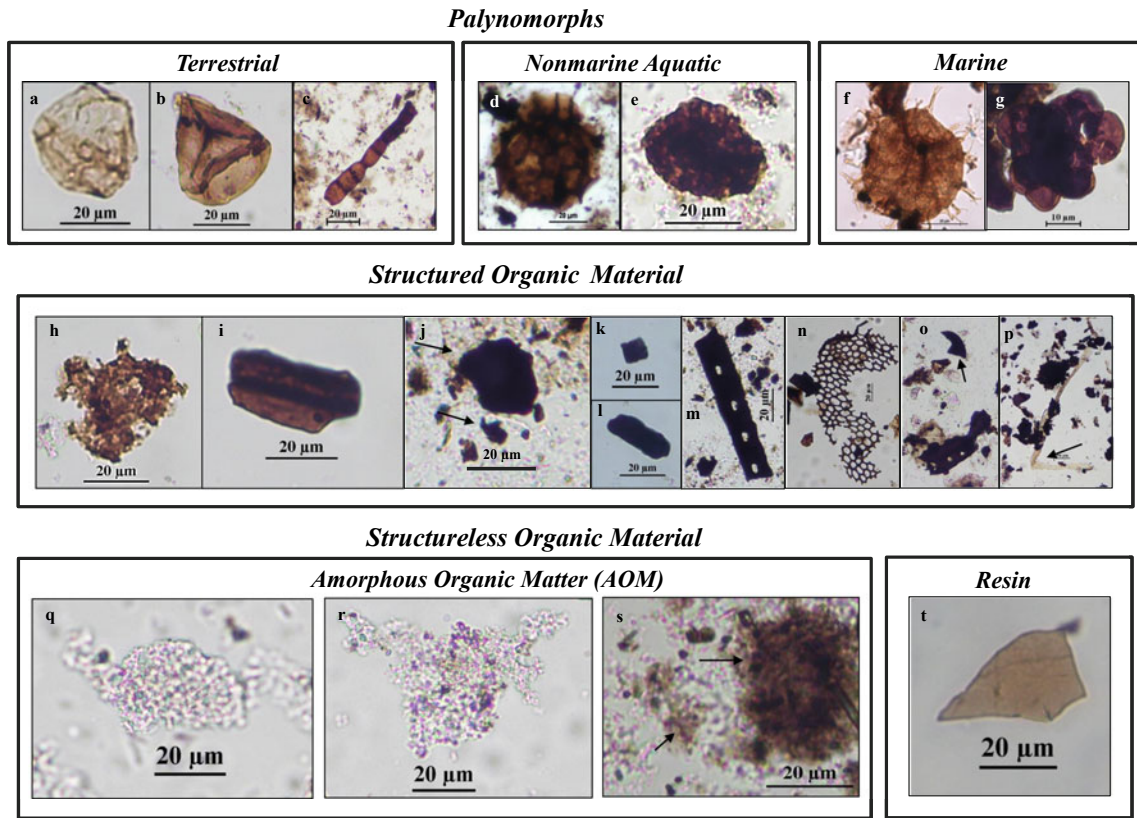


**Fig. 3** Photomicrographs of the types of particulate organic matter components identified in this study. Some components occur in minor amounts but were not point counted. **a** Stephanoporate pollen. **b** Trilete spore. **c** Fungal hyphae. **d** Water fern (*Balmeisporites* sp.). **e** Algal coenobium. **f** Dinoflagellate cyst. **g** Microforaminiferal test lining.

**h** Degraded phytoclast. **i** Structured phytoclast. **j** Opaque particles. **k** Equant-shaped opaque particle. **l** Lath-shaped opaque particle. **m** Tracheid. **n** Parenchyma. **o, p**, Zooclasts. **q, r** Marine amorphous organic matter. **s** Nonmarine amorphous material. **t** Resin

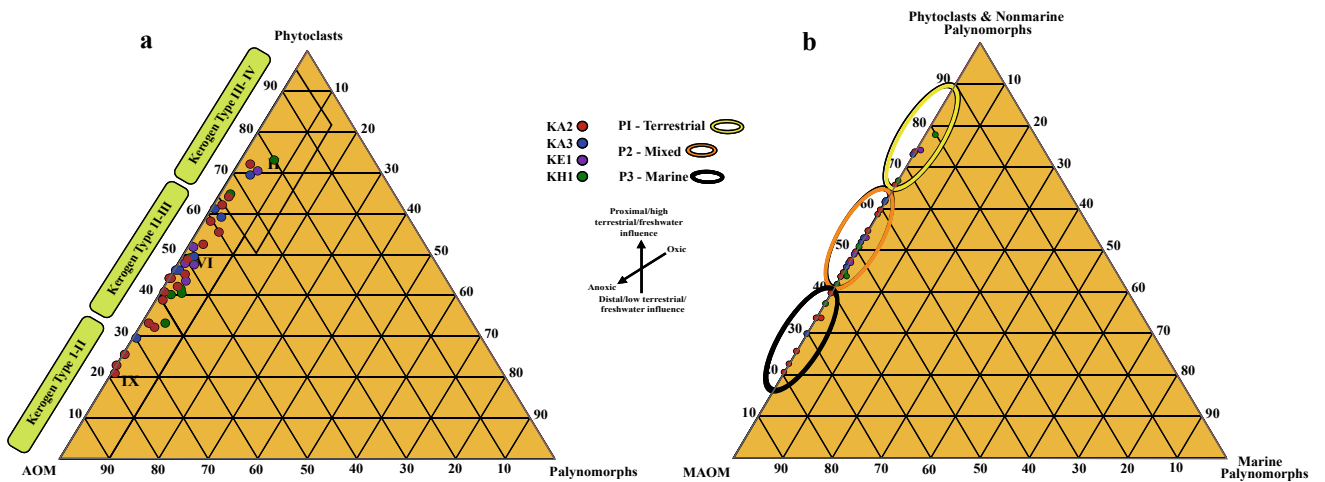


**Fig. 4** Ternary plots of particulate organic matter in the samples of wells K-H1, K-E1, K-A2, and K-A3. **a** AOM-Palynomorph-phytoclast plot (after Tyson, 1995). **b** Marine amorphous marine organic matter [MAOM]-phytoclast and nonmarine palynomorph-marine

palynomorph plot (modified from El Beialy et al., 2016) and inferred palynofacies assemblages. Yellow oval = palynofacies 1, orange oval = palynofacies 2, and black oval = palynofacies 3

### 3.2 Foraminiferal Analysis

Foraminiferal analyses were conducted on 27 shale and claystone core samples based on careful examination of well logs and composite logs (well completion report) and detailed megascopic analysis. Prior to the megascopic examination, drilling additive contaminations were removed by washing the samples with water, and then, overall lithological characteristics of each sample were described. The main documented lithological properties are described:

1. physical properties (color, grain size, angularity, cement, etc.)
2. general lithological compositions (e.g., limestone, dolomite, shale, siltstone, claystone, sand, rock fragments, algal remains, and fossils)
3. accessory materials presence (e.g., coal, ferruginous, and pyritized particles)

The nature of the core samples determines the selection of their optimum processing techniques (Feldmann et al., 1989; Green, 2001; Harris & Sweet, 1989; Kummel & Raup, 1965). The main aim of the procedure is to disintegrate rock fragments into discrete grains in order to eliminate the binding cement materials and facilitate microfossils separation. For sample processing, 20 g of each core sample were washed in water. All core fragments were crushed into smaller sizes utilizing a wooden hammer and then soaked in water. Then, the samples were transferred to separate enamel bowls filled with water. 15 ml of hydrogen peroxide (conc. 30%) was added to the mixture and kept for 48 h at room temperature. The hydrogen peroxide eliminates the cement materials allowing the sedimentary particles to be separated. The clay matrix separations were achieved by adding caustic soda to the mixture. After the previous step, the solutions were heated for 45 min to intensify the disintegration and then left to cool. Then, each sample mixture was sieved with a fine 50  $\mu\text{m}$  sieve under running water to remove the clay materials and retain microfossils and sediment fragments. Extreme caution was taken while processing to avoid sieve contamination and mixing of identification labels. Each sample was then transferred to a separate bowl and dried in an oven. Finally, the samples were microscopically examined for biostratigraphy.

## 4 Results

### 4.1 Lithology

The lithology in wells K-A2, K-A3, K-H1, and K-E1 is dominated by siltstone and fine-grained sandstone

interbedded with shale and claystone (Figs. 5, 6 and 7). The rate of sedimentation in the studied sections, which experienced terrestrial inputs from the nearby continent, is relatively high (Brownfield, 2016; Campher et al., 2009; Gallagher and Brown, 1999; Paton et al., 2007; Rouby et al., 2009). Carbonaceous streaks, mixed shallow marine algal fragments, and pyritized foraminiferal tests were noted in the core samples.

Core 1 of the K-A2 well (3984.1–3991.85 m) comprises mainly very fine-grained sandstone intercalated with shale and siltstone (Fig. 5, left). The shale is dark gray and fissile with disseminated pyrite grains toward the bottom of each interval. The sandstone is light gray to white, feebly argillaceous, tight toward the base, and moderately sorted with subangular grains. Parallel shale laminations and carbonaceous particles occur in the middle sandstone interval at 3987.31 m. The upper sandstone interval (3985.25–3984 m) contains fine-grained silty patches, is moderately hard and feebly calcareous, and very tight with poor visual porosity and rare carbonaceous matter. The siltstone is light gray and feebly calcareous with parallel shale lamination in the middle; it has carbonaceous particles and common pyrite grains in the upper portion. Bioturbation is widespread in this core. Some inter-laminated siltstone and shale preserve load casts, as well as climbing ripples and wavy laminations (Salie, 2018).

Core 2 of well K-A2 (4076.1–4083.1 m) is dominated by intercalated siltstone and shale in the lower portion, followed by alternating layers of sandstone and siltstone, coarsening-upward sandstone with intercalations of siltstone and very thin shale (Fig. 5, right). The siltstone in the lower portion of the core is medium gray with white patches and is feebly calcareous. The sandstone in the upper half of the core is light gray, massive, very tight and is locally silty with subangular to subrounded grains. The shale is dark gray, bulky, feebly carbonaceous, and often grades to siltstone.

The dominant lithology in core 1 of well K-A3 (2906–2914.5 m) is medium- to very fine-grained sandstone, which has interbeds of shale and thin siltstone below 2911.7 m (Fig. 6, left). The initial fining-upward sequence is succeeded by a coarsening-upward sequence. The sandstone varies from white to light gray in color (mud drapes forming flaser laminations), consists of well-sorted and subangular grains, and is feebly calcareous with fine carbonaceous patches in places. The shale is dark gray and fissile with some carbonaceous layers. Core 2 of well K-A3 (3875.5–3884 m) is also dominantly sandstone with thin intercalations of siltstone, claystone (silty shale), and shale (Fig. 6, right). The sandstone is light gray to white with subangular to subrounded grains and a few shale clasts and has planar laminations. The siltstone is gray and laminated. The dark gray to black shale is hard and fissile, contains pyrite grains, and transitions to claystone.

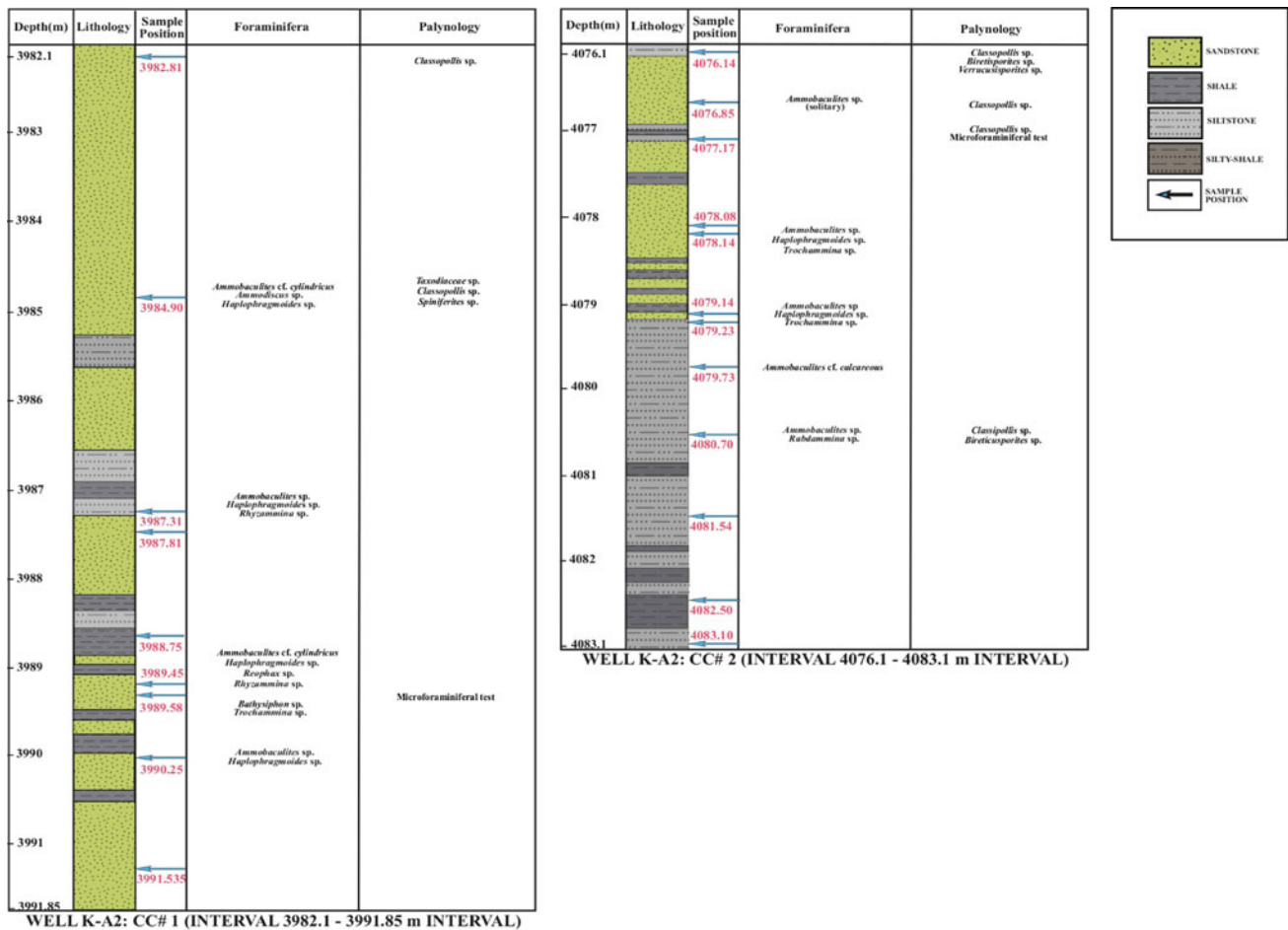


Fig. 5 Lithologic column of the well K-A2 showing the locations of samples and key foraminiferal and palynomorph taxa

The well K-H1 core spans 3066 m through 3083 m. It is dominantly sandstone which alternates with siltstone and shale layers between ~ 3073.8 and 3080.6 m (Fig. 7, left). The sandstone is gray to light gray, fine-grained, moderately sorted with planar laminations and has subangular to sub-rounded grains surrounded by mild calcareous cement; it also has common fine pyrite grains. The siltstone is dark gray, locally fissile, and transitions into claystone. The shale is dark gray and non-calcareous and has a few pyrite grains.

In the well K-E1 core (Fig. 7, right), alternating shale and sandstone transition to alternating sandstone and siltstone near the top of this segment. The siltstone is light gray to pale yellow in color, hard and compact, and argillaceous and feebly carbonaceous in places. The sandstone is light yellow to white, fine-grained, with subangular to subrounded grains, and is very tight with poor visual porosity. Fine argillaceous patches and rare carbonaceous fine flaser and wavy laminations also occur in places. The shale is dark gray, hard, and compact with some carbonaceous layers. There is occasional lenticular bedding, and low-angle cross-bedding is more apparent with decreasing depth (Salie, 2018).

## 4.2 Palynomorphs

Palynomorph abundances and diversity vary from low to barren in the four studied sections (Table 2). The recovered palynomorphs (Figs. 8, 9 and 10), which are primarily nonmarine in origin, include spores of pteridophytes (*Appendicisporites erdtmanni*, *Appendicisporites* sp., *Balmesporites* sp., *Biretisporites potoniaei*, *Camaronosporites* sp., *Cicatricasporites* sp., *Cyatheadites* sp., *Deltoidospora* sp., *Densoisporites* sp. *Gleicheniidites* sp., *Lycopodium* sp., *Undulatisporites* sp., *Verrucosisporites* sp.) and bryophytes (*Interlobites* sp., *Tauocusporites segmentatus*, *Tauocusporites* sp.). Gymnosperm (*Classopollis classoides*, *Classopollis* sp., *Ephedripites* sp., *Taxodiaceapollenites hiatus*), and angiosperm pollen grains (*Cretacaeiporites polygonalis*, *Tricolpites* sp.), along with fungal remains. Few nonmarine algae (*Chomotriletes minor*), marine palynomorphs (the dinoflagellate cysts *Dinogymnium* sp., *Exochosphaeridium* sp., *Hafniasphaera* sp., *Spiniferites* sp., *Odontochitina operculata*), and foraminiferal test linings occur. The spheroidal pollen grain

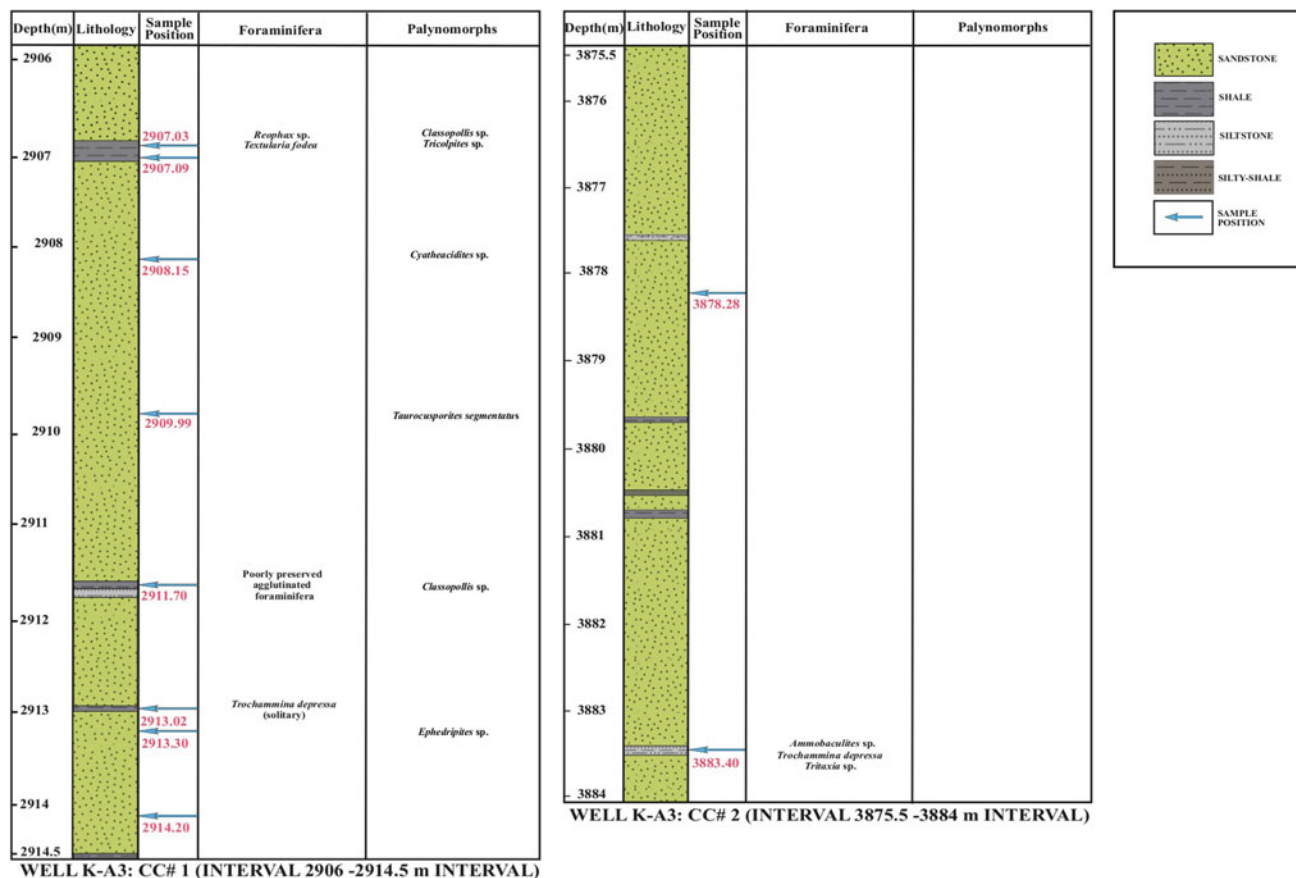


**Fig. 6** Lithologic column of the well K-A3 showing the locations of samples and key foraminiferal and palynomorph taxa

*Classopollis* sp. is the most common taxon throughout the study wells.

### 4.3 Palynofacies Analysis

The abundances of the particulate organic matter components identified in Sect. 3.1 (Table 2, Fig. 3) provide information about the depositional conditions. Structured phytoclasts, degraded phytoclasts, opaques, and zooclasts such as insect parts (noted but not counted in this study) are associated with proximity to terrestrial environments. Structureless organic materials such as amorphous organic matter or resin (tree sap) are categorized as marine or non-marine in origin. The dominant component in this study is MAOM, followed by phytoclasts (Table 2). The sizes and shapes (lath-shaped, equidimensional) of the phytoclasts, including opaques, are affected by the hydroenergetic regime and distance of transportation. Equidimensional to lath-shaped opaque ratios decrease offshore overall, from well K-A3 and K-A2 to well K-E1 (Table 2).

Previous studies have benefited from the use of multivariate statistical analyses for interpreting palynofacies

results (Kovach and Batten 1994; Oboh, 1992, Oboh-Ikuenobe & De Villiers, 2003; Oboh-Ikuenobe et al., 2005). These analyses provide comparison of complex datasets with multiple variables that are of particular use in ecological studies (Ramette, 2007). The multivariate analytical methods chosen are unique to the dataset and depend on the aim of the study. Based on cluster analysis, three palynofacies assemblages are constrained (I, II, III in Fig. 11), and an image of a representative sample from each assemblage is shown in Fig. 12.

Palynofacies assemblage I (Figs. 11 and 12) is dominated by nonmarine, mainly terrestrial components (between 60 and 80%), with only about 20–40% AOM. The AOM is mostly dispersed, although some clumped nonmarine AOM is present. The opaques are moderately rounded and both structured material such as tracheids and structureless materials including resin are present. This assemblage is divided into two subgroups (A and B). Subgroup B differs from subgroup A due to increased numbers of structured phytoclasts, terrestrial palynomorphs, and marine palynomorphs, and a decrease in AOM and opaques.

Palynofacies II (Figs. 11 and 12) is characterized by approximately 40–60% AOM, and has two subgroups (A

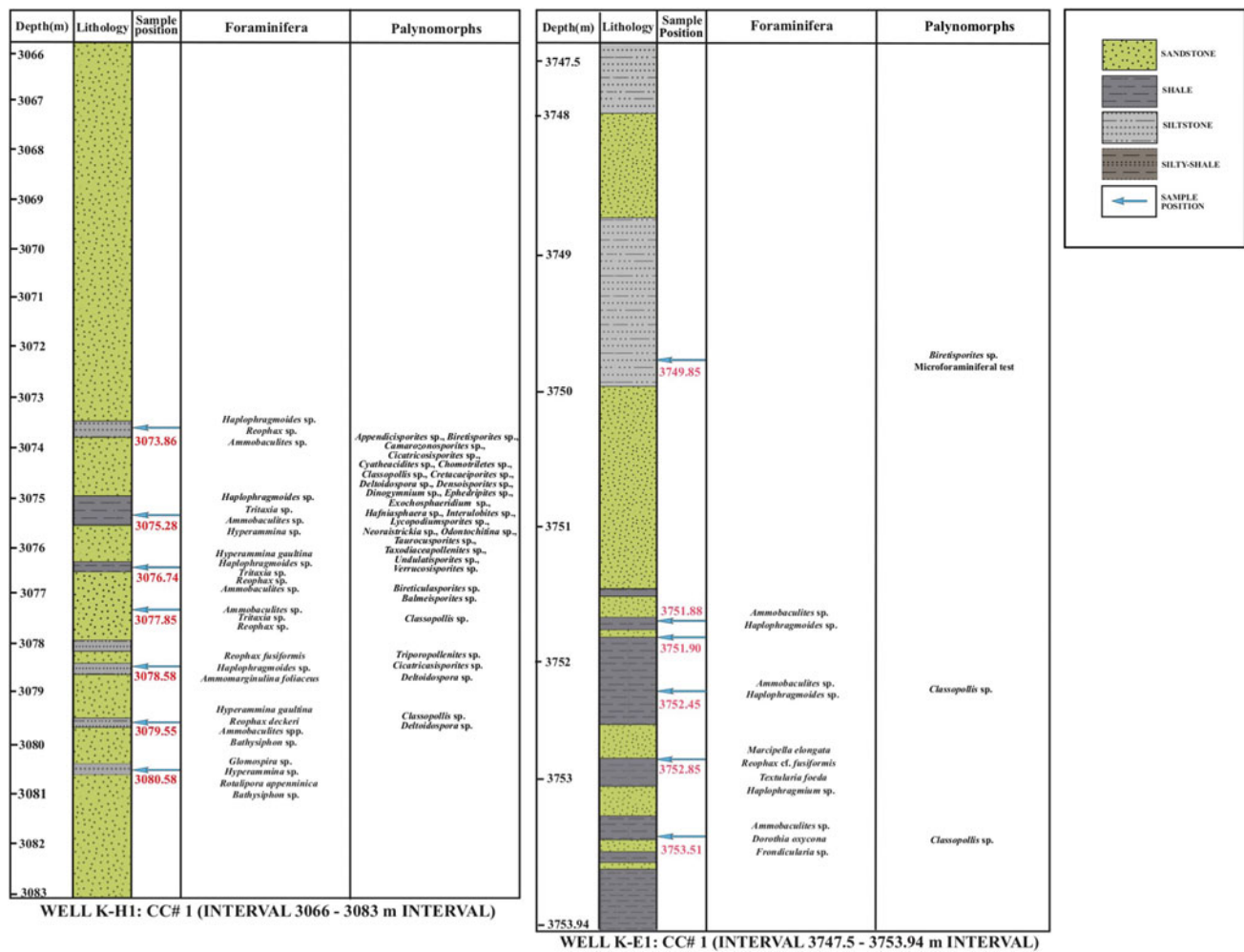


Fig. 7 Lithologic column of the wells K-E1 and K-H1 showing the locations of samples and key foraminiferal and palynomorph taxa

and B) as a result of differences in the numbers of degraded and structured phytoclasts. Subgroup A has more palynomorphs, more degraded phytoclasts (12–35%), both dispersed and clumped granular marine AOM, and rounded to well-rounded opaque particles that are fairly consistent in size. In contrast, subgroup B has a greater abundance of structured phytoclasts (12–25%), only dispersed marine AOM, bimodal-sized opaques that are both angular and rounded, and fewer palynomorphs. These subgroups are each further divided as A1, A2, B1, and B2. A1 has more rounded opaque particles, while A2 has fewer palynomorphs. In B1, palynomorphs are more common compared to B2. Overall, palynofacies assemblage II contains the highest abundance of lath-shaped opaques in this study.

Palynofacies assemblage III (Figs. 11 and 12) comprises the highest abundance (60–80%) of marine components, the lowest nonmarine input, and the lowest abundance of opaques. This assemblage contains a mix of angular and well-rounded opaques, and dispersed and granular marine

AOM. It is also further divided into two subgroups: subgroup A is differentiated by the absence of palynomorphs, whereas subgroup B contains few palynomorphs, scattered resins, and structured phytoclasts.

#### 4.4 Foraminiferal Analysis

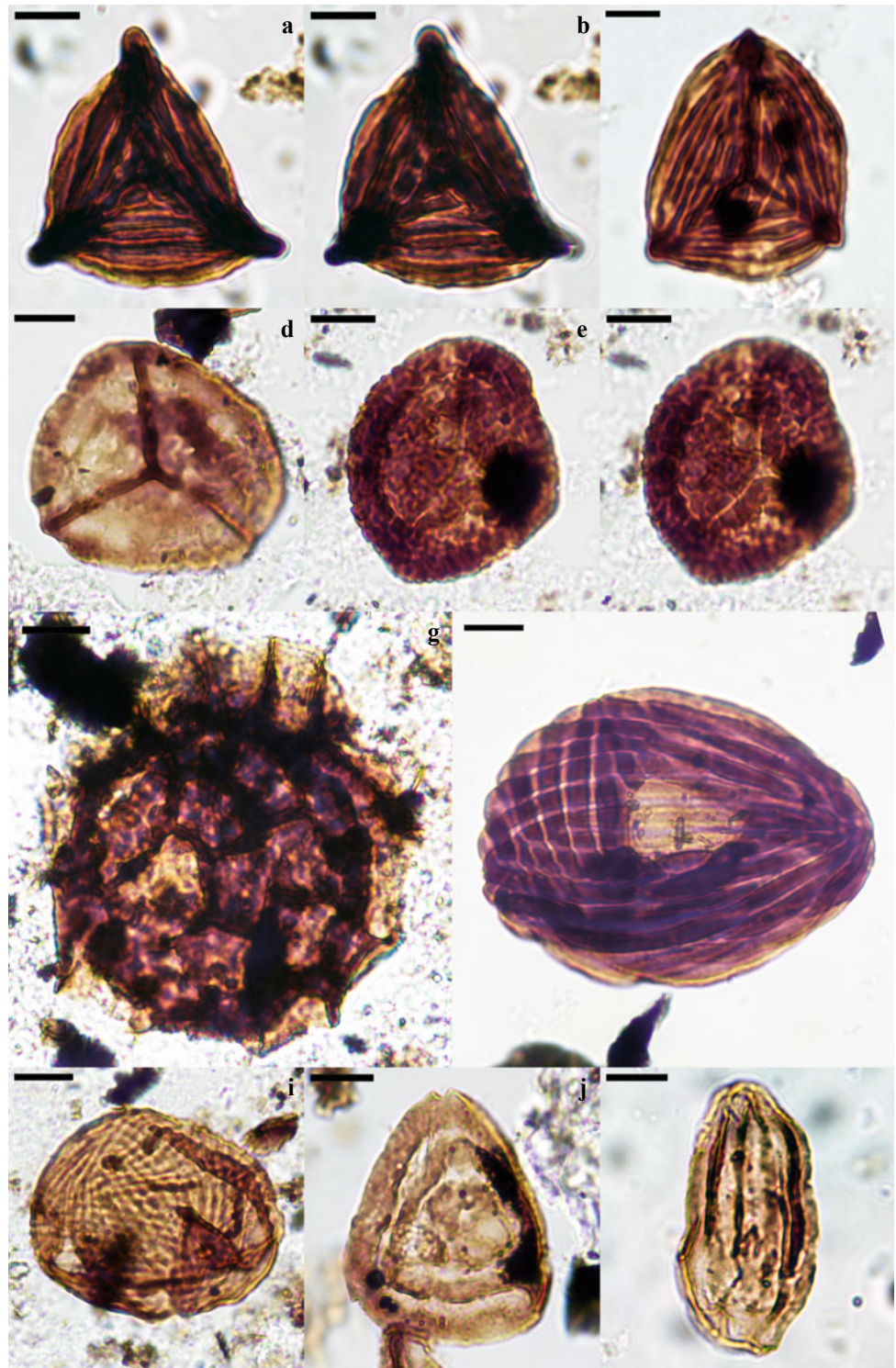
Foraminiferal frequency is moderate to low in most samples of the four wells. In general, all the samples are dominated by agglutinated foraminifera and pyritized tests that are reported in some intervals. Several agglutinated foraminifera species are recorded in the K-A2 well, such as *Ammobaculites* cf. *cylindricus*, *Ammobaculites* spp., *Ammodiscus* spp., *Bathysiphon* sp., *Haplophragmoides* sp., *Reophax* sp., and *Trochammina* sp. There is a gradual decrease in foraminiferal frequency from the lower part of the interval to the top. One core sample from the K-A3 well (CC#2, depth 3883.41 m) records very coarse textured agglutinated

**Table 2** Quantitative distribution of particulate organic matter components

Well and depth (m)	Lithology	AOM	Palynomorphs			Phytoclasts			Opaque shapes	
			MAR	SPORO	FUN				EO	LO
K-A3 2907.03	Sandstone and shale	81	+	11	+	85	29	94	133	167
K-A3 2908.15	Sandstone	210	+	2	+	22	43	23	209	91
K-A3 2909.99	Sandstone	142	+	3	+	48	28	79	109	191
K-A3 2911.70	Silty shale	159	+	2	1	39	23	76	134	166
K-A3 2913.30	Silty shale	114	1	8	+	57	21	99	117	183
K-A3 2914.20	Sandstone	145	+	7	+	62	12	74	142	158
K-A3 3878.28	Sandstone	115	1	1	+	25	98	60	155	145
K-A3 3883.40	Shale	161	+	1	+	7	109	22	154	146
K-H1 3073.86	Silty shale	148	+	2	3	38	25	84	173	127
K-H1 3075.28	Clay	61	6	13	1	73	65	81	129	171
K-H1 3076.74	Silty shale	100	+	6	+	70	11	113	165	135
K-H1 3077.85	Sandstone and silty shale	166	2	9	2	46	18	57	142	158
K-H1 3078.58	Silty shale and sandstone	165	1	10	+	53	14	57	163	137
K-H1 3079.85	Sandstone and silty shale	187	1	12	1	40	13	46	179	121
K-H1 3080.58	Silty shale	173	+	4	3	57	11	52	159	141
K-E1 3749.85	Silty shale	159	+	9	2	60	15	55	160	140
K-E1 3751.90	Shale	153	+	+	4	56	11	76	162	138
K-E1 3752.45	Shaley mudstone	75	4	10	+	90	53	68	144	156
K-E1 3752.85	Shale	142	+	2	1	61	26	68	155	145
K-E1 3753.51	Shale and sandstone	148	+	10	+	69	14	59	146	154
K-A2 3982.81	Sandstone	176	+	2	+	14	66	42	173	127
K-A2 3984.90	Mudstone and sandstone	157	+	8	+	46	43	46	140	160
K-A2 3987.31	Silty shale	167	+	1	+	9	68	55	151	149
K-A2 3987.81	Siltstone	236	+	2	+	16	30	16	130	170
K-A2 3988.75	Shaley mudstone	109	+	5	+	34	76	76	159	141
K-A2 3989.45	Shale and sandstone	180	+	2	2	39	56	21	123	177
K-A2 3990.25	Shale and sandstone	197	+	3	1	25	34	40	127	173
K-A2 3991.535	Sandstone	195	2	7	+	46	29	21	129	171
K-A2 4076.14	Silty shale	122	+	3	1	53	73	48	97	203
K-A2 4076.85	Sandstone	102	+	6	+	56	55	81	95	205
K-A2 4077.17	Silty shale	77	+	7	+	79	72	65	120	180
K-A2 4078.08	Sandstone	150	+	3	1	50	31	65	111	189
K-A2 4079.14	Mudstone	166	+	8	+	51	35	40	118	182
K-A2 4079.73	Silty shale	135	+	7	1	69	36	52	117	183
K-A2 4080.70	Silty shale	121	+	12	1	84	33	49	108	192
K-A2 4081.54	Mudstone	168	+	+	+	15	69	48	161	139
K-A2 4082.50	Sandstone and mudstone	223	+	1	+	13	49	14	174	126
K-A2 4083.10	Silty shale	232	+	+	+	4	49	15	158	142

Well locations shown in Fig. 1. Lithology shown in Figs. 2, 3 and 4. AOM Amorphous organic matter, MAR Marine palynomorphs, SPORO Pollen and spores, FUN Fungal remains, STR Structured phytoclasts, DEG Degraded phytoclasts, OPA Opaques, EO Equidimensional, LO Lath-shaped, and + Present but not point counted

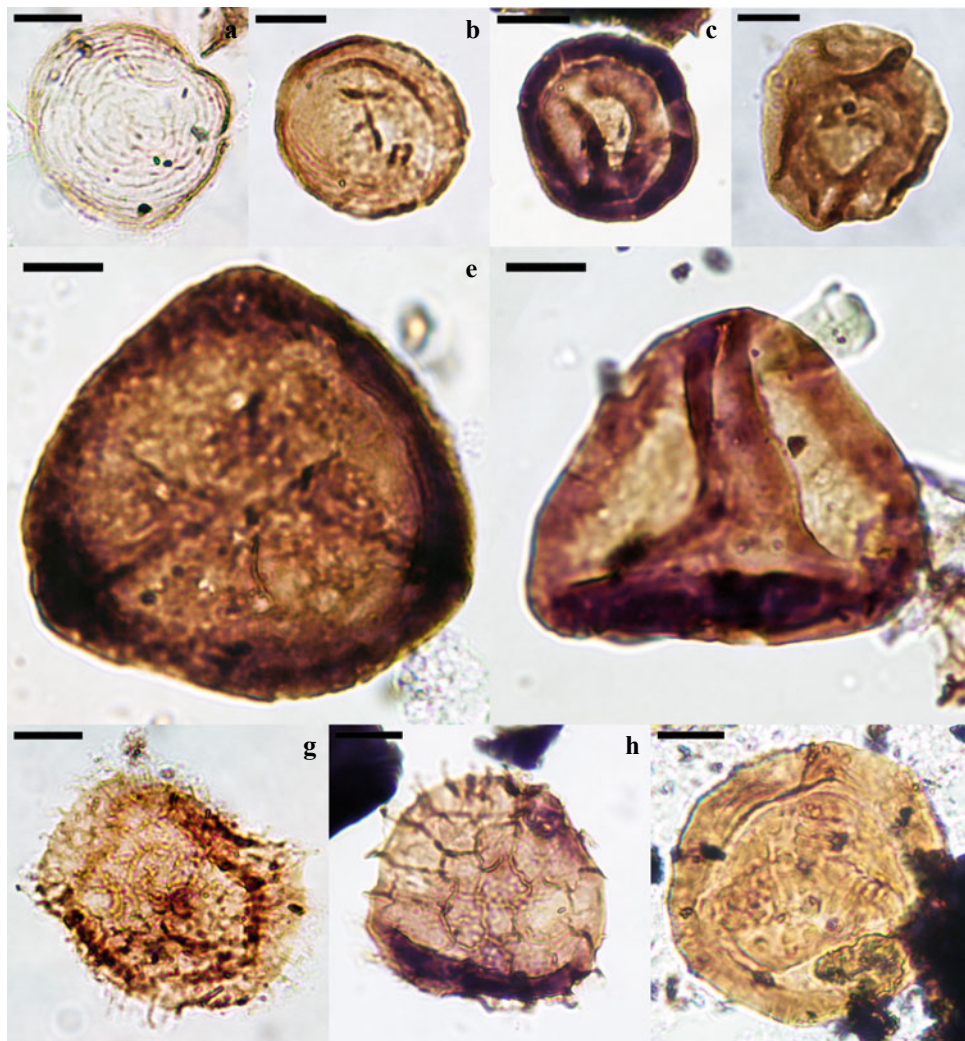
**Fig. 8** Photomicrographs of selected palynomorph taxa. Well sample numbers are noted EF = England Finder® coordinates. Scale bar is 10  $\mu$ m.  
**a, b** *Appendicisporites erdtmanii*, K-H1 3075.28-2, EF 1T25.  
**c** *Appendicisporites trichacanthus*, K-H1 3075.28B, EF 4P45.  
**d** *Biretisporites potoniaei*, K-H1 3075.28D, EF 4L44.  
**e, f** *Camarozonosporites* sp., K-H1 3075.28B, EF 2M36.  
**g** *Balmeisporites* sp., K-H1 3076.74D, EF 1P39.  
**h** *Cicatricosisporites* sp., K-H1 3075.28D, EF 3O33.  
**i** *Cicatricosisporites venustus*, K-H1 3075.28A, EF 4Q28.  
**j** *Cyatheacidites* sp., K-H1 3075.28D, EF 4B50.  
**k** *Ephedripites* sp., K-H1 3075.28C, EF 2U41



foraminifera. Some samples above this depth contain the agglutinated foraminifera *Trochammina depressa*, *Textularia* sp., and *Ammobaculites* spp. In the other core (CC#1: samples at 2907.03, 2911.70 and 2913.02 m), very rare agglutinated foraminifera are present.

In well K-H1, there is moderate to low frequency of taxa, with few calcareous benthic forms. The early Cenomanian planktonic foraminifera *Rotalipora appenninica* and *Rotalipora gandolfi* (*Rotalipora brotzeni* Zone, Caron, 1985) are present at depth 3080.58 m. Agglutinated foraminifera, such

**Fig. 9** Photomicrographs of selected palynomorph taxa. Well sample numbers are noted EF = England Finder® coordinates. Scale bar is 10  $\mu$ m.  
**a** *Chomotriletes minor*, K-H1 3075.28A, EF 2F31.  
**b** *Classopollis classoides*, K-H1 3075.28B, EF 2R52.  
**c** *Classopollis* sp., K-H1 3752.45C, EF 1O30.  
**d** *Cretacaeiporites polygonalis*, K-H1 3075.28B, EF 1S35.  
**e** *Densoisporites* sp., K-H1 3075.28-2, EF 3N30.  
**f** *Gleicheniidites* sp., K-H1 3076.74D, EF4L40.  
**g** *Exochosphaeridium* sp., K-H1 3075.28B, EF 1B40.  
**h** *Lycopodiumsporites reticulumsporites*, K-H1 3075.28D, EF 2E51.  
**i** *Taurocusporites segmentatus*, K-A3 2909.99E, EF 1K47



as *Ammobaculites* spp., *Glomospira* sp., *Haplophragmoides* spp., *Hyperammina gaultina*, *Reophax* sp., and *Tritaxia* sp. dominate the remaining samples. Calcareous benthics, including *Lenticulina angulosa* and *Lenticulina* cf. *nodosa*, are recorded in the basal part of the section. In well K-E1, the agglutinated benthic foraminifera *Ammobaculites sub-aquale*, *Haplophragmoides* spp., *Reophax* cf. *fusiformis*, *Textularia foeda*, *Dorothyia oxycona*, and *Frondacularia* sp. are recorded in varying proportion in most of the samples.

## 5 Discussion

Palynomorph and foraminiferal data provide the information used to constrain the age of the sediments in the studied wells. In addition, these two proxies have been integrated with lithological and palynofacies analyses to interpret the depositional environment, in addition to inferring the hydrocarbon potential of this segment of the Orange Basin.

### 5.1 Age Constraint

The majority of the identified agglutinated foraminifera and palynomorph taxa are long-ranging, from the Late Jurassic through the Late Cretaceous. The presence of the planktonic foraminifera *Rotalipora appenninica* and *Rotalipora gandolfi* at 3080.58 m in well K-H1, however, indicates an early Cenomanian age (Caron, 1985). In addition, the presence of the angiosperm pollen *Cretacaeiporites polygonalis*, which is constrained to the Albian–Coniacian (Ibrahim et al., 2015), at 3075.28 in well K-H1 supports this age assignment. Therefore, the inferred age of the studied sequences is early Cenomanian.

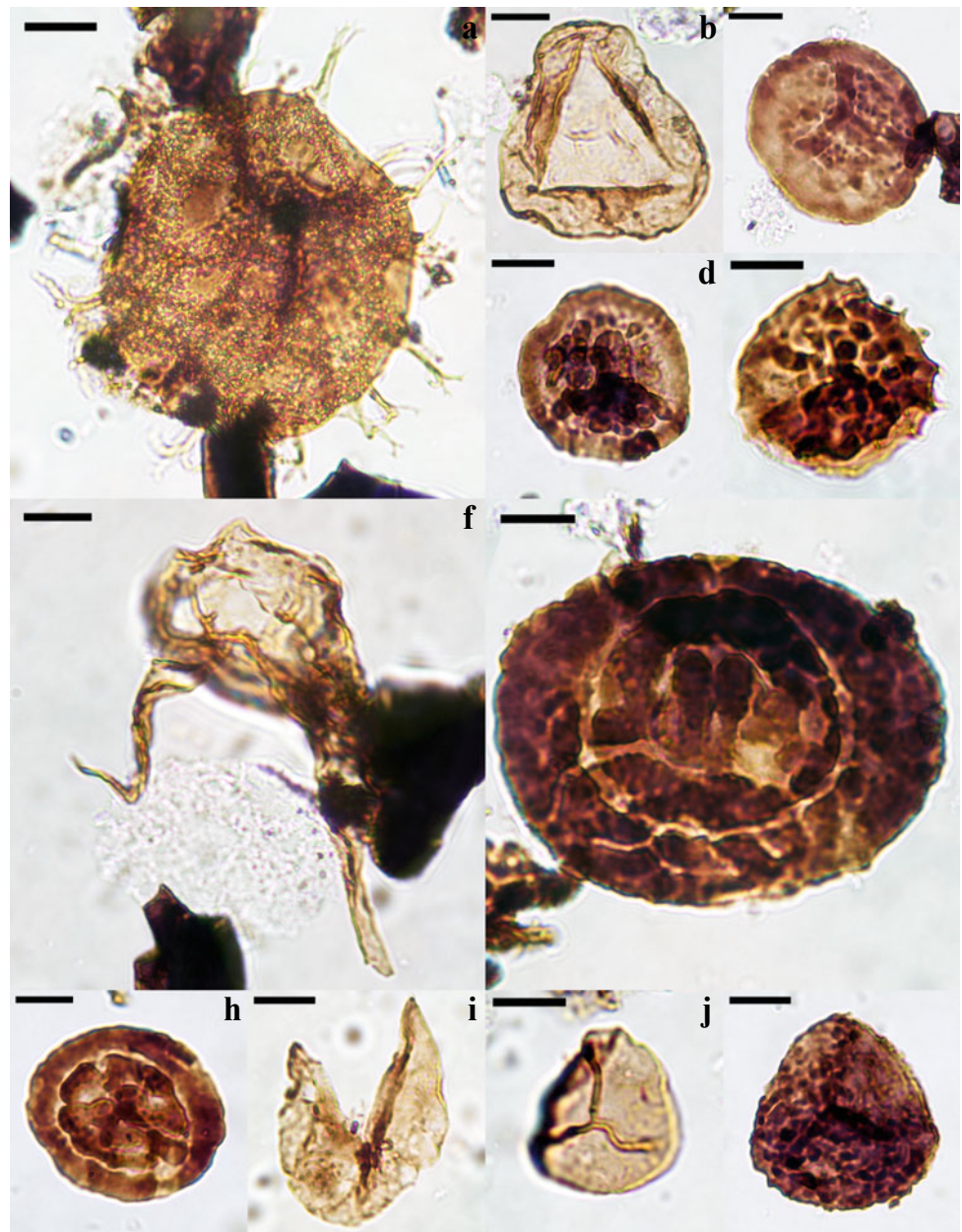
### 5.2 Paleoenvironmental Conditions

The multiple proxies generated from the lithological descriptions of the sediments, microfossils, and particulate organic matter reveal valuable insights into the depositional



**Fig. 10** Photomicrographs of palynomorph selected taxa. Well sample numbers are noted. EF = England Finder® coordinates. Scale bar is 10  $\mu\text{m}$ .

**a** *Hafniasphaera* sp., K-H1 3075.28A, EF 2R43.  
**b** *Deltoidospora* sp., K-H1 3075.28-2, EF 2O32.  
**c** *Interulobites* sp., K-H1 3752.45D, EF 3U33. **d** *Interulobites* sp., K-H1 3075.28D, EF 3S46.  
**e** *Neoraistrickia* sp., K-H1 3075.28-2, EF 1E42.  
**f** *Odontochitina operculata*, K-H1 3075.28-2, EF 3S37.  
**g** *Taurocusporites* sp. A, K-H1 3075.28A, EF 2V43.  
**h** *Taurocusporites* sp. B, K-H1 3075.28B, EF 4E31.  
**i** *Taxodiaceapollenites hiatus*, K-H1 3075.28-2, EF2H45. **j**, *Undulatisporites* sp., K-H1 3075.28D, EF 4W40.  
**k** *Verrucosiporites* sp., K-H1 3075.28D, EF 3E27



environment, sedimentary processes (e.g., energetic and redox conditions), the origins, duration of transport, and/or source proximity of particulate organic matter and palynomorphs, and indirect inferences about the paleoclimatic conditions at the time of sedimentation. The overall lithology of alternating fine-grained sandstone, siltstone, shale, and claystone in the four wells (Figs. 5, 6 and 7) is consistent with fluvio-marine type deposits reported from other African basins (e.g., Khalifa & Catuneanu, 2008; Oboh-Ikuenobe et al., 2005). Sandstone facies dominate in the study well, except for the K-E1 well which suggests high energy of deposition based on grain size. Alternatively, the presence of flaser laminations and mud drapes within the sandstone units

and occasional wavy laminations in some heteroliths suggests short periods of quiescence. While mostly shallow marine, the depositional structures suggest periodic tidal and deltaic influences (Daidu et al., 2013; Legler et al., 2014). We see no clear evidence of turbiditic deposition.

The types of microfossils in the sediments (nonmarine and marine), as well as palynofacies analysis and the presence of glauconite (Salie, 2018), provide information about the depositional environment in this part of the Orange Basin during the Cenomanian. These details suggest the sediments were deposited in a marginal to shallow marine (shelf) environment with input from the adjacent continent. The thicker overburden in the study area (Campher et al., 2009)

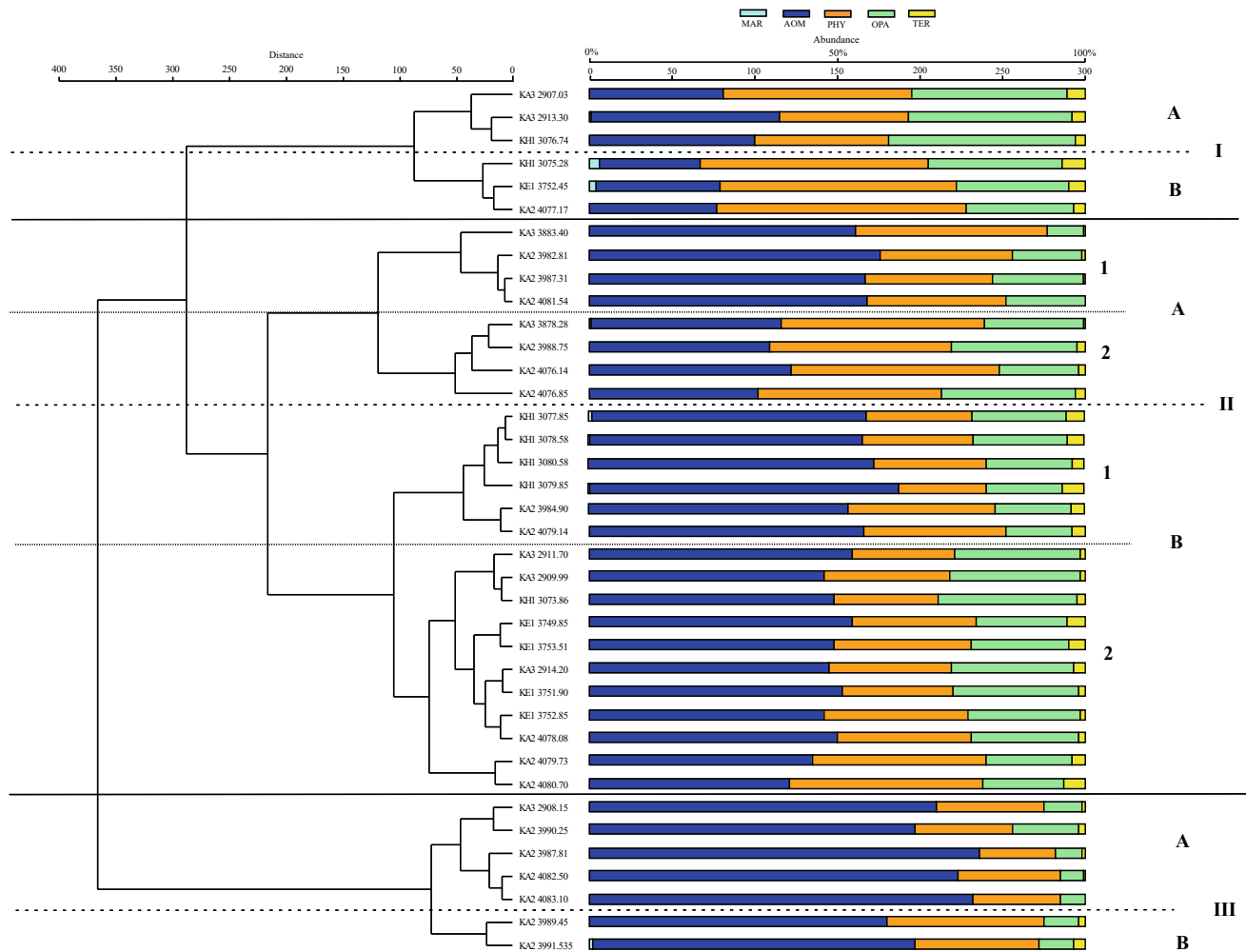


**Fig. 11** Q-mode cluster analysis (Ward's/Euclidean method) of the core samples showing the abundances of the particulate organic matter components. MAR = Marine palynomorphs; AOM = Amorphous organic matter; PHY = Structured and degraded phytoclasts; OPA =

Opales; and TER = terrestrial/nonmarine palynomorphs. Three palynofacies assemblages, each with two subgroups A and B, are recognized; I = Nonmarine, primarily terrestrially dominated, II = Mixed terrestrial and marine, and III = Marine dominated

that accompanied the high rate of sedimentation in southwestern Africa during the mid-Cretaceous (Dingle & Hendry, 1984) was likely the result of increased topography along the coast, where sedimentation outpaced the rate of accommodation space created in the basin by rifting, and higher global sea levels related to glacioeustasy (An et al., 2017; Gréselle et al., 2008; Miller et al. 2008). The absence of bioturbation except in well K-A2 provides additional evidence of a higher sedimentation rate and changing water conditions related to fluctuations in sea level (Tonkin, 2012). Sea level rise is also documented by the carbonaceous streaks, marine algal fragments, and calcareous cement in the sandstone beds in wells K-H1 and K-A2 and the upper portion of well K-A3. However, the presence of pyrite crystals (Table 1) in the samples, in addition to the high amounts of AOM (well K-E1) and few marine microfossils (Fig. 11), suggest low depositional energy and reducing

conditions with a high potential for preservation of organic material (Tyson, 1995; Zobaa et al., 2011, 2013). Since some pyritized foraminiferal tests and pyritized particulate organic matter were also recovered, the pyrite crystals may be early diagenetic in origin.

Palynofacies analysis also provides information about the type of kerogen and depositional environment. While two ternary plots of particulate organic matter both provide this information, Fig. 4b (following El Beialy et al., 2016) with palynofacies assemblages I, II, and III delineated provides more accurate data with respect to the origins of the particulate organic matter than Fig. 4a (following Tyson, 1995; see discussion in Sect. 5.3). MAOM represents the redox state at the time of deposition, while the combination of phytoclasts and nonmarine palynomorphs reflects terrestrial and nonmarine aquatic input. Additionally, the relationship between marine palynomorphs and MAOM provides a

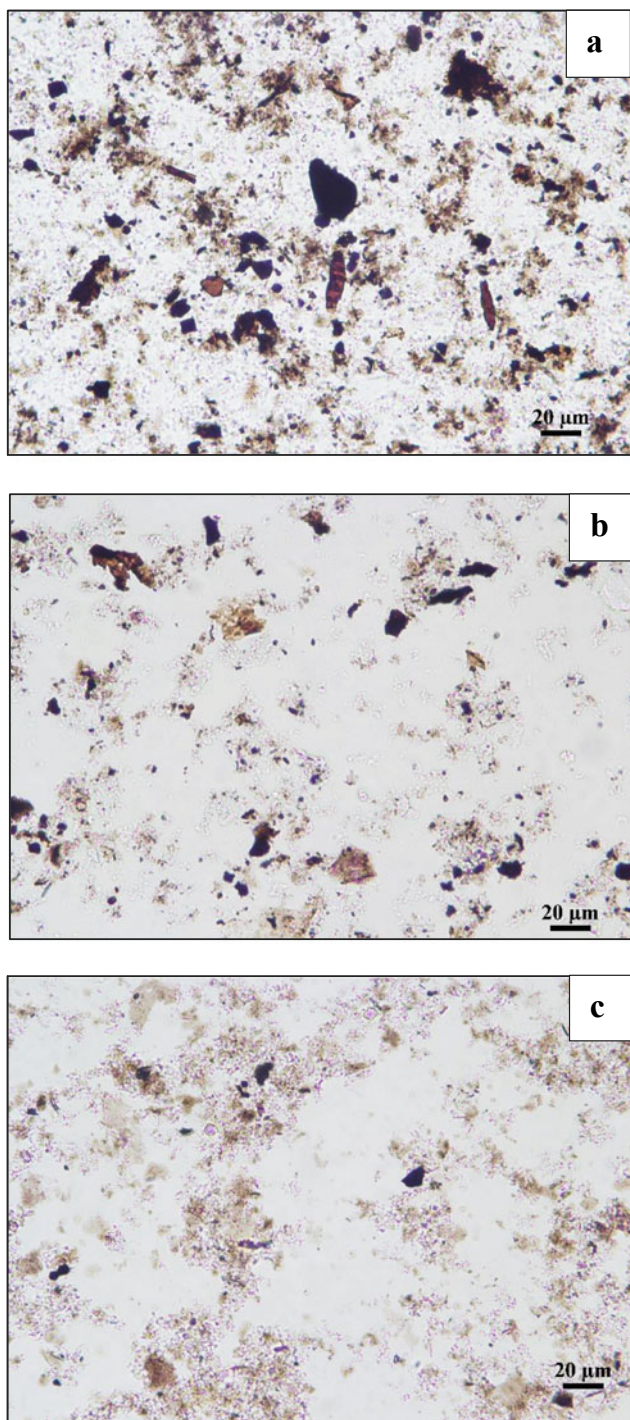


**Fig. 12** Photomicrographs of representative palynofacies assemblages. Well sample numbers are noted. EF = England Finder® coordinates. Scale bar is 20 µm. **a** Palynofacies assemblage I with primarily nonmarine organic components; well K-E1 3752.85D, EF 6GH. **b** Palynofacies assemblage II with mixed terrestrial and marine organic components; well K-H1 3079.85B, EF 2JK. **c** Palynofacies assemblage III with mainly marine organic components; well K-A2 4082.50A, EF K29

proxy for the distance between the basin and the paleo-shoreline (El Beialy et al., 2016; Tyson, 1993, 1995).

The appearance of preserved AOM can be related to its origin and how it is preserved, with its abundance in sediments attributed to an increase in paleoproductivity (Powell et al., 1990, 1992). Granular AOM is likely representative of benthic microbial mats (Emmings et al., 2019; Ercegovac & Kostic, 2006; Lückge et al., 1999; Paction et al., 2007, 2011) and may have been transported via flooding, turbidites, debris flows, bottom currents, or coastal upwelling (Emmings et al., 2019; Tyson, 1995). Additionally, the shapes and sizes of opaque particles yield information about their distance from the source. According to Tyson (1995), relatively high ratios of equidimensional to lath-shaped opaque particles (Table 2) typically represent a short distance of transport from source where the equidimensional particles have the largest sizes. In this study, the lath-shaped particles are larger (10–150 µm length for longest axis) compared to the equidimensional particles (2–50 µm length for longest axis), suggesting a longer transport distance for the terrestrial material. The type and appearance of particulate organic matter components and their abundances support transport and deposition on a continental shelf.

Palynofacies assemblages II (largest with samples from all four wells) and III (mainly K-A2 samples) are characterized by a mixed marine (>40% MAOM)/nonmarine components and preponderance (>60%) of MAOM, respectively. Foraminiferal test linings are present in some intervals. Assemblages II and III plot in the proximal suboxic-anoxic shelf (VI) and distal suboxic-anoxic basin (IX) fields, respectively, in Fig. 4. Although nonmarine (terrestrial/aquatic) organic components (Fig. 11, Table 2) dominate palynofacies assemblage I (with fewest samples from all four wells), MAOM comprises 20–40% of the total organic material, and the assemblage plots in the marginal dysoxic-anoxic basin field (II). The presence of insect parts, cuticles, and tracheids also supports this continental contribution to the basin (Table 1).

Detailed palynomorph analysis provides information about the source areas from which the spores, pollen grains, and algae were derived. The few palynomorph taxa recovered in this study, including the gymnosperm *Classopollis* sp., the pteridophytes *Deltoidospora* sp., *Cicatricasporites* sp., and *Cyatheacidites* sp., the bryophytes *Interlobites* sp. and *Taurocusporites* sp., the nonmarine algae *Chomotriletes* sp. and *Balmeisporites* sp., as well as fungal remains, are typically found in coastal environments (e.g., fluvial and deltaic) with arid hinterlands (Carvalho et al., 2017; El-Soughier 2014). Due to the configuration of the continents during the Cretaceous, the climate on the

continental interior from which these palynomorphs originated was likely arid (Scotese, 2002) with sparse vegetation (El Beialy et al., 2016). The recovered gymnosperms *Ephedripites* sp. and *Classopollis* sp. are associated with dry to semi-arid coastal environments and support this scenario (Schränk, 2010; Srivastava, 1976; Warny et al., 2019). It is possible that the absence or low abundances of palynomorphs in samples may reflect a dilution effect of abundant MAOM and phytoclasts, or the aridity and sparse vegetation in the hinterland.

The dominance of benthic agglutinated-walled foraminifera in this study is an enigma, particularly because forms such as *Ammobaculites* spp., *Trochamina* sp., and *Haplophragmodies* sp. are indicative of low salinity and low pH. They also suggest a short distance of transport since the agglutinated forms do not fare well with travel (McMillan, 2008). The agglutinated taxa provide additional support for a possible coastal or marginal marine interpretation. For example, *Ammobaculites* spp., *Haplophragmoides* sp., *Reophax* sp., and *Trochaminna* sp. are associated with hypoxic waters, and *Ammodiscus* sp. and *Glomospira* sp. are typically found in brackish delta plain and estuaries (Nagy et al., 2010). Although *Ammodiscus* and *Trochaminna* and other benthic taxa may adapt to periods of hypoxia, lower salinity, and disruption by storms in restricted marine shelf environments with deltaic influence (Nagy et al., 2010), some authors (e.g., Stevenson & McMillan, 2004) explain their presence as due to river-incised fill. Note that the presence of the calcareous benthic foraminifera *Lenticulina angulosa* and *Lenticulina* cf. *nodosa*, and the planktonic species *Rotalipora appenninica* and *Rotalipora gandolfi* in well K-H1 is consistent with fully marine, inner to middle shelf conditions.

The foregoing discussion, based on the lithology of the studied intervals in the four wells, the palynofacies, palynomorph, and foraminifera data from the studied samples, and the available information on mid-Cretaceous sediments elsewhere in the Orange Basin (e.g., Campher et al., 2009; Kuhlmann et al., 2010) suggests that the sediments were likely deposited in a highly dynamic shallow marine (inner shelf to middle shelf) paleoenvironment. This paleoenvironment experienced fluctuations in depositional energy and redox conditions, periodic continental runoff, and episodes of low salinity. Sedimentary structures, such as flaser and wavy laminations, support the deposition of the sediments in wells K-A2, K-A3, and K-E1 in the very shallow shelf closest to the Walvis Ridge. Sediments in well K-H1, which was farther from the Ridge, were deposited under more open marine (inner to middle shelf) conditions. Warm temperate to subtropical, semi-arid climate was prevalent in the hinterland.

### 5.3 Hydrocarbon Potential

The character of the particulate organic matter (kerogen I-IV) is depicted in Fig. 4, ranging from Type-I kerogen which is reflective of a marine origin and rich in MAOM and marine palynomorphs, to Type-IV kerogen which dominates terrestrially-derived (nonmarine) sediments. The positions of the samples characterizing the three palynofacies assemblages (see Figs. 11 and 12) in Fig. 4 were used to infer the types of kerogen and hydrocarbon potential. Palynofacies I has the potential to produce Type-III kerogen, which is gas prone, whereas palynofacies assemblage II is characterized by types II-III kerogen given its mixed nature, which are oil-gas prone. Palynofacies assemblage III has the potential to produce Type-I/II kerogen, and the components are highly oil-prone.

While this paleoenvironment has the potential to produce Types-II and -III kerogen, there appears to be very low primary productivity of organic matter in the water column. The low abundances of palynomorphs and foraminifera support this inference, which, together with the presence of pyrite crystals and pyritized microfossils, may also be indicative of conditions of lower salinity, lower levels of oxygenation and/or thermal maturity of sediments (Gupta & Machain-Castillo, 1993; Zobaa et al., 2011). We used the color of *Classopollis* spp., the most common palynomorph species in Types-II and -III kerogen samples to infer a thermal alteration index (TAI) of around 3. Although a preponderance of terrestrially-derived organic material and palynomorphs indicate a greater likelihood to produce gas rather than oil (Kandiyoti et al., 2006; Vandembroucke & Largeau, 2007), the low abundance of palynomorphs in these sediments belies the potential for hydrocarbon. We note here that Kuhlmann et al. (2010) used lithological interpretations of Cenomanian to Turonian outer shelf sediments in nearby blocks in the southern Orange Basin to infer gas-prone source rocks. Cole (2021) notes slightly higher productivity in well K-H1, but reports values of < 2% TOC and < 100–150 HC/g TOC HI for wells K-E1 and K-H1 with limited gas potential, irrespective of the maturity for either well. His results confirm the low potential inferred from palynological results.

## 6 Conclusions

Integrated lithology and biostratigraphy of wells K-A2, K-A3, K-H1, and K-E1 provides key information for the interpretation of this complex area within the Orange Basin. Data from terrestrial and marine palynomorphs, benthic and planktonic foraminifera, and other organic material constrain

the age and depositional conditions of this marginal marine setting with evidence of a reducing and arid nature and an inner to middle shelf transition during the early Cenomanian (based on the planktonic foraminifera *Rotalipora appenninica* and *Rotalipora gandolfi*). Additionally, this information provides insight into the hydrocarbon potential and primary productivity of organic matter, revealing the potential for Type-II and -III kerogen, albeit low productivity.

**Acknowledgements** The samples studied for this project were provided by PetroSA. We especially thank Dr. Mohamed Zobaa (University of Texas of the Permian Basin) for assisting with the taxonomic identification of palynomorphs. We also thank Dr. Annette Götz (Landesamt für Bergbau, Energie und Geologie) and an anonymous reviewer for their insightful comments which improved the quality of this paper. Funding provided by the Geoscience and Geological and Petroleum Engineering Department at Missouri University of Science and Technology, the Department of Earth Science at the University of the Western Cape, and the University of Missouri South African Education Program are gratefully acknowledged.

## References


- Adekola, S. A., Akinlua, A., Fadiya, S. L., Fajemila, O. T., & Ugwu, G. C. (2014). Palynological and paleoenvironmental analyses of selected shale samples based on terrestrial palynomorphs from two wells in the offshore Orange Basin of South Africa. *Ife Journal of Science*, 16(1), 44–59.
- Adekola, S. A., Akinlua, A., & Mangelsdorf, K. (2012). Organic geochemical evaluation of Cretaceous shale samples from the Orange Basin, South Africa. *Applied Geochemistry*, 27, 1633–1644.
- An, K., Chen, H., Lin, X., Wang, F., Yang, S., Wen, Z., Wang, Z., Zhang, G., & Tong, X. (2017). Major transgression during Late Cretaceous constrained by basin sediments in Northern Africa: Implication for global rise in sea level. *Frontiers of Earth Science*, 11, 740–750.
- Baby, G., Guillocheau, F., Braun, J., Robin, C., & Dall'Asta, M. (2020). Solid sedimentation rates history of the Southern African continental margins: Implications for the uplift history of the South African Plateau. *Terra Nova*, 32, 53–65.
- Bamford, M. K., & Corbett, I. B. (1994). Fossil wood of Cretaceous age from the Namaqualand continental shelf, South Africa. *Palaeontologia Africana*, 31, 83–95.
- Bamford, M. K., & Corbett, I. B. (1995). More fossil wood from the Namaqualand coast, South Africa: Onshore material. *Palaeontologia Africana*, 32, 67–74.
- Benson, J. M. (1990). Palynofacies characteristics and palynological source rock assessment of the Cretaceous sediments of the northern Orange Basin (Kudu 9A–2 and 9A–3 boreholes). *Communications of the Geological Survey of Namibia*, 6, 31–39.
- Boucot, A., Xu, C., & Scotese, C. (2013). Phanerozoic Paleoclimate: An atlas of lithologic indicators of climate. In G.J. Nichols & B. Ricketts (Eds.), *Concepts in sedimentology and paleontology, SEPM (Society for Sedimentary Geology)* (Vol. 11:478).
- Brown, L. F., Brown, L. F., Jr., Benson, J. M., Brink, G. J., Doherty, S., Jollands, A., Jungslager, E. H. A., Keenan, J. H. G., Muntingh, A., & Van Wyk, N. J. S. (1996). Sequence stratigraphy in offshore South Africa divergent basins. An Atlas on exploration for Cretaceous Lowstand Traps. *AAPG Studies in Geology*, 41, 138–184.
- Brownfield, M. E. (2016). Assessment of undiscovered oil and gas resources of the Orange River Coastal Province, southwest Africa. In M. E. Brownfield (Eds.), *Geologic assessment of undiscovered hydrocarbon resources of Sub-Saharan Africa, U.S. Geological Survey Digital Data Series 69–GG* (Vol. 8:14).
- Campher, C. (2009). *Geological modeling of the offshore Orange Basin, west coast of South Africa* (M.Sc. thesis). University of the Western Cape, Cape Town, South Africa.
- Campher, C. J., di Primio, R., Kuhlmann, G., van der Spuy, D., & Domoney, R. (2009). Geological modeling of the offshore Orange Basin, west coast of South America. *American Association of Petroleum Geologists Search and Discovery*, 10191, 1–5.
- Caron, M. (1985). Cretaceous planktic foraminifera. In H. M. Bolli, J. B. Saunders, & K. Perch-Nielsen (Eds.), *Plankton stratigraphy* (pp. 17–86). Cambridge University Press.
- Carvalho, M. A., Lana, C. C., Bengtson, P., & Sá, N. P. (2017). Late Aptian (Cretaceous) climate changes in Northeastern Brazil: A reconstruction based on indicator species analysis (IndVal). *Palaeogeography, Palaeoclimatology, Palaeoecology*, 485, 543–560.
- Cole, G. (2021). Orange Basin petroleum geochemistry and 3D modeling 2021. *ResearchGate*. <https://doi.org/10.13140/RG.2.2.23315.20000>
- Daidu, F., Yuan, W., & Min, L. (2013). Classifications, sedimentary features and facies associations of tidal flats. *Journal of Palaeogeography*, 2(1), 66–80.
- Davey, R. (1978). Marine cretaceous palynology of site 361, DSDP Leg 40, off Southwestern Africa. In H.M. Bolli & W.B.F. Ryan (Eds.), *Initial reports of the deep sea drilling Project, Leg 40* (pp. 889–913). Ocean Drilling Program.
- Davey, R. J., & Rogers, J. (1975). Palynomorph distribution in recent offshore sediments along two traverses off South West Africa. *Marine Geology*, 18(4), 213–225.
- De Villiers, S. E., & Cadman, A. (2001). An analysis of the palynomorphs obtained from Tertiary sediments at Koingnaas, Namaqualand, South Africa. *Journal of African Earth Sciences*, 33, 17–47.
- Dingle, R. V., & Hendy, Q. B. (1984). Late Mesozoic and Tertiary sediment supply to the Eastern Cape Basin (SE Atlantic) and palaeodrainage systems in Southwestern Africa. *Marine Geology*, 56, 13–26.
- El Beialy, S. Y., Zobaa, M. K., & Taha, A. A. (2016). Depositional paleoenvironment and hydrocarbon source potential of the Oligocene Dabaa formation, North Western Desert, Egypt: A palynofacies approach. *Geosphere*, 12(1), 346–353.
- El-Soughier, M. I. (2014). Palynology and palynofacies of the Upper Cretaceous succession of the El-Noor-IX borehole, Northwestern Egypt. *Arabian Journal Geosciences*, 7, 1297–1311.
- Emmings, J. F., Hennissen, J. A. I., Stephenson, M. H., Poulton, S. W., Vane, C. H., Davies, S. J., Leng, M. J., Lamb, A., & Moss-Hayes, V. (2019). Controls on amorphous organic matter type and sulphurization in a Mississippian black shale. *Review of Palaeobotany and Palynology*, 268, 1–18.
- Ercegovac, M., & Kostic, A. (2006). Organic facies and palynofacies: Nomenclature, classification and applicability for petroleum source rock evaluation. *International Journal of Coal Geology*, 68, 70–78.
- Feldmann, R., Chapman, R., & Hannibal, J. (1989). *Paleotechniques*. The Paleontological Society Special Publication No. 4, 5 p.
- Fensome, R. A., Williams, G. L., & MacRae, R. A. (2019). The Lentin and Williams Index of fossil dinoflagellates. AASP Contributions Series No. 50, 1173 p.
- Fischer, M., & Uenzelmann-Neben, G. (2018). Late Cretaceous onset of current controlled sedimentation in the African-Southern Ocean gateway. *Marine Geology*, 395, 380–396.
- Fossilworks, Gateway to the Paleobiology Database. <http://fossilworks.org/bridge.pl?a=home>. Accessed January 4, 2021.
- Frederiksen, N. O., Bybell, L. M., Christopher, R. A., Crone, A. J., Edwards, L. E., Gibson, T. G., Hazel, J. E., Repetski, J. E., Russ, D.

- P., Smith, C. C., & Ward, L. W. (1982). Biostratigraphy and paleoecology of lower Paleozoic, Upper Cretaceous, and lower Tertiary rocks in U.S. Geological Survey New Madrid test wells, Southeastern Missouri. *Tulane Studies in Geology and Paleontology*, 17, 23–45.
- Gallagher, K., & Brown, R. W. (1999). The denudation history of the Atlantic Margins of southern Africa and south-east Brazil and their relationship to offshore sedimentation. In N. Cameron (Ed.), *Oil and gas habitats of the South Atlantic Special Publication* (Vol. 357). Geological Society of London, The Royal Society.
- Gordon, W. (1973). Marine life and ocean surface currents in the cretaceous. *The Journal of Geology*, 81(3), 269–284.
- Green, O. R. (2001). Staining techniques used in micropalaeontology. *A manual of practical laboratory and field techniques in palaeobiology* (pp. 211–218). Springer.
- Gréselle, B., Pittet, B., & Reboulet, S. (2008). Glacio-eustasy in the Valanginian—Early Cretaceous: Evidence from the peri-voncontian zone (SE France). EGU General Assembly, Geophysical Research Abstracts 10: EGU2008-A-01039.
- Guiry, M. D., & Guiry, G. M. (2021) *AlgaeBase*. World-wide electronic publication, National University of Ireland, Galway. <https://www.algaebase.org>. Accessed January 4, 2021.
- Gupta, B. K., & Machain-Castillo, M. L. (1993). Benthic foraminifera in oxygen-poor habitats. *Marine Micropaleontology*, 20(3–4), 183–201.
- Harris, A., & Sweet, W. (1989). Mechanical and chemical techniques for separating microfossils from rock, sediment, and residue matrix. *The Paleontological Society Special Publications*, 4(1), 70–86.
- Ibrahim, M. I. A., Zobia, M. K., El-Noamani, Z. M., & Tahoun, S. S. (2015). A review of the angiosperm pollen genus *Cretaceaeporites* Hergreen, with one new species from the Upper Cretaceous of Egypt. *Palynology*, 41(1), 101–116.
- Jansonius, J., & Hills, L. V. (1976). Genera file of fossil spores and pollen (with supplements). Special Publication, Department of Geology, University of Calgary, Canada.
- Jaramillo, C., & Rueda, M. (2019). A morphological electronic database of cretaceous-tertiary and extant pollen and spores from Northern South America, v. 2019. <https://biogeodb.strsi.edu/jaramillosdb/web/morphological/>. Accessed January 4, 2021.
- Jungslager, E. H. A. (1999). Petroleum habitats of the Atlantic margin of South Africa. *Geological Society, London, Special Publications*, 153, 153–168.
- Kandiyoti, R., Herod, A. A., & Bartle, K. (2006). *Solid fuels and heavy hydrocarbon liquids: Thermal characterisation and analysis*. Energy, Elsevier.
- Khalifa, M. A., & Catuneanu, O. (2008). Sedimentology of the fluvial and fluvio-marine facies of the Bahariya Formation (Early Cenomanian), Bahariya Oasis, Western Desert, Egypt. *Journal of African Earth Sciences*, 51(2), 89–103.
- Kuhlmann, G., Adams, S., Campher, C., van der Spuy, D., di Primio, R., & Horsfield, B. (2010). Passive margin evolution and its controls on natural gas leakage in the southern Orange Basin, blocks 3/4, offshore South Africa. *Marine and Petroleum Geology*, 27(4), 973–992.
- Kummel, B., & Raup, D. (1965). *Handbook of paleontological techniques*. WH Freeman and Co.
- Legler, B., Hampson, G. J., Jackson, C. A.-L., Johnson, H. D., Massart, B. Y. J., Sarginson, M., & Ravnås, R. (2014). Facies relationships and stratigraphic architecture of distal, mixed tide- and wave-influenced deltaic deposits: Lower Sego Sandstone, Western Colorado, U.S.A. *Journal of Sedimentary Research*, 84(8), 605–625.
- Lückge, A., Ercegovac, M., Strauss, H., & Littke, R. (1999). Early diagenetic alteration of organic matter by sulfate reduction in Quaternary sediments from the Northeastern Arabian Sea. *Marine Geology*, 158, 1–13.
- McLachlan, I. R., & Pieterse, E. (1978). Preliminary palynological results deep sea drilling project, initial reports, U.S. *Government Print Office, Washington*, 40, 857–881.
- McMillan, I. K. (2003). Foraminifera defined biostratigraphic episodes and sedimentation pattern of the Cretaceous drift succession (Early Barremian to Late Maastrichtian) in seven basins on the South African and southern Namibian continental margin. *South African Journal of Science*, 99, 537–576.
- McMillan, I. K. (2008). Aragonitic-walled benthic foraminifera (*E. pistomina*) in the Cretaceous ‘mud belt’ off southern Africa, and postmortem cross-shelf transport of tests. *African Natural History*, 4, 17–24.
- Miller, K. G., Sugarman, P. J., Browning, J. V., Kominz, M. A., Hernández, J. C., Olsson, R. K., Wright, J. D., Feigenson, M. D., & Van Sickle, W. (2008). Late Cretaceous chronology of large, rapid sea-level changes: Glacioeustasy during the greenhouse world. *Geology*, 31(7), 585–588.
- Muntingh, A., & Brown, Jr. L. F. (1993). Sequence stratigraphy of petroleum plays, postrift Cretaceous rocks (lower Aptian to upper Maastrichtian), Orange basin, western offshore, South Africa. In P. Weimer & H. W. Posamentier (Eds.), *Siliciclastic sequence stratigraphy—Recent developments and applications* (Vol. 58, pp. 71–97). American Association of Petroleum Geologists Memoir.
- Muntingh, A. (1993). Geology, prospect in Orange Basin offshore western South Africa. *Oil and Gas Journal*, 91, 105–109.
- Nagy, J., Hess, S., & Alve, E. (2010). Environmental significance of foraminiferal assemblages dominated by small-sized *Ammodiscus* and *Trochammina* in Triassic and Jurassic delta-influenced deposits. *Earth-Science Reviews*, 99(1–2), 31–49.
- Oboh, F. E. (1992). Middle miocene palaeoenvironments of the Niger Delta. *Palaeogeography, Palaeoclimatology, Palaeoecology*, 92, 55–84.
- Oboh-Ikuenobe, F. E., & De Villiers, S. E. (2003). Dispersed organic matter in samples from the western continental shelf of Southern Africa: Palynofacies assemblages and depositional environments of Late Cretaceous and younger sediments. *Palaeogeography, Palaeoclimatology, Palaeoecology*, 201, 67–88.
- Oboh-Ikuenobe, F. E., Obi, C. G., & Jaramillo, C. A. (2005). Lithofacies, palynofacies, and sequence stratigraphy of Paleogene strata in Southern Nigeria. *Journal of African Earth Sciences*, 41, 79–101.
- Pacton, M., Fiet, N., & Gorin, G. E. (2007). Bacterial activity and preservation of sedimentary organic matter: The role of exopolymeric substances. *Geomicrobiology Journal*, 24(7–8), 571–581.
- Pacton, M., Gorin, G. E., & Vasconcelos, C. (2011). Amorphous organic matter—Experimental data on formation and the role of microbes. *Review of Palaeobotany and Palynology*, 166(3–4), 253–267.
- Palynodata and White. (2008). *Palynological literature information collection*. Palynodata Incorporation. <https://doi.org/10.4095/225704>. Accessed January 4, 2021.
- PAST© 2001, Hammer, Ø., Harper, D. A. T., & Ryan, P. D. (2001). Past: Paleontological statistics software package for education and data analysis. *Palaeontologia Electronica*, 4:1, art. 4, 9 p., 178kb. [http://palaeo-electronica.org/2001\\_1/past/issue1\\_01.htm](http://palaeo-electronica.org/2001_1/past/issue1_01.htm). Accessed January 4, 2021.
- Paton, D. A., di Primio, R., Kuhlmann, G., van der Spuy, D., & Horsfield, B. (2007). Insights into the petroleum system evolution of the Southern Orange Basin, South Africa. *South African Journal of Geosciences*, 110, 261–274.
- Powell, A. J., Dodge, J. D., & Lewis, J. (1990). Late Neogene to Pleistocene palynological facies of the Peruvian continental margin upwelling, Leg 112. In E. Suess, R. Von Huene, et al., (Eds.), *Proceedings of the ocean drilling program, scientific results* (Vol. 112, pp. 297–321). Ocean Drilling Program, College Station.

- Powell, A. J., Lewis, J., & Dodge, J. D. (1992). The palynological expressions of post-Palaeogene upwelling: A review. In C. P. Summerhayes, W. L. Prell, & K. C. Emeis (Eds.), *Upwelling systems: Evolution since the Early Miocene* (Vol. 64(1), pp. 215–226). Geological Society Special Publication.
- Ramette, A. (2007). Multivariate analyses in microbial ecology. *FEMS Microbiology Ecology*, 62(2), 142–160. <https://doi.org/10.1111/j.1574-6941.2007.00375.x>.
- Rouby, D., Bonnet, S., Guillocheau, F., Gallagher, K., Robin, C., Bianchetto, F., & Braun, J. (2009). Sediment supply to the Orange sedimentary system over the last 150 My: An evaluation from sedimentation/denudation balance. *Marine and Petroleum Geology*, 26, 782–794.
- Salie, S. (2018). *The effects of minerals on reservoir properties in block 3A and 2C, within the Orange Basin, South Africa*. Dissertation, University of the Western Cape.
- Sandersen, A., Scott, L., McLachlan, I. R., & PJ, Hancox PJ. (2011). Cretaceous biozonation based on terrestrial palynomorphs from two wells in the offshore Orange Basin of South Africa. *Palaeontologia Africana*, 46, 21–41.
- Schrank, E. (2010). Pollen and spores from the Tendaguru beds, upper jurassic and lower cretaceous of southeast Tanzania: Palynostratigraphical and paleoecological implications. *Palynology*, 34(1), 3–42.
- Scotese, C. R. (2002). PALEOMAP Project. <http://www.scotese.com>.
- Slimani, H., Louwye, S., & Abdelkadir, T. (2010). Dinoflagellate cysts from the cretaceous-paleogene boundary at Ouled Haddou, south-eastern Rif, Morocco: Biostratigraphy, paleoenvironments and paleobiogeography. *Palynology*, 34, 90–124.
- Sokal, R. R., & Michener, C. D. (1958). A Statistical methods for evaluating relationships. *University of Kansas Science Bulletin*, 38, 1409–1448.
- Srivastava, S. K. (1976). The fossil pollen genus *Classopollis*. *Lethaia*, 9, 437–457.
- Stevenson, I. R., & McMillan, I. K. (2004). Incised valley fill stratigraphy of the upper cretaceous succession, proximal Orange Basin, Atlantic margin of southern Africa. *Journal of the Geological Society*, 161, 185–208.
- Tonkin, N. S. (2012). Trace fossils as indicators of sedimentary environments. In D. Knaust & R. G. Bromley (Eds.), *Developments in sedimentology* (Vol. 64, pp. 507–528). Elsevier.
- Traverse, A. (2007). *Palaeopalynology* (2nd ed.). Springer.
- Tyson, R. V. (1995). *Sedimentary organic matter; organic facies and palynofacies*. Chapman and Hall, London.
- Tyson, R. V. (1993). Palynofacies analysis. In D. G. Jenkins (Ed.), *Applied micropaleontology* (pp. 153–191). Kluwer Academic Publishers.
- Tyson, R. V., & Follows, B. (2000). Palynofacies prediction of distance from sediment source: A case study from the Upper Cretaceous of the Pyrenees. *Geology*, 28, 569–571.
- Van der Spuy, D. (2003). Aptian source rocks in some South African Cretaceous basins. In T. J. Arthur, D. S. Macgregor, & N. R. Cameron (Eds.), *Petroleum geology of Africa: New themes and developing technologies* (Vol. 207, pp. 185–202). Geological Society Special Publications.
- Van der Spuy, D. (2005). *Prospectivity of the Northern Orange Basin, offshore South Africa*. Poster presented at Africa Session, Forum 23, 18th World Petroleum Congress, 25–29 September, Johannesburg, South Africa.
- Vandenbroucke, M., & Largeau, C. (2007). Kerogen origin, evolution and structure. *Organic Geochemistry*, 38(5), 719–833.
- Warny, S., Jarzen, D. M., Haynes, S. J., MacLeod, K. G., & Huber, B. T. (2019). Late Cretaceous (Turonian) angiosperm pollen from Tanzania: A glimpse of past vegetation from a warmer climate. *Palynology*, 43(4), 608–620.
- Zavada, M. S. (2004). The earliest occurrence of angiosperms in Southern Africa. *South African Journal of Botany*, 70, 646–653.
- Zobaa, M. K., El Beialy, S. Y., El Sheikh, H. A., & El Beshtawy, M. K. (2013). Jurassic Cretaceous palynomorphs, palynofacies, and petroleum potential of the Sharib1X and Ghoroud1X wells, north Western Desert, Egypt. *Journal of African Earth Sciences*, 78, 51–65.
- Zobaa, M., Oboh-Ikuenobe, F., & Ibrahim, M. (2011). The Cenomanian/Turonian oceanic anoxic event in the Razzak Field, north Western Desert, Egypt: Source rock potential and paleoenvironmental association. *Marine and Petroleum Geology*, 28(8), 1475–1482.



# Palynofacies, Organic Petrography, and Source Rock Potential of the Toarcian Quse Formation Oil Shale in the Tibetan Tethys, China

Ahmed Mansour, Thomas Gentzis, Guoqing Xia, Humberto Carvajal-Ortiz, Seare Ocubalidet, Haisheng Yi, and Haytham El Atfy 

## Abstract

The southern Qiangtang Basin located in the central Tibetan Plateau of the eastern Tethys is among the most significant petroliferous provinces in China. In this chapter, lower Toarcian sediments represented by thick oil shale succession from the Bilong co area, were studied. Geochemical screening, organic petrographic, and palynological analyses were conducted to investigate kerogen characteristics, thermal maturity, and depositional environment. The Quse and Sewa formations of the study section were divided into two groups according to time of deposition and geochemical features. The first group is represented by the early Toarcian interval and deposited during prevalent anoxia with excellent organic matter richness and hydrocarbon generation potential of kerogen Type II. Amorphous organic matter (AOM) is the foremost constituent compared to the low phytoclast content. The anoxic interval of this group is consistent with the early Toarcian oceanic anoxic event (T-OAE). The second group of the upper Bajocian-Bathonian interval refers to the Sewa Formation, which is dominated by good to very good organic matter deposited

predominantly in a dysoxic environment. Organic matter comprised varied kerogen types, including IV, III, II/III, and II, and has hydrocarbon potential that varies from poor to very good. However, the majority of samples from both groups are still in the early stage of the oil window. Paleoenvironmental conditions were variable from brackish shallow marine to distal inner-neritic shelf with enhanced organic matter preservation.

## Keywords

Kerogen • Kerogen quantity • Thermal maturity • Qiangtang Basin • Toarcian anoxia

## 1 Introduction

The oceanic anoxic event that occurred during the Toarcian stage of the Early Jurassic period (T-OAE, *ca.* 183 Ma) was responsible for substantial global depositions of organic-rich sediments (Jenkyns, 2010). This is evidenced by the regional distribution of marker marine taxa, such as ammonites and nannofossils (Chen et al., 2018; Yi et al., 2003), which undoubtedly confirm a global context of a synchronous anoxic event. The Toarcian is marked by the large-scale occurrence of petroleum-bearing basins of organic matter-rich black shale and limestone, particularly in China (Chen et al., 2005; Fu et al., 2014; Ji et al., 2014; Xia et al., 2017; Yi et al., 2013). Many of the previous works have focused on the Toarcian in the eastern Tethys Tibetan Plateau employing various approaches from macro- and micro-paleontology, paleomagnetism (e.g., Ding et al., 2013; Ma et al., 2017; Wang et al., 1997, 2019), and organic petrography as well as organic geochemistry (e.g., Chen et al., 2005; Fu et al., 2014; Ji et al., 2014; Xia et al., 2017; Yi et al., 2013). However, palynofacies analysis, organic maceral composition, and organic geochemistry investigations of the upper Quse Formation in southern Qiangtang

A. Mansour  
Geology Department, Faculty of Science, Minia University,  
Minia, 61519, Egypt

T. Gentzis · H. Carvajal-Ortiz · S. Ocubalidet  
Core Laboratories, 6316 Windfern Road, Houston,  
TX 77040, USA

G. Xia · H. Yi  
State Key Laboratory of Oil and Gas Reservoir Geology  
and Exploitation, Chengdu University of Technology,  
Chengdu, 610059, China

H. El Atfy (✉)  
Department of Geosciences, University of Tübingen,  
72076 Tübingen, Germany  
e-mail: [el-atfy@daad-alumni.de](mailto:el-atfy@daad-alumni.de)

Geology Department, Faculty of Science, Mansoura University,  
Mansoura, 35516, Egypt



Basin are absent. The southern Qiangtang Basin is a giant sedimentary archive in central Tibet, which contains a well-preserved outcrop section of organic-rich Toarcian deposits (Fu et al., 2014, 2017; Yi et al., 2003). Thus, the studied basin offers a good chance to assess potential source rocks and elucidate the environment of deposition that controlled the accumulation of organic matter (OM) in the Bilong co section.

The present work focuses on the potential intervals within the topmost part of the Quse Formation in the Bilong co section that could infer source rock. Here, we present an integrated multi-proxy approach comprised of TOC, Rock-Eval pyrolysis, organic and inorganic sulfur content, organic petrography, maceral characterization, and palynofacies to investigate kerogen quantity, quality, hydrocarbon generation potential, and thermal maturity. Although this study aimed to define source rock characteristics of the organic-rich Quse Formation, palynofacies analysis provides a reliable indicator to develop a more holistic evaluation of the prevalent environment in terms of depositional settings, type, and origin of kerogen, and oxygen regime. All of these components are fully considered in this contribution and, hence, improve the limited knowledge about the less-investigated Toarcian source rock intervals and paleoenvironments of the Quse Formation, southern Qiangtang Basin.

## 2 Geological Settings

### 2.1 Structural Settings

The Qiangtang Basin covers a large area ranging from the extreme north to central parts of the Tibetan Plateau (Fig. 1a). This basin has been influenced by successive tectonic events that resulted in a tectonic jigsaw. The basin is bound by the Jinsha suture northward and the Bangong-Nujiang suture southward, which separates the Qiangtang main basinal block from the Lhasa blocks and Hoh Xil-Songpan, correspondingly (Fig. 1b; Kapp et al., 2007; Wang et al., 2014; Yin & Harrison, 2000). The main basinal block of the Qiangtang Basin (Fig. 1c) was investigated recently. Structural data showed that the block can be subdivided into the North and South Qiangtang blocks, which are detached by Longmu Co-Shuanghu Suture Zone (LSSZ) trending toward the NWW (Fang et al., 2016). The LSSZ presents the central uplift belt. The aforementioned three suture zones that bound the Qiangtang blocks were shaped as a result of the consecutive tectonic activities of the Tethys from the Permian to the Jurassic (e.g., Ding et al., 2013; Wang et al., 1997, 2019).

In the Early Permian, strong tectonic activity resulted in the separation of the main Qiangtang Basin from eastern

Gondwana (Zhu et al., 2013). This setting contributed to further subsidence of the Qiangtang Basin, which submerged under the sea as an epicontinental shelf environment (Wang et al., 2004). Subsequently, in the Late Triassic, a fast-northward drifting resulted in a strong collision with the Hoh Xil-Songpan Block, creating a syn-tectonically foreland basin to the south of the Hoh Xil-Songpan and a thrust-fold belt system along the northern edge of the Qiangtang Basin (Li et al., 2002). Since the Early Jurassic, the paleogeographic position of the Qiangtang basinal block was at mid-paleolatitudes in the northeastern portion of the Tethys, where a hemipelagic shelf to open-ocean marine circumstances prevailed (Wang et al., 2004). This was followed by a westward collision up to the Early Cretaceous between the Qiangtang Basin and the Lhasa Block, creating yet another syn-tectonic thrust-fold and foreland basin over the Bangong-Nujiang suture. Additionally, these settings triggered a consequent closing of the Meso-Tethys due to a westward retreat of the Qiangtang Basin and thus, the termination of the Jurassic seaway that was followed by strong uplifting and erosion of the adjoining areas (Li et al., 2002; Sengör, 1987). The consecutive activity of subduction at the oceanic plate margins of the Neo-Tethys along with strong collisions of the Neo-Tethyan arcs and India with the Lhasa High did not result in tectonic configuration changes of the Qiangtang, but only minor intra-block basins were developed and have been filled with erosional red beds at sutures and fault zones during periods of active tectonic uplift, which resulted in shaping the Qiangtang Basin to its present position (Fang et al., 2016).

### 2.2 Stratigraphic Framework

The surface outcrop of the southern Qiangtang Basin contains a thick stratigraphic section that averages more than 5000 m in thickness. The southern Qiangtang Basin includes marine strata that represent, from older to younger, the Lower Jurassic Quse, Middle Jurassic Sewa, Buqu, Xiali, and the Upper Jurassic Suowa formations, which are synchronous to the equivalent rock units in the adjoining northern Qiangtang Basin (Chen et al., 2018; Ding et al., 2013; Li, 2016; Ma et al., 2017; Wang et al., 1997, 2019). The Toarcian strata are thought to be represented in the Quse Formation, which overlies the Triassic shale and limestone (Fig. 2). This is based on age-diagnostic ammonites of a typical Early Jurassic, including *Schlotheimiidae* sp. and *Hildoceratacaea* sp. (Su et al., 2015; Yi et al., 2003). The upper interval of the Quse Formation comprises black limestone and oil shale along with thick marl and calcareous mudstone (Fig. 3). The OM-rich shale and limestone are restricted only to the Quse and Sewa rock units within the Bilong co region (Fig. 2).

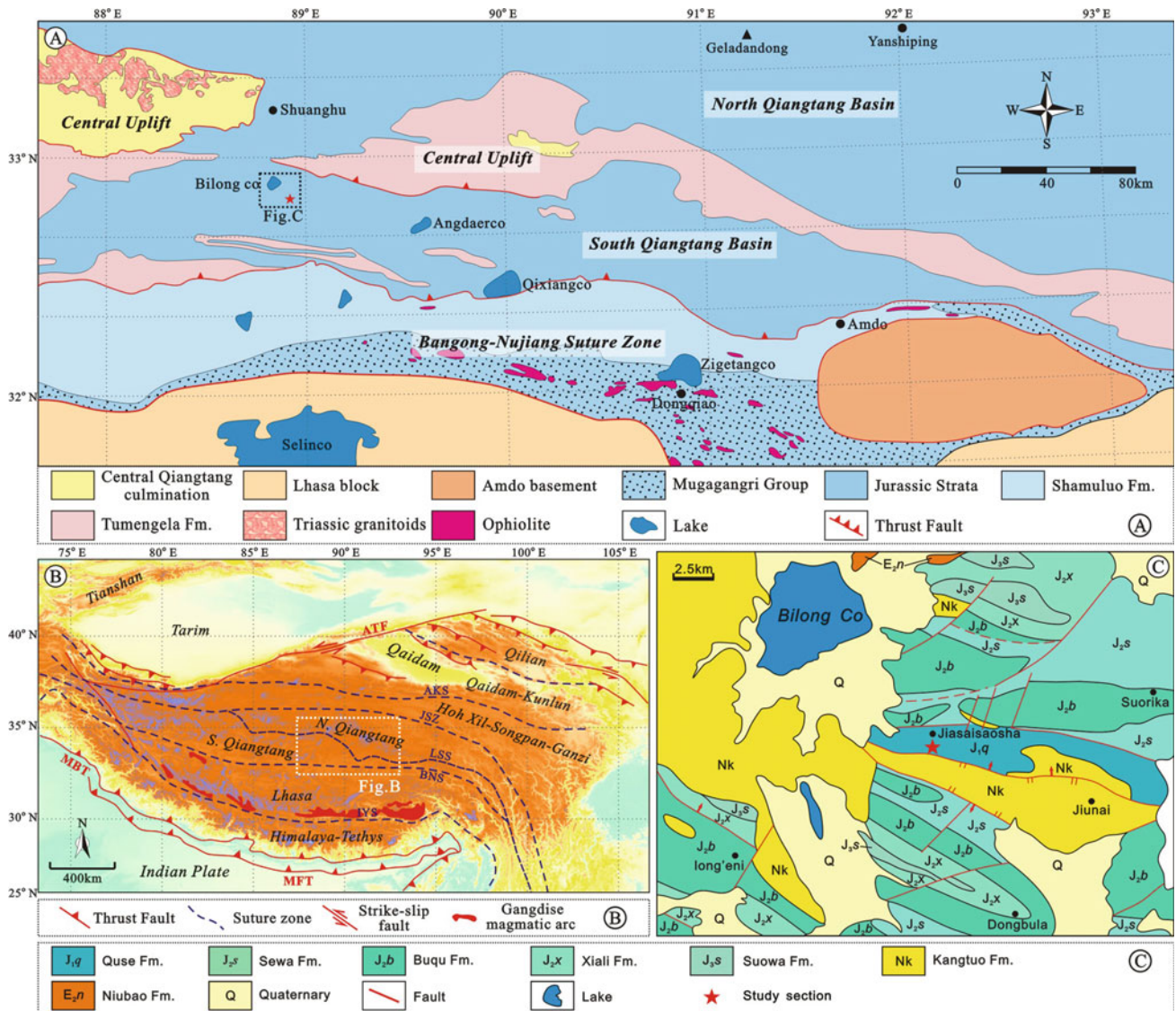


**Fig. 1** (a) Geological map of the Qiangtang basin (modified after Ma et al., 2017) showing the Bilong co area. (b) Tectonic map of the Tibetan Plateau showing the southern Qiangtang Basin and adjacent regions, ATF = Altn Tagh Fault, AKS = Anemaqen-Kunlun Suture, JSZ = Jinsha Suture Zone, LSS = Longmu Co-Shuanghu Suture, BNS = Bangong-Nujiang Suture, IYS = Indus-Yarlung Suture, MFT = Main Front Thrust, and MBT = Main Boundary Thrust. (c) Simplified geological map of the Bilongco region in the southern Qiangtang basin and location of the study section (modified from Wang et al., 2012)

The Bajocian-Bathonian Sewa Formation overlies the Quse Formation and consisted of limestone, gray marl, and mudstone facies (Yin & Chandler, 2016). The Buqu Formation is dominated by carbonate platforms rich in brachiopods *Holcothyris-Burmhirhynchia*, which are diagnostic of the late Bathonian age (Yao et al., 2011). The Callovian Xiali Formation comprised mainly fine-to coarse-grained sandstone. The Suowa Formation was formed during the Oxfordian-Kimmeridgian and is composed of shallow marine limestone with minor intercalations of black-gray calcareous mudstone and marlstone (Chen et al., 2018; Ma et al., 2017; Yao et al., 2011; Yi et al., 2005).

### 3 Material and Methods

The present study integrates organic petrographic and geochemical screening along with palynofacies analysis to qualitatively and quantitatively assess the hydrocarbon source potential of the Quse and Sewa formations. For this purpose, a number of 22 samples were collected from an outcrop section in the Bilong co, southern Qiangtang Basin, Tibet Plateau (Figs. 1, 2). All samples were tested for palynofacies analysis, random vitrinite reflectance (%VR<sub>o,r</sub>), as well as TOC and Rock-Eval® pyrolysis.

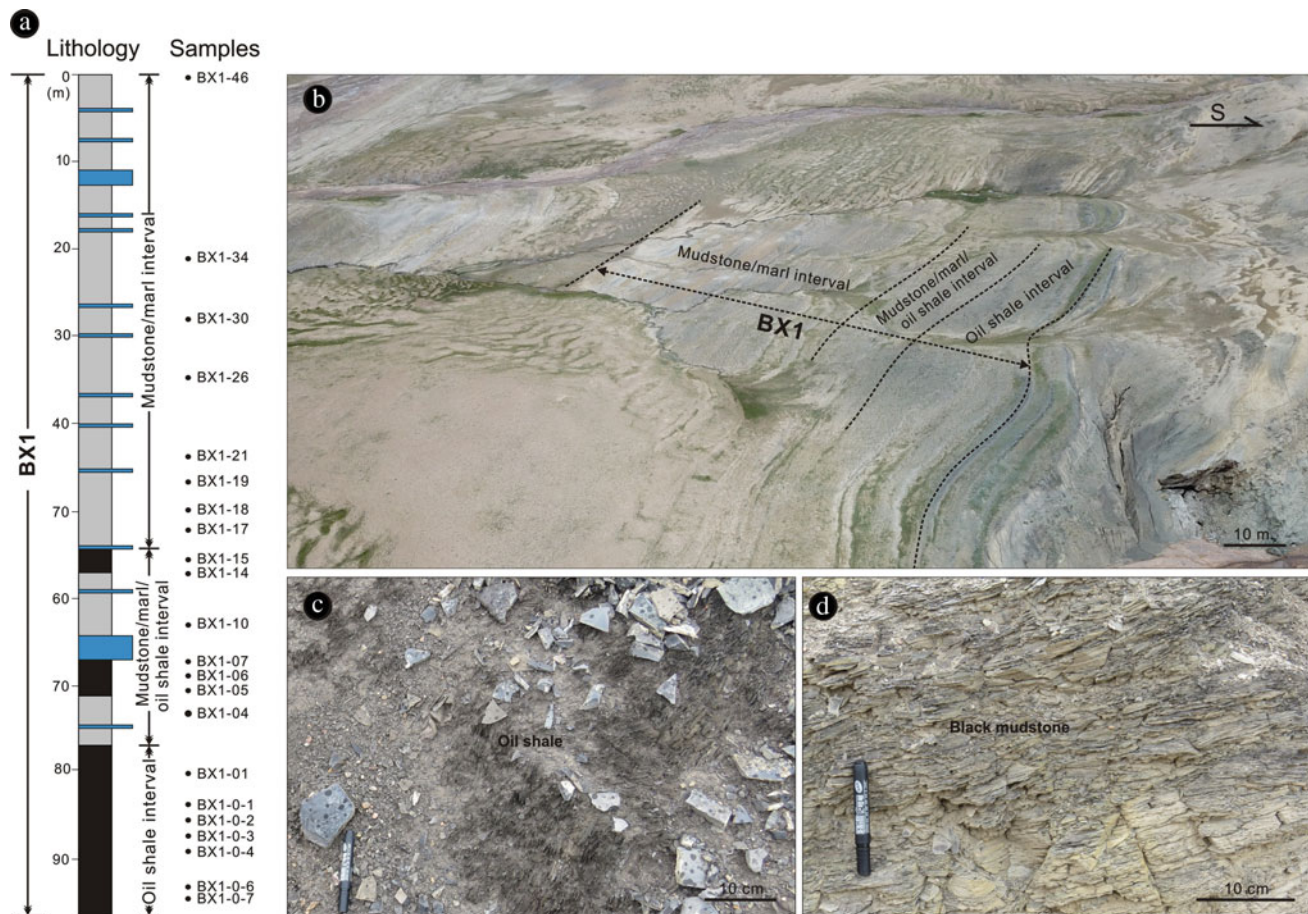


**Fig. 2** (a–d) Field photographs from the Bilong co area in the southern Qiangtang Basin illustrate the oil shales, marl, and limestone lithofacies

### 3.1 Elemental Composition, Organic Carbon, and Rock–Eval® Pyrolysis

Carbonate content was calculated from the measurement of CaO using bulk rock geochemistry analysis. 5 g of each powdered rock sample (*ca.* 0.074 mm) were soaked in a concentrated HNO<sub>3</sub> and HF acids mixture at 176–200 °C for several days. This was followed by diluting the remnant solution using deionized water to measure the major oxides (e.g., SiO<sub>2</sub>, Al<sub>2</sub>O<sub>3</sub>, CaO, MgO, FeO, Na<sub>2</sub>O, MnO, K<sub>2</sub>O, TiO<sub>2</sub>, and P<sub>2</sub>O<sub>5</sub>) using X-ray fluorescence. The analytical precision was well than  $\pm 0.5\%$  with a detection limit of 0.01%. The CaCO<sub>3</sub> content was calculated by multiplying the CaO values by 0.7146 to convert the measured calcium oxide into Ca, and the obtained result was then multiplied by 2.4973 to get the CaCO<sub>3</sub> content (Table 1). Elemental analysis of (bulk) rock samples was carried out in the Analytical Laboratory, Beijing Research Institute of Uranium Geology, China National Nuclear Corporation.

Total organic carbon (TOC) and Rock–Eval® pyrolysis measurements were conducted on all samples at the Core Laboratories facilities in Houston, USA. An aliquot of *circa*

60 mg from the fine powder of each pulverized sample was analyzed by an open system programmed pyrolysis (Rock–Eval® 6) instrument (Vinci Technologies, France) using the IFP’s Bulk-Rock technique for source rocks (e.g., Behar et al., 2001; Carvajal-Ortiz & Gentzis, 2015). The pyrolysis analysis was conducted in a nitrogen atmosphere, and the free hydrocarbons were detected using a flame ionization detector. An infrared cell detected the evolved gases of CO and CO<sub>2</sub>. During pyrolysis, samples were heated to 300 °C and stayed isothermally for 3 min, followed by a temperature increase to 650 °C with a steady rate of 25 °C/min. Pyrolysis was followed by oxidation that took place in an isolated oven. Rock–Eval pyrolysis provides a group of essential parameters, including TOC (wt%), S<sub>1</sub> (free hydrocarbons produced without cracking of kerogen, in mg HC/g rock), S<sub>2</sub> (thermally-cracked hydrocarbons at pyrolysis temperatures of 300–600 °C, same units as S<sub>1</sub>), S<sub>3</sub> (released CO and CO<sub>2</sub> due to thermal cracking of kerogen, in mg CO<sub>2</sub>/g rock), S<sub>4</sub> (residual carbon content, mg C/g rock), and S<sub>5</sub> (mineral carbon and can be used to calculate carbonate content of samples, mg CO<sub>2</sub>/g rock), and T<sub>max</sub> (the temperature at which maximum hydrocarbon released (S<sub>2</sub>))

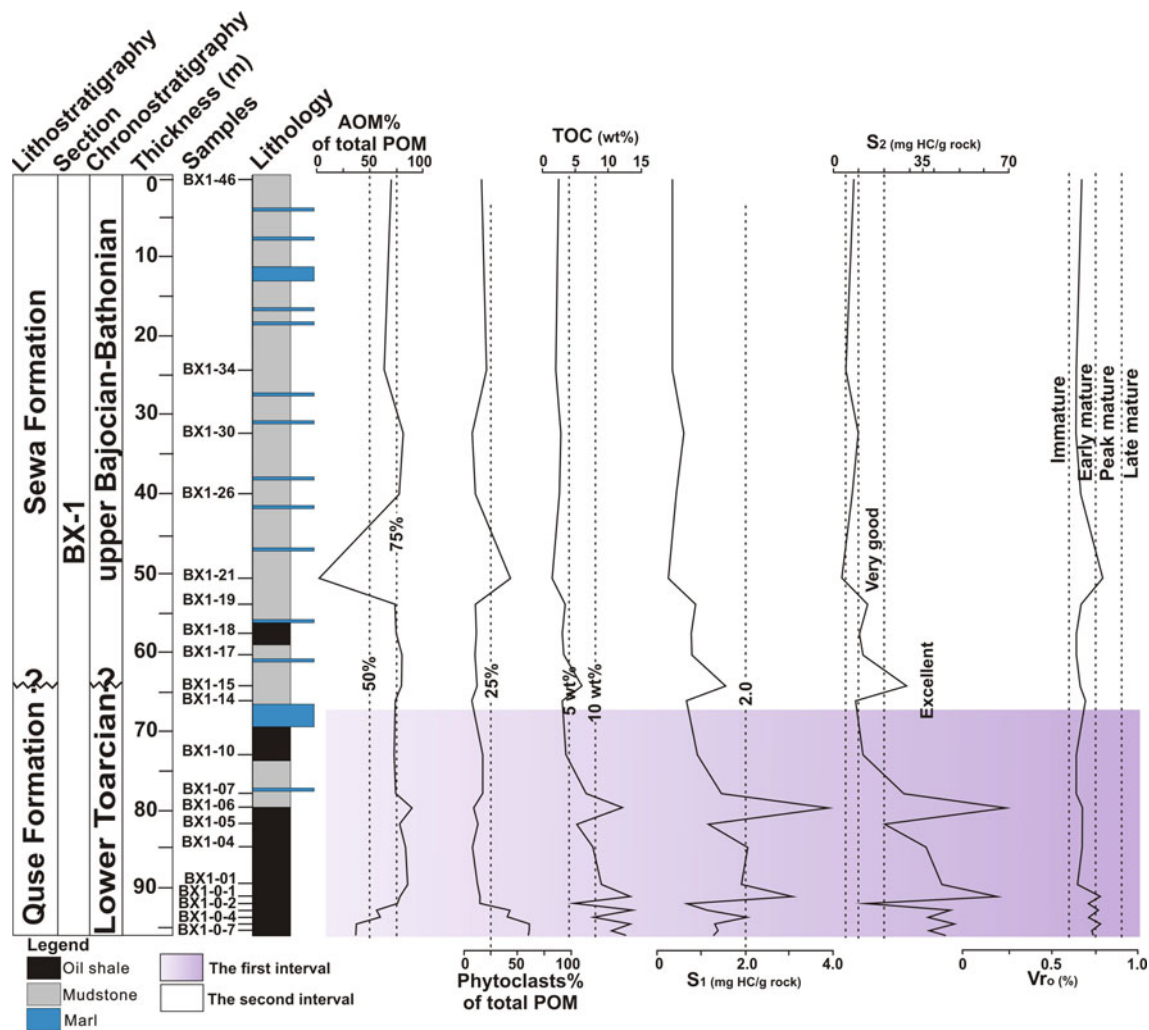


**Fig. 3** Stratigraphic distribution of the TOC/Rock–Eval pyrolysis parameters, vitrinite reflectance, as well as AOM and phytoclast contents from the upper part of the Quse Formation in the Bilong co section

during kerogen cracking, °C). Parameters such as hydrogen index ( $HI = (S_2/TOC) \times 100$ , mg HC/g TOC), oxygen index ( $OI = (S_3/TOC) \times 100$ , mg CO<sub>2</sub>/g TOC), and production index [ $PI = S_1/(S_1 + S_2)$ ] were deduced from the above-mentioned readings.

### 3.2 Sulfur Analysis

The organic sulfur proportions bounded in sedimentary OM significantly impact the source rock kinetics and consequently, thermal maturity of OM. Thus, Rock–Eval 7S® was employed to quantify the total sulfur (TS, organic, and inorganic) and to identify and quantify the sulfur species in five samples selected based on the highest TOC and S<sub>2</sub> contents. Rock–Eval 7S® has an additional oven, where sulfur compounds are converted into SO<sub>2</sub> at 900–1200 °C. SO<sub>2</sub> released during pyrolysis and oxidization is detected and measured in real time by a UV detector, followed by calculation of various

parameters, including S<sub>1</sub> S<sub>org</sub>, S<sub>2</sub> S<sub>org</sub>, residual sulfur, retained sulfur, and sulfate sulfur as well as pyritic sulfur. The basic/total sulfur IFP methodology was utilized to implement the sulfur speciation analysis. The temperature program is alike to the Basic/Bulk–Rock method that is widely applicable for source rocks exploration. It initiates at 300 °C and retains isothermally for 3 min., followed by a gradual increase of 25 °C/min. ramp until 650 °C, but with a prolonged analysis period throughout the oxidation phase (with a 20 °C/min ramp from 300 °C to 1200 °C for the complete decay of sulfate moieties). For further particulars of sulfur measurements, see Lamoureux-Var et al. (2019).

### 3.3 Organic Petrography

All samples collected from the Quse and Sewa formations were prepared for organic petrography using the whole-rock method and crushed into ca. 840 μm (–20 mesh) and

**Table 1** Organic geochemical data of TOC/Rock–Eval Pyrolysis and vitrinite reflectance along with distribution of POM composition throughout the studied succession of the Quse Formation from the southern Qiangtang Basin

Sample	CaCO <sub>3</sub> (%)	TOC (wt %)	S <sub>total</sub> (wt %)	S <sub>1</sub> (mg HC/g rock)	S <sub>2</sub> (mg HC/g rock)	S <sub>3</sub> (mg HC/g CO <sub>2</sub> )	T <sub>max</sub> (°C)	V <sub>Ro</sub> (%)	HI	OI	PI	AOM	Palynomorphs	Phytoclasts	Kerogen types
BX1-46	34.8	2.49		0.34	6.91	0.89	432	0.67	277.51	42.97	0.05	70	14.8	15.2	II > > I
BX1-34	31.3	2.02		0.35	5.23	0.78	430	0.64	258.91	45.54	0.06	63.4	15.8	20.8	II > > I
BX1-30	34.5	2.79		0.58	8.96	0.80	430	0.64	321.15	35.48	0.06	81	11.8	7.2	II > > I
BX1-26	28.8	2.51		0.39	6.71	1.07	432	0.67	267.33	52.19	0.05	77	12.6	10.4	II > > I
BX1-21	46.6	1.48		0.22	2.38	0.61	439	0.79	160.81	43.92	0.08	3.4	53.6	43	III > IV
BX1-19	39.2	3.42		0.89	13.26	0.95	432	0.67	387.72	33.92	0.06	73	16.8	10.2	II > > I
BX1-18	37.6	3.02		0.78	10.69	0.83	430	0.64	353.97	33.77	0.07	74.6	14.2	11.2	II > > I
BX1-17	37.9	3.19		0.77	11.33	0.81	430	0.64	355.17	31.35	0.06	79.4	10.8	9.8	II > > I
BX1-15	39.4	6.00		1.55	28.57	1.28	431	0.66	476.17	27.67	0.05	80.2	7.6	12.2	II ≥ I
BX1-14	28.1	2.96		0.66	8.66	1.01	433	0.69	292.57	38.85	0.07	73.8	19.2	7	II > > I
BX1-10	34.7	3.53		0.91	11.62	1.00	430	0.64	329.18	32.01	0.07	72.6	10	17.4	II > > I
BX1-07	22.1	6.72		1.45	28.12	1.78	430	0.64	418.45	34.08	0.05	74.2	8.8	17	II ≥ I
BX1-06	33.5	12.21	0.92	3.88	68.53	1.52	432	0.67	561.26	17.12	0.05	89.2	2.2	8.6	II ≥ I
BX1-05	25.4	5.19		1.15	20.02	1.19	432	0.67	385.74	25.82	0.05	78	9.4	12.6	II ≥ I
BX1-04	29.9	7.78		2.04	36.68	1.32	432	0.67	471.47	22.24	0.05	83.2	9.2	7.6	II ≥ I
BX1-01	16.2	9.01	0.53	1.91	42.49	2.20	430	0.64	471.59	32.08	0.04	85	3	12	II ≥ I
BX1-0-1	22.3	13.48	0.68	3.06	64.9	2.23	438	0.78	481.45	21.44	0.05	78	7.2	14.8	II ≥ I
BX1-0-2	24.0	4.75		0.63	12.93	1.93	434	0.71	272.21	45.05	0.05	75.6	10	14.4	II > > I
BX1-0-3	23.8	13.81		1.13	46.1	4.87	437	0.76	333.82	44.82	0.02	56.2	1.6	42.2	II
BX1-0-4	32.9	7.87		2.04	37.83	1.29	434	0.71	480.69	18.30	0.05	59.6	0.6	39.8	II
BX1-0-6	31.3	13.48	0.62	1.32	47.73	4.05	438	0.78	354.08	38.65	0.03	37.4	2	60.6	II
BX1-0-7	45.5	10.54	0.92	1.35	38.04	2.67	435	0.73	360.91	34.44	0.03	36.8	3.2	60	II

homogenized in an epoxy plug using an Epo-Thin epoxy resin and hardener (2:1 per unit volume). The epoxy plugs were grinded using 320 µm followed by 600 µm cloths and polished by means of alumina powder (0.3 µm and 0.05 µm) and H<sub>2</sub>O at two stages to get a relief-free surface. Vitrinite reflectance analysis was performed under an oil immersion objective of 50 × ( $n_{oil} = 1.514$  at 23 °C) using the reflected light microscope Zeiss Axio Imager® A2m, which is equipped with a digital camera and UV light source. The total magnification used was 500 ×. Additionally, a conventional glass standard of 0.477% was used on primary vitrinite and bitumen to measure the random reflectance values. All preparation techniques and measurements of maceral composition and vitrinite reflectance were carried out at the Advanced Technology Center, Core Laboratories, Houston, USA. Further, information on samples investigations and maceral description can be found in ASTM D7708-14 (2014) and the ISO standards (ISO 7404-part 2, 2009; ISO 7404-part 5, 2009).

### 3.4 Palynofacies Preparation of Samples

The lithologic composition of samples is represented mainly by dark-olive to black calcareous mudstone and oil shale with insignificant intercalations of marl facies. Nearly, 10 g of each sample were used for palynological analysis utilizing the preparation protocol of Wood et al. (1996). Demineralization treatment includes HCl (34%) and HF (70%) acids followed by sieving of the organic residue using a nylon mesh (10 µm). Oxidative methods were avoided to introduce reliable palynofacies results. The kerogen residue was mounted onto glass slides that were then dried and coverslips were added with a drop of Canada balsam. This step produced a permanent mount with excellent optical properties for palynofacies investigations. Two slides were prepared for microscopic investigation of each sample using a transmitted light microscope (OMAX ToupView). Palynofacies preparation was carried out at the Micropaleontology and Stratigraphy Laboratory, Minia University, Egypt.

## 4 Results and Discussion

### 4.1 Kerogen Quantity and Quality

#### 4.1.1 Geochemical Characterization

The OM quantity of the investigated succession is expressed in terms of TOC wt% (Peters & Cassa, 1994). Generally, high contents of TOC reveal high primary productivity and enhanced preservation potential during deposition at the substrate. High organic carbon content is a reliable indicator of kerogen quantity but it is insufficient to indicate source potential as a part of the TOC may be inert or reworked/recycled (Carvajal-Ortiz & Gentzis, 2015; Espitalié et al., 1985; Peters, 1986; Peters & Cassa, 1994; Rullkötter et al., 1988; Chap. 2 of this book).

In the current study, the OM richness was assessed using the TOC and Rock-Eval  $S_1$  and  $S_2$  parameters. The analyzed section from the Quse Formation showed a very good to excellent source potential with variable richness and quality. The upper Quse and Sewa formations are divided, based on age, into two intervals, which are the lower Toarcian as well as the upper Bajocian-Bathonian, respectively (Fig. 3). The first interval represents the lower Toarcian and is 30 m in thickness, showing a more prominent richness than the upper Bajocian-Bathonian section (Fig. 3). Besides, it is marked by oscillating TOC readings ranging from 3.5 to 13.8 wt% (avg. 9 wt%). Moreover, it has fair  $S_1$  values varying from 0.6 to 3.9 mg HC/g rock and high  $S_2$  content that fluctuates between 20.0 and 61.6 mg HC/g rock (Table 1, Figs. 3 and 4). The upper Bajocian-Bathonian interval of the Sewa Formation is 65 m in thickness, and encountered lower OM richness compared to the early Toarcian interval. It has good TOC content that ranges from 1.5 to 3.4 wt%, and  $S_2$  values that vary between 2.4 and 13.3 mg HC/g rock (Table 1, Figs. 3 and

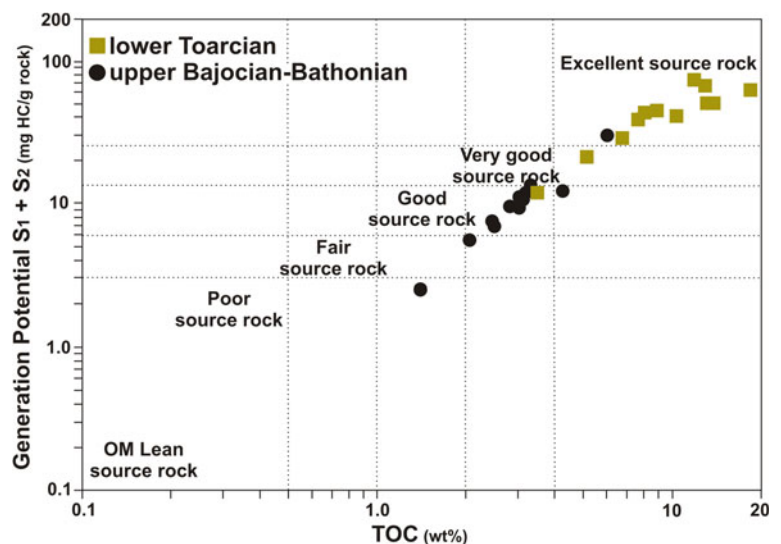
4). The lower part of the Sewa interval is more in richness. It differs in TOC and  $S_2$  from 2.9 to 6.0 wt%, and from 8.7 to 28.6 mg HC/g rock, respectively (Table 1, Figs. 3 and 4). The previous discussion reveals that the Sewa Formation possesses good to very good source potential by means of superb generative potential in the lower part of the early Toarcian section.

Several parameters and correlations evaluate the quality and kerogen types of the studied samples. The modified van Krevelen diagram (Fig. 5) is a correlation between oxygen index (OI) and hydrogen index (HI), utilized to classify various types of kerogen. The diagram reveals that the potential source rocks of the Quse and Sewa formations contain mixed kerogen Type II/III to Type II. The early Toarcian section is dominated by kerogen Type II compared to the late Bajocian-Bathonian interval. The  $S_2$  versus TOC correlation diagram is also used to typify kerogen in source rocks (Fig. 6). The correlation supports the conclusion from the modified van Krevelen diagram. It also elucidates homogeneous OM composition in the late Bajocian-Bathonian interval with a correlation coefficient of  $r = 0.99$ . On the other hand, the early Toarcian interval illustrated slightly heterogeneous OM composition with  $r = 0.89$  and variable TOC richness. This indicates rapid changes in the OM productivity and preservation and inputs during the early Toarcian and more stable conditions during the late Bajocian-Bathonian (Fig. 7).

#### 4.1.2 Organic Petrography

The organic petrographic investigation showed that the lower Toarcian interval contains oil-prone marine telalginite and lamalginite (kerogen Type II), primary vitrinite, and solid bitumen (Fig. 8). Alginite particles show a golden-yellow fluorescence, which is consistent with the early phase of oil window (Fig. 8a-b). Other types of

**Fig. 4** TOC content versus the petroleum potential ( $S_1 + S_2$ ), indicating the quality of potential source rock intervals



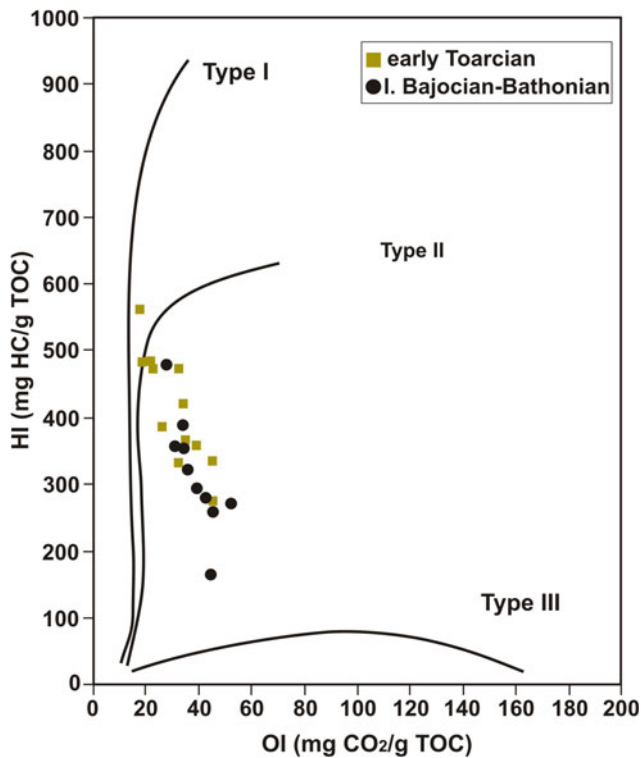


**Fig. 5** Modified van Krevelen diagram plot of the studied potential source rock intervals from the upper part of the Quse Formation, Bilong co section

oil-prone liptinites, such as amorphous filamentous algal matter and sporinite exhibit dull olive-green fluorescence (Fig. 8c-d). The upper Bajocian-Bathonian interval shows a similar petrographic composition to the lower section, but low-reflecting vitrinite, primary vitrinite, and inertinite are

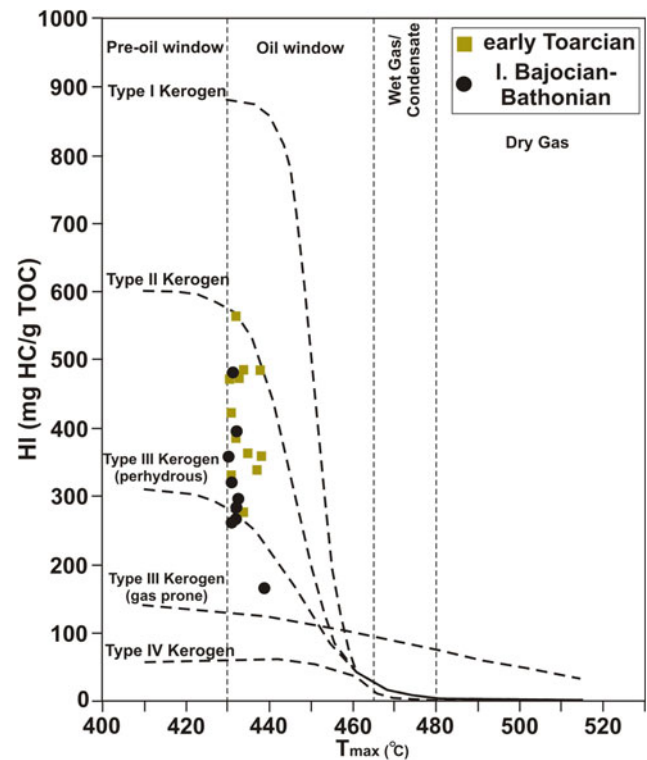


**Fig. 7**  $T_{max}$  versus HI (sensu Espitalié et al., 1985), discriminating the kerogen types and thermal maturity levels for the upper part of the Quse Formation, Bilong co section

more abundant (Fig. 9). The upper interval is rich in paly-nomorphs, especially sphaeromorphs pollen grains, which have dull-yellow fluorescence (Fig. 9b). Faunal inertinite of high maturity setting along with amorphous filamentous algal matter is also present (Fig. 9d, h).

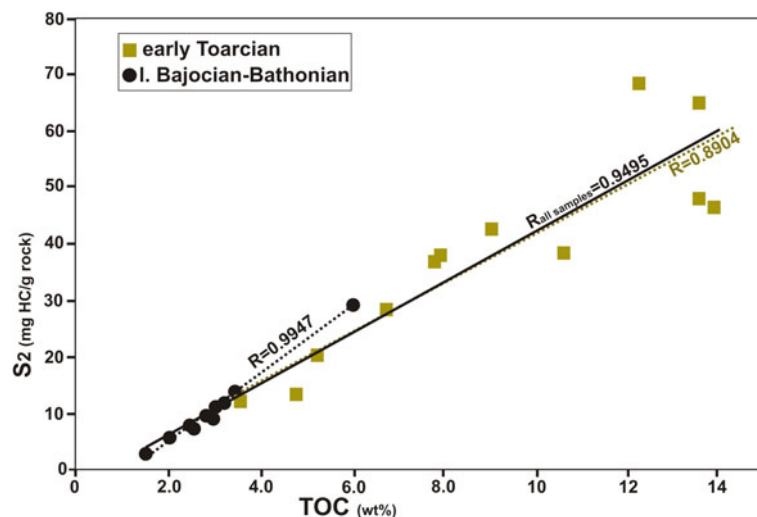


**Fig. 6** TOC versus  $S_2$  of the Quse Formation indicates the type of kerogen

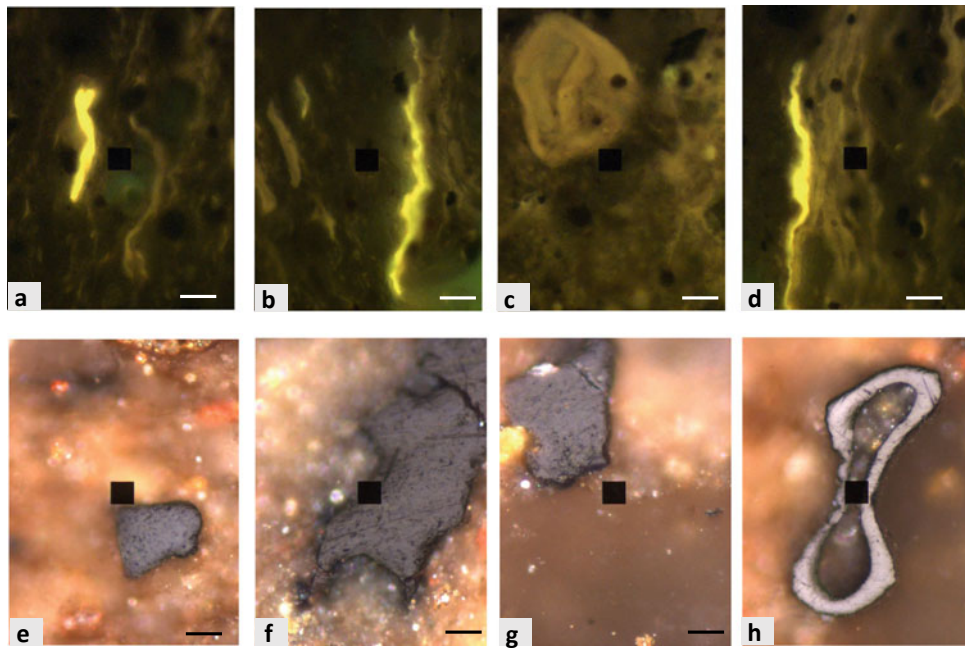


**Fig. 8** Photomicrographs of maceral composition for the first group of lower Toarcian samples. **a** BX1-04: Telalginite with golden-yellow fluorescence; **b** BX1-10: Lamalginite with golden-yellow fluorescence; **c** BX1-06: Spherical pollen grains having dull olive-green fluorescence; **d** BX1-06: Amorphous filamentous alginite with dull olive-green fluorescence; **e** BX1-04: Primary vitrinite ( $VR_{o,r} = 0.63\%$ ); **f** BX1-0-1: Angular reservoir bitumen ( $VR_{o,r} = 0.59\%$ ); **g** BX1-07: Primary vitrinite ( $VR_{o,r} = 0.66\%$ ); **h** BX1-07: Inertinite of algal or faunal origin. Photomicrographs A-D were taken under UV light. Excitation is 465 nm, combined dichroic and barrier filter has a cut at 515 nm. The scale bar is 10  $\mu\text{m}$

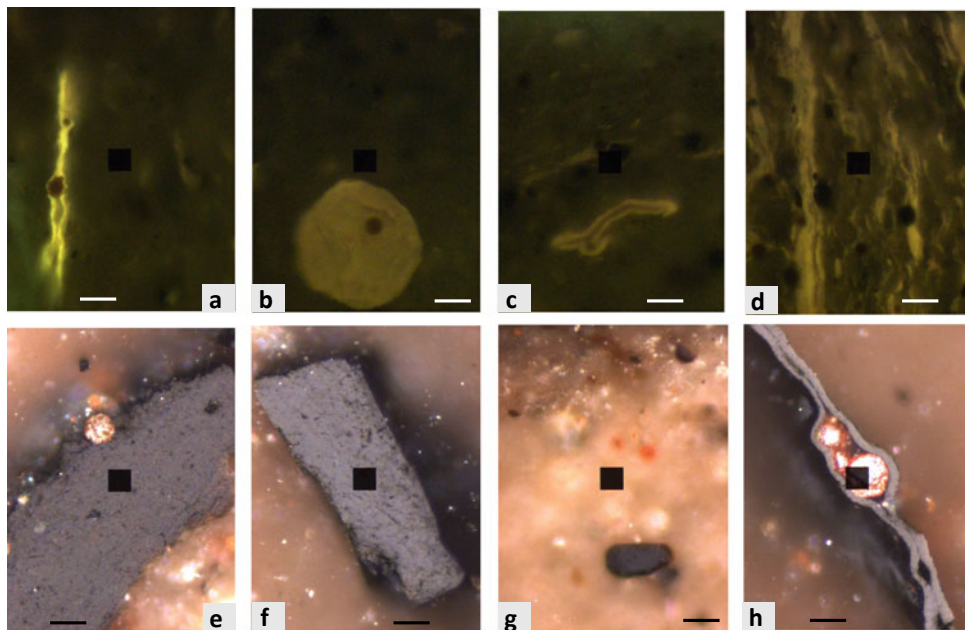


**Fig. 9** Photomicrographs of maceral composition for the second group of upper Bajocian-Bathonian samples. **a** BX1-19: Lamalginite with golden-yellow fluorescence; **b** BX1-14: Spherical pollen grains having dull-yellow fluorescence; **c** BX1-30: Compressed spore showing trilete mark and dull-yellow fluorescence; **d** BX1-26: Dull-yellow fluorescing amorphinite; **e** BX1-46: A thick band of low-reflecting vitrinite ( $VR_{o,r} = 0.47\%$ ); **f** BX1-34: A large grain of primary vitrinite ( $VR_{o,r} = 0.78\%$ ); **g** BX1-30: A small grain of primary vitrinite ( $VR_{o,r} = 0.73\%$ ); **h** BX1-46: Inertinite of faunal origin. Photomicrographs a–d were taken under UV light. Excitation is 465 nm, combined dichroic and barrier filter have a cut at 515 nm. The scale bar is 10  $\mu\text{m}$



## 4.2 Thermal Maturity Assessment

Evaluating thermal maturity levels of sedimentary OM preserved within the upper Quse and Sewa formations is one of the most important objectives of this study. Organic matter maturation in the studied strata was assessed based on Rock–Eval  $T_{\max}$  and random vitrinite reflectance ( $VR_{o,r}$ ); however, due to the scarcity of psilate spores, we could not apply visual maturity evaluation using spore coloration index.

In the Bilong co section, all samples showed comparable  $T_{\max}$  values that average 433 °C and similarly relatively low  $VR_{o,r}$  values that average 0.69% (Table 1; Fig. 3). PI values are constantly very low and do not exceed 0.07. The foregoing results designate that the OM is early mature. Thermal maturation has also been assessed using the relationship between the HI *versus*  $T_{\max}$  (Fig. 7), which further indicates an early maturation stage.

## 4.3 Palynofacies Analysis

Palynofacies as a term was first defined by Combaz (1964) as the total palynological organic material recovered from kerogen-strewn slides. Furthermore, Traverse (1988) defined it as an assemblage of palynomorphs, signifying local environmental conditions. Palynofacies analysis has been efficiently used in the visual characterization of kerogen types for hydrocarbon potential (Batten & Stead, 2005; Powell et al., 1990; Tyson, 1993, 1995). It has several advantages, which can offer reliable results of kerogen types, whereas its disadvantage is to discriminate hydrogen richness of kerogen (Powell et al., 1990). In many palynological-based kerogen quality assessment studies, AOM-rich kerogen was presumed to correspond to hydrogen-rich OM, thus the relative increase of the AOM content can be considered as an indicator of good source rock potential (Powell et al., 1982). Therefore, AOM is commonly considered a significant proxy when combined with organic geochemical investigations. For that reason, integrating the palynofacies analysis and organic geochemical results underpins the optimal appraisal of possible source rock sediments.

In this study, the particulate organic matter (POM) composition indicates substantial stratigraphic variations in the upper Quse and Sewa formations, which provide an opportunity to distinguish between various palynofacies assemblages and kerogen quality. Preserved POM encompasses both allochthonous particles such as plant pollen and spores, freshwater algae and phytoclasts derived from fluvial/riverine discharge, and autochthonous constituents such as microplanktons, foraminiferal test linings (FTLs), and AOM. Here, we used the AOM-Phytoclasts-Palynomorphs (APP) ternary plot (Tyson, 1993) to elucidate kerogen

types, proximal–distal trends, redox state, as well as relative magnitudes of terrestrial influx.

Within the stratigraphic section, the POM is dominated by moderate to high AOM (36.8–89.2%) *versus* low to moderate phytoclast contents (7–60.6%, Table 1, Fig. 3). The palynomorphs content is generally low and ranges between 0.6 and 19.2% of total content. Only sample BX1-21 exhibits different POM contents. It is composed mainly of palynomorphs of terrestrial origin (53.6%), phytoclasts (43%), and rare AOM content (3.4%, Table 1, Fig. 3). The lower Toarcian interval yielded a moderate recovery of palynomorphs of high degradation compared to high recovery and abundance for the upper Bajocian-Bathonian succession. The recovered palynomorphs from the Quse Formation are mainly terrestrial in origin, including sphaeromorphs pollen compared to low dinoflagellate cysts (dinocysts) and FTLs. Freshwater algae and pteridophyte spores along with marine prasinophytes are rare and comprise a minor percentage of the total palynomorph yield, except for sample BX1-21, which showed a peak of freshwater algae that is represented by *Schizosporis reticulatus*.

Based on the stratigraphic variation of the recovered POM, we defined different kerogen types in the Quse and Sewa formations using palynofacies analysis. The first group of samples, represents the lower Toarcian Quse Formation, plots in the palynofacies fields IX (AOM-dominated) and VI (moderate AOM and phytoclasts) of the APP ternary diagram of Tyson (1993). Fields IX and VI indicate kerogen Type II  $\geq$  I and Type II, respectively.

The second group represents the upper Bajocian-Bathonian Sewa Formation and is located mainly in the palynofacies field VIII (AOM-dominated but slightly lower than field IX) of the APP ternary diagram, except for sample BX1-21 that belong to the palynofacies field V (phytoclasts-dominated; Tyson, 1993). Field VIII infers a kerogen Type II  $\gg$  I, whereas field V is assigned to kerogen Type III  $>$  IV (Tyson, 1993).

## 4.4 Depositional Environment

The lithologic composition indicates that the Bilong co area contains significant amounts of carbonates mixed with fine siliciclastics. The carbonate content of the investigated samples is in the range of 15.7–46.6% (avg. 32%). The analyzed section is also characterized by high TOC content *versus* low TS values. The relationship between  $CaCO_3$  and TOC indicates a shallow marine environment typical of moderate carbonate production, where the organic carbon was negatively correlated with the  $CaCO_3$  content ( $r = -0.35$ ,  $P < 0.01$ ,  $n = 24$ , not shown, e.g., Bohacs et al., 2005; Ricken, 1996). In such an environment, high terrestrial input presumably enhances nutrients, resulting in water

column bioproductivity and high organic carbon accumulation and burial.

The relationship between sulfur and organic carbon is commonly used to differentiate redox levels during deposition, from oxygen-poor anoxia to well-oxygenated settings (Berner, 1984; Leventhal, 1995). Additionally, it provides insights into the activity of microbial sulfate reduction *versus* sulfide oxidation. A strong linear relationship between the former categories reveals a normal marine, oxic setting at the water–sediment interface (Berner, 1984; Leventhal, 1995). The measured total sulfur values (0.98–0.53, avg. 0.78 wt%) are low in these high TOC samples, indicating a moderate relationship between both variables ( $r = 0.50$ ,  $P < 0.05$ ,  $n = 6$ , not shown). In other words, as TOC changed with time, sulfur content increased slightly, suggesting that sulfur was controlled, to some extent, by the available OM in the water column (Mansour et al., 2020). Relative abundance of oxygen at bottom water settings can also be observed by the Rock–Eval HI and OI cross-plot. For the studied intervals, the high HI *versus* low OI values indicates reduced oxygen contents during deposition (Table 1). Higher values of HI and  $S_2$  compared to moderate TS and organically-bound sulfur reveal better preservation potential of OM probably because of the oxygen-depleted setting at the sea floor (e.g., Mansour et al., 2020).

Furthermore, palynological organic matter is widely used as a reliable proxy indicator of depositional environments under different sedimentary conditions (e.g., Tyson, 1993). Within a sedimentary basin, OM is controlled by some factors that include the type of water column, redox status, sedimentation rates, burial efficiency, proximal–distal trends, and changes in relative sea level (Batten & Stead, 2005; Berner, 1984; Powell et al., 1990; Tyson, 1993). Organic facies can be implemented to characterize the environment of deposition. Besides, palynofacies analysis is a crucial

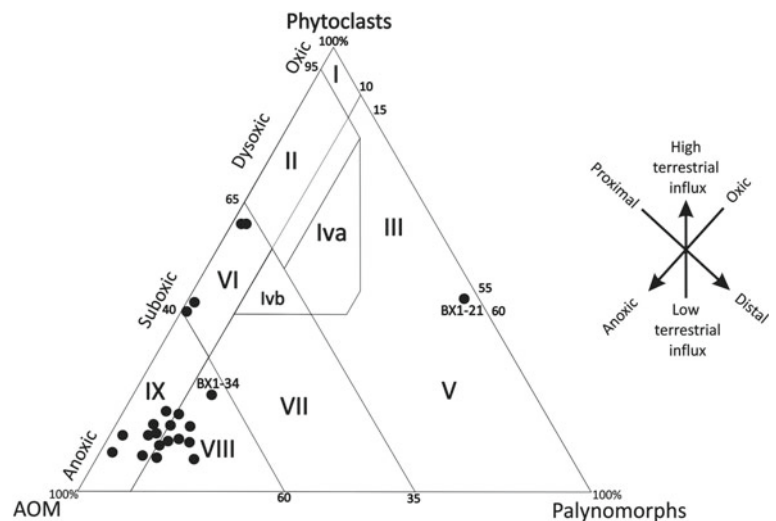
proxy for interpreting depositional environmental settings (Batten, 1996; Tyson, 1993, 1995). Relative changes in POM composition infer oxygenation conditions and thus, can provide a reliable assessment of oxic *versus* anoxic environments. Additionally, POM content is consistent with sea level transgressive–regressive trends and therefore, can provide an estimate of proximal–distal trends from the shoreline (Tyson, 1993, 1995).

In the lower Toarcian Quse Formation in the Bilong co section, most samples are dominated by rich, mixed kerogen associations with rich AOM content *versus* low to moderate content of degraded phytoclasts. Palynomorph composition is characterized by a predominance of terrestrial gymnosperm pollen grains *versus* moderate to low marine dinocysts and rare occurrences of pteridophyte spores, FTLs, freshwater algae, acritarchs, and prasinophytes. This palynofacies assemblage of the studied samples indicates a shallow marine, anoxic to dysoxic shelf environment, whereby sphaeromorphs pollen grains of terrestrial land-plants were transported either by wind action or fluvial input.

Plotting of the retrieved data on the APP ternary diagram indicates that most upper Quse samples are located in field IX, whereas Sewa samples are plotted in field VIII (Fig. 10). These two fields suggest deposition in a distal suboxic-anoxic basin and distal dysoxic shelf settings, respectively, under well-stratified water column distinctive for organic carbon-rich shales (Tyson, 1995). The lowermost oil shale interval (samples BX1-0-7 to BX1-0-3) is characterized by the highest phytoclast content (*ca.* 60.6 to 40% of total POM content, Fig. 11, Table 1), thus suggesting deposition during a high terrestrial input (Fig. 3).

Generally, the relative abundance of AOM is commonly low in marginal to shallow shelf environments and gradually increases in deeper shelf-basinal settings, where enhanced sedimentation, water column stratification, and oxygen

**Fig. 10** Plot of samples taken from the upper part of the Quse Formation on the APP ternary diagram of Tyson (1993)



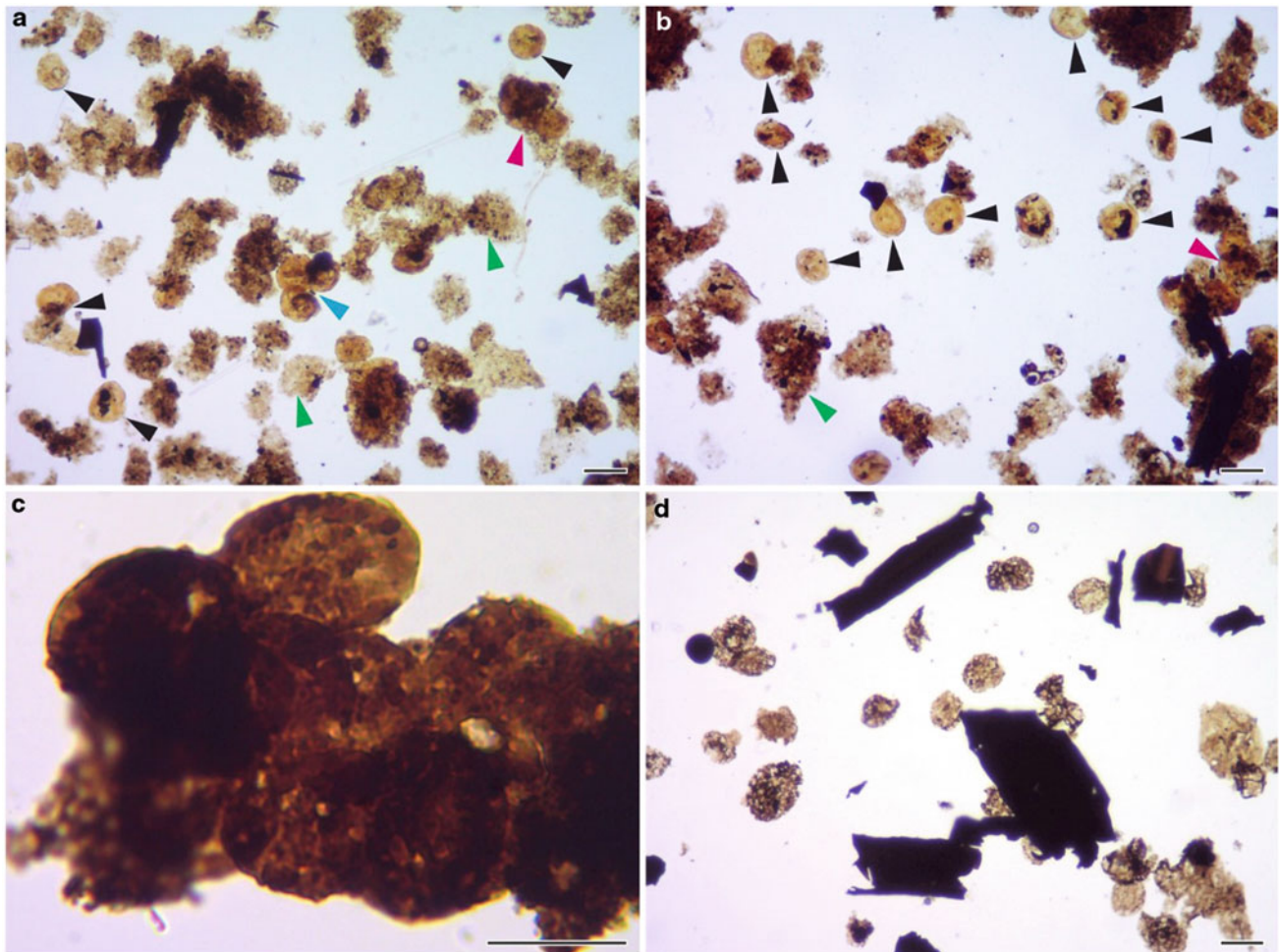


**Fig. 11** Transmitted light photomicrographs of POM components from the upper part of the Quse Formation, southern Qiangtang Basin. The scale bar is 40  $\mu\text{m}$ . **a** POM composition of the sample BX1-14 that is dominated by AOM (green arrows) and palynomorphs, mainly sphaeromorphs (black arrows), MFL (pink arrow), *Classopollis* (blue arrow) with low phytoclast content. **b** Palynofacies composition the sample BX1-07 that characterized by AOM richness (green arrows) and sphaeromorphs (black arrows) and low to moderate phytoclasts content. **c** Moderately-preserved sphaeromorphs cluster recovered from the oil shale sample BX1-0-7. **d** Charred or lath-shaped opaque phytoclast and freshwater *Schizosporis reticulatus* algae recovered from the sample BX1-21

depletion allow enhanced preservation of the available organic matter (Mansour et al., 2020; Tyson, 1993, 1995). In most samples of the studied succession, the high proportions of the AOM reveal not only deposition in a marine setting but also reduced oxygen levels and deposition in suboxic to anoxic environment (Fig. 10). This agrees with the existence of pyrite accompanying the AOM in many samples, suggesting the strong impact of microbial mats and enhanced biodegradation under reduced oxygen levels (Pacton et al., 2011).

Sample BX1-21 has a mixed content of palynomorphs (53.6% of total POM) and phytoclasts (43%) compared to very low AOM content (3.4%, Table 1). This sample plots in field V of the APP diagram (Tyson, 1993, Fig. 10), typically of a light-colored bioturbated calcareous mudstone deposited at oxic shelf conditions.

The relative abundance of sphaeromorphs infers a deposition in a basinward direction and in deeper outer neritic shelf environments (Tyson, 1993). For the studied succession, the palynomorphs content is dominated by sphaeromorphs pollen grains that are represented by *Spheripollenites psilatsu*, *Corolina torosa*, *Classopollis* sp., and *Araucariacites australis*, suggesting that the upper Quse and Sewa were deposited in a low-energy, slightly distal inner-neritic environment. The overall scarcity of psilate spores and vascular cryptogamma in the current succession can be attributed to the absence of humid conditions (Abbink, 1998). The overwhelming abundance of the *Classopollis* sp. and *Spheripollenites psilatus* is consistent with many Early Jurassic ecosystems worldwide and was used as a significant indicator of annual dry-arid conditions, allowing the development of coastal forest covers of the

Coniferophyta/Bennetitales and Cheirolepidiaceae that might have grown in the vicinity of the Bilong co (Barrón et al., 2010; Gómez et al., 2008; Mohr, 1989; Slater et al., 2019). An aquatic palynomorph association was represented by low percentages of the above plant families compared to the sphaeromorphs pollen. The association is dominated by peridinioid dinocysts that favor a high nutrient supply in shallow shelf settings, especially in areas of improved terrestrial/riverine input (Brinkhuis, 1994). This interpretation is consistent with the occurrence of freshwater *Schizosporis* algae (Appendix 1), which was triggered by freshwater/riverine supply (Batten, 1996).

Overall, the prevalent environmental circumstances during deposition of the upper interval of the Quse and Sewa formations were mainly anoxic to dysoxic, stagnant distal inner-neritic shelf conditions with a significant contribution of terrestrial/riverine discharge. Only, sample BX1-21 suggests a deposition during high terrestrial input in a shallow marine environment.

**Acknowledgements** The authors would like to thank the National Natural Science Foundation, China for funding this study (Grant No. 41772105).

## References

- Abbink, O. A. (1998). Palynological investigations in the Jurassic of the North Sea region. *Utrecht Laboratory of Palaeobotany and Palynology Contribution Series*, 8, 1–191.
- ASTM D7708-14. (2014). *Standard test method for microscopical determination of the reflectance of vitrinite dispersed in sedimentary rocks*. ASTM International, West Conshohochen, PA. [www.astm.org](http://www.astm.org)
- Barrón, E., Ureta, S., Goy, A., & Lassaletta, L. (2010). Palynology of the Toarcian-Aalenian global boundary stratotype section and point (GSSP) at Fuentelsaz (Lower–Middle Jurassic, Iberian Range, Spain). *Review of Palaeobotany and Palynology*, 162, 11–28.
- Batten, D. J. (1996). Palynofacies and petroleum potential. In: J. Jansonius, & D. C. McGregor, (Eds.), *Palynology: Principles and applications* (pp. 1065–1084). AASP Foundation.
- Batten, D. J., & Stead, D. T. (2005). Palynofacies analysis and its stratigraphic application. In E. A. M. Koutsoukos (Ed.), *Applied stratigraphy* (pp. 203–226). Springer.
- Behar, F., Beaumont, V., Penteadó, H. L., et al. (2001). Rock-Eval 6 technology: Performances and developments. *Old & Gas Science and Technology Review—IFP*, 56, 111–134.
- Berner, R. A. (1984). Sedimentary pyrite formation: An update. *Geochimica Et Cosmochimica Acta*, 48, 605–615.
- Bohacs, K. M., Grabowski, G. J., & Carroll, A. R. et al. (2005). Production, destruction, and dilution—The many paths to source-rock development (Vol. 82, pp. 61–101). SEPM Special Publication.
- Brinkhuis, H. (1994). Late Eocene to early Oligocene dinoflagellate cysts from the Priabonian type-area (Northeast Italy): Biostratigraphy and paleoenvironmental interpretation. *Palaeogeography, Palaeoclimatology Palaeoecology*, 107(1–2), 121–163.
- Carvajal-Ortiz, H., & Gentzis, T. (2015). Critical considerations when assessing hydrocarbon plays using Rock-Eval pyrolysis and organic petrology data: Data quality revisited. *International Journal of Coal Geology*, 152, 113–122.
- Chen, L., Yi, H. S., Hu, R. Z., et al. (2005). Organic geochemistry of the early Jurassic oil shale from the Shuanghu area in northern Tibet and the early Toarcian oceanic anoxic event. *Acta Geologica Sinica*, 79, 392–397.
- Chen, L., Mattioli, E., Da, X. J., et al. (2018). Calcareous nannofossils from the Jurassic black shales in the Qiangtang Basin, northern Tibet (China): New records of stratigraphic ages and palaeoceanography. *Newsletters on Stratigraphy*, 52(1), 55–72.
- Combaz, A. (1964). Les Palynofacies. *Review Micropaleontology*, 7, 205–218.
- Ding, L., Yang, D., Cai, F., et al. (2013). Provenance analysis of the Mesozoic Hoh-Xil-Songpan-Ganzi turbidites in northern Tibet: Implications for the tectonic evolution of the eastern Paleo-Tethys Ocean. *Tectonics*, 32, 34–48.
- Espitalié, J., Deroo, G., & Marquis, F. (1985). La pyrolyse Rock-Eval et ses applications (Vol. 40, pp. 563–579). Partie 1. Revue Institute Francais Petrole.
- Fang, X., Song, C., Yan, M., et al. (2016). Mesozoic litho- and magneto-stratigraphic evidence from the central Tibetan Plateau for megamonsoon evolution and potential evaporites. *Gondwana Research*, 37, 110–129.
- Fu, X., Tan, F., Feng, X., et al. (2014). Early Jurassic anoxic conditions and organic accumulation in the eastern Tethys. *International Geology Review*, 56(12), 1450–1465.
- Fu, X., Wang, J., Zeng, S., et al. (2017). Continental weathering and palaeoclimatic changes through the onset of the Early Toarcian oceanic anoxic event in the Qiangtang Basin, eastern Tethys. *Palaeogeography, Palaeoclimatology, Palaeoecology*, 487, 241–250.
- Gómez, J. J., Goy, A., & Canales, M. L. (2008). Seawater temperature and carbon isotope variations in belemnites linked to mass extinction during the Toarcian (Early Jurassic) in central and northern Spain, Comparison with other European sections. *Palaeogeography, Palaeoclimatology, Palaeoecology*, 258, 28–58.
- ISO 7404-2. (2009). *Methods for the petrographic analysis of coal—Part 2: Methods of preparing coal samples*. International Organization for Standardization. ISO 7404-2:2009(en). [www.iso.org/standard/42798.html](http://www.iso.org/standard/42798.html)
- ISO 7404-5. (2009). *Methods for the petrographic analysis of coal—Part 5: Methods of determining microscopically the reflectance of vitrinite* (p. 14). International Organization for Standardization, Geneva, Switzerland.
- Jenkyns, H. C. (2010). Geochemistry of oceanic anoxic events. *Geochemistry, Geophysics, Geosystems*, 11, Q03004.
- Ji, C. J., Xia, G. Q., Yi, H. S., et al. (2014). Aromatic hydrocarbons in the Biluo Co oil shale of the Shuanghu area, northern Tibetan Plateau, and their implications. *Oil Shale*, 31(4), 351–364.
- Kapp, P., DeCelles, P. G., Gehrels, G. E., et al. (2007). Geological records of the Lhasa-Qiangtang and Indo-Asian collisions in the Nima area of central Tibet. *Geological Society of America Bulletin*, 119, 917–932.
- Lamoureux-Var, V., Espitalié, J., & Pillot, D., et al. (2019). Rock-Eval 7S: Technology and performance. In: *29th International Meeting of Organic Geochemistry* (Vol. 1, pp. 1–2). European Association of Geoscientists and Engineers.
- Leventhal, J. S. (1995). Carbon-sulfur plots to show diagenetic and epigenetic sulfidation in sediments. *Geochimica Et Cosmochimica Acta*, 59, 1207–1211.
- Li, Y., Wang, C. S., & Yin, H. S. (2002). Filled sequence and evolution of the Mesozoic Qiangtang composite foreland basin in the Qianghai-Tibet Plateau. *Journal of Strategy*, 26, 62–79. (in Chinese with English abstract).
- Li, G. J. (2016). *Research on sedimentary facies and hydrocarbon source rocks of upper Triassic and Lower to Middle Jurassic in the*

- South Qiangtang depression, Tibet (pp. 1–85). Master Thesis, Chengdu: Chengdu University of Technology (in Chinese with English abstract).
- Ma, A. L., Hu, X. M., Garzanti, E., et al. (2017). Sedimentary and tectonic evolution of the southern Qiangtang basin: Implications for the Lhasa-Qiangtang collision timing. *Journal of Geophysical Research: Solid Earth*, *122*, 4790–4813.
- Mansour, A., Gentzis, T., & Carvajal-Ortiz, H., et al. (2020). Geochemistry and palynology of the upper Albian at the Abu Gharadig Basin, southern Tethys: Constraints on the oceanic anoxic event 1d. *Geological Journal*, *55*(9), 6338–6360. <https://doi.org/10.1002/gj.3810>
- Mohr, B. A. R. (1989). New palynological information on the age and environment of Late Jurassic and Early Cretaceous vertebrate localities of the Iberian Peninsula (eastern Spain and Portugal). *Berl Geowiss Abh Reihe A*, *106*, 291–301.
- Pacton, M., Gorin, G. E., & Vasconcelos, C. (2011). Amorphous organic matter—experimental data on formation and the role of microbes. *Review of Palaeobotany and Palynology*, *166*, 253–267.
- Peters, K. E. (1986). Guidelines for evaluating petroleum source rock using programmed pyrolysis. *AAPG Bulletin*, *70*, 318–329.
- Peters, K. E., & Cassa, M. R. (1994). Applied source rock geochemistry. In: L. B. Magoon, & W. G. Dow (Eds.), *The petroleum system—From source to trap*. AAPG Memoir, Vol. 60, pp. 93–120.
- Powell, T. G., Creaney, S., & Snowdon, L. R. (1982). Limited use of organic petrographic techniques for identification of petroleum source rocks. *AAPG Bulletin*, *66*, 430–435.
- Powell, A. J., Dodge, J. D., Lewis, J. (1990). Late Neogene to Pleistocene palynological facies of the Peruvian continental margin upwelling, Leg 112. In: E. Suess, R. Von Huene (Eds.), *Proceeding of the ocean drilling project, scientific results* (Vol. 112, pp. 297–321). ODP, College Station, Texas.
- Ricken, W. (1996). Bedding rhythms and cyclic sequences as documented in organic carbon-carbonate patterns, Upper Cretaceous, Western Interior, U.S. *Sedimentary Geology*, *102*, 131–154.
- Rullkötter, J., Leythaeuser, D., Horsfield, B., et al. (1988). Organic matter maturation under the influence of a deep intrusive heat source: A natural experiment for quantitation of hydrocarbon generation and expulsion from a petroleum source rock (Toarcian shale, northern Germany). *Organic Geochemistry*, *13*, 847–856.
- Sengör, A. M. C. (1987). Tectonics of the Tethysides: Orogenic collage development in a collisional setting. *Annual Review of Earth and Planetary Science*, *15*, 213–244.
- Slater, S. M., Twitchett, R. J., Danise, S., et al. (2019). Substantial vegetation response to Early Jurassic global warming with impacts on oceanic anoxia. *Nature Geoscience*, *12*, 462–467.
- Su, X., Yin, Y. R., Zhu, Y. H., et al. (2015). Late early Jurassic Posidonia shale facies in Qiangtang Basin and its chronostratigraphic significance. *Geological Bulletin of China*, *34*, 1617–1628. (in Chinese with English abstract).
- Traverse, A. (1988). *Paleopalynology* (p. 600). Unwin Hyman.
- Tyson, R. V. (1993). Palynofacies analysis. In D. G. Jenkins (Ed.), *Applied micropaleontology* (pp. 153–191). Kluwer Academic Publication.
- Tyson, R. V. (1995). *Sedimentary organic matter-organic facies and palynofacies* (p. 615). Chapman and Hall.
- Wang, C. S., Chang, E. Z., & Zhang, S.-N. (1997). Potential oil and gas-bearing basins of the Qinghai-Tibetan plateau, China. *International Geology Review*, *39*(10), 876–890.
- Wang, C. S., Yi, H. S., Liu, C. Y., et al. (2004). Discovery of paleo-oil-reservoir in Qiangtang Basin in Tibet and its geological significance. *Oil and Gas Geology*, *25*(2), 139–143. [in Chinese with English abstract].
- Wang, Y. S., Zhang, S. Q., Xie, Y. H., et al. (2012). *1:250000 regional geological survey report of the People's Republic of China (Angdarco Sheet)*. Publishing House of China University of Geosciences.
- Wang, C. S., Dai, J. G., Zhao, X. X., et al. (2014). Outward-growth of the Tibetan Plateau during the Cenozoic: A review. *Tectonophysics*, *621*, 1–43.
- Wang, Z., Wang, J., Fu, X., et al. (2019). Sedimentary successions and onset of the Mesozoic Qiangtang rift basin (Northern Tibet), southwest China: Insights on the Paleo- and Meso-Tethys evolution. *Marine and Petroleum Geology*, *102*, 657–679.
- Wood, G. D., Gabriel, A. M., Lawson, J. C. (1996). Chapter 3. Palynological techniques-processing and microscopy. In: J. Jansoni, & D. C. McGregor (Eds.), *Palynology: Principles and applications* (Vol. 1, pp. 29–50). AASP Foundation.
- Xia, G., Ji, C., Chen, L., et al. (2017). Biomarkers of the Lower Jurassic black shale in the Shuanghu area of the Qiangtang Basin, Northern Tibet, and their geological significance. *Oil Shale*, *34*(1), 55–69.
- Yao, H. Z., Zhang, R. J., Duan, Q. F., et al. (2011). Jurassic rocks, bivalves, and depositional environments of the source area of the Yangtze River, Qinghai Province, western China. *Science China Earth Sciences*, *54*, 1136–1148.
- Yi, H. S., Lin, J. H., Zhao, B., et al. (2003). New biostratigraphic data of the Qiangtang area in the northern Tibetan plateau. *Geology Review*, *49*, 59–65. [In Chinese with English abstract].
- Yi, H. S., Wang, C. S., Lin, J. H., Shi, Z. Q., Chen, L., Wu, X. H., Wei, Q. L., Zhang, X. Q. (2005). Jurassic ammonite fauna in the Amdo area, northern Tibet and its paleogeographic implications. *Geological Bulletin of China*, *24*(1), 41–47 (in Chinese with English abstract).
- Yi, H. S., Chen, L., Jenkyns, H., et al. (2013). The Early Jurassic oil shales in the Qiangtang Basin, northern Tibet: Biomarkers and Toarcian oceanic anoxic events. *Oil Shale*, *30*, 441–455.
- Yin, A., & Harrison, T. M. (2000). Geologic evolution of the Himalayan-Tibetan orogen. *Annual Review of Earth and Planetary Sciences*, *28*, 211–280.
- Yin, J., & Chandler, R. B. (2016). Aalenian to Lower Bajocian ammonites from the Qiangtang block (North Tibet). *Proceedings of the Geologists' Association*, *127*, 172–188.
- Zhu, D. C., Zhao, Z. D., Niu, Y. L., et al. (2013). The origin and pre-Cenozoic evolution of the Tibetan Plateau. *Gondwana Research*, *23*, 1429–1454.



# Palynology and Petroleum Source Rock Geochemistry of the Cretaceous Mancos and Gallup Formations, San Juan Basin, New Mexico

Ashton B. Faulkner and Mohamed K. Zobia

## Abstract

The organic facies, source rock potential, and depositional environments of the Cretaceous Mancos Shale and Gallup Sandstone in Rio Arriba and San Juan counties, New Mexico were investigated using palynological and geochemical approaches. Four main palynological categories were specified which are: amorphous marine organic matter (AMOM), palynomorphs, phytoclasts, and opaques. The SJ 28-6 well consisted of two primary palynofacies assemblages. Palynofacies-1 comprised 41% phytoclasts, 36% AMOM, 19% opaques, and 4% palynomorphs. Palynofacies-2 is made up of 64% phytoclasts, 30% opaques, 5% AMOM, and only 1% palynomorphs. In Burnham-1 well, a comparable palynofacies composition was observed in which Palynofacies-1 comprised 51% phytoclasts, 33% AMOM, 15% opaques, and 1% palynomorphs, while Palynofacies-2 is composed dominantly of 76% phytoclasts (degraded), 12% opaques, 2% AMOM, and 1% palynomorphs. The palynofacies variation in the two boreholes contends for a regional transfer from shallow marine inner shelf circumstances with distinct terrestrial input into higher energy, more oxygenated fluvio-deltaic settings. In terms of kerogen composition, Palynofacies-1 indicates type II-III kerogen (mixed oil- and gas-prone), while Palynofacies-2 suggests type III kerogen (mainly gas-prone). Furthermore, spores and pollen color variations within the investigated interval point to thermally mature organic facies. Geochemical data confirm palynological interpretations and offer supplementary evidence for petroleum source rock deductions.

## Keywords

San Juan Basin • Mancos • Gallup • Palynology • Geochemistry • Cretaceous • Paleoenvironment • Source-rock

## 1 Introduction

The San Juan Basin has produced oil and gas since 1921, with most of the production being gas and natural gas liquids from Upper Cretaceous blanket sandstones and coal beds. The Gallup Sandstone has historically been a conventional oil and gas target in the San Juan Basin. According to the Bureau of Indian Affairs, Division of Energy and Mineral Development, the Gallup Sandstone has produced over 920 billion cubic feet of gas and 173 million barrels of oil, making it the largest oil-producing formation in the San Juan Basin.

The Mancos Shale has been viewed as the major source rock to surrounding sandstone reservoirs in the San Juan Basin (Broadhead, 2013). Natural fractures are present in the uppermost Mancos Shale from Laramide tectonic uplift in the northwestern and southeastern flanks of the basin. These fractures have produced small volumes of oil from several vertical wells but are generally sub-economical. The Mancos lacks the dense network of open fractures needed to produce economical volumes of oil and gas; therefore, interest has shifted to unconventional methods of extraction (Broadhead, 2015).

The Mancos is highly favorable to new shale technology and advanced hydraulic fracturing techniques due to its high permeability and saturation compared to other shales (Broadhead, 2015; Toon, 2018). The Mancos Shale is believed to be emerging as a major unconventional play in the San Juan Basin. In the summer of 2017, BP drilled a horizontal Mancos well in San Juan County, New Mexico, that showed a 30-day initial production rate of 12.9 million

A. B. Faulkner  
Beryl Oil and Gas, Midland, TX, USA

M. K. Zobia (✉)  
Department of Geosciences, The University of Texas Permian  
Basin, Odessa, TX, USA  
e-mail: [zobaa\\_m@utpb.edu](mailto:zobaa_m@utpb.edu)

cubic feet of gas per day, the highest the play has seen in 14 years. It continued to produce nearly 13 million cubic feet of gas for the first 150 days of production (Toon, 2018). With this great discovery, the Mancos is believed to contain untapped potential, giving it the possibility of emerging as a major unconventional play in the San Juan Basin.

Palynofacies is a valuable tool in oil and gas exploration that can provide clues about hydrocarbon source potential, depositional paleoenvironment, kerogen type, and thermal maturity (El Beialy et al., 2016; Zobaa et al., 2011, 2013). While palynological studies have been conducted on the Mancos Shale elsewhere, there have been no palynological analyses to the authors' knowledge performed on the Mancos and Gallup formations in the San Juan Basin. The No. 148 M San Juan 28-6 Unit (SJ 28-6) in Rio Arriba County, New Mexico, and the No. 1 Burnham (Burnham-1) in San Juan County, New Mexico, both penetrate the Upper Mancos Shale and Gallup Sandstone. The SJ 28-6 well is approximately 85 km east-northeast of the Burnham-1 well (Fig. 1). Core samples from both wells were palynologically studied in order to: (1) identify palynofacies assemblages based on particulate organic matter content, (2) use palynofacies data to interpret the depositional paleoenvironment, (3) determine the kerogen type and organic thermal maturity

by means of organic matter composition and spore/pollen coloration, and (4) evaluate the overall hydrocarbon source rock potential using palynofacies data supported by programmed pyrolysis and X-Ray Diffraction analyses.

## 2 Geologic Setting

The San Juan Basin is a Paleogene structural depression that spans 160–240 km wide across northwestern New Mexico and southwestern Colorado. The San Juan Basin is characterized by its asymmetric structure, with strata dipping gently into the subsurface on the southern flank and steeply rising to the outcrop on the northern flank, north of the New Mexico-Colorado border (Stone et al., 1983). Upper Cretaceous rocks within and on the flanks of the basin are almost completely preserved and contain large oil, gas, and coal reserves (Molenaar, 1977).

Geologically, the Mancos Shale was deposited in the Late Cretaceous (Turonian-Coniacian) throughout the majority of the Western Interior Seaway, a large inland sea that separated the continent of North America into two landmasses, stretching from the Gulf of Mexico all the way to the Arctic Ocean (Fig. 2). Following this deposition, Laramide

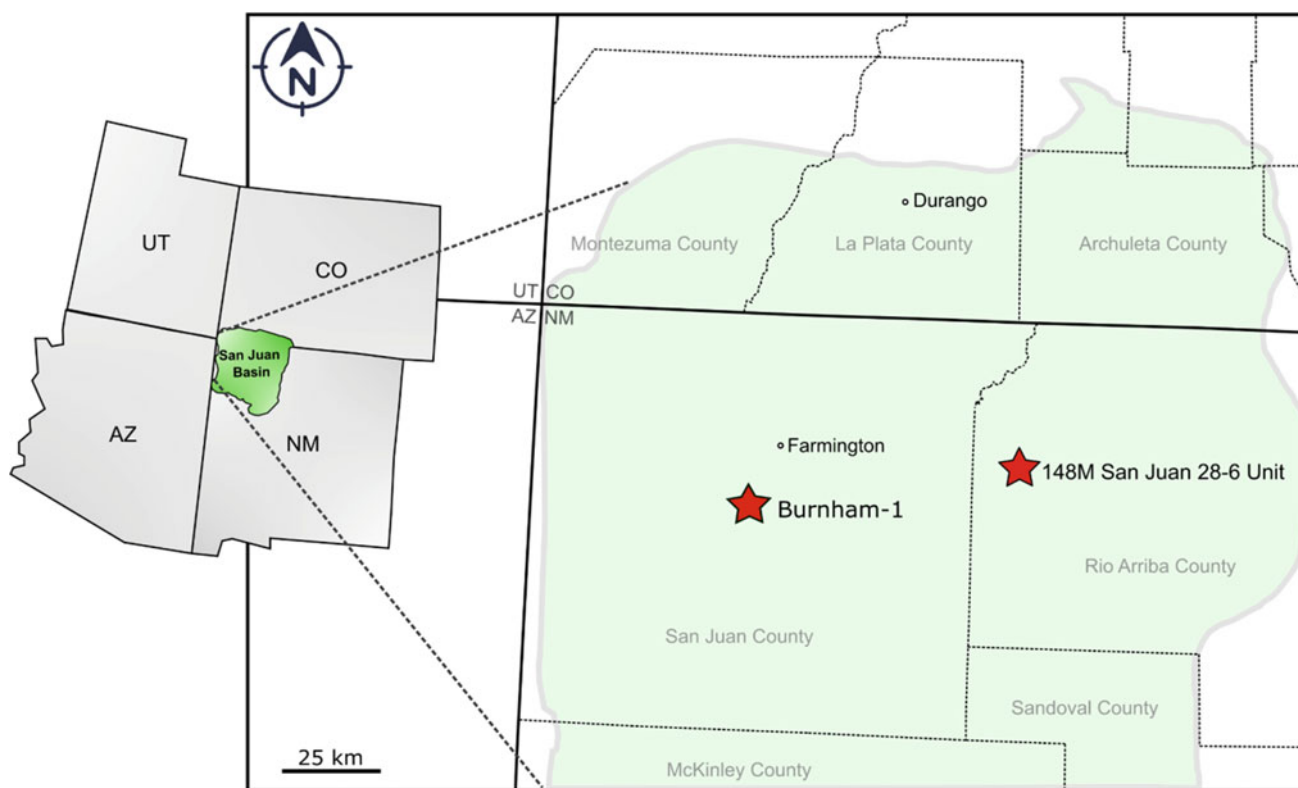


**Fig. 1** The extent of the San Juan Basin in New Mexico and Colorado with the approximate locations of the studied wells in Rio Arriba and San Juan counties, New Mexico

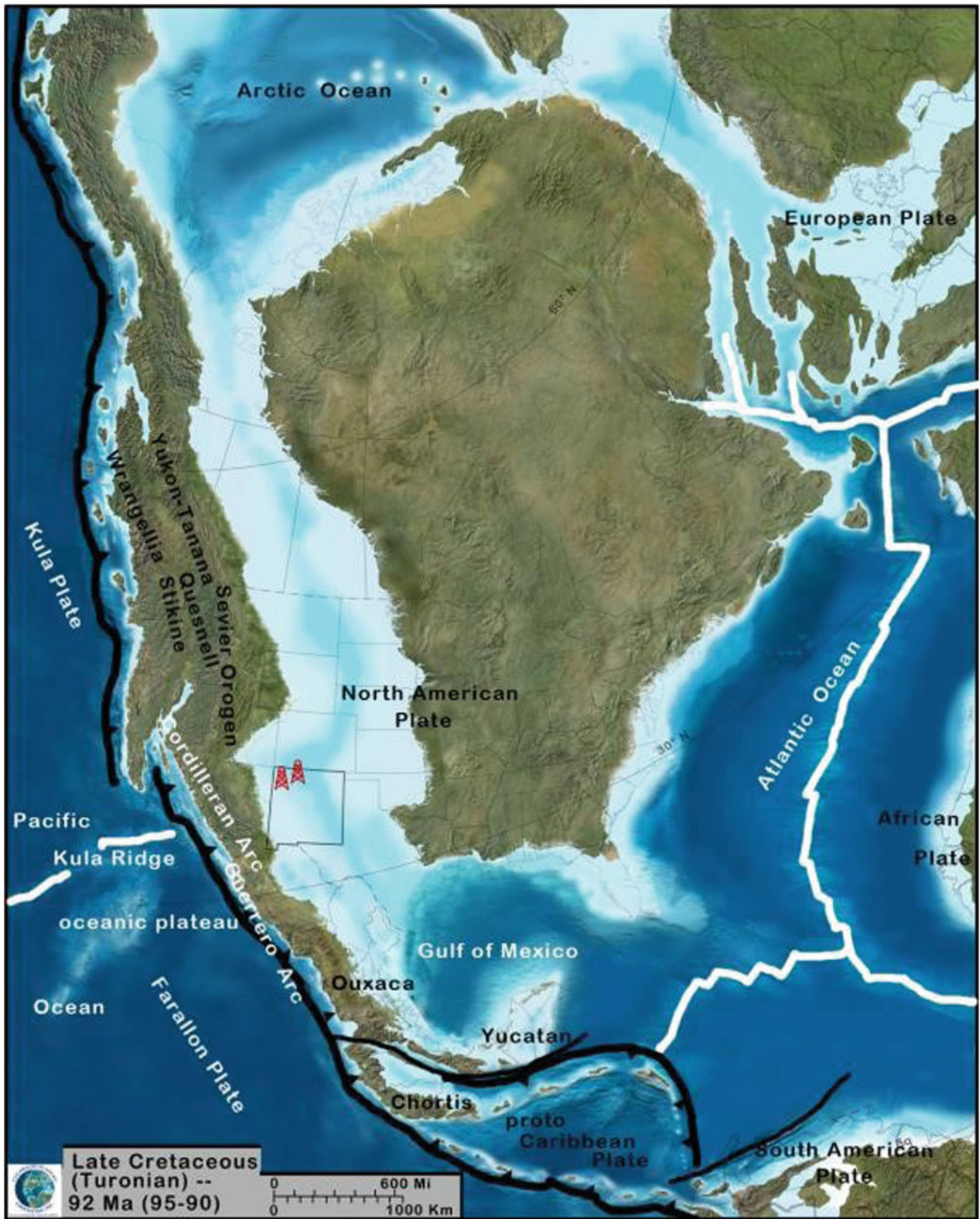


**Fig. 2** Paleogeographic map of the Late Cretaceous (Turonian) Western Interior Seaway shows the approximate location of the SJ 28-6 and Burnham-1 wells. © Ron Blakey, 2013 Colorado Plateau Geosystems Inc



compressive structural deformation formed the present-day shape of the San Juan Basin. The San Juan Basin contains over 30,000 km<sup>2</sup> of Cretaceous Mancos Shale (Broadhead, 2015). The Mancos Shale is a medium to dark gray, kerogen-rich marine shale with interbedded fine-grained sandstones and marine siltstones (Broadhead, 2015; Silver, 1951). It is bounded below by the Dakota Sandstone and is overlain by the Point Lookout Sandstone of the Mesaverde Group (Ridgely et al., 2013). In the San Juan Basin, the Mancos Shale is subdivided into the Upper Mancos Shale and Lower Mancos Shale. The Upper Mancos is separated from the Lower Mancos by the basal Niobrara unconformity in the northeast with intertongues of Gallup Sandstone in the southwestern portion of the basin (Broadhead, 2015; Ridgely et al., 2013). The Upper Mancos shale is further divided into three informal units known as Mancos A, Mancos B, and Mancos C, based on gamma-ray and resistivity logs, not on lithological changes (Broadhead, 2015). For the purpose of this study, the focus will be on the Upper Mancos Shale and the Gallup Sandstone. A generalized stratigraphic section of both units in the San Juan Basin is shown in Fig. 3.

Age	Formation	Member	Lithology	Description				
Late Cretaceous	Point Lookout Sandstone	Mancos A	[Lithology symbol: yellow dots]	Medium-grained, massive sandstone				
					Upper Mancos	Mancos B	[Lithology symbol: dark gray with dots]	Dark gray, kerogen-rich marine shale with interbedded marine siltstones and sandstones
						Mancos C		
	Lower Mancos	Gallup Sandstone	Upper Carlile Shale	[Lithology symbol: dark gray with dots]	Very dark gray, silty, marine shale with intertongues of regressive fluvial to shoreface sandstone wedges			
			Juana Lopez	[Lithology symbol: dark gray with dots]	Dark gray shale with thin beds of calcarenite, and minor very fine-grained marine sandstone			
			Lower Carlile Shale	[Lithology symbol: light gray with dots]	Light gray, calcareous marine shale grading upward into a dark gray, kerogen-rich marine shale			
			Greenhorn Limestone	[Lithology symbol: light gray with dots]	Calcareous shale with thin beds of argillaceous limestone			
			Graneros Shale	[Lithology symbol: dark gray with dots]	Dark gray, kerogen-rich marine shale grading upward into a light gray, calcareous marine shale			
	Early Cretaceous	Dakota Sandstone		[Lithology symbol: yellow dots]	Medium-grained sandstone			

**Fig. 3** Generalized stratigraphic section of the Cretaceous Mancos and Gallup formations in the San Juan Basin (Modified from Broadhead, 2015)

### 3 Materials and Methods

This study is based on 35 core samples from the Mancos and Gallup formations. The Mancos is represented by 20 samples from the SJ 28-6 well and seven samples from the Burnham-1 well, while Gallup is only represented by eight samples from the Burnham-1 well. Samples were palynologically processed and prepared in the Sedimentary Organic Matter and Hydrocarbon Source-Rock Research Laboratory at the University of Texas Permian Basin. About 15–17 g of each sample were crushed to powder using a porcelain mortar and pestle. Each sample was placed in a polypropylene beaker and treated with 100 ml of concentrated (35%) HCl to remove the carbonates. After 24 h, the samples were washed with water until they became neutral. The silicates were removed by treating the samples with 100 ml of concentrated (48%) HF for at least three days. During this treatment, samples were stirred frequently. Once the HF treatment was complete, samples were washed until neutral. With carbonates and silicates being removed, the next step was to separate the clays from the kerogen content. The samples were passed through a 125 µm brass sieve and the organic residue was collected in a 10 µm nylon sieve. Thirty-five permanent kerogen slides were mounted and prepared for a palynological examination through transmitted light microscopy. All kerogen slides were scanned for their particulate organic matter content. Two hundred organic particles were point counted and identified from each slide to statistically represent the relative abundances of kerogen content in every sample. Four main groups of palynological elements were identified: phytoclasts, opaques, palynomorphs, and amorphous marine organic matter (AMOM). Phytoclasts are defined as all terrestrial plant-derived fragments, such as cuticles and tracheids. Undegraded phytoclasts are translucent, exhibiting a clear internal structure. Degraded phytoclasts show only remnants of their original internal structure. Opaque phytoclasts are structured kerogen fragments that are black in color due to post-depositional oxidation or carbonization of translucent phytoclasts. Palynomorphs include all organic-walled microfossils of both terrestrial and marine origin (e.g., pollen, spores, freshwater algae, dinoflagellate cysts, and foraminiferal test linings). Amorphous marine organic matter (AMOM) comprise highly degraded marine algae and phytoplankton that are semitransparent with no visible internal structure (El Beialy et al., 2016; Zobia et al., 2015).

Paleoenvironmental parameters and kerogen types were determined by plotting relative abundances of organic constituents on the Zobia et al. (2015) sedimentary particulate organic matter (POM) ternary diagram. Visual thermal maturity estimations were made using Pearson's (1984) spore/pollen color chart in correlation with other maturity

scales such as thermal alteration index (TAI) and vitrinite reflectance ( $R_o$  %). Geochemical analyses were performed on multiple samples throughout the studied Mancos and Gallup intervals. Programmed pyrolysis and X-Ray Diffraction analyses were conducted at a commercial laboratory to help interpret hydrocarbon generation potential, source richness and quality, kerogen type, thermal maturity, and mineral composition. All samples and residues are stored in the Sedimentary Organic Matter and Hydrocarbon Source-Rock Research Laboratory at the University of Texas Permian Basin, Odessa, Texas.

## 4 Results

### 4.1 Palynofacies Analysis

The Mancos Shale interval within the SJ 28-6 well, depth from 2067.5 to 1848.6 m, is divided into two distinct palynofacies based on the relative abundance of palynological elements (Fig. 4). Palynofacies-1 is located within the deepest part of the section (2067.5–2003.1 m) and repeats near its middle (1966.6–1904.1 m). It is represented by phytoclasts (average abundance 41%), AMOM (36%), opaques (19%), and palynomorphs (4%). The majority of the phytoclast portion contains dark brown, degraded phytoclasts (average 36% of the total count) with opaques, mostly equant in shape (14%). Undegraded woody fragments were rare and only comprised 5% of the total count. The AMOM in this palynofacies is abundant, showing near colorless and structureless characteristics. Marine palynomorphs included dinoflagellate cysts and foraminiferal test linings but only accounted for <5% of the total count. Palynofacies-2 occurs directly above Palynofacies-1 at depths of 1997.0 and 1898.0 m. Palynofacies-2 is dominantly composed of phytoclasts (average abundance 64%) and opaques (30%) with a small presence of AMOM (5%) and palynomorphs (1%). Brown, degraded phytoclasts (44% of the total count) were abundant along with undegraded translucent phytoclasts (20%) and lath-shaped opaques (19%). Terrestrial palynomorphs encountered within this palynofacies type were dark brown, embryophyte spores but only accounted for 1% of the total count. Photomicrographs of sedimentary organic matter encountered within the SJ 28-6 well are shown in Fig. 5.

The same palynofacies were also identified in the Burnham-1 from 1310.6 to 1292.4 m (Fig. 6). Palynofacies-1 occurs within the Gallup Sandstone (1310.6–1306.4 m) and is primarily composed of phytoclasts (average abundance 51%), AMOM (33%), opaques (15%), and a few palynomorphs (1%). Dark brown, degraded phytoclasts (37% of the total count), equant and lath-shaped opaques (15%), and degraded cuticles (4%) made up the phytoclast portion of this

palynofacies. The AMOM identified were pale yellow, nearly colorless with diffuse edges. Terrestrial palynomorphs encountered were brown in color and mostly simple, thin-walled embryophyte spores and pollen (1%).

Palynofacies-2 occupies the shallower portion of the studied interval, including both Gallup and Mancos formations (1305.2–1292.4 m). It is dominantly made up of phytoclasts (average abundance 76%) and opaques (21%) with minimal AMOM (2%) and palynomorphs (1%). Dark brown, degraded phytoclasts are abundant, accounting for 56% of the total count. Undegraded translucent phytoclasts (16%) and lath-shaped opaques (13%) are common throughout this section. AMOM and palynomorphs are rare, only accounting for 3% of the total count. Photomicrographs of sedimentary organic matter encountered within the Burnham-1 well are shown in Fig. 7.

### 4.2 Spore and Pollen Coloration

Although spores and pollen are not seen in abundant numbers throughout the studied intervals, the documentation of their coloration is important to estimate thermal alteration index (TAI) and equivalent vitrinite reflectance values. Embryophyte spores identified in the SJ 28-6 well varied from brown to dark brown. Pollen grains were not seen in this well. Within Burnham-1, both spore and pollen exhibit a range of colors from orangish-brown to dark brown. These colors correlate with a TAI range of 3–4 and vitrinite reflectance values of 0.8–1.3  $R_o$ % (Traverse, 2007).

### 4.3 Pyrolysis Analysis

Pyrolysis data for the SJ 28-6 and Burnham-1 wells are shown in Tables 1 and 2, respectively. TOC values for the Mancos Shale in the SJ 28-6 well ranged from 0.83 to 2.26 wt%. In the Burnham-1 well, TOC values for the Gallup Sandstone ranged from 1.24 to 1.80 wt% and for the Mancos Shale ranged from 1.68 to 1.98 wt%.

The S1 values reflect the amount of hydrocarbons that have already been expelled from the contained organic matter. S1 values for the Mancos Shale in the SJ 28-6 well ranged from 0.19–1.38 mg HC/g rock. In the Burnham-1 well, Gallup Sandstone S1 values ranged from 0.67 to 1.41 mg HC/g rock, while those of the Mancos Shale ranged from 1.30 to 1.63 mg HC/g rock.

The S2 characterizes the hydrocarbon generating potential of the kerogen which remains in the sediment. S2 values for the Mancos Shale in the SJ 28-6 well ranged from 0.25 to 1.79 mg HC/g rock. In the Burnham-1 well, S2 values for the Gallup Sandstone ranged from 1.98 to 4.01 mg HC/g rock

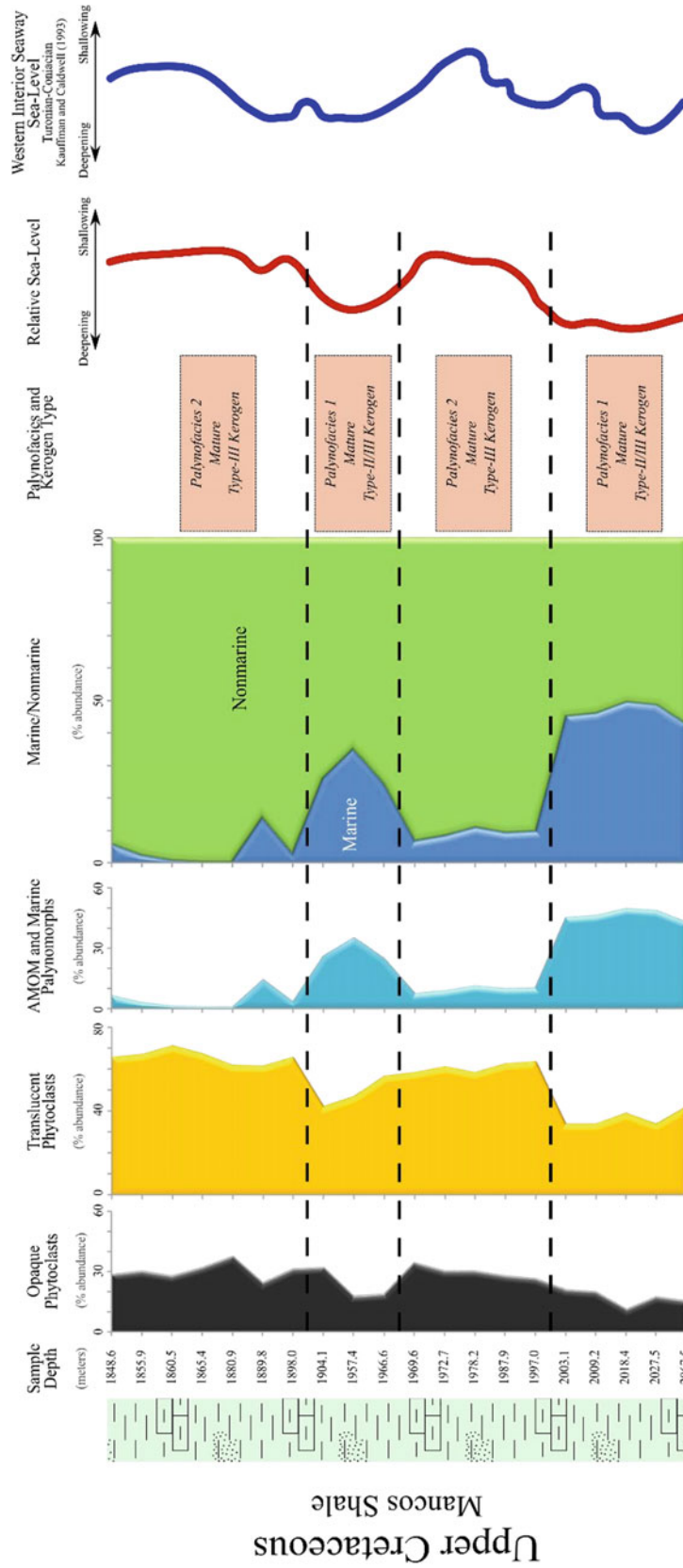


**Fig. 4** Quantitative representation of particulate organic matter encountered within the studied Mancos Shale interval in the SJ 28-6 well. Shown are lithology, sample depth, percent abundance of kerogen components, polynofacies and kerogen types, and sea-level curves. The relative sea-level (red) was approximated based on the present data and compared to Kauffman and Caldwell's (1993) Western Interior Seaway sea-level during the Turonian-Coniacian of the Late Cretaceous

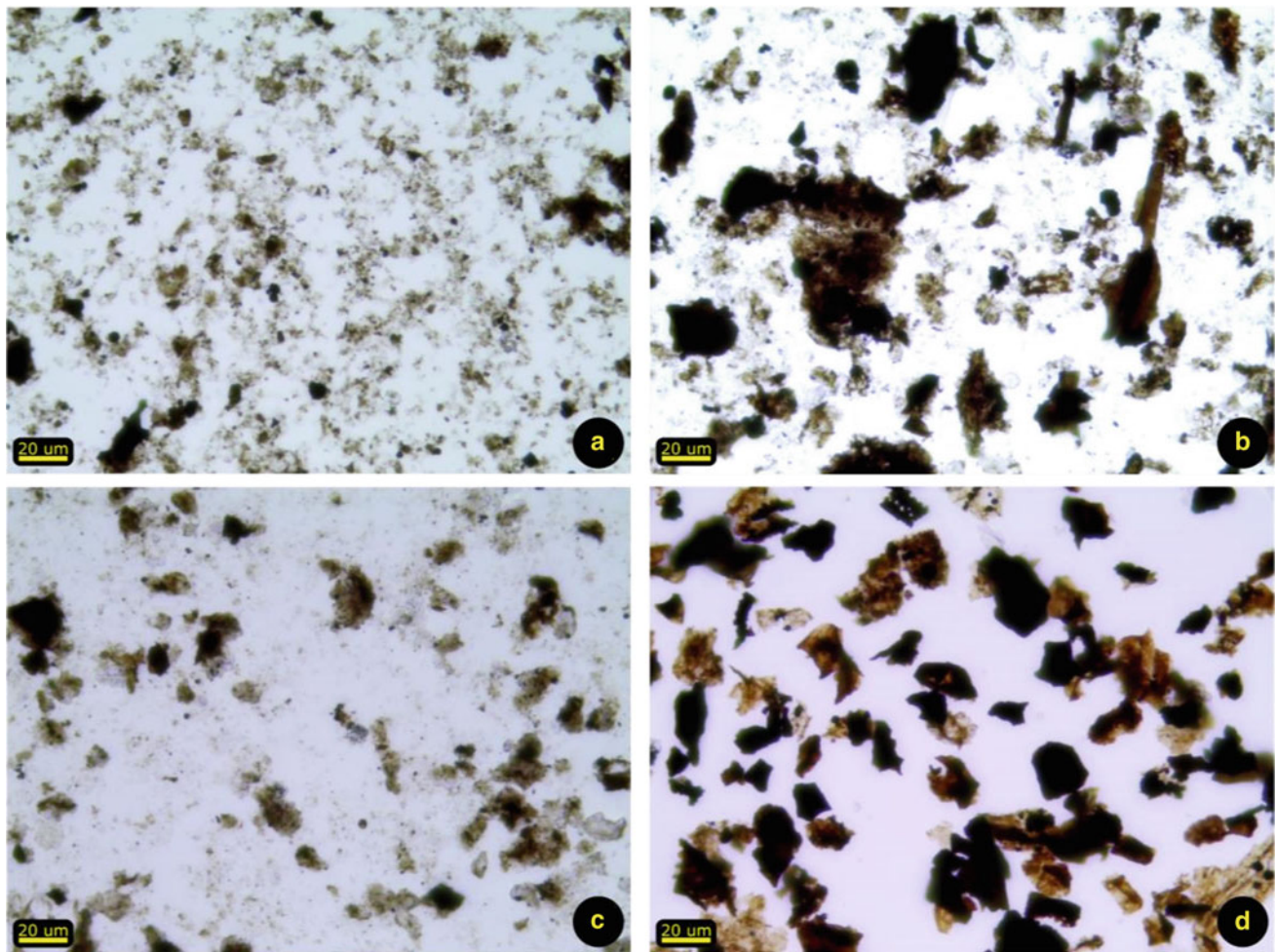


**Fig. 5** Photomicrographs of sedimentary organic matter encountered within the SJ 28-6 well, Palynofacies 1 and 2, shown from deepest to shallowest. **a** Palynofacies-1, is primarily composed of amorphous marine organic matter (AMOM) with scattered amounts of translucent and opaque phytoclasts (2067.5 m, 40× magnification). **b** Palynofacies-2, largely composed of degraded and undegraded phytoclasts,

opaques, and sparse AMOM (1978.2 m, 40× magnification). **c** Brief repeat of Palynofacies-1, an abundance of AMOM with degraded and opaque phytoclasts (1957.4 m, 40× magnification). **d** Reoccurrence of Palynofacies-2, dominantly composed of undegraded phytoclasts and opaques with a minimal presence of AMOM (1880.9 m, 40 × magnification)

and for the Mancos Shale ranged from 3.83 to 4.81 mg HC/g rock. Both S1 and S2 are used as source richness indicators.

The value which indicates the amount of carbon dioxide produced as a result of kerogen thermal breakdown is referred to as S3—measured in milligrams of CO<sub>2</sub> per gram of rock. S3 values for the Mancos Shale in the SJ 28-6 well ranged from 0.18 to 1.78 mg CO<sub>2</sub>/g rock. In the Burnham-1 well, S3 values for the Gallup Sandstone ranged from 0.21 to 0.44 mg CO<sub>2</sub>/g rock and for the Mancos Shale ranged from 0.20 to 0.36 mg CO<sub>2</sub>/g rock.

$T_{\max}$  (°C) is the temperature at which the S2 peak reaches its maximum temperature and is the primary parameter used to interpret thermal maturation.  $T_{\max}$  values for the Mancos Shale in the SJ 28-6 well ranged from 454 to 462 °C. In the Burnham-1 well,  $T_{\max}$  values for the Gallup Sandstone and Mancos Shale ranged from 438 to 442 °C.

Hydrogen Index (HI) relates to the amount of hydrogen in existing kerogen in the rock. It is expressed as milligrams of hydrocarbon per gram of TOC and is used as a source quality indicator. HI values for the Mancos Shale in the SJ 28-6 well ranged from 30 to 91 mg HC/g TOC. In the Burnham-1 well, HI values for the Gallup Sandstone ranged from 227 to 253 mg HC/g TOC and for the Mancos Shale ranged from 159 to 241 mg HC/g TOC.

Oxygen Index (OI) measures the amount of oxygen in kerogen, measured in milligrams of CO<sub>2</sub> per gram of TOC. OI values for the Mancos Shale in the SJ 28-6 well ranged from 11 to 115 mg CO<sub>2</sub>/g TOC. In the Burnham-1 well, OI values for the Gallup Sandstone ranged from 12 to 25 mg CO<sub>2</sub>/g TOC and for the Mancos Shale ranged from 10 to 18 mg CO<sub>2</sub>/g TOC.

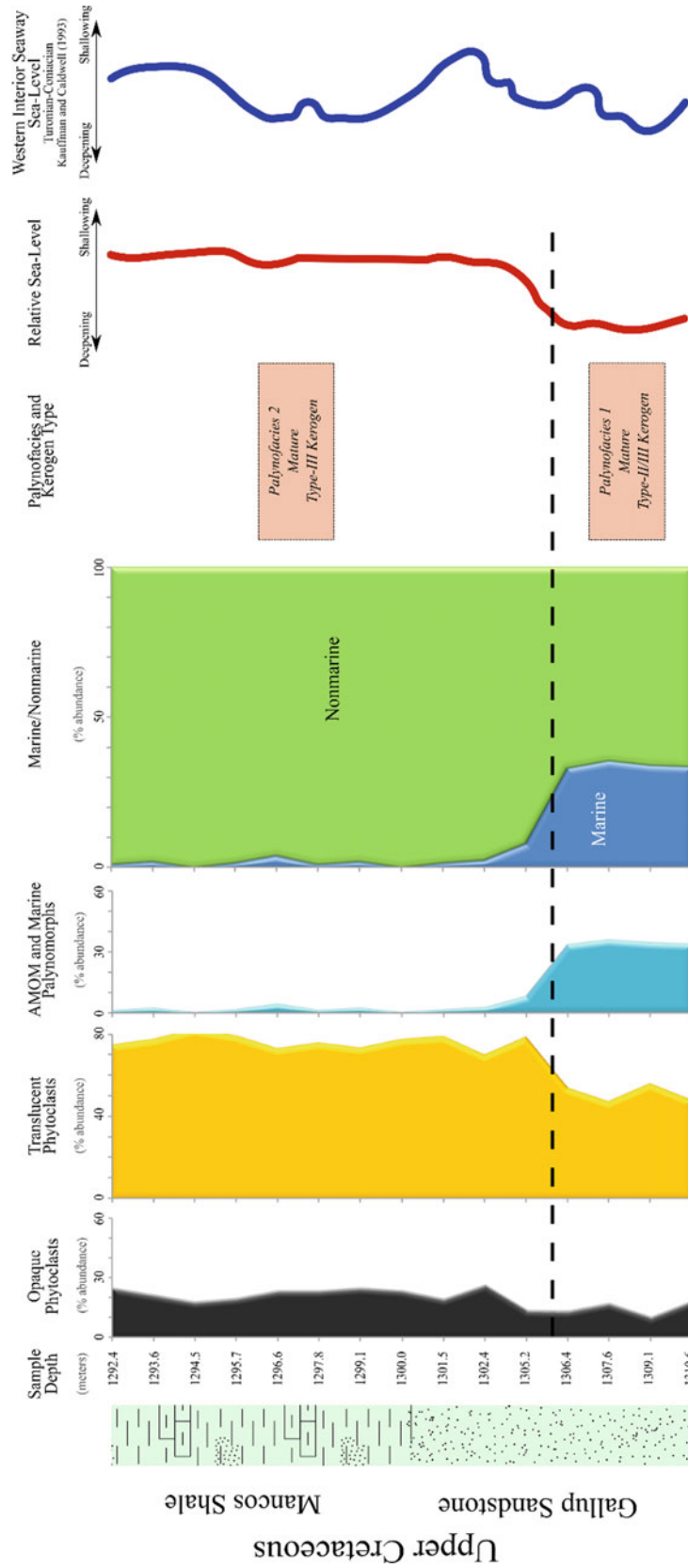


**Fig. 6** Quantitative interpretation of particulate organic matter encountered within the studied Gallup and Mancos intervals in the Burnham-1 well. Shown are lithology, sample depth, percent abundance of kerogen components, palynofacies and kerogen types, and sea-level curves. The relative sea-level (red) was inferred based on the data and compared to Kauffman and Caldwell's (1993) Western Interior Seaway sea-level during the Turonian-Coniacian of the Late Cretaceous

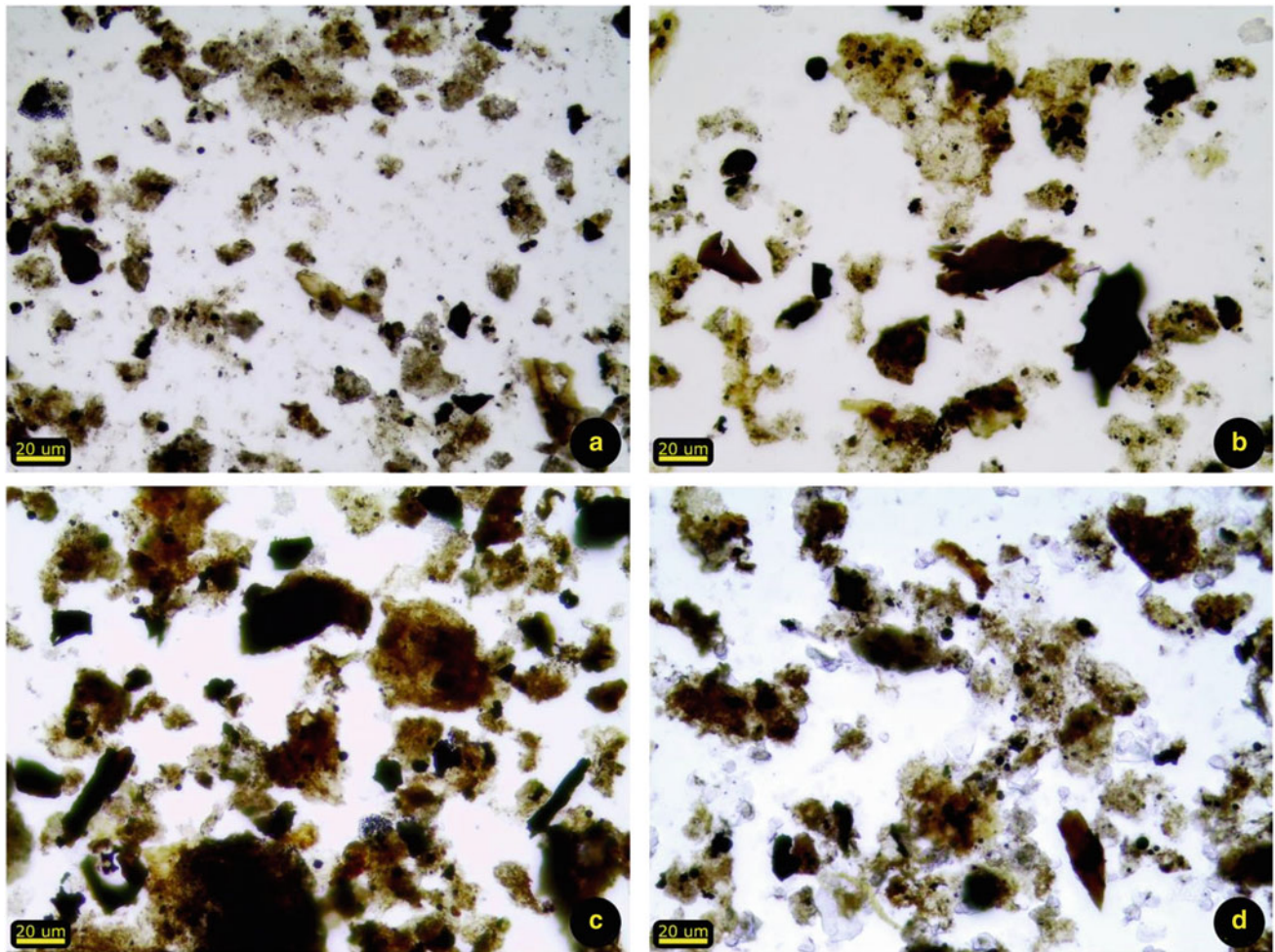


**Fig. 7** Photomicrographs of sedimentary organic matter encountered within the Burnham-1 well, Palynofacies 1 and 2, shown from deepest to shallowest. **a** Palynofacies-1, Gallup Sandstone, primarily composed of translucent and opaque phytoclasts with an abundance of amorphous marine organic matter (AMOM) (1309.1 m, 40× magnification). **b** Palynofacies-2, Gallup Sandstone, largely composed of degraded

phytoclasts with scattered amounts of undegraded phytoclasts and sparse AMOM (1301.5 m, 40× magnification). **c, d** Palynofacies-2, Mancos Shale, dominantly composed of lath-shaped opaques, degraded phytoclasts, and moderate amounts of undegraded phytoclasts with a minimal presence of AMOM (1295.7 and 1292.4, 40× magnification)

The Production Index (PI) represents the amount of hydrocarbons already generated ( $S_1$ ) to the total amount of hydrocarbons that can be generated ( $S_1 + S_2$ ). PI values for the Mancos Shale in the SJ 28-6 well range from 0.27 to 0.47. In the Burnham-1 well, PI values for the Gallup Sandstone range from 0.18 to 0.26 and for the Mancos Shale range from 0.24 to 0.25.

The ratio of free hydrocarbons to total organic carbon ( $S_1/TOC$ ) is used to identify reservoir rocks or the thermal maturity of tight source rocks (Tobey, 1999).  $S_1/TOC$  values for the Mancos Shale in the SJ 28-6 well ranged from 19 to 77. In the Burnham-1 well,  $S_1/TOC$  values for the Gallup Sandstone ranged from 37 to 85 and for the Mancos Shale ranged from 74 to 86.

Pyrolysis data can be used to calculate equivalent vitrinite reflectance values ( $R_o\%$ ), which is a thermal maturity indicator that is used to interpret the main stages of oil and gas generation. Equivalent vitrinite reflectance values for the Mancos Shale in the SJ 28-6 well range from 1.01 to 1.16. In the Burnham-1 well, Equivalent vitrinite reflectance values for the Gallup Sandstone and Mancos Shale range from 0.72 to 0.80.

#### 4.4 X-Ray Diffraction

Mineral composition for the Mancos Shale in the SJ 28-6 well had quartz and feldspar content ranging from 28 to 49

**Table 1** Pyrolysis data for the SJ 28-6 well

Sample type	Palynofacies	Depth (m)	TOC (wt %)	SI	S2	S3	$T_{max}$ (°)	HI	OI	SI/TOC	PI	% $R_0$
				mg HC/g rock	mg HC/g rock	mg CO <sub>2</sub> /g rock)		mg HC/g TOC	mgCO <sub>2</sub> /g TOC)			
Core	2	1853.3	1.19	0.22	0.52	0.46	459	44	39	19	0.30	1.10
Core	2	1861.2	0.83	0.19	0.25	0.20	454	30	24	23	0.44	1.01
Core	2	1866.7	1.69	0.35	0.96	0.18	455	57	11	21	0.27	1.03
Core	2	1888.7	1.43	0.38	0.77	1.11	461	54	77	27	0.33	1.14
Core	1	1903.4	1.42	0.47	0.74	1.49	462	52	105	33	0.39	1.16
Core	1	1957.4	1.50	0.63	0.98	0.90	456	65	60	42	0.39	1.05
Core	2	1979.3	1.39	0.56	0.86	1.60	457	62	115	40	0.39	1.07
Core	2	1997.1	1.24	0.61	0.78	0.40	456	63	32	49	0.44	1.05
Core	1	2011.2	1.96	1.21	1.79	1.30	458	91	66	62	0.40	1.08
Core	1	2027.2	1.80	1.38	1.57	1.78	457	87	99	77	0.47	1.07
Core	1	2051.4	1.82	1.21	1.46	0.74	456	80	41	67	0.45	1.05
Core	1	2066.4	2.26	1.17	1.67	0.45	457	74	20	52	0.41	1.07

**Table 2** Pyrolysis data for the Burnham-1 well

Sample type	Palynofacies	Depth (m)	TOC (wt %)	SI	S2	S3	$T_{max}$ (°)	HI	OI	SI/TOC	PI	% $R_0$
				mg HC/g rock	mg HC/g rock	mg CO <sub>2</sub> /g rock)		mg HC/g TOC	mgCO <sub>2</sub> /g TOC)			
Core	2	1292.4	1.68	1.30	3.83	0.21	440	227	12	77	0.25	0.76
Core	2	1294.5	1.98	1.47	4.68	0.36	441	236	18	74	0.24	0.78
Core	2	1296.6	1.95	1.63	4.81	0.24	438	246	12	84	0.25	0.72
Core	2	1297.8	1.89	1.63	4.79	0.20	442	253	10	86	0.25	0.80
Core	2	1300.0	1.66	1.41	4.01	0.21	442	241	12	85	0.26	0.80
Core	2	1302.4	1.24	0.69	1.98	0.22	438	159	17	56	0.26	0.72
Core	1	1306.4	1.80	0.67	3.04	0.38	440	168	20	37	0.18	0.76
Core	1	1309.1	1.75	1.24	3.44	0.44	440	196	25	71	0.26	0.76
Core	1	1310.6	1.40	0.91	2.59	0.24	440	185	17	65	0.26	0.76

wt%, carbonate content ranging from 5 to 39 wt%, and total clay mineral content ranging from 31 to 46 wt%. Mineral composition for the lower Gallup Sandstone interval in the Burnham-1 well had quartz and feldspar content of 35 wt%, carbonate content of 24 wt%, and total clay mineral content of 38 wt%. The upper Gallup Sandstone and Mancos Shale interval in the Burnham-1 well had quartz and feldspar content ranging from 34 to 55 wt%, carbonate content ranging from 24 to 36 wt%, and total clay mineral content ranging from 19 to 35 wt%. X-Ray Diffraction results for the

studied intervals within the SJ 28-6 and Burnham-1 wells are shown in Fig. 8.

## 5 Discussion

### 5.1 Hydrocarbon Source Potential

Key pyrolysis data from the SJ 28-6 and the Burnham-1 wells were plotted on geochemical logs for hydrocarbon

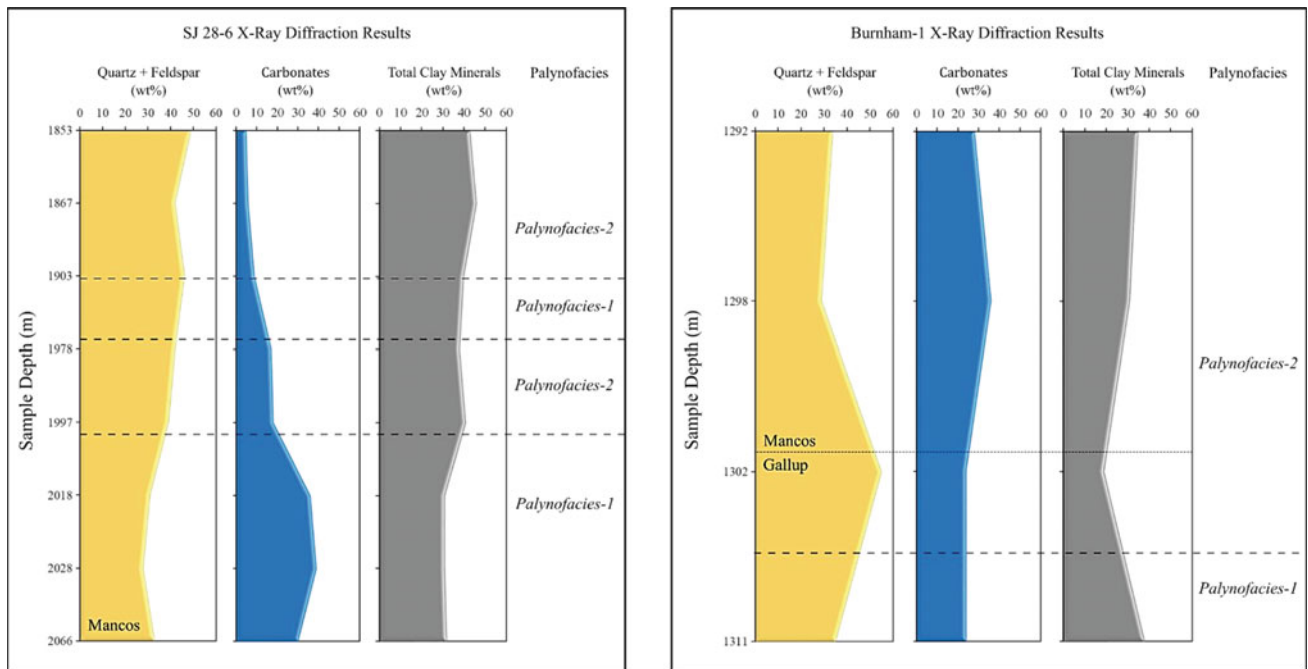


**Fig. 8** X-Ray Diffraction results for SJ 28-6 and Burnham-1 wells showing wt.% composition of quartz and feldspars, carbonates, and total clay minerals of the Mancos and Gallup formations

source interpretation (Figs. 9 and 10). The organic richness of the Mancos Shale in SJ 28-6 is good to excellent throughout the studied interval, with only one sample near the top of the interval being categorized as fair; however, the hydrocarbon source potential is poor, with S2 values <2 mg HC/g rock. Organic matter type determined by the hydrogen index values suggests the entire section to be terrestrially influenced, mainly gas-prone material, which conforms with recorded palynofacies composition (Fig. 4). Normalized oil

content places the deepest section of the Mancos as a mature stained source rock, but as it shallows it is interpreted as a low maturity source rock. Calculated maturity from vitrinite reflectance values infers that the Mancos is within the wet gas/condensate zone.

The Gallup Sandstone (1311–1300 m) within Burnham-1 has good organic richness but its hydrocarbon source potential is fair. Based on HI values, the formation is primarily derived from terrestrial material and classified as

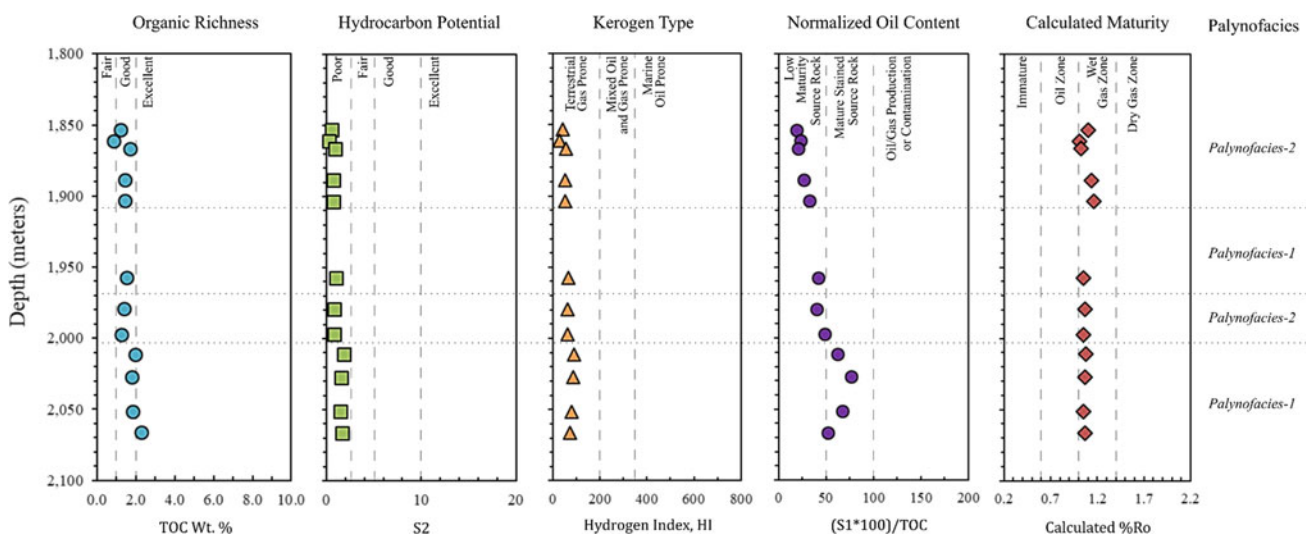


**Fig. 9** Geochemical logs of pyrolysis data for the Mancos Shale from the SJ 28-6 well showing organic richness (TOC), hydrocarbon potential (S2), kerogen type (HI), normalized oil content (S1/TOC), and calculated maturity (Ro%). Palynofacies divisions are shown for reference



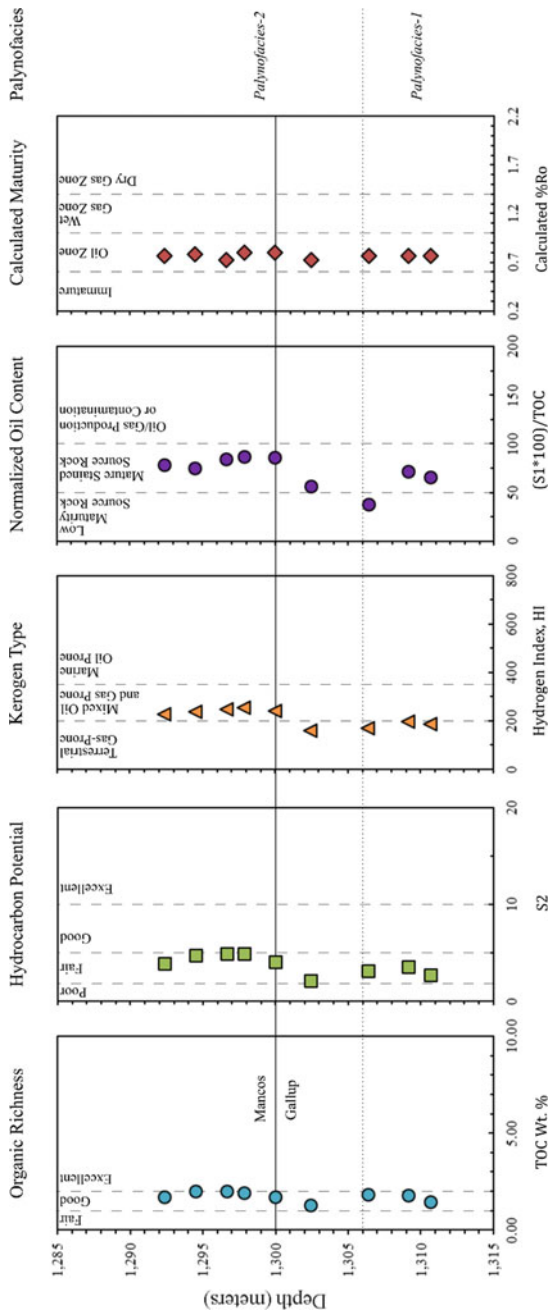


**Fig. 10** Geochemical logs of pyrolysis data for the Gallup and Mancos formations from the Burnham-1 well showing organic richness (TOC), hydrocarbon potential (SZ), kerogen type (HI), normalized oil content (SI/TOC), and calculated maturity (Ro%). Palynofacies divisions are shown for reference

gas-prone. The Gallup is mostly a mature stained source rock with calculated vitrinite reflectance values indicating maturity within the oil generation window.

The studied Mancos Shale interval (1299–1292 m) within Burnham-1 shows a good to excellent organic richness with a hydrocarbon source potential straddling the line between fair to good. According to HI values, the formation is primarily derived from mixed oil- and gas-prone organic constituents. The ratio of free hydrocarbons to TOC classifies the Mancos as a mature stained source rock. Calculated vitrinite reflectance indicates a thermally mature formation within the oil generation window.

### 5.2 Visual Kerogen Type and Thermal Maturity

According to visual kerogen analysis, Palynofacies-1 organic constituents in both studied wells suggest kerogen type II-III, mixed oil- and gas-prone organics, based on the abundance of both AMOM and phytoclasts. Palynofacies-2 in both wells was dominated by phytoclasts, suggesting kerogen type III, mostly gas-prone organics. Pyrolysis data were plotted on a Pseudo van Krevelen diagram to evaluate kerogen type and thermal maturity based on  $T_{max}$  and HI values (Fig. 11). The diagram shows that SJ 28-6 Palynofacies-1 is in between

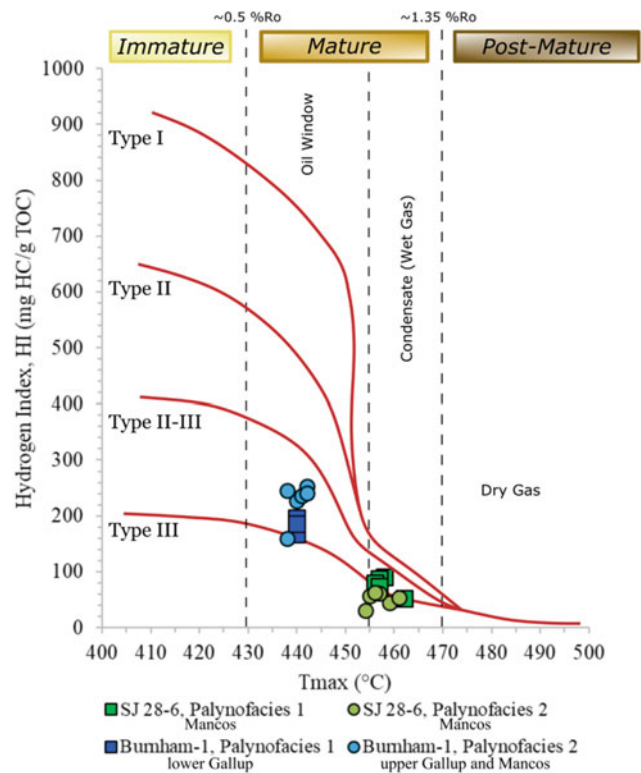


**Fig. 11** Pseudo van Krevelen diagram illustrating the kerogen type and thermal maturity of the identified palynofacies within the SJ 28-6 and Burnham-1 wells

kerogen type II-III and type III and Palynofacies-2 is kerogen type III. Both palynofacies in the Burnham-1 well are within kerogen type II-III. The studied interval within Burnham-1 is in the oil generation window with  $T_{max}$  values between 438 and 442 °C, while SJ 28-6  $T_{max}$  values of 454–462 °C plot mainly within the gas generation window. Pyrolysis data, therefore, show that the Mancos and Gallup formations within both studied intervals are thermally mature. This is independently confirmed by the observed spore and pollen exine colors which ranged from orangish-brown to dark brown on Pearson’s (1984) color standard.

### 5.3 Depositional Paleoenvironment

Cretaceous rocks within the San Juan Basin represent both continental and marine environments that were formed through transgressive and regressive cycles of the Western Interior Seaway. Approximately 2000 m of strata were deposited within the Cretaceous time (Craig, 2001). An older study on the Mancos Shale by Molenaar (1977) describes it as being deposited within a low-energy, deep offshore marine environment; however, a more recent study by Genovese (2017) interprets the formation to be deposited in a high-energy, nearshore environment within a water depth of less than 100 m. Molenaar (1974) describes the Gallup Sandstone as being deposited as northeastward delta front sandstones. To reconstruct the depositional paleoenvironments in this study, percentage abundances of organic constituents observed in each sample were plotted on the Zobaa et al. (2015) sedimentary particulate organic matter

(POM) ternary plot. This plot graphically represents the distribution of the major kerogen components in the context of paleoenvironment parameters.

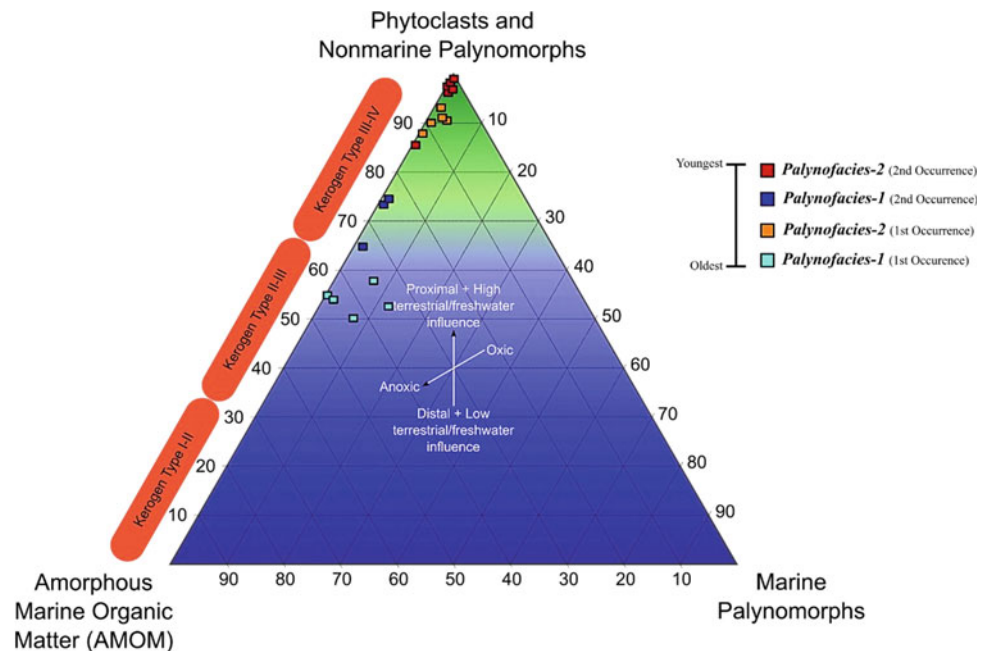
#### 5.3.1 SJ 28-6 Interpreted Paleoenvironment

According to the Zobaa et al. (2015) sedimentary POM ternary plot for the SJ 28-6 well (Fig. 12), the Mancos Shale began deposition in a terrestrially influenced, shallow marine inner shelf environment (Palynofacies-1). The abundance of terrestrial constituents combined with a moderate number of AMOM suggests the deepest portion of the Mancos was deposited in a nearshore environment with pronounced terrestrial influence. The majority of observed opaques were equant in shape, indicating the material was transported some distance from its origin to the inner shelf depositional setting.

A paleoenvironmental transition to a fluvio-deltaic setting with more oxic conditions occurred during the accumulation of Palynofacies-2 sediments. The majority of POM in this section of the Mancos Shale are of terrestrial origin, indicating high proximity to fluvio-deltaic sources and the possibility of reduced salinity (Tyson, 1993). Opaques were mostly lath-shaped and phytoclasts were well-preserved, reflecting minimal transport distance to the location of deposition.

X-Ray Diffraction data (Fig. 8) show that the deepest part of the studied Mancos section is composed of a similar amount of quartz (average 25 wt%), clay mineral content (30 wt%), and carbonates (35 wt%). Within the younger section, the average carbonate content dramatically decreases to an average of <10 wt% as quartz and clay minerals dominate

**Fig. 12** Zobaa et al. (2015) sedimentary particulate organic matter (POM) ternary plot illustrating the positions of Palynofacies 1 and 2 (Mancos Shale) in the SJ 28-6 well in the context of paleoenvironmental parameters. Palynofacies 1 and 2 are both repeated in the studied interval



with a combined average content of >85 wt%. Accordingly, by combining palynofacies and geochemical data, the studied Mancos section within the SJ 28-6 well began deposition in a shallow marine, prodelta environment where moderate amounts of sands, clays, and terrestrial phytoclasts were transported into the marine environment, intermixing with carbonates and AMOM. Subsequently, delta progradation resulted in a change to high-energy, more oxygenated, fluvio-deltaic conditions. The abundance of terrestrially derived organics and mass amounts of sands and clays argue for a delta front depositional environment. A brief transgressive occurrence led to a repeat of the prodelta (Palynofacies-1) depositional conditions until sea-levels once again regressed and high-energy, delta front deposition prevailed.

### 5.3.2 Burnham-1 Interpreted Paleoenvironment

Based on to the Zobaa et al. (2015) sedimentary POM ternary plot for the Burnham-1 well (Fig. 13), the oldest portion of the Gallup Sandstone was deposited in an oxygenated, nearshore depositional environment with freshwater influence (Palynofacies-1). An abundance of terrestrially derived organic constituents intermixed with a reasonable amount of AMOM argues for a proximal, terrestrially influenced depositional setting. Opaques included in this section were both equant and lath-shaped, suggesting a moderate distance of travel to the depositional location.

The youngest section of the Gallup Sandstone and the Mancos Shale were deposited in a more proximal, more oxic, fluvio-deltaic depositional environment (Palynofacies-2) as

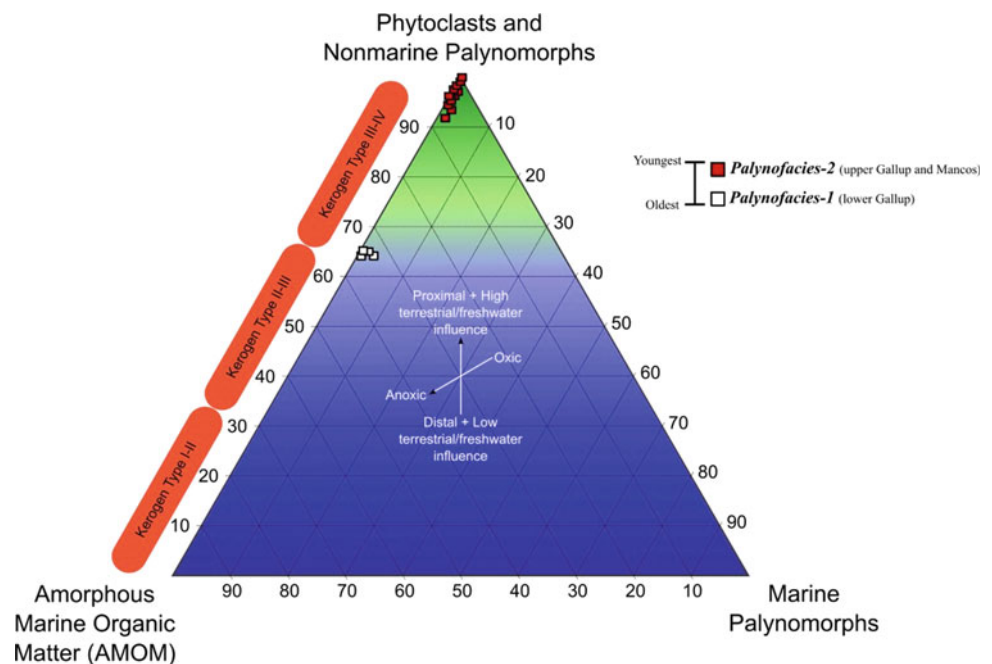
seen from the dominance of degraded phytoclasts and more frequent observations of opaques.

X-Ray Diffraction data (Fig. 8) show that the oldest Gallup Sandstone interval (Palynofacies-1) is composed of a moderate amount of quartz and feldspar (35 wt%) and clays (38 wt%) with a smaller percentage of carbonates (24 wt%). A difference in composition is noticed within the upper Gallup Sandstone and Mancos Shale (Palynofacies-2), with a greater average percentage of quartz and feldspar (39 wt%) and carbonates (29 wt%) and fewer clay minerals (28 wt%). Consequently, the sum of palynofacies and geochemical data shows that the Gallup deposition began in a proximal marine, prodelta environment which changed to a more proximal delta front setting as delta progradation likely occurred during the end of Gallup and Mancos deposition. A paleodepositional model depicting the observed delta progradation in the studied wells is shown in Fig. 14.

## 6 Conclusions

Palynofacies and organic geochemical data gathered from the Mancos and Gallup formations provided information on hydrocarbon source potential and depositional paleoenvironment in the San Juan Basin of New Mexico. Two palynofacies were identified in each well. Palynofacies-1 organic nature was similar in both wells, containing type II-III kerogen (mixed oil- and gas-prone) and was deposited in a shallow marine, prodelta environment. Organic constituents within Palynofacies-2 in both wells indicate type III kerogen (mostly gas-prone) and deposition in a delta front environment.

**Fig. 13** Zobaa et al. (2015) sedimentary particulate organic matter (POM) ternary plot illustrating the positions of Palynofacies-1 (Gallup Sandstone) and Palynofacies-2 (uppermost Gallup and Mancos formations) in the Burnham-1 well in the context of paleoenvironmental parameters



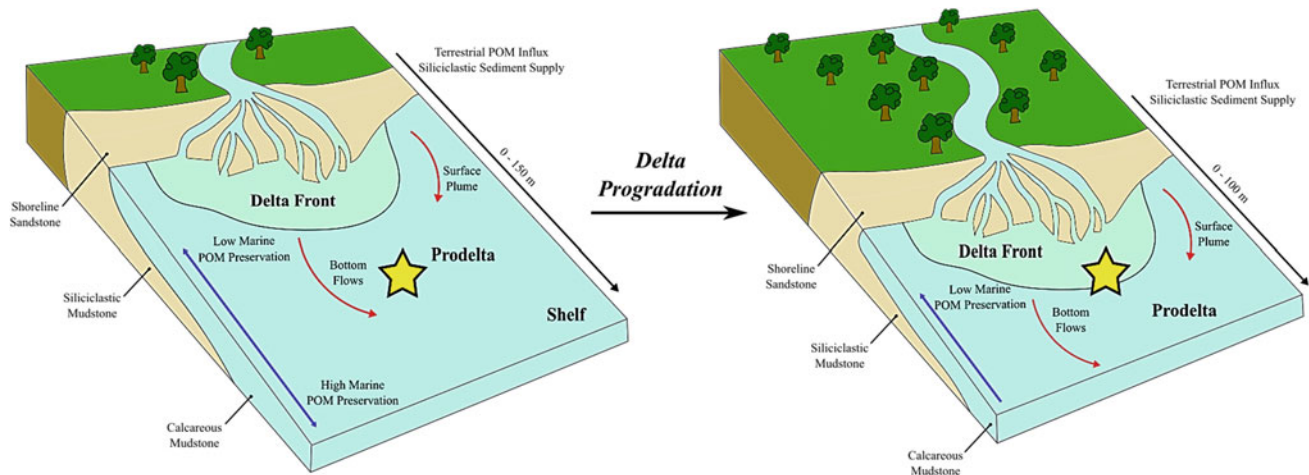


**Fig. 14** A paleodepositional model of the SJ 28-6 and Burnham-1 wells (Modified from Hart, 2016). Delta progradation resulted in a regional shift from prodelta conditions to a delta front setting. The yellow star indicates the approximate location of deposition for both wells

The Mancos and Gallup formations are both thermally mature, based on spore/pollen coloration and pyrolysis data. Despite possessing good organic richness, the hydrocarbon source potential of the Mancos Shale in SJ 28-6 is overall poor. Within Burnham-1, the hydrocarbon source potential of the Gallup Sandstone and Mancos Shale is mostly fair with good to excellent organic richness.

**Acknowledgements** The authors would like to thank Mr. Mike Party, President of Beryl Oil and Gas who generously funded this research. We wish to thank Annabelle Lopez from the New Mexico Subsurface Data and Core Library Facility for facilitating the collection of samples and providing valuable data from past studies. Special thanks to Impact Exploration Services for conducting the pyrolysis and X-Ray Diffraction analyses.

## References

- Broadhead, R. (2013). The Mancos Shale and “Gallup” zones in the San Juan Basin: geologic framework, historical production, future potential. In *San Juan Basin Energy Conference*, Farmington, New Mexico, March 18, 2013.
- Broadhead, R. F. (2015). The Upper Mancos Shale in the San Juan Basin: Three plays, conventional and unconventional. American Association of Petroleum Geologists, Search and Discovery, Document No. 10791 (39 p).
- Craig, S. D. (2001). Geologic framework of the San Juan Basin structural basin of New Mexico, Colorado, Arizona, and Utah, with emphasis on Triassic through Tertiary rocks in Regional Aquifer-System Analysis—San Juan Basin, New Mexico. U.S. Geological Survey Professional Paper 1420 (81 p).
- Dembicki, H. (2016). *Practical petroleum geochemistry for exploration and production* (1st ed.). Elsevier Science.
- El Beialy, S. Y., Zobaa, M. K., & Taha, A. A. (2016). Depositional paleoenvironment and hydrocarbon source potential of the Oligocene Dabaa Formation, north Western Desert, Egypt: A palynofacies approach: *Geosphere* (Vol. 12, No. 1, pp. 346–353). <https://doi.org/10.1130/GES01227.1>
- Genovese, C. (2017). *Detailed thin-bedded facies analysis of Mancos C in the upper Mancos Shale, New Mexico* (M.S. thesis) (63 p.). McMaster University.
- Hart, B. S. (2016). Marine mudstone source rocks in epicontinental basins: Development of a conceptual facies model and application to Cenomanian/Turonian mudstones of the Cretaceous Western Interior Seaway. In M.P. Dolam, D.K. Higley, & P.G. Lillis (Eds.), *Hydrocarbon source rocks in unconventional plays, Rocky Mountain Region* (pp. 364–421).
- Kauffman, E. G., & Caldwell, W. G. E. (1993). The Western Interior Basin in space and time. In W.G.E. Caldwell, E.G. Kauffman (Eds.), *Evolution of the western interior basin* (pp. 1–30). Geological Association of Canada, Special Paper 39.
- Molenaar, C. M. (1974). Correlation of the Gallup Sandstone and associated formations, Upper Cretaceous, eastern San Juan and Acoma Basins, New Mexico. In C.T. Siemers, L.A. Woodward, & J.F. Callendar (Eds.), *25th Annual Fall Field Conference, Guidebook* (pp. 251–258). New Mexico Geological Society.
- Molenaar, C. M. (1977). Stratigraphy and depositional history of Upper Cretaceous rocks of the San Juan Basin area, New Mexico and Colorado, with a note on economic resources. In *28th Annual Fall Field Conference, Guidebook* (pp. 159–166). New Mexico Geological Society.
- Pearson, D. L. (1984). *Pollen/spore color standard, version 2*. Phillips Petroleum Co.
- Ridgely, J. L., Condon, S. M., & Hatch, J. R. (2013). Geology and oil and gas assessment of the Mancos-Menefee composite total petroleum system in Total petroleum systems and geologic assessment of undiscovered oil and gas resources in the San Juan Basin province, exclusive of Paleozoic rocks. U.S. (97 p.). Geological Survey Digital Data Series 69-F, Chapter 4.
- Silver, C. (1951). Cretaceous stratigraphy of the San Juan Basin. In T. C. Smith, & C. Silver (Eds.), *2nd Annual Fall Field Conference, Guidebook* (163 p.). New Mexico Geological Society, San Juan Basin (New Mexico and Arizona).
- Stone, W. J., Lyford, F. P., Frenzel, P. R., Mizell, N. H., Padgett, E. T. (1983). Hydrogeology and water resources of San Juan Basin. Hydrologic report 6 (70 p.). New Mexico.
- Tobey, M. H. (1999). TOC, Rock-Eval, or SR Analyzer interpretive guidelines (11 p.). Weatherford Laboratories, Geochemical Services, Application Note 99-4.
- Toon, S. (2018). *San Juan rising in oil and gas investor* (p. 53–65). Hart Energy Publishing.

- Traverse, A. (2007). *Paleopalynology. Topics in geobiology* (2nd ed.). Springer
- Tyson R. V. (1993). Palynofacies analysis. In D.J. Jenkins (Ed.), *Applied micropalaeontology*: (pp. 153–191). Kluwer Academic Publishers.
- Zobaa, M. K., Oboh-Ikuenobe, F. E., & Ibrahim, M. I. (2011). The Cenomanian/Turonian oceanic anoxic event in the Razzak Field, north Western Desert, Egypt: Source rock potential and paleoenvironmental association. *Marine and Petroleum Geology*, 28, 1475–1482.
- Zobaa, M. K., El Beialy, S. Y., El-Sheikh, H. A., & El Beshtawy, M. K. (2013). Jurassic–Cretaceous palynomorphs, palynofacies, and petroleum potential of the Sharib-1X and Ghoroud1X wells, north Western Desert, Egypt. *Journal of African Earth Sciences*, 78, 51–65.
- Zobaa, M. K., El Beialy, S. Y., Taha, A. A., & Oboh-Ikuenobe, F. E. (2015). Improved graphical representation of sedimentary organic matter as paleoenvironmental parameters. In *2015 Geological Society of America Annual Meeting*, Baltimore, Maryland, Abstract (Vol. 47, Issue 7, p. 365).



# Petroleum System Analysis of the Main Paleozoic Source Rocks in Western Iraq: A 1D Basin Modelling Approach

Qusay Abeed

## Abstract

Three 1D models were built to study the petroleum potential of the primary Paleozoic source rocks (Ordovician–Silurian) in the Western Desert of Iraq using information and data based on geo-related information from Akkas\_1, Khleisia\_1, and Key Hole\_5/1 wells. Results of 1D basin modelling indicated no significant hydrocarbon quantities have been generated from the Akkas hot shale in both Khleisia\_1 and Akkas\_1 wells. Thus, the economic hydrocarbons discoveries in these two wells are likely charged by Akkas hot shale where it has experienced higher maturity. Using source rock maturity and hydrocarbon charge indications, this study has speculated three possible hydrocarbon migration pathways; from the east, towards the border with the Mesopotamian Basin, in which stratigraphic correlations have shown that the Paleozoic successions are buried to greater depth intervals or toward the south and southwest Akkas field, in which another stratigraphic correlation has shown that the Akkas Formation has gained significantly greater thickness, which has increased the burial depth. Another possible migration pathway could be the upward migration through the faults from the deeper Khabour Formation. Further study of the area between Akkas\_1 well and Key Hole 5/1, is recommended where the Akkas hot shale is expected to be at oil window maturity. A 3D basin model is highly recommended to indicate accurate migration pathways and petroleum accumulation.

## Keywords

Akkas hotshale • Iraq • Paleozoic • Basin modeling • Source rocks

## 1 Introduction

Although the Western Desert represents around one-third of the Iraqi total surface area, its petroleum potential has been poorly explored and only a little is known about its petroleum systems (Fig. 1). While the Mesozoic successions in Iraq are known to host the main working petroleum systems, the Paleozoic petroleum system is considered the prominent play in western and southwestern Iraq (Al-Hadidy, 2007).

The Paleozoic succession of the Iraqi Western Desert constitutes mainly alternations of siliciclastic lithologies and anhydrite with some carbonate intercalations (Fig. 2). These formations represent various marine depositional environments varying between outer and inner neritic shelves with local lagoons and upwelling currents (Al-Ameri & Baban, 2002; Al-Hadidy, 2007).

The Ordovician Khabour Formation was deposited in a shallow marine environment. It consists of stacked transgressive and regressive cycles that are controlled by the change in eustasy. The Silurian Akkas Formation hot shale sections were deposited in an open marine environment (Al-Juboury & Al-Hadidy, 2009).

The Akkas\_1 well comprises the reference sections of the Khabour, the Akkas, the Pirispiki Red Beds, Kaista, Ora, and Harur formations. In this well, the Silurian Akkas Formation consists of two members which are named after the towns of Hoseiba and Al-Qaim in the western Iraqi provenance of Al-Anbar. The Khabour Formation consists of seven members (K1–K7) referred to as Khabour valley in northern Iraq, where its type section is exposed (Al-Hadidy, 2007).

This study aims to characterize the generation, expulsion, and migration of the Paleozoic hydrocarbons in western Iraq (i.e. Ordovician Khabour and Silurian Akkas formations). It represents the first attempt to use basin modelling techniques to study the Paleozoic petroleum system of western Iraq, a similar study, specifically for this area and study wells, has not been published so far.

Q. Abeed (✉)  
Halliburton, Landmark Solutions, Abingdon, UK  
e-mail: [Qusay.Abeed@halliburton.com](mailto:Qusay.Abeed@halliburton.com)

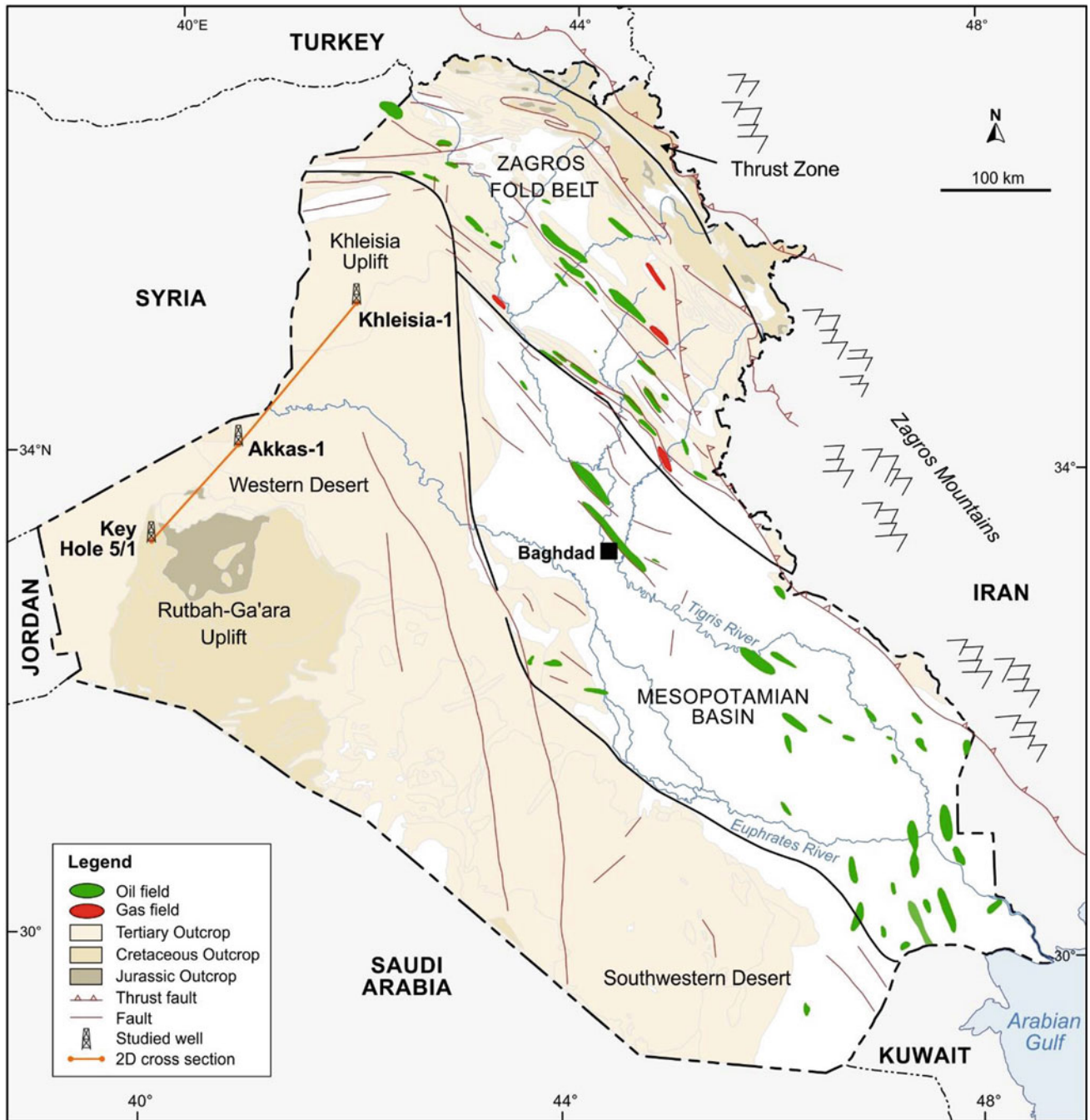


**Fig. 1** Base map showing major hydrocarbon accumulations in Iraq. The well locations as well as the schematic 2D cross-section panels are shown in (Fig. 9), (modified after Pitman et al., 2004)

## 2 Paleozoic Petroleum System of Western IRAQ

### 2.1 Source Rocks

At the end of the Ordovician period, a major transgression impacted Gondwana, which resulted in the deposition of the

outer shelf, graptolite-rich shales (Jassim & Goff, 2006). The most prominent Paleozoic source rocks in the Arabian Peninsula and North Africa are the Silurian hot shales (Boote et al., 1998; Lüning et al., 2000). These organic-rich hot shales represent the primary source rocks for the non-associated, “sweet” light oils and gas discovered in the Akkas field and Khleisia\_1 well located in the Western Desert of Iraq (Al-Ameri, 2010; Al-Hadidy, 2007; Alkhafaji et al., 2015; Aqrawi, 1998).

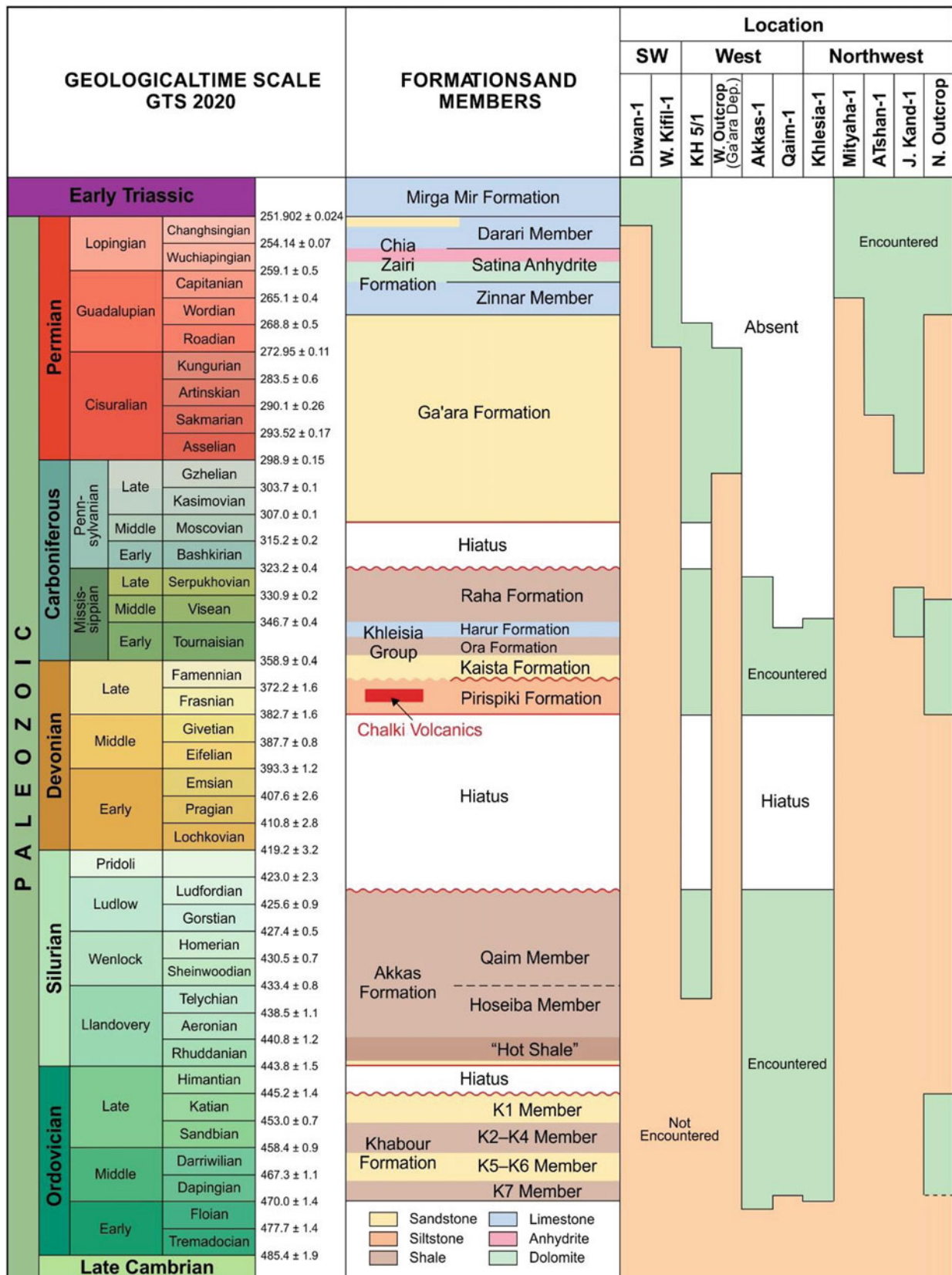


**Fig. 2** The paleozoic stratigraphic column shows the encountered successions in the studied wells and some other wells in different regions in Iraq (modified after Al-Hadidy, 2007). The lithological unit ages were calibrated to GTS 2020 (Cohen et al., 2013; updated)



The black shales in the Ordovician Khabour Formation, the Lower Carboniferous Ora Shale Formation, and the Upper Permian Chia Zairi Formation can also be considered potential regional source rocks, but significantly less important than the hot shale. For example, geochemical parameters such as Rock–Eval pyrolysis and the total organic carbon (TOC) values of the Khabour Formation in the Akkas oilfield indicated a low potentiality, although this could be derived from the high maturity of the studied succession (Alkhafaji et al., 2015; Jassim & Goff, 2006).

Petrographic investigation and bitumen composition analyses indicated that Akkas and Khabour Formations contain predominantly amorphous organic matter of marine origin (i.e. Type-II kerogen (Alkhafaji et al., 2015).

## 2.2 Reservoirs

The primary Paleozoic reservoir rocks in the study area are the upper Ordovician K1-K4 sandstone members of the Khabour Formation. Moreover, the Qaim Member of the Silurian Akkas Formation acts as a potential regional reservoir (Al-Hadidy, 2007; Al-Juboury & Al-Hadidy, 2009). Further, potential reservoirs may be found in the Carboniferous Ga'ara sandstones and the carbonates of the Permian Chia Zairi Formation in the Southwestern Desert (Al-Hadidy, 2007; Aqrawi, 1998).

The Khabour K1 and K2 members in the Akkas field have an average porosity of (7.6, 6.6%) and average permeability of (0.13, 0.08 mD) respectively with fractures along two orientations and provide preferential flow directions (Al-Hadidy, 2007).

## 2.3 Trap Formation

The trap in the Akkas oil field is structural, based on the seismic interpretations and well data. It is considered a basement-controlled, “flat-top” anticline bounded by “door” faults along its flank (Al-Hadidy, 2007).

The Widyman Basin, located in the western and southwestern deserts, includes approximately 155 prospects that vary in length from 1 to 46 km, with seven greater than 20 km. The Triassic and Paleozoic formations are the main targets. They differ in shape and size (Fox & Ahlbrandt, 2002).

## 3 Methods

### 3.1 Petroleum Systems Modelling

Three well locations were selected to perform a 1D basin model to numerically simulate the burial history and petroleum

generation of potential Palaeozoic source rocks located in western Iraq (i.e. Akkas\_1, Khleisia\_1, and Key Hole 5/1). The Akkas\_1 well represents the deepest penetration in the Akkas oil field and the Khleisia-1 well is located northward. They represent discovery of light and sweet oil (Al-Hadidy, 2007).

The models were created using basin modelling software (Permedia 14.0.0®) from Halliburton-Landmark Solutions. Formation tops and lithology were mainly derived from published work (Al-Hadidy, 2007) and accomplished from other resources (e.g. Buday & Jassim, 1987; Jassim & Goff, 2006; van Bellen et al., 1959).

Total organic carbon (TOC) analysis was performed on samples from the Akkas Formation in the Akkas\_1 well (Alkhafaji et al., 2015) and found to be ranging between (0.16–6.97 wt %) with the highest values measured in the basal part of the Hoseiba Member, which assigned for the “hot shale” interval. Results from a palynostratigraphic analysis indicate marginally mature source rock (Al-Ameri, 2010; Al-Ameri & Baban, 2002).

The Akkas Formation intervals in the Khleisia\_1 and Akkas\_1 wells share the same geochemical source rock properties and depositional environments (Aqrawi, 1998 and the references therein).

## 4 Basin Modelling Input Data

The boundary conditions of the wells (Akkas\_1, Khleisia\_1 and Key Hole 5/1) were implemented and calibrated using present-day observed temperatures with paleo-temperature indicators (i.e. Ro\_Equiv [%]) to provide insights into the burial history of the Paleozoic main source rocks.

The paleo sea-level curve (Snedden & Liu, 2010) was used and calibrated to GTS2012. The matrix conductivity of the different lithologies is calculated using published models (Sekiguchi, 1984).

### 4.1 Akkas\_1 Well

Information on stratigraphy, hiatuses, and lithology was accomplished from published work (e.g. Al-Hadidy, 2007; Aqrawi, 1998; Buday & Jassim, 1987; Jassim & Goff, 2006; van Bellen et al., 1959). Geochemical data required to evaluate source rock potential and thermal maturity in the well (e.g. TOC wt.%, Hydrogen indices HI (mg HC/gTOC), and Ro\_equiv.%) were collected from Al-Ameri (2010), Al-Hadidy (2007), Al-Khafaji (2013), Aqrawi (1998) (Fig. 3).

### 4.2 Well Khleisia\_1

The 1D model of the Khleisia\_1 well used stratigraphic data and lithology from Al-Hadidy (2007), Aqrawi (1998),

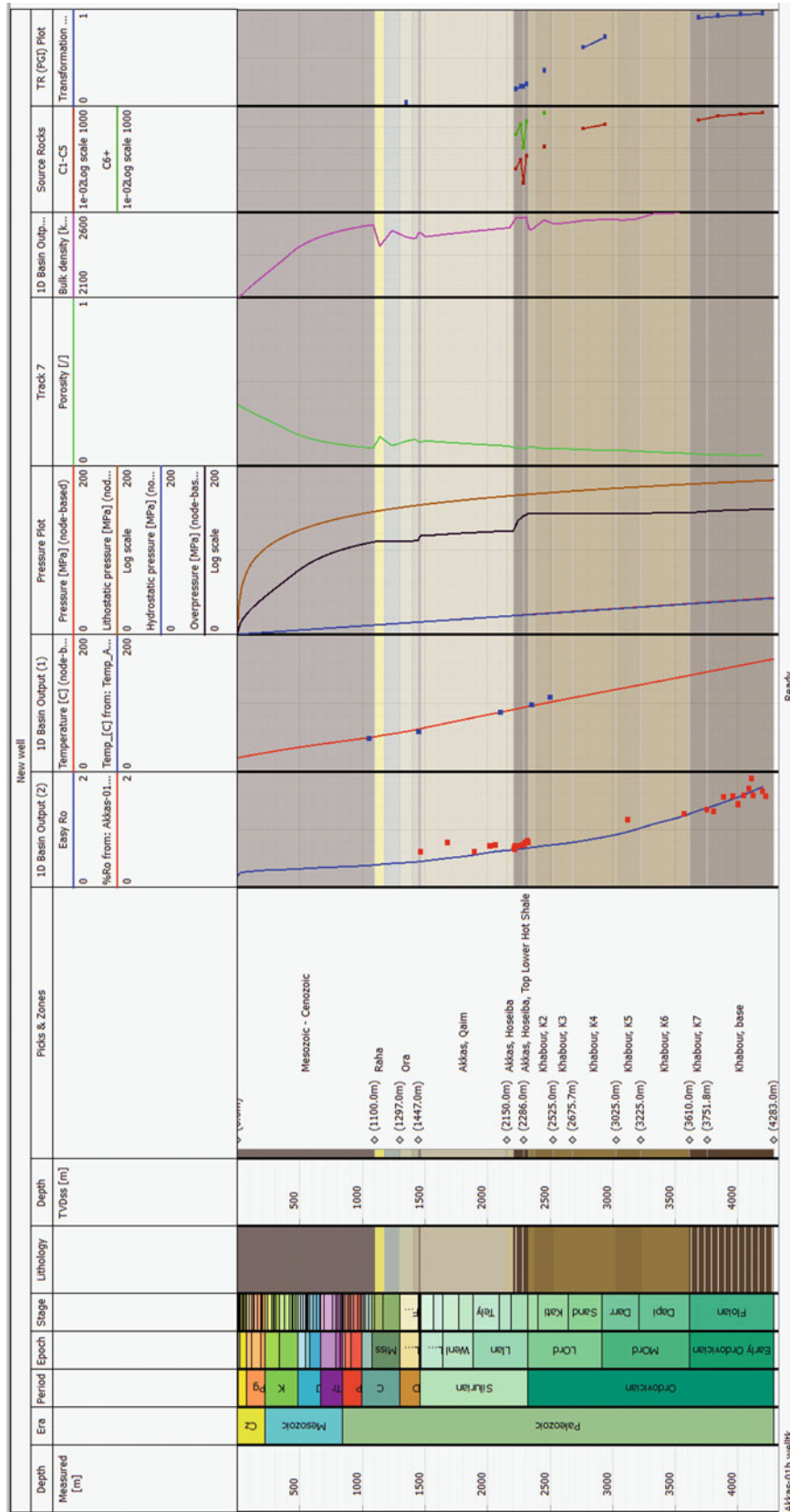


Fig. 3 Depth profile showing the input parameters used for the calibration and evaluation of the petroleum source rock as well as the extracted outputs of Akkas\_1 well

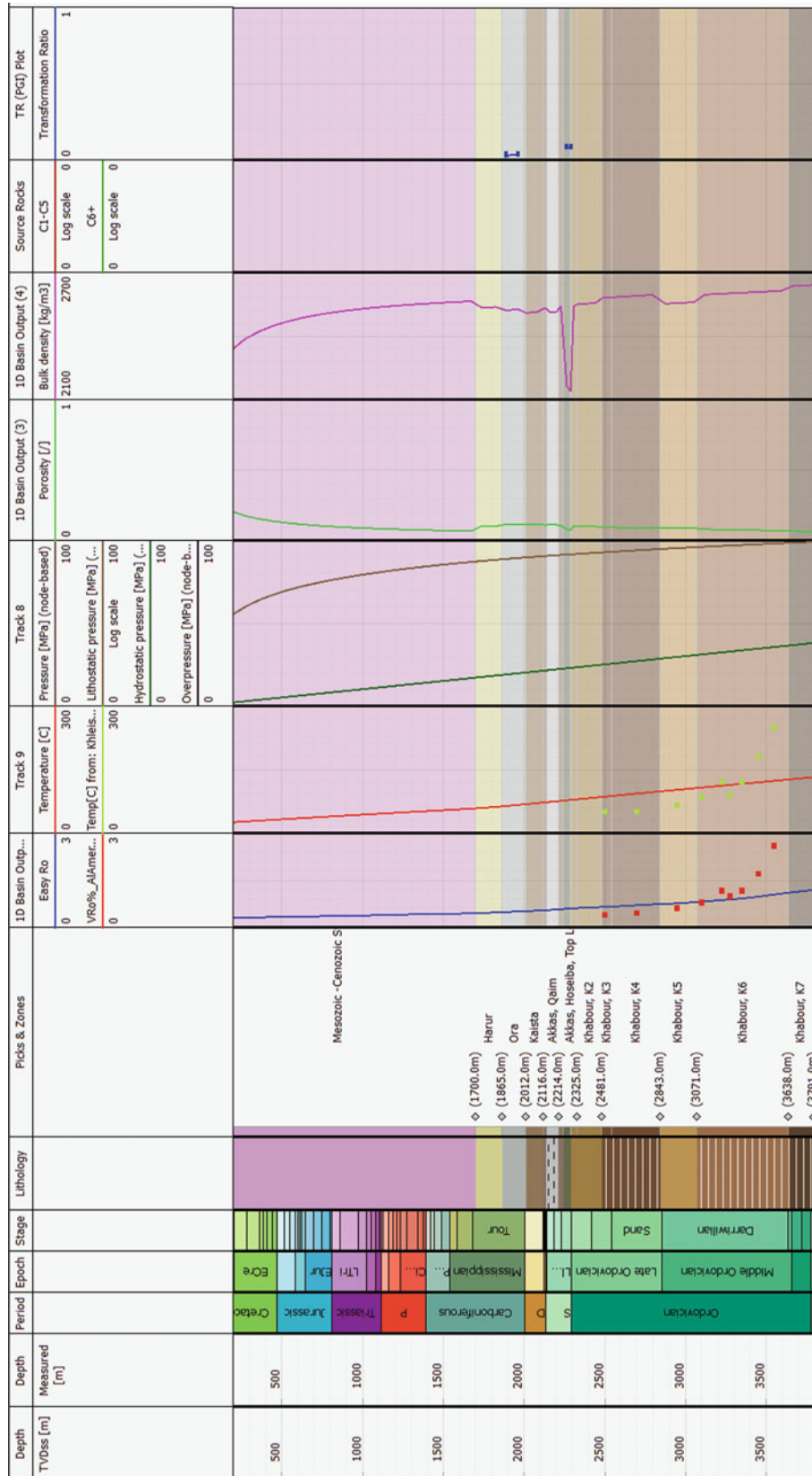


Fig. 4 Depth profile plot showing the input parameters used for the calibration and evaluation of the petroleum source rock as well as the extracted outputs Kheleisia\_1. TR [%] indicates no significant hydrocarbon generation in the hot shale

**Table 1** Formation tops in (m) of the modelled wells (modified after Al-Hadidy, 2007)

Formations/Members	Akkas_1	Khleisia_1	Key hole 5/1
RTKB	287	293	
Mesozoic-present day	1100-0 <sup>a</sup>	1700-0 <sup>a</sup>	–
Ga'ara	Absent	Absent	0.0
Raha	1100	Absent	670
Harur	1177	1700	854
Ora	1297	1865	940
Kaista	1402	2012	1240
Pirispiki	1447	2116	1313
Akkas/Qaim	1463	2139	1333
Akkas/Hoseiba	2150	2214	
Upper hot shale	2205	2243	
Lower hot shale	2286	2286	3333 <sup>b</sup>
Khabour/ K1	2327	2291	
Khabour/ K2	2375	2325	
Khabour/ K3	2525	2481	
Khabour/ K4	2675	2540	
Khabour/ K5	3025	2843	
Khabour/ K6	3225	3071	
Khabour/ K7	3610	3638	
T.D (m)	4238	3791	3333 <sup>b</sup>

<sup>a</sup> Inferred depth

<sup>b</sup> The basal Akkas hot shale is interpreted to be at a depth of about (3333 m) in well Key Hole\_5/1 according to stratigraphic correlation by Aqrabi (1998 and the references therein). Accordingly, the T.D. of the well was extended to this value in the 1D model of well Key Hole 5/1.

Buday and Jassim (1987), Jassim and Goff (2006), van Bellen et al., (1959). Input geochemical data of source rocks and maturity were used from Al-Ameri and Baban (2002). The geochemical analysis indicates significantly low TOC (wt%) content for the Khabour Formation indicating low to non-petroleum potential of the formation in this well (Fig. 4). The Akkas hot shale interval in the same well was considered to have similar source rock potential as in the Akkas\_1 well (Salleh & Mokhtar, 1995, in Aqrabi, 1998).

### 4.3 Well Key Hole 5/1

Key Hole\_5/1 is a relatively shallow “water well” that did not penetrate the main Paleozoic hot shales interval of the Akkas Formation (Table 1). “Ludlovian” rocks were penetrated for 270 m without reaching the Silurian succession base (Al-Haba et al., 1994, in Aqrabi, 1998).

The Silurian succession can reach 2000 m thick in the Rutbah-Ga'ara Uplift area in the Western Desert, based on correlations with its equivalent rock units in eastern Jordan and northern Saudi Arabia. Thus, the Akkas Formation thickness was increased to 2000 m in the model of well Key

Hole\_5/1 to speculate on the possible maturity of the hot shale interval.

### 4.4 Source Rock Kinetics

Hydrocarbon kinetics is a key aspect to quantify petroleum generation capacity and determining the petroleum generation timing. In this study, the models used the source rock kinetics of Pepper and Corvi (1995) that classified the source rock kinetics based on their common organofacies. It assumes that the amount of hydrocarbon generated is a function of the TOC and initial hydrogen index (HI) of immature source rock. Kerogen Type-II was assigned in the model for both Khabour and Akkas formations based on the study of Alkhafaji (2015).

## 5 Results and Discussion

Simulating thermal history is vital, as it represents the main factor influencing petroleum generation. The 1D model from the well (Key Hole 5/1) provides insights into the burial

history around Ga'ara Uplift by implementing the same temperature boundaries (heat flow and surface temperature) from the other two wells.

## 5.1 Source Rock Maturity

### 5.1.1 Akkas\_1 Well

The model indicates that the source rocks hosted in the Akkas Formation entered the oil window (generation onset (i.e. 0.6–0.7 Ro%)) in the Early Jurassic–Middle Jurassic (~200–165 Ma), while the top part of the hot shale reached the oil window later in the Middle Jurassic–Late Jurassic (~165–140 Ma) (Fig. 5a).

The Khabour Formation (K1, K2 and K3 members) attained the oil window in the Carboniferous and Permo-Triassic times (~330, 265, 225 Ma), respectively, and they continue in the main oil window until the present-day. High rates of subsidence of the Khabour Formation in the Akkas\_1 well caused the lower members K4–K7 to enter the early oil window as early as the Late Silurian (~420 Ma) and they are within the main oil - late gas maturity in the present day. K7 member, which represents the deepest penetrated part of the Khabour Formation is within the dry gas maturity with Ro% between (1.2–2%).

The temperature profile shows that the hot shale interval of the Akkas Formation is sitting in the present day within a temperature of around 100 °C, the temperature increases towards the bottom of the well reaching ~160 °C in the deepest part (Fig. 5b).

Better matching between modelled vitrinite reflectance and measured values was accomplished in the model using a fixed surface temperature of 20 °C and a steady heat flow of 60 mW/m<sup>2</sup>.

### 5.1.2 Khleisia\_1 Well

The whole Paleozoic succession has experienced less thermal maturity level than in the Akkas\_1 well. The Akkas Formation hot shales are thermally immature (less than 0.6 Ro%) as indicated by the burial history of the model (Fig. 6a).

The calculated Ro% showed a good matching with the upper part of the curve, however, a clear mismatch is present at the bottom of the well (Fig. 4). The K2–K6 members of the Khabour Formation have attained oil window maturity (i.e. 0.6–0.7 Ro%). While the middle part of K6 and K7 members are in the gas window (0.9–1.2 Ro%). However, the Khabour Formation was not considered a source rock in the model due to the significant low TOC values reported for this formation by (Al-Ameri & Baban, 2002). Yet, a high level of maturity depicted in the Khabour Formation can imply the low hydrocarbon generation potential in the present day (Alkhafaji et al., 2015).

The temperature profile of the Khleisia\_1 well shows that the hot shales interval of the Akkas Formation is within a temperature of around 70 °C in the present day and, the temperature increases towards the bottom of the well reaching ~130 °C (Fig. 6b).

### 5.1.3 Well Key Hole 5/1

Based on a regional stratigraphic correlation (Al-Haba et al., 1994 in Aqrabi, 1998), the hot shale of the Akkas Formation could have experienced additional burial due to the interpreted high thickness of the formation in the well. Accordingly, in the present day, the basal Akkas hot shale in well Key Hole\_5/1 could be located in a deeper stratigraphic depth compared to its stratigraphic location in the Khleisia\_1 and Akkas\_1 wells.

A 1D model for the well Key Hole\_5/1 was created. If existed, the basal Akkas hot shale interval is interpreted in the model to be in the early- main gas window around Ga'ara Uplift in the present day (i.e. 0.9–1.2 Ro%) (Fig. 7a).

The temperature profile illustrated in the burial history shows that the base of the Akkas Formation is at a subsurface temperature of about 140 °C (Fig. 7b).

## 5.2 Hydrocarbon Generation, Migration Interpretation, Accumulation, and Entrapment

### 5.2.1 Akkas\_1 Well

The 1D model indicates that the hot shale interval investigated in the Akkas Formation has not achieved the suitable levels of thermal maturity to produce commercial quantities of hydrocarbons in the well (Fig. 5). The Transformation ratio, which represents the amount of kerogen converted to hydrocarbon is only ~0.2 in the present day for both lower and upper hot shales (Fig. 8). The kitchen of the light oil and sweet gas found the well could be located to the south or to the east of the field, where the hot shale interval has been stratigraphically buried to greater depth intervals. Another possible source is the deeper Khabour Formation; however, the petroleum potential of this formation is a matter of debate (Al-Ameri, 2010; Al-Ameri & Baban, 2002; Al-Hadidy, 2007; AlKhafaji et al., 2015; Aqrabi, 1998). In addition, the notably high amounts of (TOC [wt.%] and S<sub>2</sub> [mgHC/g rock]) reported in the hot shale interval within the Akkas Formation (Al-Hadidy, 2007; Al-Khafaji, 2013) could also confirm that these hot shales have not yet generated significant amounts of hydrocarbons. The discovered hydrocarbons in the well are mature (have low H<sub>2</sub>S and high API; (Al-Hadidy, 2007)), indicating generation from highly mature source rocks. Such elevated temperatures are found in deeper zones of the basin in normal geological settings (e.g. no effect from igneous intrusions, etc.). These

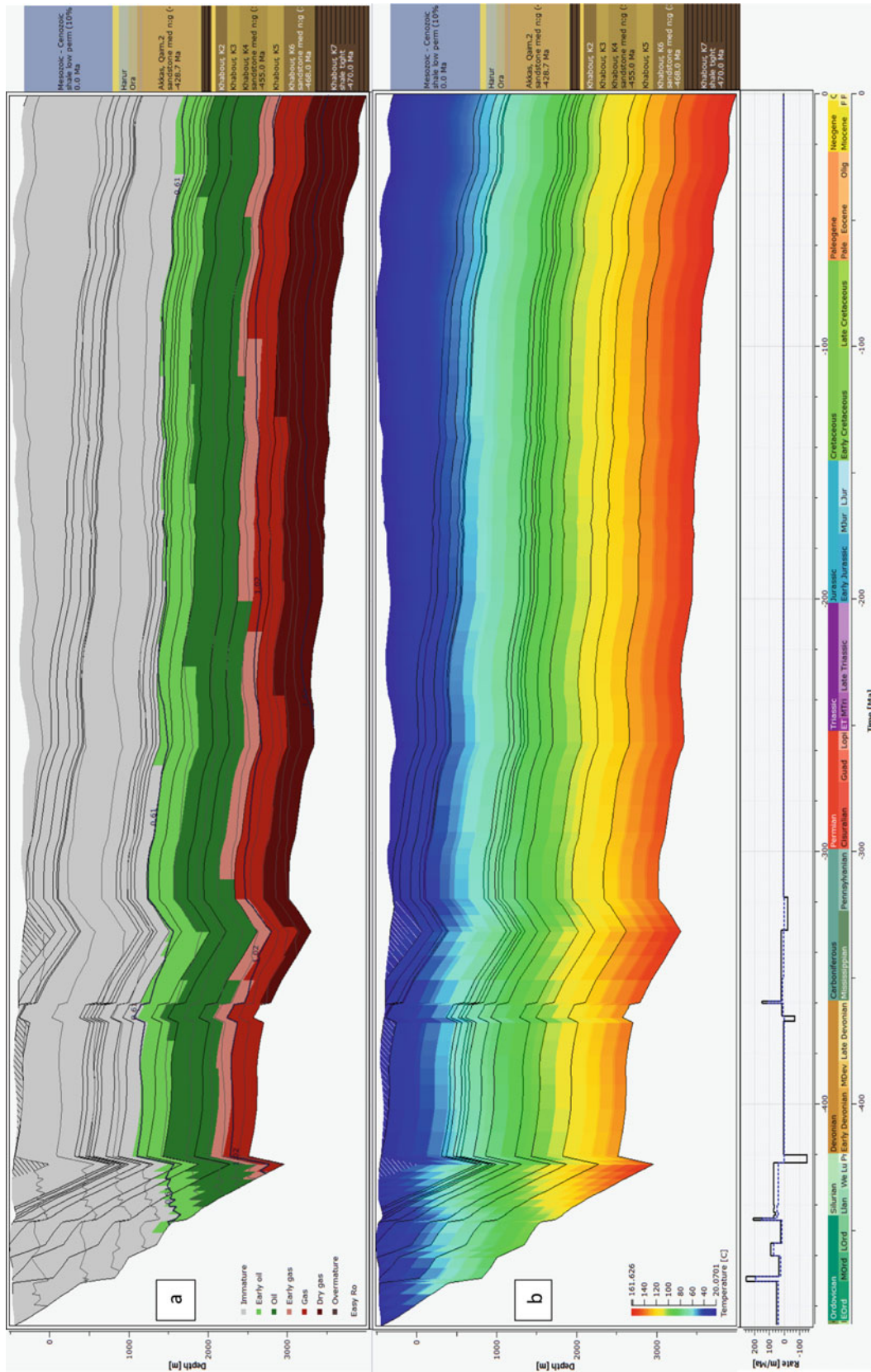


Fig. 5 Burial history model with subsidence curve of Akkas\_1 well showing: a Easy Ro [%] overlay, b Temperature [°C] overlay

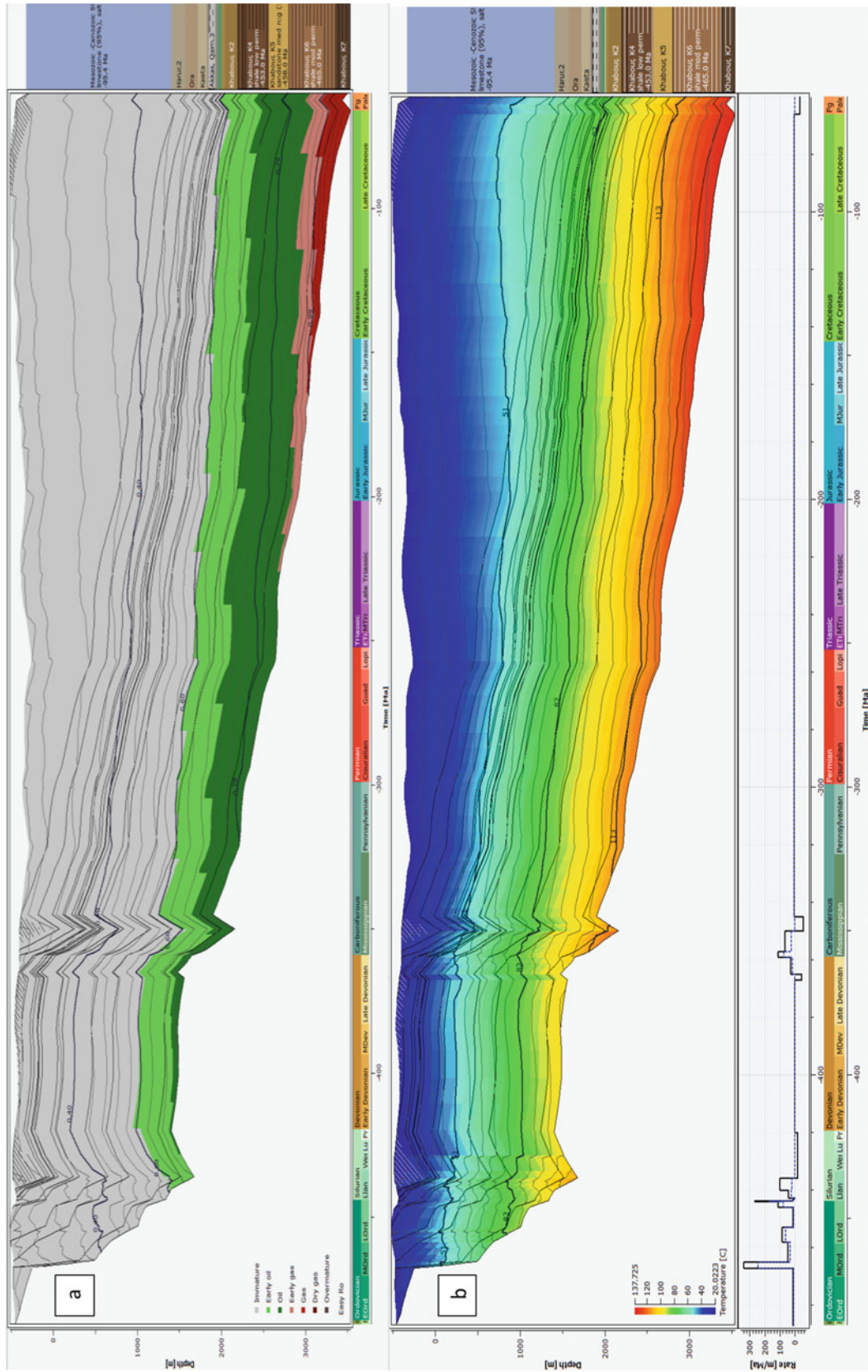
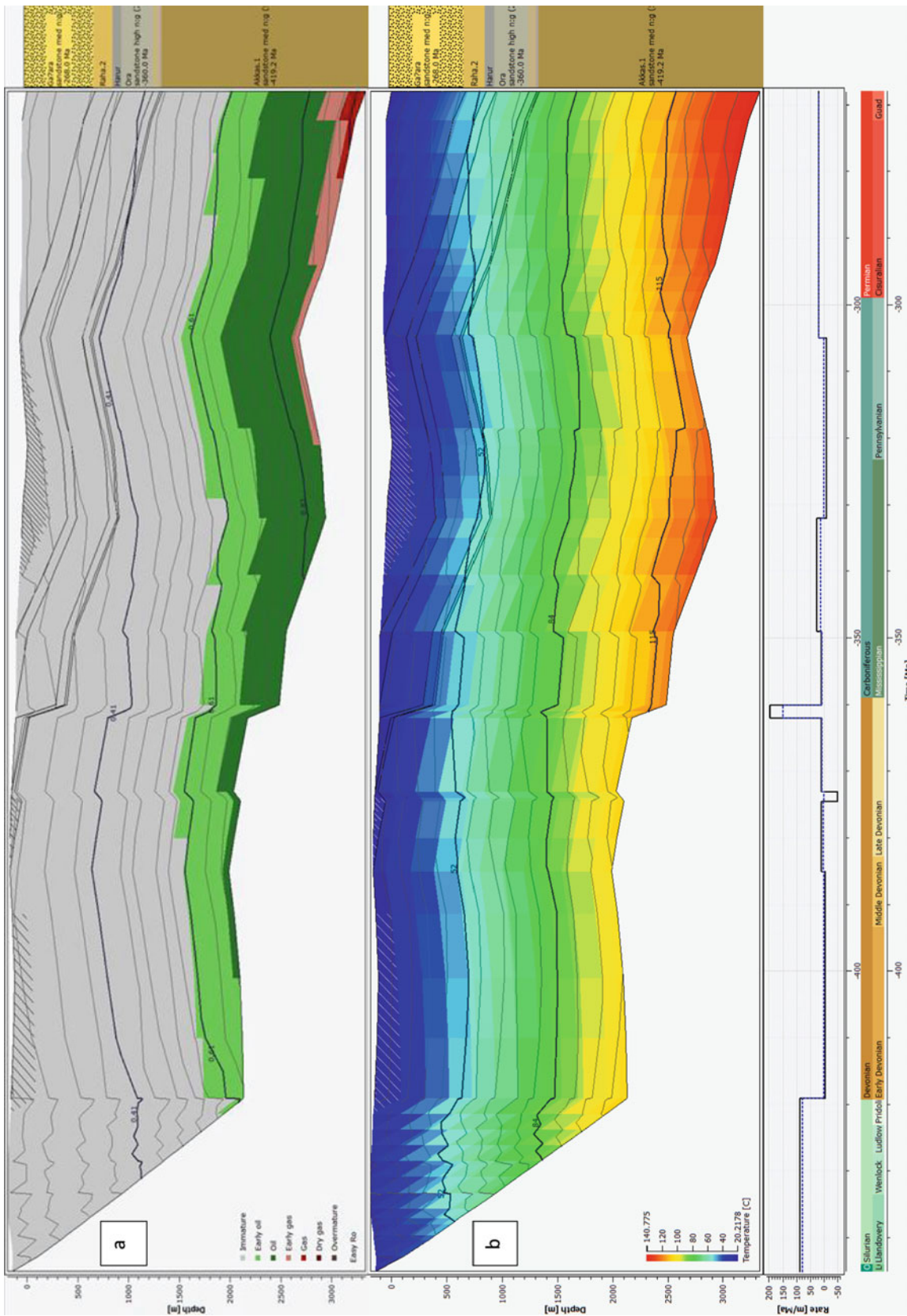
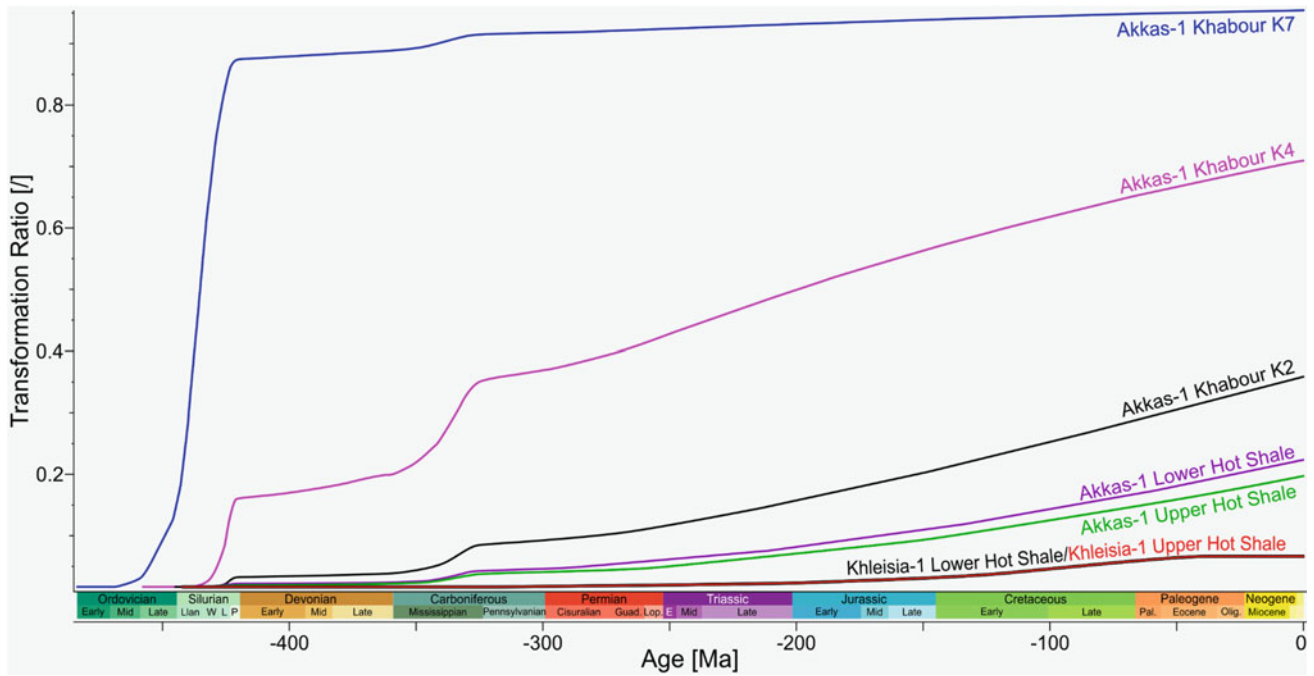


Fig. 6 Burial history model with subsidence curve of Khleisia\_1 well showing: a Easy Ro [%] overlay, b Temperature [°C] overlay



**Fig. 7** Burial history model with subsidence curve of well Key Hole\_5/1 showing: **a** Easy Ro [%] overlay, **b** Temperature [°C] overlay





**Fig. 8** Transformation ratio (TR) versus Age plot for the Akkas hot shale and selected Khabour members in Akkas\_1 and Khleisia\_1 wells. It indicates that the hot shale in both wells has not significantly contributed to the oil generation. However, the TR of the Khabour Formation was significantly higher for different members

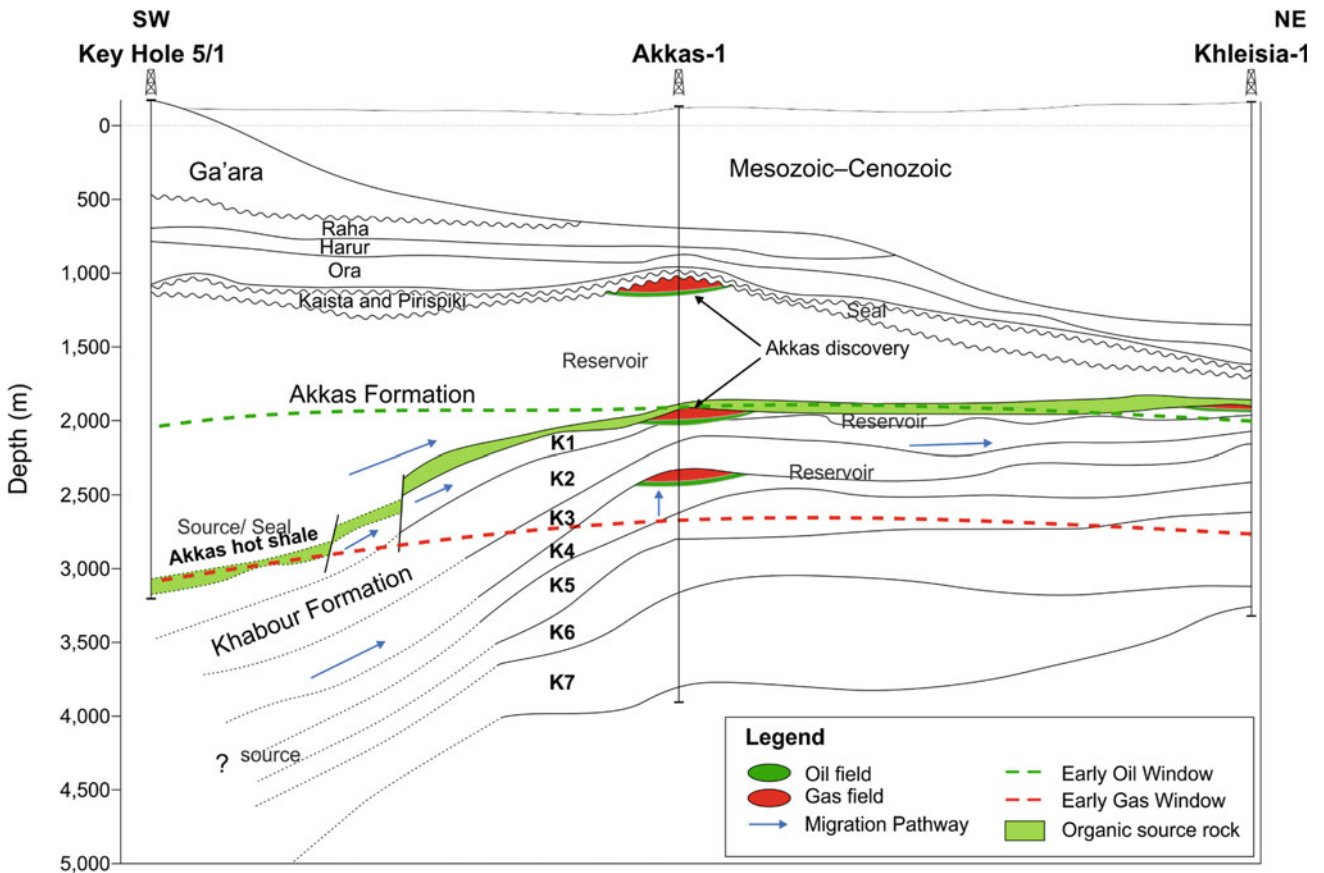


**Fig. 9** A schematic cross-section between the wells showing the stratigraphy, source rock maturity and the possible migration pathways (vertical and lateral SW), formation tops used in this figure are from (Al-Hadidy, 2007). This figure is for illustration purposes only with no horizontal scale

hydrocarbon accumulations are likely to result by lateral migration of hydrocarbons through the faults system and the unconformities from the Akkas hot shale interval located in deeper areas of the basin and/or from Khabour Formation (Fig. 9).

The stratigraphic seals are the most dominant seal types in the basin. Condensed shale layers (e.g. Akkas and Khabour shales) and unconformity surfaces with very low porosity have formed good seals to the entrapped hydrocarbons.

### 5.2.2 Khleisia\_1 Well

The hot shale interval is immature and has not contributed to the hydrocarbon generation in the well with a Transformation Ratio of less than 0.1 (Fig. 8). The mature light and sweet oils (42° API) discovered in the Khleisia\_1 well (Al-Hadidy, 2007) have most likely migrated from deeper parts of either the Khabour Formation or from the hot shales sections hosted in the Akkas Formation that are buried to deeper intervals to the east or the southwest of the well.

The temperature profile on the burial history model of the well (Fig. 6b) indicates that the hot shales are located within a temperature of around 70 °C in the present day and that they have not experienced higher temperatures in the past. This is rather cold to generate any hydrocarbons, considering the type of kerogen interpreted to the hot shale (i.e. Kerogen Type II).

### 5.2.3 Well Key Hole 5/1

Due to the lack of geochemical data, source rock potential was not modelled in this well. However, the burial history model of this well shows useful insights into the maturity of the Paleozoic strata. It indicates that the Akkas basal hot shale in the well has passed the oil window and that they might be in the gas window in the present day (Fig. 7a).

### 5.2.4 Erosion

For the paleothermal analysis, modelled Ro- depth trends were constructed to estimate the number of eroded strata in the well Akkas\_1 similar to the published technique (Dow, 1977). This trend estimates an amount of 850 m of strata are missing in the well (Fig. 10).

This approach did not apply to the Khleisia\_1 well, the trend of the vitrinite reflectance in the well suggested by (Al-Ameri & Baban, 2002), is showing a sharp increase in the lower part of the trend which makes this method inapplicable. Also, the well Key Hole\_5/1 lacks information on vitrinite reflectance. As such, the amount of eroded sediment for both wells Khleisia\_1 and Key Hole\_5/1 is an estimation in this study.

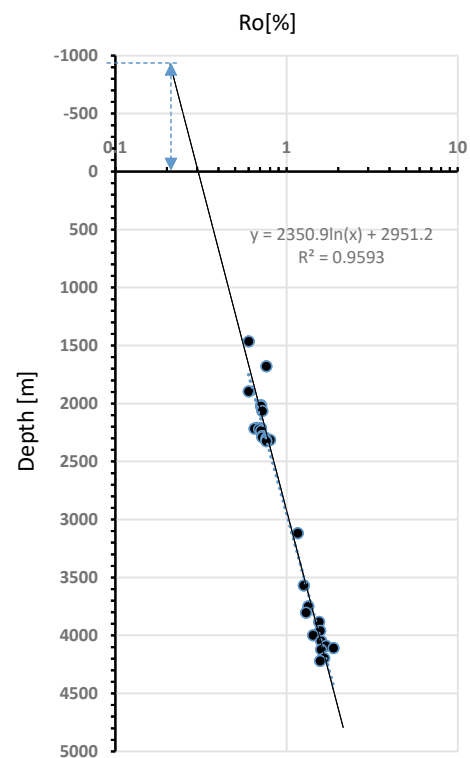


**Fig. 10** Showing the calculated erosion in Akkas\_1 well (method after Dow, 1977), an estimate of 850 m of sediments were eroded in the good vicinity

## 6 Conclusions

Although the hot shale interval is considered the major Paleozoic source rock in the Western Desert, it has not attained the high level of thermal maturity to generate significant quantities of hydrocarbon. Consequently, the discovered hydrocarbons, which are characterized by high API and low H<sub>2</sub>S in both (Akkas\_1 and Khleisia\_1) wells must have been generated elsewhere in the basin and migrated vertically (via the faults) or laterally (through the widely distributed unconformities). There are three possible interpretations for source of these hydrocarbons; the hydrocarbon generated from more mature intervals of the Khabour Formation migrated upward. Second generated to the east of the Akkas and Khleisia fields where the Paleozoic successions have been buried to a greater depth. The final interpretation indicated that hydrocarbons could have been migrated from the south and southwest where regional correlation indicated that Akkas Formation has probably reached ~2000 m in thickness, where the hot shale achieved elevated thermal maturity. As a result, the kitchen of the discovered hydrocarbons could be located to the east of Akkas\_1 and

Khleisia\_1 well or to the south of Akkas\_1 well, which makes both areas interesting for further hydrocarbon exploration.

**Acknowledgements** The Author wants to articulate sincere gratitude to Prof. Ali Al-Juboury from the University of Mosul, Iraq for providing his recent work on the studied region and for a discussion on the petroleum geology of the Western Desert of Iraq. Thanks to Allesia Nawell and Rachel Hopper from Neftex Predictions-Landmark for helping in re-drafting some of the study figures. I'd like also to thank Halliburton-Landmark Solutions for providing a technical review and for the permission of publishing this work.

## References

- Al-Ameri, T., & Baban, D. (2002). Hydrocarbon generation potential of the Lower Palaeozoic succession. *Western Iraqi Desert Iraqi Journal of Science*, 43(3), 77–119.
- Al-Ameri, T. K. (2010). Palynostratigraphy and the assessment of gas and oil generation and accumulations in the Lower Paleozoic, Western Iraq. *Arabian Journal of Geosciences*, 3, 155–179.
- Al-Hadidy, A. H. (2007). Paleozoic stratigraphic lexicon and hydrocarbon habitat of Iraq. *GeoArabia*, 12(1), 63–130.
- Al-Juboury, A. I., & Al-Hadidy, A. H. (2009). Petrology and depositional evolution of the Paleozoic rocks of Iraq. *Marine and Petroleum Geology*, 26(2), 208–231.
- Alkhafaji, M. W., Aljubouri, Z. A., Aldobouni, I. A., & Littke, R. (2015). Hydrocarbon potential of Ordovician-Silurian successions in Akkas field. *Western Desert of Iraq. AAPG Bulletin*, 99(4), 617–637.
- Al-Khafaji, M. W. A. (2013). *Organic geochemistry of Khabour and Akkas formations (Ordovician- Silurian) of Akkas Field, Western Iraq* (Dissertation). University of Mosul.
- Aqrabi, A. A. M. (1998). Paleozoic stratigraphy and petroleum systems of the western and southwestern deserts of Iraq. *GeoArabia*, 3(2), 229–248.
- Boote, D. R. D., Clark-Lowes, D. D., & Traut, M. W. (1998). Palaeozoic petroleum systems of North Africa. In D.S. MacGregor, R.T.J. Moody, & D.D. Clark-Lowes (Eds.), *Petroleum geology of North Africa* (pp. 7–68). Geological Society of London, Special Publications No. 132
- Buday, T., & Jassim, S. Z. (1987). *The regional geology of Iraq, tectonism, magmatism and metamorphism*. State Establishment of Geological Survey and Mineral Investigation.
- Cohen, K. M., Finney, S. C., Gibbard, P. L., Fan, J.-X. (2013). The ICS International Chronostratigraphic Chart. *Episodes*, 36, 199–204. <http://www.stratigraphy.org/ICSChart/ChronostratChart2020-03.pdf>
- Dow, W. G. (1977). Kerogen studies and geological interpretations. *Journal of Geochemical Exploration*, 7, 79–99.
- Fox, J. E., & Ahlbrandt, T. S. (2002). Petroleum geology and total petroleum systems of the Widyian Basin and Interior Platform of Saudi Arabia and Iraq. *United States Geological Survey Bulletin*, 2202E, 26 p.
- Jassim, S. Z., & Goff, J. C. (2006). *Geology of Iraq*. Dolin, Prague and Moravian Museum, 486 p.
- Lüning, S., Craig, J., Loydell, D. K., Štorch, P., & Fitches, B. (2000). Lower Silurian 'hot shales' in North Africa and Arabia: Regional distribution and depositional model. *Earth-Science Reviews*, 49, 121–200.
- Pepper, A. S., & Corvi, P. (1995). Simple kinetic models of petroleum formation. Part I: Oil and gas generation from kerogen. *Marine and Petroleum Geology*, 12(3), 291–319.
- Pitman, J. K., Steinshouer, D., & Lewan, M. D. (2004). Petroleum generation and migration in the Mesopotamian Basin and Zagros Fold Belt of Iraq: Results from a basin-modelling study. *GeoArabia*, 9(4), 41–72.
- Sekiguchi, K. (1984). A method for determining terrestrial heat flow in oil basinal areas. In R.L. Cermak & D.S. Chapman (Eds.), *Terrestrial heat flow studies and the structure of the lithosphere, tectonophysics* (Vol. 103, pp. 67–79).
- Snedden, J.W., & Liu, C. (2010). A compilation of phanerozoic sea-level change, coastal onlaps and recommended sequence designation. In *Search and Discovery Article 40594*. AAPG.
- van Bellen, R. C., Dunnington, H. V., Wetzel, R., & Morton, D. (1959). *Lexique Stratigraphique International*. Asie, Fasc 10a, Iraq, Paris. Reprinted as Stratigraphic Lexicon of Iraq in 2005 by GeoArabia, 239 p.



# Source Rock Quality and Continuous Petroleum System in the Ranikot Formation (Kirthar Foldbelt, Pakistan) Based on Principal Organic Geochemistry

Michał Makos, Richard J. Drozd, Ishtiaq Noor, Zdzisław Kołodziejczyk, Mateusz Górniak, Ihtesham Ul Wahab, Muhammad Javid Akhtar, and Shifaat Alam Muhammad

## Abstract

Geochemical and petrophysical studies have been carried on the Ranikot Formation in four wells drilled within the Kirthar Range. The Palaeocene Ranikot Formation is untested to date and requires detailed investigation to evaluate its generative potential. The Ranikot section is dominated by clay components (up to 60%), and thus, the unit of interest can be called the Ranikot shale. It was deposited in the shoreface system exhibiting intercalations of sandstones and mudstones formed as thin beds. Lithology and properties of the source section allow considering the formation as a hybrid unconventional petroleum system with organic-rich shales and organic-lean sandstones. The generative potential of the

Ranikot shale has been analysed using the wireline logging, X-ray diffraction (XRD), total organic carbon (TOC)/Programmed pyrolysis, kerogen composition and vitrinite reflectance. Average organic richness in individual wells varies from 1.6 to 2.2% TOC. The inferred source intervals reach the thickness between 120 and 200 m. There is a progressive and fairly uniform increasing TOC trend with depth, and it clearly corresponds to mudlogging gas readings, even up to 11–46% of gas. Moreover, there is also overpressure recorded (up to 4500 psi) with pore pressure gradient of 0.59 psi/ft. Pyrolysis S<sub>2</sub> and HI yields vary from 0.5 to 3.1 mg HC/g rock and 32 to 143 mg HC/g TOC, respectively. Kerogen composition indicates diverse relation of gas-prone to oil-prone type, which reflects mixed-type organic matter. The northern section of the study area is enriched in type-III kerogen (up to 86%) with very small amount of inertinite (1–6%). The southern section, however, contains much more type-II kerogen (22–74%), but contribution of inertinite reaches even up to 77%. Thermal maturity of the most perspective interval indicates an easterly increasing trend between 0.8 to 1.13% Ro. Therefore, depending on kerogen composition and its thermal maturity, the transformation ratio of organic matter varies between 50 and 90%. The calculated original TOC and hydrocarbon potential is then 1.7–3.2% and 2.8–10 mg HC/g rock, respectively. The gas generation potential is between 5.6 and 7 m<sup>3</sup>/m<sup>3</sup> (243 and 306 Mcf/ac-ft). According to the source section net thickness, the volume of gas generated at the maturity level of around 1.1% Ro was between 0.84 and 1.1 BCM/km<sup>2</sup> (76 and 100 Bcf/mi<sup>2</sup>).

M. Makos (✉) · M. Górniak · I. Ul Wahab · M. J. Akhtar  
Polish Oil and Gas Company (PGNiG SA) Pakistan Branch,  
6th Floor, Ufone Tower Building, Jinnah Avenue, Blue Area,  
Islamabad, Pakistan  
e-mail: [michal.makos@pgnig.pk](mailto:michal.makos@pgnig.pk)

M. Górniak  
e-mail: [mateusz.gorniak@pgnig.pk](mailto:mateusz.gorniak@pgnig.pk)

I. Ul Wahab  
e-mail: [Ihtesham.wahab@pgnig.pk](mailto:Ihtesham.wahab@pgnig.pk)

M. J. Akhtar  
e-mail: [javid.akhtar@pgnig.pk](mailto:javid.akhtar@pgnig.pk)

R. J. Drozd  
Stratum Reservoir, Houston, USA  
e-mail: [rjdrozd@sbcglobal.net](mailto:rjdrozd@sbcglobal.net)

I. Noor  
HyRes Geoscience, Islamabad, 44000, Pakistan  
e-mail: [ishtiaq.noor@hyresgeoscience.com](mailto:ishtiaq.noor@hyresgeoscience.com)

Z. Kołodziejczyk  
Polish Oil and Gas Company (PGNiG SA), Exploration and  
Production Branch in Warsaw, 25A Kasprzaka St. 01-224,  
Warsaw, Poland  
e-mail: [zdzislaw.kolodziejczyk@pgnig.pl](mailto:zdzislaw.kolodziejczyk@pgnig.pl)

S. A. Muhammad  
Pakistan Petroleum LTD., Gerry's Center, Justice Abdul Rasheed  
Road, 7th Avenue, Sector G-6/1, Islamabad, Pakistan  
e-mail: [a\\_shifaat@ppl.com.pk](mailto:a_shifaat@ppl.com.pk)

## Keywords

Shale gas • Unconventional play • Source rock analysis • Ranikot formation • Southern Indus Basin

## 1 Introduction

Growing of Pakistan's economy will require higher energy consumption, putting huge pressure on the limited domestic energy resources. Gas accounts for about 50% of the total present energy consumption. Lack of internal production forces Pakistan to import from neighbouring countries. Increasing internal production is preferred, but these become more challenging in the existing petroleum provinces. Conventional reservoirs have been the major exploration targets; however, during the last few years, the unconventional tight gas reservoirs within the Kirthar Foldbelt have become a target. A recent EIA Report (2013) presents the unconventional shale gas resources in the Sembar and Ranikot formations at 0.9 BCM/km<sup>2</sup> (83 Bcf/mi<sup>2</sup>) and 0.2 BCM/km<sup>2</sup> (17 Bcf/mi<sup>2</sup>), respectively. These very general data need to be verified in detail across the basins using new well data.

Shale resource systems are described as continuous organic-rich source rocks that may be both a source and a reservoir rock for the production of petroleum (oil and gas) or may charge and seal petroleum in juxtaposed, continuous organic-lean intervals (Jarvie, 2012). In this context, both the primary migration processes that occur within the source interval, and secondary migration into non-source horizons, need to be considered (Welte & Leythausen, 1984). Further, some migration away from the resource system into other reservoirs may also have occurred. Two basic types of producible shale resource systems (gas- and oil-producing systems) exist, and their classification depends on the amount of gas versus oil. Additionally, the reservoir lithofacies, mudstone contribution, maturity of the source rock and the storage mechanism are factors controlling the type of continuous petroleum system. Among the shale oil systems, three sub-types are distinguished: tight shale, hybrid shale and fractured shale. Diversity of shale gas systems is slightly more complicated and relates mostly to the gas origin and reservoir lithology. The combination gas system produces both gas and oil, condensate or natural gas liquids, in mudstones or hybrids at thermal maturity between 0.8 and 1.4% Ro. Mudstone dry gas systems produce hydrocarbons from organic-rich shale at high thermal maturity over 1.4% Ro and mudstone wet gas system with hydrocarbons generated at low maturity below 0.8% Ro. The most common is the hybrid dry gas system with combination of organic-rich mudstones and organic-lean carbonate or sand intervals at high thermal maturity over 1.4% Ro (Jarvie, 2012). All of these systems contain thermogenic gas. Biogenic shale gas systems exist, but they are of minor significance. Although the industry commonly describes these systems as shale plays, these are truly mudstones. They should be considered as petroleum systems (Magoon & Dow, 1994), regardless of

reservoir lithofacies or quality, because all the components and processes are applicable (Jarvie, 2012).

The aim of this paper is to introduce the Palaeocene Ranikot Formation in the Kirthar Foldbelt as an unconventional petroleum system. Using the standard geochemical procedure (e.g. Jarvie et al., 2007), the unconventional petroleum potential of the source section has been described. A comprehensive examination of geochemical processes and shale characteristics controlling generation, storage and access were applied to evaluate the Ranikot resource system properly.

## 2 Geological Setting

The Indus Basin is sub-divided into northern, central and southern areas (Fig. 1) with the primary commercial oil and gas discoveries being restricted to the southern and central sectors, collectively termed the Lower Indus Basin (Bender & Raza, 1995). At the end of Jurassic, the Indo-Pakistan Plate drifted away from the Pangea supercontinent (van Hinsbergen et al., 2011). During the Cretaceous, most Pakistan territory was a passive margin, followed by formation of the Bela Ophiolite during the Palaeocene (Loosveld et al., 1996). In the Eocene–Pliocene, passive margin deposition resumed (Bender & Raza, 1995). Continental collision of the Indo-Pakistan and Eurasian plates occurred during the Neogene–Quaternary (Matthews et al., 2016).

The Kirthar Foldbelt is located between the Lower Indus Basin on the east and Balochistan Basin on the west. On the north, the Kirthar Range is bounded by the Sulaiman Foldbelt and its southern boundary contacts with Makran and Offshore Indus basins. The Kirthar Foldbelt is the product of oblique collision between the Indian Plate and the Helmand Block of the Eurasian Plate, and six mega sequences from Jurassic to Quaternary reflect the tectonic evolution of the area (Bannert et al., 1992). The Kirthar Foldbelt is a prolific gas and gas condensate producer with major fields like Bhit, Mazarani, Zamzama and Sari-Hundi, which confirm the presence of a dynamic petroleum system in this tectonostratigraphic province (Wandrey et al., 2004). A generalized stratigraphic column is given in Fig. 2.

The deltaic deposits of the Cretaceous Goru and Sembar formations were formed in the passive margin setting (Bender & Raza, 1995). They represent primary source intervals that charged most of gas fields in the Kirthar region (Ahmad et al., 2012; Raza et al., 1990). Clastic sedimentation stopped during the major transgression of the Turonian Anoxic Event. Deepwater carbonates (limestones) of Parh Formation were deposited at Coniacian–Campanian time. The Campanian–Maastrichtian section in the Kirthar Foldbelt is represented by a thick sequence of low stand turbidite

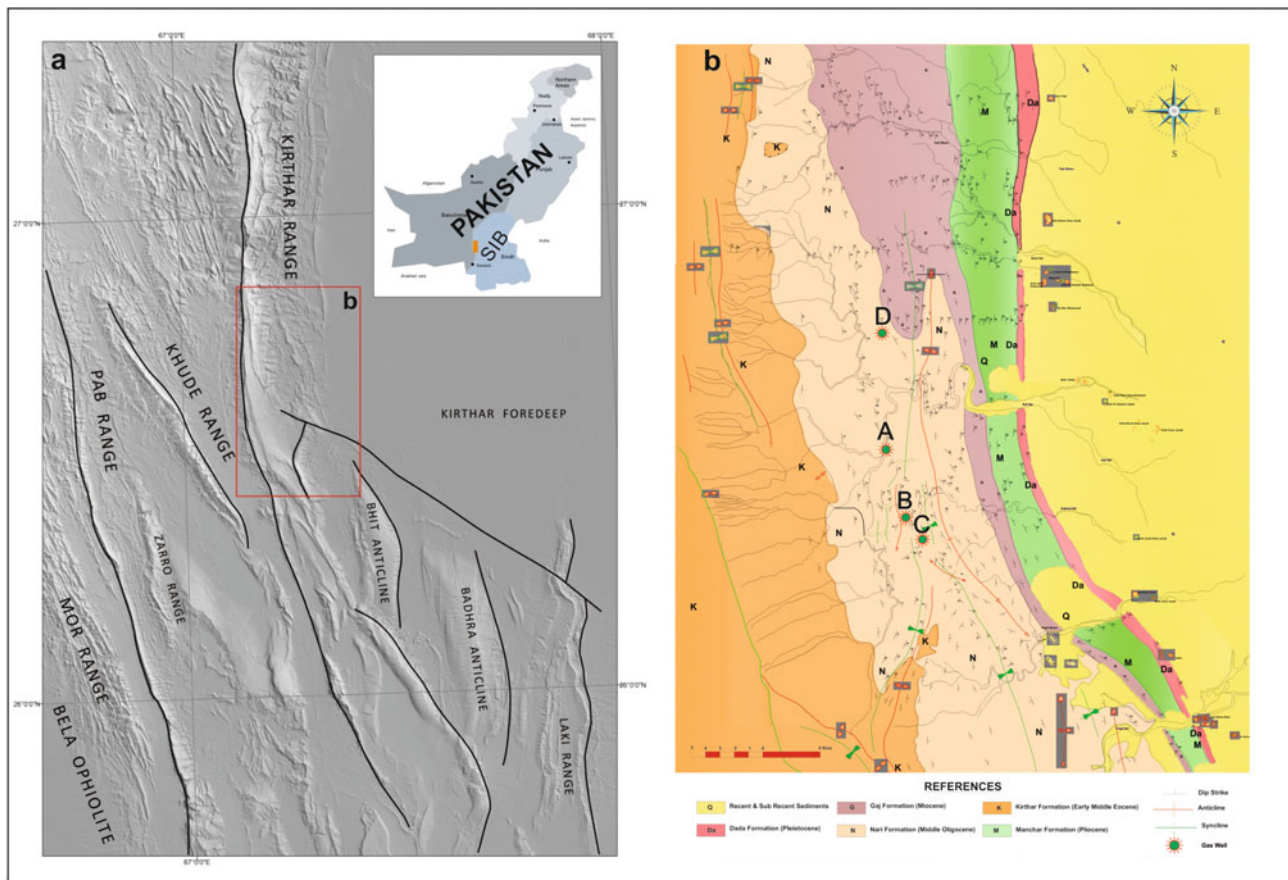


**Fig. 1** Location of the study area (digital elevation model)—**a** Surface geological map of the study area; **b** SIB—Southern Indus Basin

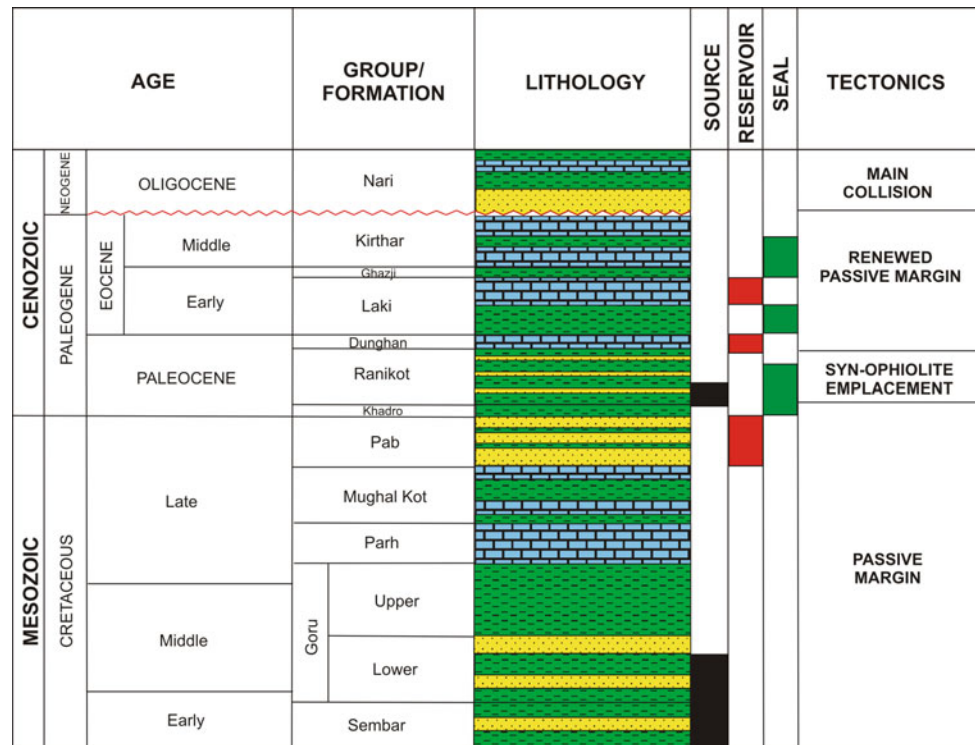
sandstones of Mughal Kot Formation (Vail et al., 1977). The subsequent Late Maastrichtian high stand led to deposition of the 200-m-thick section of Pab Formation sandstones on the marine shelf (Bender & Raza, 1995). Collectively, these deposits are the conventional gas exploration target in the Kirthar basin. Relative sea-level rise at the end of the Cretaceous terminated Pab sandstones deposition. The shelf area was then dominated by deposition of the shale section of the Palaeocene Ranikot Formation.

Further evolution of the Indo-Pakistan landmass is related to its movement and collision with the Euro-Asia plate. During the Early Eocene, the shelf area was dominated by deposition of carbonates of the Laki and Kirthar formations, separated by the Laki Shale interval deposited during the temporal deep-water setting. The whole Eocene section is composed of renewed passive margin sequences. The Oligocene/Miocene deformation phase resulted in deposition of the thick shelfal clastic section of Nari and Gaj formations (Smewing et al., 2002). The main phase of deformation in the Kirthar Foldbelt occurred with an early phase of compressional tectonics during Pliocene when large N-S folds (e.g. Bhit and Badhra) were formed (Treloar & Izatt, 1993).

The interior part of foldbelt has been uplifted of 2–4 km in total during the Neogene/Pleistocene times.

The Ranikot section consists of an upper carbonate unit containing dominantly fossiliferous limestone interbedded with dolomitic shale, calcareous sandstone and abundant bituminous material. This unit is interpreted to be deposited in a restricted marine depositional environment (EIA, 2013), which may be conducive to preservation of marine and terrigenous organic matter. West of the Karachi Trough axis, the Ranikot Formation becomes predominantly shale and is interpreted to have been deposited in a deep marine setting (EIA, 2013). Cutting samples evaluated in the present investigation consist predominantly of clastics (clay, quartz) with only minor carbonate influence (Fig. 3). Calcite is elevated (>10%) only in the upper 50 m of the sampled interval, and siderite is moderately abundant (up to 10%) lower in the section. Clay components dominate on average, and thus, the unit of interest can be called the Ranikot shale. Within the southern portion of the Lower Indus Basin, EIA (2013) has identified over 10,000 km<sup>2</sup> of area where the Ranikot shale appears to be prospective for oil and associated gas (Ro of 0.7–1.0%). No publically available data have

**Fig. 2** Lithology and stratigraphy of the Kirthar Foldbelt with major tectonic events and petroleum system elements



been reported on shale gas exploration or development for Pakistan beyond the estimates contained in EIA (2013) and Sheikh and Gao (2017). The unconventional potential of the Ranikot shale is untested to date and is the major aim of current investigation.

composition and vitrinite reflectance. All laboratory analyses were performed by the Stratum Reservoir (former Weatherford Labs.).

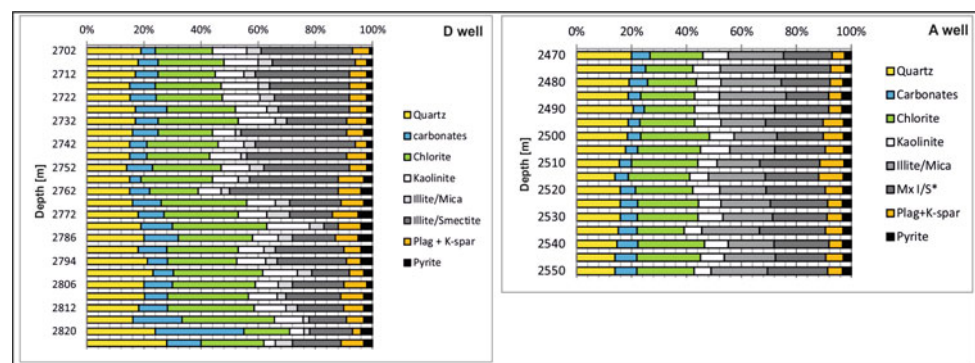
### 3 Methods

Four wells located in the Kirthar Range drilled the Ranikot Formation of which thickness is between 360 and 470 m (Fig. 1). The formation is composed of shale intervals with high content of clay minerals intercalated by layers enriched with quartz and coarser fractions which are interpreted as sandstones (Fig. 4). The hydrocarbon potential of the Ranikot shale was investigated using wireline logging, X-ray diffraction (XRD), programmed pyrolysis, kerogen

### 3.1 Wireline Logging

The Ranikot Formation deposited in the shoreface system is composed of intercalations of sandstones and mudstones formed as thin beds. The log data were used as indirect indicators for thin beds because core was not available. The petrophysical tools included gamma ray, short and deep resistivity, borehole images and electrical images (Passey et al., 2006). The electrical image log from the Lower Ranikot section (2700–2818 m) in the D well was internally statistically interpreted, aiming at accurate prediction of sand fraction contribution. The Sand Count module (Stratum

**Fig. 3** Mineralogical (XRD) composition of the Ranikot section in the A and D wells



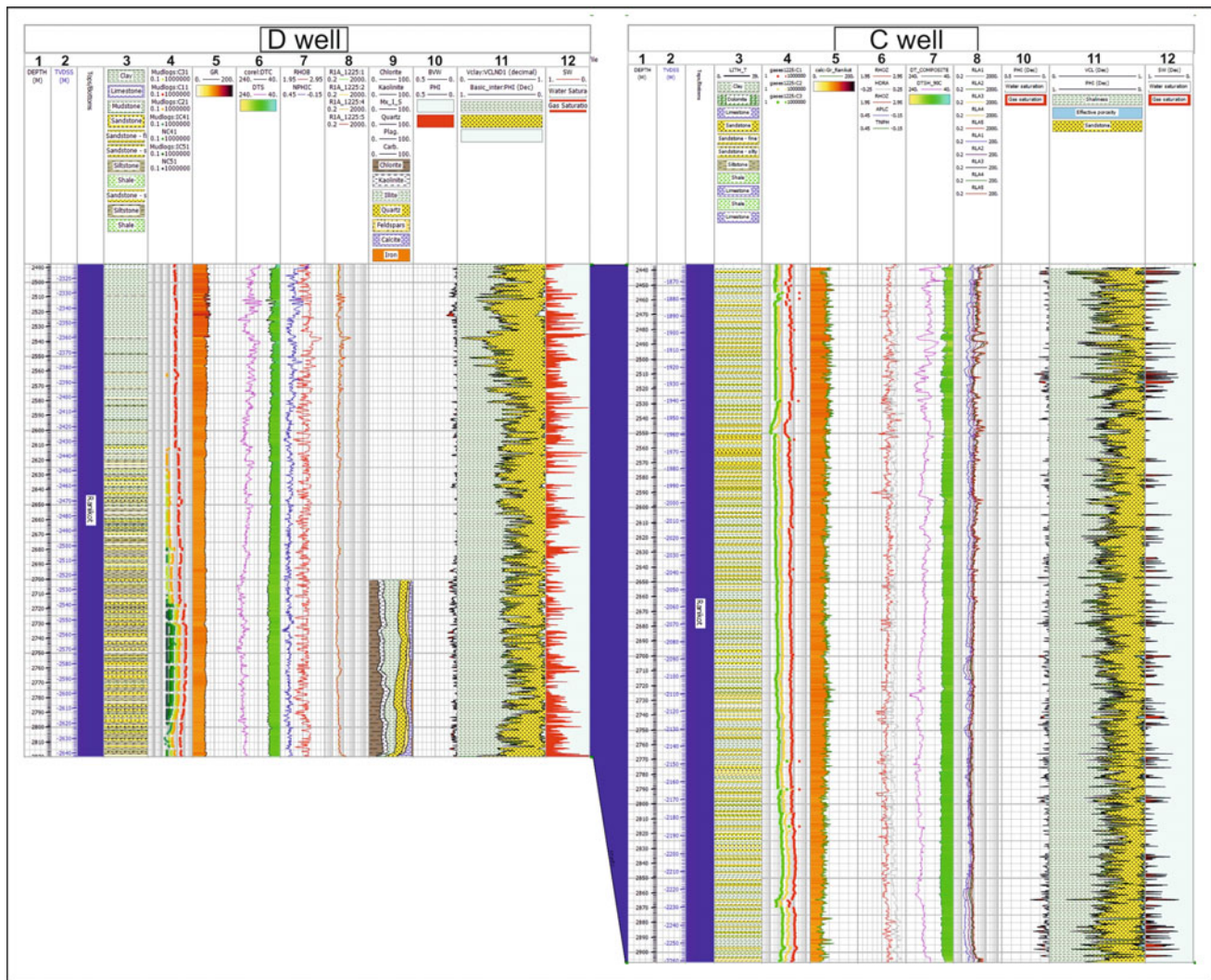


**Fig. 4** Petrophysical interpretation and correlation of the Ranikot well logs in the C and D wells

Reservoir) was used to identify thin sand/silt units, which are beyond resolution of the conventional logs. An HMI synthetic resistivity curve (SRES\_IMAGCAL) has been generated by scaling the HMI image with a shallow resistivity curve LLS to get high-resolution HMI shallow resistivity from electrical image. SRES\_IMAGCAL curve was used to identify thin sand/silt units which are beyond the resolution of the conventional logs either by software or manually. Sandstone layers of thickness less than 2 m are recognized as thin beds of sand.

## 3.2 XRD

XRD data were collected on 176 cutting samples from all four wells. Based on mineralogy of the samples, lithofacies variations, reservoir quality and brittleness were evaluated.

The general cut-off of 50% total clay content is considered as a critical value for shale reservoirs for hydraulic fracturing susceptibility. In these wells, however, the relationship between chlorite and smectite content is crucial due to their opposite influence on rock brittleness. Even when the brittleness calculated from the total clay content is positive, the smectite plasticity is a negative factor. Sample preparation procedures follow those of Bish and Reynolds (1989) and Moore and Reynolds (1997).

## 3.3 Source Rock Analysis

### 3.3.1 Programmed Pyrolysis

Two hundred thirty-one (231) cutting samples were recovered from the Palaeocene Ranikot succession drilled in four study wells. The source rock characterization was performed



using the Source Rock Analyser (Drozd et al., 2009; SRA, 2012) in the total organic carbon (TOC) mode. The samples were washed, dried and ground, and then analysed to yield free oil content (S1); residual hydrocarbon potential (S2), the amount of CO<sub>2</sub> produced during kerogen pyrolysis (S3), total organic carbon (TOC) and thermal maturity (Tmax). The instrument thermal program applies the standard open-system heating process: free hydrocarbons are detected in an inert atmosphere by heating to 340 °C, followed by a temperature ramp of 25 °C/min to 640 °C. CO<sub>2</sub> and CO are detected by an IR cell, hydrocarbons by FID. The temperature at which the S2 peak reaches a maximum (Tmax) is a measure of the source rock maturity. Repeatability of Tmax is 1 °C to 3 °C, depending on the instrument, program rate and sample size and sample heterogeneity. Tmax values for samples with S2 peaks less than 0.2 mg HC/g rock are often inaccurate and are rejected unless a definitive kerogen peak is noted from the pyrogram. CO and CO<sub>2</sub> released between 300° and 390 °C are collected as the S3 peak, providing an assessment of the oxygen content of the rock. The typical source rock parameters such as hydrogen index (HI), oxygen index (OI) and production index (PI) are derived from the measured data (Behar et al., 1997; Langford and Blanc-Valleron, 1990; Espitalie et al., 1977; Peters, 1986).

### 3.3.2 Organic Matter Assessment by Optical Microscopy

Selected samples from each well were studied by organic petrology methods for determination of the kerogen maceral composition and thermal maturity. Visual kerogen assessments complement chemical assessments by recording information from the macerals that make up the sedimentary organic matter. Vitrinite macerals and their reflectance of incident light under oil immersion are used to assess the thermal maturity of the sample. Vitrinite reflectance (% R<sub>o</sub>) increases with increased depth of burial (i.e. increased thermal exposure) and is an indication of the maximum temperature to which these particles have been exposed. The reflectance microscope measures the amount of reflected light relative to the incident light and expresses this ratio as a percentage. The in situ population must be identified and must exclude vitrinite derived from cavings and reworked organic matter. Reworked vitrinite that was redeposited in the sediments may have higher reflectance that will skew the measurements towards higher R<sub>o</sub> values if not recognized and removed from the average. In cuttings samples, cavings from overlying less mature sediments may skew the average towards lower values. Generally, when cavings are excluded, the lowest reflecting population is found to be indicative of the indigenous population, but this evaluation is made in combination with visual kerogen assessments, programmed measurements and data for the extent of kerogen conversion.

Maceral composition is an assessment of the percentages of various organic particles found in kerogen samples. These particles are related to the oil and gas potential of the organic matter and are generally described as amorphous, exinitic, vitrinitic, inertinitic or solid bitumen percentages. The former two macerals are primarily oil-prone particulate matter, whereas vitrinite particles are indicative of gas-prone organic matter. Inertinite is very hydrogen-poor and has no potential for generation of commercial quantities of hydrocarbons. The presence of solid bitumen is indicative of in situ generated hydrocarbons, migrated hydrocarbons or contamination. Other observations from visual kerogen assessment include the quality of the organic matter.

### 3.4 Generated Gas Volumetric Calculation

The results of programmed pyrolysis and visual kerogen assessment were used to calculate the amount of generated hydrocarbons from the Ranikot shale source section using the methodology of Jarvie et al. (2007):

$$HC_{gen} = S2_o - S2 = \Delta S2 \quad (1)$$

$$S2_o = 0.01(HI_o \times TOC_o) \quad (2)$$

$$HI_o = \left(750 \frac{\% \text{ type I}}{100}\right) + \left(450 \frac{\% \text{ type II}}{100}\right) + \left(125 \frac{\% \text{ type III}}{100}\right) + \left(50 \frac{\% \text{ type IV}}{100}\right) \quad (3)$$

$$TOC_o = \frac{83.33 \times HI \times TOC}{[HI_o \times (1 - TR) \times (83.33 - TOC) + HI \times TOC]} \quad (4)$$

$$TR = 1 - \frac{HI \times \left[1200 - \left(\frac{HI_o}{1 - PI_o}\right)\right]}{\left[HI_o \times \left(1200 - \frac{HI}{1 - PI}\right)\right]} \quad (5)$$

The volume of generated hydrocarbons (HC<sub>gen</sub>) is expressed as the difference (ΔS2) of the original hydrocarbon potential (S2<sub>o</sub>) and residual hydrocarbon potential (S2) Eq. (1). The original hydrocarbon potential (S2<sub>o</sub>) is given by formula (2), where HI<sub>o</sub> is the original hydrogen index calculated based on the visual kerogen composition according to formula (3). This formula assumes a fixed HI<sub>o</sub> for each kerogen type, which is not accurate in detail and is adequate for these general assessments. TOC<sub>o</sub> is the original organic carbon content (before maturation) and is calculated by Eq. (4) following Peters et al. (2005), where 83.33 is the carbon fraction in generated petroleum, and TR is the transformation ratio of the organic matter into petroleum calculated using Eq. (5), where PI<sub>o</sub> is the original production

index at the assumed level of 0.02 and PI is the present-day measured production index from pyrolysis. 1200 is the maximum amount of hydrocarbons that could be formed assuming 83.33% carbon in hydrocarbons.

$\Delta S2$  indicates the amount of generated hydrocarbons but does not differentiate between oil and gas. Therefore, assuming that primary generation of oil and gas can occur only from the oil-prone and gas-prone kerogens, respectively, the amount of generated oil is:

$$V_{oil} = (\Delta S2 \times \% \text{ type-II} + S1) \times 21.89 \text{ bbl/ac-ft, or} \quad (6a)$$

$$V_{oil} = (\Delta S2 \times \% \text{ type-II} + S1) \times 0.02 \text{ bbl/m}^3, \quad (6b)$$

The amount of generated gas is then:

$$V_{gas} = \Delta S2 \times \% \text{ type-III} + 131.34 \text{ Mcf/ac-ft, or} \quad (7a)$$

$$V_{gas} = \Delta S2 \times \% \text{ type-III} \times 3 \text{ m}^3/\text{m}^3 \quad (7b)$$

Moreover, after the primary oil and gas generation, secondary gas generation occurs as a result of oil cracking by consequent heating of the source rock at the thermal maturity over 1% Ro. According to Tian et al. (2006), the oil is cracked completely at the 2% Ro. Thus, the amount of gas generated at the specific thermal maturity is calculated as follows:

$$V_{total\ gas} = V_{oil} \times R + V_{gas} \quad (8)$$

where  $R$  is the oil cracking factor, determined by the thermal maturity and estimated based on the plot of Tian et al. (2006).

## 4 Results and Discussion

### 4.1 Distribution of Lithofacies and Mineralogy

The Ranikot Formation is a thin-bedded, laminated reservoir, where relatively thicker mudstone horizons are intercalated by thin sandstone layers. The formation within the study area was deposited in a distal lower shoreface system (Bodnar, 2015).

The electrical image log from the Ranikot Section (2500–2818 m) in the D well was internally statistically interpreted, aiming at accurate prediction of sand fraction contribution. Net-to-gross sandstone fraction is 20% of the entire section. Electrical images sometimes give different results than core photos, and final determination may be affected by many factors limiting understanding of the real sand fraction content. Sandstone cumulative thickness of 38.2 m was interpreted in the Dwell based on the Sand Count module, corresponding to ~10% in the total formation (Fig. 5).

Based upon these calculations, we infer that the most prospective section of the Ranikot Formation contains 10–20% of sandstone.

Mineralogy of cutting samples from the Ranikot shale intervals are dominantly clay ranging from 34 to 73% (Fig. 3). Clay types are chlorite (18–25%), kaolinite (10–13%), mixed-layered illite/smectite (10–24%) and illite/mica (4–8%). Good unconventional shale reservoirs exhibit less than 10% mixed-layered illite/smectite with total clay content less than 50%. The Ranikot shale, especially in the D and B locations, is within the range of unfavourable mineralogy. The Ranikot shale interval also was found to contain abundant quartz, generally ranging from 17 to 43% and averaging 27%. These results are more encouraging for potential brittleness and fracture development. Carbonates are minor constituents and make up on average only 13%. Considering the interpreted shallow marine depositional environment, the mineralogy suggests significant clastic input (clays and quartz) into more proximal marine depositional setting.

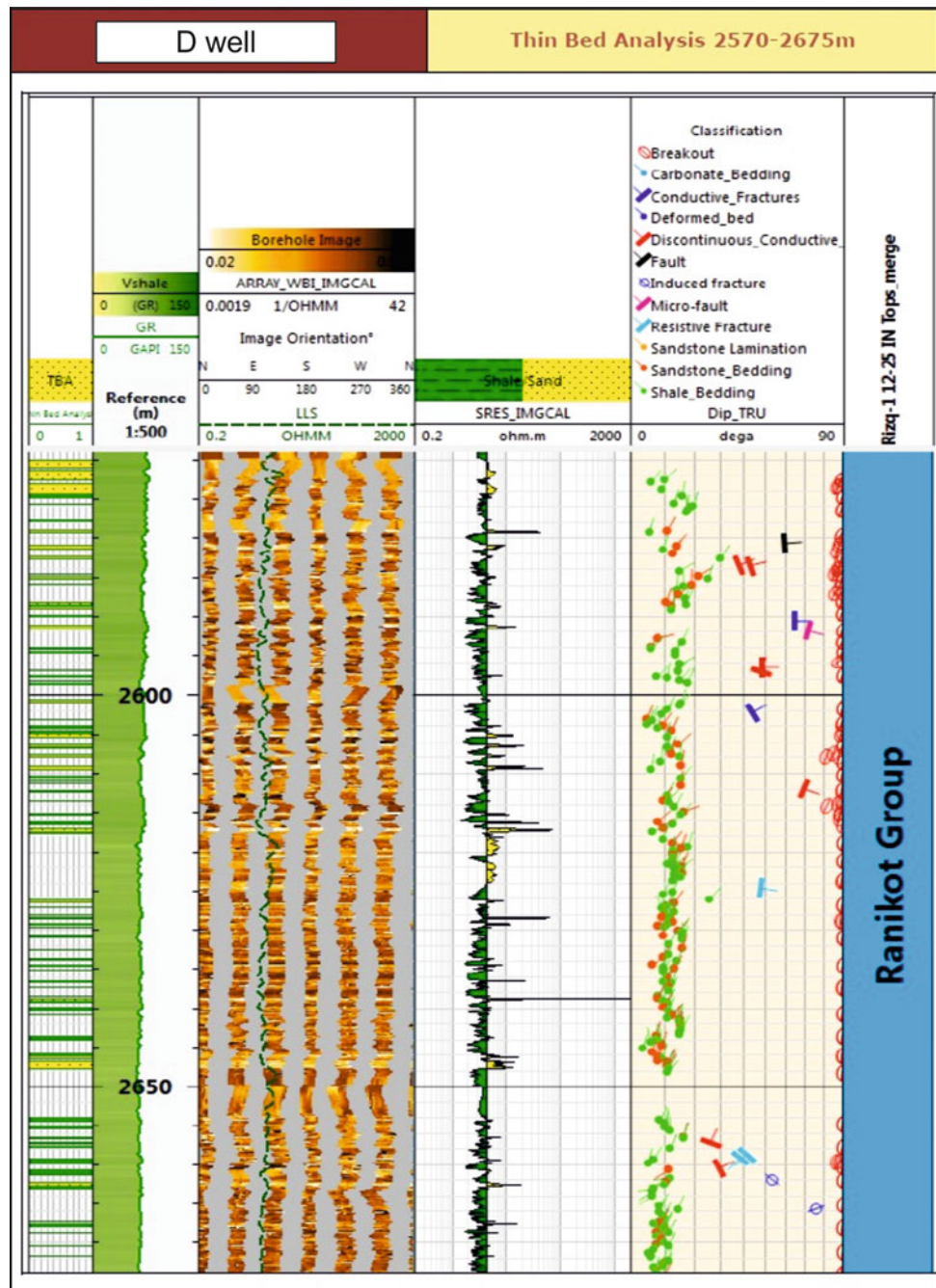
Porosity and permeability are the key parameters for unconventional reservoir characterization. Since the XRD study revealed chlorite as being the dominant clay mineral, its fine texture and dispersed pore lining likely affect the reservoir quality and may be the possible cause of the low resistivity recorded in profile of the Lower Ranikot Formation. Well-developed chlorite in pore filling cement and authigenic chlorite both reduce cementation and preserve reservoir properties.

The shale/sandstone Ranikot Formation in the study area is commonly over pressured throughout the entire section. Overpressure starts to increase from the top of Laki shale and reaches the highest values in the Ranikot section.

In all wells drilled on the Kirthar Range, borehole conditions in the Ranikot Formation were very bad. Enormous washouts, breakouts and rugosity were observed throughout the entire logged interval. High overpressure requires high density mud, which also strongly affects wireline logs quality. Poor-quality logs and thinly laminated reservoir both imply difficulties in petrophysical evaluation. Interpreted petrophysical parameters like porosity, permeability and water saturation are unreliable and do not reflect true formation properties. The reservoir quality of the Lower Ranikot section is rather poor and tight in nature and has similar properties to these of the Pab sandstones in the area. Effective porosity is in the range between 0 and 10% with rather low permeability. Sandstone intervals are gas saturated.

In general, the Ranikot Formation in the study area is thinly bedded and strongly over pressured section exhibiting low porosity and permeability and always containing gas (Fig. 4). Despite the low reservoir parameters, the analysed

**Fig. 5** HMI interpretation of thin beds within the 2570–2675 m section of the Ranikot Formation in the D well



rocks have potential to give high rates initial production due to high overpressure. Additionally, natural fractures and also probable microfractures may increase the gas inflow.

#### 4.2 Present-Day Generative Potential

The average measured geochemical parameters for the Ranikot shale in each of the four wells are reported in Table 1 and Fig. 6. Average present-day TOC values are

1.63, 1.75, 2.17 and 1.9% in the D, A, B and C wells, respectively. Depth trends in organic richness show that the highest TOC values are located near the base of the sampled interval, which corresponds to gas readings throughout the Ranikot sections in all four wells. Pyrolysis S2 yields vary from 0.1 to 4.8 mg HC/g rock. The inferred source intervals, however, indicate the average values from 0.5 mg HC/g rock in the D well to 2.9 mg HC/g rock in the B well, showing poor to fair remaining potential for hydrocarbon generation. This reflects relatively higher

**Table 1** Rock-Eval results

Depth (m)	S1 (mgHC/g rock)	S2 (mgHC/g rock)	Tmax (°C)	S3 (mgCO <sub>2</sub> /g rock)	TOC (%)	HI (mgHC/gTOC)	OI (mgCO <sub>2</sub> /gTOC)	PI	R <sub>0</sub> (%)	TR (%)
<i>B well</i>										
2400	0.24	0.65	413	1.78	1.60	41	111	0.27		86
2405	0.11	0.30	420	1.51	1.66	18	91	0.27		94
2410	0.17	0.41	424	1.50	1.69	24	89	0.29		92
2415	0.26	0.65	423	1.31	1.60	41	82	0.29		86
2420	0.28	0.72	413	1.35	1.56	46	86	0.28		84
2425	0.37	0.94	417	1.60	1.60	59	100	0.28		79
2430	0.80	2.06	422	2.00	1.43	144	139	0.28		45
2435	0.66	1.58	407	1.54	1.39	114	111	0.29		58
2440	0.52	1.27	416	1.73	1.58	81	110	0.29		71
2445	0.42	1.02	424	1.36	1.64	62	83	0.29		78
2450	0.45	1.05	427	1.56	1.85	57	85	0.30	0.92	24
2455	0.34	0.95	423	1.62	1.75	54	93	0.26		81
2460	0.30	0.72	412	1.29	1.69	43	77	0.30		85
2465	0.22	0.58	425	1.01	1.59	36	63	0.28		88
2470	0.21	0.50	424	1.17	1.61	31	72	0.30		89
2475	0.25	0.62	427	1.04	1.60	39	65	0.29		86
2480	0.43	0.96	409	0.95	1.56	61	61	0.31		78
2485	0.40	0.91	414	1.13	1.57	58	72	0.30		80
2490	0.43	1.12	424	1.23	1.62	69	76	0.28		75
2495	0.43	1.00	414	1.67	1.78	56	94	0.30		80
2500	0.53	1.34	420	1.58	1.82	74	86	0.28		74
2505	0.87	2.09	416	1.52	1.82	115	84	0.29	0.97	72
2510	0.81	1.95	414	1.45	1.95	100	74	0.29		63
2515	0.58	1.34	414	1.70	1.88	71	90	0.30		75
2520	0.49	1.06	429	1.26	2.01	53	63	0.32		81
2525	0.30	0.64	417	1.15	1.91	34	60	0.32		88
2530	0.43	0.78	416	1.38	2.38	33	58	0.36	1.02	90
2535	0.24	0.35	417	0.98	2.17	16	45	0.41		95
2540	0.16	0.28	421	1.36	1.93	15	70	0.36		95
2545	0.22	0.38	419	2.15	1.96	19	110	0.37		94
2550	0.12	0.27	414	1.02	1.47	18	69	0.31		94
2555	0.30	0.63	421	1.58	2.05	31	77	0.32		89
2560	0.42	0.62	426	1.53	1.98	31	77	0.41		89
2565	0.21	0.50	430	1.72	1.83	27	94	0.29		91
2570	0.33	0.91	430	1.48	1.99	46	74	0.27	0.85	87
2575	0.21	0.76	433	1.05	1.58	48	67	0.22		83
<i>A well</i>										
2400	0.06	1.49	435	0.85	2.06	72	41	0.04		79
2405	0.22	2.41	430	0.88	2.23	108	40	0.08		68
2410	0.55	3.17	426	0.38	2.07	153	18	0.15		53
2415	0.14	2.06	429	0.79	2.12	97	37	0.06		71

(continued)

**Table 1** (continued)

Depth (m)	S1 (mgHC/g rock)	S2 (mgHC/g rock)	Tmax (°C)	S3 (mgCO <sub>2</sub> /g rock)	TOC (%)	HI (mgHC/gTOC)	OI (mgCO <sub>2</sub> /gTOC)	PI	R <sub>0</sub> (%)	TR (%)
2420	0.34	2.18	434	0.42	1.42	153	30	0.14		53
2425	0.46	2.38	421	0.17	1.35	177	13	0.16		44
2430	0.15	2.3	429	0.68	2.08	111	33	0.06		67
2435	0.16	2.08	434	0.64	2.09	99	31	0.07		71
2440	0.15	2.51	434	0.71	2.36	106	30	0.06		68
2445	0.24	2.88	430	0.81	2.44	118	33	0.08		64
2450	0.22	2.46	431	0.83	2.27	108	37	0.08		68
2455	0.28	2.69	421	1	2.32	116	43	0.09		65
2460	0.59	4.02	433	0.81	2.04	197	40	0.13		37
2465	0.46	2.91	430	0.6	2.04	143	29	0.14		56
2470	0.26	2.29	432	1.04	2.09	110	50	0.10	0.81	56
2475	0.78	4.48	433	0.33	1.79	250	18	0.15		25
2480	0.22	2.33	430	1.09	2.28	102	48	0.09		60
2485	0.73	4.8	432	0.42	2.05	234	21	0.13		60
2490	0.21	3.56	434	1.01	2.58	138	39	0.06	0.83	65
2495	0.18	3.27	435	0.87	2.26	145	38	0.05	0.84	67
2500	0.3	2.92	431	0.65	2.05	142	32	0.09		66
2505	0.48	3.97	429	0.93	2.35	169	40	0.11	0.83	47
2510	0.4	4.06	432	0.92	2.23	182	41	0.09		47
2515	0.52	4.47	435	0.78	2.18	205	36	0.11		32
2520	0.47	4.31	435	0.69	2.21	195	31	0.10	0.77	48
2525	0.38	3.26	432	0.47	2.27	144	21	0.10		61
2530	0.31	3.08	432	0.55	2.28	135	24	0.09		63
2535	0.21	3.13	432	0.83	2.33	134	35	0.06		51
2540	0.22	3.36	430	0.94	2.5	134	38	0.06		71
2545	0.27	3.21	429	1.48	2.51	128	59	0.08		73
2550	0.31	3.64	433	0.95	2.57	142	37	0.08	0.78	43
<i>C well</i>										
2720	0.21	1.39	353	0.35	1.80	77	20	0.13	1.07	84
2735	0.32	1.62	392	0.47	2.05	79	23	0.16		84
2755	0.23	1.56	354	0.39	2.02	77	19	0.13		84
2760	0.24	1.58	354	0.38	1.98	80	19	0.13		84
2765	0.23	1.44	346	0.38	1.88	76	20	0.14		84
2770	0.14	1.44	435	0.34	1.53	94	22	0.09		80
2775	0.17	1.65	440	0.35	1.59	104	22	0.09		78
2780	0.17	1.56	434	0.38	1.71	91	22	0.10		80
2785	0.15	1.25	430	0.33	1.51	83	22	0.11		83
2790	0.21	1.33	437	0.31	1.46	91	22	0.14		81
2795	0.23	1.94	435	0.38	1.59	122	24	0.11		74
2800	0.37	2.05	432	0.47	1.64	125	29	0.15		73
2805	0.31	2.15	436	0.41	1.48	145	28	0.13		69
2810	0.26	1.43	434	0.37	1.70	84	22	0.15	1.07	84

(continued)

**Table 1** (continued)

Depth (m)	S1 (mgHC/g rock)	S2 (mgHC/g rock)	Tmax (°C)	S3 (mgCO <sub>2</sub> /g rock)	TOC (%)	HI (mgHC/gTOC)	OI (mgCO <sub>2</sub> /gTOC)	PI	R <sub>0</sub> (%)	TR (%)
2815	0.17	1.45	433	0.34	1.75	83	19	0.11		83
2820	0.10	1.04	426	0.48	2.03	51	23	0.09		90
2825	0.06	1.00	374	0.36	2.05	49	17	0.05		90
2830	0.04	1.00	426	0.38	2.13	47	18	0.04		91
2835	0.07	1.13	425	0.37	2.05	55	18	0.06		89
2840	0.12	1.43	417	0.35	2.10	68	17	0.08		86
2845	0.71	4.35	382	0.43	2.23	195	19	0.14	1.07	56
2850	0.27	1.63	354	0.36	1.97	83	18	0.14		83
2855	0.26	1.59	429	0.38	1.85	86	21	0.14		82
2860	0.31	1.38	419	0.37	1.93	72	19	0.19		85
2865	0.32	1.84	360	0.32	1.97	93	16	0.15		81
2870	0.29	1.47	352	0.31	1.72	85	18	0.16		83
2875	0.42	2.25	370	0.42	2.08	108	20	0.16	1.10	78
2880	0.16	1.42	360	0.47	2.02	70	23	0.10		86
2885	0.27	1.18	342	0.50	2.38	50	21	0.19		90
2890	0.26	1.48	430	0.65	2.27	65	29	0.15		87
2895	0.24	1.45	375	0.44	2.07	70	21	0.14	1.13	84
<i>D well</i>										
2700	0.23	0.60	468	1.00	1.47	40	68	0.28		81
2705	0.17	0.47	476	0.75	1.31	36	57	0.27		83
2710	0.23	0.59	455	1.16	1.45	41	80	0.28	1.07	81
2715	0.19	0.51	477	0.66	1.63	31	40	0.27		86
2720	0.17	0.45	480	1.23	1.49	30	82	0.28		86
2725	0.26	0.65	439	0.98	1.48	44	66	0.28		79
2730	0.15	0.38	460	1.21	1.53	25	79	0.29		88
2735	0.16	0.39	333	1.03	0.91	43	113	0.29		80
2740	0.12	0.30	473	1.13	1.51	20	75	0.29		91
2750	0.10	0.26	464	1.16	1.46	18	79	0.29		92
2755	0.17	0.41	417	0.78	1.45	28	54	0.29		87
2760	0.12	0.31	477	1.12	1.64	19	68	0.28	1.08	92
2765	0.17	0.42	485	1.00	1.79	24	56	0.29		88
2770	0.09	0.14	463	1.41	1.90	7	74	0.40		97
2775	0.21	0.47	477	0.81	1.86	25	44	0.31		88
2784	0.31	0.75	440	1.57	1.88	40	84	0.29	1.09	80
2788	0.24	0.57	468	0.76	1.74	33	44	0.29		84
2792	0.32	0.87	480	0.66	1.48	58	44	0.27		71
2796	0.11	0.37	479	0.88	1.51	25	58	0.22		88
2804	0.15	0.51	457	0.86	1.58	32	54	0.23		84
2806	0.30	0.74	470	0.95	2.02	37	47	0.29		80
2810	0.20	0.66	442	0.95	1.57	42	61	0.24		77
2816	0.33	0.83	486	1.30	2.16	38	60	0.28		79
2818	0.32	0.81	483	1.31	2.23	36	59	0.29	1.09	80

level of primary thermal conversion in the D well than in other locations.

All measured values reflect the thermal history of the formation at the present day. The inferred Ranikot source interval reaches a thickness of 120 m in the D well up to 200 m in the B well. Moreover, there is also overpressure recorded (up to 4500 psi) with pore pressure gradient of (0.59 psi/ft) and gas readings reach 15–45%.

Figure 7 is a kerogen quality plot of the Ranikot source section data from the three study wells. The data in all the wells generally range from 1.4 to 2.6% TOC, with measured S2 values less than 5 mg/g. The D well measurements plot in the field of Type IV inert kerogen, while the C well data plot as Type III. The measurements from the B well plot in the field of Type II/III kerogen with higher S2 yields than the other three wells. These are present-day values and have been reduced from the original kerogen properties on immature samples. The HI and Tmax values are obtained from the pyrolysis and TOC measurements on the samples at present-day conditions. While these parameters are also influenced by thermal maturity, they clearly indicate that the HI and present-day generative potential in the D well is partly consumed due to increasing thermal conversion of kerogen.

An original TOC<sub>o</sub> of 1.5–2.0% is considered a minimum for generation and expulsion of hydrocarbons during thermal maturation (Lewan, 1994; Pepper, 1992). However, 1.0% TOC is used as the minimum cut-off for an effective source rock, which is able to generate and expel a limited volume of hydrocarbons, of which commerciality is questionable (e.g. Peters and Cassa, 1994). In this study, the present-day TOC value of 1.5% has been accepted as the minimum value for a productive source rock.

Measured HI ranges from 11 to 250 mg HC/g TOC. The highest average value (143 mg HC/g TOC) is observed in the B well where the Ranikot shale is at the lowest level of conversion, and they decrease towards the deeper location in the D and C wells where the source rock is more thermally matured. The generally low, but variable measured HI values seem to correlate with minor fluctuations in TOC and indicate the kerogen contains mixed gas- and oil-prone components. Pyrolysis S1 values vary between 0.02 and 0.96 mg HC/g rock. There is no clear trend in the S1 values with depth, although the apparent leanest values tend to occur at the top of the zone.

The oil saturation index (OSI) ranges from 3 to 56. The highest values for this ratio are in the basal section of the sampled source rock interval, where TOC values are also relatively high. OSI values in more mature rocks within the condensate/wet gas window are typically lower (< 25) because volatile hydrocarbons may have been lost during sample recovery and handling, and the higher maturity experienced by the rocks.

### 4.3 Thermal Maturity

Measuring reflectance on indigenous vitrinite was very challenging on the Ranikot samples because they were dominated by reworked or caved particles. Measured vitrinite reflectance (VR) values from selected cutting samples in all four wells are plotted with depth in Fig. 6. Measured VR varies over a range from 0.8 to 1.13% Ro, reflecting a clear W-E increasing trend (Fig. 8). These values are in agreement with basin modelling results presented by Sheikh and Giao (2017) for the well in the Southern Indus Basin. Their data indicate that at the depth of around 3000 m, the level of thermal maturity should have reached at least 1% Ro. Moreover, the recently published results of gas analyses from the Pab sandstone reservoir within the Kirthar Range evidence that these hydrocarbons were generated at the maturity level of around 1.9–2% Ro from deep source rocks, probably Sembar/Goru formations (Laughrey et al., 2020). It means that the Ranikot shale located 2000 m shallower should have reached thermal maturity of around 1% Ro. Although the total sampled interval is small, there is also a general trend or increasing reflectance with depth. These measured VR would place the entire Ranikot shale within the oil- to wet gas-windows for type-II kerogen. There are hints of lower mature material evident in spore colouration and liptinite fluorescence, but the interpretive reliability of these data is low.

The VR data do not correlate directly with Tmax values even using the newer Tmax-Ro correlation of Drozd and Knowles (2016). The calculated vitrinite reflectance equivalent values based upon the Tmax measurements are generally too low, up to 0.6% reflectance equivalent. An exception is the D well where the Tmax equivalent reflectance is 0.17% higher than the measured value. These differences are not atypical in section with mixed kerogen and significant reworked material. The reworked material will contribute to the S2 peak (and hence Tmax), but not to the indigenous vitrinite measurement.

Production Index (PI) values have large variation from 0.04 to 0.4. The very low to moderately high PI values are generally consistent with thermal maturity indicators. The relatively low PI values reflect the low S1 yields and low OSI's. Low residual liquid content is interpreted as a positive factor in the Ranikot shale for the recovery of gas because any liquids would potentially block the micropore network.

### 4.4 Kerogen Composition and Transformation Ratio

The kerogen assemblage in the Ranikot is interpreted to be a complex mixture of oil-prone and gas-prone organic matter,

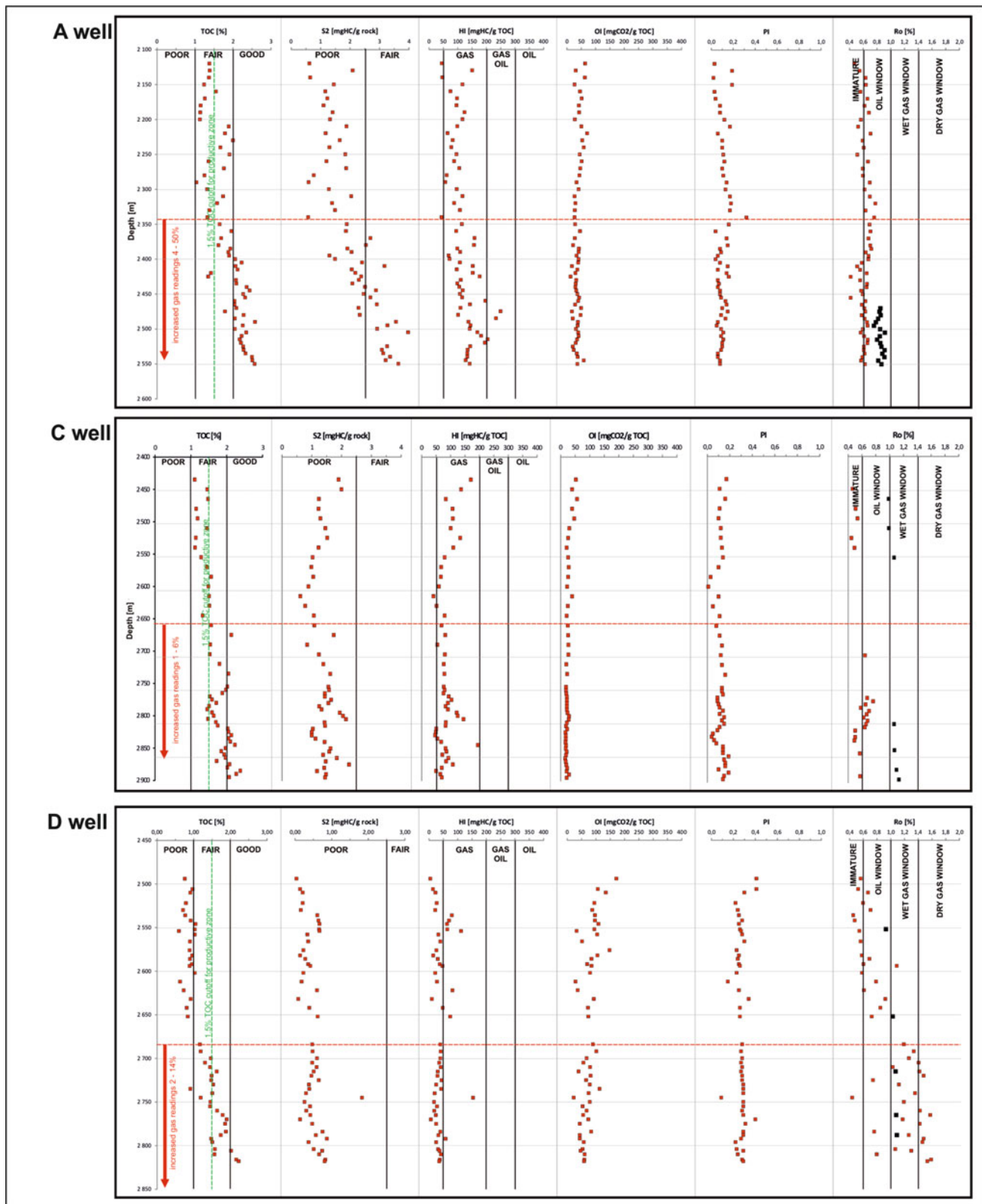


**Fig. 6** TOC and Rock-Eval-based geochemical logs from the A, C and D wells. TOC—total organic carbon, S2—residual hydrocarbon potential, HI—hydrogen index, OI—oxygen index, PI—production index, Ro—thermal maturity in vitrinite reflectance scale (red squares—Tmax based values; black squares—microscope reflectance measurements)



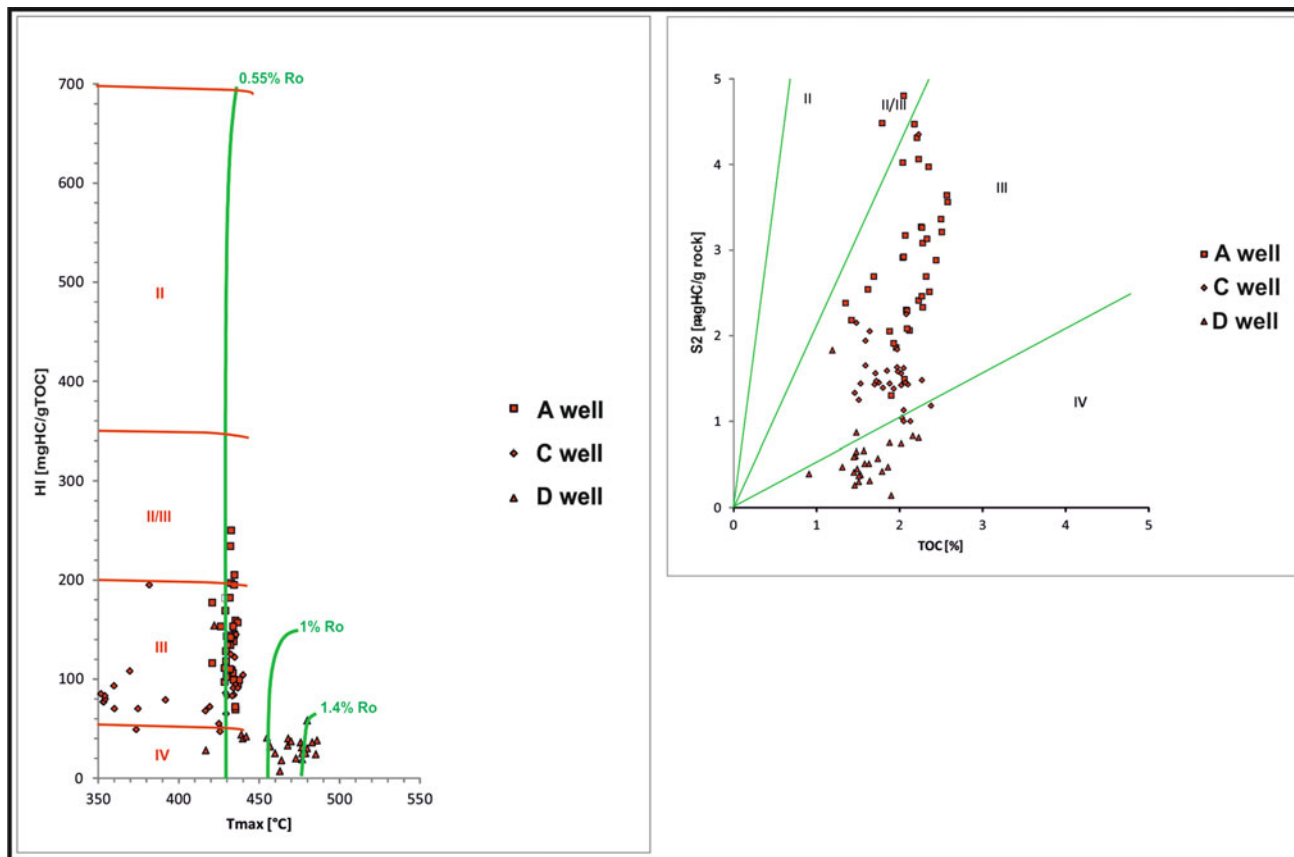


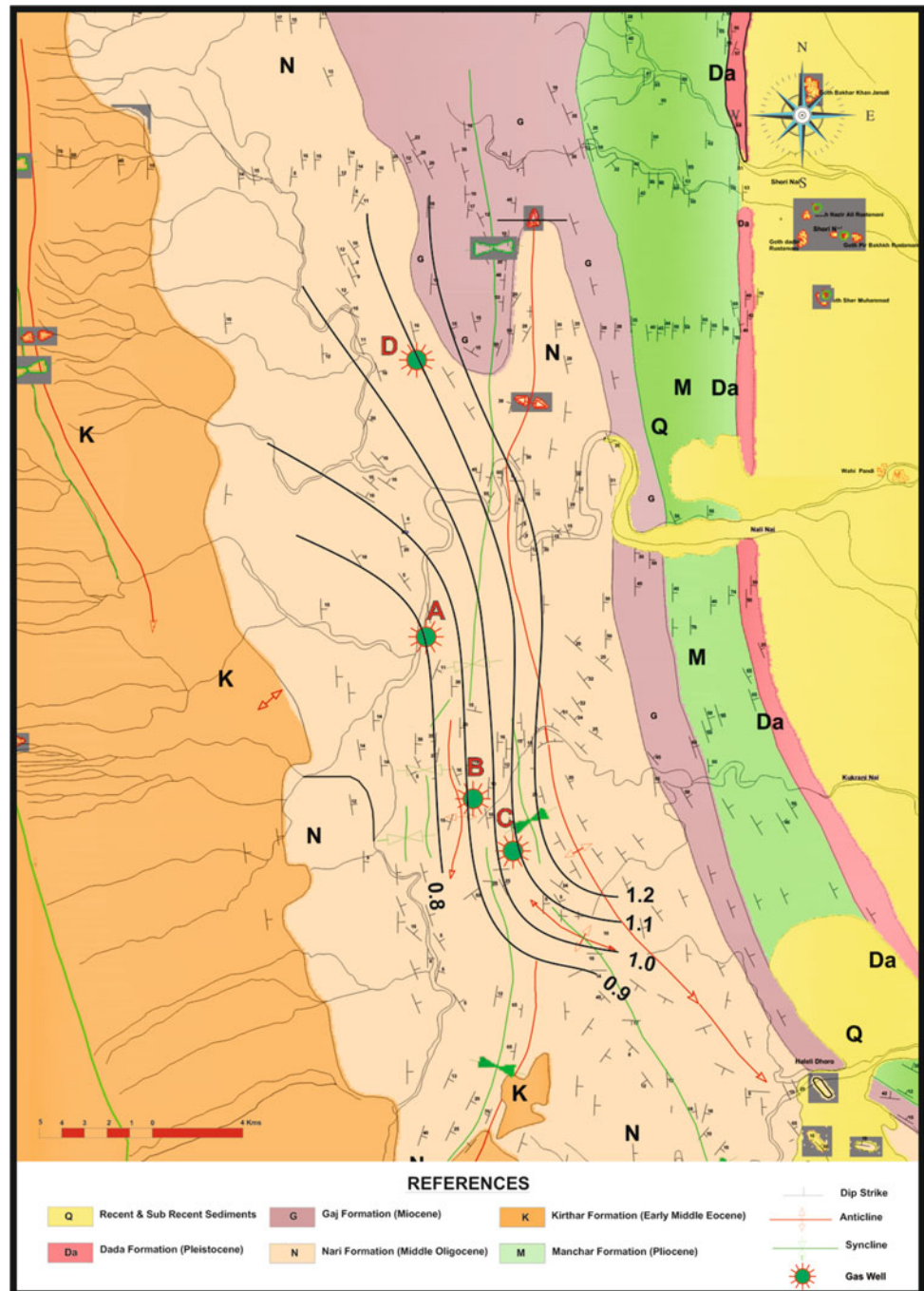
**Fig. 7** Quality of organic matter in the Ranikot shale based on Rock-Eval analysis. Note the decreasing HI and S2 readings according to increasing maturity of organic matter

along with minor to significant amounts of inert organic matter, based on visual kerogen assessment (Fig. 9). The Ranikot organic matter in the D well show a dominance of structured terrigenous woody particles (vitrinite) ranging from 75 to 85% (average 79%). Liptinite, in the form of marine amorphous organic matter (AOM), is the secondary major kerogen type and ranges from 12 to 20% with an average abundance of 18%. The AOM is non-fluorescent, which would be expected given the thermal maturity level of these samples, and typically occurs as thin brown wisps. Structured alginite and other liptinite macerals are absent. Solid bitumen is rare but was observed in some samples as trace amounts or up to 10%. The occurrence of solid bitumen would suggest a source rock that was capable of generating at least minor amounts of liquid hydrocarbons. Inertinite is generally low from 1 to 6%. The maceral compositions of kerogen in the A, B, C wells are similar with predominant amounts of type-II kerogen in the form of AOM between 41 and 63%. There is also an admixture (6–8%) of type-I kerogen observed. The gas-prone humic organic matter is very rare between 4 and 13% on average. Some vitrinite particles show evidence of oxidation. Unfortunately, inertinite occurs at the level up to 40% on

average. The higher concentration of inert organic matter is characteristic for shallower, more north-westward locations of the Ranikot Formation in the A and B wells. The mix of marine and non-marine organic matter in all samples with moderate to low TOC suggests an updip depositional location that is between basin margin and its more central part (Bohacs et al., 2013).

Transformation ratios were calculated using Eq. (5), and the average kerogen compositions are summarized in Table 2. Original hydrogen index ( $HI_o$ ) can be computed from visual kerogen using formula (3). The average estimated  $HI_o$  values for the Ranikot shale are between 240 and 364 mg HC/g rock in the A, B, C wells and 180 mg HC/g rock in the D well, confirming the variable contribution of oil-prone kerogen to the source rock. The extent of organic matter conversion was determined using Eq. (5), where the present-day values were measured via programmed pyrolysis. Using these values, the extent of fractional conversion of  $HI_o$  to petroleum in the Ranikot shale varies from 55 to 84%. The transformation ratio increases with depth between the B and C wells. This is consistent with the changes in thermal maturity. In the C and D wells, the TR values are well above 50%, recommended minimum threshold for shale oil

**Fig. 8** Thermal maturity of the lower section of Ranikot shale based on vitrinite reflectance data



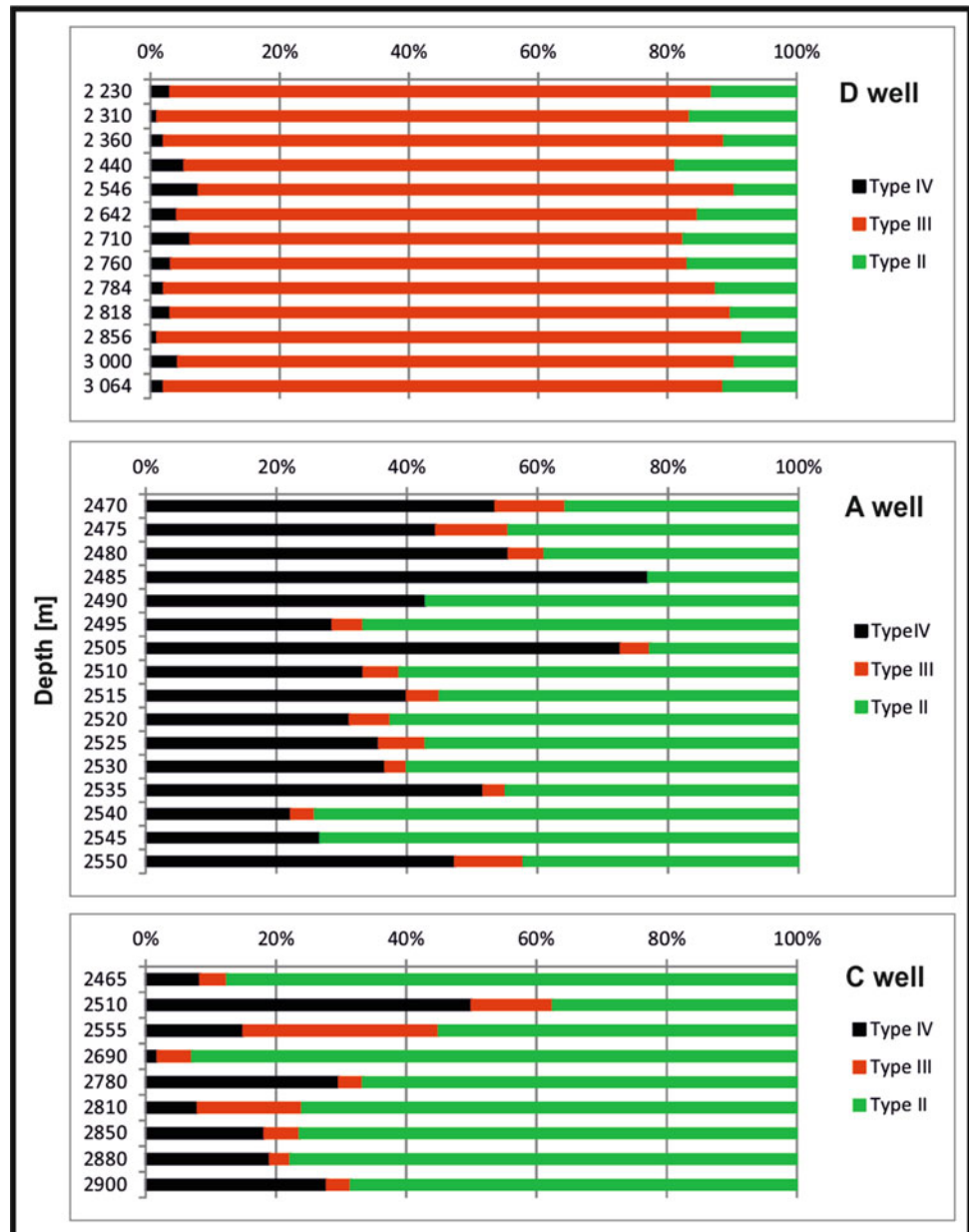
systems, and exceed 80% which is common thermogenic shale gas systems.

#### 4.5 Original Generative Potential

Generative potential of the source rock depends on the original quantity of organic matter ( $TOC_o$ ) and the original type of organic matter ( $HI_o$ ) (Peters et al., 2005). This original potential is decreased during the petroleum

generation processes reflected in the measured TOC and HI. Ranikot shale samples exhibit a range of conversion into hydrocarbons depending upon thermal maturity. The extent of kerogen conversion, the volume of expelled hydrocarbons and the expulsion efficiency were estimated using the method described by Jarvie et al. (2007) and Peters et al. (2005). The estimated original TOC for the Ranikot shale source rock samples before petroleum expulsion varies from 1.9 to 2.5% (Table 2). When the  $TOC_o$  and  $HI_o$  are known, then the original hydrocarbon potential ( $S2_o$ ) of the source

**Fig. 9** Kerogen composition within the Ranikot shale in the B, C and D wells



rock can be calculated from Eq. (2). For the Ranikot shale source section, the  $S2_o$  values vary from 3.3 in the D well to 9.1 mg HC/g rock in the C well. The original  $HI_o$  (Table 2) values indicate that the kerogen assemblage was mixed Type II/III in the A, B, C wells and Type III in the D well (Fig. 10).

#### 4.6 Hydrocarbon Yield Calculation

The amount of generated hydrocarbons is expressed as the difference between  $S2_o$  and  $S2$  values (Eq. 1) and is

summarized in Table 2. The  $\Delta S2$  in the Ranikot shale source section varies from 2.8 mg/g rock in the D well to 7.5 mg HC/g rock in the C well. It is a challenge to determine the amount of hydrocarbons retained in the rock compared to what was generated because a substantial quantity may have been expelled, or have been lost prior to analysis. However, many attempts of reserves estimations based on geochemical data have been made (e.g. Jarvie et al., 2007; Schmoker, 1994). The model of Schmoker (1994) has been widely used in many petroleum basins (e.g. Badics and Veto, 2012; Demirel et al., 2001; Mancini et al., 2008). A major uncertainty is how much oil and gas is produced from particular

**Table 2** Original generative potential of the Ranikot source rock calculated based on model by Jarvie et al. (2007)

	S1 (mgHC/g rock)	S2 (mgHC/g rock)	Tmax (°C)	TOC (%)	HI (mgHC/g TOC)	PI	Type-I (%)	Type-II (%)	Type-III (%)	Type-IV (%)	HI <sub>o</sub> (mgHC/g TOC)	Plo	TR (%)	TOC <sub>o</sub> (%)	S2 <sub>o</sub> (mgHC/g rock)	ΔS2 (mgHC/g rock)
A well	0.33	3.09	430.98	2.17	143	0.09	6	42	5	41	279	0.02	55	2.54	7.33	4.33
B well	0.38	0.89	419.82	1.75	52	0.30	0	45	13	42	240	0.02	82	2.08	4.98	4.09
C well	0.24	1.60	n.a	1.89	86	0.12	6	68	6	21	364	0.02	82	2.50	9.09	7.50
D well	0.20	0.52	460.37	1.63	32	0.28	0	18	79	4	179	0.02	84	1.86	3.34	2.80

types of kerogen at a given thermal maturity. This issue has a special significance in case of organic matter composed of different, gas-prone and oil-prone kerogens (Hunt, 1991; Tissot & Welte, 1984) as found in the study wells. Our calculations assume that significant amounts of oil and gas are generated only by oil-prone and gas-prone kerogen, respectively. The oil cracking ratio by Waples (2000) and Tian et al. (2006) was applied to estimate the extent of primary oil cracking and then the volume of cracked gas. Based upon the measured thermal maturity, the average oil cracking in the D well reached 25% and in the B well it was negligible (~1%). Results of calculations of hydrocarbon yields are presented in Table 3.

The S2<sub>o</sub> of the Ranikot source section ranges from 3.3 mgHC/g rock in the D well to 9.1 mgHC/g rock in the C well. In the area of Rehman gas field, the composition of organic matter (Fig. 9) indicates 45–73% of oil-prone kerogen with 6 to 13% of gas-prone kerogen and inertinite reaches of 42%. The D well area has abundant gas-prone kerogen (79%) with secondary oil-prone kerogen (17.5%) and low inert organic matter (3.5%). The primary potential for oil and gas generation are 1.9–5.5 mgHC/g rock and 0.2–0.5 mgHC/g rock, respectively, from oil-prone kerogen. The gas-prone dominated kerogen yields between 0.49 and 2.21 mgHC/g rock. The amount of final product depends on the level of thermal conversion and the secondary oil cracking to gas (between 1 and 25% in the study area).

The Ranikot source section in the A well area could have generated 0.006 bbl/m<sup>3</sup> (8 bbl/ac-ft) of oil and 6.66 m<sup>3</sup>/m<sup>3</sup> (290 Mcf/ac-ft) of gas during the primary process. Oil cracking into gas supplied another 0.4 m<sup>3</sup>/m<sup>3</sup> (16 Mcf/ac-ft) of gas for a total gas potential of 7 m<sup>3</sup>/m<sup>3</sup> (306 Mcf/ac-ft). The S1 peak reflects the amount of oil retained in rock (0.0035 bbl/m<sup>3</sup>; 4.4 bbl/ac-ft). Assuming the D well source rock net thickness of 120 m, the total generated hydrocarbons volume is 0.84 BCM/km<sup>2</sup> (76 Bcf/mi<sup>2</sup>) of gas and 720 Mbbl/km<sup>2</sup> (1.8 MMbbl/mi<sup>2</sup>) of oil.

Within the range of A, B, C wells area, the Ranikot source section exhibits diverse quality and maturity of organic matter. In the A well, the primary generation process produced 0.03 bbl/m<sup>3</sup> (36 bbl/ac-ft) of oil and 0.6 m<sup>3</sup>/m<sup>3</sup> (69 Mcf/ac-ft) of gas. In the C well generation processes produced 0.07 bbl/m<sup>3</sup> (90 bbl/ac-ft) of oil and 1.6 m<sup>3</sup>/m<sup>3</sup> (63 Mcf/ac-ft) of gas. The low maturity section (B well) produced very minor amount of secondary gas (0.07m<sup>3</sup>/m<sup>3</sup>; 3.3 Mcf/ac-ft). At higher maturities secondary cracking generated significant additional gas. Total generated gas reaches 5.57 m<sup>3</sup>/m<sup>3</sup> (243 Mcf/ac-ft) in the C well location (1.13% Ro). With a net source rock thickness of around 200 m, 14.6 MMbbl/km<sup>2</sup> (37.8 MMbbl/mi<sup>2</sup>) of oil and 1.1BCM/km<sup>2</sup> (100 Bcf/mi<sup>2</sup>) of gas were generated.

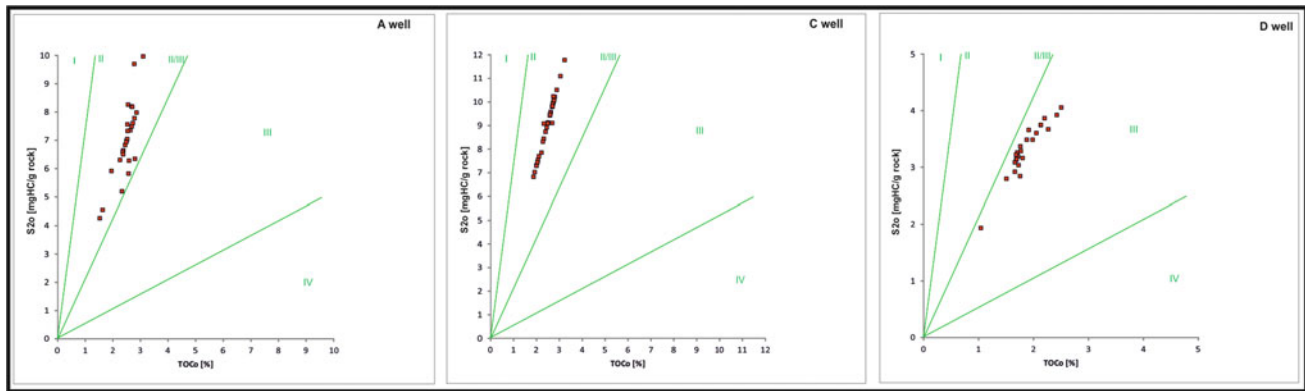


**Fig. 10** Original generative potential of the Ranikot shale in the B, C and D wells.  $TOC_o$  and  $S_{2_o}$  calculated based on Eqs. 2–4. Note the original quality of kerogen indicates its mixed character with significant

contribution of oil-prone organic matter in the southern area. In the northern area, the kerogen is more gas prone

**Table 3** Volumetric calculation of hydrocarbon generated from the Ranikot source rock, according to model by Jarvie et al. (2007)

	Free oil (bbl/ac-ft)	Primary oil (bbl/ac-ft)	% oil cracked	Total oil (bbl/ac-ft)	Primary gas (Mcf/ac-ft)	Secondary gas (Mcf/ac-ft)	Total gas (Mcf/ac-ft)	Total gas ( $m^3/m^3$ )	Gas equivalent (Mcf/ac-ft)	Gas equivalent ( $m^3/m^3$ )	ExEf
A well	7.2	46	1	45	28	3.3	31	0.70	568	13.04	0.92
B well	8.2	40	10	36	68	24.8	93	2.13	537	12.33	0.91
C well	5.2	120	25	90	63	179.8	243	5.57	98	22.58	0.97
D well	4.4	11	25	8	290	16	306	7.03	367	8.43	0.93

#### 4.7 Shale Gas Reserves and Risk Assessment

The Ranikot shale interval in the Kirthar Block is considered as a moderate geochemical risk source rock for gas production (Fig. 11). The average TOC content of 1.6–2.2% is only slightly below the generally accepted limit of 2% TOC for economical petroleum generation. There are zones within the upper section of the Ranikot interval that are organically lean, but other zones that exceed the 2% TOC threshold can be a viable unconventional shale gas target. The difference in the dominant original kerogen types in the A–C (oil-prone) and D (gas-prone) areas is a significant uncertainty. Such a large change in primary kerogen deposition within the same formation and at two locations only 10 km apart is a concern for a regional assessment and will require further investigation to be resolved.

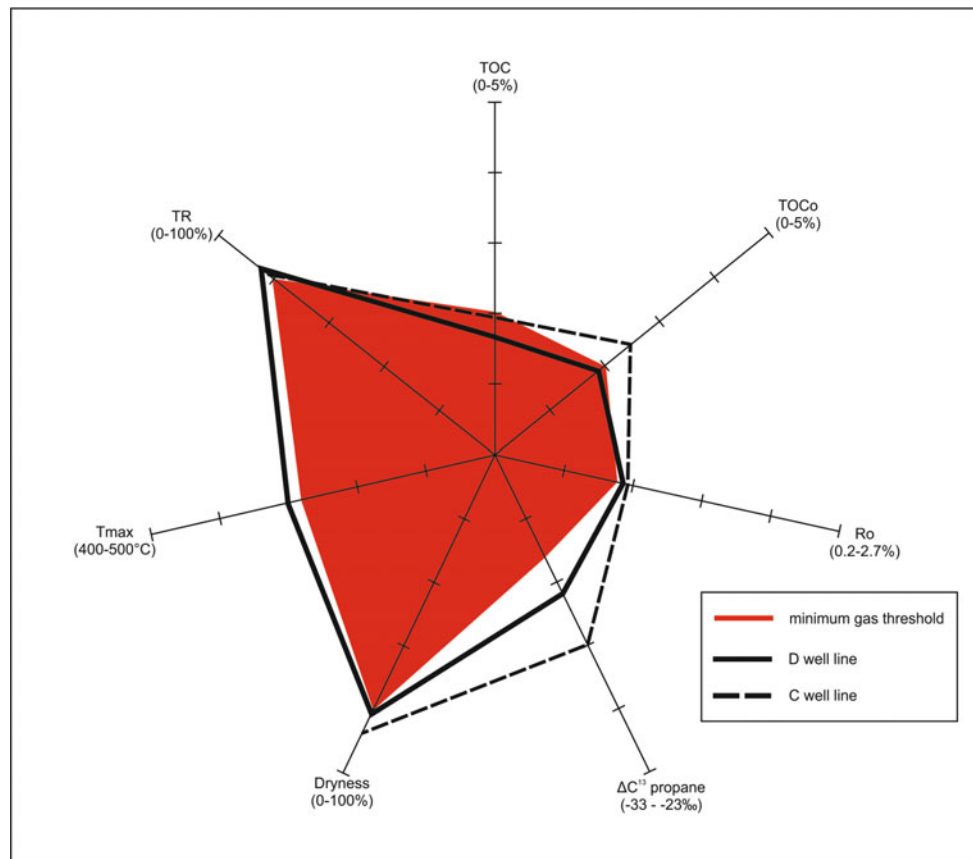
Most  $T_{max}$  values determined for the Ranikot shale cuttings samples are considered unreliable due to either to low values (A well) or to high values (D well). More reliable organic petrography measurements place the Ranikot shale source interval in condensate/wet gas window (1.0–1.13% Ro). At this level of thermal alteration, the source rock should be sufficient to generate/expel significant amounts of

hydrocarbons from these mixed, oil- and gas-prone source facies. The measured transformation ratios are above 80% which is the recommended minimum for shale gas systems.

Volumes of generated hydrocarbons are presented in Table 3. The calculated yields are based on mass balance and are likely to be slightly overestimated. They do not represent recoverable products. This is very difficult to assess how much hydrocarbons can be produced from the unconventional reservoir without performing production tests in drilled wells. Therefore, at the early stage of basin evaluation, only general extrapolations are possible based on reasonable assumptions. For this purpose, analogue data from other producing shale plays were used. As more detailed information becomes available, the initial assessment of the play must be reevaluated.

According to the production data from the Barnett shale play (Fort Worth Basin, Texas, USA), approximately 60% of the total generation potential is lost as a consequence of expulsion and migration from the source rock during primary generation. Another 15% is lost during oil cracking and its conversion into pyrobitumen. Only 25% of the total generation potential is retained gas (Jarvie et al., 2007). When this model is considered for the Ranikot shale and the

**Fig. 11** Assessment of the Ranikot shale as a source rock for gas generation. C and D well lines are outside the red area indicating the potential for hydrocarbon production from the Ranikot shale system



total potential of the source section ranges between 0.84 and 1.1 BCM/km<sup>2</sup> (76 and 100 Bcf/mi<sup>2</sup>), the gas-in-place (GIP) reserves will be then between 0.21 and 0.28 BCM/km<sup>2</sup> (19 and 25 Bcf/mi<sup>2</sup>) in the locations of D and C wells, respectively. For comparison, the Barnett Shale (core section) GIP is estimated to 2.2 BCM/km<sup>2</sup> (200 Bcf/mi<sup>2</sup>). The long-term average recovery factor for Barnett Shale play is 6–7%, which gives recoverable gas resources of around 0.14 BCM/km<sup>2</sup> (12.8 Bcf/mi<sup>2</sup>). That means EUR of around 0.045 BCM/well (1.6 Bcf/well) (8 horizontal wells/mi<sup>2</sup>). In case of the Ranikot shale, assumption of 7% recovery factor gives recoverable resources of 0.015 BCM/km<sup>2</sup> (1.3 Bcf/mi<sup>2</sup>), which means EUR of 4.5 MMCM/well (0.16 Bcf/well).

However, the Barnett analogy is too much conservative for the Ranikot reservoir. The Ranikot Formation is composed of thin layers of siltstones and mudstones, which are interbedded with relatively thinner layers of sandstone. The Barnett is a massive mudstone without significant interbedded units. Therefore, the Ranikot should be interpreted as a hybrid unconventional petroleum system with organic-rich shales and organic-lean sandstones (Jarvie, 2012). Assuming that the formation is a self-sealing reservoir, the amount of generated and expelled hydrocarbons from the shale section may have been retained within the sandstone section. It is

difficult to estimate the volume of hydrocarbons lost to the reservoir under such conditions. However, the presence of saturated sandstones layers and increased reserves, especially within the large structures explored at the Kirthar Range, can be expected. Hence, the GIP reserves could be much higher than these calculated via conservative Barnett analogue. Also, recovery factors are likely larger in a hybrid system compared to typical mudstone unconventional systems. Thus, the recoverable resources of the Ranikot shale source section can be significantly higher than 4.5 MMCM/well (0.16 Bcf/well). Using minimum values for the sandstone layers: thickness—12 m; porosity—5%; HC saturation—55%; recovery factor—40%, the estimated recoverable reserves in the Ranikot shale are 0.082 BCM/km<sup>2</sup>, or about 27 MMCM/well (3 wells/km<sup>2</sup>).

## 5 Conclusions

The Ranikot Formation in the Southern Indus Basin (Kirthar Foldbelt), composed of organic shales and intercalations of sandstones (10–20% net thickness), exhibits gas saturation with overpressure of 4500 psi and pore pressure gradient of 0.59 psi/ft. Thickness of the most perspective section varies between 120 and 200 m. The average TOC ranges between

1.6 and 2.2%. The HI and level of organic matter conversion depend on the thermal maturity ranging from the peak oil window to the wet gas window. Organic matter is composed of mixed-type kerogen with diverse contribution of type-II, type-III and type-IV. Based on all geochemical data, the Ranikot shale source intervals should be considered a high risk for shale gas play. However, the Ranikot Formation is a hybrid system with modest organic richness, acceptable thermal maturity and sufficient transformation ratio confirmed by gas composition. Under these conditions, the Ranikot shale is considered only a moderate risk for commercial shale gas production.

At the maturity of around 1.1%Ro, the Ranikot shale could have generated between 5.6 and 7 m<sup>3</sup>/m<sup>3</sup> (243 and 306 Mcf/ac-ft) of gas. According to the interpreted thickness of the source interval, the volume of generated gas was between 0.84 and 1.1 BCM/km<sup>2</sup> (76 and 100 Bcf/mi<sup>2</sup>). These hydrocarbons were expelled and migrated, but in some part were retained in the source rock. Moreover, some part of expelled gas was retained in the sandstones layers within the Ranikot Formation. Therefore, the absolute minimum volume of recoverable gas resources in the Kirthar Range is around 4.5 MMCM/well (0.16 Bcf/well). In general, the unconventional resources should be considered as a significant contributor to the overall energy balance of Pakistan, and the Ranikot shale has a potential to be one of these resources.

**Acknowledgements** Authors would like to thank Polish Oil and Gas Company (PGNIG SA) and Pakistan Petroleum Limited (PPL) for all necessary permissions and providing the data set for interpretation and publication. We also thank Wayne Knowles and Tim Ruble (Stratum Reservoir) for significant suggestions and lot of discussions on results of this study.

## References

- Ahmad N., Mateen, J., Shehzad, K., Mehmood, N., Arif, F. (2012). Shale gas potential of lower cretaceous Sembar formation in middle and lower Indus Sub-Basins, Pakistan. In: *Search and Discovery*. Article #10392 Adapted from oral presentation at PAPG/SPE Annual technical conference 2011, Islamabad, Pakistan, November 22–23, 2011
- Badics, B., & Vető, I. (2012). Source rocks and petroleum systems in the Hungarian part of the Pannonian Basin: The potential for shale gas and shale oil plays. *Marine and Petroleum Geology*, 31(1), 53–69.
- Bannert, D., Cheema, A., Ahmed, A., & Schäffer, U. (1992). The structural development of the Western Fold Belt, Pakistan. *Geologisches Jahrbuch*, B80, 3–60.
- Behar, F., Vandenbroucke, M., Tang, Y., Marquis, F., & Espitalié, J. (1997). Thermal cracking of kerogen in open and closed systems; determination of kinetic parameters and stoichiometric coefficients for oil and gas generation. *Organic Geochemistry*, 26, 321–339.
- Bender, F. K., & Raza H. A. (Eds.) 1995. *Geology of Pakistan* (p. 414).
- Bish, D. L., & Reynolds, R. C. Jr. (1989). Sample preparation for X-ray diffraction. In D. L. Bish and J. E. Post (Eds.), *Modern powder diffraction reviews in mineralogy*, (Vol. 20, pp. 73–99). Mineralogical Society of America.
- Bodnar, D. (2015). Thinly bedded pay in clastic reservoirs, recognition, geological occurrence, understanding, and quantification. In AAPG Asia Pacific Region, Geoscience technology workshop, modern depositional systems as analogues for petroleum reservoirs, April 21–22, 2015, Wellington, New Zealand.
- Bohacs, K., Macquaker, J., Grabowski, G., Lazar, R., & Demko, T. (2013). Local expression of regional and global factors in mudstone-reservoir occurrence, character, and distribution in Toarcian platform/ramp source-rock settings, NW Europe. In Houston Geological Society—Applied Geoscience Conference, February 18–19.
- Demirel, I. H., Yurtsever, T. S., & Guneri, S. (2001). Petroleum systems of the Adiyaman region, Southeastern Anatolia, Turkey. *Marine and Petroleum Geology*, 18(3), 391–410.
- Drozd, R. J., & Knowles, W. R. (2016). Vitrinite reflectance and programmed pyrolysis Tmax measurements, How can I use both in an operational setting? In Joint Meeting: The Society for Organic Petrology, The Palynological Society & The International Committee for Coal and Organic Petrology, September 18–23, 2016, Houston, Texas.
- Drozd, R. J., Weldon, W. D., Schrynmeeckers, R., Maende, A., Leroux, B., & Hossein, A. (2009). *Onsite pyrolysis—Using real-time technology to evaluate reservoir properties*, Poster 24th International meeting on organic geochemistry. Bremen.
- EIA. (2013). *Annual energy outlook* (pp. 60–62). US Energy Information Administration.
- Espitalié, J. M., Madec, M., Tissot, B., Mennig, J. J., & Leplat, P. (1977). Source rock characterization method for petroleum exploration. *Proceedings of the Annual Offshore Technology Conference*, 3, 439–448.
- Hunt, J. (1991). Generation of gas and oil from coal and other terrestrial organic matter. *Organic Geochemistry*, 17(6), 673–680.
- Jarvie, D. M., Hill, R. J., Ruble, T. E., & Pollastro, R. M. (2007). Unconventional shale-gas systems: The Mississippian Barnett Shale of north-central Texas as one model for thermogenic shale-gas assessment. *American Association of Petroleum Geologists Bulletin*, 91, 475–499.
- Jarvie, D. M. (2012). Shale resource systems for oil and gas: Part 1—Shale-gas resource systems. In J. A. Breyer (Ed.), *Shale reservoirs—Giant resources for the 21st century: AAPG Memoir* (Vol. 97, pp. 69–87).
- Langford, F. F., & Blanc-Valleron, M.–M. (1990). Interpreting programmed pyrolysis data using graphs of pyrolyzable hydrocarbons vs. total organic carbon. *AAPG Bulletin*, 74(6), 799–804.
- Laughrey, C. D., Makos, M., Gorniak, M., ul Wahab, I., Shifaat Alaam, M., Noor, I., Naem Kahn, R. (2020). Origin of carbon dioxide, nitrogen, and hydrocarbons in upper cretaceous Pab sandstone tight-gas reservoirs, Middle Indus Basin, Pakistan: Noble gas and stable isotopic evidence for crustal and magmatic components. AAPG ACE 2020.
- Lewan, M. D. (1994). Assessing natural oil expulsion from source rocks by laboratory pyrolysis. In L. B. Magoon & W. G. Dow (Eds.), *The petroleum system—from source to trap*. AAPG Memoir, Vol. 60, pp. 201–211.
- Loosveld, R. J. H., Bell, A., & Terken, J. J. M. (1996). The tectonic evolution of interior Oman. *GeoArabia*, 1, 28–51.
- Magoon, L. B., & Dow, W. G. (1994). The petroleum system. In L. B. Magoon, and W. G. Dow, (Eds.), *The petroleum system: From source to trap: AAPG Memoir* (Vol. 60, pp. 3–24).
- Mancini, E. A., Li, P., Goddard, D., Ramirey, V., & Talukdar, S. C. (2008). Mesozoic (Upper Jurassic and lower cretaceous) deep gas

- reservoir play, central and eastern Gulf coastal plain. *AAPG Bulletin*, 92(3), 283–309.
- Matthews, K. J., Maloney, K. T., Zahirovic, S., Williams, S. E., Seton, M., & Müller, R. D. (2016). Global plate boundary evolution and kinematics since the late Paleozoic. *Global and Planetary Change*, 146, 226–250.
- Moore, D. M., & Reynolds, R. C. (1997). *X-ray diffraction and the identification and analysis of clay minerals* (2nd ed., p. 332). Oxford University Press.
- Passey, Q. R., Dahlberg, K. E., Sullivan, K. B., Yin, H., Brackett, R. A., Xiao, Y. H., & Guzmán-García, A. G. (2006). Petrophysical evaluation of hydrocarbon pore-thickness in thinly bedded clastic reservoirs. AAPG Archie Series (No. 1, pp. 133–153).
- Pepper, A. S. (1992). Estimating the petroleum expulsion behavior of source rocks: A novel quantitative approach. In W. A. England, and A. L. Fleet (Eds.), *Petroleum migration*. Geological Society (London) Special Publication, Vol. 59, pp. 9–31.
- Peters, K. (1986). Guidelines for evaluating petroleum source rock using programmed pyrolysis. *The American Association of Petroleum Geologists Bulletin*, 70(3), 318–329.
- Peters, K. E., & Caasa, M. R. (1994). Applied source rock geochemistry. In L. B. Magoon, & W. G. Dow (Eds.), *The petroleum system: From source to trap*. AAPG Memoir, Vol. 60, pp. 93–117.
- Peters, K. E., Walters, C. C., & Moldowan, J. M. (2005). *The biomarker guide biomarkers and isotopes in the environment and human history* (Vol. 1). Cambridge University Press.
- Raza, H. A., Ali, S. M., & Ahmen, R. (1990). Petroleum geology of Kirthar sub-basin and part of Kutch basin. *Pakistan Journal of Hydrocarbon Research*, 2(1), 29–74.
- Schmoker, J. W. (1994). Volumetric calculation of hydrocarbons generated. In L. B. Magoon, & W. Dow (Eds.), *The petroleum system from source to trap* (Vol. 60). American Association of Petroleum Geologists Memoir, pp. 323–329.
- Sheikh, N., & Giao, P. H. (2017). Evaluation of shale gas potential in the lower cretaceous Sembar formation, the Southern Indus Basin, Pakistan. *Journal of Natural Gas Science and Engineering*, 44, 162–176.
- Smewing, J. D., Warburton, J., Daley, T., & Ul Haq, N. (2002). Sequence Stratigraphy of the southern Kirthar Foldbelt. *Geological Society of London Special Publications*, 195, 273–299.
- SRA. (2012). *Source Rock Analyzer*. <https://weatherford.com/en/documents/>, Accessed June, 2014.
- Tian, H., Wang, Z., Xiao, Z., Li, X., & Xiao, X. (2006). Oil cracking to gases: Kinetic modeling and geological significance. *Chinese Science Bulletin*, 51(22), 2763–2770.
- Tissot, B. P., & Welte, D. H. (1984). *Petroleum formation and occurrence* (p. 699). Springer-Verlag.
- Treloar, P. J., Izatt, C. N. (1993). Tectonics of the Himalyan collision between the Indian plate and the Afghan block: A synthesis. In: P. J. Treloar, & M. P. Searle, (Eds.), *Himalayan tectonics*. Geological Society (London) Special Publications, Vol. 7(4), pp. 69–87.
- Vail, P., Mitchum Jr, R. M., & Thompson, S. (1977). Seismic stratigraphy and global changes of sea-level, Part 4: Global cycles of relative changes of sea level. *American Association Petroleum Geological Memoirs*, 26, 83–97.
- Van Hinsbergen, D. J. J., Steinberger, B., Doubrovine, P. V., & Gassmöller, R. (2011). Acceleration and deceleration of India-Asia convergence since the Cretaceous: Roles of mantle plumes and continental collision. *Journal of Geophysical Research*, 116.
- Wandrey, C. J., Law, B. E., & Haider, A. S. (2004). Sembar Goru/Ghazij composite total petroleum system, Indus and Sulaiman-Kirthar Geologic Provinces, Pakistan and India. In *US Geological Survey Bulletin 2208-B* (pp. 1–23).
- Waples, D. (2000). The kinetics of in-reservoir oil destruction and gas formation: Constraints from experimental and empirical data, and from thermodynamics. *Organic Geochemistry*, 31, 553–575.
- Welte, D., & Leythausen, D. (1984). Geological and physicochemical conditions for primary migration of hydrocarbons. *Naturwissenschaften*, 70, 133–137.





# Characterization of the Upper Cretaceous-Paleogene Black Shale of the Southern Tethys Margin, Egypt

Rania Abu-Ali<sup>1</sup>, Ahmed El-Kammar, and Jochen Kuss

## Abstract

The Late Cretaceous-Paleogene times witnessed a deposition of widespread anoxic black shales in Egypt, resulting from an extensive high productivity upwelling system that existed along the southern Tethyan margin. These organic-rich sedimentary rocks from the Quseir, Dakhla, Duwi and Esna formation were recently studied through three exploration wells drilled in the Safaga area of the Eastern Desert of Egypt. The studied wells are Mohamed Rabah, Um El-Huaitat, and Wassief. The study evaluates the organic richness and quality as well as thermal maturity of the black shale intervals and their potential source rock. Furthermore, the stable carbon isotopes ( $\delta^{13}\text{C}_{\text{org}}$ ) were measured on the selected bulk kerogen samples. Rock-Eval<sup>®</sup>  $T_{\text{max}}$  values indicate a predominance of immature organic matter, with several marginal mature intervals. In the current study, the  $\delta^{13}\text{C}_{\text{org}}$  is not a reliable tool for determining the organic matter origin. The studied black shales from the Duwi, Dakhla, and Esna formations show good to excellent source rock qualities, derived from mostly marine organic matter, with promising oil to mixed gas and oil hydrocarbon potentiality. The siltstone-mudstone facies of the Quseir Formation (lower part of the succession), however, show high terrestrial input, reflected by a wide range of kerogen types (from type I to type III).

## Keywords

Late cretaceous-paleogene • Black shale • Rock-Eval pyrolysis • TOC% •  $\delta^{13}\text{C}_{\text{org}}\text{‰}$  • Egypt

R. Abu-Ali (✉) · A. El-Kammar  
Department of Geology, Cairo University, Giza, Egypt  
e-mail: [mrانيا@sci.cu.edu.eg](mailto:mrania@sci.cu.edu.eg)

R. Abu-Ali · J. Kuss  
Department of Geosciences, Bremen University,  
Bremen, Germany

## 1 Introduction

The term Black shale refers to organic-rich fine-grained sedimentary rocks of high economic importance for either conventional or unconventional systems. Due to the increased demand for fossil fuels and the coeval decline in conventional reserves, black shales become more important as a potential future energy resource. The Upper Cretaceous to Paleogene sequences in the Middle East are characterized by regional anoxic black shale occurrences, enriched in different stratigraphic levels of various local basins (Abed et al., 2005; Almogi-Labin et al. 1990a, 1993; Ashckenazi-Polivoda et al., 2010, 2011; Holbourn et al., 1999; Inan et al., 2010). The studied black shales are accompanied by various amounts of inorganic constituents that are lithologically expressed by calcareous shales, marlstones, limestones, and phosphoritic beds, rich in organic matter.

The Campanian Quseir Formation was mainly deposited in oxic to dysoxic conditions, with the exception of the intercalated phosphate-rich beds that show anoxic signatures, while the calcareous-rich facies of the Late Campanian–Maastrichtian Duwi and Dakhla formations indicates marine-proper depositional conditions, again interrupted by phosphate beds and phosphatic-rich facies (Abu-Ali, 2019). The sediments of the Early Paleogene Dakhla Formation reflect fluctuations between anoxic deep marine and dysoxic shallow water depositional conditions, formed during oscillating sea-level that continued into the Esna Formation when anoxic marine conditions alternate with dysoxic events (Abu-Ali, 2019). The described paleoenvironmental conditions were responsible for the organic-rich sediment depositions during several intervals of the Late Cretaceous-Paleogene succession.

There is an increasing interest in the organic-rich sedimentary rocks in the region of Quseir-Safaga since the pioneer study of Mustafa and Ghaly (1964). Several earlier studies focused on the source rock, particularly as an oil

shale deposits (El-Kammar, 1987, 1993; Khaled et al. 1997; Malak et al., 1977; Rasmy & Basily, 1983). In addition, there are important contributions by the TU Berlin scientific team in the period from 1978 until 1990 (e.g., Barthel & Böttcher, 1978; Klitzsch et al., 1990; Schrank, 1984, 1987; Schrank & Perch-Nielsen, 1985). Furthermore, Robison and Tröger (1983) investigated the geology with a focus on organic geochemistry of the Dakhla Formation in different areas in Egypt and determined extractable hydrocarbons ranging from 3.8 to 5.9% organic carbon and 550–2400 ppm HC in the Quseir-Safaga region. Several previous studies indicated that isotope and organic geochemistry data can be effectively integrated for paleoenvironmental deductions (Bechtel et al., 2012; Hayes et al., 1987; Westerhausen et al., 1993). Abd El-Rahiem et al. (2014) evaluated the black shale from the Rabah Mine (Safaga) to get an organic matter-rich concentrate, which can be used in a retorting process as a source of energy. Mineralogically, the studied black shale samples contain bituminous calcareous claystone, quartz, apatite, and pyrite with 28% organic matter. They upgraded the organic matter and obtained a concentrate with 59% assaying and 85% recovery. Makled et al. (2014) studied the sequence stratigraphy and the paleoenvironmental setting of the late Campanian-early Maastrichtian oil shale of the Duwi Formation from six phosphate mines, Eastern Desert, Egypt; El-Nakheil, Wassief, Um Huaitat, Mohamed Rabah, El-Beida and Younis. They integrated the geochemical constraints with the palynofacies data to predict the depositional settings. They concluded that sediments with low TOC content were deposited in a low stand system tract, while the sediments with intermediate TOC content took place in a high stand system tract during active paleoproductive and upwelling settings, whereas high TOC sediments content took place in a transgression system tract with a low sedimentation rate. Baioumy and Lehmann (2017) investigated the redox-sensitive trace elements (Ni, V, Mo, Cu, U, Re, Cr, Mn, Sb, Cd, and Tl) of the black shale beds in the Duwi Formation of North-eastern Egypt to examine their depositional settings. These shales are characterized by high concentrations of redox-sensitive trace metals content, Ni/Co, V/Ni, V/(V + Cr), and V/(V + Ni) ratios. Alternately, the studied shales have low concentrations of Mn, low V/Mo and Th/U ratios. They concluded that the Duwi Formation black shales originated in high productivity reducing marine conditions. Fathy et al. (2017) investigated the mineralogical and geochemical characteristics of 3 surface oil shale horizons from the Maastrichtian Duwi and Dakhla strata (El-Nakheil and El-Beida mines), the Eastern Desert (Egypt). They investigated the chondrite-normalized REE patterns and documented that these patterns are notable for the enrichment of LREE, reduction of HREE, negative Eu-anomaly, and distinctive shale-like post-Arcean Australian shale (PAAS)-normalized REE patterns.

Additionally, they recognized that the total content of REE is positively compared with Si, Na, K, Al, Fe, Mn, and Ti. This indicates that the REE of the studied oil shales is resulting from terrigenous sources. In addition, they documented significant signs of chemical weathering such as petrogenesis, sediment recycling, and tectonic setting of source material of oil shales. Abou El-Anwar et al. (2019) investigated the marine black shale of the Duwi Formation in the Quseir area to determine their depositional environment. The mineralogical investigations revealed that these black shales are mainly composed of kaolinite, montmorillonite, calcite, quartz, gypsum, and pyrite of detrital and authigenic sources. They suggested that these minerals may be developed from basic volcanic rocks due to severe chemical weathering under the prevailing semi-arid circumstances. They added that these black shales are enriched in redox-sensitive combined with sulfide-forming trace metals, which indicate a euxinic condition. Fathy et al. (2018) investigated geochemical proxies (organic and inorganic) as well as clay minerals and molecular fossils of two oil shale horizons of the Maastrichtian Duwi and Dakhla strata. They recorded that detrital smectite is the dominant clay mineral in the Duwi oil shales, while kaolinite prevails in the Dakhla Formation. They concluded that during a general Maastrichtian cooling trend, the studied Maastrichtian oil shales were accumulated in warm, arid to humid greenhouse climatic conditions. Additionally, the oil shales of the Dakhla Formation took place in deeper marine settings than those of the Duwi Formation. Abu-Ali et al. (2019) discussed the sea-level changes and the consistent depositional processes during the Late Cretaceous-Early Paleogene sequences within three sites in the Eastern Desert. The facies interpretations are obtained from biostratigraphic, lithostratigraphic, microfacies, and geochemical data (major oxides, TiO<sub>2</sub>/CaO and CaO/P<sub>2</sub>O<sub>5</sub> ratios, TOC%, and rare earth elements (REE) and Ce-anomaly). Moreover, Abu-Ali et al. (2020) investigated the geochemical characteristics along the Upper Cretaceous-Lower Paleogene organic-rich sedimentary succession of three shallow wells in the Safaga area, Egypt. They determined five geochemical influencing factors on the studied strata, defining 80% of the total variances; terrestrial, phosphorites, anoxia as well as argillaceous marine sediments and/or marine shale and earliest diagenesis. For the studied black shales and phosphorites, they identified seven lithofacies; limestone, dolomitic rocks, marlstone, siltstone-mudstone, calcareous shale, phosphorite, and phosphatic rocks. They documented the geochemical characteristics of the studied geological formations, the Quseir, the Duwi, the Dakhla, and the Esna formations, and their depositional conditions. Some of the documented geochemical characters were considered consistent chemostratigraphic signs and differentiate among the various depositional environments of the investigated succession.

The current study explores the southern Tethyan depositional archives along the Upper Cretaceous-Paleogene, the main host of the shallow black shales in the Safaga area. The available organic geochemical data allow for characterizing and evaluating the organic-rich sequences. The main objective of this chapter is to characterize the Upper Cretaceous-Paleogene black shale in the Safaga region, an unconventional source of the future energy mix. We estimated the quantity, quality, and thermal maturity, and the stable carbon isotope signature ( $\delta^{13}\text{C}_{\text{org}}$ ) of the bulk organic matter of these valuable organic-rich sedimentary source rocks. For a detailed discussion on biostratigraphy, microfacies, and inorganic geochemical features of the currently studied succession, see Abu-Ali et al. (2019, 2020).

## 2 Geologic Setting and Distribution

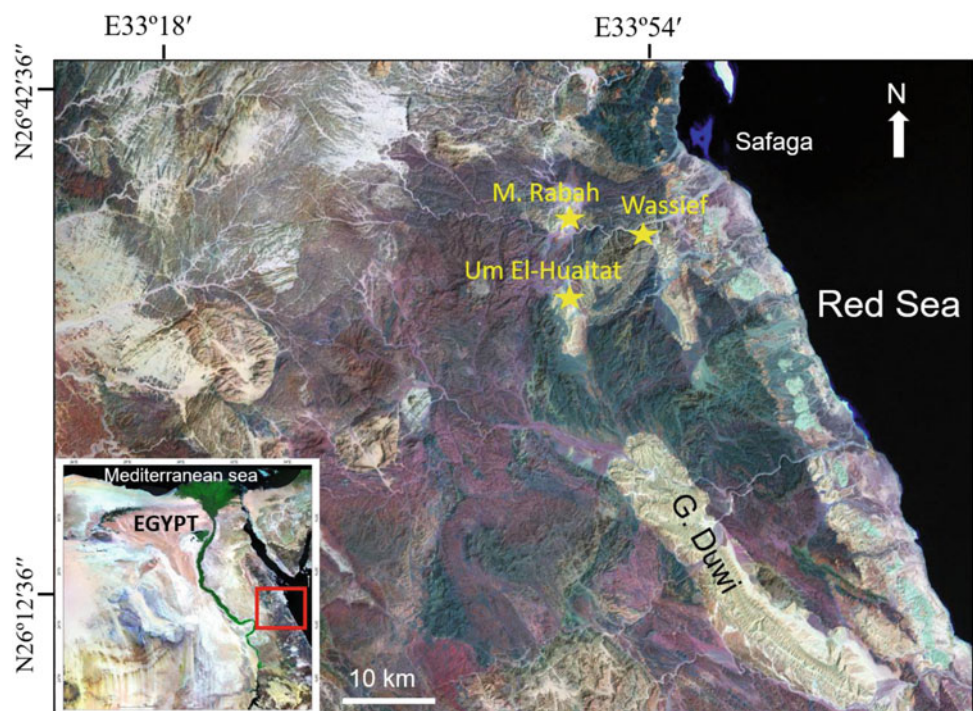
Within the Upper Cretaceous-Paleogene succession of Egypt, local anoxic conditions prevailed and contributed to organic-rich sedimentary rocks “black shales”. Similar black shales are known from various Tethyan localities (e.g., Jordan, Israel, and Syria). In Egypt, they are widely distributed from the Eastern Desert through the Nile Valley to the Western Desert. The study area is located in the Eastern Desert, southwest of Port Safaga, Red Sea range, between latitudes  $26^{\circ} 30'$  and  $26^{\circ} 36' \text{ N}$  and longitudes  $33^{\circ} 46'$  and  $33^{\circ} 56' \text{ E}$ , which is represented by three shallow boreholes (Fig. 1). This area belongs to the Southern Levant upwelling

system (Makled 2014). The total depths of the studied wells are 197 m, 91.5 m, and 227 m for Um El-Huaitat (U), Mohamed Rabah (M,) and Wassief (W) boreholes, respectively. The W and U boreholes penetrated the following formations from top to base: the Thebes, Esna, Dakhla, Duwi, and Quseir formations; the M borehole did not reach the Quseir Formation. The subsequent is a brief discussion on the aforementioned rock units, from older to younger (Fig. 2).

The **Quseir Formation** (Ghorab, 1956) is generally composed of varicolored non-fossiliferous silty shale and mudrock, except for the presence of limited terrestrial plant remains. In its lower part, it comprises laminated varicolored silty shale with scattered pyrite crystals, limonitic spots, hematite and glauconite pellets, and some coal relics. The upper part consists of multicolored mudrocks (e.g., brown, green, and black) with a few phosphate grains. All facies reflect terrestrial environments—the Late Cretaceous-Paleogene transgressive event started after the deposition of the Quseir Formation. Moreover, it was dated as Campanian (Hassanein et al., 1993; Malak et al., 1977).

The **Duwi Formation** (Ghorab, 1956) unconformably overlies mudrocks of the Quseir Formation. Two phosphate beds mark the lower and upper boundaries of the Duwi Formation, which is predominantly comprised black fossiliferous phosphatic limestone, enriched in organic matter and with dispersed pyrite crystals. It was deposited in shallow to open marine environments (middle to outer neritic settings). An unconformable boundary to the Dakhla Formation above

**Fig. 1** Satellite images showing the location of the study areas



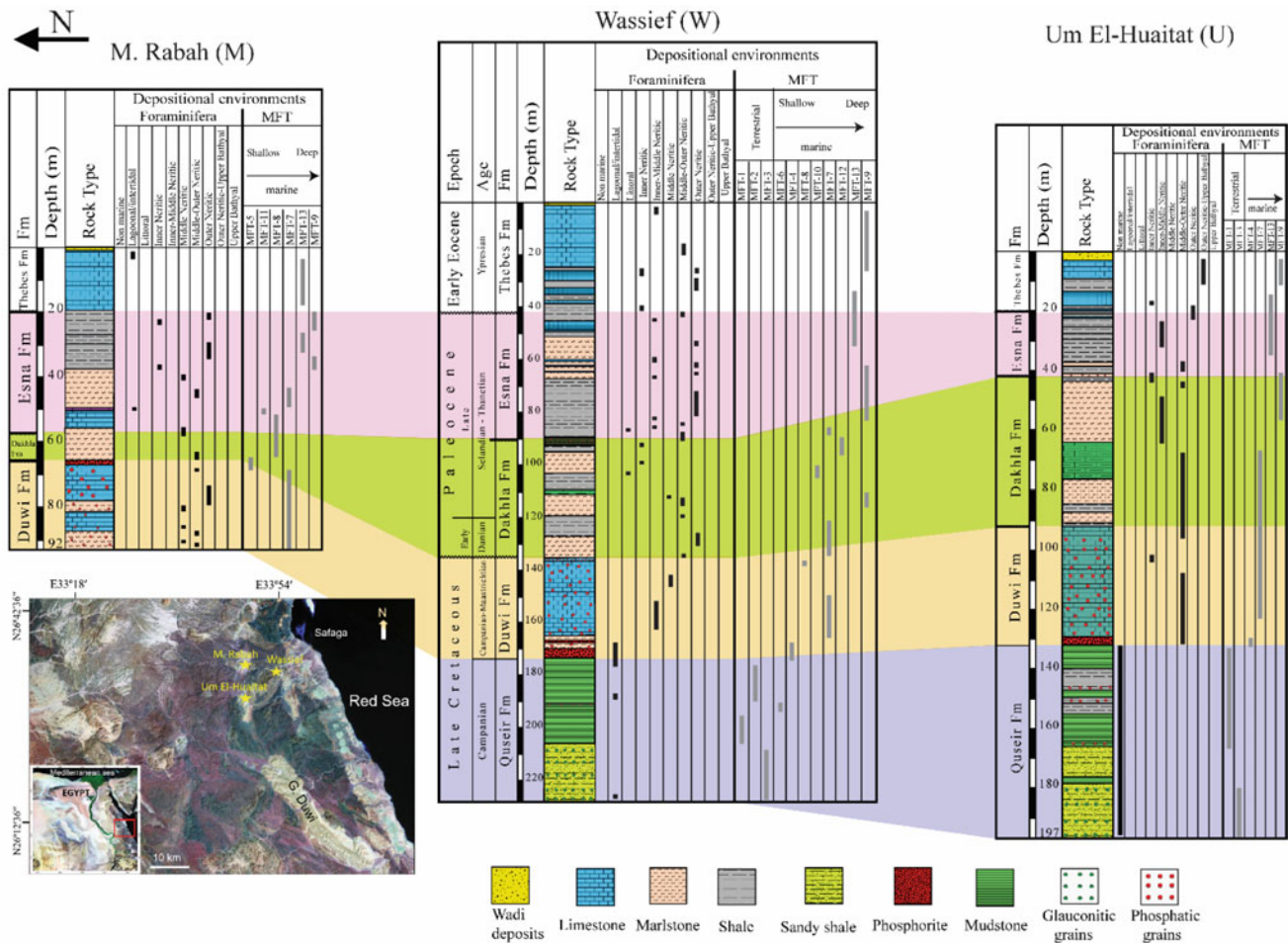


**Fig. 2** Summary of the lithologies and the depositional environments of the sedimentary succession of the Upper Cretaceous-Paleogene strata of the study three wells

is marked by an abrupt lithological change in all three boreholes: phosphatic limestones of the Duwi Formation are overlain by marlstones, calcareous shales, and phosphorites to marlstones of the Dakhla Formation above. The Duwi Formation spans a late Campanian–Maastrichtian age (Abu-Ali et al., 2019; Hewaidy, 1979).

The **Dakhla Formation** (Said, 1961) consists of dark gray to black fossiliferous argillaceous limestone, marlstone, and calcareous shale with scattered pyrite crystals and was deposited in a wide range of depositional environments from inner neritic to open marine middle to outer neritic environments. The black shales of the Dakhla Formation are highly enriched in organic matter (El-Kammar, 1987). The age of the Dakhla Formation was assigned to a Maastrichtian-late Paleocene (Obaidalla, 2000).

The boundary between the Dakhla- and the overlying Esna Formation reflects a hiatus, as evidenced by the absence of the Tarawan Formation (late Paleocene). In the M borehole, this surface separates marlstones of the Dakhla

Formation from limestones of the Esna Formation, whereas black, poorly fossiliferous, phosphatic, and/or glauconitic mudstones with some pyrite crystals occur in W and U boreholes at this boundary.

The **Esna Formation** (Beadnell 1905) consists of dark greenish-gray fossiliferous calcareous shales to marlstones with sporadic pyrite crystals, deposited in the middle to outer neritic environments and occasionally in restricted inner neritic environments. At the base of the Esna Formation, some phosphatic and glauconitic grains occur in both W and U boreholes, whereas dolomitic limestones characterize the lowermost part of the Esna Formation in the M borehole. The late Paleocene age was assumed for the Esna Formation (Abu-Ali et al., 2019).

The **Thebes Formation** (Said, 1990) comprised white to yellowish-white fossiliferous limestones with brown cherts. The lower part of the Thebes Formation in the W and M boreholes consists of intercalations of light greenish-gray fossiliferous weathered calcareous shale, as well as

**Table 1** Summary of different MFTs with their characteristic features (modified after Abu-Ali et al., 2019)

Siliciclastic lithofacies	Phosphoritic lithofacies	Carbonate lithofacies
<b>(MFT-1) Silty to sandy mudrock</b>	<b>(MFT-4) Phosclast packstone to phosclast grainstone</b>	<b>(MFT-6) Non-fossiliferous mudstone</b>
Dull brownish non-fossiliferous, non-laminated clayey material, with angular to sub-angular, mainly of silty size quartz grains as well as some fragmented glauconitic and phosphatic grains	Fossiliferous, chiefly silicified fish bones, and shark teeth, skeletal phosphatic grains as well as disseminated pyrite crystals and detrital quartz grains	Massive non-fossiliferous mud matrix and partly micro-sparite
		<b>(MFT-7) Phosphatic foraminiferal pack/grainstone</b>
		Fossiliferous, well-preserved planktonic and benthonic foraminifera with enrichment of phosphatic grains and organic matter
		<b>(MFT-8) Bioclastic foraminiferal packstone</b>
		Fossiliferous, rich in bioclasts
<b>(MFT-2) Organic-rich silty mudrock</b>	<b>(MFT-5) Phosoid packstone to phosoid grainstone</b>	<b>(MFT-9) Bioclastic foraminiferal wackestone</b>
Non-fossiliferous mudrock including laminated terrestrial organic matter flakes as well as angular to sub-angular quartz grains	Fossiliferous phosphatic lithoclasts as well as phosoids in a carbonate matrix	Consists of fossiliferous, with various bioclasts
		<b>(MFT-10) Glauconitic phosphatic foraminiferal Wacke-Packstone</b>
		Poorly fossiliferous, with some glauconitic and phosphatic grains
<b>(MFT-3) Fine-grained sandstone/glauconite intercalations</b>		<b>(MFT-11) Non-fossiliferous dolomitic mudstone</b>
Non-fossiliferous, laminated angular to sub-angular, well-sorted quartz grains as well as coarse sub-rounded to well-rounded glauconitic pellets. In addition, detrital phosphatic grains can be detected		Non-fossiliferous, massive, dolomitized mudstone, with few phosphatic grains
		<b>(MFT-12) Dolomitic glauconitic mudstone</b>
		Poorly fossiliferous, dolomitized mudstone with few framboidal pyrite as well as phosphatic and glauconite grains
		<b>(MFT-13) Dolomitic bioclastic wackestone</b>
		Poorly fossiliferous, massive with some fossil remains, dolomitized mudstone

yellowish and greenish-white fossiliferous weathered silty to argillaceous limestones, deposited in open marine environments with intermittent restricted intervals. Said (1990) documented an Early Eocene age of the Thebes Formation.

The stratigraphy (both litho- and biostratigraphy) and microfacies characteristics of the described five formations of all three boreholes were documented in Abu-Ali et al., (2019, 2020), including paleoenvironmental reconstructions, based on the distribution of 13 microfacies types MFT (see Table 1; Fig. 2).

### 3 Materials and Methodology

Three hundred sixty-eight cores were retrieved from three shallow boreholes in the Safaga area, namely: Wassief (W), Um El-Huaitat (U), and Mohamed Rabah (M). The boreholes were drilled by the Egyptian Mineral Resources Authority (EMRA) and DanaGas© Egypt in 2009.

In 2009, the Total Organic Carbon (TOC) content (wt%) of 368 samples and the basic/bulk Rock-Eval pyrolysis of

193 samples were measured in the laboratories of Stratochem Service<sup>©</sup> (Egypt). The samples were primarily dissolved in HCl, and then TOC content was measured by combustion in a LECO C230 combustion furnace—the resulting carbon dioxide was quantitatively logged by infrared absorption. The basic/bulk Rock-Eval pyrolysis was used to determine  $S_1$ ,  $S_2$ ,  $S_3$ , and  $T_{max}$ , and to calculate hydrogen index (HI), oxygen index (OI), and production index (PI). In 2017, 115 samples with  $\geq 3\%$  TOC were selected for stable carbon isotopes measurements on bulk organic matter ( $\delta^{13}C_{org}$ ). The weight of material treated to obtain 30  $\mu\text{g}$  of organic carbon differs depending on the lithology and the TOC content of the sample. The selected samples were processed with 1% HCl to remove the inorganic carbon. Then, the samples were dried on a hot plate. The records of bulk organic carbon isotope were measured by Thermo Delta Plus Gas Isotope Ratio Mass Spectrometer with Thermo Flash 1112 Elemental Analyzer at the ZMT, Bremen, Germany. The standard deviation of house standard (Peptone) over the measurement period was 0.10‰ for  $\delta^{13}C_{org}$ .

## 4 Results and Discussion

### 4.1 Organic Matter Richness

The organic matter content is designated by TOC% values that range from 0.03 to 9.44% in the W core, 0.1–12.97% in the U core, and 0.8–8.71% in the M core. Considering the whole sequence, the TOC content of both, the Duwi and the Dakhla formations, can be categorized as excellent to good source rocks, respectively (Table 2). The vertical TOC variations along the studied sequence show a maximum in TOC content (up to 13%) at the boundary between the Dakhla and the Esna formations, especially in the W and U cores (Fig. 3). The high concentration of organic matter, at

the beginning of the deposition of the Duwi Formation, indicates a relatively high productive water with rapid sedimentation under anoxic conditions.

### 4.2 Hydrocarbon Potentiality

Organic matter (kerogen) type and its hydrocarbon products as well as estimation of thermal maturity are vital factors in evaluating the potentiality of source rocks. These parameters were estimated from data of the Rock-Eval pyrolysis on samples containing  $\geq 2\%$  TOC ( $n = 193$ ).

#### 4.2.1 Organic Matter Quality (Kerogen Type)

The quality of organic matter and its origin allows for calculating the paleoenvironmental depositional conditions: Hydrogen index ( $HI = [S_2/TOC]*100$ ) and oxygen index ( $OI = [S_3/TOC]*100$ ) values were calculated from data of the Rock-Eval pyrolysis to determine the kerogen types. The HI-values range from 110 to 123 (W), 17 to 813 (U), 1175 and 728 (M), while the OI-values range from 8 to 38 (W), 8 to 37 (U), and 12 to 49 (M)—see Table 3. Plots of HI-values versus OI-values were used to determine the kerogen types on a modified van Krevelen plot (Fig. 4). A detailed zonation of hydrocarbon potentiality is delineated based on the HI-values versus TOC-values (Fig. 5). Generally, the plots show that kerogen types range from type I to mixed types II and III. The latter type occurs in the Esna Formation and indicates mixed marine and terrestrial sources that can produce fair oil hydrocarbons. The kerogen types of the Dakhla Formation show a wider range of mixed type I and II, with the dominance of type II, thus indicating greater amounts of marine organic matter that produces mainly fair oil hydrocarbons but scarcely gas and oil (W) or gas (M) hydrocarbons. The Duwi Formation contains the best quality kerogen types: type I in U and mainly type I with few exceptions of mixed types I + II in W and M cores. In M core, few

**Table 2** Summary of statistical data of the TOC (wt%) for the study geological formations of the three study cores, at a confidence level of 95%

Core	Formation	Mean (Min.–Max.)	Standard deviation
Wassief (W)	Esna ( $n = 41$ )	1.5 (1.1–2.1)	0.3
	Dakhla ( $n = 44$ )	2.8 (0.6–9.4)	1.4
	Duwi ( $n = 37$ )	4.7 (1.4–7.6)	1.6
	Quseir ( $n = 43$ )	1.2 (0.03–5.7)	1.2
Um El-Huaitat (U)	Esna ( $n = 21$ )	1.6 (1.2–2.7)	0.3
	Dakhla ( $n = 51$ )	2.8 (0.8–13)	1.7
	Duwi ( $n = 24$ )	4.5 (1.3–8)	1.4
	Quseir ( $n = 45$ )	1.4 (0.1–6.1)	1.3
M. Rabah (M)	Esna ( $n = 27$ )	1.9 (1–4.1)	0.8
	Dakhla ( $n = 9$ )	2.2 (0.8–3.9)	1
	Duwi ( $n = 26$ )	5.3 (2.1–8.7)	1.8

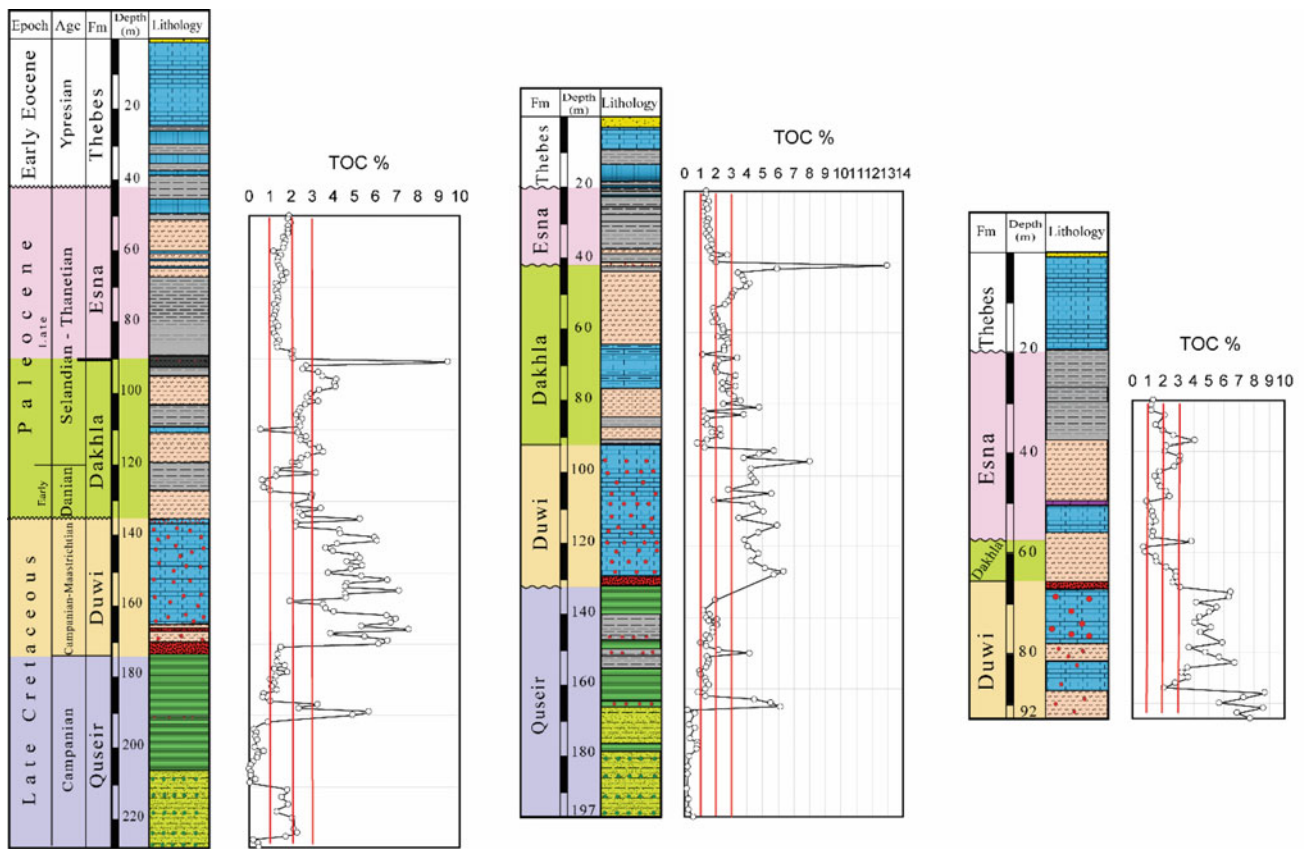


**Fig. 3** Vertical distribution of TOC% along the Upper Cretaceous-Paleogene succession of, from left to right, Wassief, Um El-Huaitat, and Mohamed Rabah areas, respectively

**Table 3** Summary of statistical data of the calculated HI & OI of the studied rock units within the three cores, at a confidence level of 95%

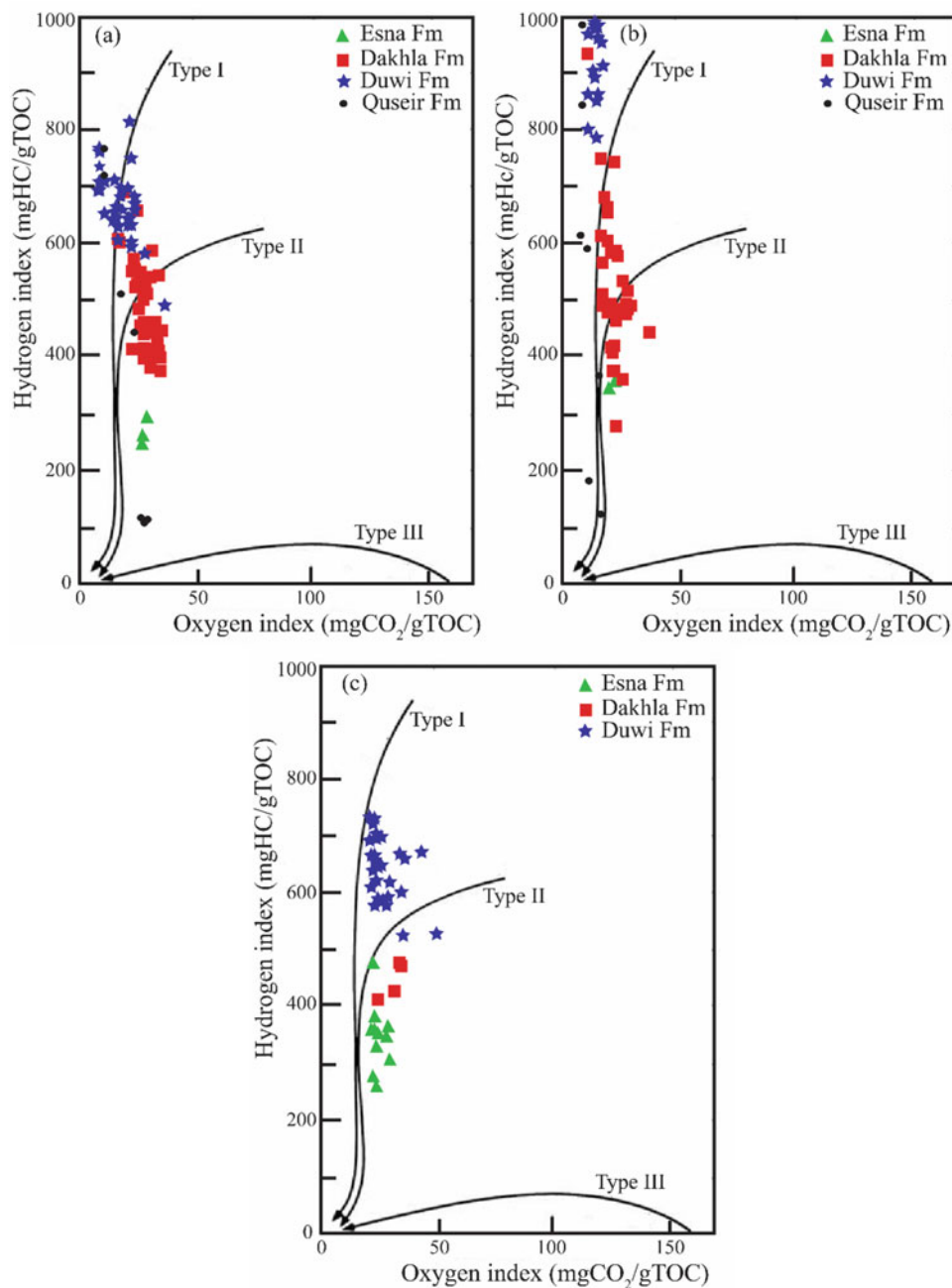
Formation	Area	Hydrogen index (HI)		Oxygen index (OI)	
		Mean (Min.–Max.)	Standard deviation	Mean (Min.–Max.)	Standard deviation
Esna	Wassief ( <i>n</i> = 3)	273.3 (258.1–296.9)	20.7	27.1 (26–28.1)	1.1
	Um El-Huaitat ( <i>n</i> = 2)	346.5 (338.2–354.7)	11.7	21.1 (19.4–22.7)	2.3
	M. Rabah ( <i>n</i> = 11)	345.9 (256.4–483.3)	58.7	23.5 (19.5–28.5)	2.9
Dakhla	Wassief ( <i>n</i> = 37)	489.8 (367.8–688.5)	80	27 (16.8–33.8)	4.2
	Um El-Huaitat ( <i>n</i> = 38)	518.6 (287.1–934.7)	124.9	21.6 (11.5–36.5)	4.5
	M. Rabah ( <i>n</i> = 5)	355.1 (17.3–468.4)	191	26.4 (12–32.9)	8.7
Duwi	Wassief ( <i>n</i> = 34)	670.2 (492.2–813.4)	59.9	17.7 (7.6–37.5)	6.5
	Um El-Huaitat ( <i>n</i> = 22)	957.7 (791.5–1175.1)	91.1	13.6 (10.5–17.4)	1.9
	M. Rabah ( <i>n</i> = 27)	638.7 (523.2–727.8)	57.4	26.4 (19.3–49)	7.1
Quseir	Wassief ( <i>n</i> = 7)	398.9 (109.9–763.9)	285.6	21 (10.7–28.5)	7.4
	Um El-Huaitat ( <i>n</i> = 7)	557.6 (123.1–984.7)	334.3	11 (7.6–16.3)	3.3

samples reach the margin of gas and oil source, thus indicating a mainly marine origin of organic matter, with oil hydrocarbon potentiality. The few analyzed samples of the Quseir Formation, in both W and U cores, show highly

variable kerogen types (from type I to type III), indicating high terrestrial influences.

Dean et al. (1986) proposed that the HI is linked not only to the source of the kerogen but also to the preservation

**Fig. 4** Modified van Krevelen diagram showing kerogen types of the study formations of **a** Wassief, **b** Um El-Huaitat, and **c** M. Rabah cores (Quseir Formation was not punched) (after Waples, 1985)



level. Based on this assumption, the studied HI-values indicate a very good to excellent organic matter preservation.

#### 4.2.2 Thermal Maturity of Organic Matter

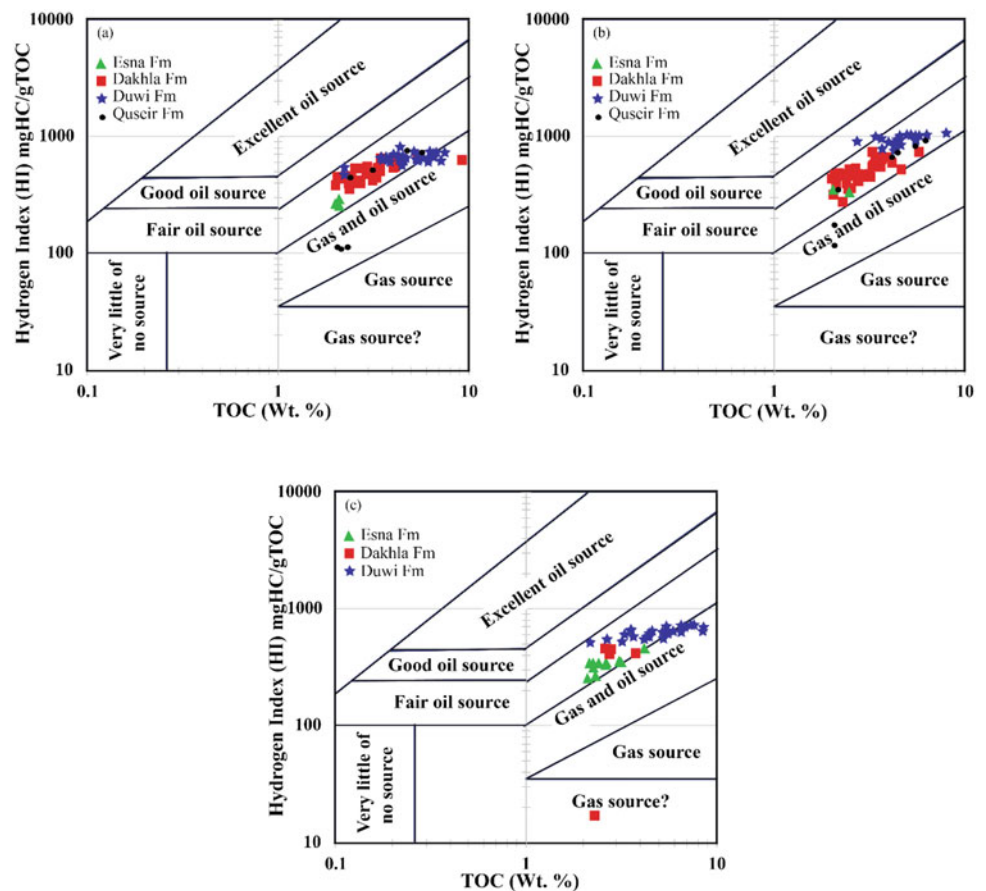
$T_{\max}$  is the temperature of the maximum development degree of non-volatile hydrocarbons ( $S_2$ ). Here we used it as a parameter to estimate the thermal maturity of organic matter that is immature when  $T_{\max}$  values are less than 435 (Fig. 6). Only a few samples reach the marginal oil window or marginal mature stage ( $\geq 435$ ).

#### 4.3 Bulk Organic Carbon Isotopes

Tyson (1995) documented that the  $\delta^{13}\text{C}_{\text{org}}$ -signature can be used in a wide range of applications in oil source rock correlation, chemostratigraphy, paleoceanography, and paleoenvironmental analysis. The  $\delta^{13}\text{C}_{\text{org}}$ -signature of bulk organic matter as a reliable tool in chemostratigraphy studies is still a matter of great controversy. Galimov (2006) assumed that isotope chemistry is infrequently employed for organic geochemistry data interpretation, but the majority of



**Fig. 5** Relationship between TOC (wt%) and HI of the study formations of **a** Wassief, **b** Um El-Huaitat, and **c** M. Rabah cores (Quseir Formation was not punched) (after Jackson et al., 1985)



studies are empirical, and some theoretical misinterpretation may occur. However, the  $\delta^{13}\text{C}_{\text{org}}$ -signature may be used as a sea-level indicator as positive  $\delta^{13}\text{C}$  excursion is related to sea-level rise (Immenhauser et al., 2008; Jarvis et al., 2002). Moreover, Galimov, (op. cit.) indicated that the biological sign is transformed throughout diagenesis according to the organic matter source and the environmental settings. Tyson (1995) documented that organic materials express significant variation in their isotope ratios dependent on their composition, the carbon source, and the metabolic trails that participated in their formation. We tried to deduce the organic matter origin from stable organic carbon isotopic records.

#### 4.3.1 Critical Arguments for Interpreting Fossil $\delta^{13}\text{C}_{\text{org}}$ values

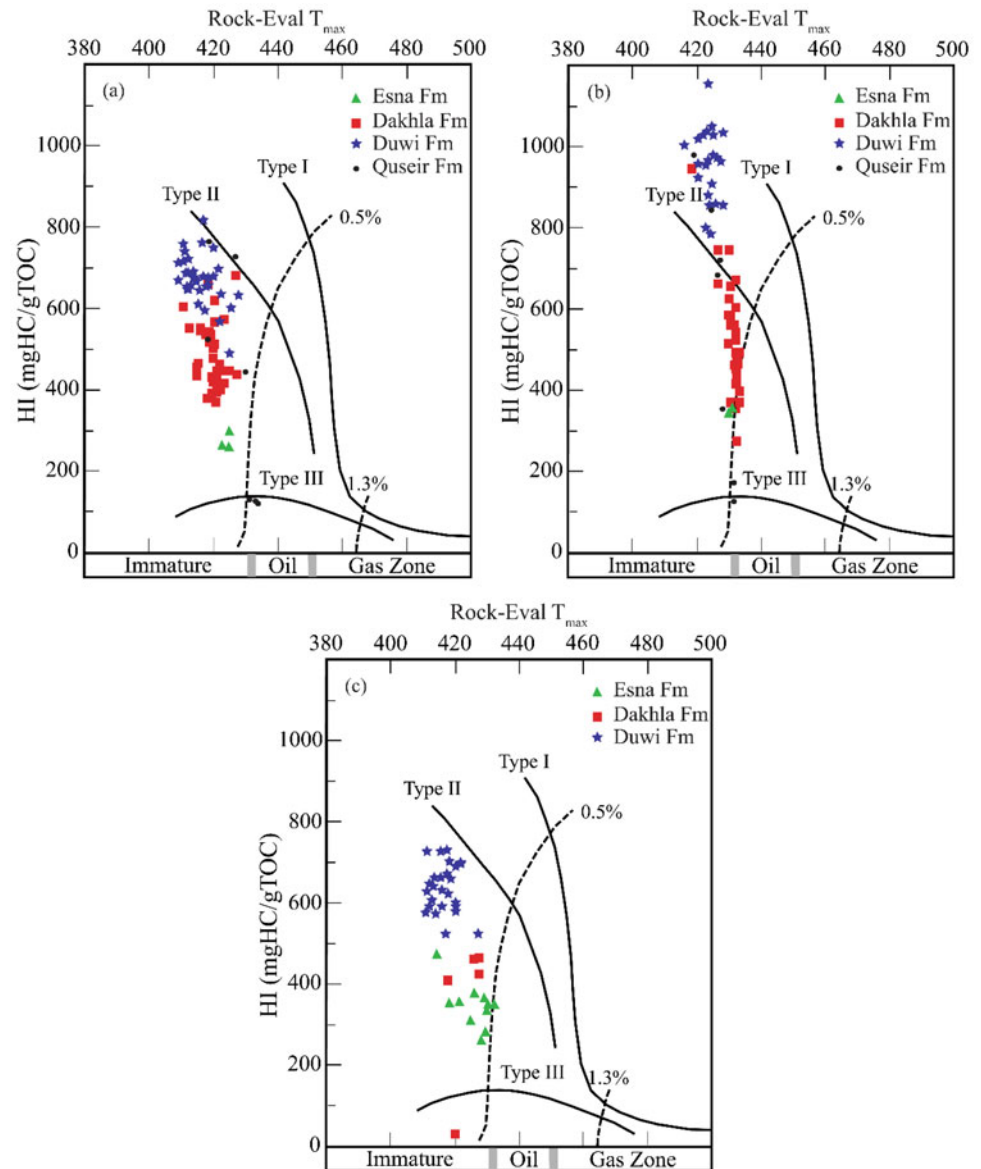
The recent terrestrial C3 plants synthesize organic matter which is depleted in  $\delta^{13}\text{C}$  (between  $-23$  and  $-33\%$ ), while the marine organic matter has higher  $\delta^{13}\text{C}$  values (between  $-17$  and  $-23\%$ ); the highest  $\delta^{13}\text{C}$  values (between  $-9$  and  $-17\%$ ), however, lead back to C4 plants that colonize arid environments (Dean et al., 1986; Farquhar et al., 1989; Holail et al., 1995; and Saltzman & Thomas, 2012).

Similarly, Tyson (1995) documented  $\Delta\delta^{13}\text{C}$  values for C3 land plants of about  $-20\%$ , while marine phytoplankton ranges between  $-22$  and  $-36\%$ .

Thus, the variations in the composition of the organic carbon isotope ( $\delta^{13}\text{C}_{\text{org}}$ ) are managed by fractionation throughout photosynthesis in both marine and terrestrial environments (e.g., Wagner & Herrle, 2014). Photosynthesis favors uptake of  $^{12}\text{C}$  due to the dynamic fractionation in the organic matter (Tiwari et al., 2015).

In addition, Saltzman and Thomas (2012) documented that  $\delta^{13}\text{C}$  values in marine phytoplankton depend on temperature: in the tropics,  $\delta^{13}\text{C}$  values reach up to  $-13\%$ , while at high latitudes  $\delta^{13}\text{C}$  values are as low as  $-32\%$ . Wang et al. (2014) suggested that the  $\delta^{13}\text{C}_{\text{org}}$  values of shallow marine carbonates are weightier than  $-30\%$  which may be controlled by photosynthesis. Whereas those from deep water dark siliceous and black shale sedimentary strata are lighter than  $-32\%$ , possibly resulting from chemoautotrophic taxa and methanotrophs under an anoxic environment. The highest negative (light) values of carbon isotope are linked to microbiologically-produced methane (Wagner & Herrle, 2014).

**Fig. 6** Relationship between HI and  $T_{max}$  of the study formations of **a** Wassief, **b** Um El-Huaitat, and **c** M. Rabah cores (Quseir Formation was not punched) (after Jackson et al., 1985)



On the other hand, Galimov (2006) emphasized that the suggested ranges of  $\delta^{13}C_{org}$ -values, valid for present-day conditions, are not transferable similar to marine  $\delta^{13}C_{org}$ -values older than the Oligocene. Similarly, Tyson (1995) reported that  $\delta^{13}C$ -values of pre-Neogene marine organic matter are consistently lighter (5–7‰) than younger marine materials, nearly indistinguishable from that of recent terrestrial C3 plants.

Other important factors that may have triggered fossil  $\delta^{13}C$ -measurements are diagenetic processes, bacterial activity, mixing of sources, i.e., marine as well as terrestrial organic matter, and/or changes in the availability of carbon to photosynthetic organisms (Carvajal-Ortiz et al., 2009; Dean et al., 1986; Macko et al., 1994; Meyers, 1994; Maslin

& Swann, 2005). Differential elimination of  $^{13}C$ -enriched fractions during diagenetic processes can lead to depletion in the  $\delta^{13}C_{org}$  (Lehmann et al., 2002; Meyers, 1994). Dean et al. (1986) suggested that the high availability of  $CO_2$  may cause larger carbon isotope fractionation due to the higher discrimination of the phytoplankton to  $^{12}C$ . Macko et al. (1994) suggested that the preferential loss of isotopically enriched (e.g., amino acids) or depleted (e.g., lipids) elements during diagenetic processes can lead to variation in the organic carbon stable-isotope values. Under anoxic environments, organic matter may be additionally depleted cat  $^{13}C$  due to the influence of bacterial biomass, and the  $^{13}C$  depletion increases by organisms involved in the anaerobic cycling of methane carbon (Galimov, 2006;

Macko et al., 1994). The latter recorded that some micro-organisms like methane-oxidizing archaea yield enormously isotopically-light mixtures such as isoprenoid ethers and crocetane with very low  $\delta^{13}\text{C}$  readings ( $-50$  to  $-70\text{‰}$  and down to  $-100\text{‰}$ ). Galimov (1999) documented that volcanic activities lead to the induction of an anoxic regime which increases the inflow of nutrients to the ocean and the bioproductivity in turn. In addition, oxygen-deficient conditions are good for organic matter preservation that lead to the anomalous enrichment of carbonates in the  $^{13}\text{C}$  isotope, while the organic carbon is fairly depleted in  $^{13}\text{C}$ . The same author added that oxygen circulation, during global cooling, results in the recycling of most of the deposited organic matter leads to an increase of bioproductivity as well as the depletion of carbonates at  $^{13}\text{C}$ , while the organic carbon is relatively enriched in  $^{13}\text{C}$ .

Werne and Hollander (2004) informed that the processes affecting the  $\delta^{13}\text{C}_{\text{org}}$  are complex and much less understood and its interpretation is more complicated. Consequently, the modest method of differentiation between marine and terrestrial organic matter, especially for pre-Oligocene organic matter, is not generally viable and should be investigated with caution.

### 4.3.2 Discussion

The following discussion will focus on the correlation of  $\delta^{13}\text{C}_{\text{org}}$ -signatures with TOC%- and HI-values as well as with the vertical variations of the  $\delta^{13}\text{C}_{\text{org}}$  values comparing the three studied successions (Fig. 9). We selected a total of 115 samples of the Duwi to Dakhla formations, with  $> 3\%$  TOC-values for measuring the  $\delta^{13}\text{C}_{\text{org}}$  signature. The correlation between  $\delta^{13}\text{C}_{\text{org}}$  and organic matter is not significant. However, there is a weak positive coherence between TOC and  $\delta^{13}\text{C}_{\text{org}}$  (Fig. 7). Tyson (1995) reported similar weak correlations between  $\delta^{13}\text{C}$  and TOC that may be due to variations in the initial ratio of terrestrial to marine organic matter, or to the unequal content of carbon for the various organic fractions, or the initial metabolizing content, as well as the rate and extent of its pre- and post-burial utilization, humification degrees, and microbial production and changes in redox conditions.

A weak correlation between HI and  $\delta^{13}\text{C}_{\text{org}}$  for the study of geological formations is illustrated in Fig. 8, with a slight difference between the Duwi and the Dakhla formations, due to their different sources of organic matter (see HI-values in Fig. 4). Although the HI data do not properly correlate with  $\delta^{13}\text{C}_{\text{org}}$ -values, the range of  $\delta^{13}\text{C}_{\text{org}}$ -values is nearly the same. Accordingly, in the present case, the  $\delta^{13}\text{C}_{\text{org}}$  is not a trustable tool to precisely define the organic matter origin.

The vertical variation of the  $\delta^{13}\text{C}_{\text{org}}$ -values along the studied Upper Cretaceous-Paleogene succession is illustrated in Fig. 9.  $\delta^{13}\text{C}_{\text{org}}$  ranges are about  $-38$  to  $-25\text{‰}$ ,  $-37$  to  $-26\text{‰}$  and  $-36$  to  $-27\text{‰}$ , for M, W, and U cores,

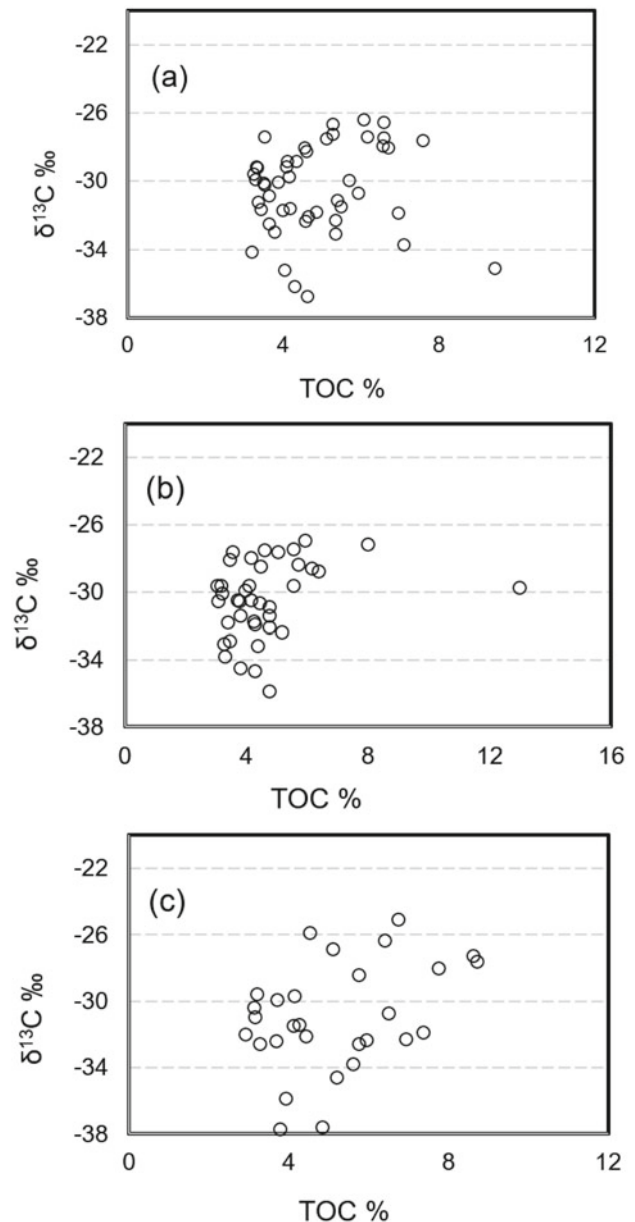


**Fig. 7** Relationship between TOC and  $\delta^{13}\text{C}_{\text{org}}$  of **a** Wassief, **b** Um El-Huaitat, and **c** M. Rabah cores

respectively. At first glance, it appears these values may be misinterpreted as the terrestrial origin of organic matter. This deceptive suggestion is incompatible with the conclusion of kerogen characterization and typology (Sect. 4.2.1). Furthermore, the recognized values (as low as  $-38\text{‰}$ ) are much lighter than those of terrestrial plants. This inconsistency is also observed in several previous studies, e.g., Cretaceous DSDP sites (Dean et al., 1986), sub-recent kerogens of the northern Red Sea (Botz et al., 2007), Mississippian black shales of the Barnett Formation (Hoelke 2011), Late Cretaceous phosphates and oil shales in the Negev (Schneider-Mor et al., 2012).

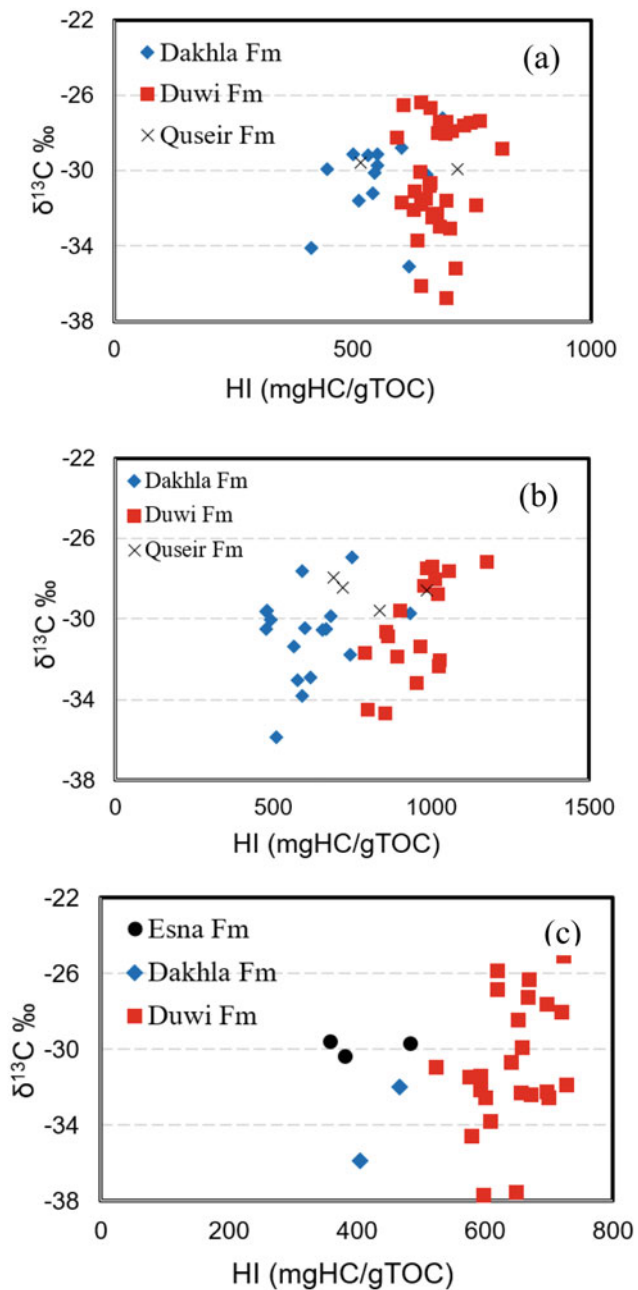


**Fig. 8** Relationship between HI and  $\delta^{13}\text{C}_{\text{org}}$  of **a** Wassief, **b** Um El-Huaitat, and **c** M. Rabah cores

Instead, the bulk organic carbon isotope values of the studied Duwi Formation are characterized by high variability and fluctuations which match well with the diversity of Total Foraminifera Number (TFN) data (Abu-Ali et al., 2019). Additionally, there is one (at 82 m in M. Rabah core) or two (at 153 and 161 m in W and at 109.5 and 125.5 m in U cores) distinctive abrupt negative shifts. At the uppermost part of the Duwi Formation, there is a distinguishing

negative shift with a magnitude of about  $-6$ ,  $-7$ , and  $-7\%$  in all three cores (W, U, and M). Also, a negative  $\delta^{13}\text{C}_{\text{org}}$ -excursion at the boundary between the Dakhla and the Esna rock units especially in the W and U cores. The extreme depletion of  $\delta^{13}\text{C}$  values may indicate a severe anoxic environment. This suggestion can be confirmed by the anomalous enrichment of the redox-sensitive elements and/or ratios (e.g., U, Mo, Ni/Co) (Abu-Ali et al., 2020).

The anomalous deficient (light)  $\delta^{13}\text{C}$  values throughout the study successions may suggest that the Cretaceous-Paleogene organic matter has an isotopically lighter  $\delta^{13}\text{C}$  signature than modern plankton organic matter. A possible explanation for this severe  $\delta^{13}\text{C}$  depletion is the effect of anaerobic methanogenic bacterial action under reducing conditions.

In summary, it can be concluded that the signature of  $\delta^{13}\text{C}_{\text{org}}$  is not a simple reliable tool to differentiate between terrestrial and marine organic matter in the Cretaceous-Paleogene rocks. However, it seems that the signature of  $\delta^{13}\text{C}_{\text{org}}$  confirms the well-established stratigraphic boundaries of the Upper Cretaceous-Paleogene of the study area.

## 5 Summary and Conclusions

The Upper Cretaceous-Lower Paleogene sedimentary successions of three cores drilled near Port Safaga (Red Sea coastal area of Egypt: W, U, and M) were studied with respect to sedimentological and organic geochemical data. The studied organic matter is immature, but sporadically few samples reach a marginal mature stage. The relationship between  $\delta^{13}\text{C}_{\text{org}}$  and organic matter is not straightforward but there is a weak positive consistency between TOC and  $\delta^{13}\text{C}_{\text{org}}$ . The HI results do not accurately match with the  $\delta^{13}\text{C}_{\text{org}}$  data. Consequently, in the existing case, the  $\delta^{13}\text{C}_{\text{org}}$  is not a reliable tool to precisely define the origin of organic matter. The extreme depletion of the  $\delta^{13}\text{C}_{\text{org}}$ -values throughout the study successions may indicate an effective anaerobic methanogenic bacterial action under a severe anoxic environment.

The limited analyzed samples of the siltstone-mudstone facies of the Quseir Formation, in both cores W and U, show a wide range of kerogen types (from type I to type III). We conclude that the Quseir Formation was deposited pre-transgressive, under oxic to dysoxic conditions within terrestrial environments, except for the phosphatic beds which show clear signatures of anoxic conditions. The major transgression started after the deposition of the Campanian Quseir Formation with organic-/phosphatic-rich sediments of the Duwi Formation that shows the highest average values of TOC wt%. Additionally, the Duwi Formation is well

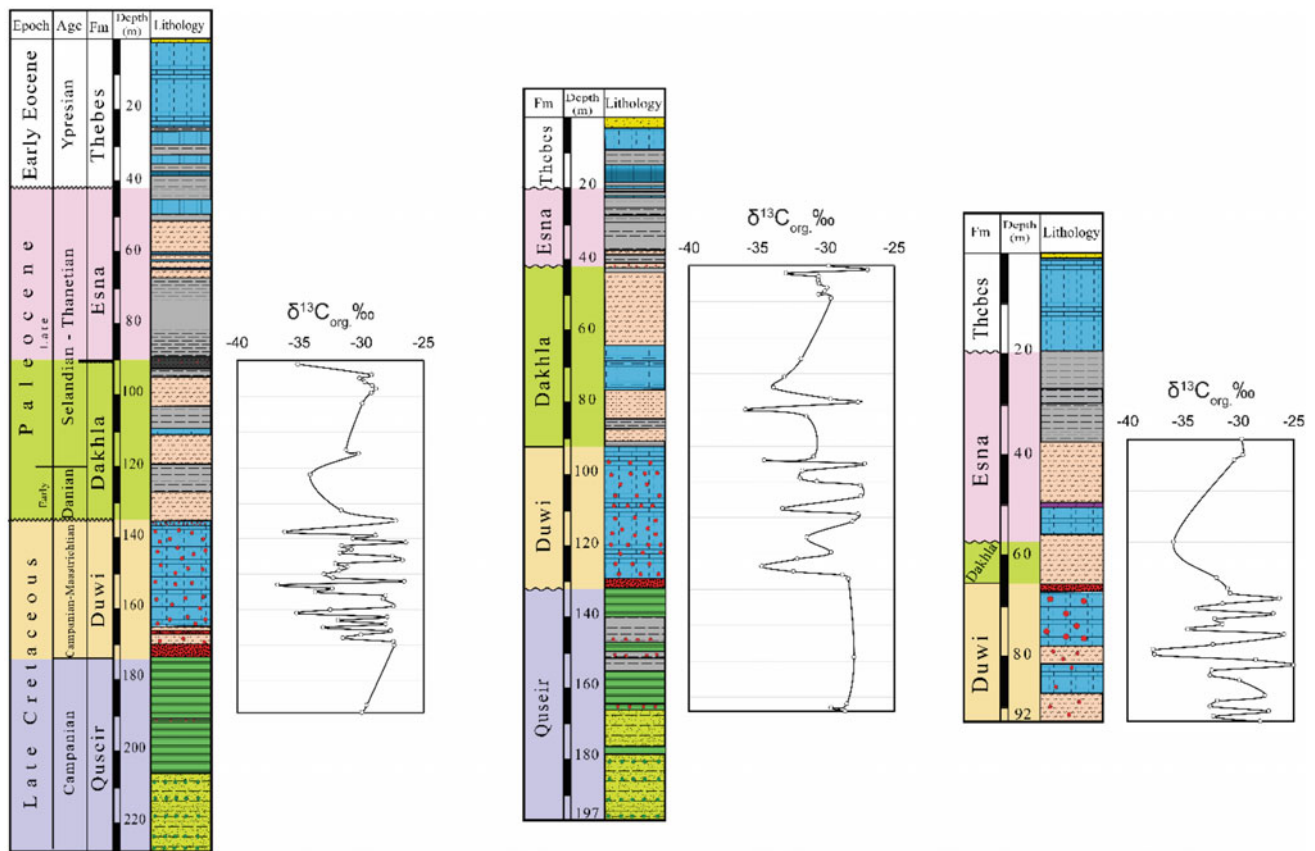


**Fig. 9** Vertical distribution of the  $\delta^{13}\text{C}_{\text{org}}$  along the Upper Cretaceous-Paleogene succession of, from left to right, Wassief, Um El-Huaitat, and Mohamed Rabah areas, respectively

thought-out an excellent source rock with the highest quality of kerogen (mainly type I) derived from organic matter of marine source with oil hydrocarbon potentiality. The Duwi Formation is distinguished by a diagnostic instability in bulk organic carbon isotope values. Furthermore, there is one (in M core) or two (in W and U cores) characteristic abrupt negative shifts. At the uppermost part of the Duwi Formation, there is a distinctive negative shift.

The above-mentioned parameters depicted the commencement of shifting the depositional settings toward more marine-proper settings throughout the Late Cretaceous transgression. The Duwi Formation was deposited mainly in shoals and a restricted nearshore shallow lagoon to anoxic open marine conditions, demonstrating a deposition under middle to outer neritic conditions. The Dakhla Formation is categorized as a good source rock with mixed kerogens types I + II with relative dominance of type II mainly of marine organic matter. The studied rocks of the Dakhla Formation imply a wide array of depositional settings formed during vacillating sea-level with erratic shallow water intervals. The boundary between the Dakhla and the Esna formations is characterized by abrupt environmental

changes as designated by an anomalous enrichment in the TOC content as well as a characteristic negative  $\delta^{13}\text{C}_{\text{org}}$  excursion, especially in both Wassief and Um El-Huaitat samples. These aforesaid characters specify a falling sea-level, probably associated with strong anoxic or even euxinic evaporative environments. The Esna Formation comprises mixed kerogen of type II + III of mixed marine and terrestrial sources which can produce oil and gas hydrocarbons. The obtained data concludes that black shale in the Safaga region is promising for hydrocarbons potentiality. It is suitable for in situ retorting or application as an energy donor for electric power stations. For an improved assessment of Egyptian unconventional resources, detailed organic geochemical analyses such as oil saturation index (modified OSI), biomarker, and isotope correlations, among others should be carried out.

**Acknowledgements** The authors gratefully acknowledge DanaGas© Egypt for providing the core samples. Additionally, they would like to thank the DAAD for funding the corresponding author during her Ph.D. in Bremen, Germany. We would like also to thank the editors for their great efforts and particular thanks to PD Dr. Haytham El Atfy for the kind invitation and support to present this chapter.

## References

- Abd El-Rahiem, F. H., Hassan, M. S., Selim, K. A., & Abdel-Khalek, N. A. (2014). Characterization and beneficiation of the Egyptian black shale for possible extraction of organic matter. *International Journal of Mining Science and Technology*, *24*, 177–182.
- Abed, A. M., Arouri, K. R., & Boreham, C. J. (2005). Source rock potential of the phosphorite bituminous chalk–marl sequence in Jordan. *Marine and Petroleum Geology*, *22*, 413–425.
- Abou El-Anwar, E. A., Mekky, H. S., & Abdel Wahab, W. (2019). Geochemistry, mineralogy and depositional environment of black shales of the Duwi Formation, Qusseir area, Red Sea coast, Egypt. *Carbonates and Evaporites*, *34*, pp. 883–892.
- Abu-Ali. (2019). *Chemostratigraphy and paleo-environments of the Upper Cretaceous-Lower Tertiary sedimentary sequences in Safaga area, Red Sea, Egypt* (Ph.D. Thesis). Faculty of Science, Cairo University, 150 pp.
- Abu-Ali, R., & El-Kammar, and Kuss, J. (2020). Chemostratigraphy of the Upper Cretaceous-Paleogene organic-rich succession on the southern Tethys margin in Egypt. *Journal of African Earth Sciences*. <https://doi.org/10.1016/j.jafrearsci.2020.103779>
- Abu-Ali, R., El-Kammar, A., Zakaria, A., El-Shafeiy, M., & Kuss, J. (2019). Paleo-environmental reconstructions of the Upper Cretaceous– Paleogene successions, Safaga, Egypt. *Journal of African Earth Sciences*, *149*, 170–193.
- Almogi-Labin, A., Bein, A., & Sass, E. (1990). Agglutinated foraminifera in organic-rich neritic carbonates (Upper Cretaceous, Israel) and their use in identifying oxygen levels in oxygen-poor environments. In C. Hemleben, M. A. Kaminski, W. Kuhnt, & D. B. Scott (Eds.), *Paleoecology* (pp. 565–585). Kluwer Academic Publishers.
- Almogi-Labin, A., Bein, A., & Sass, E. (1993). Late Cretaceous upwelling system along the southern Tethys margin (Israel): Interrelationship between productivity, bottom water environments and organic matter preservation. *Paleoceanography*, *8*, 671–690.
- Ashckenazi-Polivoda, S., Abramovich, S., Almogi-Labin, A., Schneider-Mor, A., Feinstein, S., Püttmann, W., & Berner, Z. (2011). Paleoenvironments of the latest Cretaceous oil shale sequence, Southern Tethys, Israel, as an integral part of the prevailing upwelling system. *Palaeogeography, Palaeoclimatology, Palaeoecology*, *305*, 93–108.
- Ashckenazi-Polivoda, S., Edelman-Furstenberg, Y., Almogi-Labin, A., & Benjamini, C. (2010). Characterization of lowest oxygen environments within ancient upwelling environments: Benthic foraminifera assemblages. *Palaeogeography, Palaeoclimatology, Palaeoecology*, *289*, 134–144.
- Baioumy, H. M., & Lehmann, B. (2017). Anomalous enrichment of redox-sensitive trace elements in the marine black shales from the Duwi Formation, Egypt: Evidence for the late Cretaceous Tethys anoxia. *Journal of African Earth Sciences*, *133*, 7–14.
- Barthel, K. W., & Böttcher. (1978). Abu Ballas formation—A significant lithostratigraphic unit of the former “Nubia Series”. *Mitteilungen der Bayerischen Staatssammlung für Paläontologie und Historische Geologie*, *18*, 155–166.
- Bechtel, A., Jia, J., Strobl, S. A. I., Sachsenhofer, R. F., Liu, Z., Gratzner, R., & Püttmann, W. (2012). Palaeoenvironmental conditions during deposition of the Upper Cretaceous oil shale sequences in the Songliao Basin (NE China): Implications from geochemical analysis. *Organic Geochemistry*, *46*, 76–95.
- Botz, R., Schmidt, M., Wehner, H., Hufnagel, H., & Stoffers, P. (2007). Organic-rich sediments in brine-filled Shaban- and Kebrüt deeps, northern Red Sea. *Chemical Geology*, *244*, 520–553.
- Carvajal-Ortiz, H., Mora, G., & Jaramillo, C. (2009). A molecular evaluation of bulk organic carbon-isotope chemostratigraphy for terrestrial correlations: An example from two Paleocene-Eocene tropical sequences. *Palaeogeography, Palaeoclimatology, Palaeoecology*, *277*, 173–183.
- Dean, W. E., Arthur, M. A., & Claypool, G. E. (1986). Depletion of  $^{13}\text{C}$  in Cretaceous marine organic matter: Source, diagenetic, or environmental signals? *Marine Geology*, *70*, 119–157.
- El-Kammar, M. M. (1987). *Stratigraphical and mineralogical studies on the black shale at Quseir area, Red Sea Coast, Egypt* (M. Sc. thesis) Faculty of Science, Cairo Uni., 157 pp.
- El-Kammar, M. M. (1993). *Organic and inorganic components of the Upper Cretaceous–lower tertiary black shales from Egypt and their hydrocarbon potentialities*. (Ph. D. thesis). Faculty of Science, Cairo Uni., 226 pp.
- Farquhar, G. D., Ehleringer, J. R., & Hubick, K. T. (1989). Carbon isotope discrimination and photosynthesis. *Annual Review of Plant Physiology and Plant Molecular Biology*, *40*, 503–537.
- Fathy, D., Wagreich, M., Gier, S., Mohamed, R. S. A., Zaki, R., & El Nady, M. M. (2018). Maastrichtian oil shale deposition on the southern Tethys margin, Egypt: Insights into greenhouse climate and paleoceanography. *Palaeogeography, Palaeoclimatology, Palaeoecology*, *505*, 18–32.
- Fathy, D., Wagreich, M., Zaki, R., Mohamed, R.S.A., & Gier, S. (2017). *Geochemical fingerprinting of Maastrichtian oil shales from the Central Eastern Desert, Egypt: Implications for provenance, tectonic setting, and source area weathering*. Wiley. <https://doi.org/10.1002/gj.3094>
- Galimov, E. M. (1999). The causes of the global variations of carbon isotopic composition in the biosphere. *Geochemistry International*, *37*, 699–713.
- Galimov, E. M. (2006). Isotope organic geochemistry. *Organic Geochemistry*, *37*, 1200–1262.
- Ghorab, M. A. (1956). A summary of a proposed rock stratigraphic classification of upper cretaceous rocks in Egypt. *Journal of Geological Society, Egypt*.
- Hassanein, A. M., Dardir, A. A., & Hewaidy A. A. (1993). Contribution to the stratigraphy of the upper cretaceous/lower tertiary succession in Wasif area, Eastern Desert, Egypt. *Annals of the Geological Survey of Egypt*, *19*, 181–206.
- Hayes, J. M., Takigiku, R., Ocampo, R., Callot, H. J., & Albrecht, P. (1987). Isotopic compositions and probable origins of organic molecules in the Eocene Messel Shale. *Nature*, *329*, 48–51.
- Hewaidy, A. (1979). *Stratigraphy of the cretaceous and lower tertiary rocks in Wasif area, Eastern Desert, Egypt* (M.Sc. Thesis). Al Azhar Uni., Cairo, 129 pp.
- Hoelke, J. D. (2011). *Chemostratigraphy and paleoceanography of the Mississippian Barnett formation, southern Fort Worth basin, Texas, USA* (M.Sc. thesis). Faculty of the Graduate School of The University of Texas at Arlington, 96 pp.
- Holail, H., Abd Alla, M., & El Dahhar, M. (1995). Mineralogical and geochemical evaluation of the Upper Cretaceous black shales, Safaga district, Egypt. *Qatar Uni. Science Journal*, *15*(1), 205–214.
- Holbourn, A., Kuhnt, W., El Albani, A., Pletsch, T., Luderer, F., & Wagner, T. (1999b). Upper Cretaceous palaeoenvironments and benthonic foraminiferal assemblages of potential source rocks from the western African margin, Central Atlantic. In N. R. Cameron, R. H. Bate, & V. S. Clure, (Eds.), *The oil and gas habitats of the South Atlantic* (Vol. 153, pp. 195–222). Geological Society, London, Special Publications.
- Immenhauser, A., Holmden, C., & Patterson, W. P. (2008). Interpreting the carbon-isotope record of ancient shallow epeiric seas: Lessons from the recent. In Pratt & Holmden (Eds.), *Dynamics of Epeiric seas*. Geological Association of Canada, Special paper V. 48.
- Inan, S., Ugur, F. A., Inan, T., Yalcin, M. N., & Mann, U. (2010). Relationship between organic matter, sulphur and phosphate contents in Upper Cretaceous marine carbonates (Karabogaz

- Formation, SE Turkey): Implications for early oil generation. *Journal of Petroleum Geology*, 34, 319–337.
- Jackson, K. S., Hawkins, P. J., & Bennett, A. J. R. (1985). Regional facies and geochemical evaluation of southern Denison Trough. *The APEA Journal*, 20, 143–158.
- Jarvis, I., Mabrouk, A., Moody, R. T. J., & de Cabrera, S. (2002). Late Cretaceous (Campanian) carbon isotope events, sea-level change and correlation of the Tethyan and Boreal realms. *Palaeogeography, Palaeoclimatology, Palaeoecology*, 188, 215–248.
- Khaled, K. A. (1997). On the nature of kerogen in oil shale beds of Safaga phosphate mines, Red Sea, Egypt. In *3rd Conference on Geochemistry, Alexandria, Egypt* (pp. 1–17).
- Klitzsch, E., Gröschke, M., & Hermann-Degen, W. (1990). Wadi Qena: Paleozoic and Pre-Campanian cretaceous strata. In R. Said (Ed.), *The geology of Egypt* (pp. 321–328). Balkema, Rotterdam, Netherlands.
- Lehmann, M. F., Bernasconi, S. M., Barbieri, A., & McKenzie, J. A. (2002). Preservation of organic matter and alteration of its carbon and nitrogen isotope composition during simulated and in situ early sedimentary diagenesis. *Geochimica Et Cosmochimica Acta*, 66 (20), 3573–3584.
- Macko, S. A., Engel, M. H., & Qian, Y. (1994). Early diagenesis and organic matter preservation—A molecular stable carbon isotope perspective. *Chemical Geology*, 114, 365–379.
- Makled, W. A., Mostafa, T. F., & Maky, A. F. (2014). Mechanism of Late Campanian-Early Maastrichtian oil shale deposition and its sequence stratigraphy implications inferred from the palynological and geochemical analysis. *Egyptian Journal of Petroleum*, 23, 427–444.
- Malak, E. K., Philobos, E. R., Abdou, I. K., & Ashry, M. M. (1977). Some petrographical, mineralogical and organic geochemical characteristics of black shales from Quseir and Safaga, Red Sea area, Egypt. *Desert Institute Bulletin, A.R.E.*, 27(1), 1–15.
- Maslin, M. A., & Swann, G. E. A. (2005). Isotopes in marine sediments. In M. J. Leng (Ed.), *Isotopes in paleoenvironmental research* (pp. 227–290). Springer, Dordrecht, Netherlands.
- Meyers, P. A. (1994). Preservation of elemental and isotopic source identification of sedimentary organic matter. *Chemical Geology*, 114, 289–302.
- Mustafa, A., & Ghaly, E. L. (1964). Survey of Quseir shales and other carbonaceous shales in Egypt. *Journal of Chemical & Engineering Data*, 9(4), 557–567.
- Obaidalla, N. A. (2000). Planktonic foraminiferal biostratigraphy and faunal turnover events during the Late Cretaceous-Early Tertiary along the Red Sea Coast, Egypt. *Journal of African Earth Sciences*, 31(3/4), 571–595.
- Rasmy, M., & Basily, A. B. (1983). Spectrographic study of trace elements in some Egyptian black shales associated with phosphate deposits. *Chemical Geology*, 39, 115–123.
- Robison, V. D., & Tröger, U. (1983). Geology and organic geochemistry of Dakhla Shale, Egypt. (Abstract), *American Association of Petroleum Geologist Bulletin*, 63(3), 542, Tulsa.
- Said, R. (1961). Tectonic framework of Egypt and its influence on distribution of foraminifera: American Association of Petroleum Geologist. *Bulletin*, 45, 198–218.
- Said, R. (1962). *The geology of Egypt* (337 pp). Elsevier Science Ltd., Rotterdam, Netherlands.
- Said, R. (1990). Red Sea coastal plain. In R. Said (Ed.), *The geology of Egypt* (pp. 345–359). Balkema.
- Saltzman, M. R., & Thomas, E. (2012). Carbon isotope stratigraphy. In F. M. Gradstein, J. G. Ogg, M. D. Schmitz, & G. M. Ogg, (Eds.), *The geologic time scale* (Vol. 2, pp. 207–232). Elsevier.
- Schneider-Mor, A., Alsenz, H., Ashckenazi-Polivoda, S., Illner, P., Abramovich, S., Feinstein, S., Almogi-Labin, A., Berner, Z., & Püttmann, W. (2012). Paleooceanographic reconstruction of the late Cretaceous oil shale of the Negev, Israel: Integration of geochemical, and stable isotope records of the organic matter. *Palaeogeography, Palaeoclimatology, Palaeoecology*, 319–320, 46–57.
- Schrank, E. (1984). Organic geochemical and palynological studies of a Dakhla Shale (Late Cretaceous) in Southeast Egypt—Part A: succession of microfloras and depositional environment. *Berliner Geowissenschaftliche Abhandlungen*, 50, 189–207.
- Schrank, E. (1987). Paleozoic and Mesozoic palynomorphs from Northeast Africa (Egypt and Sudan) with special reference to Late Cretaceous pollen and dinoflagellates. *Berliner Geowissenschaftliche Abhandlungen*, 75(1), 249–310.
- Schrank, E., & Perch-Nielsen, K. (1985). Late Cretaceous palynostratigraphy in Egypt with comments on Maastrichtian and Early Tertiary calcareous nannofossils. *Newsletter on Stratigraphy*, 15(2), 81–99.
- Tiwari, M., Singh, A. K., & Sinha, D. K. (2015). Stable isotopes: Tools for understanding past climate conditions and their applications in chemostratigraphy. In M. Ramkumar (Ed.), *Chemostratigraphy concepts, techniques and applications* (pp. 65–92). Elsevier.
- Tyson, R. V. (1995). *Sedimentary organic matter: Organic facies and palynofacies* (pp. 395–415). Springer-Science and Business Media, B.v.
- Wagner, T., & Herrle, J. O. (2014). *C-Isotopes* (pp. 1–8). Springer.
- Wang, X. Q., Shi, X. Y., Jiang, G. Q., & Tang, D. J. (2014). Organic carbon isotope gradient and ocean stratification across the late Ediacaran-Early Cambrian Yangtze Platform. *Science China Earth Sciences*, 57(5), 919–929.
- Waples, D. W. (1985). *Geochemistry in petroleum exploration* (232 p). Boston International Human Resources Development Corporation.
- Westerhausen, L., Poynter, J., Eglinton, G., Erlenkeuser, H., & Sarnthein, M. (1993). Marine and terrigenous origin of organic matter in modern sediments of equatorial East Africa: The  $\delta^{13}\text{C}$  and molecular record. *Deep-Sea Research*, 40, 1087–1121.
- Werne, J. P., & Hollander, D. J. (2004). Balancing supply and demand: Controls on carbon isotope fractionation in the Cariaco Basin (Venezuela) Younger Dryas to present. *Marine Chemistry*, 92, 275–293.
- Youssef, M. I. (1957). Upper Cretaceous rocks in Kosseir area. *Bulletin Institute Desert Egypt*, 7(2), 35–53.